

The Tectonics and Mineralisation of the  
Black Angel Pb-Zn Deposits, Central West Greenland.

A thesis submitted in fulfilment of  
the requirements for a degree of Ph.D.  
of the University of London.

by

Andrew John Carmichael BSc. (Hons.).

Department of Earth Sciences,  
Goldsmiths' College,  
University of London.

June 1988.

# IMAGING SERVICES NORTH

Boston Spa, Wetherby

West Yorkshire, LS23 7BQ

[www.bl.uk](http://www.bl.uk)

**CONTAINS MAPS.**

## IMAGING SERVICES NORTH

Boston Spa, Wetherby  
West Yorkshire, LS23 7BQ  
[www.bl.uk](http://www.bl.uk)

CONTAINS  
PULLOUTS

## LIST OF CONTENTS

	Page Number
List of Contents	(ii)
List of Figures	(iix)
List of Tables	(xvi)
Abstract.	1
Chapter 1 Introduction to the Marmorilik area	2
1.1 Introduction	2
1.2 Aims of the thesis	4
1.3 Methodology	4
1.4 Previous work	7
1.5 Thesis structure	9
1.6 Acknowledgements.	10
Chapter 2 Regional geology of the Rinkian mobile belt	11
2.1 Introduction	11
2.2 Tectono-stratigraphy of the Rinkian mobile belt	15
2.2.1 Archean Umanak Gneiss Complex	15
2.2.2 Karrat Group Supracrustals	17
2.2.2i Qeqertarsuaq Formation	17
2.2.2ii Marmorilik Formation	19
2.2.2iii Kangidleq Formation	21
2.2.2iv Nukavsak Formation	21
2.2.3 Igneous complexes	23
2.3 Structure and metamorphism of the Rinkian mobile belt	24
2.3.1 Introduction	24
2.3.2 Basement gneiss tracts	24
2.3.3 Basement gneisses and supracrustals	25
2.3.4 Metamorphism	28
2.4 Mineralisation in the Rinkian mobile belt	28
2.4.1 Meta-clastic hosted mineralisation	29

## LIST OF CONTENTS

	Page Number
List of Contents	(ii)
List of Figures	(iix)
List of Tables	(xvi)
Abstract.	1
Chapter 1 Introduction to the Marmorilik area	2
1.1 Introduction	2
1.2 Aims of the thesis	4
1.3 Methodology	4
1.4 Previous work	7
1.5 Thesis structure	9
1.6 Acknowledgements.	10
Chapter 2 Regional geology of the Rinkian mobile belt	11
2.1 Introduction	11
2.2 Tectono-stratigraphy of the Rinkian mobile belt	15
2.2.1 Archean Umanak Gneiss Complex	15
2.2.2 Karrat Group Supracrustals	17
2.2.2i Qeqertarssuaq Formation	17
2.2.2ii Marmorilik Formation	19
2.2.2iii Kangidleq Formation	21
2.2.2iv Nukavsak Formation	21
2.2.3 Igneous complexes	23
2.3 Structure and metamorphism of the Rinkian mobile belt	24
2.3.1 Introduction	24
2.3.2 Basement gneiss tracts	24
2.3.3 Basement gneisses and supracrustals	25
2.3.4 Metamorphism	28
2.4 Mineralisation in the Rinkian mobile belt	28
2.4.1 Meta-clastic hosted mineralisation	29

	Page Number	
4.4.3	En-écheleon folds	112
4.4.4	Sinistral shear zones	113
4.5	D4 Late Extension Phase Deformation.	114
4.6	Tectonic evolution of the Marmorilik area	126
4.6.1	D1 Early Recumbent Phase Deformation	126
4.6.2	D2 South Verging Fold and Fault Phase Deformation	126
4.6.3	D3 Sinistral Shear Phase Deformation	127
<b>Chapter 5</b>	<b>Metamorphism of the Marmorilik area</b>	<b>132</b>
5.1	Introduction	132
5.2	Basement gneiss metamorphism	133
5.3	Karrat Group metamorphism	133
5.3.1	Field relationships and mineral assemblages	133
5.4	Mineral compositions	145
5.5	Metamorphic grade and P/T regimes	145
5.6	Primary sediment chemistry	154
<b>Chapter 6</b>	<b>Mineralisation of the Black Angel deposits and the Marmorilik area</b>	<b>156</b>
6.1	Introduction.	156
6.2	(Della Valle)-Myers-SLGL-Ark-Garde	159
6.3	Nunngarut deposit	160
6.3.1	Introduction	160
6.3.2	The Nunngarut orebody: Form and structure	160
6.4	Uvkussigsat and MP 5 zone	161
6.5	Black Angel deposits	169
6.5.1	Introduction	169
6.5.2	Previous mine work	169
6.5.3	The Black Angel ore zones	170

	Page Number
6.5.4 Mine stratigraphy	170
6.5.4 a Introduction	170
6.5.4 b Stratigraphic location of the ore zones	171
6.5.4 c Hangingwall & Footwall stratigraphic variation	173
6.5.5 Mine structure	179
6.5.6 Ore petrology	190
6.5.6 a Introduction	190
6.5.6 b Ore facies	193
Banded ore facies	193
Porphyroclastic ore facies	193
Recrystallised ore facies	199
Massive pyritic ore facies	201
Primary textures	202
6.5.6 c Ore facies distribution	237
6.5.6 d Ore stratigraphy	239
6.5.7 Geochemistry of the ore horizon	244
6.5.7 a Introduction	244
6.5.7 b Metal distribution patterns	245
6.5.7 c Mineral chemistry	253
 Chapter 7	
Lead isotope analysis of the Black Angel deposits and mineralisation of the Marmorilik area	258
7.1 Introduction	258
7.2 Methods of study	258
7.3 Results	260
7.4 Model age dates	263
7.5 Discussion	266
7.5.1 Lead source	266
7.5.2 Comparative studies	269
7.6 Conclusions	273

	Page Number
Chapter 8	
Stable isotope study of the Black Angel deposits and host rocks	274
8.1	274
8.2	275
8.3	275
8.3.1	275
8.3.2	281
8.3.3	283
8.4	284
8.5	287
8.5.1	287
8.5.2	288
8.5.2 a	288
8.5.2 b	293
8.6	297
Chapter 9.	298
9.1	298
9.2	298
9.2.1	298
9.2.2	309
9.3	312
9.3.1	312
9.3.2	315
9.3.3	324
9.4	326
9.4.1	326

	Page Number
9.4.2 A comparison of the Black Angel deposits with carbonate-hosted deposits	326
9.4.3 Models of ore genesis	333
9.4.4 Alternative models of ore genesis	338
9.5 Exploration potential in the Marmorilik area	341
9.5.1 Regional exploration potential	341
9.5.2 Local exploration potential	341
Chapter 10 Conclusions	344
10.1 Introduction	344
10.2 Tectono-stratigraphy	344
10.3 Tectonic evolution	344
10.4 Metamorphism	346
10.5 Mineralisation	346
10.6 Exploration potential	349
Appendix 1 Lead isotope preparation	351
Appendix 2 Stable isotope preparation	353
Appendix 3 Etch techniques	355
References	356

## LIST OF FIGURES

Chapter 1	Page Number
Figure 1.1 Geological setting of the Marmorilik in the Rinkian Mobile Belt	3
Figure 1.2 Oblique air photographs illustrating the topography and exposure in the Marmorilik area	6
Figure 1.3 Geological location map of the study area	8
Chapter 2	
Figure 2.1 Correlation of the Rinkian Mobile Belt into Canada	12
Figure 2.2 Simplified stratigraphic column for the units in the Rinkian Mobile Belt	13
Figure 2.3 Tectono-stratigraphic correlation through the Rinkian and Nagssugtoqidian Mobile Belts	14
Figure 2.4 Geological map of the Rinkian Mobile Belt	16
Figure 2.5 Simplified reconstruction of the sedimentological setting of the Karrat Group	18
Figure 2.6 Ternary diagrams of analyses from the Kangidleq Formation volcanics	20
Figure 2.7 Geological map of the Talorssuit dome and the Ata granite	22
Figure 2.8 Geological map of the Marmorilik-Rinks Isbrae district.	26
Figure 2.9 Simplified structural cross-sections through the Marmorilik-Rinks Isbrae district.	27
Figure 2.10 Palaeogeographical setting of the Rinkian Mobile Belt in the Proterozoic supercontinent.	30
Figure 2.11 Polar wandering curves for the Laurentian shield for the period 2000-1750 Ma.	30

Chapter 3	Page number
Figure 3.1a Simplified Lithological map of Marmorilik area	33
Figure 3.1b 1:20 000 lithological map of the Marmorilik area	back pocket
Figure 3.2 Simplified tectono-stratigraphic column for the Karrat Group of the Marmorilik area	34
Figure 3.3 Previous classifications of the Karrat Group stratigraphy in the Marmorilik area	36
Figure 3.4 Lithologies of the Umanak Gneiss Complex	38
Figure 3.5 Internal tectono-stratigraphic correlation of the Marmorilik Formation	41
Figure 3.6 Stratigraphic sections through the Qeqertarsuaq Formation	42
Figure 3.7a Lithologies of the Qeqertarsuaq Formation and the Lower Marmorilik Formation (Unit 1)	45
Figure 3.7b Tectono-stratigraphic column through Unit 1	48
Figure 3.8i Tectono-stratigraphic column through Unit 2	48
Figure 3.8 Lithologies of the Lower Marmorilik Formation (Unit 2) massive dolomitic marbles	50
Figure 3.9 Lithologies of the Middle Marmorilik Formation (Unit 3) graphitic calc/dolomites	53
Figure 3.10 Lithologies of the Upper Marmorilik Formation (Unit 4) Coarse calcitic marbles	56
Figure 3.11 Lithologies of the Upper Marmorilik Formation (Units 5 & 6) and the Nukavask Formation	59
 Chapter 4	
Figure 4.1a 1:20000 tectonic map of the Marmorilik area	back pocket
" 4.1b&c Cross-sections through the Marmorilik area	62
Figure 4.2 A tectonic map of D1 deformation structures.	70
Figure 4.3 A map of the study and D1 homogeneous sub-areas	71

	Page number
Figure 4.4 Tectono-metamorphic packages of the southerly basement/supracrustal contact	72
Figure 4.5 D1 basement structures	74
Figure 4.6 Line drawing of a D1 extensional fault system	76
Figure 4.7 Simplified tectonic map of the south-east Little South Lake	77
Figure 4.8 D1 extensional structures	79
Figure 4.9 D1 folds and associated structures	81
Figure 4.10 Geological map of the 1085 Peak	82
Figure 4.11 Cross-section through the 1085 Peak	83
Figure 4.12 Deformation structures observed on the 1085 Peak	84
Figure 4.13 Geological map and cross-section of the (Nunnarsugssuaq) Uvkusigssat Peninsula	85
Figure 4.14 Structural interpretation of the Black Angel nappe	87
Figure 4.15 Dip isogon analysis of D1 folds	88
Figure 4.16 t plots of D1 folds	89
Figure 4.17 D1 stereographic data	90
Figure 4.18 Geological map of the Magdlak Peninsula	92
Figure 4.19 A tectonic map of D2 deformation structures	97
Figure 4.20 Tributary fold	99
Figure 4.21 D2 deformation fold structures	101
Figure 4.22a Dip isogon analysis	102
Figure 4.22b t plots of D2 folds	103
Figure 4.23 D2 foliations.	105
Figure 4.24 A structural interpretation of the Fishing Lakes cliffwall	107
Figure 4.25 D2 deformation stereographic data	108
Figure 4.26 D2 tectonic slide systems and the D3 Tributary-Nunngarut Fault	110

	Page Number
Figure 4.27 A tectonic map of D3 deformation structures	115
Figure 4.28 A 3D image of D3 deformation structures	116
Figure 4.29 D3 folds and associated shear faults	118
Figure 4.30 D3 deformation structures	120
Figure 4.31 D3 shear fault system	122
Figure 4.32 D3 microfaults and joints	124
Figure 4.33 Summary stereogram of D3 structures	125
Figure 4.34 Tectonic evolution of the Marmorilik area	129
Figure 4.35 Uplift and basin formation in shear zones	130
Figure 4.36 Sequential development of structures in a shear zone	131
<b>Chapter 5</b>	
Figure 5.1 AFM diagram for mineral assemblages in the Marmorilik Formation carbonates	134
Figure 5.2 Tremolite microtextures	137
Figure 5.3 Phlogopite and scapolite microtextures	140
Figure 5.4 Graphite and baryte microtextures	143
Figure 5.5 AFM diagram for mineral assemblages in the metapelites of the Marmorilik Formation	144
Figure 5.6 Chemical composition diagrams of tremolite and phlogopite	146
Figure 5.7 Isobaric Pf-T-Xco <sub>2</sub> diagram for reactions in siliceous dolomite marbles	146
Figure 5.8 Isobaric T-Xco <sub>2</sub> diagram at 2 kb. pressure for reactions in siliceous dolomite marbles	148
Figure 5.9 Isobaric T-Xco <sub>2</sub> diagram at 5 kb. pressure for reactions in siliceous dolomite marbles	148
Figure 5.10 Stabilities of phases as a function of fs <sub>2</sub> and fo <sub>2</sub> and 6kb in the system C-O-S-Ca-Ti-Fe	150

	Page Number
Figure 4.27 A tectonic map of D3 deformation structures	115
Figure 4.28 A 3D image of D3 deformation structures	116
Figure 4.29 D3 folds and associated shear faults	118
Figure 4.30 D3 deformation structures	120
Figure 4.31 D3 shear fault system	122
Figure 4.32 D3 microfaults and joints	124
Figure 4.33 Summary stereogram of D3 structures	125
Figure 4.34 Tectonic evolution of the Marmorilik area	129
Figure 4.35 Uplift and basin formation in shear zones	130
Figure 4.36 Sequential development of structures in a shear zone	131
 Chapter 5	
Figure 5.1 AFM diagram for mineral assemblages in the Marmorilik Formation carbonates	134
Figure 5.2 Tremolite microtextures	137
Figure 5.3 Phlogopite and scapolite microtextures	140
Figure 5.4 Graphite and baryte microtextures	143
Figure 5.5 AFM diagram for mineral assemblages in the metapelites of the Marmorilik Formation	144
Figure 5.6 Chemical composition diagrams of tremolite and phlogopite	146
Figure 5.7 Isobaric Pf-T-Xco <sub>2</sub> diagram for reactions in siliceous dolomite marbles	146
Figure 5.8 Isobaric T-Xco <sub>2</sub> diagram at 2 kb. pressure for reactions in siliceous dolomite marbles	148
Figure 5.9 Isobaric T-Xco <sub>2</sub> diagram at 5 kb. pressure for reactions in siliceous dolomite marbles	148
Figure 5.10 Stabilities of phases as a function of fs <sub>2</sub> and fo <sub>2</sub> and 6kb in the system C-O-S-Ca-Ti-Fe	150

	Page Number
Figure 5.12 Mole % FeS in sphalerite	151
Figure 5.13 Calibration curves of mole % FeS in sphalerite vs pressure	151
 Chapter 6	
Figure 6.1 Map of mineralised zones in the Marmorilik area	157
Figure 6.2 Stratigraphic setting of mineralised zones	158
Figure 6.3 Stratigraphic setting of the Myers-Ark zone	162
Figure 6.4 Stratigraphic and tectonic setting of mineralisation in the Lower Marmorilik Formation	163
Figure 6.5 Schematic representation of tectonic setting of the Ark mineralised zone	164
Figure 6.6 Cross-section through the Myers mineralised zone	165
Figure 6.7 Geological map of the Nunngarut deposit	166
Figure 6.8a Cross-section through the west Nunngarut zone	167
Figure 6.8b Cross-section through the east Nunngarut zone	167
Figure 6.9 Detailed section through the Nunngarut deposit	168
Figure 6.10 Tectono-stratigraphic setting of the Black Angel deposits	175
Figure 6.11 Isometric section of the Black Angel deposits	176
Figure 6.12 Hangingwall lithological map	177
Figure 6.13 Footwall lithological map	178
Figure 6.14 I zone ore horizon contacts	183
Figure 6.15 Tectonic map of the Black Angel deposit	184
Figure 6.16 Geological map of the Black Angel deposits' haulage level	back pocket
Figure 6.17 Detailed mine cross-sections	back pocket
Figure 6.18 North verging D1 nappe structures	186
Figure 6.19 Isoclinal F1 folds in the K area, Cover zone	187
Figure 6.20 Stope wall cross-sections	188

	Page Number
Figure 6.21 Simplified sections along KI and CB II ramps	189
Figure 6.22 Ore facies distribution map	204
Figure 6.23 Layered ore tectonite textures	206
Figure 6.24 Pyrite microtextures	208
Figure 6.25 Porphyroclastic ore facies	210
Figure 6.26 Breccia-textured ore tectonite	212
Figure 6.27 Breccia-textured ore in Stope L66, Cover zone	213
Figure 6.28 Breccia-textured and Buckshot ore microtextures	215
Figure 6.29 Micaceous fabrics in massive ore	216
Figure 6.30 Sketch of foliated pyrrhotite ore	217
Figure 6.31 Pyrrhotite microtextures	219
Figure 6.32 Pyrite/pyrrhotite microtextural relationships	221
Figure 6.33 Field relationships and microtextures of tectonites from the porphyroclastic ore facies	223
Figure 6.34 Recrystallised ore facies	225
Figure 6.35 Microtextures of tennantite-rich ore	227
Figure 6.36 Arsenopyrite microtextures	229
Figure 6.37 Sheared galena microtextures	231
Figure 6.38 Detailed mapping of Stope I 170, I zone	232
Figure 6.39 Foam textured ore tectonite	234
Figure 6.40 Primary microtextures	236
Figure 6.41 Ore thickness variation map	241
Figure 6.42 Ore stratigraphy of the Angel and Cover zones	242
Figure 6.43 Fence diagram of Tributary zone ore stratigraphy	243
Figure 6.44 Zn metal concentration map	246
Figure 6.45 Pb metal concentration map	247
Figure 6.46 Fe metal concentration map	248
Figure 6.47 Zn x ore thickness concentration map	250
Figure 6.48 Pb x ore thickness concentration map	251
Figure 6.49 Zn / Zn + Pb concentration map	252

	Page Number	
Figure 7.1	Map of lead isotope sample locations	259
Figure 7.2	Distribution patterns of lead isotope analyses	262
Figure 7.3	Stacey and Kramers growth curve	264
Figure 7.4	Cumming and Richards growth curve	264
Figure 7.5	Black Angel lead isotope data plotted on a Plumbotectonics plot	267
Figure 7.6	Lead isotope compositions from the Navan deposit	270
Figure 7.7	Comparison of lead isotope compositions from carbonate-hosted ore deposits	270
Figure 7.8	Lead isotope compositions on galena from the Balmat-Edwards deposits	271
 Chapter 8		
Figure 8.1	Stratigraphic Variation of $\delta^{34}\text{S}$ , $\delta^{13}\text{C}_{\text{gr}}$ , $\delta^{13}\text{C}_{\text{c}}$ and $\delta^{18}\text{O}_{\text{c}}$ through the Marmorilik Formation	278
Figure 8.2	Sulphur isotopic compositions from the Black Angel deposits and surrounding mineralisation	279
Figure 8.3	Equilibrium isotopic fractionation factors among carbon compounds relative to $\text{H}_2\text{CO}_3(\text{ap})$ .	280
Figure 8.4	Equilibrium isotopic fractionation factors among sulphur compounds relative to $\text{H}_2\text{S}$ .	285
Figure 8.5	Temperature curves for the fractionation of sphalerite and galena	286
Figure 8.6a	Schematic presentation of sulphur isotopic data of some Mississippi Valley-type deposits	290
Figure 8.6b	Sulphur isotope distributions of M.V.T ores compared with other sulphur bearing environments	290
Figure 8.7	Sulphur isotope distributions for the Irish deposits	291

	Page Number
Figure 8.8 Sulphur isotope distributions carbonate and shale-hosted deposits	292
Figure 8.9 Distribution pattern for $\delta^{34}\text{S}$ values of $\text{H}_2\text{S}$ and sulphide minerals when sulphate of $\delta^{34}\text{S} = +20\%$ is reduced by various mechanisms	294
Figure 8.10 Plot of $\delta^{34}\text{S}$ against $^{206}\text{Pb} / ^{204}\text{Pb}$ for galena and pyrite from the Black Angel deposits	295
 Chapter 9	
Figure 9.1 Tectonic models for gneiss dome formation	300
Figure 9.2 Rotation of compressional structures by backthrusts	302
Figure 9.3 Strain patterns developed in diapiric models	303
Figure 9.4 Summary of models of lithospheric extension	306
Figure 9.5 Initiation of a warped detachment fault	307
Figure 9.6 Deformation predicted through continent-continent collision of the Ketilidian and Archean blocks	307
Figure 9.7 Orientation of the southern basement/supracrustal margin between Marmorilik and the Nunarssussuaq	310
Figure 9.9 Core-mantle microtextures	320
Figure 9.10 Pyrrhotite ductility with respect to other sulphides	322
Figure 9.11 Geological setting of Irish and MVT deposits	330
Figure 9.12 Deposits of the McArthur River Basin	335
Figure 9.13 Model of ore genesis for the Black Angel deposits	337
Figure 9.14 Convective cell model	338

## List of Tables

		Page Number
Table 4.1	Deformation events in the Marmorilik area	64
Table 4.2	Summary of the stereographic data from the Marmorilik area	91
Table 5.1a	Microprobe analyses of pyrite encapsulated sphalerite from the Black Angel deposits.	152
Table 5.1b	Microprobe analyses of matrix sphalerite from the Black Angel deposits	152
Table 6.1	Mineralised zones in the Marmorilik area	159a
Table 6.2	Mineralised zones in the Black Angel deposits	169a
Table 6.3	Summary of the mineralogy and textures in the ore facies of the Black Angel deposits	191
Table 6.4	Summary of mineral and ore facies formation w.r.t. deformation events in the Marmorilik area	192
Table 6.5	Microprobe analyses of pyrite from the Black Angel and Nunngarut deposits	254
Table 6.6	Microprobe analyses of arsenopyrite from the Black Angel deposits	254
Table 6.7	Microprobe analyses of tennantite from the Black Angel deposits	256
Table 6.8	Microprobe analyses of pyrrhotite from the Black Angel and Nunngarut deposits	256
Table 7.1	Lead isotope analyses from the Black Angel deposits and surrounding mineralisation	261
Table 8.1a	Carbon and Oxygen isotope analyses from carbonates of the Marmorilik Formation	276
Table 8.1b	Sulphur isotope analyses from the Black Angel deposits and host rocks	276
Table 8.1c	Oxygen isotope analyses from unmetamorphosed and metamorphosed carbonates	277

		Page Number
Table 8.2	Equilibrium isotopic fractionation factors of carbon compounds with respect to CO <sub>2</sub>	280
Table 8.3	Equilibrium isotopic fractionation factors of sulphur compounds with respect to H <sub>2</sub> S	285
Table 9.1	Features of basement massifs as compared with possible mechanisms of formation	299
Table 9.2	Metamorphism of sulphides-a summary	313
Table 9.3	Synopsis of the physical properties of sulphides	316
Table 9.4	Summary of the deformation mechanisms and microstructures formed during ductile deformation	317
Table 9.5	Microstructures developed in the Black Angel sulphides during the tectonic evolution of the Marmorilik area.	319
Table 9.6	Comparative features of carbonate-hosted Pb-Zn deposits	327
Table 9.7	Metal concentrations of potential source rocks	334

## Abstract

The 13.5 M Tonne Black Angel Zn-Pb-Ag-Fe deposit at Marmorilik, West Greenland (71° 10' N, 51° 45' W) consists of six massive, stratabound to discordant sulphide lenses hosted in poly-deformed, poly-metamorphosed evaporite bearing carbonates of the Early Proterozoic Upper Marmorilik Formation. This study is an analysis of the tectonics and mineralisation of the orebodies. The research programme involved detailed and regional structural and stratigraphic mapping, section measuring, extensive underground mapping and sampling, logging of drill cores, detailed mineralogical and textural studies, and stable and lead isotopic analyses.

The deposits occur within the Karrat Group supracrustal sequence of the Mid-Proterozoic (1860 - 1680 ma.) Rinkian mobile belt, an upper greenschist to granulite facies terrain composed of Archean and Early Proterozoic tectono-stratigraphic units. Four deformation phases have been recognised within the supracrustals of the Marmorilik and Nukavsek Formations. Three penetrative phases have been assigned to the polyphase Rinkian event and are namely, D1 - an early recumbent nappe phase, D2 - a south verging fold and slide phase and D3 - a sinistral shear event. Peak metamorphic conditions of upper greenschist facies in the mine area were attained after this deformation, which was succeeded by an extensional D4 deformation (Late Precambrian) associated with dolerite dyke intrusion.

The mineralisation occurs as folded and boudinaged massive sulphide lenses within a narrow, highly deformed, east-west trending mineralised corridor in the Marmorilik Formation carbonates. The ores consist of tectonised, metamorphosed and recrystallised medium to coarse grained sphalerite, galena, pyrite, pyrrhotite and chalcopyrite with subordinate tennantite and arsenopyrite. Primary void-fill (marcasite/early pyrite) textures occur in metamorphic pyrite grains. Intense shearing at the ore/host rock contacts has produced discordant relationships and the inclusion of rafted calcitic marble and pelitic clasts, quartz eyes, and fluorite vein fragments within the sulphides. Ten types of ore tectonites have been recognised and these have been classified, according to their mineralogy and texture, into four distinct ore facies associations. The ore facies associations are related to particular deformation structures. Those belonging to D1 and D3 are the most significant. D1 produced large ENE-WNW trending recumbent overfolds and thickening of the ore lenses and D3 gave rise to ESE-WNW trending periclinal folds with substantial ore thickening and remobilisation in the fold hinge regions.

Lead isotope analyses on galenas from the deposits and surrounding carbonate hosted mineralisation indicate strongly homogenised 'orogene' to upper crustal leads. Minor changes in the ore lead source are possibly indicated by a bimodal distribution of the data. Stable carbon, oxygen and sulphur isotope analyses on the sulphides and carbonate host material gave homogenised results indicative of a strong metamorphic overprint. S-isotope geothermometry on sphalerite-galena pairs gives a temperature of 470° C for the D3 deformation.

The geological setting, mineralogical associations and primary textural features of the Black Angel deposits indicates that they were probably formed as stratabound Mississippi Valley Type massive sulphide ores which were subsequently highly deformed and metamorphosed such that the primary depositional, textural and isotopic signatures are no longer preserved.

## **CHAPTER 1**

### **1.1 Introduction**

This thesis is an analysis of the tectonics and mineralisation of the 13.5 M Tonne Black Angel Zn-Pb-Ag-Fe deposit, Marmorilik, West Greenland (71° 10' N, 51° 45' W) (Fig. 1.1). The orebodies are massive, stratabound to discordant sulphide lenses hosted by poly-deformed, poly-metamorphosed evaporite-bearing carbonates of the Early Proterozoic Upper Marmorilik Formation of the Rinkian Mobile Belt (Fig. 1.1).

The deposits were first discovered by N. A. Anderson in 1938, who found sulphide boulders at the base of the Black Angel Mountain (Fig. 1.2 b) and correlated these occurrences with a rusty weathering horizon set high up in the Black Angel cliffwall (Fig. 1.2 b). In 1966 Cominco Ltd. took up an exploration license on the Marmorilik area and later an exploitation license after 6 exploration drill holes had defined the high grade economic Angel ore zone. Production work in the mine started in 1974, under the control of Greenex A/S, with the ore being crushed on site in the purpose built mining township of Marmorilik (Fig. 1.2a). In 1986 Boliden AB and the Danish Government took over the running of the mine after Cominco Ltd / Greenex A/S ran into financial difficulties due to a major drop in world zinc and lead prices.

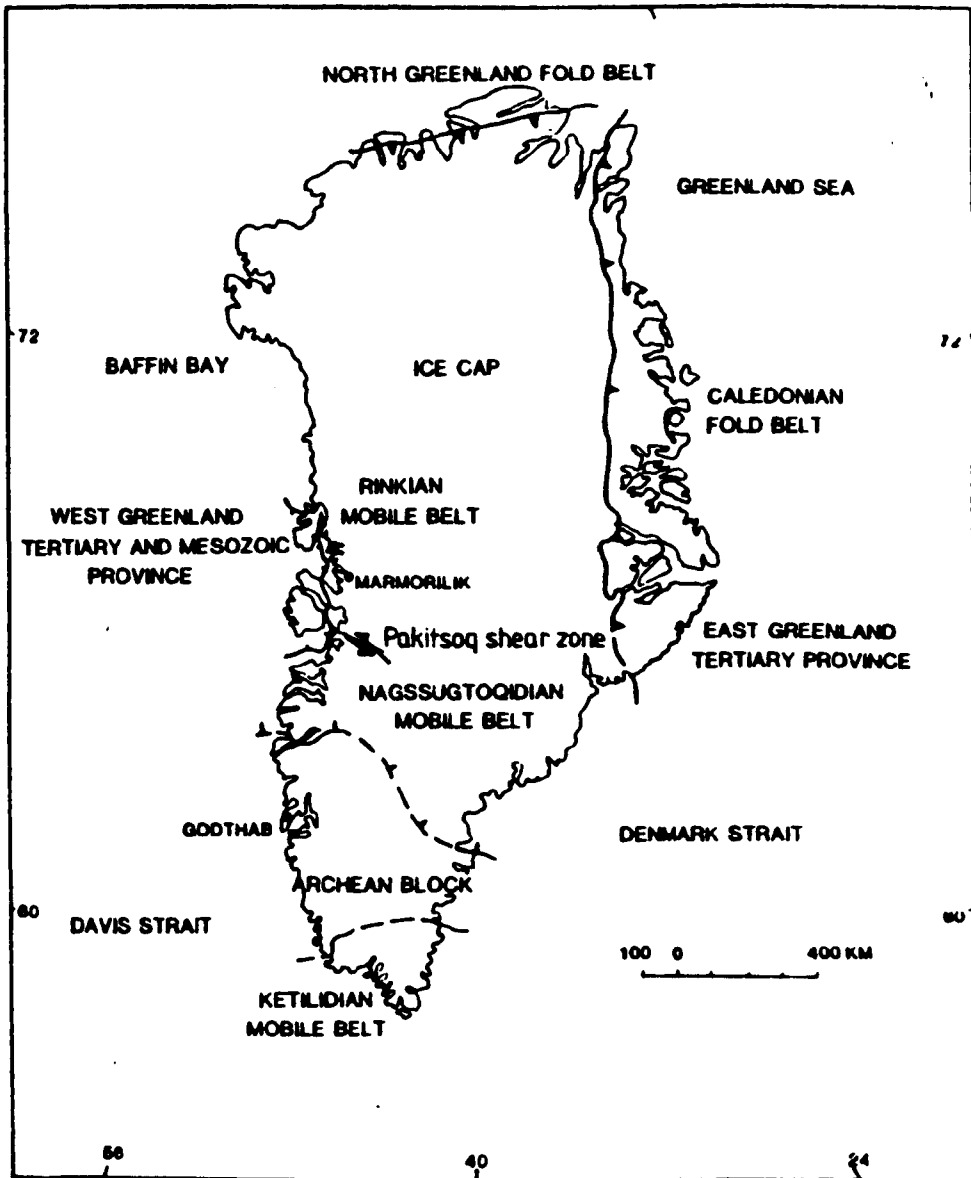


**Figure 1.1** Geological setting of Marmorilik in the Rinkian Mobile Belt

## 1.2 Aims of the Thesis.

This thesis aims to establish:-

- i) the structural setting and tectonic evolution of the Black Angel deposits, both in terms of the local structure and regional tectonics.
- ii) the effects of tectonism on the sulphide deposits and host rocks and in particular the relationships between structure and the distribution of ore grades, thicknesses, mineralogy and textures.
- iii) a genetic model for the formation of the ore deposits.
- iv) a geological basis<sup>for</sup> the potential for further exploration both in the vicinity of the known pre-existing deposits and also regionally in hither to unexplored parts of the Rinkian mobile belt.

## 1.3 Methodology.

The research programme involved detailed and regional structural and stratigraphic mapping, section measuring, extensive underground mapping and sampling, logging of drill cores, detailed mineralogical and textural studies, and stable and lead isotopic analyses.

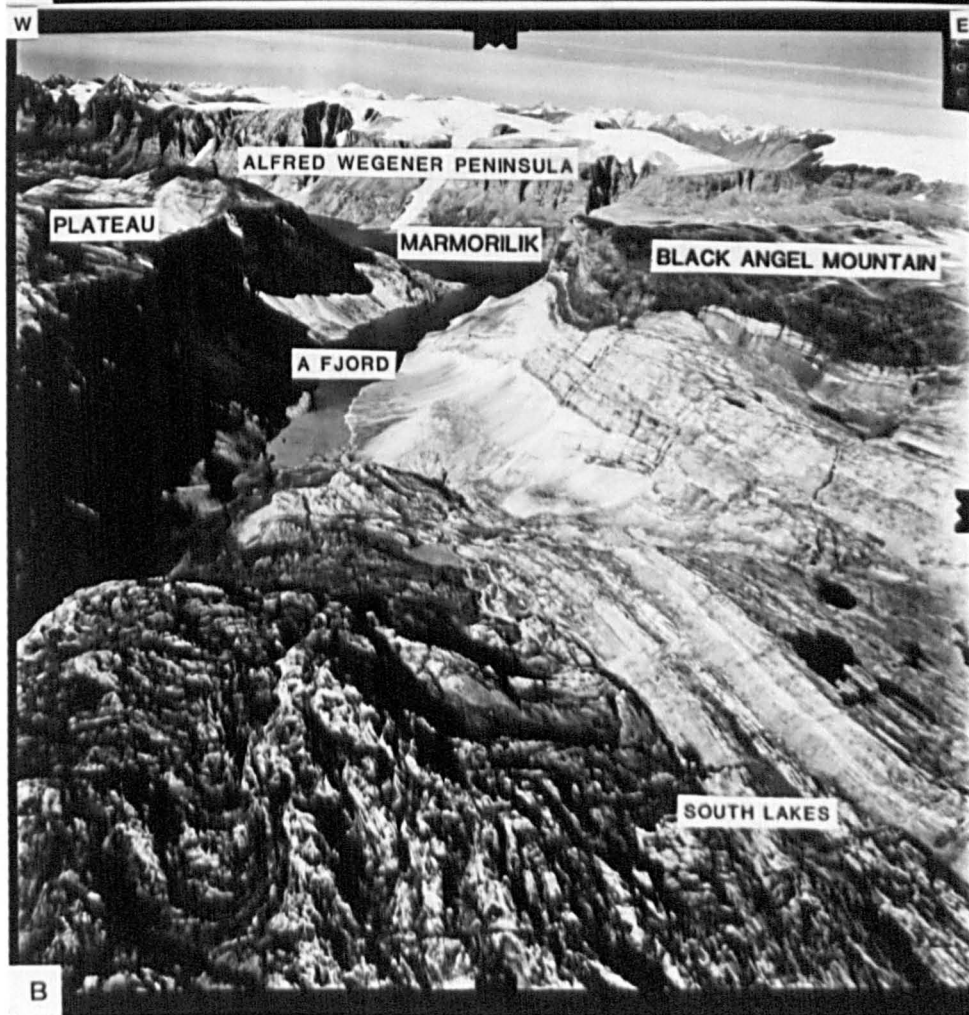
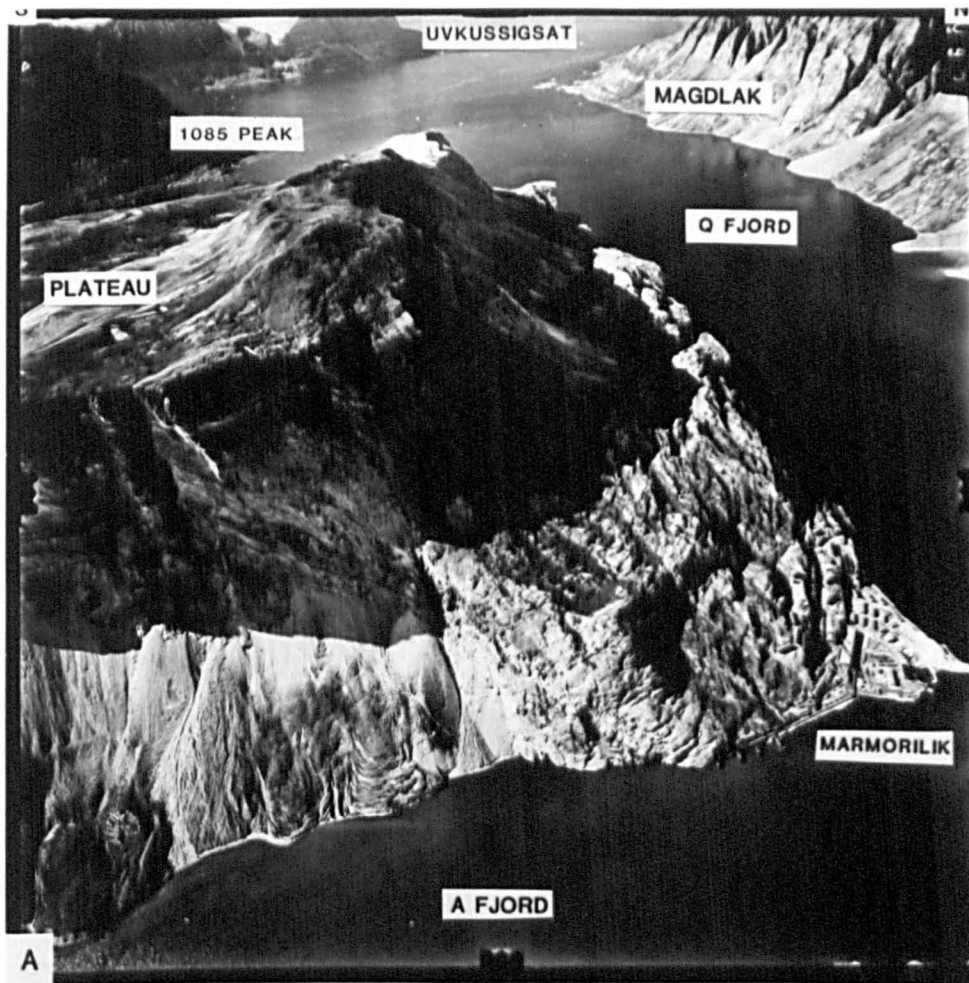
Four separate periods of field work, totalling nine months in all, were carried out in the Marmorilik region between July 1984 and November 1985. Surface mapping was carried out over a 90 km<sup>2</sup> of the Marmorilik area and two isolated areas to the west of Marmorilik around the Peak 1085 and the Magdlak Peninsula (Fig 1.3). The mapping was on scales of 1:5000, 1:10000 and 1:20000 using maps and aerial photographs produced by the Geodetic survey, Copenhagen, Denmark.

The field area is rugged and dominated by the Black Angel and Marmorilik mountain plateaux, which lie at an elevation of between 600-1100 metres (Fig. 1.2 a & b). The plateaux are split by the Agfardlikavsa fjord and bounded to the north by the Quamarajuk fjord. Precipitous cliffwalls occur along both of these fjords. Surface mapping, by traverse from drill camps, was restricted to the mountain plateaux and the more accessible lower lying regions of the South Lakes area which are

## Figure 1.2

A) An oblique aerial photograph showing the rugged precipitous topography of the western half of the Marmorilik area. The Agfardlikavsa fjord and Marmorilik Plateau (height 940 m) are in the foreground. Reconnaissance mapping trips were made to the 1085 Peak and the Magdlak peninsula. Uvkussigsat (Nunnarsugsuaq) is 25 km. away.

B) An oblique aerial photograph taken from the well exposed South Lakes areas, looking northwards along the Agfardlikavsa fjord towards Marmorilik and the high pinnacle peaks of the Alfred Wegener peninsula (height 1600 m, 10 km. away).



characterised by moderate rolling relief at an altitude of 500 metres. Exposure varies from 30% on the plateaux to 80% in the South Lakes region.

Underground mapping involved both general mine mapping and detailed 3-dimensional stope mapping and was carried out at scales varying from 1:25 to 1:3000. The maps used were prepared by Greenex A/S mine surveyors. Access to the mine was afforded by two 1.5 km. long free spanning cable cars that enter the eastern cliffwall of the Agfardlikavsá Fjord at heights of 520 and 600 metres (Fig. 4.14).

Sampling of the sulphides and host rocks was carried out during both underground and surface mapping, in order to provide i) material for petrological and microprobe studies and ii) a specific sample set for a lead and stable isotope analysis of the Black Angel deposits

#### **1.4 Previous Work**

Regional mapping of the Rinkian Mobile belt (Fig. 2.4) was performed by the Grønlands Geologiske Undersøgelse (G.G.U.) in 1967 and 1968. A regional appraisal of the belt is given in Escher and Watt (1976). Since this time a number of studies have been carried out on the structure of parts of the belt including the Umanak District (Pulvertaft, 1986), the Ikerasak District and the Svartenhuk Peninsula (Grocott, 1984 & 1987). Radiometric dating of the basement and supracrustals was carried out by Kalsbeek (1981, 1984) and Andersen and Pulvertaft (1985).

Little work has been published on the Black Angel deposits or the Marmorilik area. Owing to the operational format of the Black Angel Mine, previous work in and around the deposit has been separated into surface work and mine work.

Surface work by Cominco exploration geologists has focussed on particular drilling programs that have highlighted the difficulties of stratigraphic and structural interpretation in this highly deformed terrain. Much work on restricted parts of the Marmorilik area (Fig. 1.3) have been carried out by:- Black Angel Mountain (Elder, 1967; Myers, 1973;

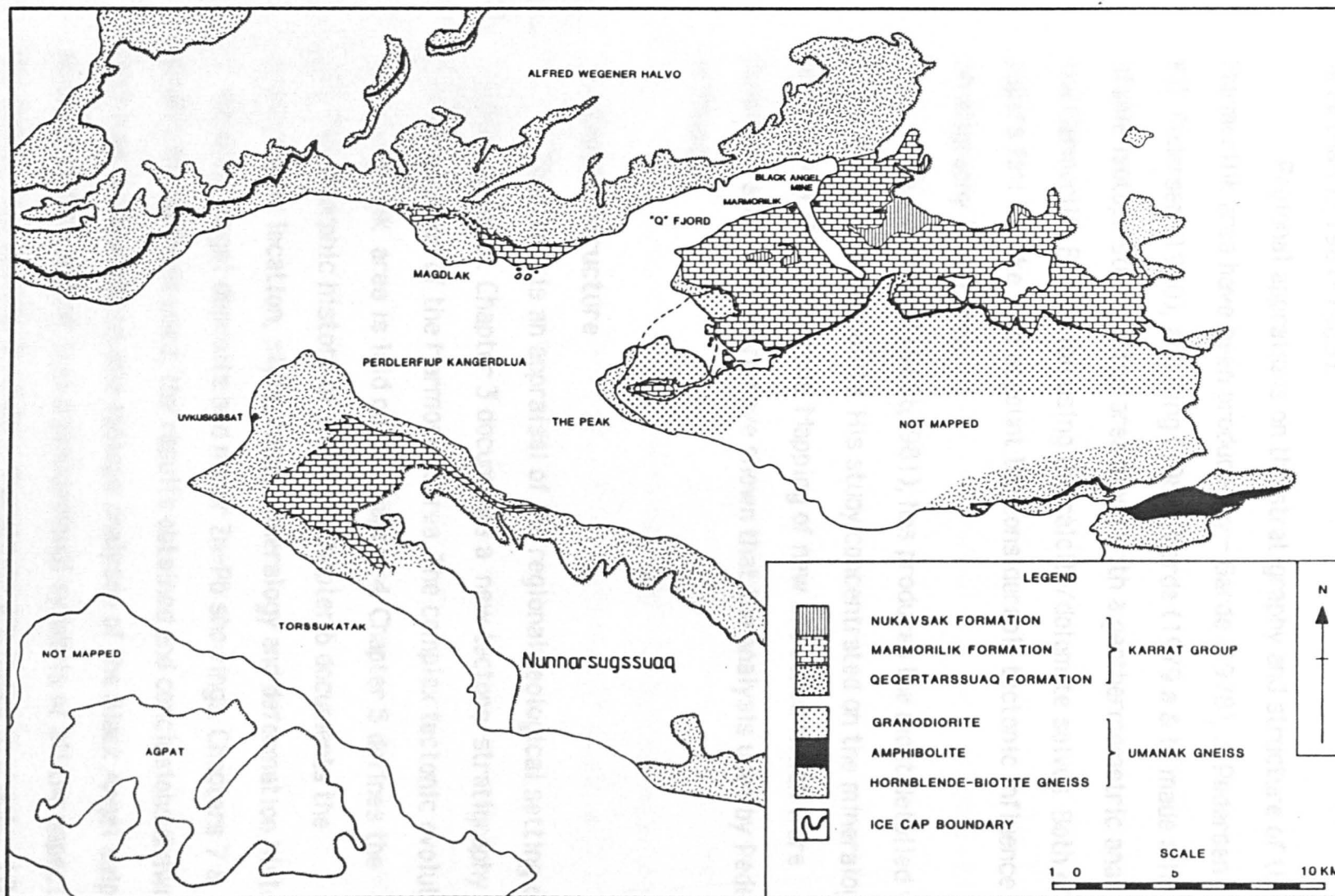


Figure 1.3 Geological map of the study area

Gannicott, 1976-1979; Nicholls, 1981; Harris, 1985),  
 Uvkusigssat and Aqpat island (Della Valle, 1977)  
 Aqpat Island (Gannicott, 1976 & 1979). Marmorilik Plateau and South Lakes  
 area (Harris, 1981-1985).

Regional appraisals on the stratigraphy and structure of the Marmorilik area have been produced by:- Garde (1978), J. Pedersen (1980), F.D. Pedersen (1980), and King (1981). Garde (1979 a & b) made a limited stable isotope study of the area along with a geothermometric analysis of the Marmorilik Formation using the calcite/dolomite solvus. Both of these papers fail to take into account the considerable tectonic influence on the stratigraphy in the area.

F.D. Pedersen (1980b, 1981), has produced the most detailed work on the Black Angel deposits. His study concentrated on the mineralogy and structure of the Angel zone. Mapping of new ore zones which were developed after this work have shown that the analysis used by Pedersen is flawed.

## 1.5 Thesis Structure

Chapter 2 is an appraisal of the regional geological setting of the sulphide deposits. Chapter 3 documents a new tectono-stratigraphy for the Karrat Group of the Marmorilik area. The complex tectonic evolution of the Marmorilik area is laid out in Chapter 4. Chapter 5 defines the poly-metamorphic history of the area. Chapter 6 documents the stratigraphic location, style, form, mineralogy and deformation histories of the Black Angel deposits and minor Zn-Pb showings. Chapters 7 & 8 detail the methods used, the results obtained and conclusions drawn from both lead isotope and stable isotope analyses of the Black Angel sulphides and host rocks. Chapter 9 is a discussional synopsis of all the aspects of the thesis. Conclusions from this discussion are listed in chapter 10.

## **1.6 Acknowledgements.**

I would firstly like to acknowledge Dr. K.R. McClay for giving me the opportunity to work on the Black Angel deposits and also for his support both during fieldwork in Greenland and during the period of thesis preparation. Funding for the project by N.E.R.C (CASE) award with Greenex A/S is greatly acknowledged. Secondly I would like to thank Erik Sprunk Jansen of Greenex A/S and John Collins of Cominco Ltd. for the efforts they made in order to get the project off the ground. Many thanks and best wishes go to Frank van der Stijl, Mogens Lind, Bjarne Jensen, Ernst Nielsen, Jauni Hansen-Haug and Kurt Christensen of Greenex A/S and in particular Colin Harris of Cominco Europe Ltd for their companionship and support during fieldwork in Greenland.

Dr. Ian Swainbank and Dr. Baruch Spiro are gratefully acknowledged for giving their time, assistance and expertise during the preparation and analysis of the lead and stable isotope material at the British Geological Survey, Gray's Inn Road, London.

John Maddicks is thanked for his help with the making of thin section material. Tom Easter is heartily thanked for his help with the production of photographic material in the thesis.

I must not forget the input of valuable discussion from my colleagues at Goldsmiths' College and Royal Holloway and Bedford New College. Lastly I owe my greatest thanks to my parents and Angela who encouraged me at every stage of this thesis.

## Chapter 2. Regional Geology of the Rinkian Mobile Belt

### 2.1 Introduction.

The Rinkian mobile belt is a complexly deformed, (1860-1680 Ma), poly-metamorphic, greenschist-granulite facies tectonic terrain. It consists of reworked Archean mafic and acid gneisses, migmatites and granodiorites (Umanak Gneiss Complex) and Early Proterozoic Karrat Group Supracrustals which contain the significant Zn-Pb mineralisation (Fig. 2.2). The stratigraphic relations in the belt are masked by the severe Rinkian polyphase deformation and polymetamorphism.

The Rinkian mobile belt is bounded to the north by the North Greenland Fold Belt (Dawes, 1976) (Fig 1.1), to the south by the Pakitsoq sinistral shear zone, which separates the Rinkian and Nagssugtoqidian mobile belts (Ramberg, 1949; Escher et al., 1976). To the west, the rocks of the Rinkian mobile belt are overlain by a Cretaceous-Tertiary cover sequence dominated by plateau basalts. Despite this the belt has been correlated with the late Aphebian Foxe Fold Belt, in eastern Canada (Henderson and Tippett 1981, Henderson 1983, Andersen and Pulvertaft 1985) (Fig. 2.1).

The Archean Gneisses give Rb-Sr ages at 2600 ma. (Kalsbeek, 1981; Andersen and Pulvertaft, 1985). The age of the Karrat Group sedimentation is obscured by Rinkian metamorphism and deformation. K-Ar and Rb-Sr dating defines the Rinkian deformation as an early/mid Proterozoic event which occurred between 1860-1680 ma. (Larsen and Møller, 1968; Bridgwater, 1971; Kalsbeek, 1981; Andersen and Pulvertaft, 1985), and which can therefore be correlated with the Hudsonian deformation event in Canada.

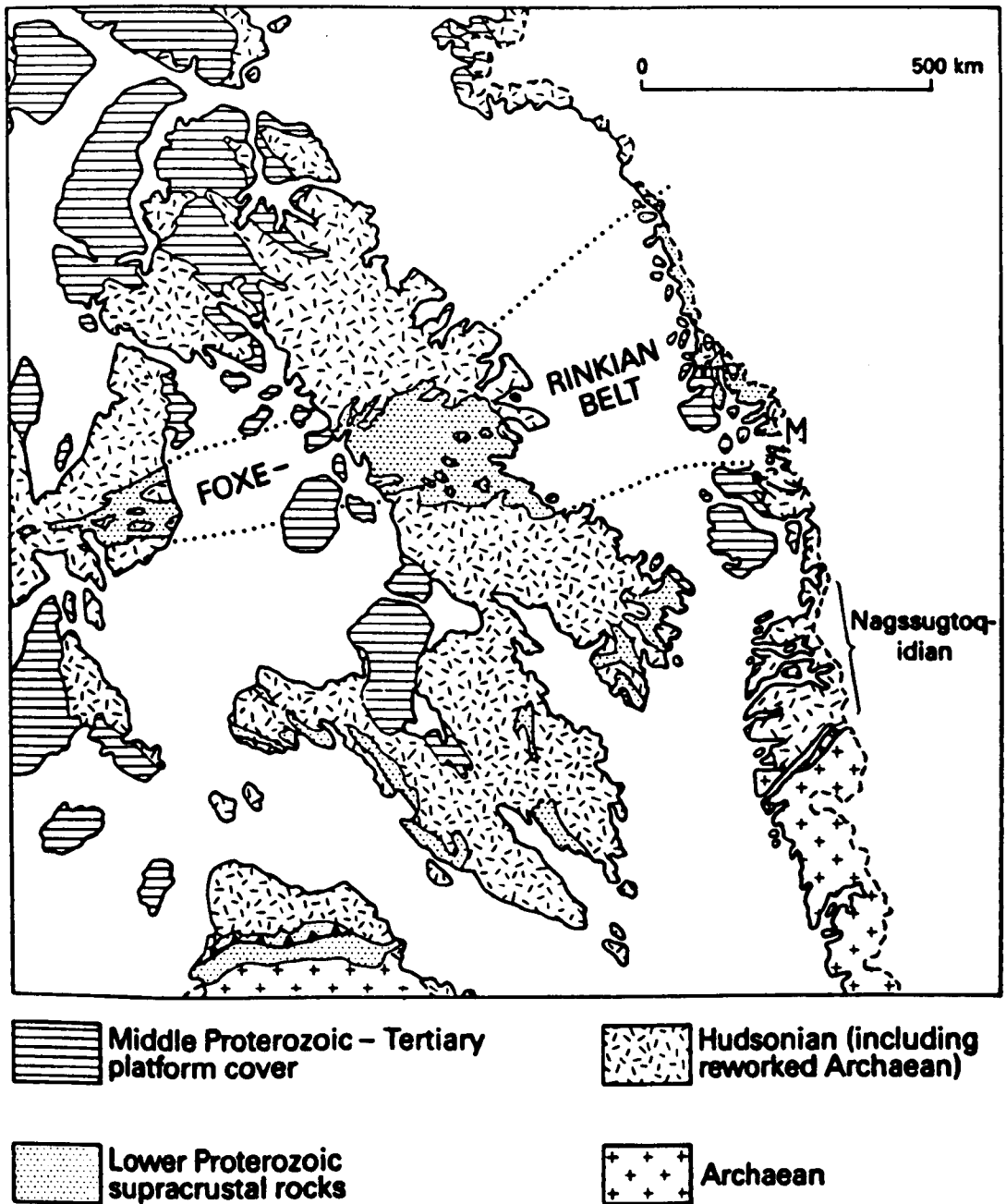


**Figure 2.1** Map showing the correlation of the Rinkian mobile belt with the Foxe fold belt of Canada. The pre-drift fit is from Le Pichon et al. (1977) modified to avoid overlap in the Canadian arctic islands  
 M = Marmorilik (After Andersen and Pulvertaft, 1985)

**Figure 2.2**  
**GENERALISED STRATIGRAPHIC COLUMN FOR THE RINKIAN MOBILE BELT**

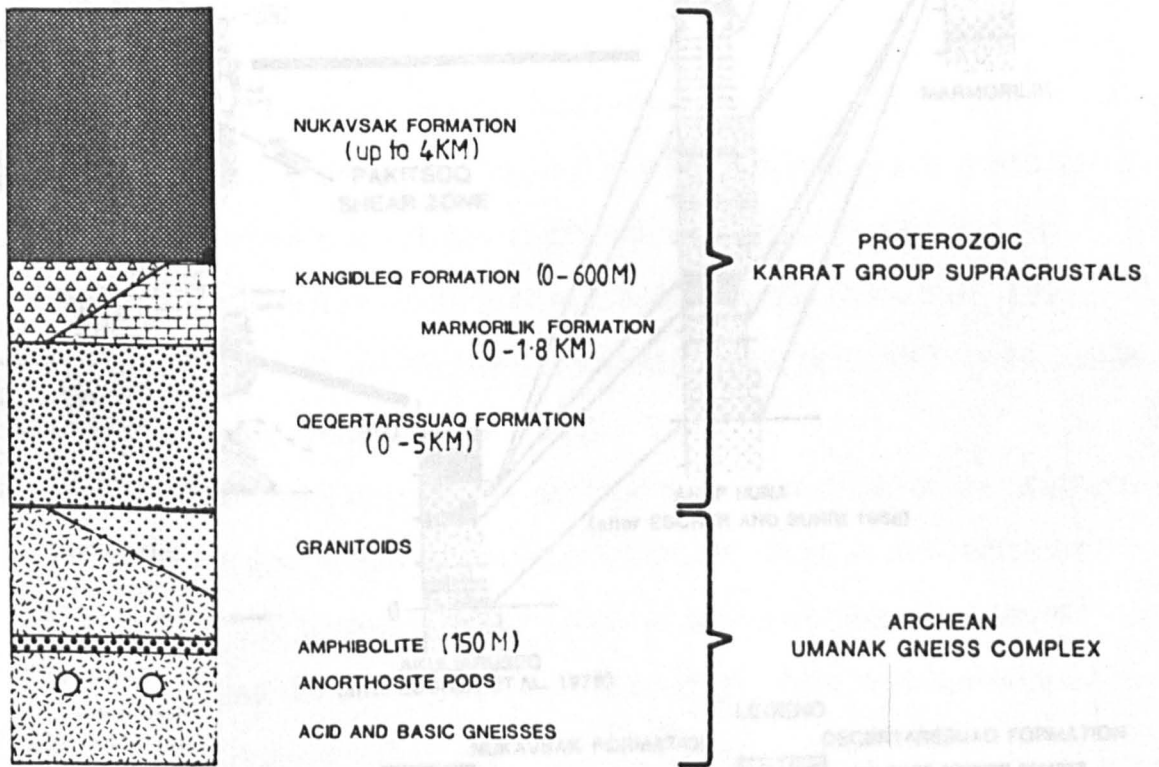


**Figure 2.3** Tectono-stratigraphic correlation of the Karrat Group through the Rinkian and Nagssugtoqvia mobile belts  
 Thickness ticks = 200m

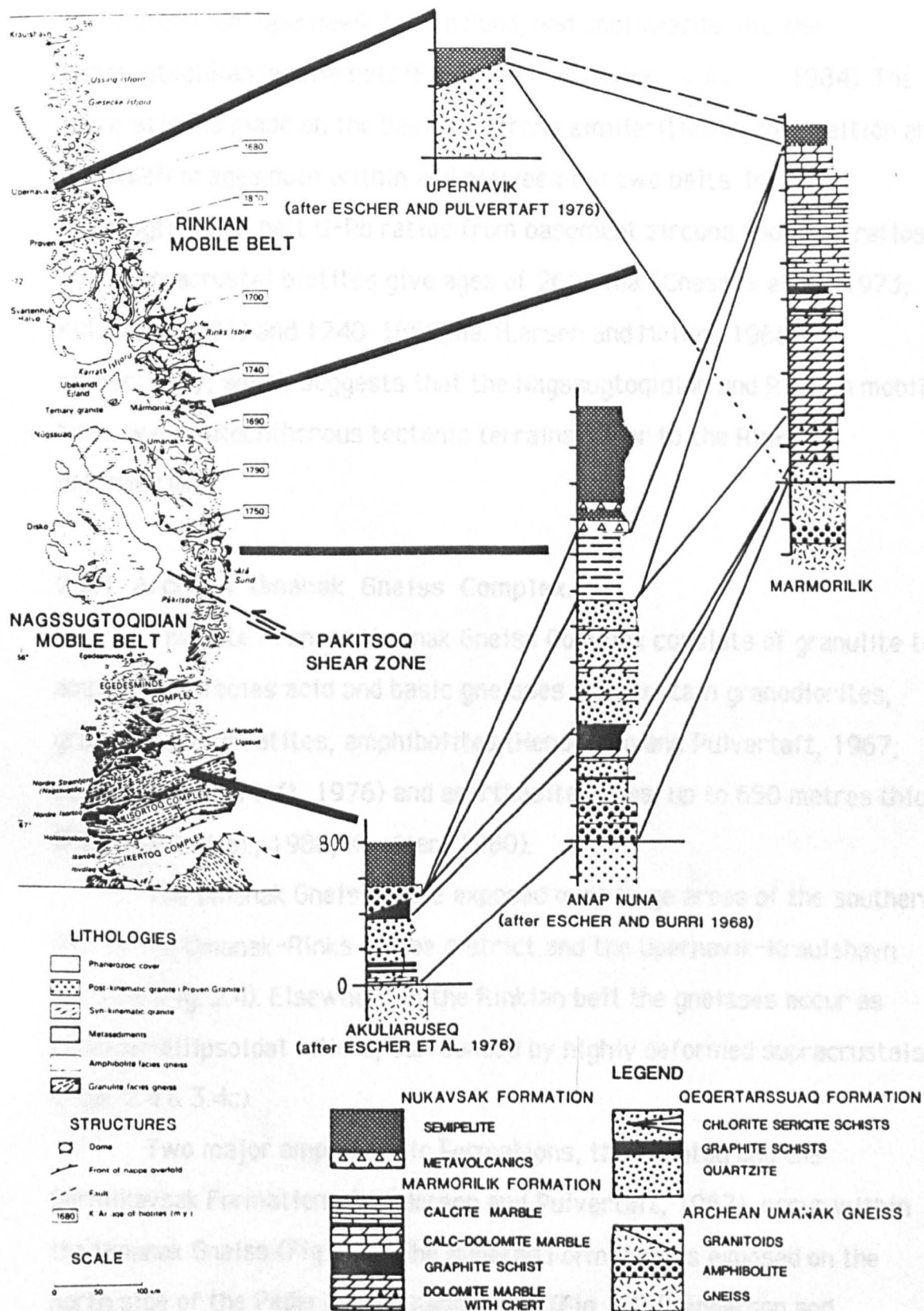


**Figure 2.3** Tectono-stratigraphic correlation of the Karrat Group through the Rinkian and Nagssugtoqidian mobile belts  
Thickness ticks = 200m

## 2.2 Tectono-Stratigraphy of the Rinkian mobile belt.

The tectono-stratigraphic units of the Rinkian mobile belt can be correlated from Upernavik to Ata Sund, and southwards into the Nagssugtoqidian mobile belt (Fig. 2.3) (Kalsbeek et al., 1984). The correlation is made on the basis of strong similarities in composition and radiometric ages both within and between the two belts. In the Nagssugtoqidian belt U-Pb ratios from basement zircons and K-Ar ratios from supracrustal biotites give ages of 2600 ma. (Chessex et al., 1973; Kalsbeek, 1981) and 1740-1650 ma. (Larsen and Møller, 1968) respectively, which suggests that the Nagssugtoqidian and Rinkian mobile belts were autochthonous tectonic terrains, prior to the Rinkian deformation.

### 2.2.1 Archean Umanak Gneiss Complex.

The Late Archean Umanak Gneiss Complex consists of granulite to amphibolite facies acid and basic gneisses that contain granodiorites, granitoids, migmatites, amphibolites (Henderson and Pulvertaft, 1967; Garde and Pulvertaft, 1976) and anorthosite zones, up to 650 metres thick (Pulvertaft et al., 1980; Knudsen, 1980).

The Umanak Gneisses are exposed over large areas of the southern half of the Umanak-Rinks Isbrae district and the Upernavik-Kraulshavn district (Fig. 2.4). Elsewhere in the Rinkian belt the gneisses occur as circular-ellipsoidal inliers, surrounded by highly deformed supracrustals (Figs. 2.4 & 3.4c).

Two major amphibolitic Formations, the Nunataq and the Sermikavsak Formations (Henderson and Pulvertaft, 1967), occur within the Umanak Gneiss (Fig. 2.2). The Nunataq Formation is exposed on the north side of the Pederlerfiup Kangerdlua (Fig 1.3) (Henderson and Pulvertaft, 1967) and consists of amphibolitic hornblende schists with intercalations of semipelitic schist and minor amounts of siliceous to semipelitic schists, quartzites, dolomite, calc-silicates and graphitic

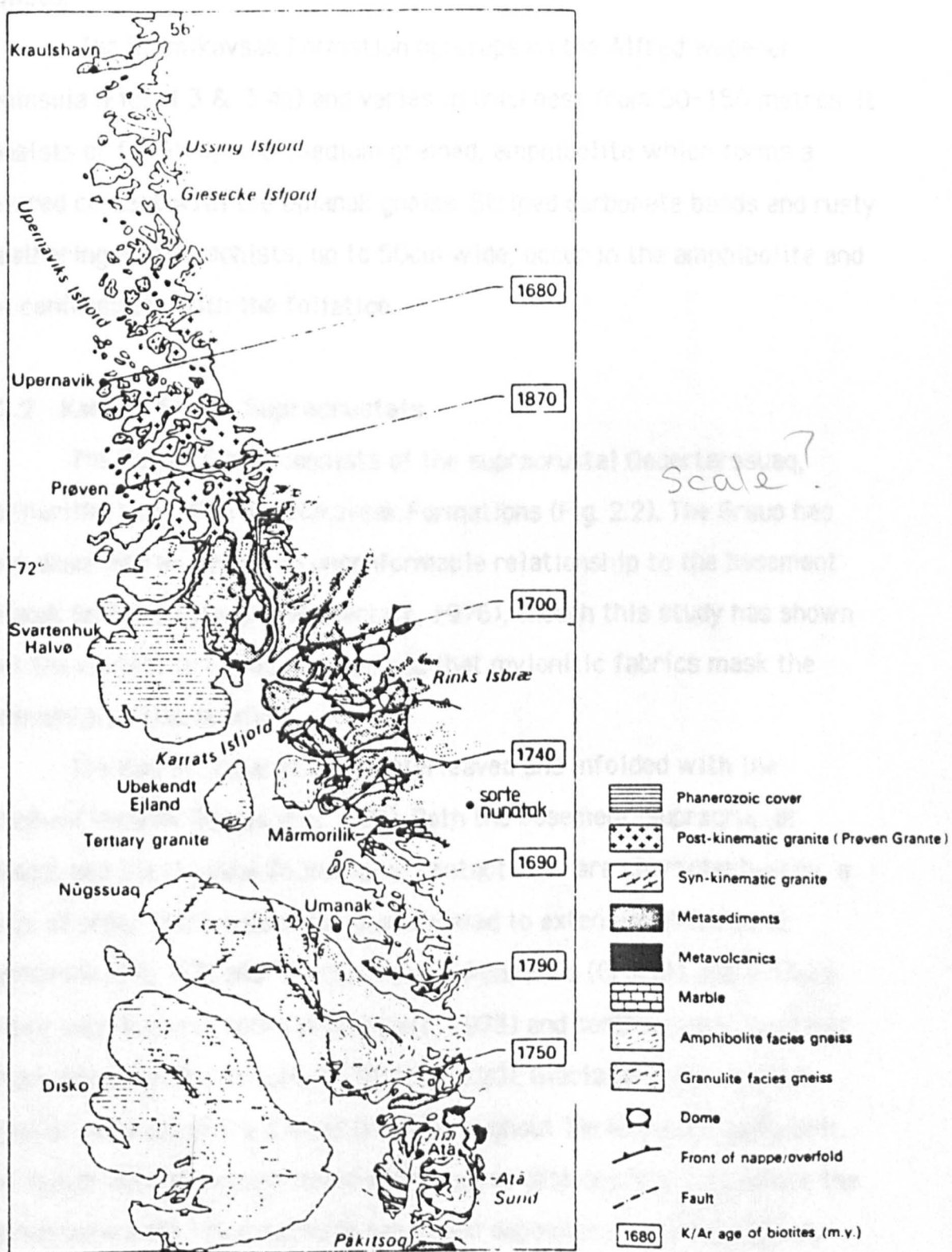


Figure 2.4 Geological map of the Rinkian Mobile Belt  
(After Escher and Pulvertaft, 1976)

schists.

The Sermikavsak Formation outcrops on the Alfred Wegener peninsula (Figs. 1.3 & 3.4a) and varies in thickness from 50-150 metres. It consists of foliated, fine-medium grained, amphibolite which forms a sheared contact with the Umanak gneiss. Striped carbonate bands and rusty weathering biotite schists, up to 50cm wide, occur in the amphibolite and are conformable with the foliation.

### **2.2.2 Karrat Group Supracrustals.**

The Karrat Group consists of the supracrustal Qeqertarsuaq, Marmorilik, Kangidleq and Nukavsak Formations (Fig. 2.2). The Group has been described as having an unconformable relationship to the basement Umanak Gneiss (Garde and Pulvertaft, 1976), though this study has shown that the contact is highly sheared and that mylonitic fabrics mask the sedimentary relationships.

The Karrat Group is often interleaved and infolded with the basement Umanak Gneiss (Fig. 4.20). Both the basement-supracrustal contact and the internal formational contacts are characterised by a range of shear fabrics such as those related to extensional faults at Marmorilik (Fig. 4.3) and the Svartenhuk Peninsula (Grocott and Vissers, 1984); ductile shear zones (Pulvertaft, 1973) and contractional faults at Nunarssugssuaq (Pulvertaft, 1973) (Fig. 4.20). Glacial erosion created isolated outcrops of the Karrat Group throughout the Rinkian mobile belt. The major outcrop occurs in the Rinks Isbrae district (Fig 2.4), where the supracrustals are interpreted to have been deposited in a rifted, gently south-north subsiding, ensialic basin (Allen and Harris, 1979) (Fig 2.5).

#### **1) Qeqertarsuaq Formation.**

This is the basal Formation of the Karrat Group, which according to Garde and Pulvertaft (1976) and Garde (1978) rests unconformably upon the basement Umanak Gneisses and thickens northwards from 10 metres

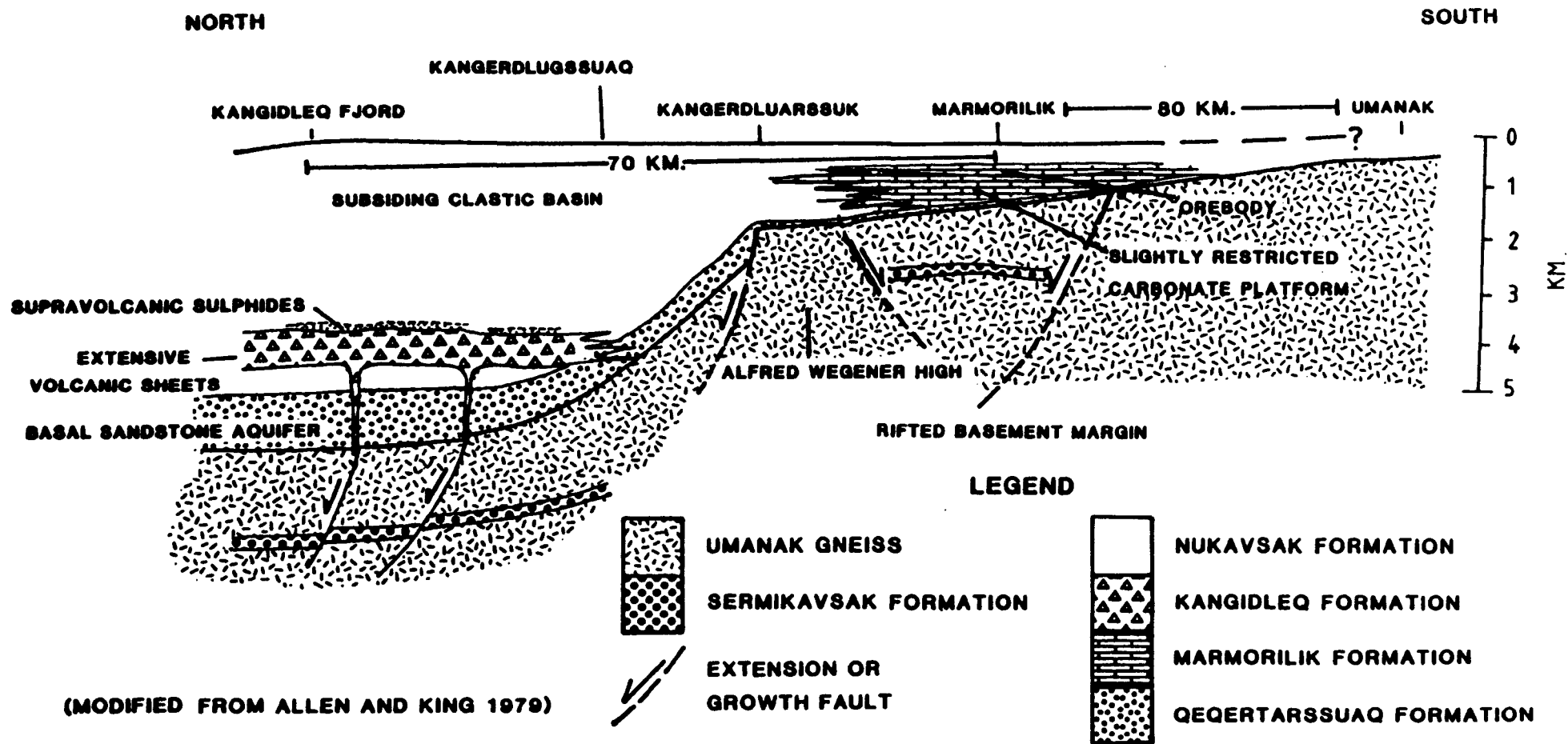


**Figure 2.5** Simplified reconstruction of the sedimentological setting of the Karrat Group. (After Allen and Harris, 1979).

south of Marmorilik to 3000 metres or more in the Rinks Isbrae district (Fig 2.4). The rocks represents an amphibolite-greenschist facies metamorphosed clastic shelf sequence consisting of interbedded metaquartzites, metapsammities and metasiltstones (semi-pelites) with local calc-silicate schists and sulphide-bearing units.

## ii) Marmorilik Formation.

The Marmorilik Formation is a greenschist facies carbonate succession that lies conformably upon the Qeqertarsuaq Formation and outcrops discontinuously for 120 miles from the Nugssuaq Peninsula to the Sorte Nunatak (Fig. 2.4). The maximum outcrop width (6 km) and maximum stratigraphic thickness (600 metres) is developed at Marmorilik. North of the Alfred Wegener peninsula (Fig. 2.4), the Marmorilik Formation thins rapidly and becomes interdigitated with the Qeqertarsuaq Formation (Fig. 2.5). In the Umanak area thin carbonate horizons that possibly represent the Marmorilik Formation (Pulvertaft, 1981 & 1986; Grocott<sup>et al</sup>, 1987) are infolded with the basement gneisses, whilst in the Ata Sund district, probable correlatives of the Marmorilik Formation (Escher and Burri, 1968), are interbedded with quartzites in the supracrustal units (Fig. 2.3).

The Marmorilik Formation consists of impure calcitic and dolomitic marbles (Fig. 2.3). In its lower units massively bedded siliceous dolomitic marbles host both disseminated and massive lead-zinc mineralisation in sub-economic quantities. Interbanded graphitic calcite/dolomite marbles overlie the massive dolomitic marbles and develop disseminated lead-zinc mineralisation. Coarse evaporite bearing calcitic marbles form the uppermost units of the Formation and host the massive stratabound Black Angel lead-zinc ore bodies. Diopside has been reported in the Marmorilik Formation (Gannicott, 1976; Pulvertaft, 1979) but greenschist facies assemblages containing tremolite/actinolite, scapolite, talc, phlogopite, biotite, quartz, dolomite and calcite are more

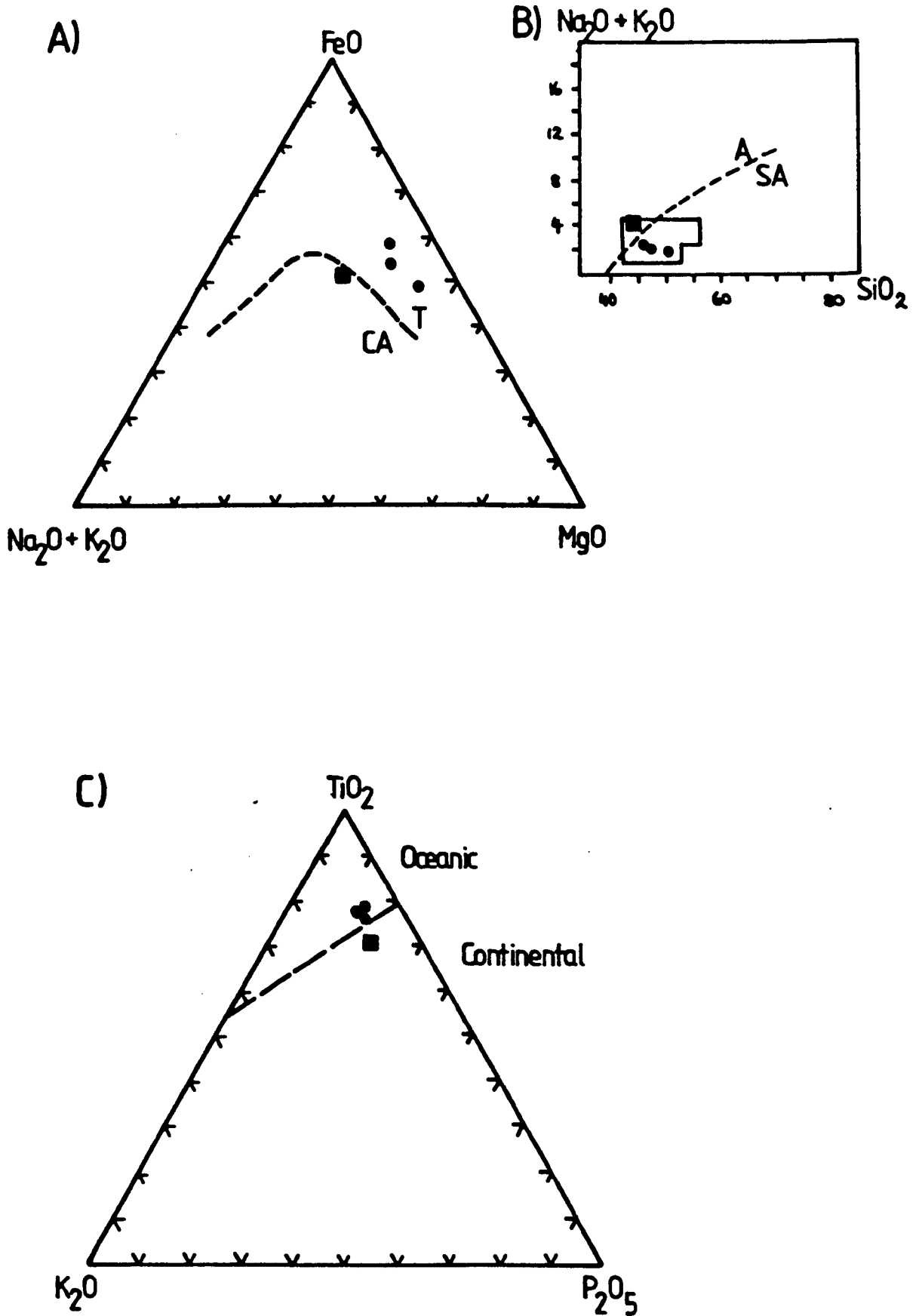


**Figure 2.6** Ternary diagrams of analyses from the Kangidleg Formation volcanics (circles) and Nunataq Formation (squares). A) AFM diagram B)  $\text{Na}_2\text{O} + \text{K}_2\text{O}$  vs  $\text{SiO}_2$  C)  $\text{TiO}_2$ - $\text{K}_2\text{O}$ - $\text{P}_2\text{O}_5$  (Pearce et al., 1975)

common (Garde, 1978; Pedersen, 1980).

### iii) Kangidleq Fm.

The Kangidleq Formation (Allen and Harris 1979) consists of metabasic to intermediate volcanics (sub-alkaline oceanic tholeiites, Fig. 2.6) that conformably overlie the Qeqertarssuaq Formation (Fig. 2.5) for 50 x 60 km. in the northern Rinks Isbrae district (Fig. 2.4). The volcanics consist of agglomeratic, tuffaceous or pillow flow breccias and occur in sheet form, varying in thickness from 25-75 metres (Ingia Fjord) to an estimated 400-600 metres on the east side of Kangidleq Fjord (Fig. 2.8). The volcanic fragments are vesicular and range in size from 1-50 cm., often being cemented by carbonate. Rare andesitic flows occur in the agglomeratic units.

### iv) Nukavsak Formation.

The Nukavsak Formation is the uppermost Formation in the Karrat Group (Fig. 2.2). It mantles the underlying Formations and dominates the outcrop north of the Alfred Wegener peninsula, where the total thickness of the succession is in excess of 5000 metres (Fig. 2.5). It has gradational stratigraphic contacts between the Qeqertarssuaq and Marmorilik Formations, but the contact between the Kangidleq and the overlying Nukavsak Formation is sharp and marked for over 50% of its length by a gossanous sulphide band (Allen and Harris, 1979).

The Formation is typically of greenschist metamorphic grade, though in the Upernavik-Kraulshavn district, it is represented by red brown granulite facies gneisses (Fig. 2.3) (Henderson and Pulvertaft, 1967; Escher and Pulvertaft, 1976). It is sub-divided into two lithologically monotonous members. The basal member consists of granular semipelites (quartz-plagioclase-biotite schists) with graphitic, biotitic and pyritic intercalations and a massive, 5-30 metres thick, graphite-pyrrhotite horizon. This horizon consists of rounded quartz clasts which are held in a



Figure 2.7 Geological map of the Talorssuit dome and the Ata granite (After Escher and Burri, 1968)

foliated graphitic-pyrrhotitic matrix (Pedersen and Gannicott, 1979). On the Svartenhuk peninsula, a 75 metre thick succession of metavolcanics composed of pillow basalts, pillow breccias and hyaloclastite tuffs lie directly above the graphite-pyrrhotite horizon (Grocott, 1984). Elsewhere the graphite-pyrrhotite horizon is overlain by a rhythmic alternation of sandstones and shales, with minor conglomeratic units, in which sedimentary structures representing  $T_{a-e}$  bouma beds are found (Grocott, 1984). The Formation has been interpreted as a metamorphosed greywacke/turbidite suite (Grocott <sup>et al</sup>, 1987).

### 2.2.3. Igneous Intrusions.

The Rinkian mobile belt contains two major Proterozoic granitoid plutonic complexes; the Ata Granite (Escher and Burri, 1968), the Proven Granite (Escher and Pulvertaft 1968), and granite sheets in the Svartenhuk Peninsula (Grocott, 1981 & 1983). A suite of dolerite dykes cut all earlier structures.

The Ata Granite occurs as a 2000 metre thick granite sheet along the basement-supracrustal contact, to the north of the Talorssuit dome in the Ata Sund district (Figs. 2.3, 2.4 & 2.7). Granodiorite to quartz diorite is developed at the sheet's sheared margins.

The Proven Granite is a large granitic plutonic complex that outcrops for over 2500 km<sup>2</sup> from south-east Proven to the Upernavik Isstrom (Fig. 2.4). The central part of the complex consists of coarse grained granite, with rapakivi-textured orthoclase phenocrysts. Highly sheared granitoid augen gneisses are present at the granite margins. Charnockitic and enderbitic compositions are developed to the north-west of the intrusion. Intense granite net veining occurs in the intruded Nukavsak Formation supracrustals.

Sheets of two-mica granite cut the Nukavsak Formation in the Kingiussap Auvfa, Svartenhuk Peninsula. The sheets are intruded syntectonically during D1 (Grocott and Visser, 1984), parallel to S1

cleavage and cross-cut D1 folds.

Two NW-SE trending 300 km. long dolerite dykes cross-cut all earlier structures in the Rinkian Mobile Belt. In the Marmorilik area these dykes are up to 100 meters wide and are associated with minor dolerite sills. Similar dykes have been recognised in eastern Canada and have been correlated with either the Mackenzie dyke swarm, 941-1040 Ma., (Fahrig and Jones, 1969) or the Franklinian dykes on Baffin Island, 700 Ma., (Fahrig et al., 1971).

## 2.3 Structure and Metamorphism of the Rinkian Mobile Belt.

### 2.3.1 Introduction.

The Rinkian mobile belt is characterised by fabrics with no obvious regional strike, generally low dips and highly variable tectonic transport directions (Henderson & Pulvertaft 1967). It is therefore structurally distinct from the southerly Nagssugtoqidian mobile belt (Ramberg, 1949; Escher et al., 1976) where consistent ENE planar fabrics are developed (Fig. 2.3). The most striking feature of the belt is the presence of basement gneiss domes which are mantled by polydeformed supracrustals (Grocott 1987) (Fig. 2.4 & 2.8). Other areas are characterised by extensive sub-horizontal basement gneiss tracts.

### 2.3.2 Basement Gneiss tracts

Basement gneisses dominate the outcrop in the Umanak (Henderson and Pulvertaft, 1967; Grocott, 1980; Pulvertaft et al., 1980) and Upernavik-Kraulshavn (Henderson and Pulvertaft, 1967) districts (Fig. 2.4). In these areas it is impossible to distinguish between Archean and Proterozoic structures (Grocott, 1980 & <sup>Grocott et al.</sup> 1987). Ductile deformation structures include large sheath-like and refolded recumbent isoclinal nappes as developed in the Upernavik region (Escher and Pulvertaft, 1968), high angle shear zones at Ikerasak (Grocott, 1980 + 1984) and curvilinear thrust fronts, with opposing senses of tectonic transport, e.g. Umanak

region (Grocott, 1980; Henderson and Pulvertaft, 1967).

### 2.3.3 Basement Gneisses and Supracrustals

Basement gneisses and Karrat Group supracrustals are deformed into basement domes with 'pinched in' supracrustal basins, which have been termed 'mantled gneiss domes', (Figs. 2.8 & 2.9) (Henderson and Pulvertaft, 1967; Henderson, 1969; Escher and Pulvertaft, 1976; Grocott *et al.*, 1987) in the Ata Sund district (Escher and Burri, 1968) (Fig. 2.7) and the Marmorilik-Rinks Isbrae district (Henderson and Pulvertaft, 1967; Pulvertaft, 1973; Escher and Pulvertaft, 1976; Garde, 1978; Pedersen, 1980; Pulvertaft, 1986). These structures are clearly products of Proterozoic (Rinkian) deformation. The domes are steep sided (Fig. 3.4c), overturned (Fig. 2.9), circular to ellipsoidal structures with gneissic cores, which vary in size and diameter from less than 2km. to more than 25 km. In the Rinks Isbrae district five major domes occur in a vague ESE-WNW trending belt (Henderson 1969) (Fig. 2.8). This tectonic elongation is also developed in the Snepynamiden and Qaersukavsak domes (Fig. 2.8).

Curvilinear high angle extensional shear faults occur within the basement gneisses (Escher and Burri 1967) and also along the basement-supracrustal boundary (Grocott, Van Den Eeckhout and Vissers 1987). The Karrat Group rocks above this contact contain low angle extensional shear systems (Wernicke and Burchfiel, 1982). Recumbent to asymmetric, chevron to isoclinal, non-cylindrical folds are present above these low angle dislocations (Fig. 2.9). The folds have axial traces that are parallel to, but verge away from, the basement-supracrustal boundary at Marmorilik (Fig. 4.3) and the Svartenhuk Peninsula (Grocott and Vissers 1984).

Two large nappes, the Nunarssugssuaq nappe and the Kigarsima nappe (Henderson, 1969), are present in the Marmorilik-Rinks Isbrae district (Fig. 2.8). The Nunarssugssuaq nappe emplaces Umanak Gneisses

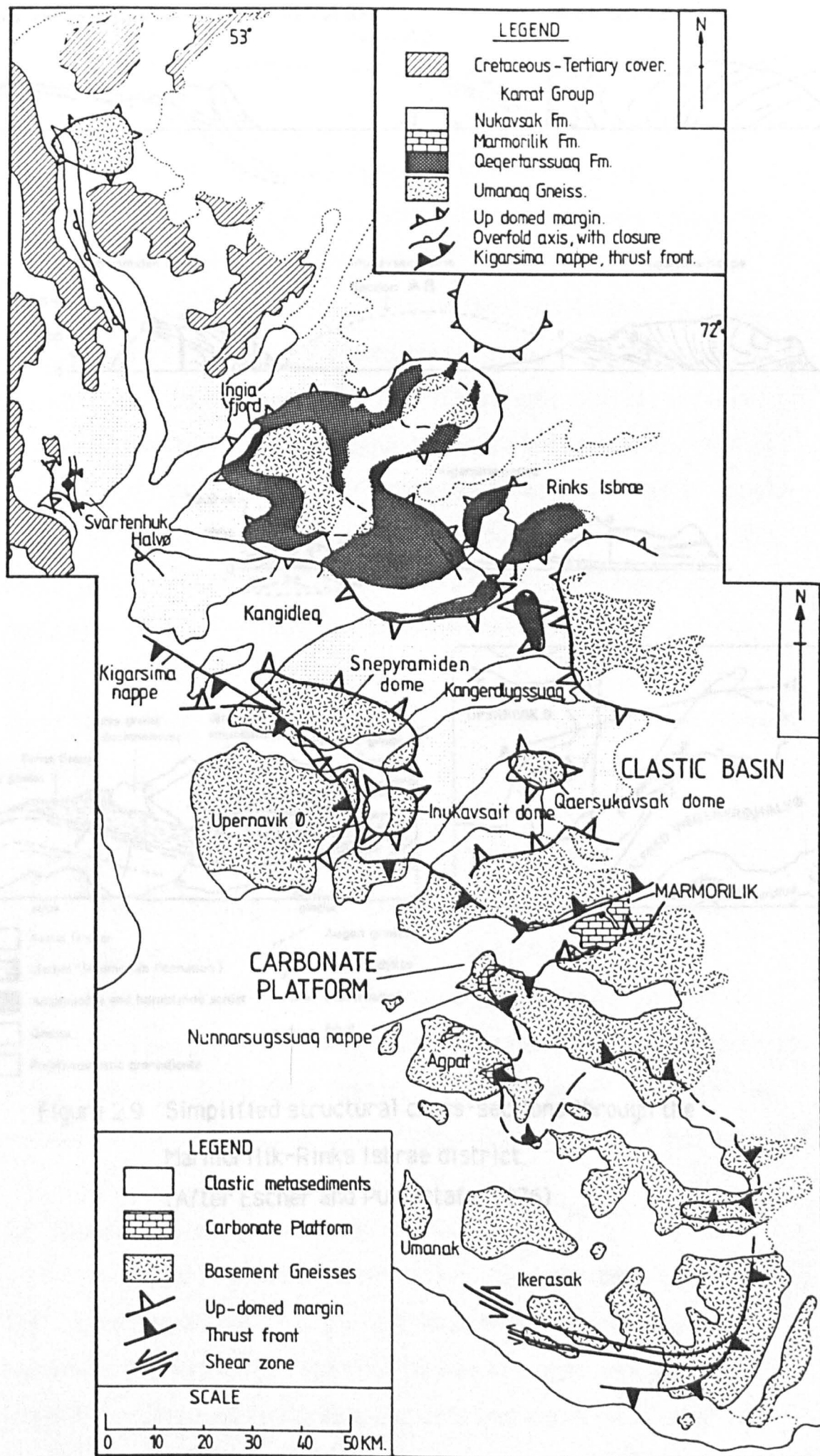


Figure 2.8 Geological map of the Marmorilik-Rinks Isbrae district. (Modified from Escher and Pulvertaft, 1976)

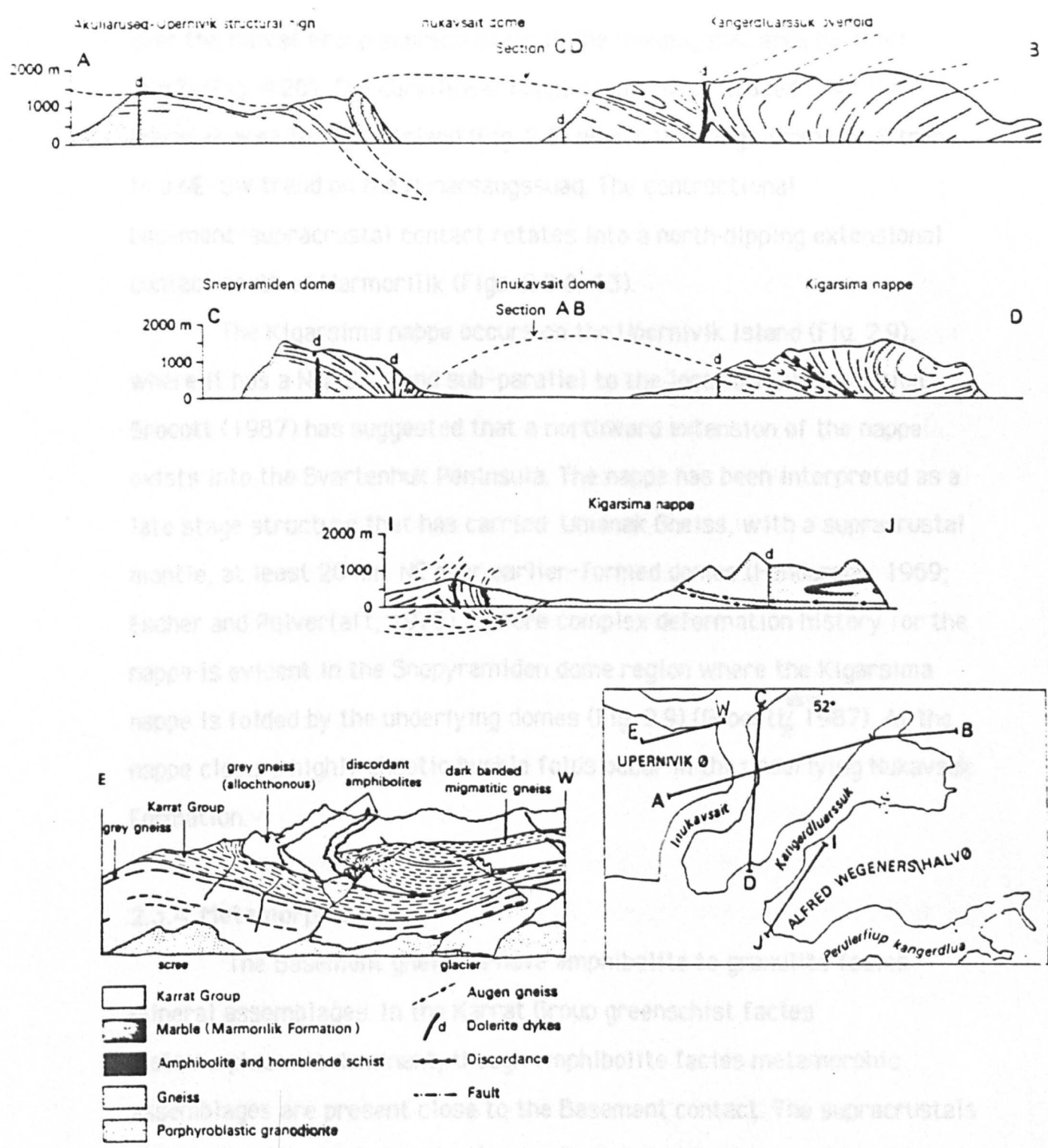


Figure 2.9 Simplified structural cross-sections through the Marmorilik-Rinks Isbrae district. (After Escher and Pulvertaft, 1976)

2.4 Mineralisation in the Rinkian Mobile Belt

Zn-Pb-Fe sulphides constitute the dominant mineralisation type in the Rinkian mobile belt. They are restricted to the Karrat Group and in particular the Marmorilik Formation. Traces of copper mineralisation occur in the basement gneisses on Agpat Island and on the southern

over the Karrat Group supracrustals in the Uvkusigssat area (Grocott 1987) (Fig. 4.20). The curvilinear nappe front can be traced from the Ikerasak area to Agpat Island (Fig. 2.8) where it swings from a N-S trend to a NE-SW trend on the Nunarssugssuaq. The contractional basement-supracrustal contact rotates into a north-dipping extensional contact south of Marmorilik (Figs. 2.8 & 4.3).

The Kigarsima nappe occurs on the Upernivik Island (Fig. 2.9), where it has a NW-SE trend sub-parallel to the local domal elongation. Grocott (1987) has suggested that a northward extension of the nappe exists into the Svartenhuk Peninsula. The nappe has been interpreted as a late stage structure that has carried Umanak Gneiss, with a supracrustal mantle, at least 20 km. NE over earlier-formed domes (Henderson, 1969; Escher and Pulvertaft, 1976). A more complex deformation history for the nappe is evident in the Snepyramiden dome region where the Kigarsima nappe is folded by the underlying domes (Fig. 2.9) (Grocott <sup>et al.</sup>, 1987). At the nappe closure highly chaotic buckle folds occur in the underlying Nukavsak Formation.

### 2.3.4 Metamorphism

The Basement gneisses have amphibolite to granulite facies mineral assemblages. In the Karrat Group greenschist facies metamorphism is dominant, though amphibolite facies metamorphic assemblages are present close to the Basement contact. The supracrustals attain granulite facies in the Upernavik district. Further aspects of the metamorphic evolution in the Marmorilik area are discussed in chapter 5.

### 2.4 Mineralisation in the Rinkian Mobile Belt.

Zn-Pb-Fe sulphides constitute the dominant mineralisation type in the Rinkian Mobile belt. They are restricted to the Karrat Group and in particular the Marmorilik Formation. Traces of copper mineralisation occur in the basement gneisses on Agpat Island and on the southern

cliffwall of the Alfred Wegener peninsula near Marmorilik.

#### 2.4.1 Karrat Group meta-clastic-hosted mineralisation

Minor disseminated Cu, Zn, Pb, Fe mineralisation is hosted in the calc-silicate and quartzitic units of the Qeqertarssuaq Formation, near Marmorilik (Garde, 1978; F.D. Pedersen, 1980a). Weakly persistent Cu-Fe sulphide mineralisation occurs in the semipelite units overlying the basal quartzites (F.D. Pedersen, 1980a). This consists of disseminated chalcopyrite, pyrite and pyrrhotite in the fine grained clastic beds, with chalcocite and bornite in the interbedded buff dolomite lenses.

Allen & Harris (1979) and Grocott & Vissers (1984) recognised pyrrhotite-bearing black shales, siliceous siltstones, pyritic quartz biotite schists, siliceous pyritic limestone and rare 1-1.5 metre beds of pyrrhotite-graphite schists in the Qeqertarssuaq Formation along the Kangidleq Fjord (Fig. 2.8).

The black graphitic schists of Nukavsak Formation contain massive to disseminated, stratabound graphitic, pyrrhotite and pyrite mineralisation (Fig. 3.2). The 5-30 metres thick foliated graphitic pyrrhotite/pyrite horizon, recognised by Pedersen and Gannicott (1979), is widespread over approximately 2500 km<sup>2</sup> of the Rinks Isbrae district (Allen and Harris, 1979).

#### 2.4.2 Karrat Group carbonate-hosted mineralisation

Major massive and disseminated, carbonate-hosted, stratabound and stratiform Zn-Pb-Fe-Ag sulphide mineralisation is present in the Marmorilik Formation (Myers, 1973; Garde, 1978; F.D. Pedersen, 1980a & King 1981). The sulphide lenses contain sphalerite, galena and pyrite with chalcopyrite, pyrrhotite, tennantite and arsenopyrite. Near Marmorilik Zn-Pb mineralisation occurs at ten stratigraphic levels (F.D. Pedersen, 1980a; J. Pedersen, 1980; King, 1981), with massive accumulations at four stratigraphic horizons (Fig. 3.2).

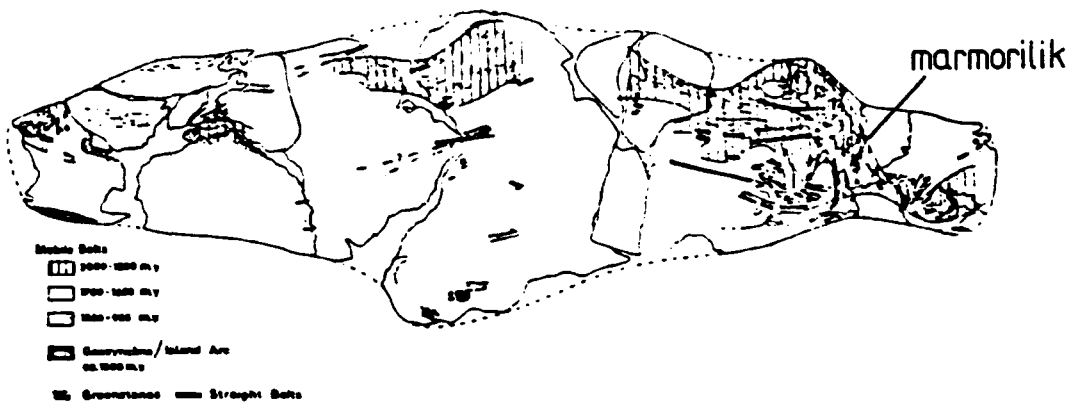


Figure 2.10 Palaeogeographical setting of the Rinkian Mobile Belt in the Proterozoic supercontinent. (After Piper, 1980)

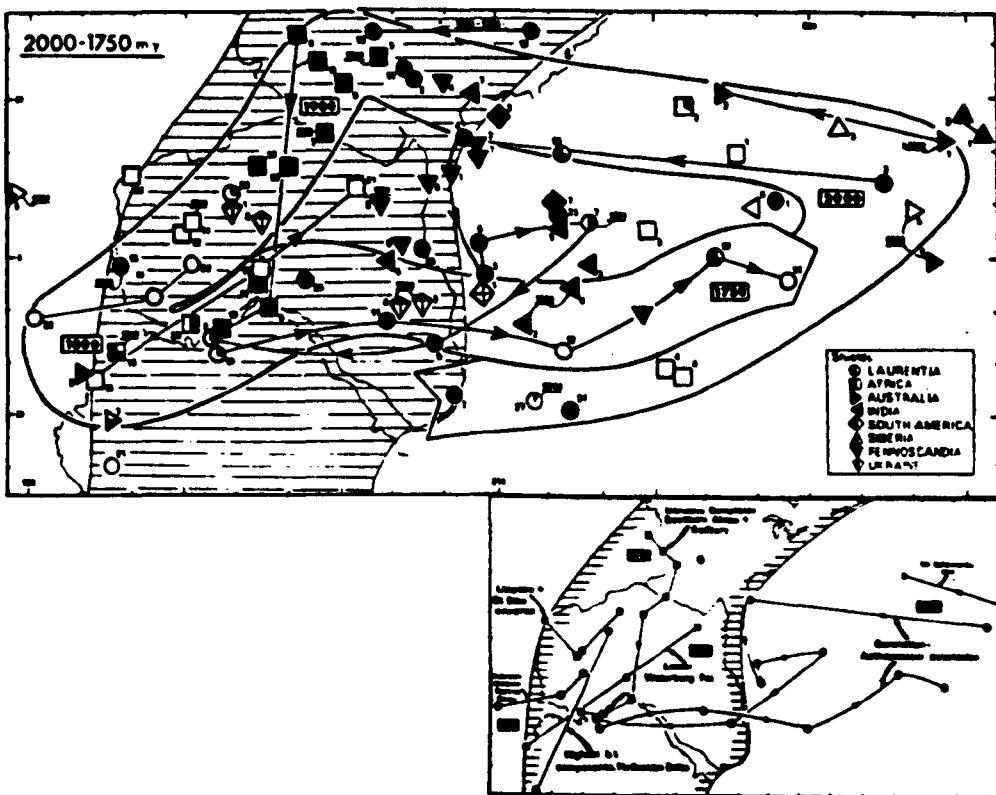


Figure 2.11 Polar wandering curves for the Laurentian shield for the period 2000-1750 Ma. (After Piper, 1980)

## **2.6 Palaeotectonics and Palaeogeography of the Rinkian Mobile Belt.**

During Karrat Group sedimentation and Rinkian tectonism, the Earth's continental crust consisted of a single lens shaped body or supercontinent (Fig 2.10) (Piper 1983). The Archean craton of Greenland, was located centrally within the Laurentian shield towards the western margin of the supercontinent (Fig 2.10). Karrat Group sedimentation is therefore thought to have taken place within a gently subsiding ensialic basin (Fig. 2.5). The classification of the Kangidleq Formation volcanics as sub-alkalic tholeiites give further credence to this tectonic setting for the Karrat Group sedimentation (Fig. 2.6). The correlation of supracrustal sediments across the Nagssugtoqidian-Rinkian Mobile Belt boundaries (Fig. 2.2), and eastwards into the Foxe Fold Belt (Henderson and Tippett, 1980. and J.R. Henderson, 1983), suggests that the ensialic basin was of a large lateral extent.

Polar wandering curves constructed from the palaeomagnetism of the Hurorian red beds and Nippissing diabase (Roy and Lapointe, 1976) indicate that the Laurentian shield was in high latitudes from 2200-2000 ma., and in intermediate to low latitudes from 1900-1500 Ma. (Fig 2.11). The presence of marine carbonates and evaporitic beds within the Marmorilik Formation is consistent with the palaeomagnetic data, and suggests that Karrat Group sedimentation took place within low latitudes.

## Chapter 3. Tectono-Stratigraphy of the Marmorilik area.

### 3.1 Introduction

This chapter presents the results of a detailed analysis of the stratigraphy of the Marmorilik area (Figs. 3.1 & 3.2). Units of the Umanak gneiss complex outcrop at the northern and southern margins of the map area, while the younger supracrustals are restricted to a central, east-west trending, structural corridor (Fig. 3.1).

Previous regional and detailed classifications of the stratigraphy (Hendersen and Pulvertaft, 1967; Garde, 1978; J. Pedersen, 1979; F.D. Pedersen, 1980; King, 1981), are summarised in Figure 3.3. These studies focussed on the identification and correlation of lithological units across the area and paid little attention to the effects of the Rinkian deformation. This resulted in oversimplification in the documentation of the Marmorilik stratigraphy, particularly with respect to repeated, inverted and structurally omitted tectonic units.

A new tectono-stratigraphy has been established (Fig. 3.2), by means of detailed 1:10000 lithological mapping, section measuring (in the less deformed areas) and cliffwall analyses. Stratigraphic correlations are necessarily broad-scale because of the widespread metamorphic recrystallisation of the original sedimentary fabrics, dolomitisation and dedolomitisation of the carbonate sequence and tectonic brecciation, extensional thinning and thrust repetition of the sedimentary succession.

The new tectono-stratigraphy has i) redefined the overall stratigraphic succession in the map area, ii) documented a new internal stratigraphy for the Marmorilik Formation (Fig. 3.5) and iii) has recognised the presence of the Qeqertarsuaq Formation in the area for the first time. The re-interpretation is of particular importance in a) defining the styles, displacements and relative timing of the deformation structures in the area and b) placing the area's significant economic ore grade and gossanous sulphide showings into a tectono-stratigraphic framework (Fig. 6.2).

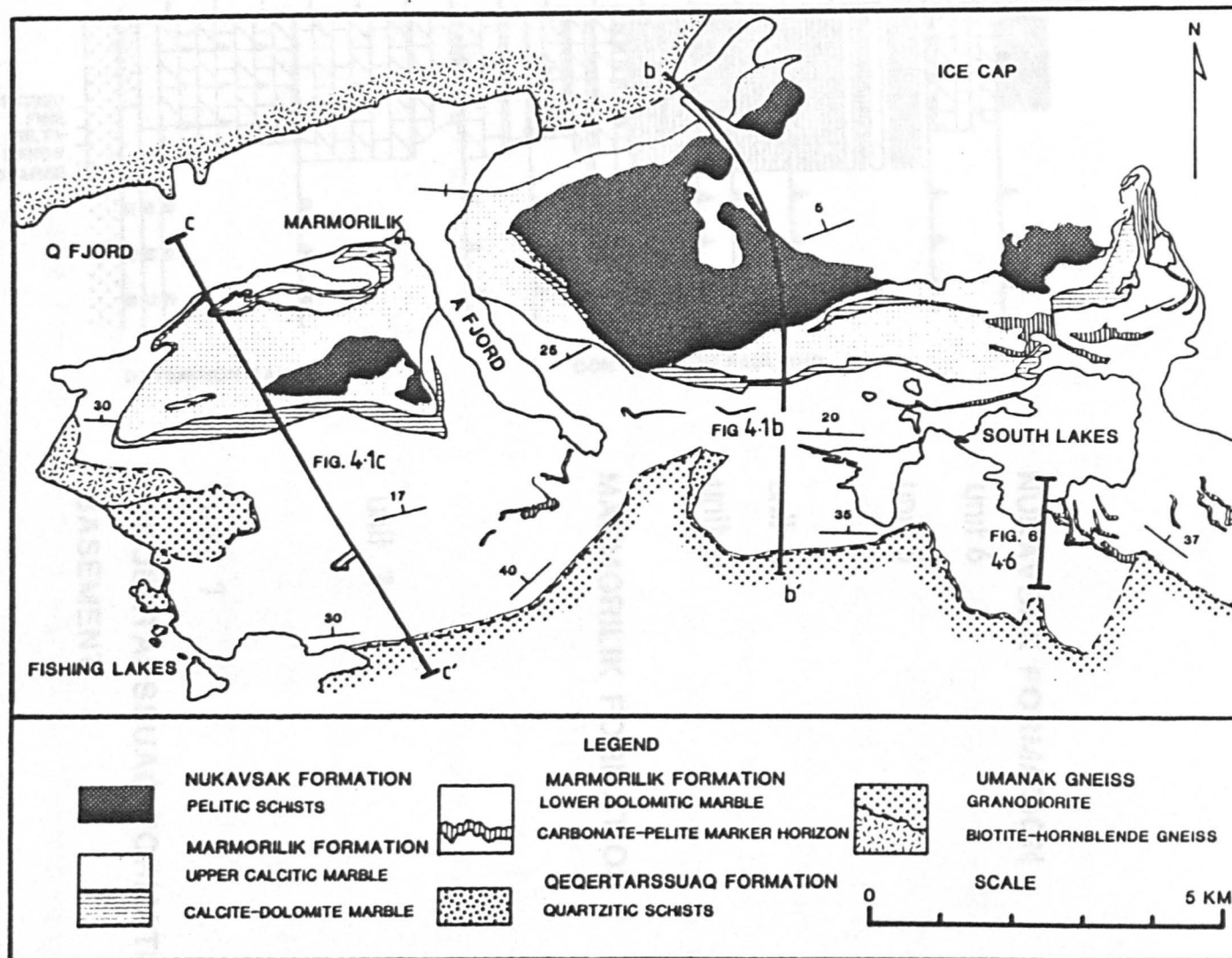
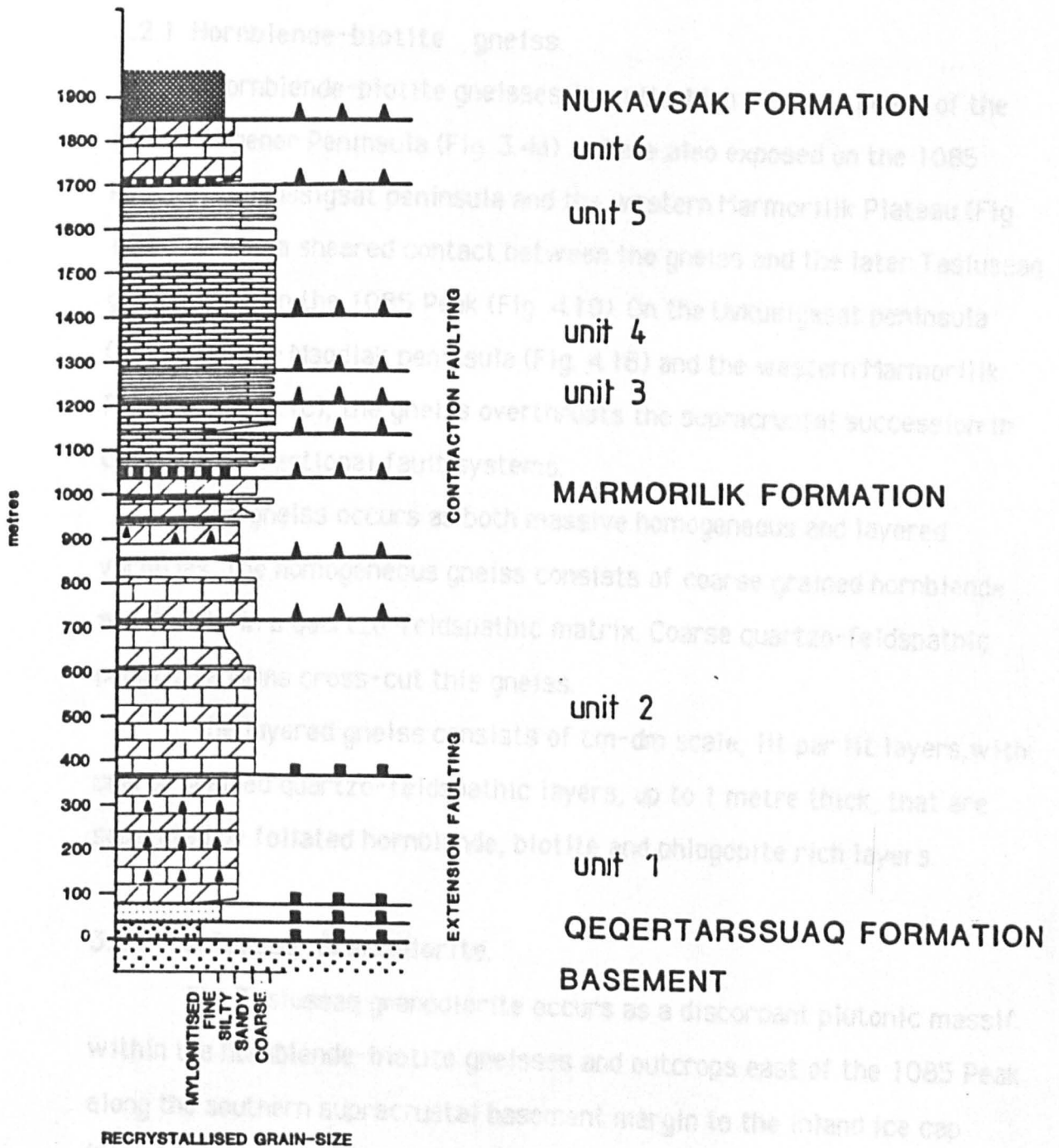


Figure 3.1 Simplified lithological map of the Marmorilik area  
(see also Fig 3.1 b in the back pocket)



**Figure 3.2** Simplified tectono-stratigraphic column for the Karrat Group of the Marmorilik area

### 3.2 Basement Umanak Gneiss Complex.

The basement can be sub-divided into three easily recognisable units. These are:

- i) Hornblende Biotite gneiss
- ii) Tasiussaq Granodiorite
- iii) Sermikavsak Amphibolite Formation

#### 3.2.1 Hornblende-biotite gneiss.

Hornblende-biotite gneisses form the high pinnacle peaks of the Alfred Wegener Peninsula (Fig. 3.4a) and are also exposed on the 1085 Peak, the Uvkussigsat peninsula and the western Marmorilik Plateau (Fig 1.3). There is a sheared contact between the gneiss and the later Tasiussaq granodiorite on the 1085 Peak (Fig. 4.10). On the Uvkusigssat peninsula (Fig. 4.13), the Magdlak peninsula (Fig. 4.18) and the western Marmorilik Plateau (Fig. 4.1c), the gneiss overthrusts the supracrustal succession in complex contractional fault systems.

The gneiss occurs as both massive homogeneous and layered varieties. The homogeneous gneiss consists of coarse grained hornblende and biotite in a quartzo-feldspathic matrix. Coarse quartzo-feldspathic pegmatite veins cross-cut this gneiss.

The layered gneiss consists of cm-dm scale, lit par lit layers, with coarse grained quartzo-feldspathic layers, up to 1 metre thick, that are separated by foliated hornblende, biotite and phlogopite rich layers.

#### 3.2.2 Tasiussaq Granodiorite.

The Tasiussaq granodiorite occurs as a discordant plutonic massif within the hornblende-biotite gneisses and outcrops east of the 1085 Peak along the southern supracrustal basement margin to the inland ice cap (Figs 1.3 & 3.1). It extends southwards 15km to the Perdlerfiup Kangerdlua. The granodiorite contacts are strongly sheared (Figs. 3.4f & 4.5) and in most cases the original contacts are obliterated. The

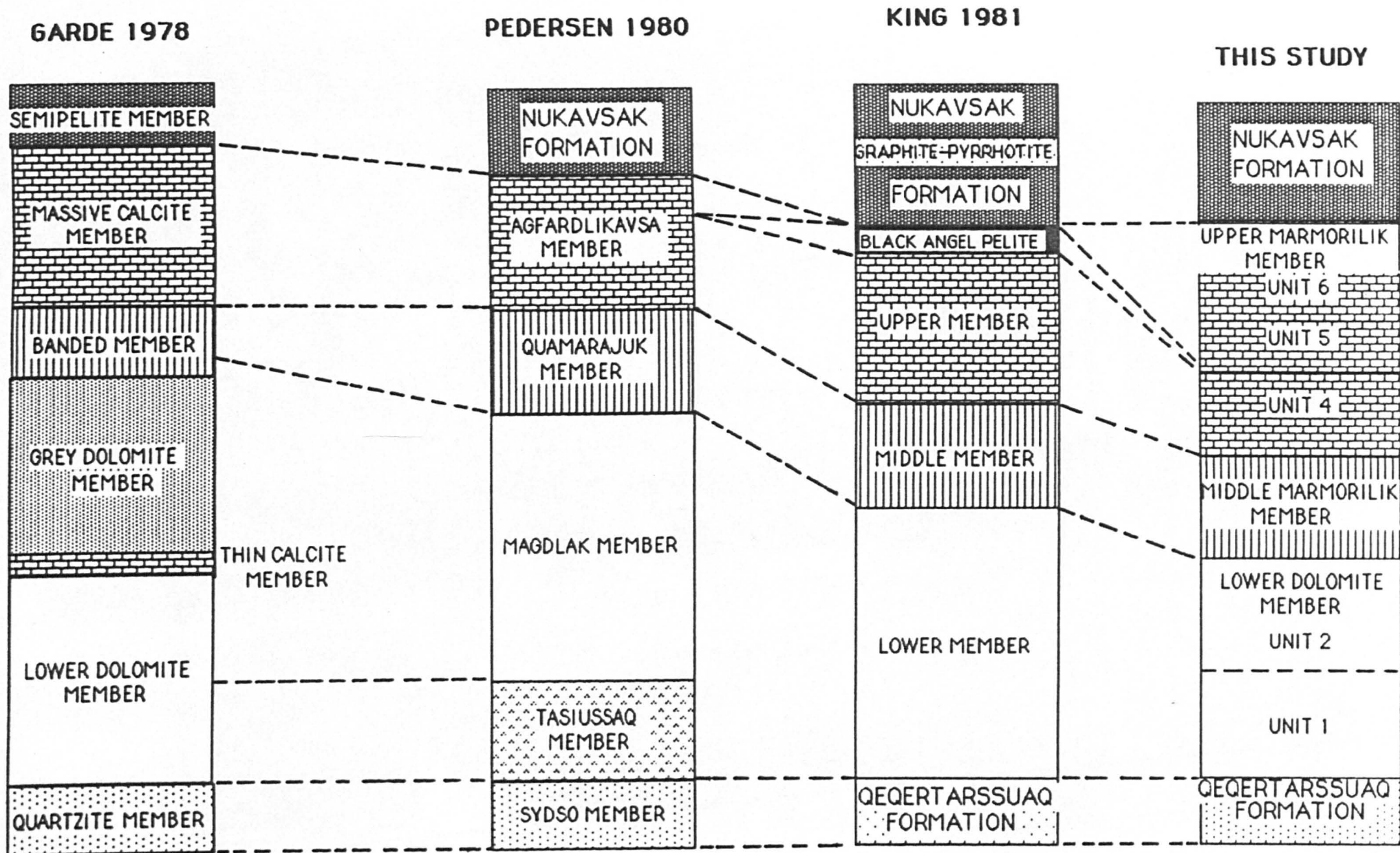


Figure 3.3 Previous classifications of the Karrat Group stratigraphy in the Marmorilik area

### Figure 3.4 Umanak Gneiss Complex.

A) The Alfred Wegener cliffwall north-west of Marmorilik. The cliffwall is composed of banded and massive Umanak Gneiss in which a the 150 metre thick amphibolitic Sermikavsak Formation is developed. Width of photo 25 km. Height of cliff 1650 metres.

B) The folded unconformity between the basement Umanak gneiss (Light grey) and the Karrat Group supracrustals (Dark grey) made up predominantly of pelitic schists of the Nukavsak Formation. Western end of the Kangerdlugssuaq fjord looking north. Height of cliff 1000 metres.

C) Circular, differentially eroded, gneiss dome surrounded by dark grey steeply dipping units of the Nukavsak Formation. Western end of the Kangerdlugssuaq fjord. Height of dome 600 metres.

D) Foliated granodiorite (bottom) cross-cut by a relatively undeformed fine grained microgranite dyke (top). Southern Agfardlikavsua fjord. Location 121. Pencil for scale (on contact).

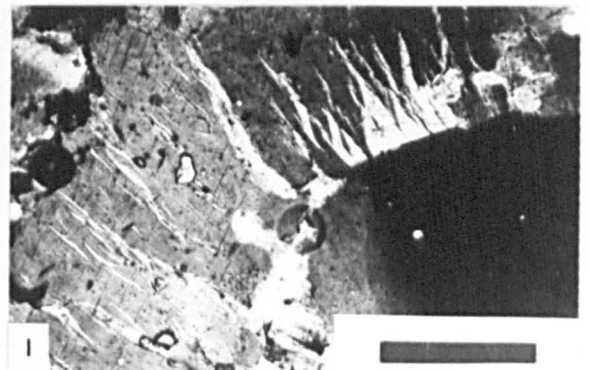
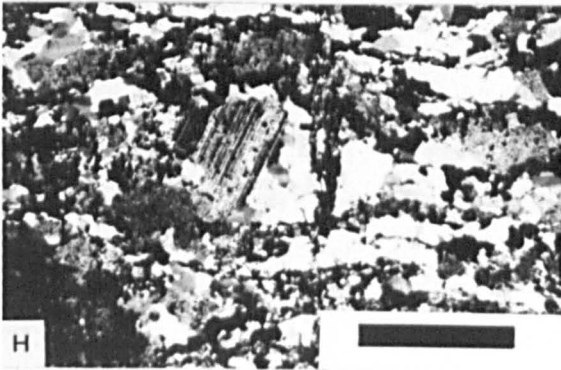
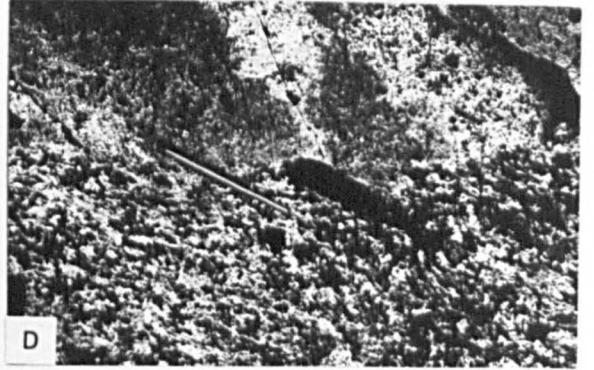
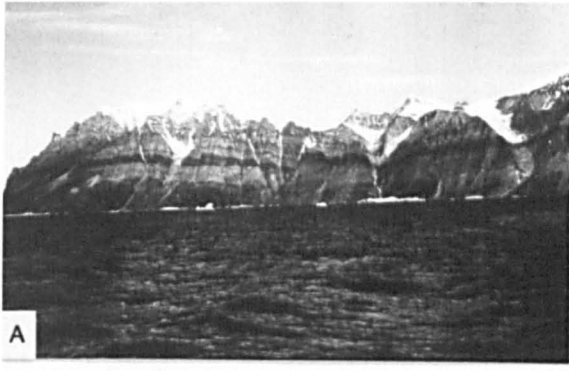
E) Boudinaged and fractured amphibolite pods of the Sermikavsak Formation incorporated within pale Umanak Gneiss. south-eastern Magdlaq Peninsula. Scale bar 2 metres.

F) Foliated granodiorite, developing C/S fabric, with feldspathic augen and phlogopite/muscovite matrix. Location South Lakes area. Scale bar 50 cm.

G) Photomicrograph of 'sieve like' albitic poikiloblasts post-tectonically (D1) overgrowing a biotitic matrix. Slight rotation (D3) of poikiloblasts indicates a sinistral shear. Specimen 17d of mafic pod found at Location 17. South lakes area. XPL Scale bar 500 $\mu$ .

H) Photomicrograph of lamellar twinned augen like albitic phenocrysts and ribbon like quartz domains found in the foliated granodiorite of (F). Thin section 500a. XPL Scale bar 500 $\mu$ .

I) Photomicrograph showing a rounded, strained, quartz grain (bottom right) mantled by a deformed microcline grain in which flame like deformation twins are developed. Specimen 695b Western Marmorilik Plateau. XPL Scale bar 160 $\mu$ .



granodiorite is dominantly homogeneous (Fig. 4.5b) and consists of 3-4 cm euhedral, simply twinned, zoned, plagioclase ( $An_{50}$ ) and orthoclase feldspar phenocrysts set in an allotriomorphic, coarse grained, quartzo-feldspathic matrix with accessory hornblende and biotite. Towards the basement margins the feldspar phenocrysts become augen like (Fig. 3.4h), the quartz grains are extended into ribbons, and large amounts of phlogopite occur.

A suite of medium grained, leucocratic, light pink to flesh coloured, 5 m wide, micogranitic dykes (Fig. 3.4d) cross-cut the granodiorite in conjugate arrays. They are transected at the basement-supracrustal contact. The dykes have fine grained, 0.1- 1mm, chilled margins and consist of 1 mm euhedral to subhedral, stubby prismatic, microcline and sodic plagioclase phenocrysts in an allotriomorphic quartzo-feldspathic matrix, which contains acicular, biotite and chlorite. The feldspar phenocrysts are strained and show lanceolate deformation bands and cataclastic fracturing.

The granodiorite also contains boudinaged mafic pods, up to 2 m wide, that are concentrated along the supracrustal-basement contact. The pods consist of anhedral embayed quartz, albitic plagioclase and microcline feldspars, up to 0.8 mm., held in a dark green to black biotite-rich foliated matrix with sinistral shear fabrics (Fig. 3.4g). The embayed feldspathic phenocrysts are overgrown by a high relief anhedral mineral.

### **3.2.3 Sermikavsak Amphibolite Formation.**

The Sermikavsak Formation outcrops within the Hornblende-biotite gneiss of the Alfred Wegener Peninsula (Fig. 3.4a). It consists of a thick 100-150 metre, dark green to black, foliated amphibolite band. It occurs with highly sheared tectonic contacts against the enclosing gneiss. On the Magdlak Peninsula the amphibolite band is boudinaged and occurs as rounded pods which lie randomly within the

gneiss (Fig. 3.4e). The amphibolite consists of coarse grained, 1–5 mm., prismatic hornblende and platy biotite that define a foliation within a medium grained quartzo-feldspathic matrix. Irregular, 1–50 cm. wide, quartzo-feldspathic pegmatite veins cut the amphibolite foliation.

### 3.3 Karrat Group Supracrustals.

Representative stratigraphic sections of the Karrat Group show i) a rapid variation in the thickness of the supracrustal succession (Fig. 3.5) and ii) that some tectono-stratigraphic units preferentially act as slip horizons (Fig. 3.5). Many low angle extension faults are present at the base of the succession, particularly in the southern and western Marmorilik region (Fig. 4.2). These detachments fault out the Qeqertassuaq Formation and the lower units of the Marmorilik Formation. A number of contraction faults at the top of the supracrustal sequence cause tectonic thickening and repetition in the Middle and Upper Marmorilik Formation (Fig. 4.22). In the field area the top of the Nukavsak Formation isn't present, so estimates of stratigraphic thickness are not given.

#### 3.3.1 Qeqertarssuaq Formation.

In this thesis the basal unit of the Karrat Group has been assigned to the Qeqertarssuaq Formation (Figs. 3.1 & 3.2) and is correlated with psammities and metapelites to the north of the Alfred Wegener peninsula (Fig. 2.5). This unit was previously considered to be the basal member of the Marmorilik Formation (Garde, 1978 and F.D. Pedersen, 1980).

Quartzites and tremolitic, calc-silicate schists, 0–60 metres thick, belonging to the Qeqertarssuaq Formation occur along the southern basement/supracrustal margin, striking in a roughly east-west trend from the 1085 Peak to the inland ice-cap (Fig. 3.1). There are also outcrops on the western Marmorilik Plateau and the Magdlak Peninsula.

In a generalised stratigraphic section the highly sheared basement contact is overlain by up to 5 metres of thin-bedded, 20 cm,

E

W

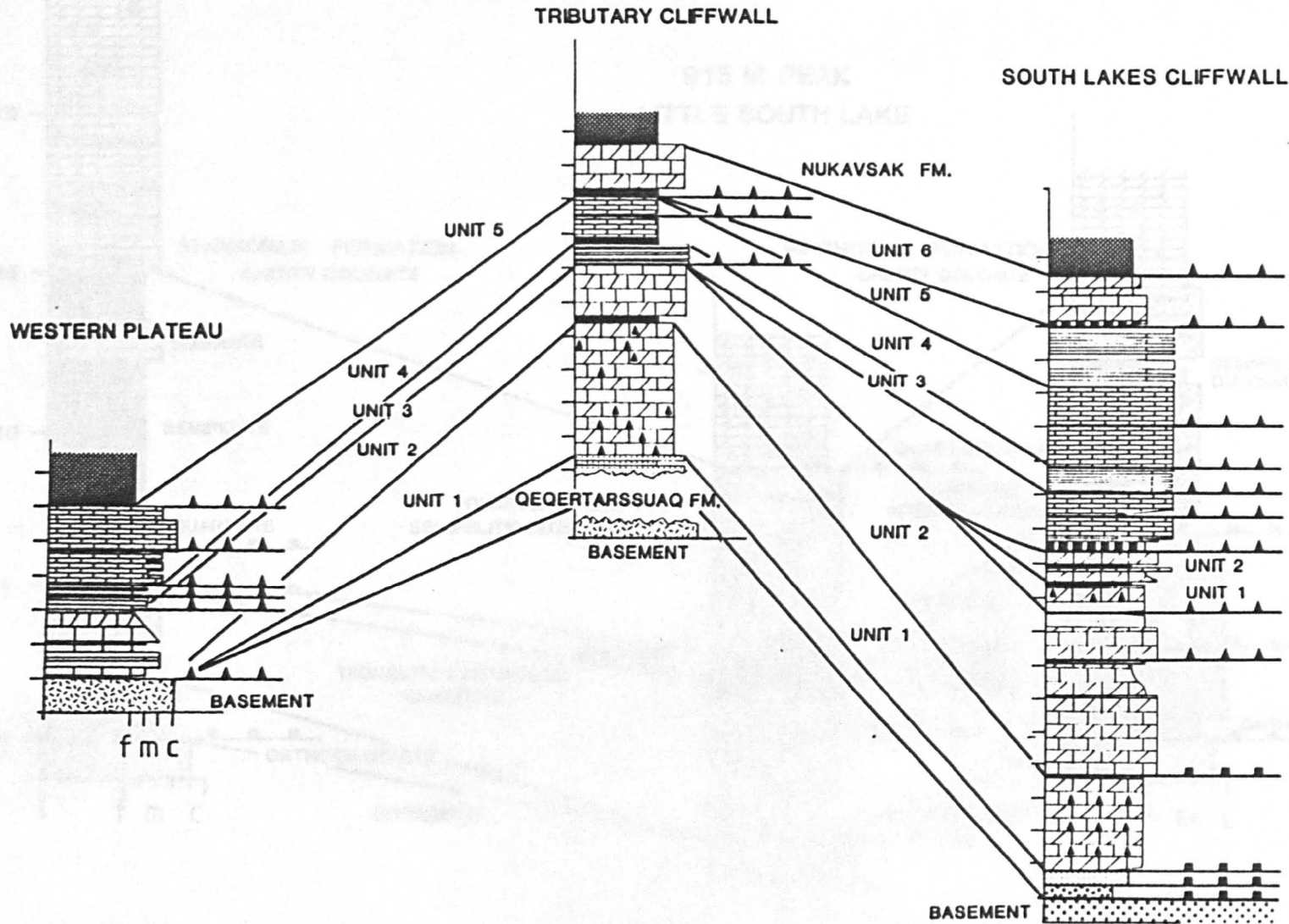


Figure 3.5 Internal tectono-stratigraphic correlation of the Karrat Group and Marmorilik Formation

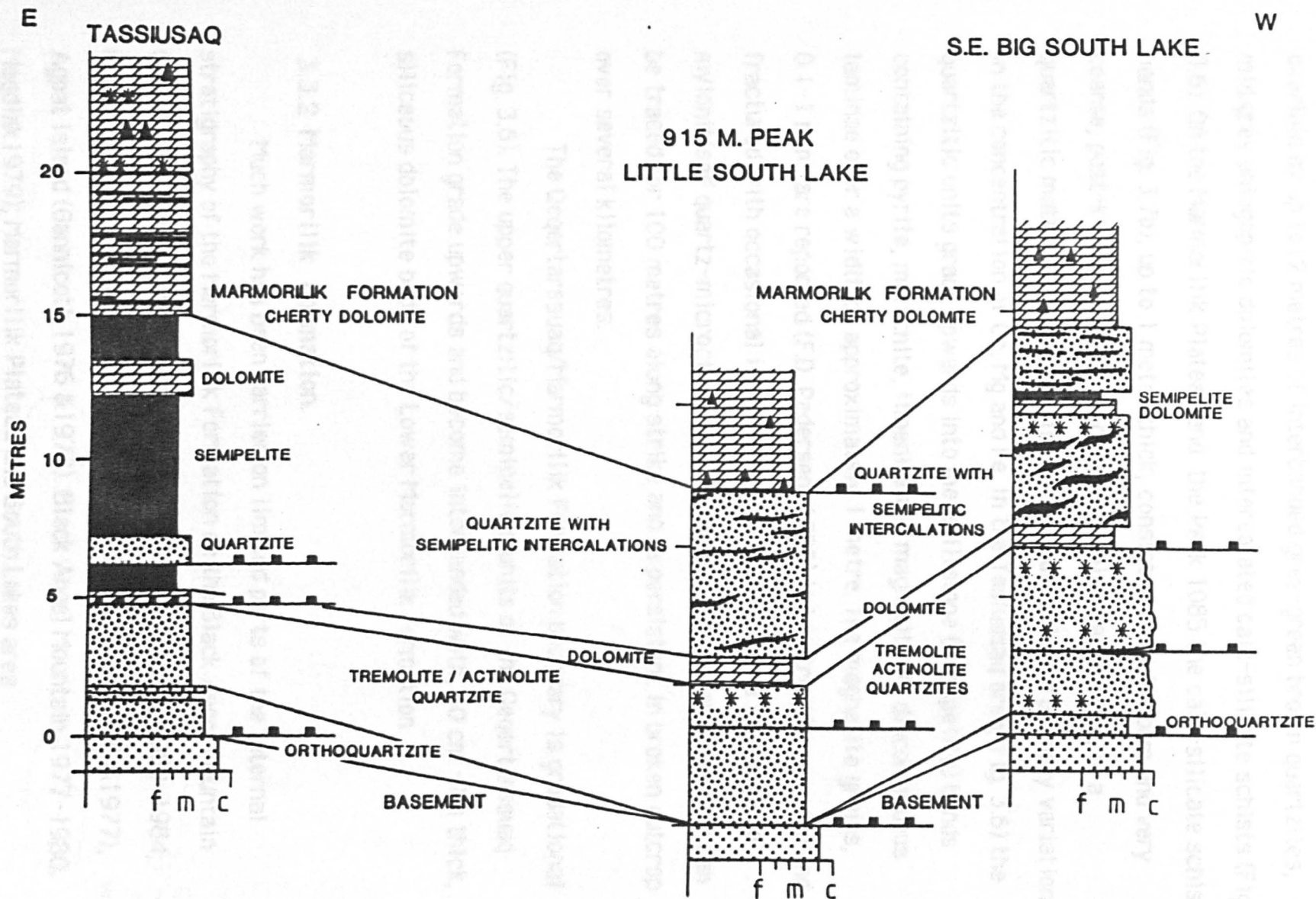


Figure 3.6 STRATIGRAPHIC TEMPLATE SHOWING THE INTERNAL STRATIGRAPHY OF THE QEQERTARSSUAQ FORMATION

orthoquartzites with flattened symmetrical ripple marks (wavelengths 10cm. and flattened amplitude 2cm) (Fig. 3.7a). Possible deformed cross-beds occur in the upper quartzite beds. The orthoquartzites are overlain by up to 12 metres of interbanded grey-green brown quartzites, mid grey phlogopitic dolomites and intercalated calc-silicate schists (Fig. 3.6). On the Marmorilik Plateau and the Peak 1085 the calc-silicate schist bands (Fig. 3.7b), up to 1 metre thick, consist of rosetteform and very coarse, post-kinematic (D3), acicular crystals of actinolite, in a quartzitic matrix. These actinolite-rich bands reflect a primary variation in the concentration of Ca, Mg and Fe. In the Tasiussaqa area (Fig. 3.6) the quartzitic units grade upwards into metasilstone (semipelite) bands containing pyrite, malachite, ilmenite and magnetite in discontinuous laminae over a width of approximately 1 metre. The magnetite grains, 0.1-1 mm., are reported (F.D. Pedersen, 1980) to be strongly corroded and fractured with occasional ilmenite rims and are set in a fine grained mylonitised quartz-microcline-biotite matrix. This mineralised unit can be traced for 100 metres along strike and is persistent in broken outcrop over several kilometres.

The Qeqertarssuaq/Marmorilik Formation boundary is gradational (Fig. 3.6). The upper quartzitic/semipelitic units of the Qeqertarssuaq Formation grade upwards and become interbanded with, 30 cm - 1m thick, siliceous dolomite beds of the Lower Marmorilik Formation.

### 3.3.2 Marmorilik Formation.

Much work has been carried on limited parts of the internal stratigraphy of the Marmorilik Formation on the Black Angel Mountain (Elder, 1967; Myers, 1973; Gannicott, 1977-1980; Nicholls, 1980-1984; Harris, 1985), Uvkusigsat and Agpat Island (Della Valle, 1976 & 1977), Agpat Island (Gannicott, 1976 & 1977). Black Angel Mountain 1977-1980. Magdlak 1979), Marmorilik Plateau and South Lakes area (Harris, 1981-1985). Regional appraisals of the Marmorilik Formation

Give  
 name X  
 1976 unit  
 1977 unit

## Figure 3.7 Qeqertarsuaq Formation and Lower Marmorilik Formation

### Qeqertarsuaq Formation

A) North dipping quartzites of the basal Qeqertarsuaq Formation, with flattened symmetrical ripples on the upper bedding surface indicating correct way-up. The southerly granodioritic basement is in the background. Location 233 Peak 915, South Lakes area. Hammer for scale on upper bedding surface.

B) Interbanded actinolite schists (dark) and dolomitic marbles of the Qeqertarsuaq Formation. The actinolite bands develop an F1 shear fold that has been rotated and now lies in an upright position. Location 842. 1085 Peak. Scale bar 50cm.

### Unit 1 Cherty Dolomitic Marbles

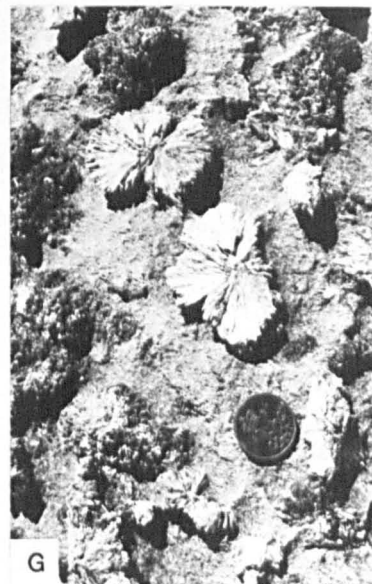
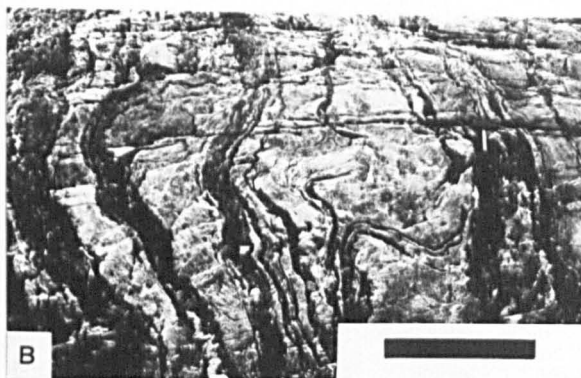
C) Massive siliceous unit, interbanded with dolomitic marbles, boudinaged into large rods. The boudinage has caused irregular folding within the dolomitic bands. Location 46. Tassiusaq.

D) Graded scapolite-bearing units composed of randomly orientated scapolite prisms in a dolomitic matrix. The scapolite decreases upwards indicating a vague relict 'way-up'. Location 9. South Lakes area. Pencil for scale.

E) Thin, folded, quartzitic units interbanded with massive dolomitic marbles. Location . South Lakes area. Hammer for scale.

F) Tremolite rosettes replacing dolomite and combining to form massive tremolitic units. Location 41b. South Lakes area. Lens cap for scale.

G) Close up of undeformed tremolite rosettes held in a dolomitic matrix. Location 7. South Lakes area. Krone (size of a 10p) for scale.



stratigraphy have been produced by:- Hendersen and Pulvertaft (1967), Garde (1978), J. Pedersen (1979), F.D. Pedersen (1980a), King (1981).

The new tectono-stratigraphy erected for the Marmorilik Formation is depicted in figures 3.2 & 3.5. Rinkian tectonism has caused large variations in thickness within the Formation, between 500 and 1800 metres, which create problems of map unit correlation (Fig. 3.5).

The Marmorilik Formation has been subdivided into the Lower, Middle and Upper Marmorilik members (Fig 3.2). The Lower Marmorilik member rests with a sheared contact on the Qequeratarssuaq Formation and consists of siliceous dolomite marbles (Unit 1) and massive dolomitic marbles (unit 2). The lower member outcrops in the southern Marmorilik area (Figs. 3.1 a & b) and the Magdlak Peninsula. The Middle Marmorilik member (unit 3) occurs as a 60-80 metre thick unit (Fig. 3.2) in the South Lakes cliffwall, mid-Marmorilik Plateau and Tributary cliffwall (Fig. 3.1). It is a highly tectonised graphitic calc/dolomite marble succession that lies with a thrust contact above the lower Marmorilik member. The Upper Marmorilik member consists of three map units that outcrop in the northern Marmorilik Plateau and the Black Angel mountain (Fig. 3.1). It is dominated by coarse calcitic marbles (unit 4) overlain by calcitic/dolomitic marbles (unit 5) and dolomitic marbles with calcite (unit 6).

### **Unit 1. Siliceous Dolomitic Marble**

This unit is up to 250 metres thick (Fig. 3.5 & 3.7h) and is the least deformed unit in the Marmorilik Formation. It consists of an interbedded sequence of white-light grey weathering, massively bedded, dolomitic marbles with alternating interbands of tremolitic dolomite marble, scapolitic dolomite marble (Fig. 3.7d), coarsely recrystallised quartz, and fine grained semipelites. The quartz bands, up to 1 metre thick, are totally recrystallised and deformed in asymmetric folds (Fig. 3.7e),

pinch and swell structures and rounded to ellipsoidal boudins (Fig. 3.7c). Seen in isolation the latter could be mistaken for conglomeratic material. Massive white-light green tremolite and actinolite bands, up to 10 metres thick, occur on the southern Marmorilik Plateau and in the South Lakes area. These bands are concentrated towards the base of the unit and contain coarse, up to 10 cm, tremolite and actinolite rosettes (Fig. 3.7f & g) that interlock to form massive bands containing interstitial coarsely recrystallised quartz and minor dolomite.

Unit 1 contains light brown to black weathering semipelitic bands, up to 10 metres thick, (Fig. 3.1). They consist of fine grained, 0.01-0.5 mm, quartz with subordinate albite with a granoblastic to slightly elongate crystal form parallel to a phlogopite/graphite foliation. The graphite occurs as xenoblastic and platy grains along the foliation planes.

Laterally discontinuous impure, silty, graphitic, grey dolomitic marble occurs within the siliceous dolomite. This graphitic dolomite is 0-15 metres thick (Fig. 3.7 h) and contains coarse grained, 2.5 mm, embayed and anhedral calcite and quartz domains in a finer grained, up to 0.2 mm, dolomitic matrix (Fig. 5.4a & b). The dolomite matrix shows an elongation in the crystal fabric parallel to a phlogopite and graphite foliation in which grains exhibit lobate and sutured boundaries. Minor fine grained pyrite, up to 0.2 mm., overgrow the coarse calcite domains.

The top of unit 1 is often marked by a distinctive semipelite band (Fig. 3.7h). This is faulted out in the western South Lakes area and Marmorilik Plateau along an early D1 extension fault (Fig. 3.5).

## **Unit 2. Light Grey Dolomitic marble**

Unit 2 is the upper unit of the Lower Marmorilik member (3.2). It rests conformably on the upper semipelite of unit 1 in the Tributary area and with an extensional fault contact on the siliceous dolomites in the South Lakes area (Fig. 3.5). In the Western Marmorilik Plateau unit 1 is absent and unit 2 is thrust directly onto the basement gneiss (Fig. 3.5).

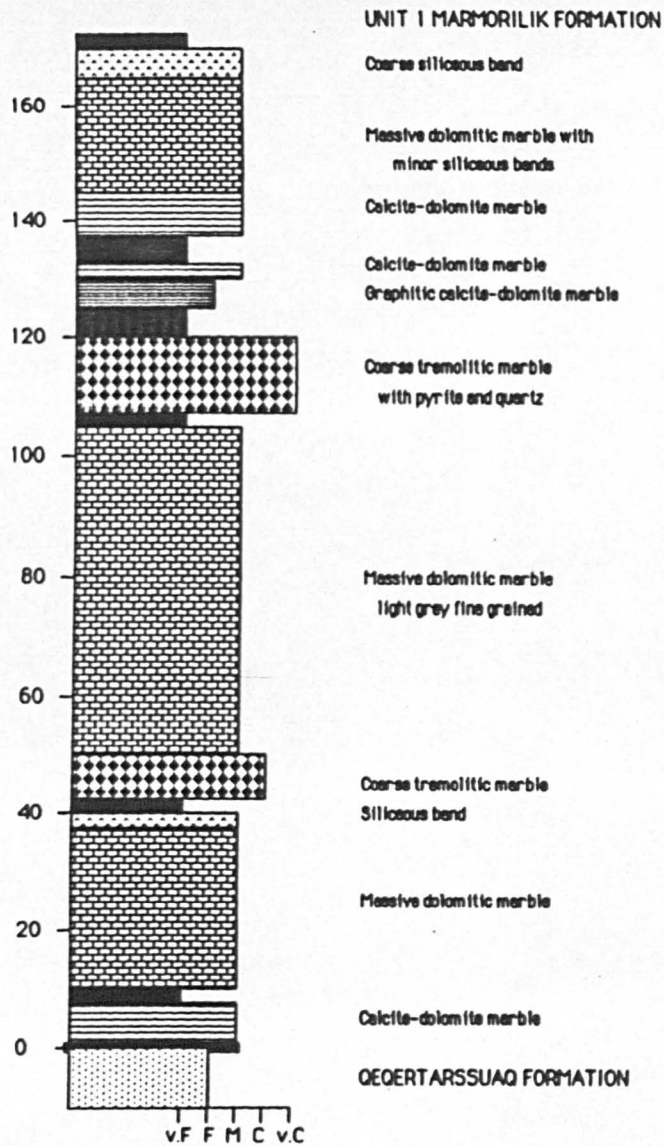


**Figure 3.7h** litho-log of Unit 1, Marmorilik Formation

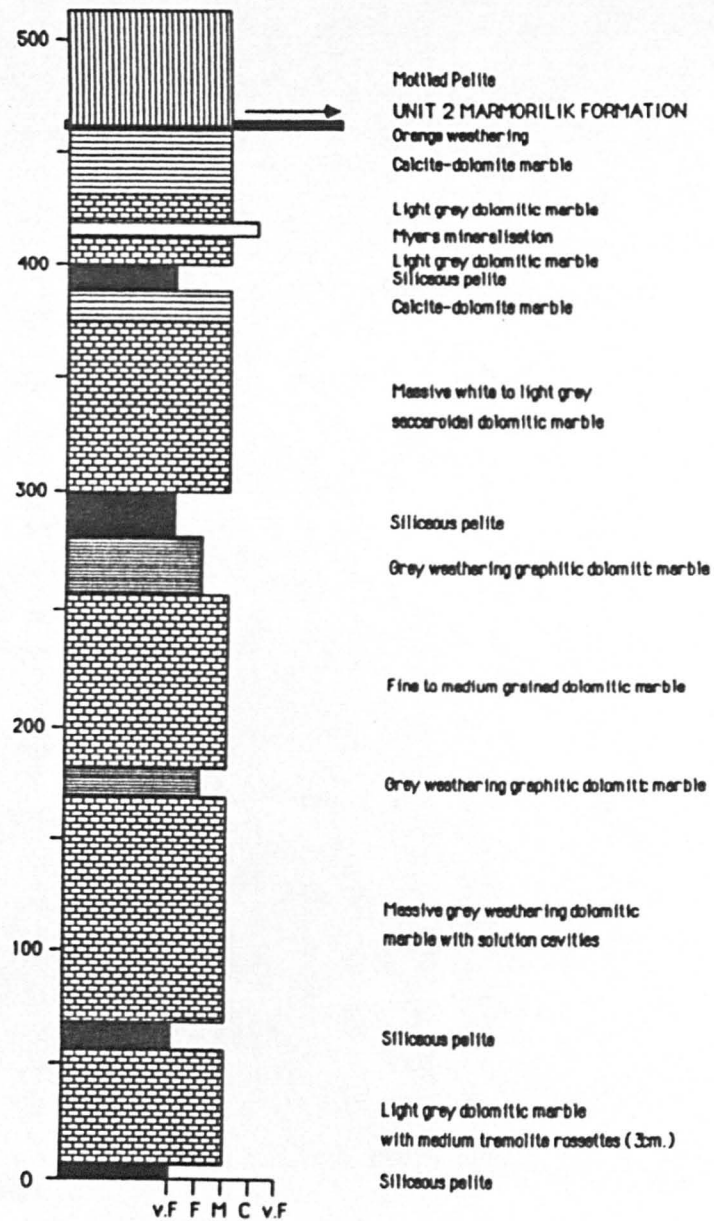


**Figure 3.8i** litho-log of Unit 2, Marmorilik Formation

### Figure 3.8 Unit 2 Massive Dolomite marbles.

A) A view looking northwards from location 39 of the lower South Lakes cliffwall, showing the massive dolomitic marbles of Unit 2, Marmorilik Formation. The dolomites are interbanded with pelitic schists (foreground).

B) Foliated silty, graphitic, and siliceous dolomitic marbles. The siliceous dolomites are transposed into thin lenses and cross-cut by a D3 shear zone. Location 39. South Lakes area. Lens cap for scale.

C) Interbanded calcite-pelite rhythmite ('mottled pelite'). The rhythmite shows sub-vertical banding, with low angle, north dipping, extensional cleavages parallel to pencil. Location 643. Nunngarut zone. Map board for scale.

D) Photomicrograph of 'mottled pelite'. Polycrystalline quartz bands ( $S_1$ ) are interbanded with phlogopitic micaceous units. Crenulated  $S_2$  fabrics develop the V shaped wedge in which pyrite sub-hedra are formed. Thin section 460a. Nunngarut zone. Scale bar 500 $\mu$ .

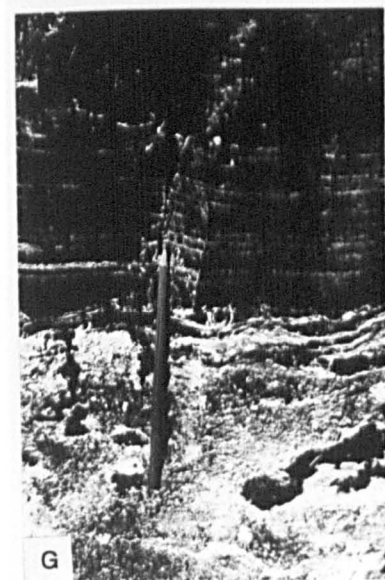
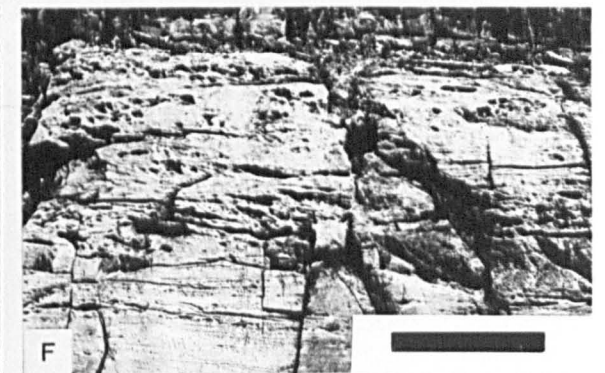
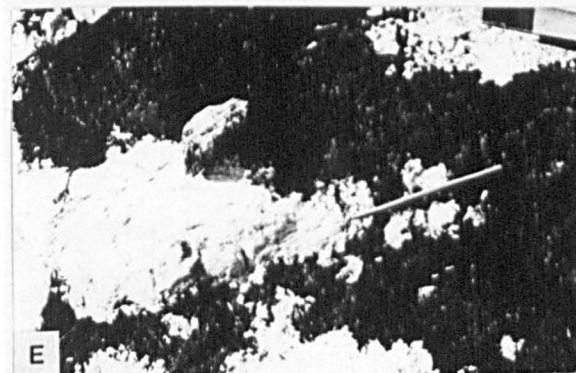
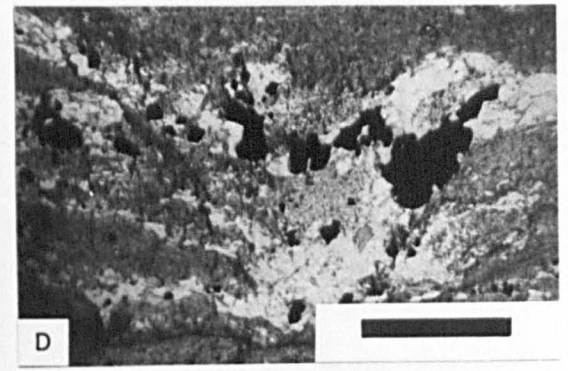
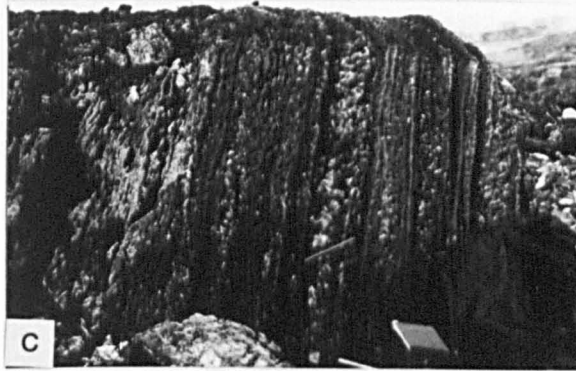
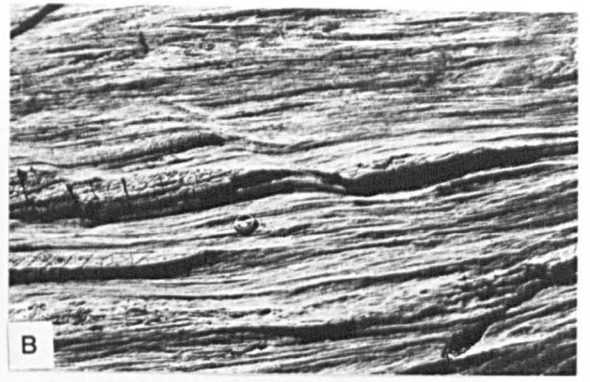
E) Photograph of coarsely recrystallised sphalerite hosted in white, fragmented, dolomite marble. Location 618. CSL 12 showing. South Lakes Glacier. Pencil for scale.

F) Massive foliated dolomite marble containing large ellipsoidal solution vugs. Location 796. Magdlak Peninsula. Scale bar 1.5 metres.

G) Mylonitic, laminated, siliceous unit (Dark) overlying a dolomite cataclastite (crush rock). A sharp, sheared contact is developed between the units. Location 23. North of South lakes cabin. Pencil for scale.

H) Thin pyritic, with minor sphalerite, bands (mid-grey) interbanded with folded dolomitic marble (light grey). Location 266. South Lakes area. Width of photo 1 metre.





Unit 2 is up to 230 metres thick (Fig. 3.2) and composed of buff weathering light grey to white, medium grained, saccharoidal dolomite marbles (Figs. 3.8a, d & i). These contain minor siliceous interbeds, which are more prominent towards the base. Semipelites (Fig. 3.8c & d) and thin calcite and calcite dolomite bands, with disseminated and sub-economic, massive lead-zinc mineralisation (Fig. 3.8e & h), are interbanded with the massive dolomites.

Unit 2 contains light grey massive dolomite marbles near its base, with minor siliceous interbeds and tremolite rosettes, up to 3 cm (Fig. 3.8i). On the Magdlak Peninsula these rocks contain large circular to ellipsoidal solution cavities (Fig. 3.8f), 1-20 cm. long, parallel to the cleavage, in which coarse, >5 mm, sparry dolomite and idioblastic pyrite, 2 mm, are preserved. The massive fine-medium grained dolomite marble is overlain by a 0-5 m thick semipelite bed above which a thick sequence of, up to 80 m, white saccharoidal phlogopitic dolomite marble is present (Fig. 3.8a & i). These are medium to coarse grained massively bedded units containing a strong phlogopitic foliation. Disseminated pyrite, sphalerite and coarse grained galena generally occur in D1 and D2 fold hinge zones (Fig. 3.8h).

The white saccharoidal dolomite is overlain by a graphitic dolomite and a 10 metre thick semipelite (Fig. 3.8i). Randomly orientated, sometimes rotated, scapolite grains, up to 3cm, are common in the graphite marble (Fig. 5.3e & f). The massive homogeneous medium to dark grey, phlogopite, graphite, pyrite dolomitic marble sequence above this semipelite contains interbeds of calcite marble, which in the South Lakes area are up to 50 metres thick, and orange weathering calcite-dolomite marbles up to 15 metres thick. It is this upper massive dolomitic marble which hosts the most important lead-zinc mineralisation in the Lower Marmorilik Formation (Fig 3.8e & 6.3).

### Figure 3.9 Unit 3 Middle Marmorilik Formation.

A) A view of the eastern Agfarlikavsá cliffwall showing the location of the thin unit of the Middle Marmorilik Formation (M) above a D2 tectonic slide (dotted line). Height of cliff 1050 metres.

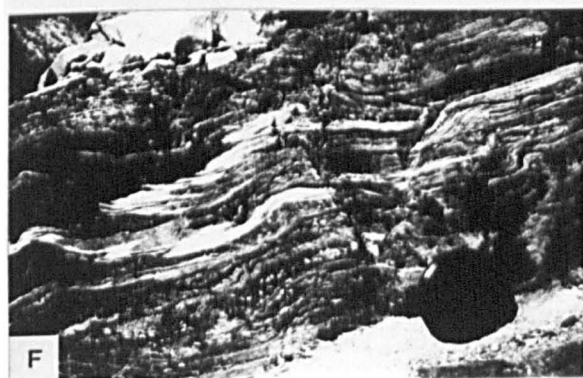
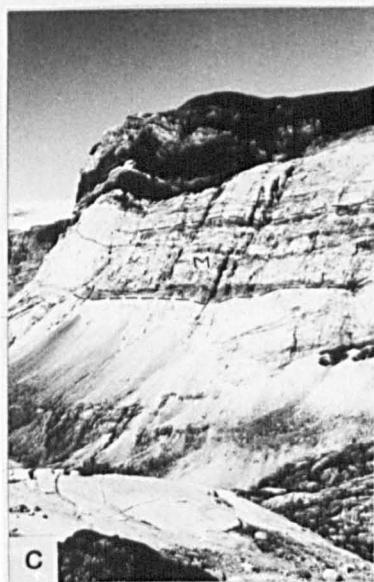
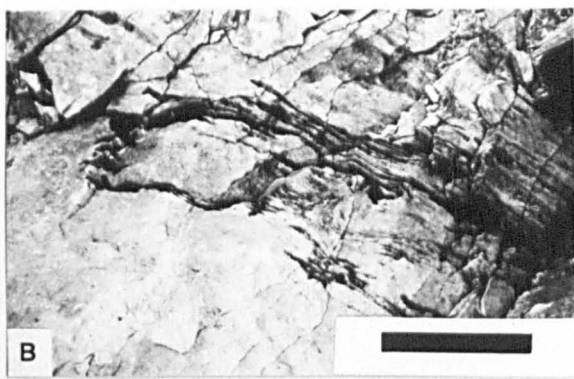
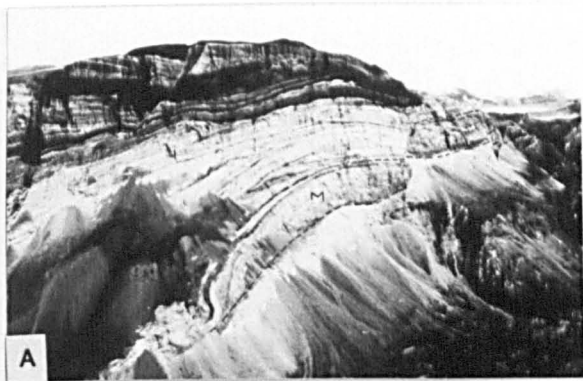
B) Isoclinally folded graphitic bands within white saccaroidal dolomite. Location 75. North of Marmorilik township.

C) Western South Lakes cliffwall showing the grey weathering interbanded graphitic calc/dolomites and calcite/dolomite marbles of Unit 3 (M). The upper and lower unit contacts are marked by tectonic slide zones (dashed). Height of cliff 500 metres.

D) Mylonitic graphitic calcite/dolomite marble. Tectonic slide zone at Location 628 near the South Lakes Glacier. Lens cap (centre top) for scale.

E) Thin interbanded calcite dolomite marbles. The calcite marble shows recessive weathering. Location 223. Northern Big South Lake. Compass clinometer for scale.

F) Isoclinally folded graphitic calcite/dolomite marble. Location 629c. North of the South Lakes Glacier. Lens cap for scale.



### **Unit 3. Graphitic Calcite-Dolomite marble**

This unit is the most easily recognised in the Marmorilik region, due to its distinctive interbanded blueish-grey to white resistant weathered appearance (Fig. 3.9a & c). It has an outcrop width of up to 100 metres (Fig. 3.2) and is bounded by two major tectonic slide zones (Fig. 3.5). Contraction faulting and transposition of the banding are present within the unit.

The base of the unit is marked by a few metres of indurated mylonitised graphitic calcite-dolomite marbles (Fig. 3.9d) with elongate coarse calcite and quartz domains. Similar mylonite zones occur at spaced intervals, 3-10 metres, through Unit 3 and are associated with highly sheared and isoclinally folded shear fabrics (Fig. 3.9f).

In the less strained zones, massive calcite, dolomite (Fig. 3.9e) and strongly foliated graphitic calcite-dolomite marbles (Fig. 3.9b,d & f) are interbanded on a metre scale. The calcite-dolomite marbles contain irregular-granoblastic and polygonised coarse grained quartz and calcite domains. Fine grained graphite and phlogopite folia anastomose around these domains which lie in a fine grained, dynamically recrystallised matrix of elongate dolomite (Fig. 5.4a & b).

Disseminations and streaks of fine to coarse grained sphalerite and galena lie parallel to the foliation and occur in sheared form throughout Unit 3. The greatest concentrations occur in the MP 5 zone (Fig 6.1).

### **Unit 4. Coarse Calcite Marble**

The coarse calcite marble is the lowest and dominant unit of the Upper Marmorilik member (Fig. 3.2). It varies in thickness from 110 metres in the Tributary area to 240 metres in the Western Marmorilik Plateau (Fig.3.5). It forms the slightly recessive creamy white weathering upper South lakes and Agfardlikavsá Fjord cliffwalls (Figs. 3.9a & 3.10a). that host the stratabound zinc-lead-iron-silver Black Angel deposits. For a

### Figure 3.10 Upper Marmorilik Formation Calcitic Marbles.

A) Field photograph of the northern Marmorilik Plateau cliffwall showing massive white calcitic marbles interbanded with pelitic schists and dolomites. The Upper Marmorilik Formation marbles (Unit 5) are overlain by pelitic schists of the Nukevsak Formation (Dark grey).

B) Drill core from the Black Angel Mountain showing thin irregular to wispy anhydritic bands (light grey) within coarse calcitic marbles. Lens cap for scale.

C) Massive and layered one found within fluoritic (left core) coarsely recrystallised calcitic marble. Drill Hole V 118. Lens cap for scale.

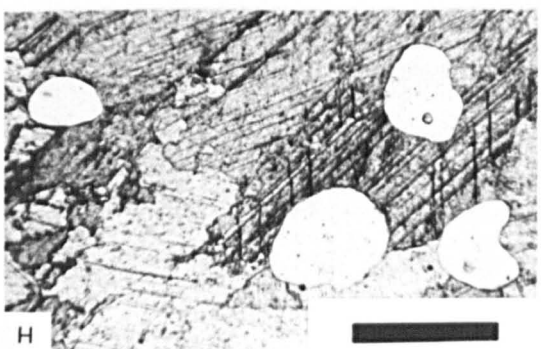
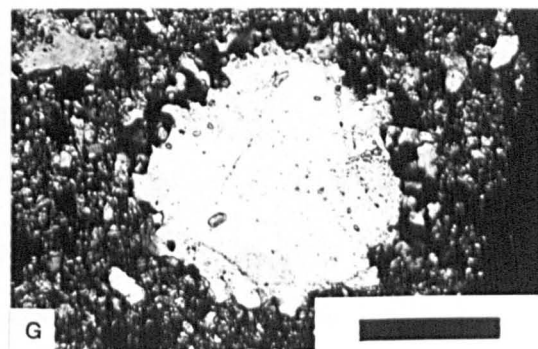
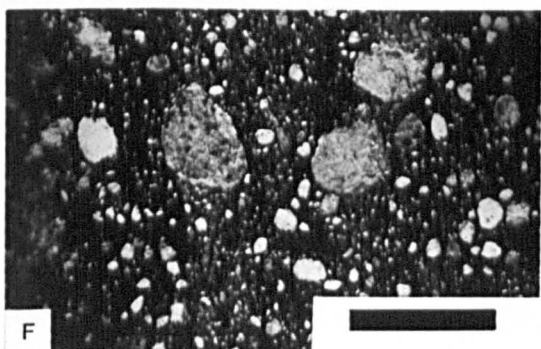
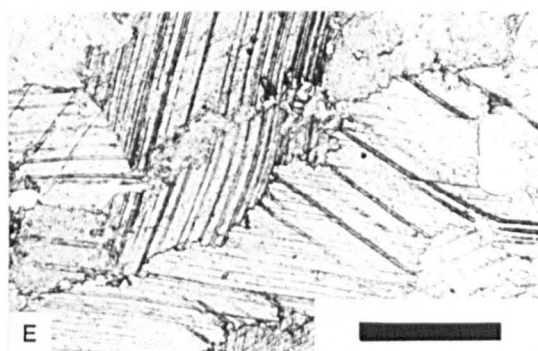
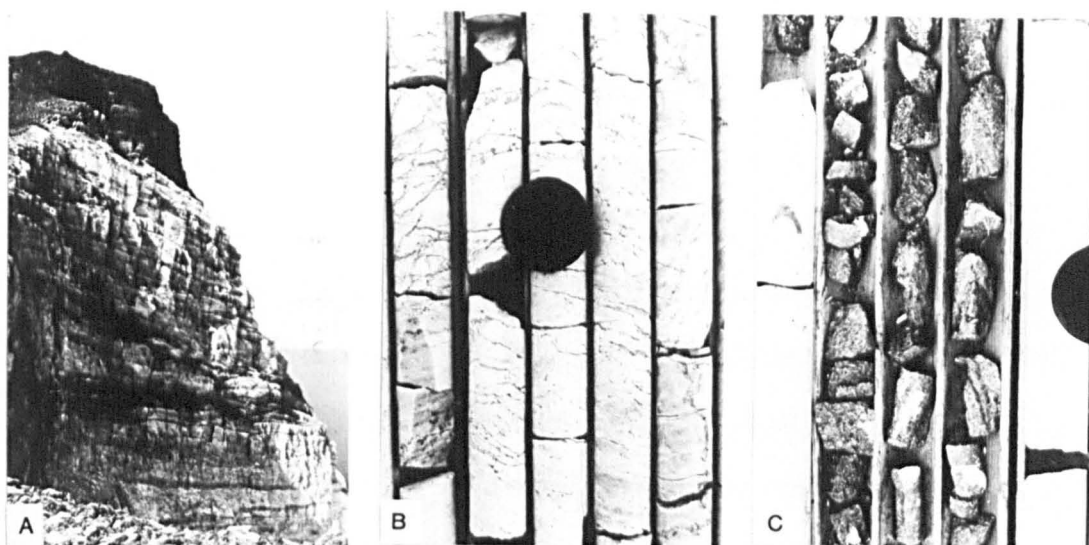
D) A slab of phlogopitic foliated calcite marble. The early  $S_1$  foliation is crenulated by a later  $S_2$  fabric (left - right). Tributary cliffwall.

E) Photomicrograph of coarsely recrystallised calcitic marble. The coarse marble grains show serrated grain boundaries and slightly bent annealing twins. Thin section 391. Northern Marmorilik Plateau. PPL. Scale bar 500 $\mu$ .

F) Photomicrograph of a quartz calcite mylonite. The large, rounded, highly strained quartz eyes are held in a fine grained, dynamically recrystallised calcitic matrix (Black). Thin section 395a. Northern Marmorilik Plateau. XPL. Scale bar 500 $\mu$ .

G) Close up of a quartz fragment in (F). The centre of the grain is unstrained with finer grained sub-grains forming at the quartz margins. XPL. Scale Bar 160 $\mu$ .

H) Quartz eyes set within coarsely recrystallised calcitic marble. Thin section 391. Northern Marmorilik Plateau. PPL. Scale bar 500 $\mu$ .



more detailed review of <sup>the</sup> deposits' stratigraphic setting see section 6.5.4.

This unit is quite monotonous, consisting of thick sequences of cream-light orange weathering massively bedded, coarsely recrystallised calcite marbles in which a strong phlogopitic foliation is often developed (Figs. 3.10a & c). Unit 4 also contains 1-30 metre thick chert and semipelite bands (Fig. 3.10a), anhydritic (Fig. 3.10b) and gypsiferous beds, up to 30 cm thick, and salmon pink manganese-rich calcite marbles.

Calc-silicate mylonites occur in bands up to 1.5 metres wide. These contain sub-rounded to tabular quartz fragments ('quartz eyes')(Fig. 3.10f-h), up to 2mm in diameter. These occur as indented, sutured, and highly strained grains with undulose extinction, cataclastic fracturing and sub-grain development (Fig. 3.10g). The quartz eyes are set in a fine grained, polygonal calcite matrix (Fig. 3.10f), which exhibits relict dynamically recrystallised textures.

The top of unit 4 is strongly sheared in the Western Marmorilik Plateau and the Tributary cliffwall where it is overthrust by the Nukavsak Formation and Unit 6, respectively (Fig. 3.5). In the South Lakes cliffwall, interbanded calcite and dolomite marbles of unit 5 conformably overlie unit 4 (Fig. 3.5).

### **Unit 5. Interbanded Calcite and Dolomite marbles**

This unit is up to 170 metres thick and restricted to the South Lakes cliffwall and the middle Marmorilik Plateau (Fig. 3.5). It is made up of cm-m interbands of granoblastic, coarse, calcite marbles and finer grained, white to light grey, saccharoidal dolomite marbles (Fig. 3.10a & 3.11h). The calcite marble occurs in early extension veins that are subsequently deformed and transposed within the dolomite marbles. Minor, 1mm, phlogopite and biotite crystals define a weak foliation. Metre thick, mylonitised, semipelite and chert bands are tectonically interbanded with the marbles.

## Figure 3.11 Nukavsak and Upper Marmorilik Formation

### Nukavsak Formation

A) Field photograph of the northern Marmorilik Plateau cliffwall showing the Upper Marmorilik Formation marbles are overlain by pelitic schists of the Nukavsak Formation (Dark grey). Height of cliff 200 metres.

B) Drill core of graphitic, biotitic pelitic schists of the Nukavsak Formation. Minor recrystallised calcite forms in boudinaged lenses. Drill hole V 216.

C) Folded and crenulated biotite schists of the Nukavsak Formation.  $S_1$  cleavage runs left-right. Location 408. Northern Marmorilik Plateau cliffwall. Pencil for scale.

D) Photomicrograph of  $S_2$  crenulated graphitic, biotitic, siliceous pelitic schists of the Nukavsak Formation. The  $S_1$  fabric (left-right) contains quartz ribbons. Thin section 9. Tributary cliffwall.

### Upper Marmorilik Formation

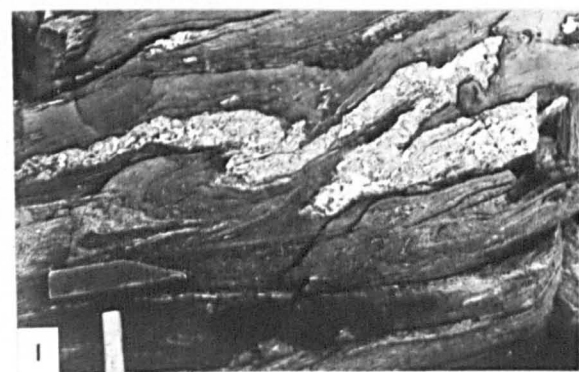
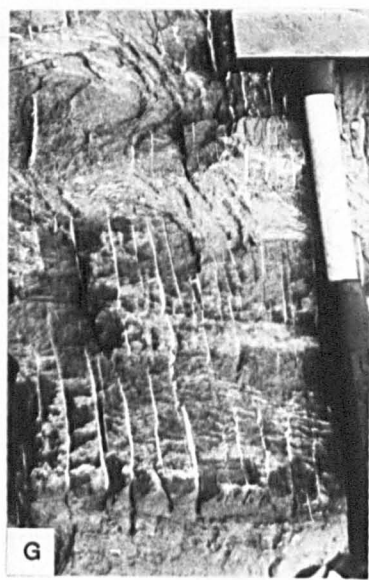
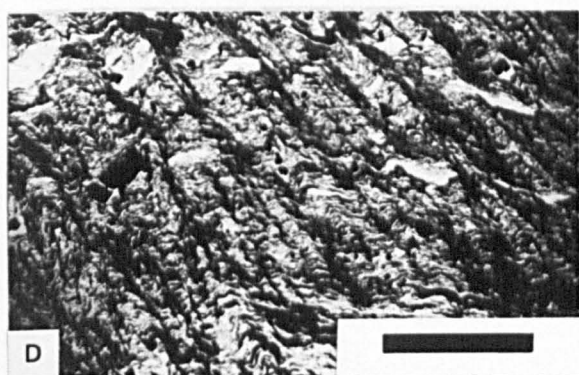
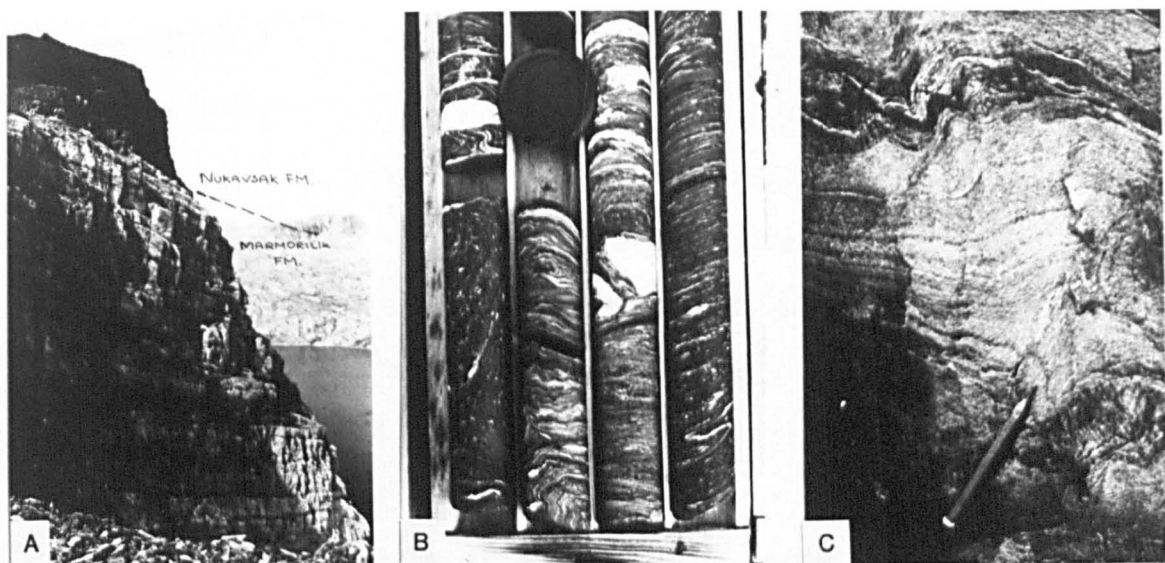
E) Grey banded marbles of unit 6. Dark grey dolomitic marbles contain an en-échelon (Imbricated) array of coarsely recrystallised calcite filled extension fractures (D1 extension veins?). Location. Drift 23, Black Angel mine. Ruler for scale.

F) Grey banded marble. Coarse calcitic marble and fine grained dark grey dolomitic marble developing in foliated bands. Location. Drift 23, Black Angel mine. Ruler for scale.

G) Calcite filled fractures in silty graphitic marble of Unit 6 Marmorilik Formation. Location 786. Black Angel Mountain.

H) Interbanded buff weathering dolomitic and recessive weathering calcitic marble. Location 745. Black Angel Mountain. Hammer for scale.

I) Coarsely recrystallised siliceous band (D1 extension vein?) within graphitic dolomitic marble of Unit 6. Location 747. Black Angel Mountain.



## **Unit 6. Grey Banded Marbles**

This unit is restricted to the Black Angel Mountain plateau and is the uppermost unit in the Marmorilik Formation. It consists of a 0-120 metre thick sequence of interbanded mid-dark grey, fine grained, graphitic dolomite marbles (Fig. 3.11e,f & i) and coarse grained calcitic marbles. The semipelite content increases upwards as the Marmorilik Formation grades into the basal Nukavsak Formation.

### **3.3.3 Nukavsak Formation.**

The Nukavsak Formation outcrops as a tectonic slide block on the top of the Marmorilik and Black Angel Plateaux (Fig. 3.5 & 3.11a). It consists dominantly of monotonous quartz-plagioclase-biotite-graphite schists (Fig. 3.11b) with very strong slaty and crenulation cleavages (Fig. 3.11c & d). Intercalations of grey banded marbles and highly sheared graphitic schists occur near the base. The schists show elongate quartz grains that are aligned parallel with the foliation. On the Black Angel Plateau a 5-30 metre thick quartz-biotite-graphite-pyrrhotite-pyrite schist occurs about 100 metres above the base of the Formation, that is characterised by alternating bands of coarse grained quartz and medium to coarse grained pyrrhotite and pyrite.

## CHAPTER 4: The Structure of the Marmorilik Region

### 4.1 Introduction

In the Marmorilik area the Karrat Group is held in an east-west trending, flat lying, synformal, trough that is fault bounded to the north and south by upstanding basement blocks (Figs 4.1a, b & c). Complexly refolded, east-west trending, folds and flat lying contraction faults are present in the supracrustal sequence. The stratigraphy is inverted along the northern margin where basement gneisses are infolded and thrust over the Karrat Group supracrustals. The southern margin of the supracrustal belt is structurally the correct way up and is marked by an extensional mylonitised detachment surface.

This study demonstrates that previous detailed structural studies by Garde (1978) and Pedersen (1980a & b) were inadequate. Garde (1978) postulated that the main deformation events were an early recumbent fold phase followed by thrusting and the formation of a major open synform. Pedersen (1980a & b) established that three phases of deformation had affected the Karrat Group in the Marmorilik region, but confused the relative timing of the tectonic events and failed to recognise that the structures evolved in linked tectonic systems. In both of these previous studies little attention was paid to the kinematics of the deformation. As a consequence, this thesis completely re-evaluates the structural evolution of the Marmorilik area. Detailed structural analysis was carried out at key locations with particular attention focussed upon the kinematics of the structural history.

The area was mapped at scales between 1:5000 and 1:20000. Figure 4.1a is a 1:20,000 scale map compiled from two field seasons of structural mapping which incorporates some earlier data from studies by Garde (1978) and Pedersen (1980a). Regional and mine mapping of the area was undertaken in an attempt to deduce a tectonic history of the Black Angel Deposits. Structural mapping was generally restricted to the supracrustal units. Limited traverses into the basement and along the

FIGURE 4.1b Geological cross-section through South Lakes area and Tributary cliffwall

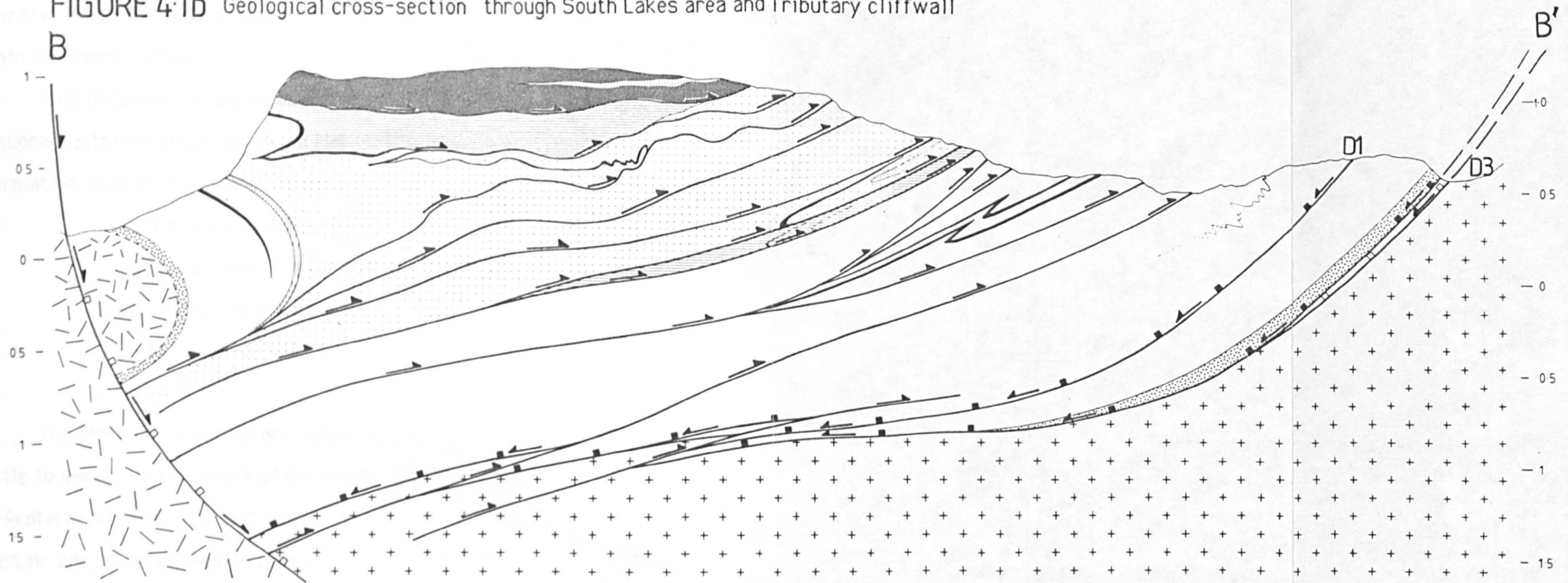
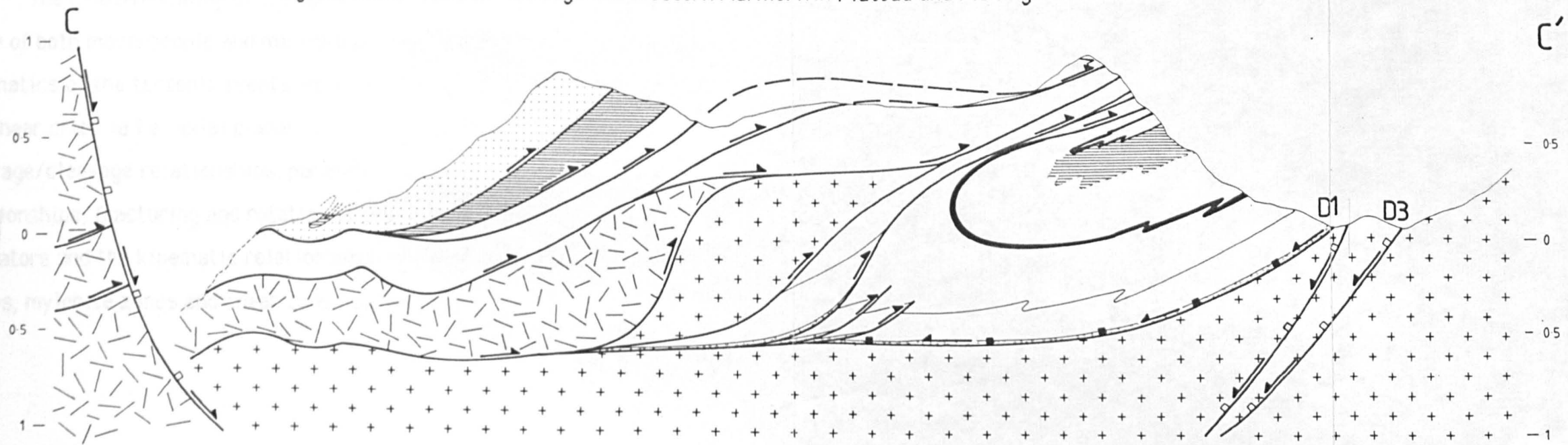


FIGURE 4.1c Geological cross-section through the western Marmorilik Plateau and Fishing Lakes cliffwall



KEY AS FOR FIG. 4.1a (vertical=horizontal scale)

and Fig 3.1b

basement-supracrustal contact were made in order to determine the tectonic relationships at these contacts, and also the state of strain and kinematic controls that the basement may have had upon deformation within the Karrat Group.

This detailed remapping has led to a new tectonic interpretation for supracrustal deformation in the Marmorilik area. Four phases of deformation have been defined (Table 4.1):-

- i) Early recumbent phase.
- ii) South verging fold and fault phase.
- iii) Sinistral shear phase.
- iv) Late extension phase.

The first three events are interpreted to be pervasive, polyphase, ductile to semi-brittle deformation events associated with Mid-Proterozoic (Rinkian) tectonism. The last deformation phase, of uncertain age, is an extensional event associated with NNW-SSE oriented dolerite dyke filled faults (section. 2.2.3).

The relative timing of the tectonic events have been defined by a study of both macroscopic and microscopic overprinting relationships. The kinematics of the tectonic events were established by analysing vergence and shear criteria i.e.: axial planar structures, bedding/cleavage and cleavage/cleavage relationships, parasitic fold orientations and relationships, fracturing and rotation of phenocrysts, sense of shear indicators and the kinematic relationships of shear structures (e.g. fault planes, mylonite zones and shear zone boundaries).

Table 4.1: Summary of deformation phases in the Marmorilik area

DEFORMATION EVENT	STRUCTURES FORMED	VERGENCE DIRECTION	ORIENTATION OF STRUCTURES	METAMORPHIC ASSEMBLAË
<b>D1 EARLY RECUMBENT PHASE</b>	EXTENSIONAL FAN SYSTEMS RECUMBENT NAPPE STRUCTURES	NORTH VERGING	DOMINANTLY EAST-WEST	MUSCOVITE-PHLOGOPITE-QUARTZ-DOLOMITE-
<b>D2 FOLD AND SLIDE PHASE</b>	OVERTHRUST NORTHERN BASEMENT SOUTHERLY INCLINED FOLDS. IMBRICATE TECTONIC SLIDES WITH BASEMENT INCORPORATION	SOUTH TO SOUTH EAST VERGING	EAST-WEST TO NORTH-EAST-SOUTH WEST	PHLOGOPITE-BIOTOTE-MYLONITE
<b>D3 SINISTRAL SHEAR PHASE</b>	TRANSTENSIONAL HALF-GRABEN BASIN BASEMENT SHEAR ZONES EN-ECHELON FOLDS EN-ECHELON SINISTRAL SHEARS	SINISTRAL SHEAR	ENE-WSW BOUNDING FAULTS WNW-ENE EN-ECHELON FOLDS N-S SYNTHETIC SHEARS	TREMOLITE-SCAPOLITE-ACTINOLITE-PHLOGOPITE-MUSCOVITE-QUARTZ-DOLOMITE
<b>D4 EXTENSION PHASE</b>	DOLERITE DYKE FILLED FAULTS D3 REACTIVATED SILLS	O <sub>1</sub> VERTICAL O <sub>2</sub> HORIZONTAL O <sub>3</sub> HORIZONTAL	N-S DYKES NE-SW SILLS	MINOR CONTACT METAMORPHISM

## 4.2 D1 Early Recumbent phase deformation

### 4.2.1. Introduction.

This deformation phase is a progressive ductile deformation in which both southerly extensional and northerly compressional tectonic fabrics are developed (Fig 4.2). All kinematic indicators suggest that a northerly tectonic transport direction occurred during this deformation phase.

D1 structures are best preserved in the southern Marmorilik area (Fig. 4.2). Overprinting and transposition of D1 fabrics by later tectonic events has taken place in the central and northern Marmorilik areas.

### 4.2.2 Southern extensional domain.

The southern extensional domain is characterised by ductile, extensional systems in both the supracrustals and the granodioritic basement massif. The domain is sub-divided into four tectono-metamorphic packages (Fig. 4.4) :- a) Crystalline Granodiorite basement b) Mylonitic granitoid gneiss c) Mylonitic basement/supracrustal decollement zone d) ductile to semi-ductile extended supracrustal cover. These four packages exhibit many similarities to those of the Cordilleran metamorphic core complexes (Coney, 1980; Naruk, 1986).

Six structural sub-areas have been classified in the southern Marmorilik region. The orientation of four tectonic packages in the sub areas are represented stereographically in Figure 4.17. The sub-areas are (Fig.4.3):- i) Ark area. ii) South Lakes area. iii) Southern 'A' Fjord and eastern Plateau. iv) Western Plateau v) Peak 1085. vi) Uvkussigat (Nunarssugssuaq).

An extended basement/cover contact is present in sub areas (i)-(iv), where relatively consistent structural orientations occur. An overturned basement/cover contact is present in sub areas (v) and (vi), and is associated with complex extensional and contractional structures. The four tectono-metamorphic packages of sub-areas (i)-(iv) are as follows:-

### **a) Granodioritic basement**

The undeformed granodiorite (3.2.2) consists of alkali and plagioclase feldspar phenocrysts in a quartzo-feldspathic matrix with accessory hornblende, muscovite and biotite (Fig. 3.4).

### **b) Granitoid Gneiss**

Discrete curvilinear, extensional, north-side down, ductile shear zones occur in the granodiorite. They increase in width and frequency towards the basement contact (Figs. 4.1 b & c.). The shear zones consist of spaced foliation planes composed of biotite, muscovite and hornblende, which wrap around elongate, fractured and boudinaged feldspathic porphyroclasts (Fig. 4.5a, c, d & e.). The S1 foliation planes contain an extensional crenulation cleavage (Fig. 4.5b) (Watkinson, 1984; Lister and Snoke, 1984), that lies parallel to fractures within the elongate porphyroclasts (Fig. 4.5c).

Below the basement/supracrustal contact the shear zones combine to form a 100 metre wide zone of granitoid gneiss. The deformation is very intense at the contact, and the feldspathic porphyroclasts are so highly extended as to be almost unrecognisable (Fig. 4.5e). The porphyroclasts are set within a dominantly mylonitised matrix, that locally becomes phyllonitic, with up to 60% phlogopite. Very strong north-south trending mineral stretching lineations occur on schistosity planes.

### **c) Mylonitic decollément**

The basement/supracrustal contact is a sharply defined feature (Figs. 4.4 & 4.5a), which is marked by a low angle, schistose to mylonitic zone (Fig. 4.1 a & b). In places, e.g. the eastern Marmorilik Plateau, lensoidal basement wedges are interleaved with the supracrustal Qeqertarsuaq Formation. The basement lenses are up to 20 metres wide and are bounded on all sides by mylonitised supracrustal fabrics.

The mylonitic zones occur as bands up to 2 metres wide, separated by isoclinally, intrafolially folded calc-silicate units (Fig. 4.5f). The mylonitic foliation intersects the mylonite zone boundaries at an angle between  $85^\circ$  and  $89^\circ$ . Strain within the supracrustals decreases away from the basement contact, with the mylonite zones becoming thinner in the massive quartzites of the Qeqertarssuaq Formation (Fig. 4.8c).

#### **d) Semi-ductile extension of the cover sequence**

Semi-ductile extensional fan systems and recumbent overfolds occur in the extended cover sequence of the southern South Lakes area (Fig. 4.6 & 4.7), but are masked by D2 overprinting in the Fishing Lakes cliffwall and the southern Marmorilik Plateau.

The extensional fan systems consist of discrete, 2-3 metre wide, low angle extension faults (Figs. 4.6 & 4.8a), with planar and ramp-flat geometries (Gibbs, 1984; McClay and Ellis, 1987). The ramp-flat faults form duplexed fault zones that consist of an extensional roof and floor fault or mylonite zone (Fig. 4.8c). These faults bound a series of dolomitic horse blocks (Figs. 4.8f & g.), which are cut by a system of steeply north dipping, 2-15 cm. wide, link faults. En-échélon, south dipping, high angle antithetic faults, hangingwall half-grabens and rollover structures (Hamblin, 1965) occur above listric fault ramps (Fig. 4.6).

In the dolomitic fault blocks asymmetric, northerly verging, inclined to recumbent folds occur (Figs. 4.9). The folds are characterised by curved fold axial planes and doubly plunging periclinal (in some cases reclined) sheath-like fold axes (Fig. 4.7 & 4.9a & c). Folded pinch and swell structures (Fig. 4.9b) are present on the upper fold limbs which indicate a progressively changing stress regime during fold development. Refracting axial planar cleavage (Fig. 4.9f) and quartzitic mullion and rod structures (Fig. 4.9g & h) occur in the northerly inclined folds. The cleavage is flatter to the north and often becomes concentrated

as slip planes or decollément horizons above which recumbent folds are accommodated. The folds increase in magnitude northwards through the supracrustal sequence (Figs. 4.9 & 4.10).

### **Deformation west of Marmorilik**

In sub-areas (v) and (vi) of the Peak 1085 (Figs. 4.10, 4.11 & 4.12) and the Nunarsugssuaq Peninsula (Fig. 4.13), the southerly basement/supracrustal contact is rotated into an upright and then an overturned attitude (Fig. 9.7). Complex refolded deformation fabrics are formed in association with the progressive rotation of the contact in both of these sub-areas.

#### **Sub-area (v) Peak 1085**

On the Peak 1085 (Fig. 4.3 & 4.10), the supracrustals are deformed into a tight, north verging, overturned, 'pinched in', synform between two bulbous, north verging, basement antiforms (Fig. 4.11). The four tectonic-metamorphic packages, associated with extension during the early recumbent phase deformation, are refolded about the synform (Fig. 4.11). Small scale structures such as mylonitic calc-silicates of the Qeqertarsuaq Formation, with intrafolial shear folds and an associated S1 cleavage, are folded by later stage, north verging, coaxial, folds (Fig. 4.12 a & b).

#### **Sub-area (vi) Nunarsugssuaq Peninsula**

On the Nunarsugssuaq Peninsula (Fig. 4.3 & 4.13), the supracrustals lie in a tight to isoclinal, southerly inclined synform bounded to the north and south by basement gneisses. The southern supracrustal/basement contact is marked by a shallow southerly dipping, northerly verging, contractional slide zone. The slide has reactivated an early extension fault and emplaced imbricated, basement gneisses over the Karrat group supracrustals (Fig. 4.13). At the northern contact, basement gneisses are deformed into a south verging, recumbent, tight to isoclinal,

D2 (section 4.3) antiform and pinched in synform pair (Fig. 4.13). These folds extend southwards into the supracrustal units of the Karrat Group, where they are transected by north verging, low angle, contraction faults associated with the northerly directed overthrusting of the basement.

#### 4.2.3 Northern contractional domain.

Large scale compressional structures, such as overturned recumbent nappes with minor low angle contraction faults, dominate the northern Marmorilik area (Fig. 4.2 & 4.14) and are linked to the southerly extensional fault systems by a flat lying, highly sheared, structural zone in the central Marmorilik area (Fig. 4.26 & 6.10).

The northern domain can be subdivided structurally into two distinct sub-areas, that are cut by a D3 sinistral shear zone. The sub areas (Fig. 4.3) are; vii) Marmorilik, Tributary and west Plateau area and viii) Magdlak Peninsula (Fig. 4.18).

Sub area (vii) is dominated by the Black Angel nappe (Fig. 4.14). This major nappe is a refolded, recumbent, isoclinal, synformal anticline. It is an east-west trending, sub-horizontal to gently south dipping, north verging, non-cylindrical structure which has a wavelength of approximately 500 metres and an amplitude of 1-2 km. Strong parasitic folding, with saddle reef and nipple fold accommodation structures (Fig. 4.15a) occur in the tectonically thickened and refolded nappe closure (Fig.4.14). Commonly the limbs are attenuated and transposed by a penetrative axial planar cleavage. Class 2 similar folds lie on the correct way up limbs, whilst Class 3 folds are found on the overturned sheared limbs (Fig. 4.15 & 4.16). The structurally correct way up fold limbs are attenuated and boudinaged. The boudins occur as 'fish mouth' structures (Fig. 4.9e). Quartz is recrystallised in the boudin necks. The overturned fold limbs are sheared out along forelimb and out of syncline tectonic slides (Figs. 4.14 & 6.18) on which phlogopitic mineral stretching lineations occur.

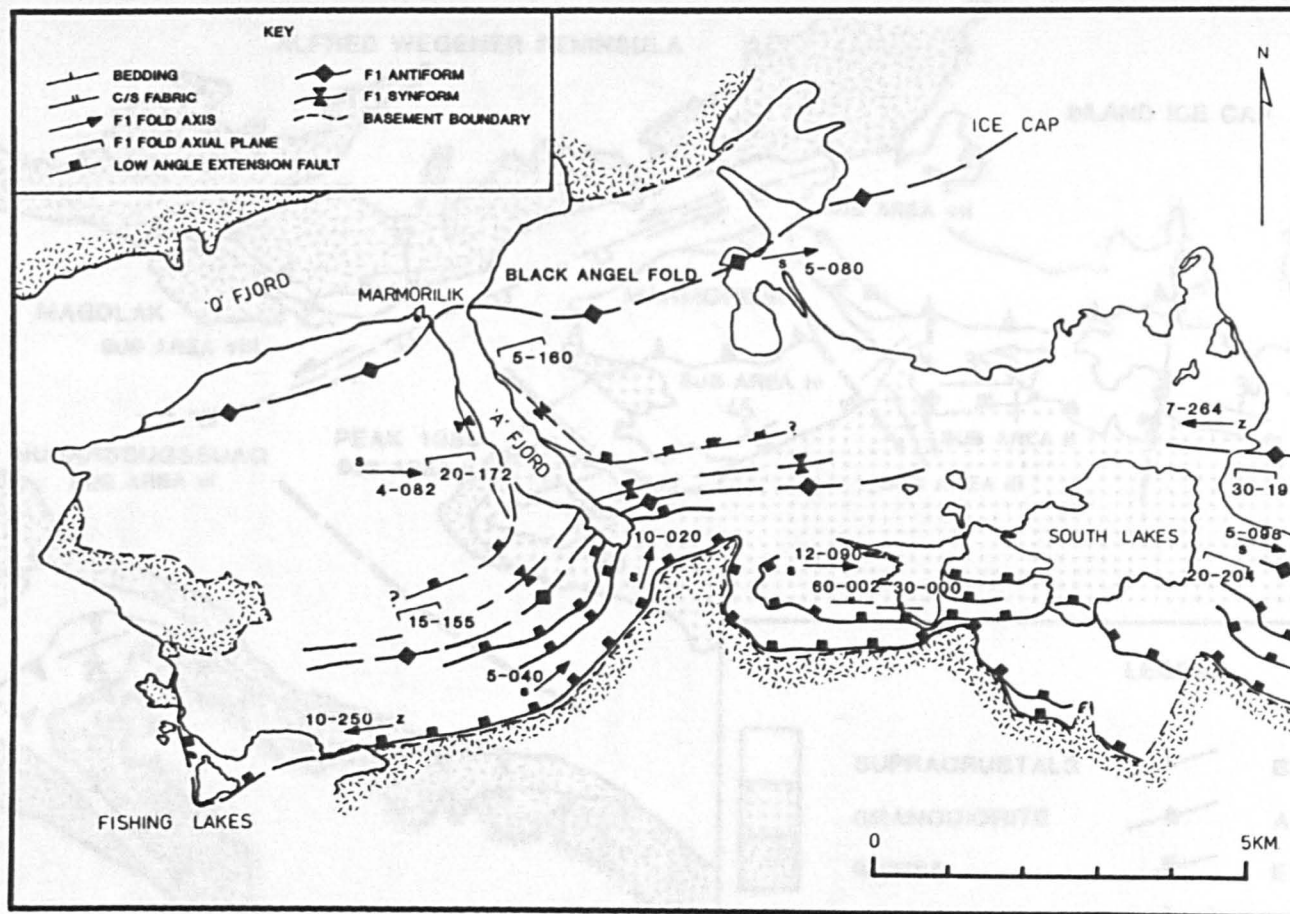


**Figure 4.2** A map of D1 deformation structures in the Marmorilik area.

Figure 4.3 Map showing the D1 homogeneous sub-areas of the study area

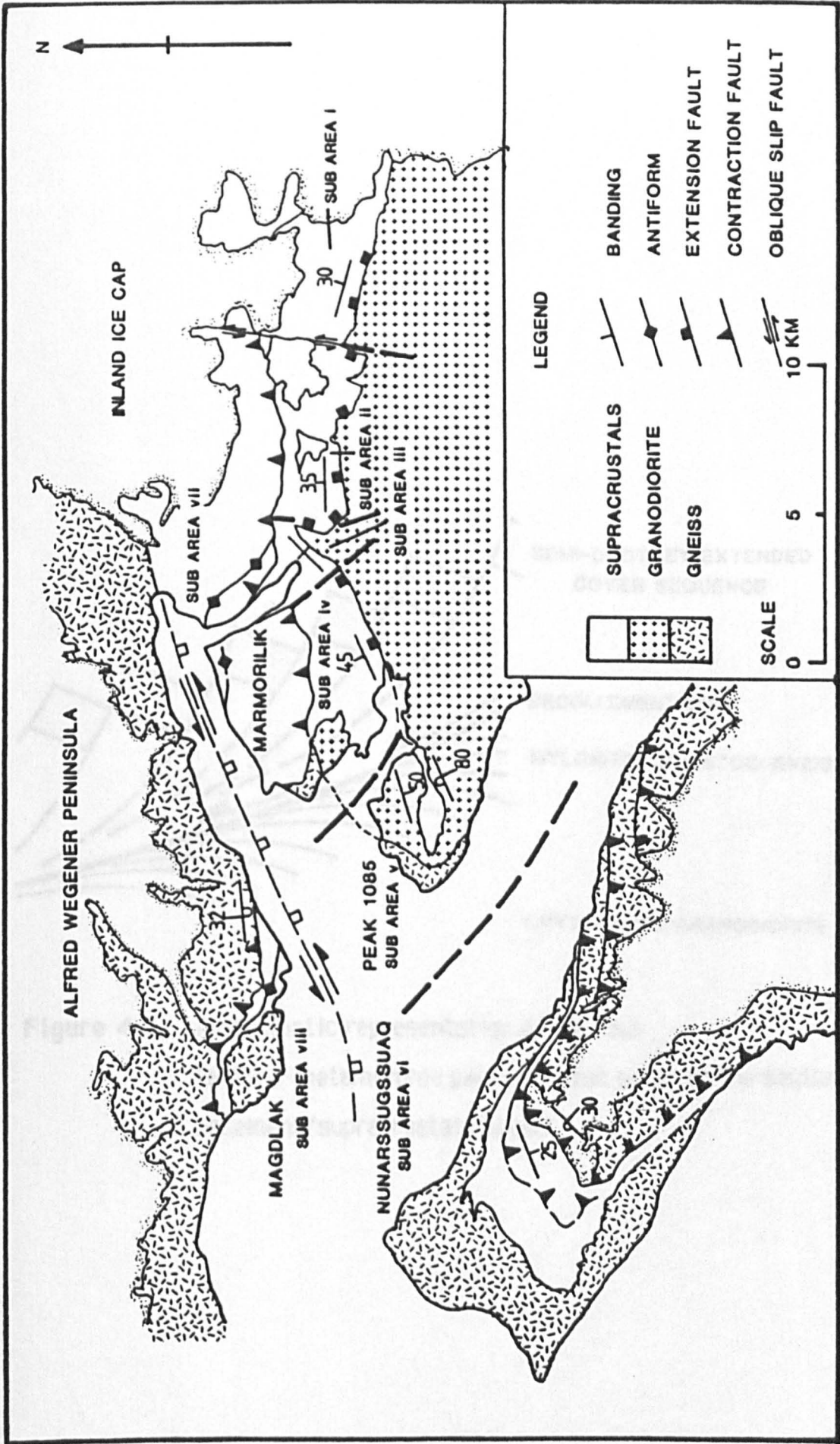
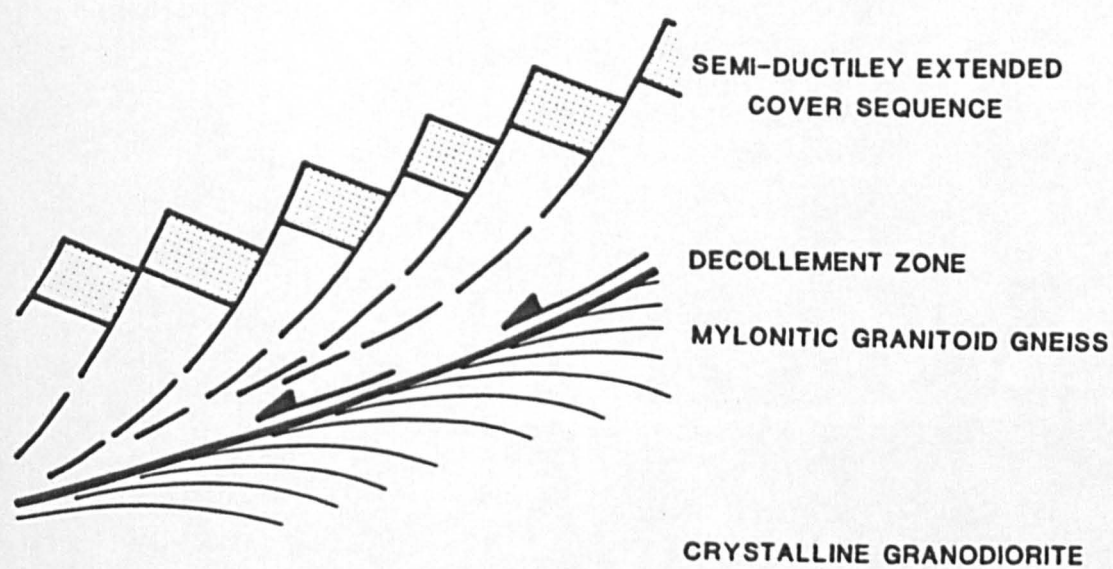


Figure 4.3 Map showing the D1 homogeneous sub-areas of the study area



**Figure 4.4** A schematic representation of the four tectono-metamorphic packages that occur on the southerly basement/supracrustal contact.

## Figure 4.5 D1 Basement Structures

- A) Field photograph showing the basement/supracrustal contact at the southern Agfardlikavsá fjord. Note the steep to southerly overturned contact and the northerly verging folds developed in the supracrustals. Scale bar 300metres.
- B) Granodiorite gneiss forming a well developed C/S fabric that indicates a sinistral sense of shear. Location 17, southern basement/supracrustal contact Little South Lake. Scale bar 5cm.
- C) An antithetic D1 dextral shear zone developed in relatively homogeneous granodiorite. Location 120, south of the Agfardlikavsá fjord.
- D) Close up of a severely extended feldspar megacryst within a granodioritic gneiss. The high angle north dipping fractures indicate dextral shear. Location 231, Peak 915, South Lakes.
- E) Highly sheared and strongly altered granitoid gneiss located close to the basement/supracrustal contact. Note the high matrix content and extended ribbon like feldspathic phenocrysts. Location 72, Fishing Lakes cliffwall.
- F) North verging folds with minor 'out of syncline' slides developed in anisotropic calc-silicate units of the Qeqertarsuaq Formation, just above the basement/supracrustal contact (located in the stream bed). Location 72, Fishing lakes Cliffwall.

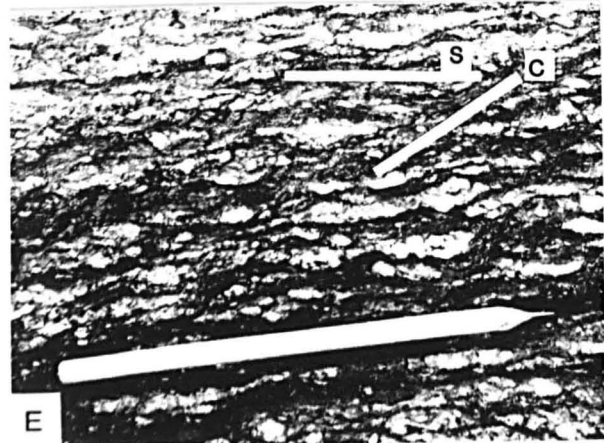
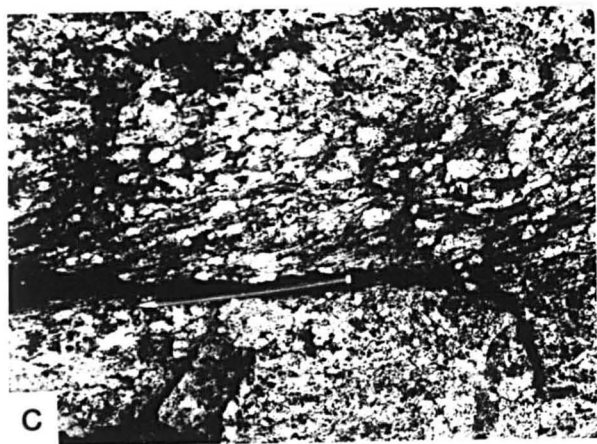
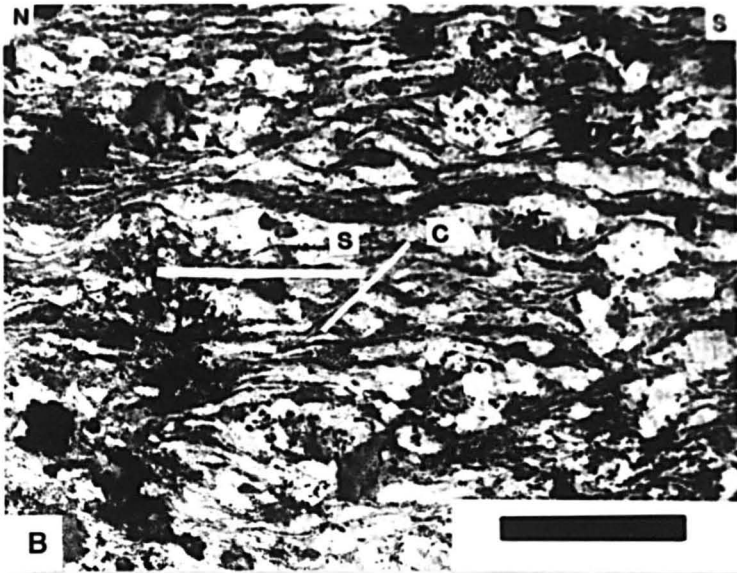
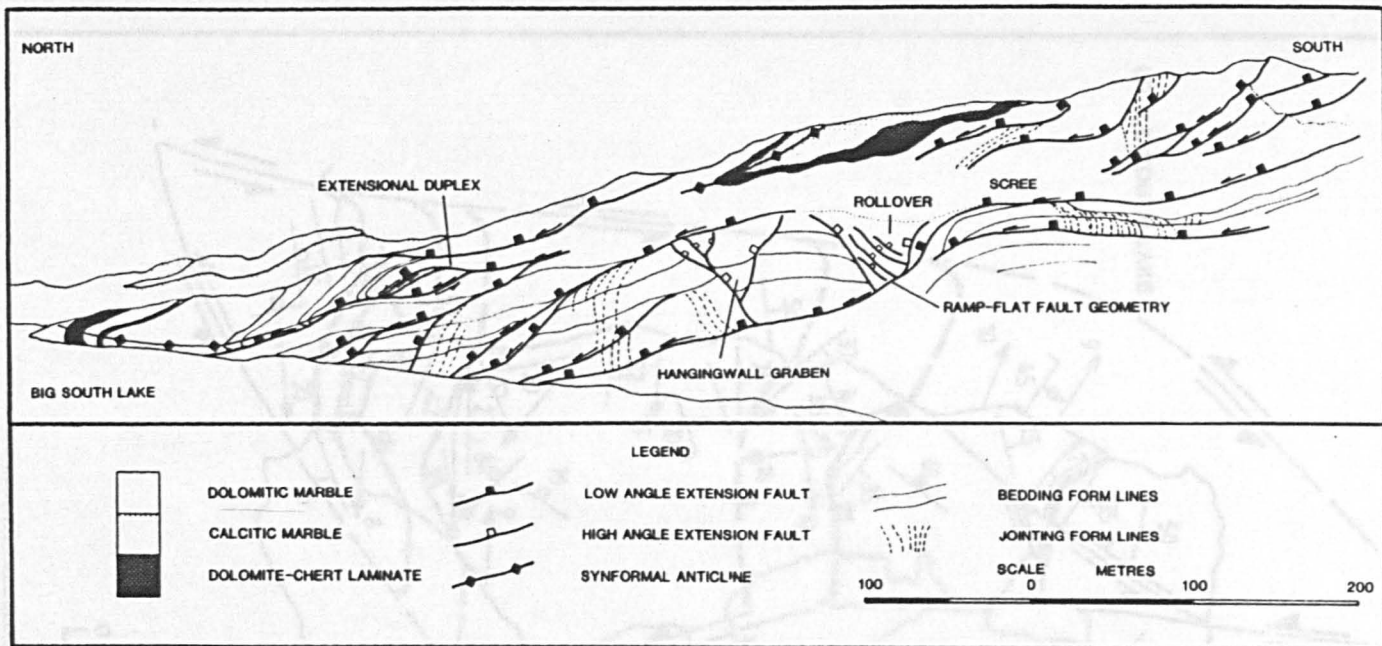


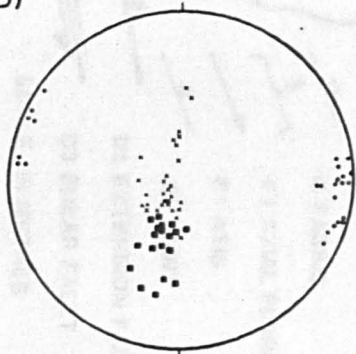
## Figure 4.6 Line Drawing of an Extensional Fault System

- A) Line drawing of the south-eastern edge of the Big South Lake. Low angle D1 extensional faults occur in an imbricated and duplexed systems above a major ramp-flat fault. To the north (left) the extended units are deformed into north verging D1 flexures.
- B) Stereogram showing the scatter of poles to D1 extension faults (squares), S1 cleavages (crosses) and the plunge of F1 fold axes (open circles).
- C) Sketch of C/S fabric development in granitoid gneiss of the southerly basement massif. Note the fractured, extended and augen-like feldspathic megacrysts.
- D) Sterogram showing the distribution of poles to C fabrics (circles) and poles to S1 cleavage in the granitoid gneiss of the southerly basement massif.

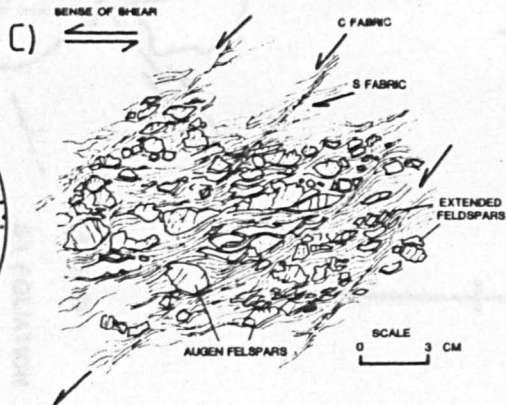
A)



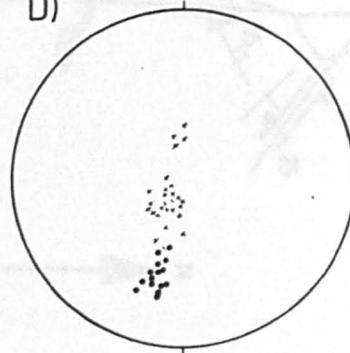
B)



C)



D)



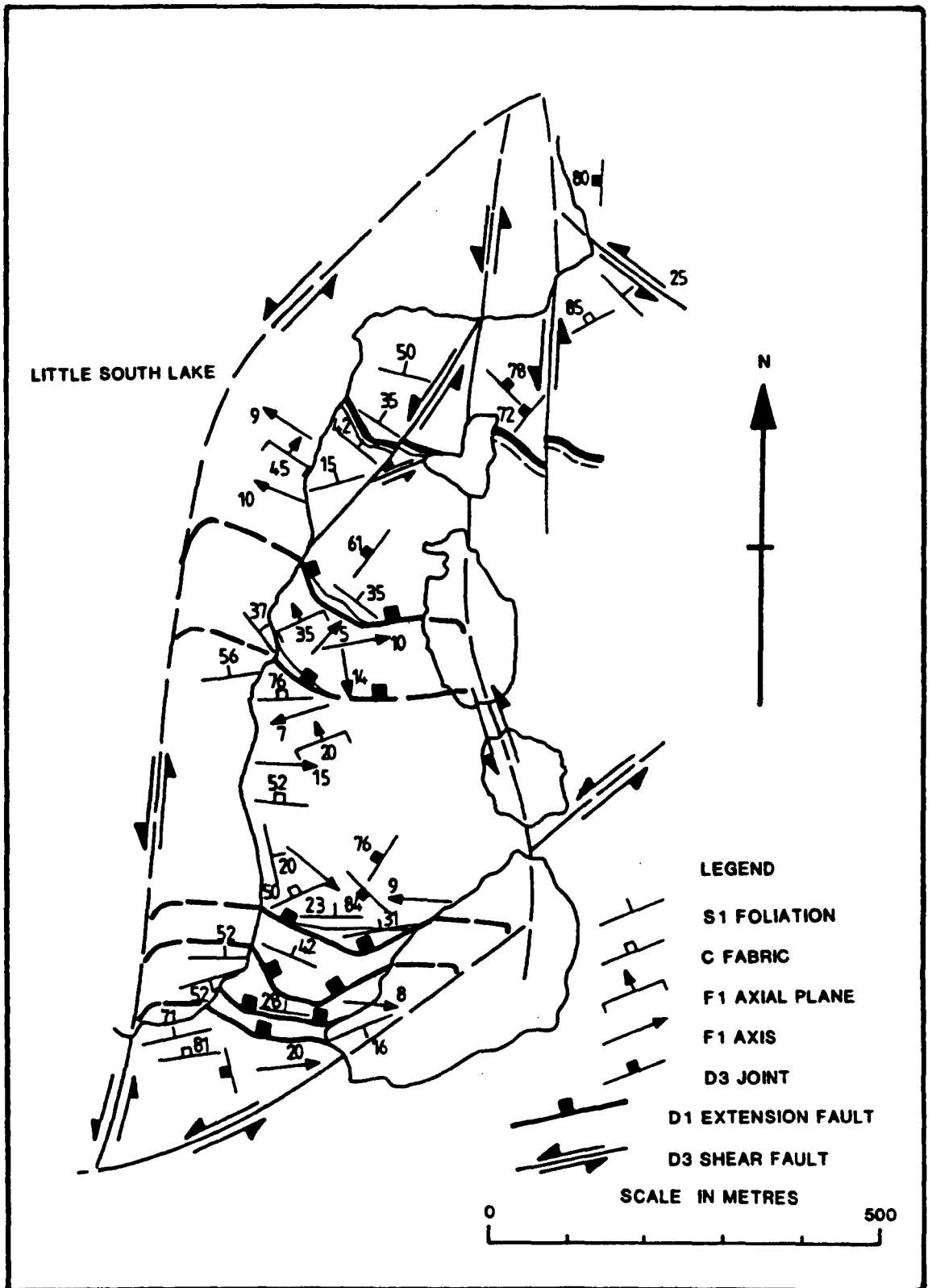


Figure 4.7 Simplified tectonic map of the south-east Little South Lake

## Figure 4.8. D1 Extensional Structures

A) D1 extension fault trace. Note the steeply north dipping units (right) in the footwall and the relatively shallowly dipping units in the hangingwall (left) of the fault. Location 283, South lakes.

B) Open D1 flexure in the immediate footwall of a D1 extension fault. The siliceous dolomitic marble shows a refraction and northward rotation or fanning of the S1 cleavage. Close to location 11, South Lakes.

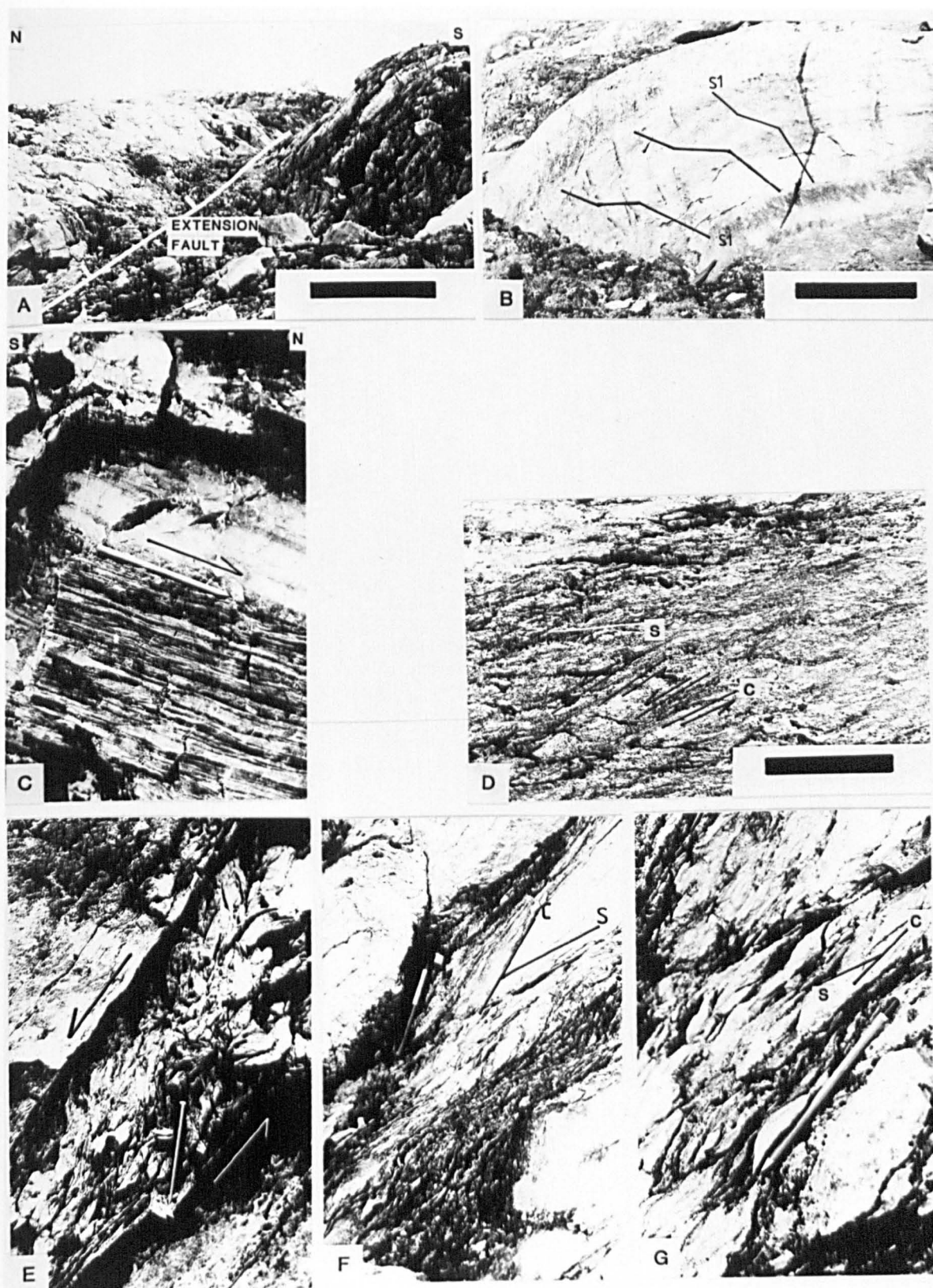
C) Mylonitic fabrics developed in low angle extensional shear zones in the quartzitic units of the Qeqertarsuaq Formation. Location 233, Peak 915, South Lakes.

D) C/S fabric relationships developed in phlogopitic dolomite marbles of unit 1 Lower Marmorilik Formation. The C/S fabric indicates a sinistral sense of shear. Location 370, southern South Lakes.

E) A close up of a thin, 50cm. thick, D1 extensional fault zone. The deformation is restricted to the footwall block in which a chaotically deformed sequence of duplexed and imbricated extensional microfaults are developed. Location 146, South-east Little South Lake.

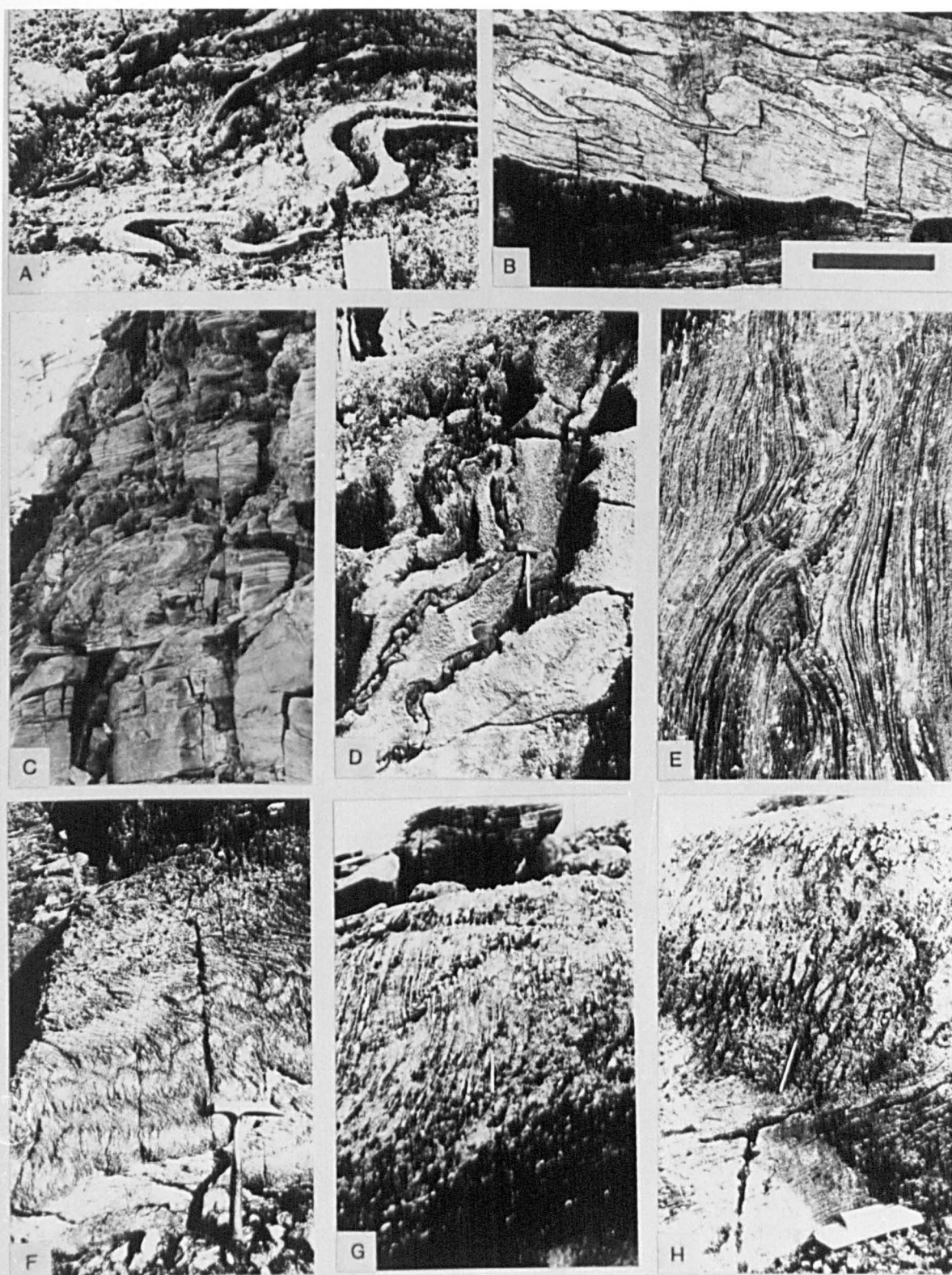
F) Photograph of conjugate D1 extensional fault zones, that bound a large lozenge shaped extensional horse block. Note the C/S fabric relationships indicating sinistral displacement and a northerly tectonic transport. Location 249, south of Big South Lake.

G) Close up of the microfaulting developed in the D1 extensional fault system of (F). Note the lozenge shaped (micro)horse blocks that are held in an extensional duplex system.



## Figure 4.9 D1 Folds and Associated Structures

- A) Doubly plunging, sheath like, reclined D1 folds developed in siliceous bands within dolomitic marble (unit 2, Marmorilik Formation). Location 101, South Lakes. Compass clinometer for scale.
- B) Assymetric northerly verging, folded pinch and swell structures developed in siliceous layers within dolomitic marble. Scale bar 50 cm. Location 25, north of Little South Lake.
- C) Chaotically deformed rootless folds formed in a D1 shear zone. The folds are developed in interbanded dolomitic sandstones and siltstones of the Lower Marmorilik Formation. Location 716, south Marmorilik Plateau. Hammer for scale.
- D) Siliceous bands forming northerly verging disharmonic folds in dolomitic marbles. Location 271, south Little South Lake.
- E) 'Fish mouth' internal boudins formed in interbanded graphitic dolomitic sandstones and siltstones. Location 94, north west Marmorilik Plateau. Pencil for scale.
- F) Strongly refracted D1 axial planar cleavage, with minor slip accomodated along cleavage planes. Location 42, Fishing Lakes cliffwall.
- G) Quartz rodding developed parallel to D1 fold axes in siliceous dolomitic marbles of the lowermost Marmorilik Formation. Note the D3 sinistral shear zone cross cutting the rods. Pencil for scale. Location 104, south of Little South Lake.
- H) Transposition of a siliceous band, into elongate lenses, by an upright D1 cleavage. The intense cleavage refracts into a massive basal dolomitic marble. Location 280, south of Little South Lake.



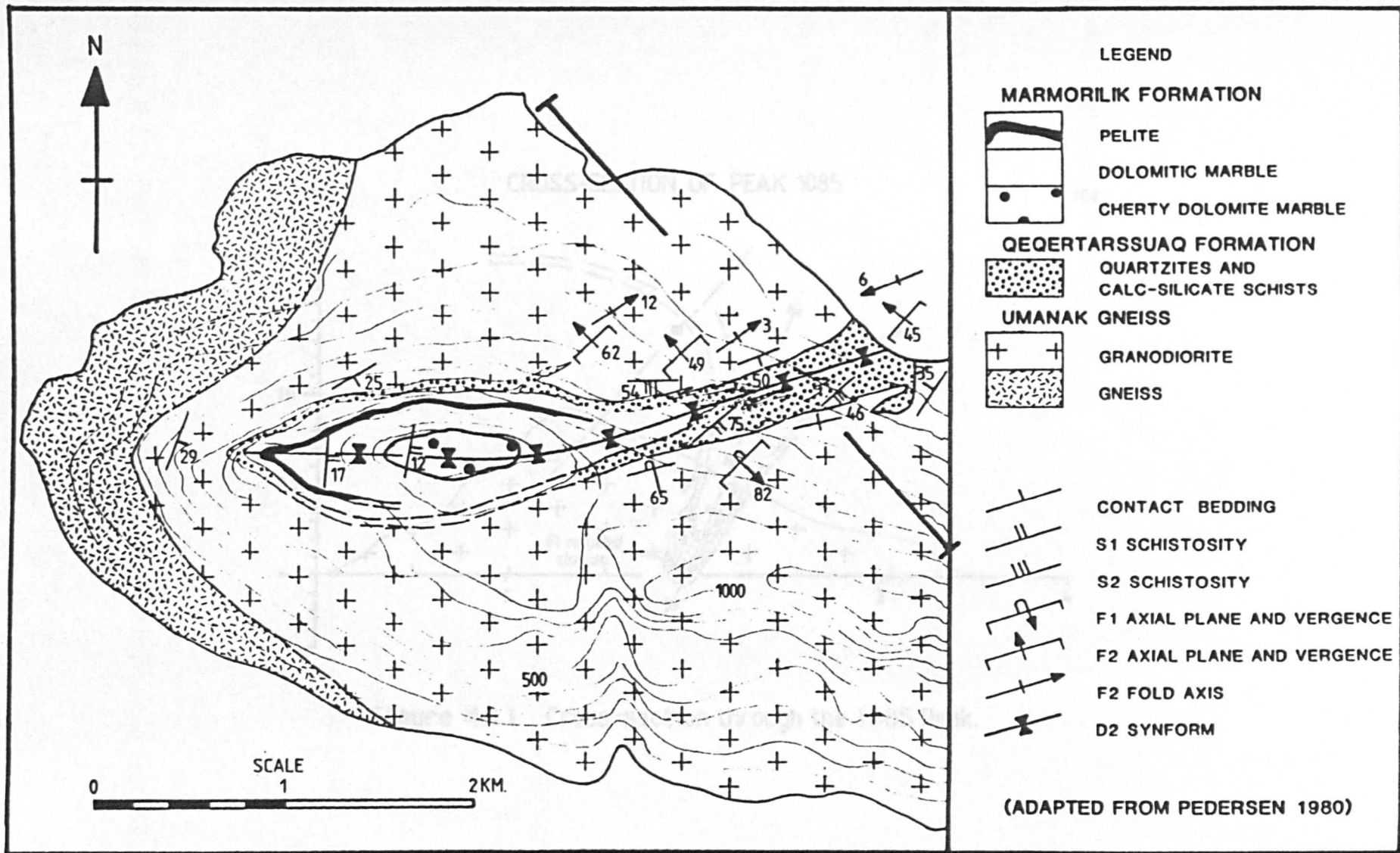
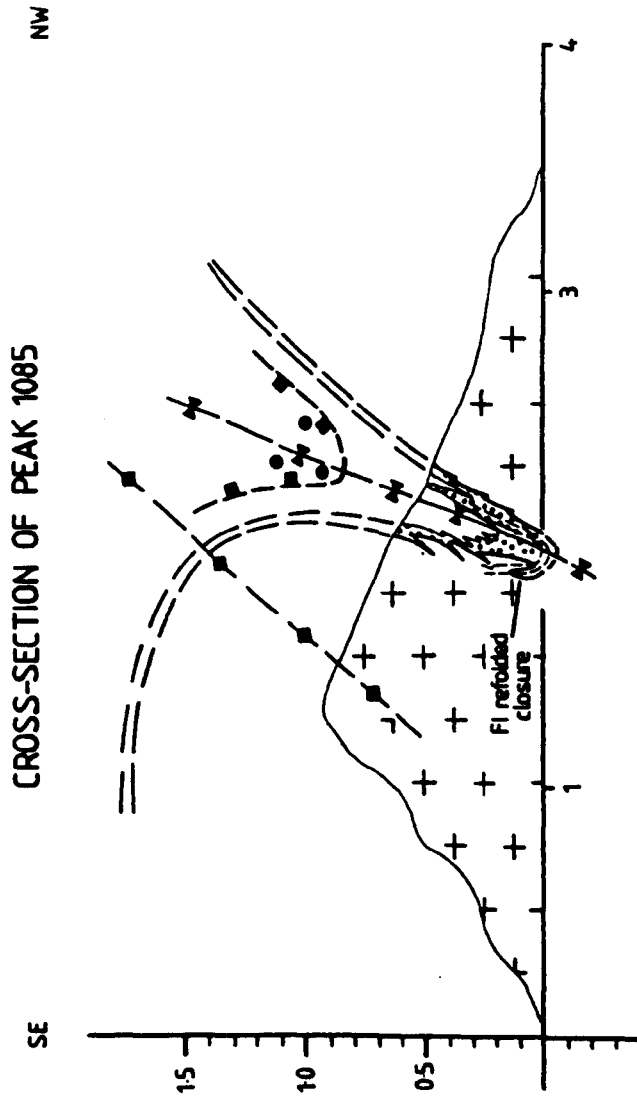
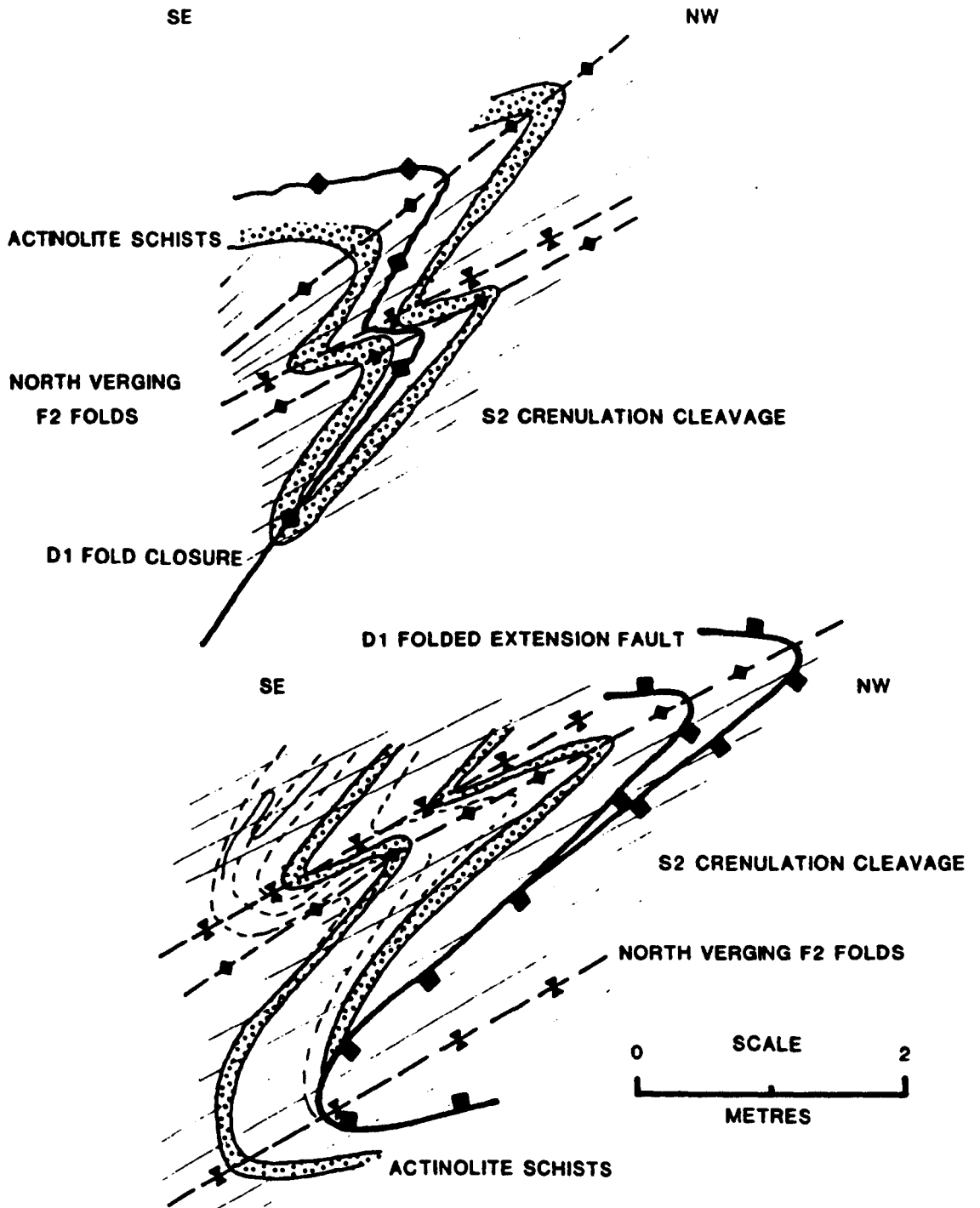


Figure 4.10 Geological map of the 1085 Peak.

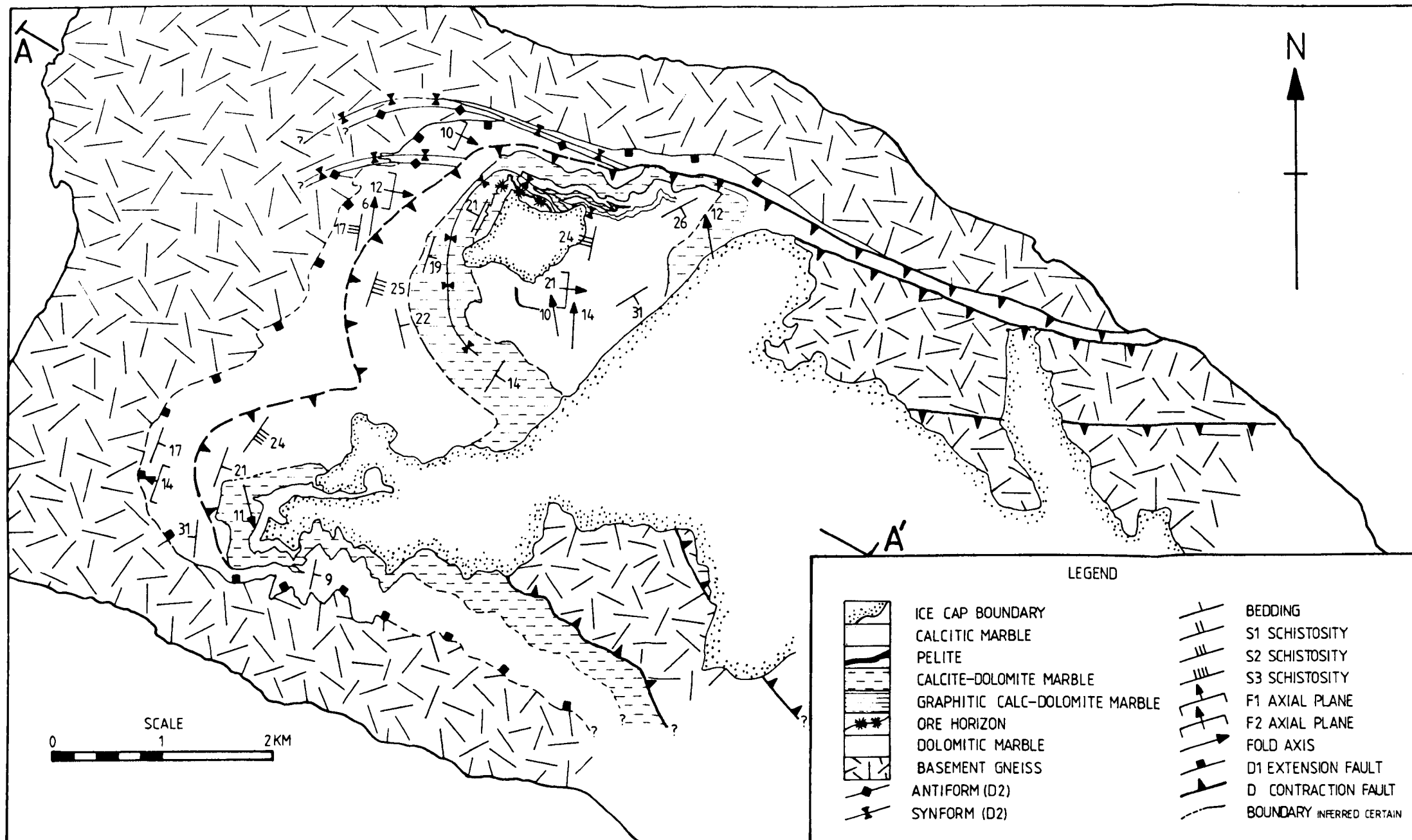


**Figure 4.11** Cross-section through the 1085 Peak.



**Figure 4.12** Refolded deformation structures observed on the 1085 Peak.

# LITHO-TECTONIC MAP OF THE UVKUSIGSSAT PENINSULA



## CROSS SECTION OF THE UVKUSIGSSAT PENINSULA

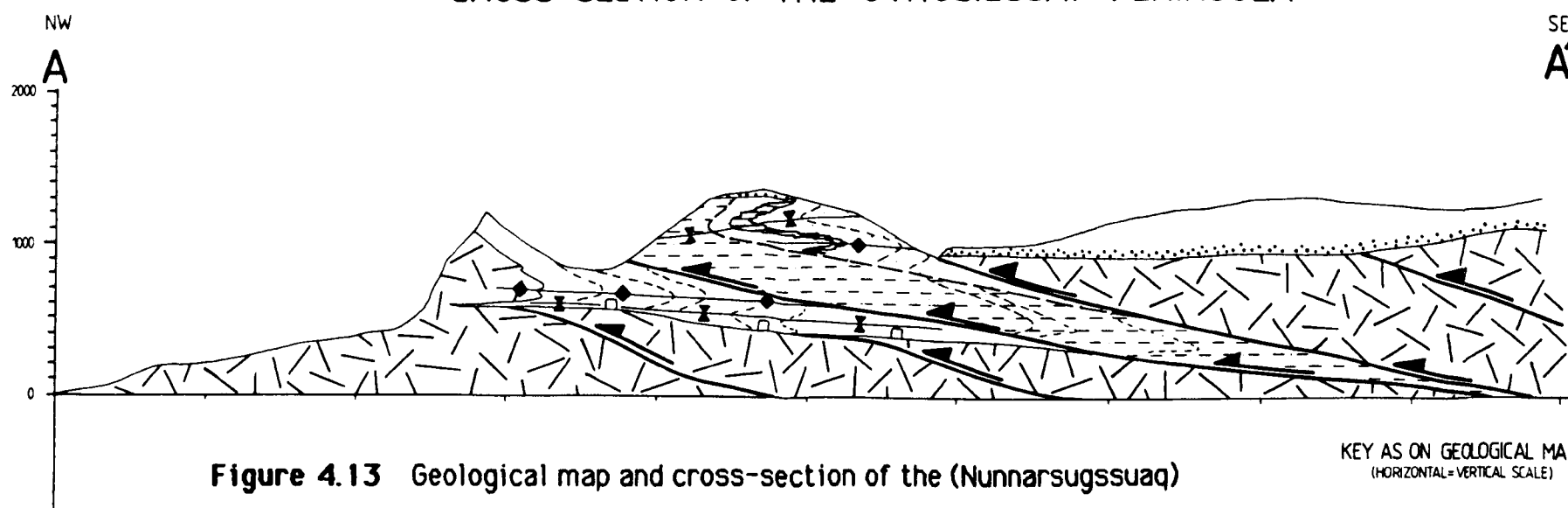


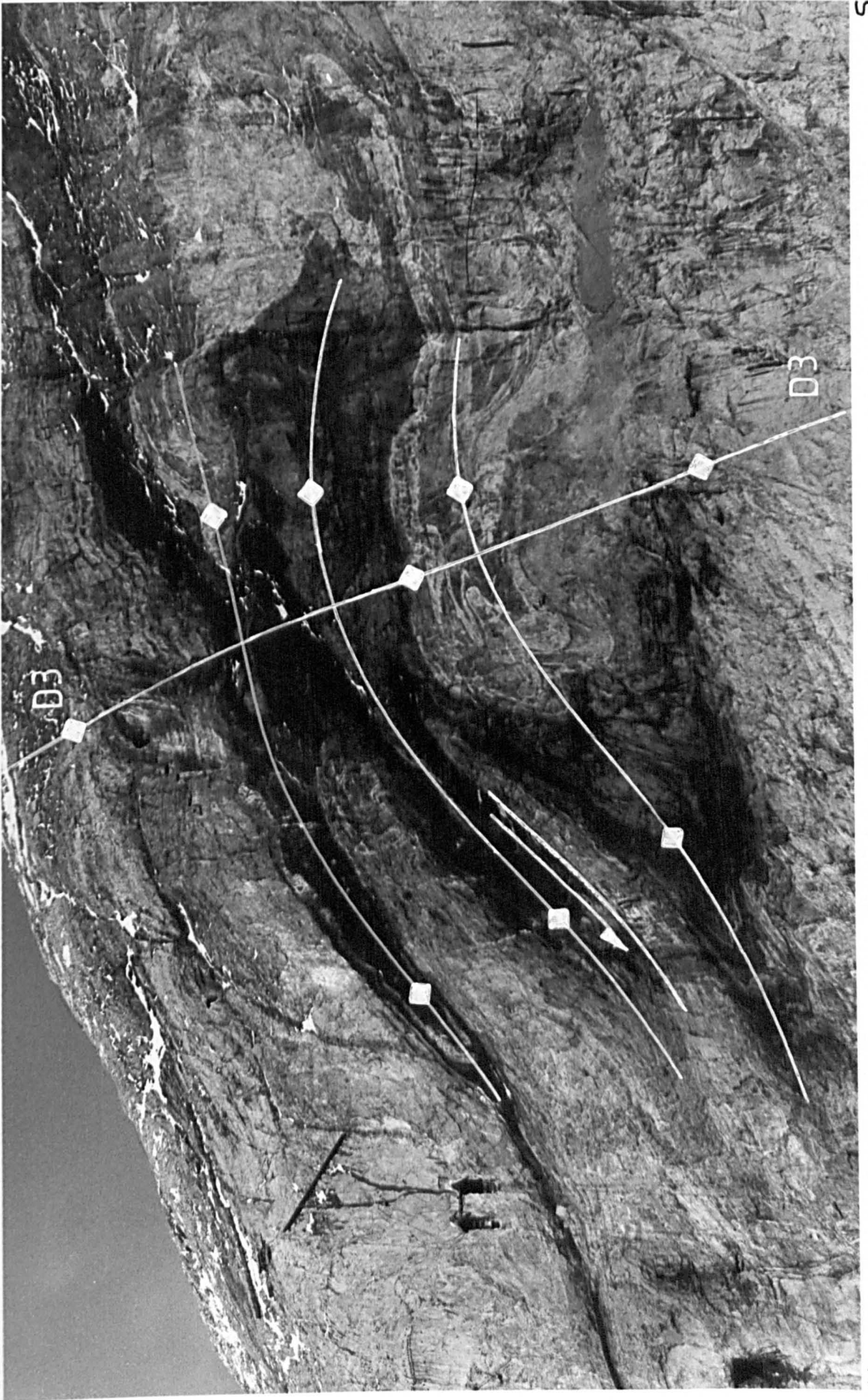
**Figure 4.13** Geological map and cross-section of the (Nunnarsugssuaq)

Uvkusigssat Peninsula (Modified from Pedersen, 1980).

KEY AS ON GEOLOGICAL MAP  
(HORIZONTAL=VERTICAL SCALE)

## Figure 4.14 Structural Interpretation of the Black Angel Nappe

Photograph of the Black Angel cliffwall showing the D1 Black Angel nappe and the entrance to the Black Angel mine (double black holes with cable car  $\approx$  3 m high). The nappe is composed of a siliceous pelite that is infolded with calcite/dolomite marbles in the fold hinge. The D1 structure with severely attenuated fold limbs, parasitic folds and associated north verging out of syncline tectonic slides is refolded about an open, southerly inclined D3 fold. The Angel zone ore horizon outcrops as a dark weathering, structurally correct 'way up', horizon within calcite marbles above the upper D1 parasitic fold hinge. Height of photograph 240 metres.

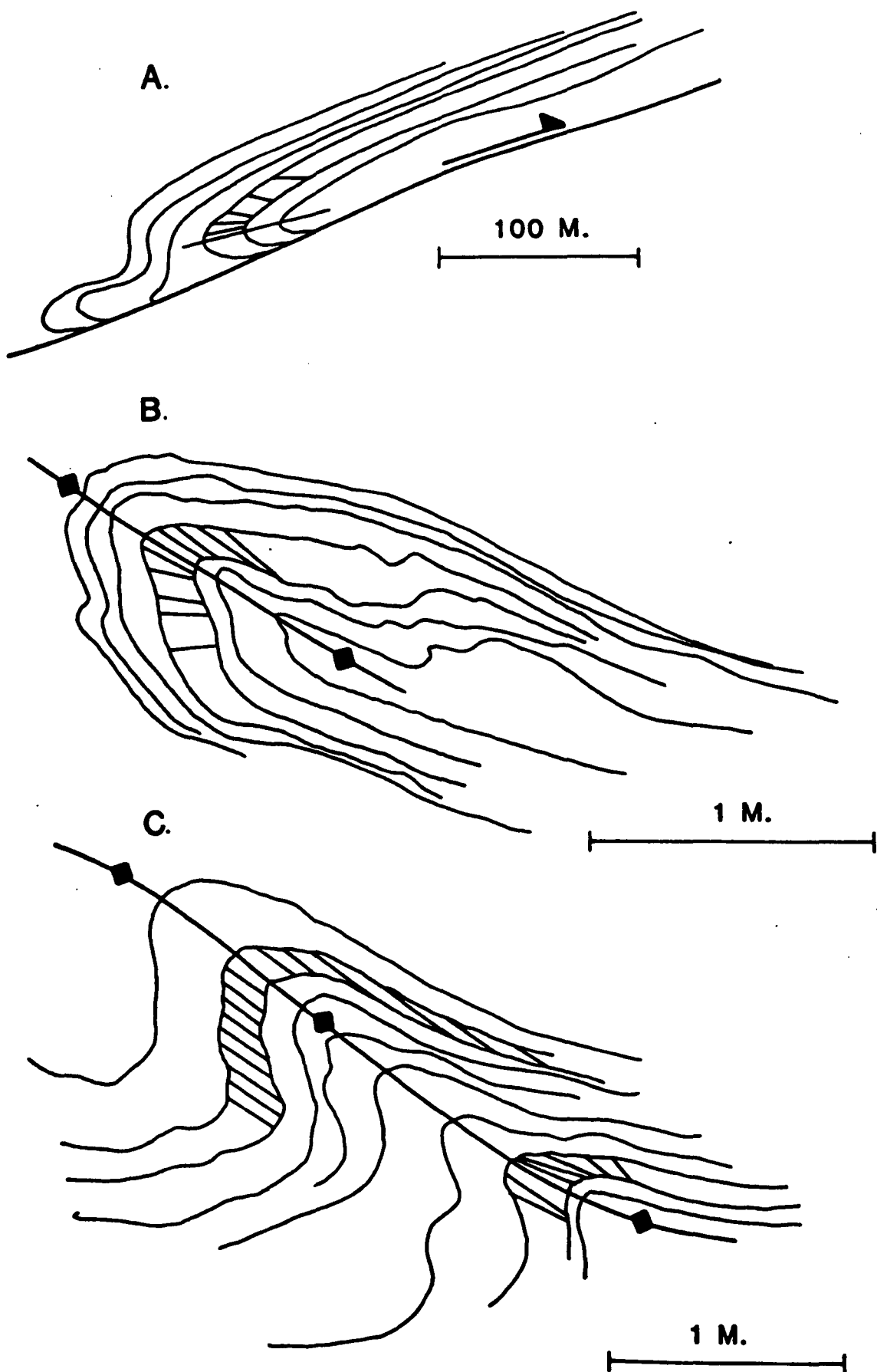


S

N

Figure 4.15

## DIP ISOGONS CONSTRUCTED ON D1 FOLDS



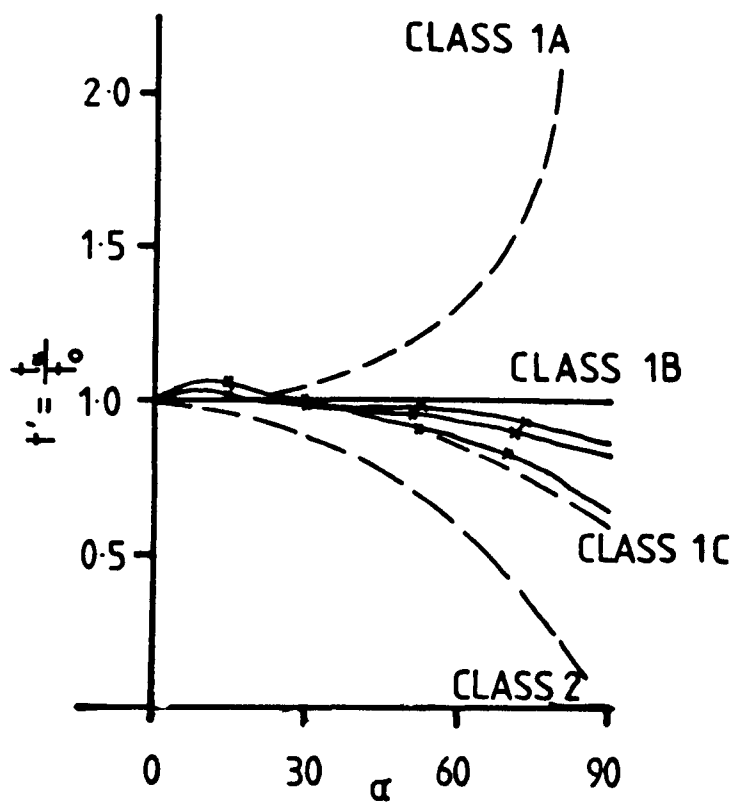


**Figure 4.16**  $t_\alpha$  plot of D1 folds. The folds are class 1C flattened parallel folds

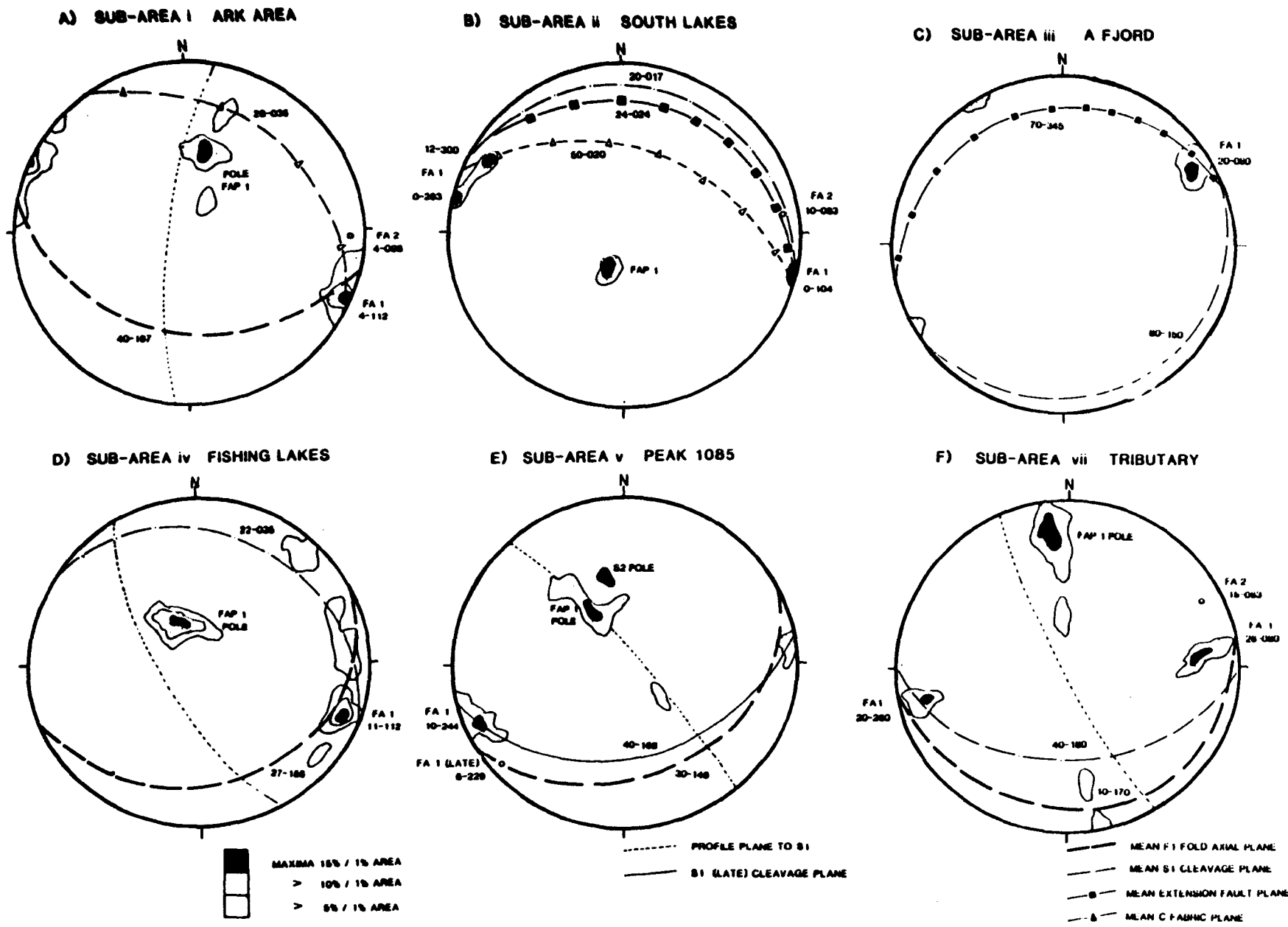
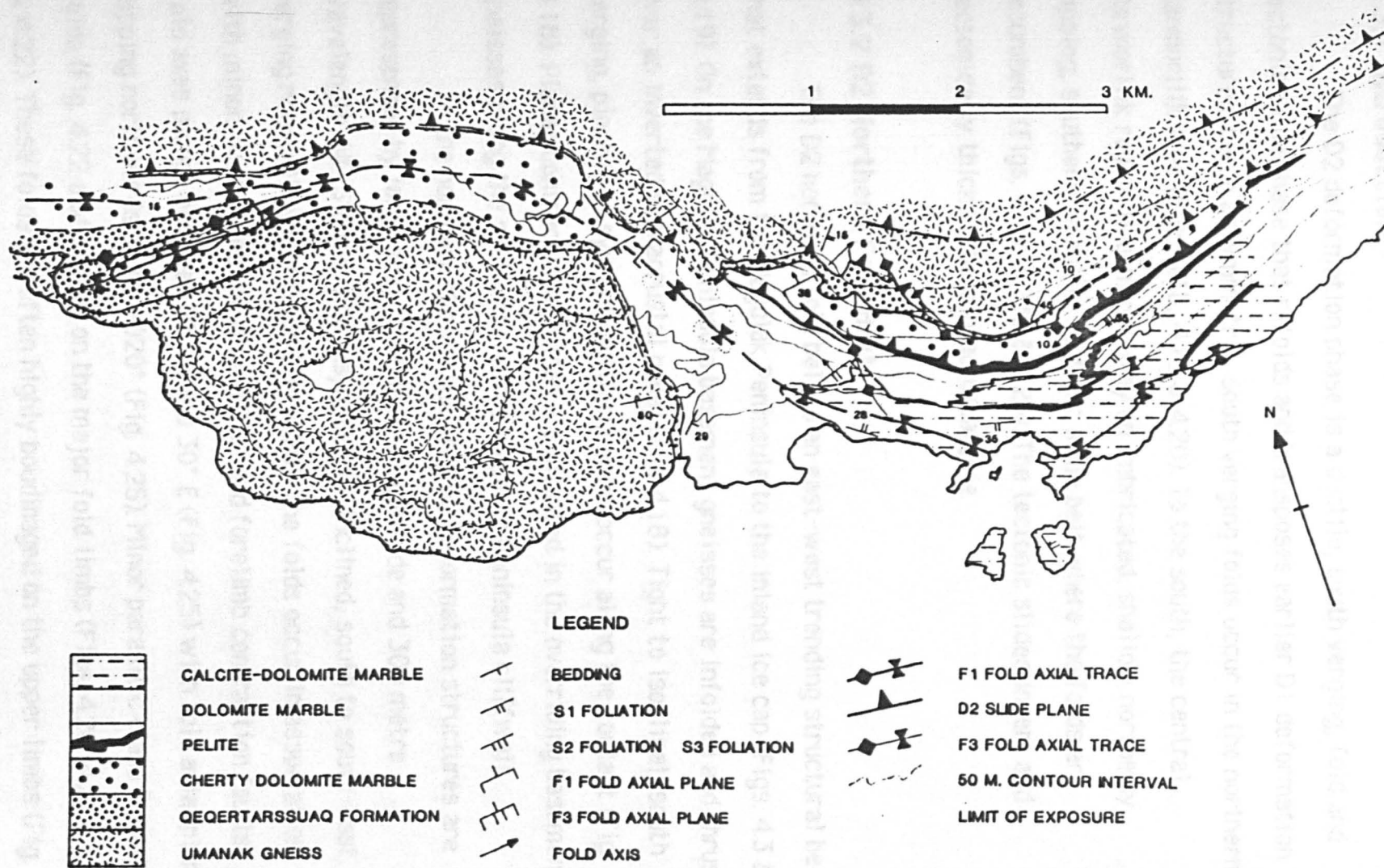


Figure 4.17 Summary diagrams of D1 stereographic data.

**Table 4.2: Summary of Stereographic data from homogeneous sub-areas for D1 and D2 deformation phases**

<b>D1 Structures</b>					
<b>Structure Sub-area</b>	<b>FAP 1</b>	<b>FA 1</b>	<b>S1</b>	<b>Extension fault</b>	<b>'C' fabric</b>
<b>i) Ark area</b>	40-197	4-112	26-201	28-306	46-311
<b>ii) South Lakes</b>	28-021	0-283 12-300	20-017	24-024	50-020
<b>iii) 'A' Fjord</b>	81-152	20-060	80-150	70-345	---
<b>iv) Fishing Lakes</b>	27-158	25-067 12-048	32-326	31-348	---
<b>v) Peak 1085</b>	30-149 39-170(L)	6-257 (R) 6-229 (L)	--- 40-168(L)	--- ---	--- ---
<b>vi) Uvkussigset</b>	---	---	---	---	---
<b>vii) Tributary</b>	10-170	26-080 20-260	40-180	---	---
<b>viii) Magdlek</b>	---	---	---	---	---
<b>D2 Structures</b>					
<b>Structure Location</b>	<b>FAP 2</b>	<b>FA 2</b>	<b>T 2</b>	<b>S 2</b>	<b>Slip vector</b>
<b>Tributary</b>	33-344	16-060	28-356	36-337	24-345
<b>Fishing Lakes Cliffwall</b>	31-330	20-045	32-347	18-350	10-300
<b>W. Marmorilik Plateau</b>	60-356	14-272	72-356	60-356	20-280
<b>South Lakes Cliffwall</b>	33-001	14-266 5-306	35-359	34-358	32-352
<b>Marmorilik Plateau</b>	40-001	30-065 10-079	23-018	30-012	40-001
<b>Nukavsak Formation</b>	38-334	11-052	26-026	36-338	24-000

**Figure 4.18** LITHO-TECTONIC MAP OF THE MAGDLAK PENINSULA (Adapted from Pedersen, 1980b)



## **4.3 D2 South Verging Fold and Fault phase**

### **4.3.1 Introduction.**

The D2 deformation phase is a ductile, south verging, fold and tectonic slide phase that refolds and transposes earlier D1 deformation structures. Large asymmetric, south verging folds occur in the northern Marmorilik area (Figs 4.1b, 4.19 & 4.20). To the south, the central Marmorilik region is dominated by an imbricated, shallow northerly dipping, southerly verging, tectonic slide belt where the folds are recumbent (Figs. 4.19, 4.23a & 4.26). The tectonic slides invert and tectonically thicken the supracrustal pile.

### **4.3.2 D2 Northern Fold Belt.**

The D2 northern fold belt is an east-west trending structural belt that extends from the Magdlak Peninsula to the inland ice cap (Figs. 4.3 & 4.19). On the Magdlak Peninsula basement gneisses are infolded and thrust over an inverted supracrustal panel (Fig. 4.18). Tight to isoclinal, south verging, pinched in synform antiform pairs occur along the contact (Fig. 4.18). Planar contractional slides are situated in the overriding basement gneisses along the southerly Alfred Wegener Peninsula cliffwall.

In the northern Marmorilik area D2 deformation structures are represented by large scale, 250 metre amplitude and 300 metre wavelength, NE-SW trending, asymmetric, inclined, south to south-east verging non-cylindrical folds (Fig. 4.20). The folds occur in association with minor out of syncline (Fig. 4.21d) and forelimb contraction faults. Fold axes plunge between 25° W and 30° E (Fig. 4.25) with fold axial planes dipping northwards at 40°-020° (Fig. 4.25). Minor parasitic class 2 similar folds (Fig. 4.22 a & b) occur on the major fold limbs (Figs. 4.20, 4.21 c, d & e & 4.22). These folds are often highly boudinaged on the upper limbs (Fig. 4.21 e & f) and thrust out along minor, southerly verging, contraction faults on the lower overturned limbs. A strong axial planar S2 crenulation cleavage occurs. These planes characterise the diffuse contacts between

dark grey dolomitic marbles and white calcitic marbles (Fig. 4.20), and occur parallel to minor, bleached, contractional fault zones (Fig. 4.26d & 4.23). The diffuse and bleached zones indicate strong fluid flow during cleavage development.

D1 fabrics are refolded into type 3, generally Z on S, fold interference patterns (Fig. 4.21b & g). S1 phlogopitic foliations are crenulated (Fig. 4.23b, d & e) and D1 contractional fault zones are re-folded. The D1 Black Angel nappe (Fig. 4.14) does not show a strong refolding by D2 folds, as the nappe closure is interpreted to lie on an overturned D2 fold limb below the D2 Tributary fold.

### **4.3.3. Central contraction belt.**

#### **a) Tectonic slide zones**

The D2 fold belt grades southwards into the central D2 contraction belt (Fig. 4.19). The D2 contraction belt is characterised by a sequence of five major, imbricated, east-west trending, north-north-west dipping (23-018), southerly verging planar and ramp flat tectonic slide<sup>1</sup> zones (Fig. 4.1b & c, 4.23a, 4.25 & 4.26). Above the shallow ramps, low amplitude snakeshead geometries and ramp anticlines are formed (Fig. 4.26) that fold the topographically higher slides zones. Map scale duplexes (Boyer and Elliot, 1981) occur in both the South Lakes cliffwall (Figs. 4.1a & 4.19) and the western Marmorilik Plateau, where basement gneisses and granodiorites are incorporated into a thick skinned duplex (Fig. 4.1c) as individual horses, bounded by high angle link faults (72-356°, S.V.15-268),

---

<sup>1</sup>The term tectonic slide is used as defined by Fleuty (1964). That being:-' a fault formed in close connection with folding, which is broadly conformable with a major geometric feature (either fold limb or axial surface) of the structure, and which is accompanied by thinning and/or excision of members of the rock succession affected by the folding'

The tectonic slides cut previously deformed strata and as a consequence rarely emplace stratigraphically older rocks on top of stratigraphically younger rocks and therefore are not considered in terms of the classic foreland fold and thrust systems (Boyer and Elliot, 1982).

Granodiorite wedges, quartzites and calc-silicate schists are tectonically repeated by imbricated footwall collapse structures in the Fishing Lakes area (Figs. 4.1c and 4.24). The stacked tectonic panels 'tip out' eastwards along the Fishing Lakes cliffwall (Fig. 4.1a), where the tectonic slides are folded above a ramp that consists of a rigid D1 synformal-anticline fold core (Fig. 4.24). A D2 tectonic klippe of the Nukavsak Formation caps both the Marmorilik and Black Angel plateaux (Fig. 4.19, 4.21a).

The slide zones shear out D1 folds (Figs. 4.24 & 4.26) to produce cut off angles of between 0°-90°. In the South lakes, Ark and western Plateau areas, D1 extensional faults are reactivated by D2 south verging tectonic slides (Fig. 6.5). This is best seen in the western Marmorilik Plateau (Figs. 3.1 & 4.1a & c) where a D1 extensional fault (inferred through the omission of unit 1 stratigraphy) now clearly shows dextral, ie south verging, kinematic indicators (Fig. 4.23c).

The sub-horizontal slide zones (35-359°, Fig. 4.25) are 1.5 to 10 metre wide and located at or close to Formation and unit boundaries (Figs 3.1 & 4.1, 4.21 a & 4.23a). They are marked by highly sheared mylonitic fabrics and very closely spaced crenulation cleavages (Figs. 3.9, 4.23b & c) which show a strong parallelism. Smaller scale mylonite zones occur within individual slide bound tectonic panels (Unit 3 section 3.3.2), along with intrafolial condom folds (Fig. 4.23c) and strong mineral stretching lineations, with mean slip vectors of 32-353 (Fig. 4.25). Slip vectors vary in orientation between separate tectonic slide panels (Fig. 4.25 and Table 4.2).

## **b) Tectonic slide panels**

The tectonic slide-bound panels contain non-cylindrical, recumbent to shallowly inclined, tight to isoclinal, southerly verging folds with either tightly 'pinched in' or 'sheared out' synformal hinges (Fig. 4.22 & 4.24). Fold axial planes in the slide panels are much shallower than those

of the northerly fold belt (Figs. 4.20 & 4.26). t plots indicate that the F2 folds are similar class 2 to flattened class 3 folds (Fig. 4.22).

Crenulation cleavages are axial planar to the F2 folds (Fig. 4.23d). The cleavage type, orientation and intensity varies according to the lithology and the relative proximity of slide zone surfaces. In the capping Nukavsak Formation klippe, very strong closely spaced crenulation cleavages fan upwards from a sub-horizontal orientation within the slide zone to become axial planar to small scale, upright chevron folds (Figs. 3.11 c & d, 4.23e). In the calcite and calcite-dolomite marble units of the Upper and Middle Marmorilik Formation, S2 cleavages are orientated at very low angles to the tectonic slide surfaces (Figs. 3.9d & f, & 4.25). The foliation planes are most strongly developed in the more anisotropic calcite-dolomite and graphitic calcite-dolomite marbles of unit 3, where an intense transposition of earlier bedding and D1 fabrics has occurred. The cleavage traces are picked out by the alignment of graphite, insoluble clay residues and phlogopite/muscovite micas that wrap around elongate coarse calcite and slightly finer dolomite grains (Fig. 5.5 a & b).

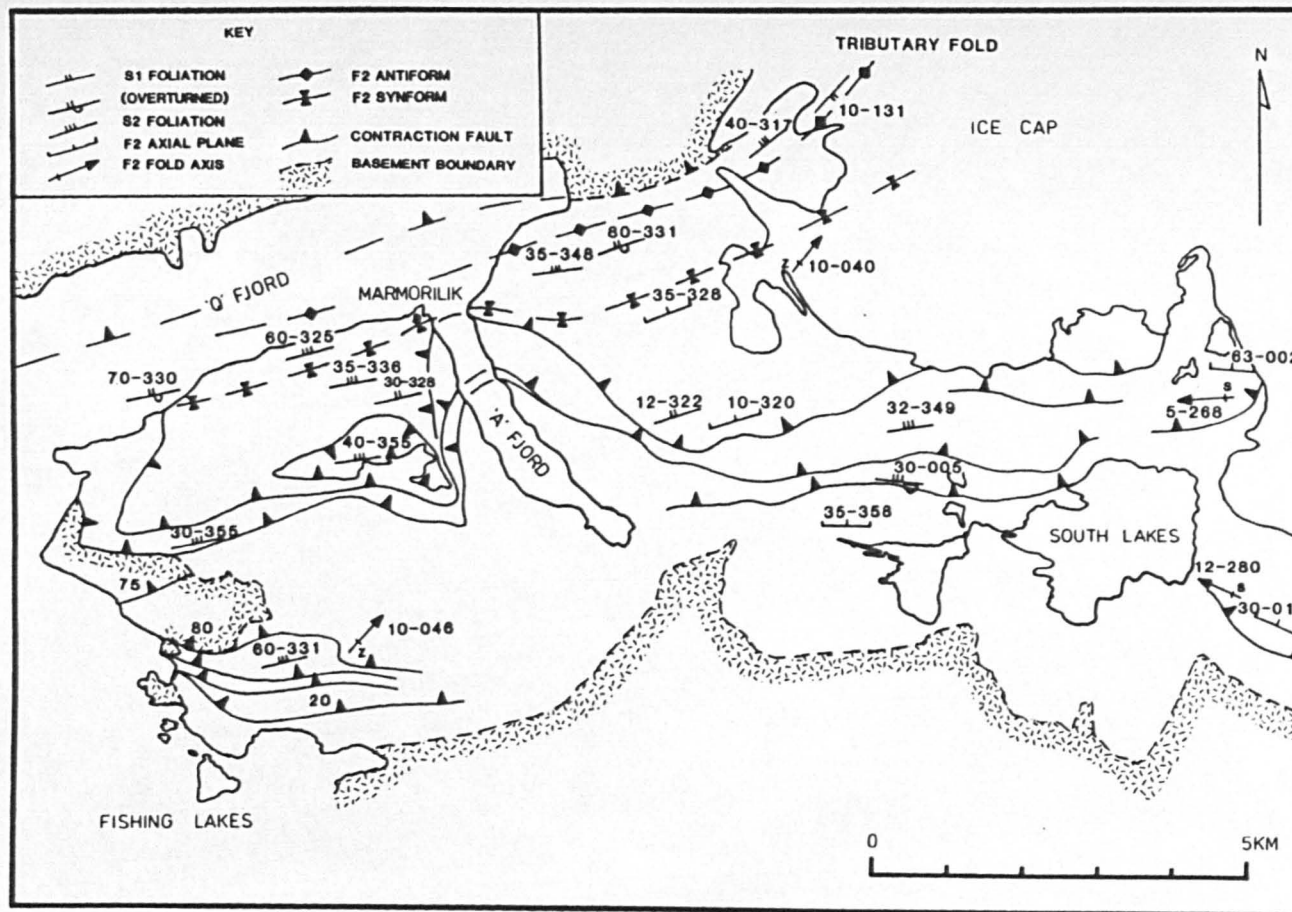


**Figure 4.19** A map of D2 deformation structures in the Marmorilik area

## Figure 4.20 The D2 Tributary Fold

A) The Tributary fold; a D2 SSE verging, asymmetric, overturned, antiform-synform pair with a strong D2 axial planar crenulation cleavage, which parallels the inclined dolomite (grey) calcite (white) bands in the antiformal fold hinge. The fold is developed in a thick siliceous-pyritic pelite. The Tributary mineralised showing is located below the synformal hinge. Scale bar 250 metres.

SE

NW



## Figure 4.21 D2 Deformation Fold Structures

A) An oblique photograph of the upper South Lakes cliffwall looking northwards. Recumbent isoclinal F2 folds are transected by a D2 tectonic slide that emplaces the Nukavsak Formation (dark grey-black) over the interbanded grey banded dolomitic and calcitic marbles (unit 6) of the Marmorilik Formation. Scale bar 300 metres.

B) Southerly verging F2 folds refold isoclinal F1 folds into a type 3 fold interference pattern. Dolomitic marbles of the Upper Marmorilik Formation. Location 771, north Black Angel Plateau.

C) Type 3 fold interference patterns formed by northerly verging F2 folds refolding an isoclinal F1 closure. South Lakes Cliffwall

D) Asymmetric D2 folds in thick and thinly banded chert units within calcitic marble. Location 1532, north wall Drift 23, Black Angel mine.

E) Assymmetric D2 folds with imbricated 'out of synform' slides (with bleached zones) developed in chert banded calcitic marbles. Location 1532, north wall Drift 23, Black Angel mine.

F) D2 boudins formed in a recrystallised calcite band that is set in a dark grey dolomitic marble. East wall Nunngarut drift E-F (45m). 1.5 metre rule for scale.

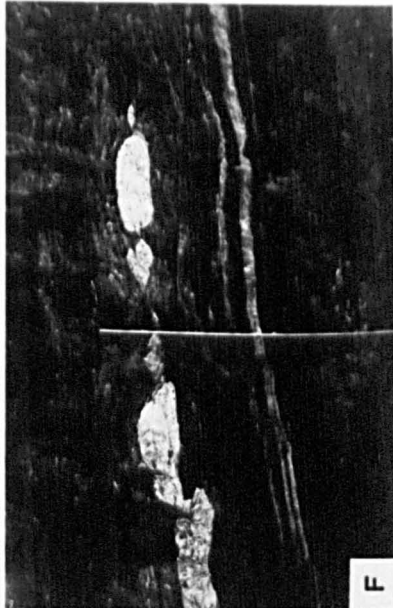
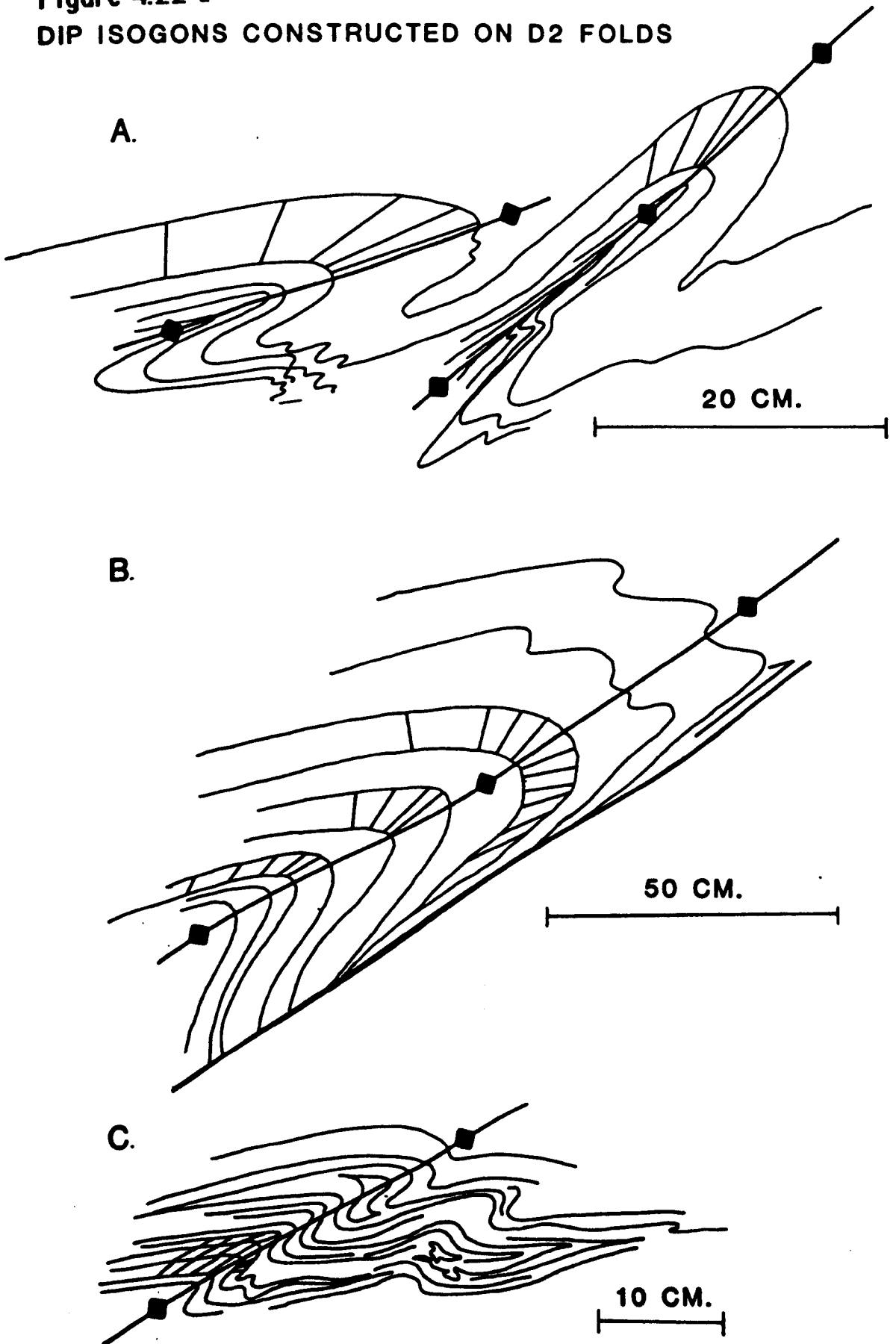
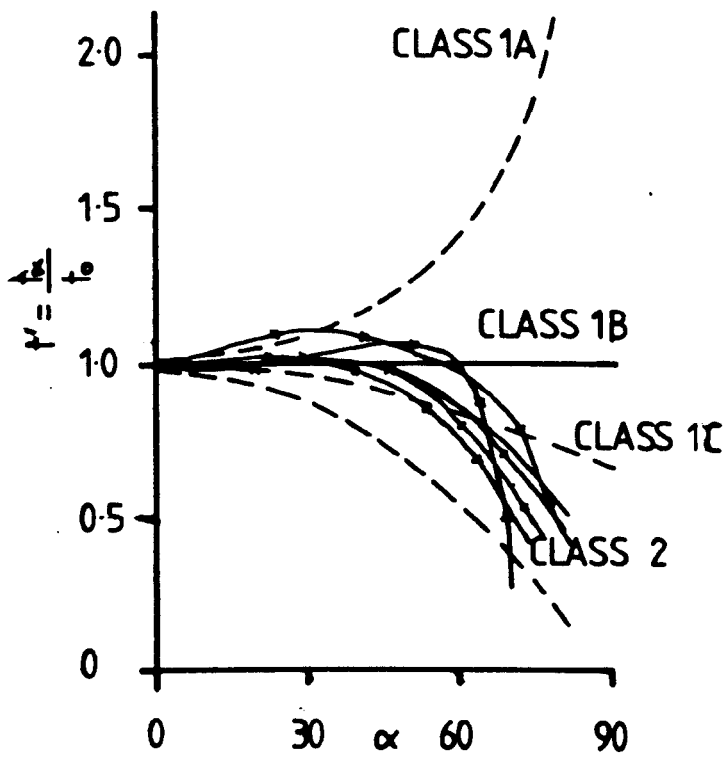


Figure 4.22 a

## DIP ISOGONS CONSTRUCTED ON D2 FOLDS





**Figure 4.22b**  $t_w$  plot of D2 folds. The folds are class 2 similar folds

## Figure 4.23 D2 Foliations

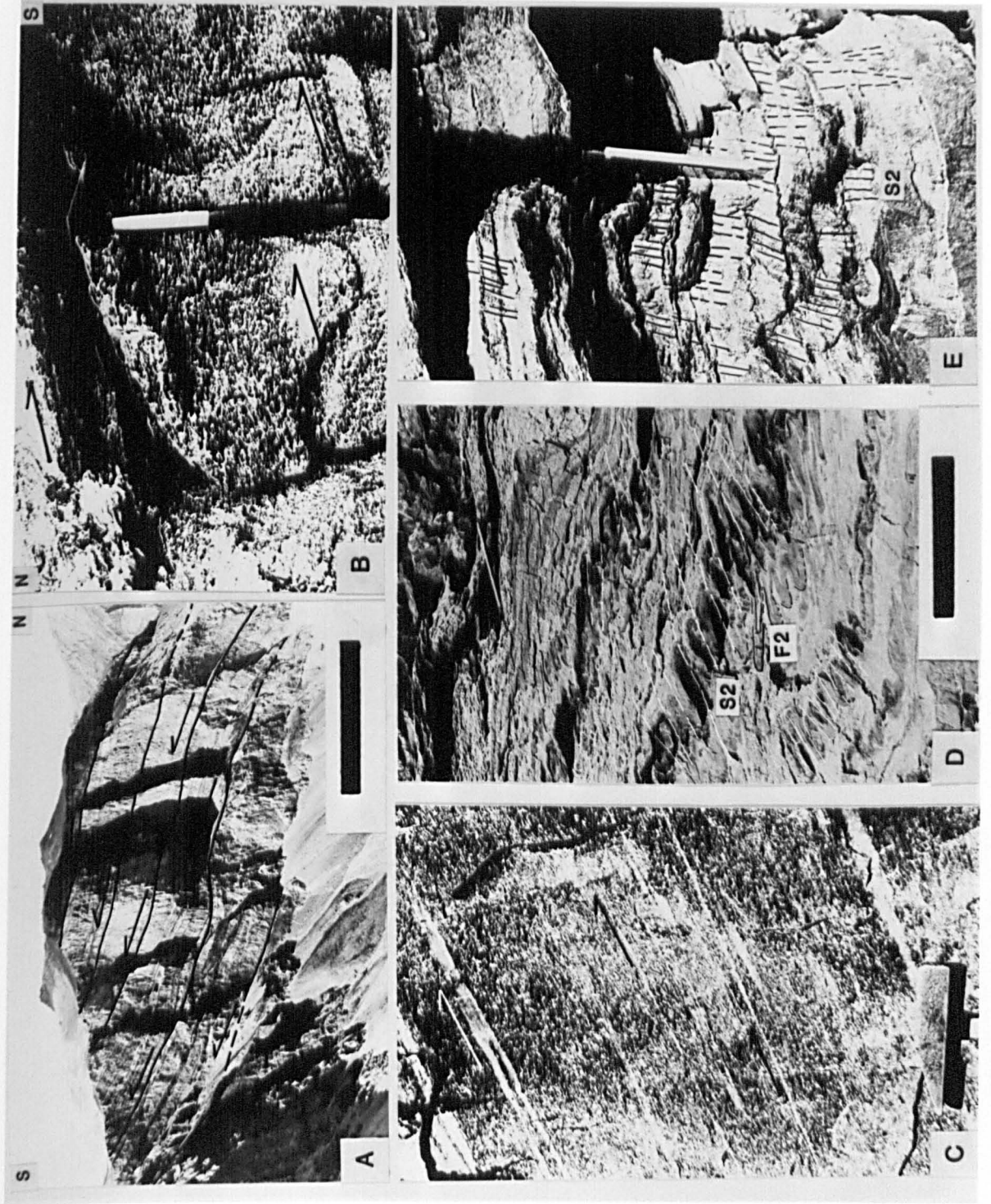
A) Photograph of the western Agfardlikavsá cliffwall highlighting the southerly verging low angle imbricated D2 tectonic slides. South verging, northerly inclined, isoclinal folds are developed within the tectonic slide panels. D1 northerly verging structures are formed below the lowermost (sole) slide. Scale bar 300 metres.

B) 'Mottled Pelite' showing throughgoing northerly inclined mylonitic shear zones (with sense of shear indicated) and asymmetric southerly verging D2 'z' folds. Location 214, near Myers showing, north South Lakes.

C) Mylonitic granodiorite, developed in a D2 tectonic slide zone, with D2 intrafolial isoclinal folds parallel to the mylonitic foliation. Location 502, western Marmorilik Plateau.

D) Competent dolomitic band transposed into an S2 crenulation cleavage. Location 516, south Marmorilik Plateau. Pencil for scale.

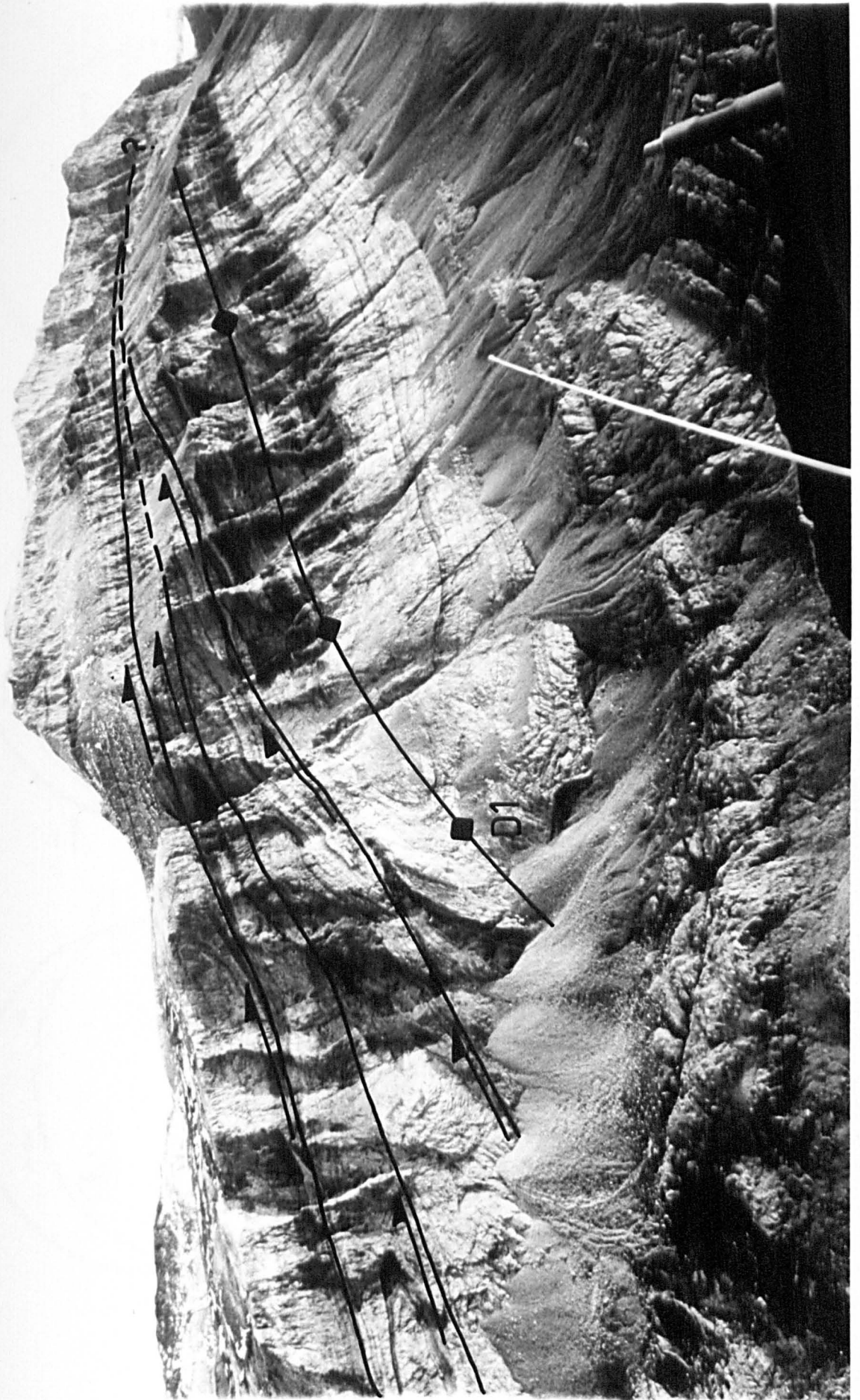
E) Upright S2 crenulation cleavage developed in S1 foliated biotite schists of the Nukavsak Formation. Pencil for scale. Location 401, northeast Marmorilik Plateau.



## Figure 4.24 A Structural Interpretation of the Fishing Lakes Cliffwall

An oblique aerial photograph of the spectacular Fishing Lakes cliffwall (sub-perpendicular to the D2 tectonic transport direction). A D1 anticlinal-synform fold core is transected by low-angle imbricated D2 tectonic slide zones. Southerly verging, D2 tight-isoclinal folds occur in the tectonic slide blocks. The D1 fold core is thought to have acted as a rigid footwall block during D2 deformation. Width of cliffwall 10 km. Height 1100m.





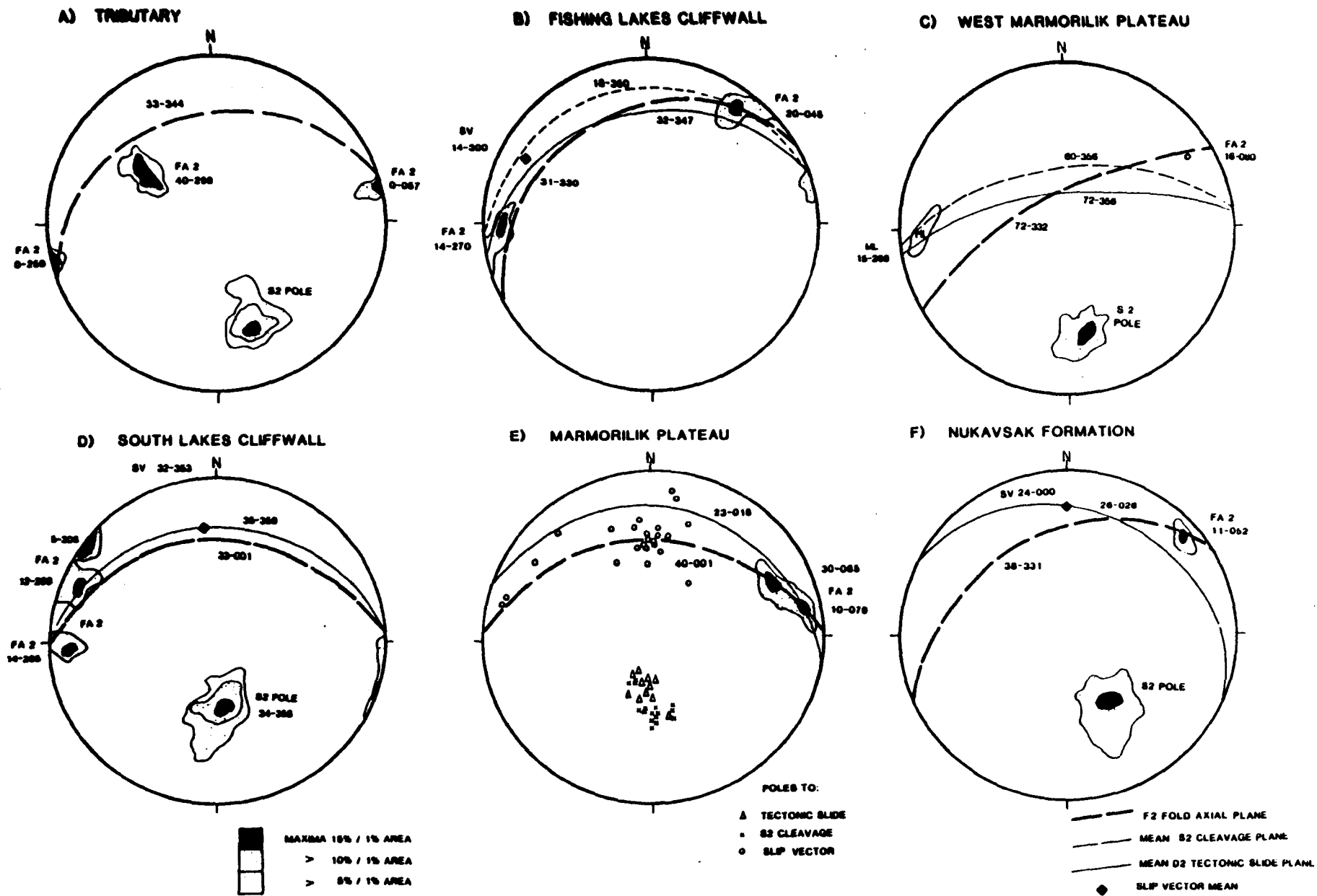


Figure 4.25 Summary stereograms of D2 deformation stereographic data

## Figure 4.26 D2 Tectonic slide systems and the D3 Tributary-Nunngarut fault

Photograph of the eastern Agfardlikavsa cliffwall showing the imbricated D2 low angle tectonic slide zones of the central contraction belt. The slide zones transect D1 recumbent isoclinal folds (centre). Low angle ramps and snakeshead structures are developed toward the top of the sequence (middle left). South verging, tight to isoclinal D2 folds are formed in the D2 slide blocks, especially where a high anisotropy encountered e.g. the interbanded carbonate-pelite succession (top). The D3 Tributary Nunngarut sinistral shear fault (right) cross-cuts all earlier structures. It shows here an apparent dip-slip displacement of 180 metres.

S

N



## **4.4 D3 Sinistral Shear Phase**

### **4.4.1 Introduction.**

D3 deformation in the Karrat Group supracrustals is dominated by a major sinistral shear zone (Fig. 4.27). The shear zone is bounded by two steeply dipping sinistral shear zones, the Quamarajuk and Fishing Lakes faults (Figs. 4.1b &c, 4.27 & 4.28).

Two distinct tectonic structures are present within the sinistral shear zone:- i) en-échélon high angle, ductile to semi-ductile, NNE-SSW trending, WNW side down, sinistral shear zones with antithetic dextral splays and ii) periclinal en-echelon, WNW-ESE trending, north-easterly verging, asymmetric folds.

The shear zones are dominant in the south and east of the study area, whilst the en-echelon folds occur in the northern Marmorilik area (Figs. 4.27 & 4.28). In the Black Angel deposits the sinistral shear zones cross-cut the en-echelon folds (Fig. 6.15 & 6.16).

### **4.4.2 Sinistral shear-bounding faults.**

The southerly Fishing Lakes fault is a 5-10 metre wide, 30°-45° northerly dipping, ductile, sinistral shear zone that has its maximum displacement at the Fishing Lakes cliffwall. It reactivates the originally extended basement-supracrustal contact in the Fishing Lakes area (Fig. 4.1a, c & 4.27) then cuts previously undeformed granodiorite, until it is deflected into the supracrustal pile south of the Little South lake (Fig. 4.28). Here the shear zone is transected by higher angle, NE-SW trending, west side down, D3 sinistral shear zones that cut both the basement and supracrustals (Fig. 4.1a & 4.27).

The northerly Quamarajuk fault is unexposed but is interpreted to be an oblique slip, semi-ductile, shear zone with an inferred minimum dip slip displacement of 600 metres (Fig. 4.1b). The fault is inferred to trend WSW-ESE along the Quamarajuk fjord, south of the Magdlak area, and then between the Karrat Group and the basement gneisses along the Alfred

Wegener Glacier to the inland ice-cap (Fig. 4.27 & 4.30a). This interpretation was made on the basis of several observations:-

i) the presence of a major downbend in D1 and D2 structures in the northern Marmorilik area (Figs. 4.30a), analogous to rollover development associated with a listric extension fault (McClay and Ellis, 1987). ii) the juxtaposition of topographically higher basement gneisses of the Alfred Wegener Peninsula against the Karrat Group supracrustals (Fig. 4.1b), iii) the geometrical association of en-échelon shear zones and folds in the supracrustal pile (Figs. 4.27 & 4.28) and iv) the lack of D3 sinistral shear zones in the Magdlak Peninsula (Fig. 4.18).

#### **4.4.3 En-échelon folds.**

En-échelon, doubly plunging, periclinal, ESE-WNW trending, open to closed, upright to northerly verging folds (Figs. 4.29a & 4.33) are found locally along the southern margin of the Quamarajuk ('Q') Fjord fault. The fold axial traces are inferred to intersect the fault at an angle of between 30°-40° showing a clockwise sense of rotation (Fig. 4.27). The fold axial planes are rotated from an upright to northerly inclined structures from the middle of the Black Angel mountain towards the 'Q' fjord (Fig. 4.30a). The fold axial traces are cross-cut at approximately 80° by later D3 sinistral shear faults (Fig. 4.27) (section 4.4.4). Folds are accommodated by differential slip of material on axial planar microshears and microlithons (Fig. 4.291c & d). Extensional kink structures occur above semi-brittle fracture tips (Fig. 4.29b).

Very complex outcrop patterns result from D3 refolding of earlier tectonic fabrics (Fig. 4.14 & 6.16). The earlier type 3 fold (D1-D2) interference patterns are overprinted by type 1, dome and basin, interference patterns as result of periclinal D3 refolding (Fig. 6.16).

#### 4.4.4 Sinistral shear zones.

To the south and east of Marmorilik, NNE-SSW trending, WNW side down (76-304°, S.V. 30-208, Fig. 4.33), sinistral shear zones occur as en-échelon arrays. They are high angle, ductile to semi-ductile structures (Fig. 4.30c & d) with antithetic dextral splays (Fig. 4.30 e & g). The shear zones vary from small scale closely spaced semi-ductile zones in the Ark area to semi-brittle, listric and planar oblique slip faults in the hangingwall block of the Tributary-Nunngarut fault (Fig. 4.26, 4.30a & b). These oblique slip faults decrease in displacement northwestwards and intersect the Quamarajuk Fault at approximately 90° (Figs. 4.27 & 4.28).

The Tributary-Nunngarut fault is a steep, braided fault zone of 180 metres apparent dip slip displacement on the 'A' fjord cliffwall (Fig. 4.26). The fault flattens out into a low angle, east-west trending, extensional structure on the Marmorilik Plateau (Fig. 4.27 & 6.7), that tips out in the Fishing Lakes cliffwall.

Individual shear zones vary both in width (1cm-20m) and displacement (1cm-180m) through the area (Fig. 4.30 c & f). The rotation of the external schistosity into the shear zone plane varies between 60°-85° from semi-ductile to ductile shear zones respectively (Fig. 4.30 c-g). Transtensional duplexes (Fig. 4.31) and antithetic accommodation features occur within the semi-ductile shear zones of the South Lakes area (Fig 4.27). Antithetic dextral (R') reidal shears (Fig. 4.30g) offset the rotated schistosity, whilst conjugate shear sets fracture the more competent massive dolomitic lenses (Fig. 4.32g & h). These fractures are oriented with their acute bisectrix parallel to the  $O_1$  direction.

The shear zone fault blocks are relatively undeformed and exhibit a limited number of synthetic and antithetic accommodation features (Fig. 4.32). These include extensional, NE-SW trending, upright fractures with a north-west side down dextral or sinistral offset (Fig. 4.32 b,c & d), extensional calcite-filled tension gashes (Fig. 4.32f), conjugate fractures

(70-307° and 57-061° Fig. 4.33) (Fig. 4.32g & h) and semi-ductile to brittle, planar, rotational joints (Fig. 4.32a).

The joints become closer spaced within the more brittle siliceous units (Fig. 4.32a) and also adjacent to the major shear zones. In the more micaceous-shaley units extension within the shear zone fault blocks is taken up by ductile shearing along earlier anisotropic schistosity planes.

A minimum estimate for the cumulative sinistral, west side down, displacement on the 20 major D3 shear zones in the supracrustal shear zone, has been estimated at 1.7 km by using the formula (Ramsey and Graham, 1970):-

$$S = \int_0^x Y \, dy$$

where S = displacement, Y = Angular shear strain, x = shear zone width

#### **4.5. D4 Late Extension Phase**

D4 deformation is a non-penetrative event that consists of linearly extensive, sub-vertical, north-south trending, faults. The faults are sometimes filled with dolerite dykes, up to 150 metre wide, which are associated with minor sills. Extensive small scale fracturing and en-échelon, north-south trending, west side down, joints are developed in the Black Angel mine. The faults are often observed as open zones or filled with a carbonate/talc fault gouge. Microfracturing in the ore horizon occurs, with offsets of up to 2 metres on the Black Angel sulphide body. The age of this deformation is debatable (Sect. 2.2.3), but it is likely to be late Pre-Cambrian (≈1000-700 ma.).

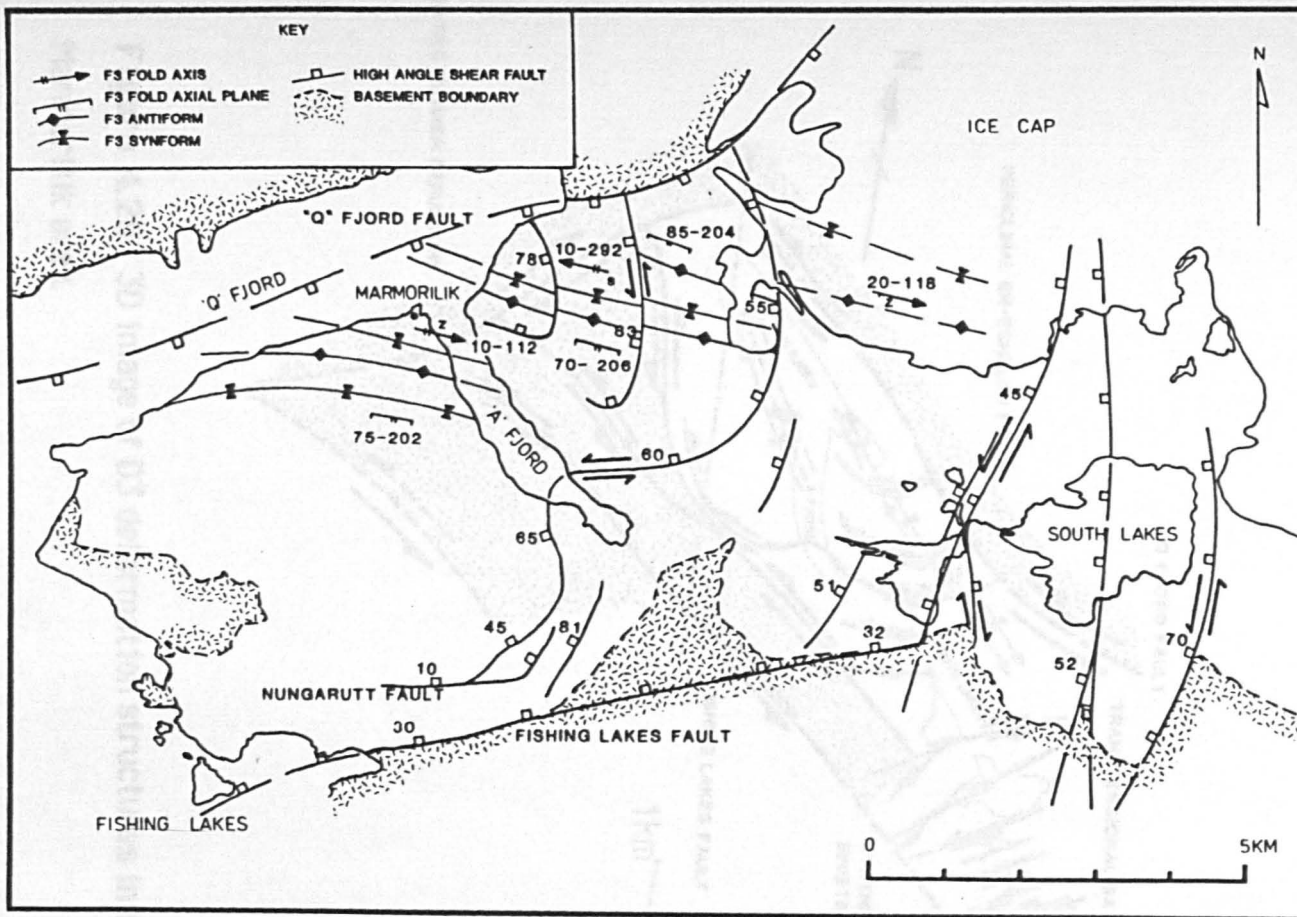


**Figure 4.27** A map of D3 deformation structures in the Marmorilik area.

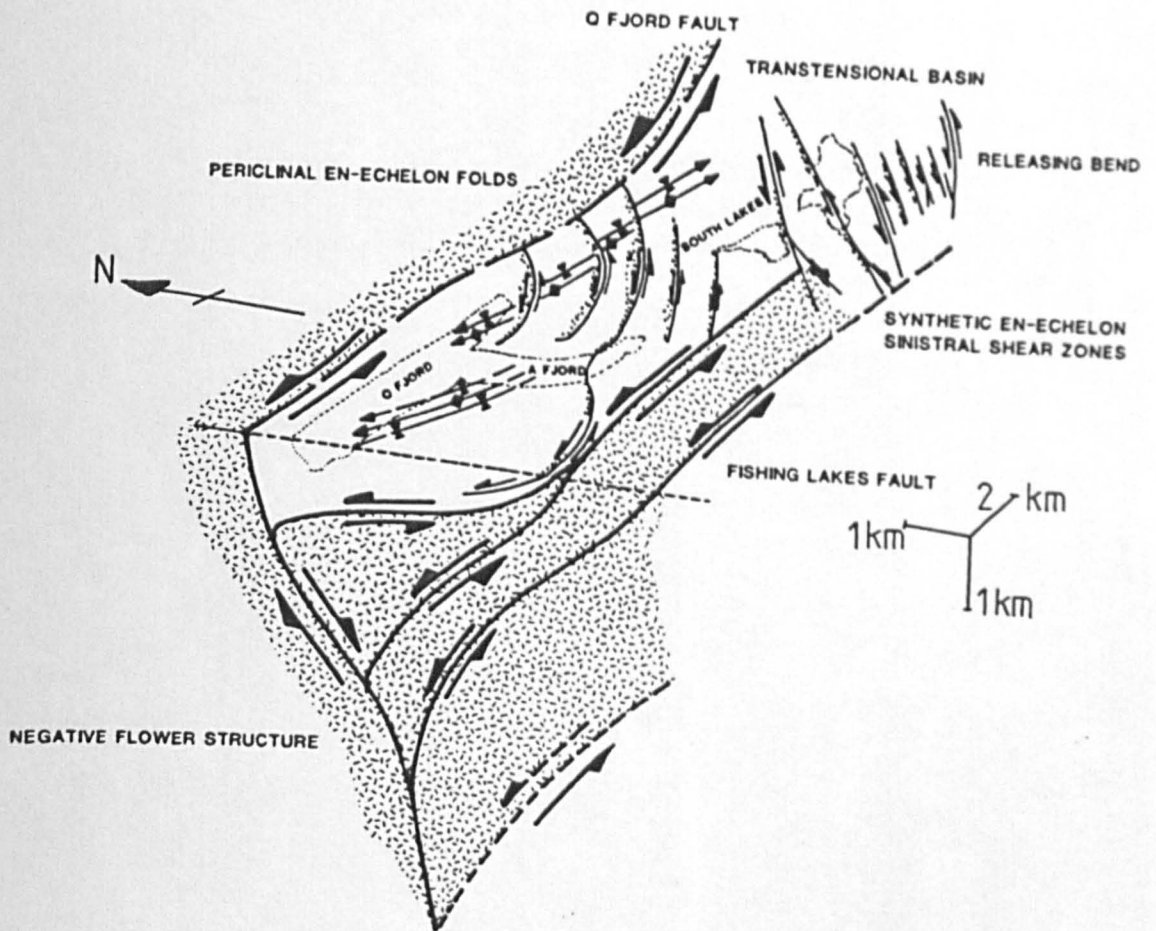


**Figure 4.28** 3D image of D3 deformation structures in the Marmorilik area.

## Figure 4.29 D3 Folds and Associated Shear Faults

A) D3 north verging asymmetric fold with a nipple like synformal hinge filled with massive recrystallised ore. 1.5 metre rule for scale. Stope D24, Angel zone, Black Angel mine.

B) A D3 semi-brittle shear fault with antithetic calcite filled tension gashes tips out into a D3 extensional kink zone. Ruler divided into 20 cm. sections. Location 1630, Drift 23, Black Angel mine.

C) Steeply east dipping D3 dextral shear fault (a fault in the Tributary fault system) showing a stepped ramp-flat geometry. The footwall marbles are bleached indicating a high fluid flow during deformation. The hangingwall block shows D3 shear folds developed by slip on synthetic microfaults. Location 1532, Drift 23, Black Angel mine.

D) Interbanded grey banded calcite and dolomite marbles are sheared into a D3 synform which abutts a D3 steeply east dipping sinistral shear zone. Calcite filled tension gashes are formed in the shear zone. Location 1628, Drift 23, Black Angel mine.

E) A close up of a sharp D3 semi-ductile, west dipping, sinistral shear fault. Talc and graphite occur on the shear zone plane. The hangingwall pyrite laminated calcite marbles are bleached adjacent to the shear zone. Location 1628, Drift 23, Black Angel mine.

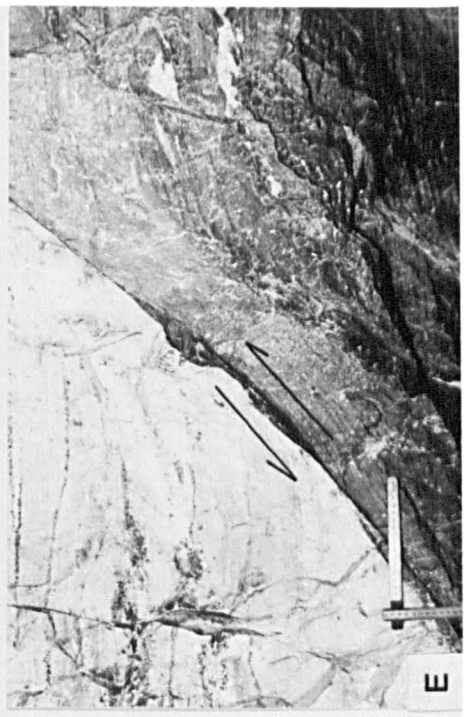
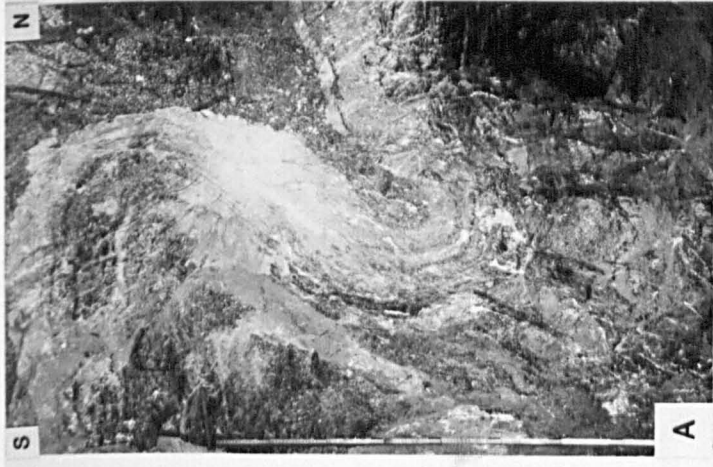
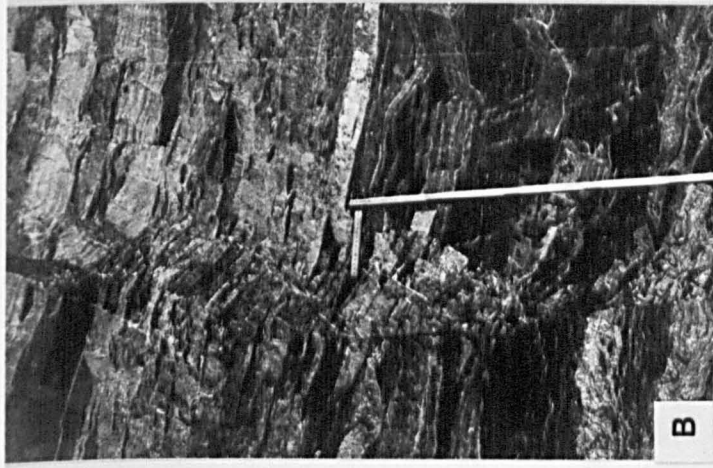


## Figure 4.30 D3 Deformation Structures

A) A view of the eastern 'A' fjord cliffwall taken from the 'Q' fjord. The trace of the inferred northerly sinistral shear bounding fault is marked. The axial trace of the D3 rollover antiform is shown refolding the D1 Black Angel nappe. Antithetic shear faults, that accommodate the rollover downbend and rotation, are developed to the south of the cliffwall. Width of photo 6 km. Height of cliffwall 1050 m.

B) Close up of the southerly antithetic, listric, north-west side down, sinistral shear fault that occurs in an en-echelon array of faults to the south of the eastern 'A' fjord cliffwall. The fault cross-cuts the southerly verging F2 folds. Scale bar 150 m.

C) A photograph showing an early S1 foliated fabric becoming progressively rotated into a steeply westward dipping plane of a semi-ductile D3 sinistral shear fault. Hammer for scale. Location 39, South Lakes area.

D) Close up of the D3 shear fault in (C). In the shear zone the S1 fabric is sub-parallel to the eroded shear zone margin. The internal shear zone foliation is cross-cut by a later lower angle  $R_1$  fabric.

E) Antithetic semi-ductile, sub-vertical, D3 shear zone. The S1 foliation is deformed into D3 shear folds at the margins of the shear zone. near Location 13, South Lakes area.

F) An en-echelon array of northwest dipping (top left) D3 semi-brittle, sinistral, microshear zones. Location 18, South Lakes Cabin.

G) A ductile, antithetic, dextral, shear zone developed in dolomitic sandstones and siltstones. Intersecting shear joints occur in the more competent dolomitic sandstone lenses (transposed by S1 foliation). Location 39, South Lakes.

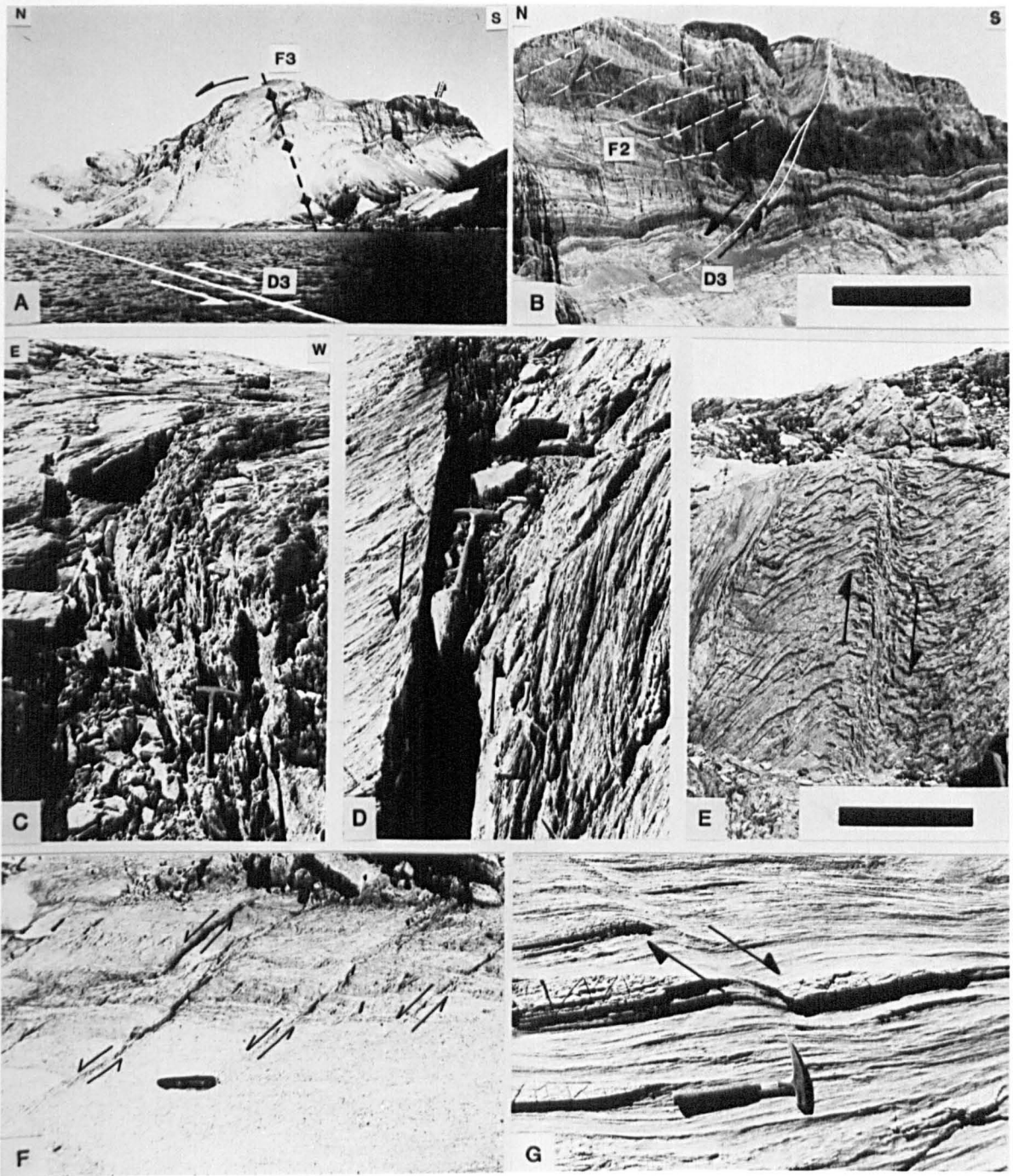


### Figure 4.31 D3 Transtensional Shear Fault System

Photographic montage of a D3 semi-brittle sinistral shear fault system developed in massive dolomite marbles on the northeastern shore of the Little South Lake. The montage shows a high angle, northwesterly dipping, bounding fault to the right (south) of the frame. The hangingwall block is dissected by a series of transtensional synthetic, high angle, semi-brittle, rotational shear faults that form into transtensional duplexes. Towards the centre of the frame, the fault spacing decreases and ramp-flat geometries occur. Scale bar 2m.



## Figure 4.32 D3 Microfaults and Joints

A) An en-echelon set of D3 antithetic, rotational, planar-concave, east side down extension joints cross-cutting an early S1 foliation. Location 25, north Little South Lake.

B) Synthetic northwest side down en echelon fractures developed in a foliated dolomitic marble. Location 369, north Nunngarut zone, Marmorilik Plateau.

C) En-echelon, planar-convex, rotational fractures that are developed in a synthetic D3 shear zone in the hangingwall of the Nunngarut fault. Location 440, north Nunngarut zone, Marmorilik Plateau.

D) Westerly dipping synthetic extension joints in the hangingwall of a sinistral shear zone. Location 25, north Little South Lake.

E) En-echelon sinistral and dextral microshear faults formed in an S1 foliated graphitic dolomitic marble. Transected D3 similar folds form due to differential slip on the D3 microlithons. Location 456, north Nunngarut zone, Marmorilik Plateau.

F) Sub-vertical calcite filled tension joints cross-cutting S1/S2 foliated grey banded calcite-dolomite marbles. Location 747, north Black Angel Plateau.

G) Conjugate and intersecting shear faults developed in relatively undeformed massive dolomitic marbles at the centre of a large sinistral shear fault zone. Location 39, south South Lakes.

H) Interbanded dolomitic S1 foliated siltstones and sandstone lenses to the east of a ductile dextral D3 shear (top right). Intersecting shear joints are differentially formed in the more competent dolomitic sandstones. The conjugate fractures give way to dextrally displaced west dipping microfaults. Location 39, south South Lakes.

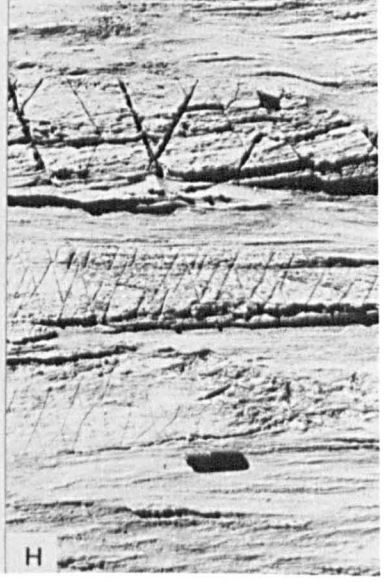
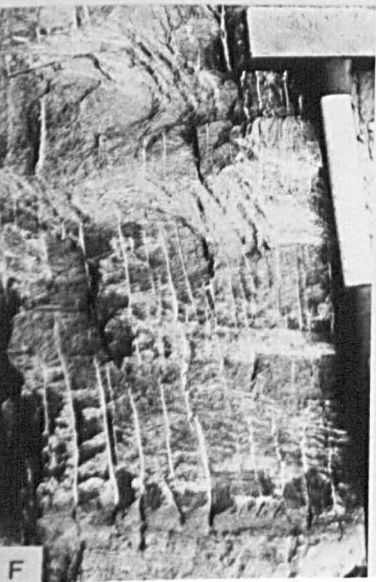
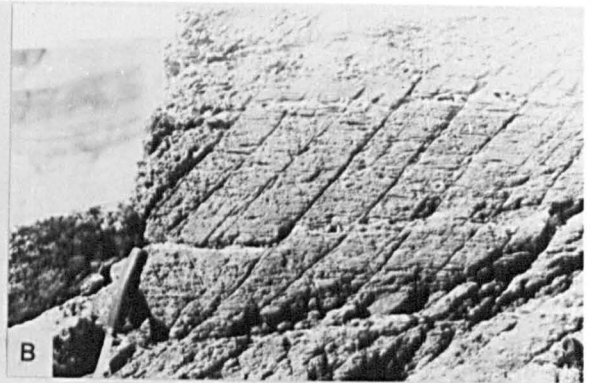
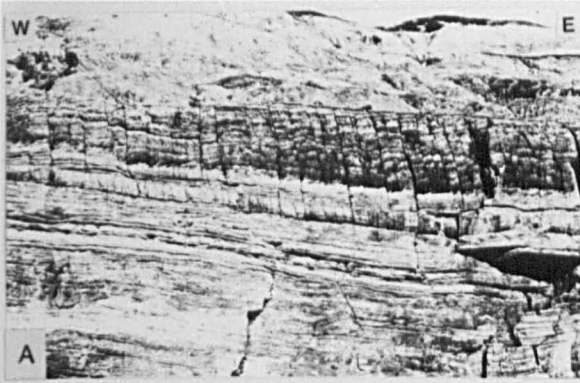
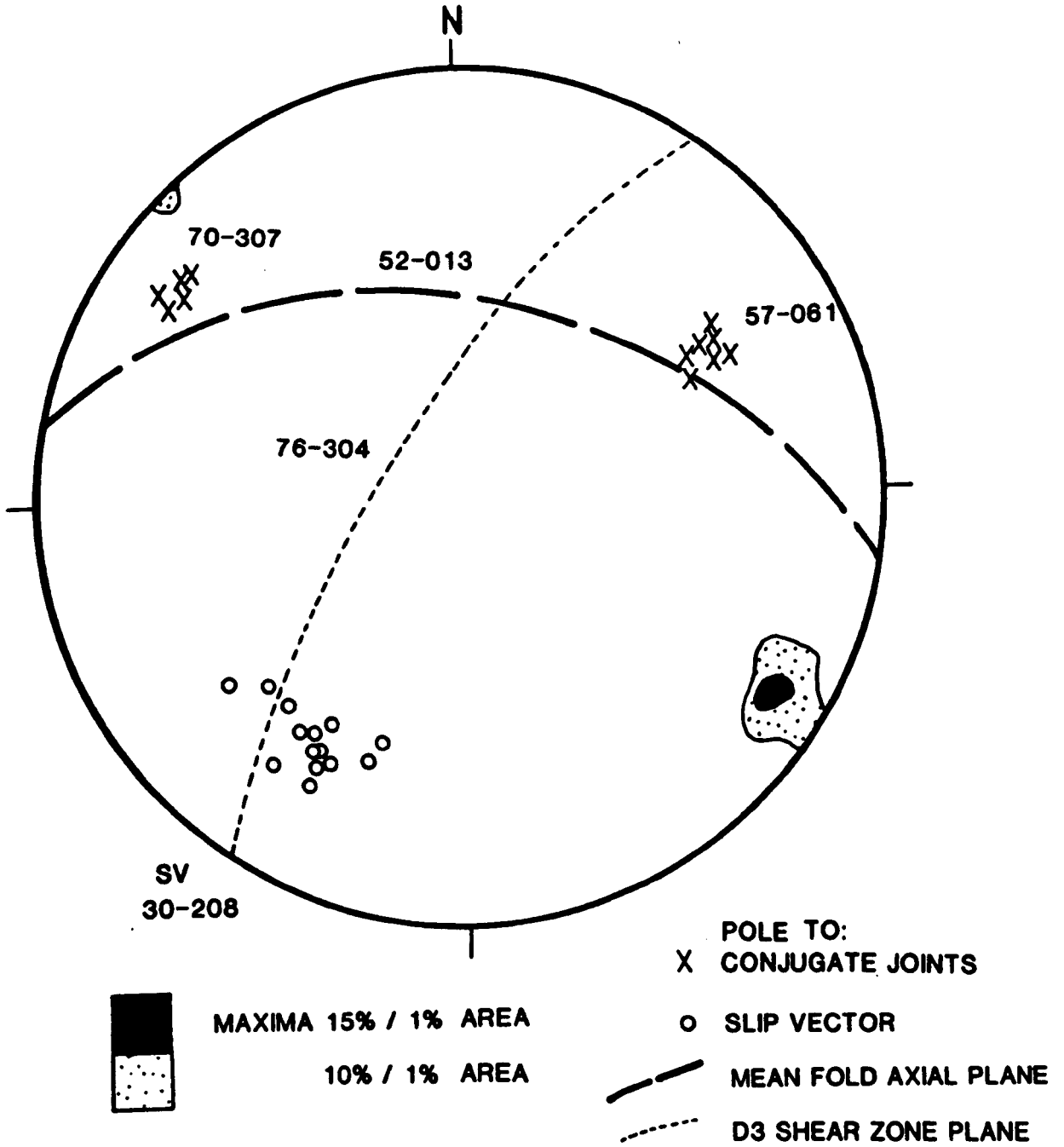


Figure 4.33  
D3 SUMMARY STEREOGRAM



## **4.6 Tectonic Evolution of the Marmorilik area**

Polyphase deformation in the Marmorilik area took place under ductile conditions and is characterised by complex vertical basement and sub-horizontal supracrustal motions. Vertical basement motions were probably associated with both extensional/transensional and diapiric processes. Mechanisms of basement uplift are discussed fully in chapter 9.2.

### **4.6.1 D1 Early Recumbent Phase Deformation**

The structures developed during the D1 deformation phase are - i) extensional fault systems which occur in the south of the area, consisting of four tectonic packages (Fig. 4.4), that verge northwards off a granodioritic basement massif, ii) central flat-lying intensely sheared zone (Fig. 4.26) and iii) a northern non-cylindrical, recumbent nappe structure (Fig. 4.14) with small-scale contraction faults. These are interpreted to represent geometrically linked systems within a northerly propagating gravity slide block, that was initiated by a basement uplift to the south (Fig. 4.34a). The low angle extensional listric fans, high angle extension faults and rollover structures represent the trailing edge of a gravity slide block. The large recumbent isoclinal folds, bedding plane slip and tectonic sliding in the northern Marmorilik area represent leading edge compressional structures in the toe end of a major nappe.

### **4.6.2 D2 South Verging Fold and Fault Phase**

The second deformation phase produced structures with a southerly sense of vergence, but a colinearity with the earlier D1 trends (Fig. 4.1a). The impetus for this reversal in the tectonic transport direction is accounted for by the generation of an uplifted and overthrust (section 4.3.2) basement massif (to the north) on the Alfred Wegener peninsula. Overthrusting of the northern basement gneisses onto the supracrustals led to the formation of a southerly propagating fold and

slide belt in the Karrat Group (Fig. 4.34b). Basement incorporation into the stacked tectonic slide systems to the west of Marmorilik (Fig. 4.1c) suggests that the sole thrust for this deformation lay in the southerly granodioritic massif.

The presence of tectonic slides, the non-cylindricity of the folding and the rotational nature of the deformation (fold axial planes were rotated from inclined to recumbent orientations in the central Marmorilik region (Fig. 4.20 & 4.26)) suggests that the rocks were highly ductile and deformed by a process of heterogeneous simple shear. The sub-horizontal nature of the tectonic slides is enhanced by highly anisotropic fabrics that were developed during  $D_1$  extensional fault and cleavage formation.  $D_1$  anisotropy is also thought to be responsible for the strong colinearity between  $D_1$  and  $D_2$  structures.

### 4.6.3 D3 Sinistral Shear Phase

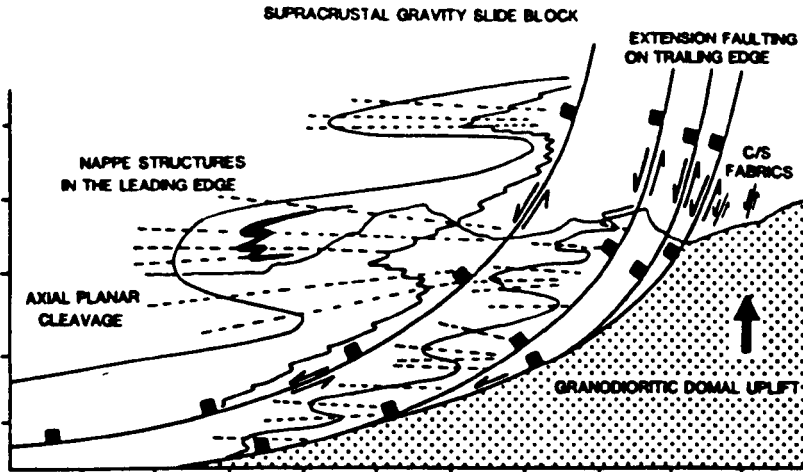
Structures formed in the sinistral shear phase are mechanically linked to the formation of a major crustal shear zone (Fig. 4.28). From both field and experimental studies of transcurrent fault systems, the controls on structural type, orientation and relative timing of the tectonic features developed within these systems is better understood (Tchalenko, 1970; Wilcox et al., 1973; Rodgers, 1980; and Harding, 1985; Woodcock & Fisher, 1986).

Three major D3 shear structures are present in the Marmorilik area, they are:- i) synthetic sinistral shear faults ii) en-echelon periclinal folds and iii) through-going shear zone bounding faults. From the association of these structures, the shear zone has been interpreted as a right-stepping, transtensional shear zone (Fig. 4.35) that developed into a synformal, negative flower structure (Harding, 1985)(Figs. 4.28 & 4.34c). Studies on the relative timing of the structures within shear zones has been carried out by Wilcox et al., (1973) (Fig. 4.36). On applying their

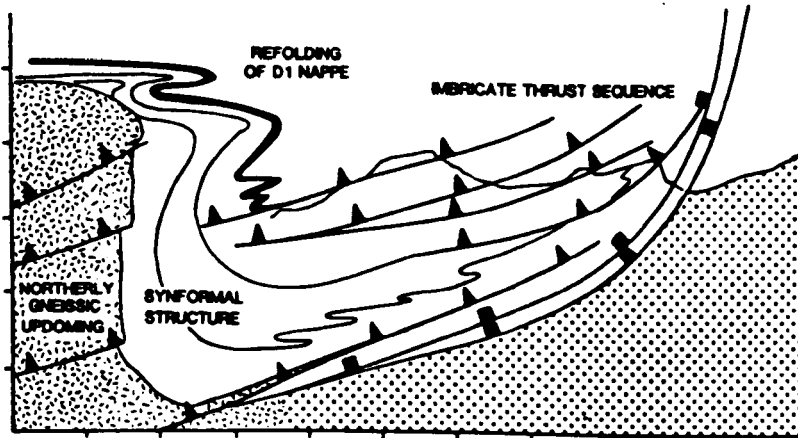
findings to the Marmorilik area, it is suggested that the en-echelon periclinal folds were the first structures to develop. These features accommodated a roll-over structure (Hamblin, 1965), with a sense of oblique slip, that was produced in the supracrustal hangingwall block of the Quamarajuk fault as a major half graben developed (Fig. 4.30 a & b, 6.10).

As sinistral shear proceeded, the roll-over downbend was accommodated and cross-cut by synthetic reidal shears (Fig. 4.36b), such as the Tributary-Nunngarut Fault (Fig. 4.26) and the structures in its hangingwall block (Figs. 4.30b). The last structures to be developed were the throughgoing west-east trending bounding faults, in particular the southerly Fishing Lakes fault. This fault propagated eastwards, but terminated abruptly against a zone of oblique slip faults in the Little South Lakes area (Fig. 4.28). This fracture zone is interpreted to have imparted a pseudoplasticity upon the area (Wilcox et al., 1973) that allowed the region to deform uniformly without being cut by the wrench fault. The pseudoplasticity allowed a rapid translation of the sinistral displacement on the Fishing Lakes wrench fault to be accomplished within a short distance.

**A D1 DEFORMATION: EARLY RECUMBENT PHASE**



**B D2 DEFORMATION: SOUTH VERGING FOLD AND FAULT PHASE**



**C D3 DEFORMATION: SINISTRAL SHEAR PHASE**

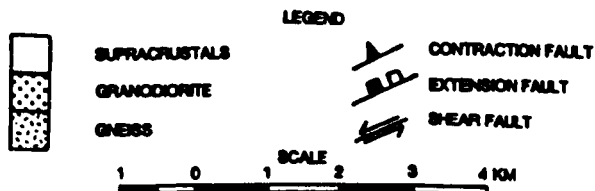
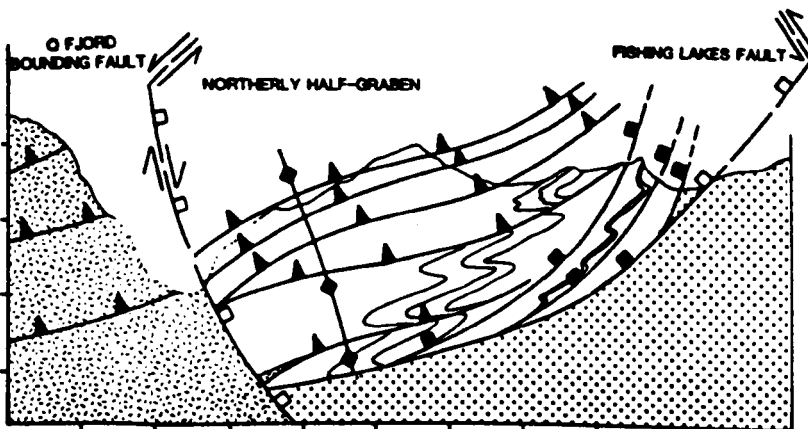


**Figure 4.34** Simplified cross-sections to represent the tectonic evolution of the Marmorilik area.

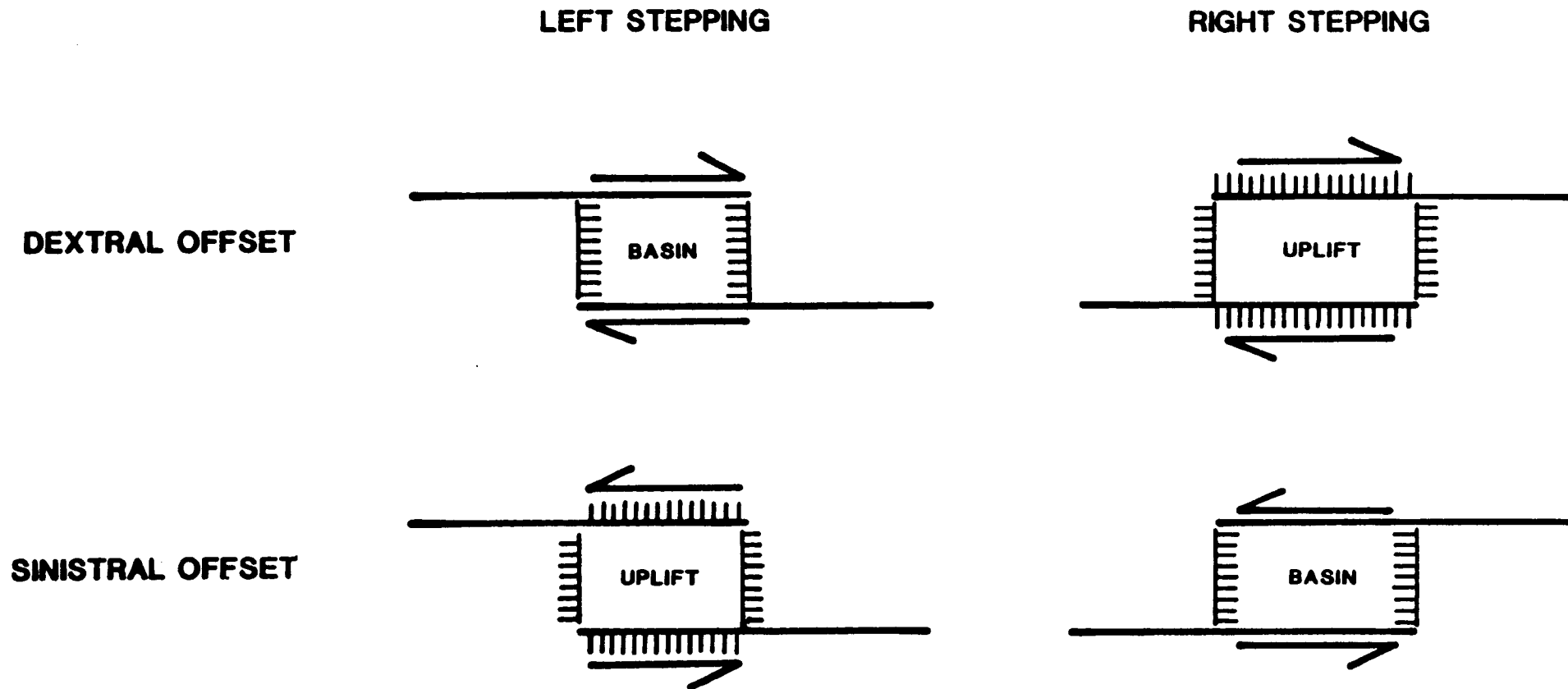
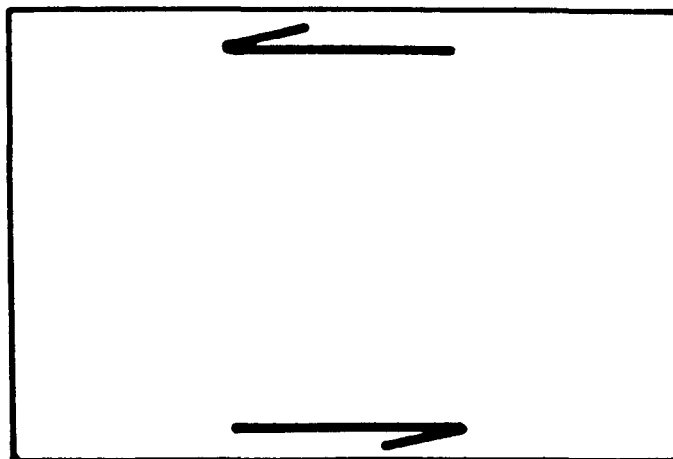
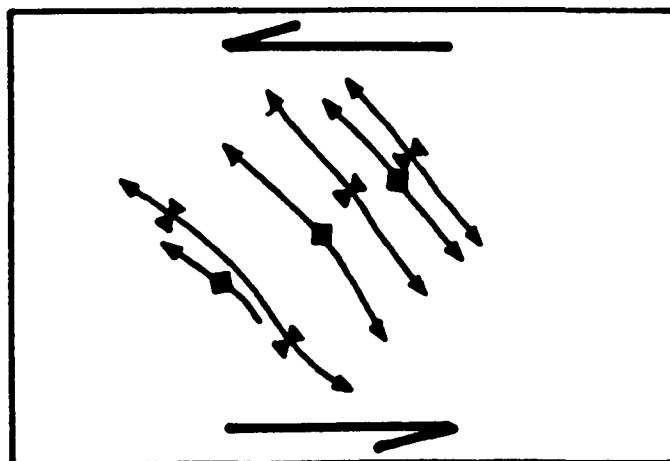


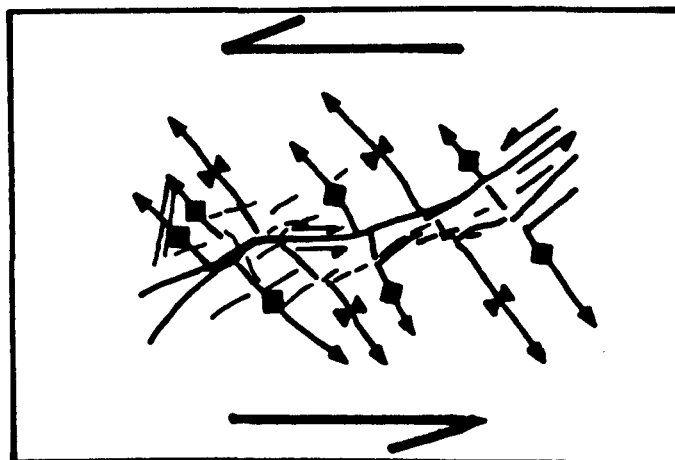
**Figure 4.35** The development of uplifts and basins in right and left stepping, dextral and sinistral shear systems  
(After Rodgers, 1980)



UNDEFORMED STRATA WITH SINISTRAL SHEAR INITIATED



EN-ECHELON PERICLINAL FOLDS



EN-ECHELON FOLDS CROSS-CUT BY SYNTHETIC REIDAL SHEAR

**Figure 4.36** Sequential development of accomodation structures associated with the development of a sinistral shear zone.  
(After Wilcox et al., 1973).

## **CHAPTER 5: Metamorphism of the Marmorilik area**

### **5.1 Introduction**

The metamorphic grade of the Basement Umanak Gneiss Complex varies from granulite to greenschist facies, whereas metamorphism in the Karrat Group is marked by greenschist-amphibolite facies (Henderson and Pulvertaft, 1967; Garde, 1978; Pedersen, 1980a & b).

A comprehensive study of the metamorphic evolution of the Marmorilik area is beyond the scope of this thesis. This chapter specifically assesses i) the P/T conditions of the successive deformation phases, and ii) the pre-metamorphic character of the supracrustal package. A detailed description of sulphide metamorphism and deformation is given in chapters 6 and 9.

The metamorphism has been studied through observations on the field relationships between the metamorphic mineral assemblages and deformation structures. These data are supplemented by petrographic observations and microprobe analyses. The peak metamorphic grade of the supracrustal sequence has been established by i) stable isotope analyses of coexisting sphalerite and galena pairs within the Black Angel deposits (section 8.4) ii) Carbon isotope analyses on free graphite and the graphite-bearing carbonate rocks (section 8.3.1) and iii) microprobe analyses of sphalerites for application of the FeS geobarometer.

## 5.2 Basement Gneiss metamorphism

Earlier work has shown that three phases of metamorphism have affected the basement gneisses. An Archean age, granulite facies event is indicated by the presence of relict blue coloured quartz crystals in the Tassiusaq granodiorite. The granulite facies metamorphism is overprinted by retrogressive amphibolite facies mineral assemblages, thought to have been associated with the generation of the late Archean, Sermikavsak Formation (Escher and Pulvertaft, 1976).

Retrogressive phyllonitic shear zones (Fig. 4.5e) consisting of hornblende, tremolite, and phlogopite cross-cut the Basement Gneiss Complex. These formed during amphibolite-greenschist facies metamorphism associated with the Rinkian event

## 5.3 Karrat Group metamorphism

### 5.3.1 Mineral assemblages and field relationships

#### a) Qeqertarssuaq Formation

Metamorphic assemblages of the Qeqertarssuaq Formation are :-

Diopside-tremolite-dolomite-quartz+epidote

Actinolite-chlorite-phlogopite-dolomite

Phlogopite-biotite-chlorite-quartz-graphite

Little evidence of metamorphism is apparent in the orthoquartzitic bands of this unit (Fig. 3.7a). A weak D1 phlogopite schistosity occurs in the less pure quartzites.

Actinolitic and tremolitic schists (Fig. 3.7b) containing interstitial diopside and quartz and interbanded with quartzites and dolomite marbles, are deformed by D1 folds in the Fishing Lakes area (Fig. 4.5f) and by both D1 & D2 folds in the Magdlaq peninsula (Fig. 4.18). The actinolite/tremolite bands consist of coarse grained, up to 10cm., idiomorphic bladed-acicular grains and rosettes which occur in the quartzites (Fig. 5.2a) and represent post-D3 growth. Actinolite

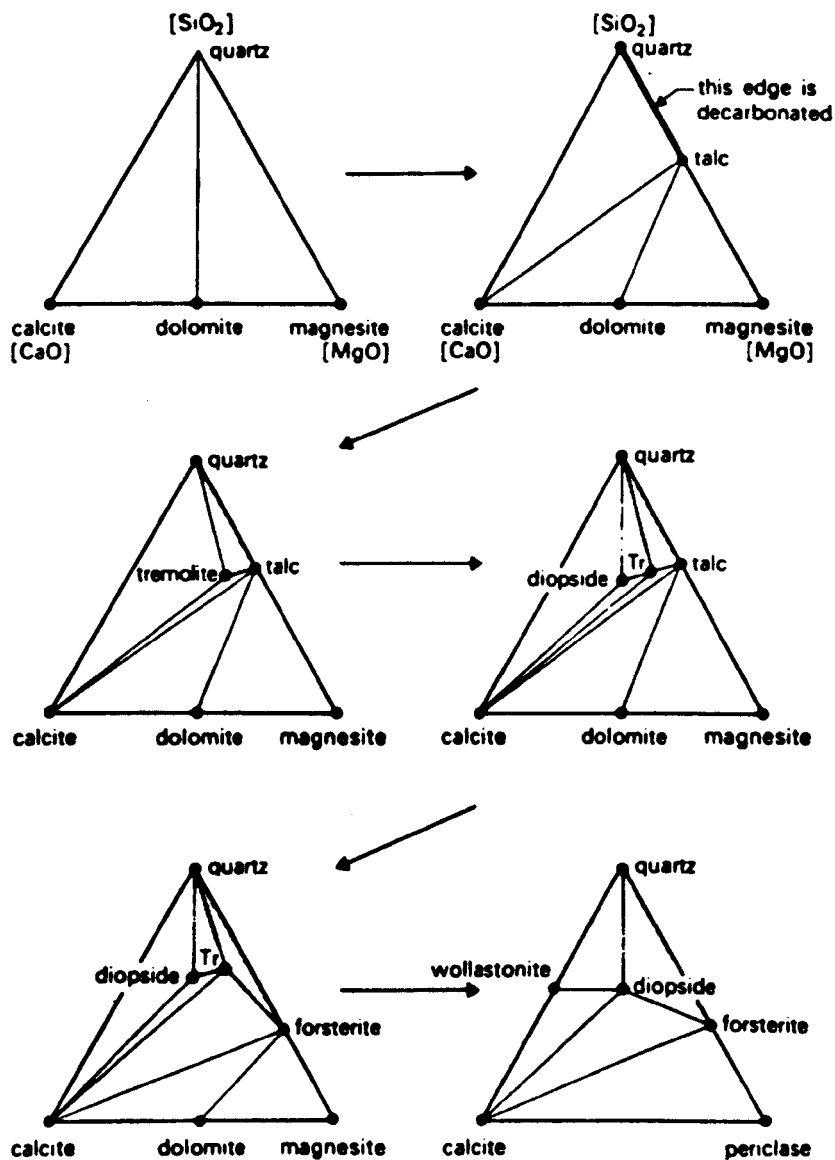


**Figure 5.1** AFM diagram for mineral assemblages in the siliceous Marmorilik Formation carbonates (From Winkler, 1979)

occurs in the western Marmorilik region whilst tremolite dominates the calc-silicate units in the east of the area.

Phlogopite (talc)-chlorite-quartz-graphite folia of the metapelitic units of the Qeqertarssuaq Formation are overgrown by syn-post D3 diopside, quartz and occasionally epidote porphyroblasts ( Garde, 1978; Pedersen, 1980a). The foliations are often crenulated.

## **b) Marmorilik Formation**

Tremolite, scapolite, phlogopite, biotite and chlorite occur in the Marmorilik Formation carbonates. Typical carbonate metamorphic assemblages are (Fig. 5.1):-

In the dolomite marbles

dolomite-calcite-quartz-phlogopite+albite+K-feldspar  
 dolomite-calcite-tremolite-phlogopite+albite+K-feldspar  
 dolomite-calcite-tremolite  
 dolomite-calcite-talc and calcite-tremolite-talc  
 dolomite-scapolite-graphite-phlogopite-quartz

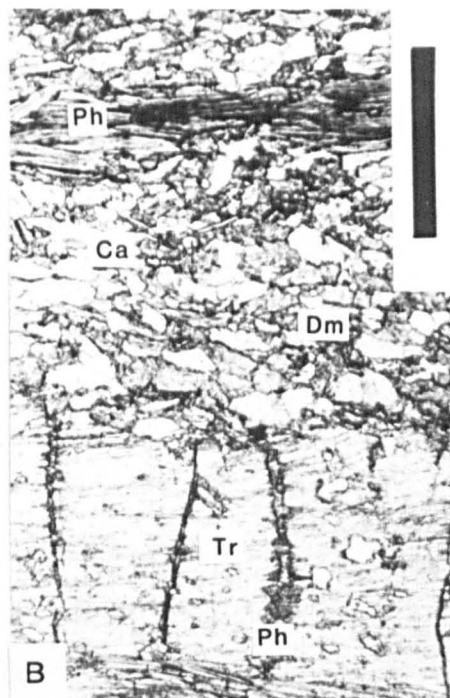
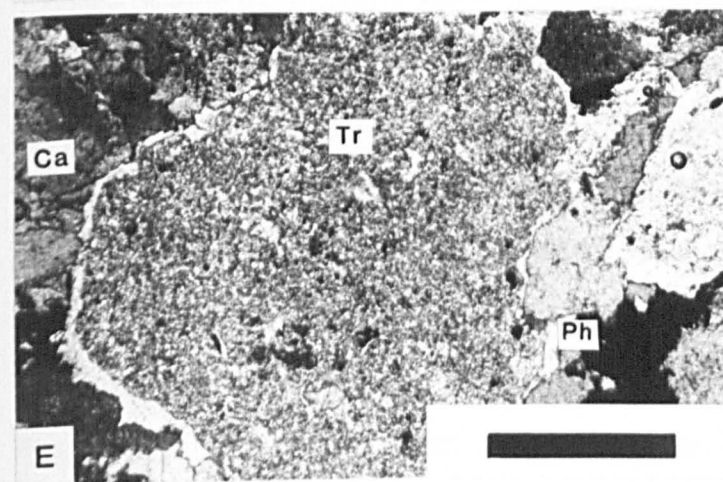
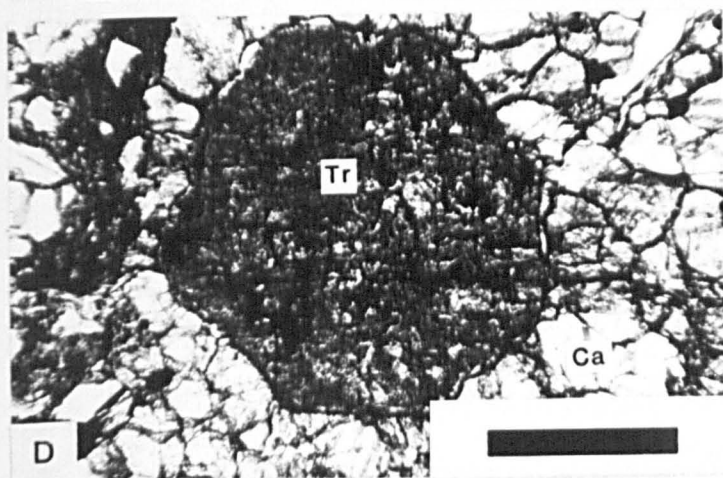
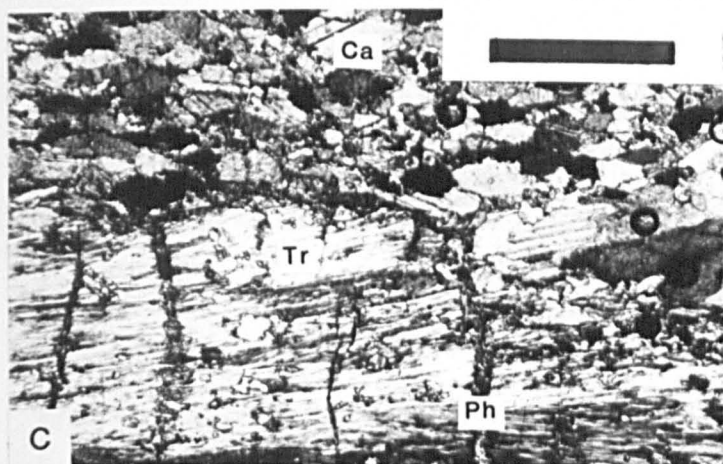
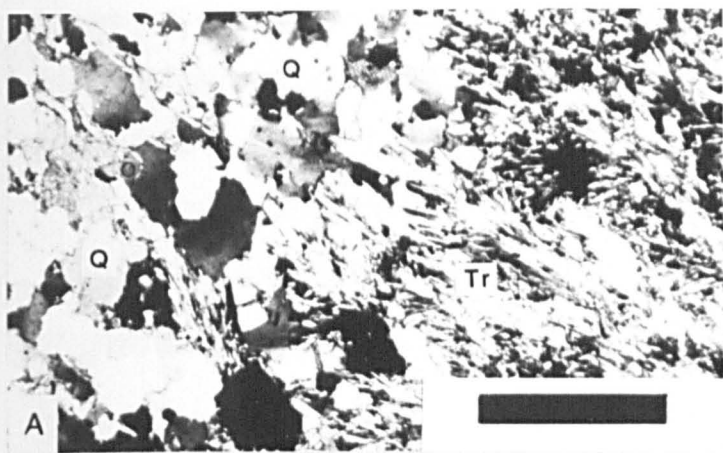
In the calcite marbles

Calcite-quartz-phlogopite+dolomite+albite+K-feldspar  
 Calcite-quartz-muscovite +albite+K-feldspar  
 Calcite-quartz-muscovite-biotite-albite-K-feldspar  
 Calcite-quartz-tremolite-phlogopite+albite  
 Calcite-scapolite-phlogopite-quartz  
 accessory chlorite and talc

Tremolite (Figs. 3.7f & g & 5.2) and scapolite (Fig. 3.7d & 5.3d-f) are the commonest metamorphic silicates in the Marmorilik Formation. Massive tremolitic units, up to 50 metres thick, are commonly found in the Lower Marmorilik member (Unit 1) of the South Lakes area (Fig. 3.7f & h), in the dolomite marbles (Unit 2) of the Nunngarut zone (Fig. 6.7) and the Middle Marmorilik member. The tremolitic units are composed of very coarse grained, up to 6 cm., light green to silvery white, tremolite

## Figure 5.2. Tremolite microtextures

- A) A photomicrograph of a coarse grained D3 tremolite rosette (Tr), consisting of fibrous acicular crystals, in a moderately strained quartzitic matrix (Q). Thin section 17a from the Qeqertarsuaq Formation, Location 17, South Lakes area. XPL. Scale Bar 500 $\mu$ .
- B) Phlogopite foliated calcitic marble, with minor dolomite, overgrown by a tremolite grain aligned parallel to the S2 foliation. Slight elongation of the calcite grains occurs parallel to the foliation. Specimen 234 a, South Lakes area. Scale bar 300 $\mu$ .
- C) A coarse grained prismatic tremolite crystal (Tr) overgrowing a phlogopitic (talc ?) calcite matrix (Ca). The tremolite (Tr) is retrogressed to phlogopite (Ph) along N-S fractures. Specimen 234 a, South Lakes area. Scale bar 300 $\mu$ .
- D) Cross-section of a tremolite crystal (Tr) set in a coarse grained calcitic matrix. Thin section V 216. Drill hole V 216. Black Angel Mountain. Scale 500 $\mu$ .
- E) An altered tremolite grain, now made of phlogopite (talc ?) and undifferentiated clay minerals, rimmed by fine grained phlogopite (Ph) and set in a calcitic matrix (Ca). Thin section XPL. Scale bar 500 $\mu$ .



rosettes ('knotenschiefer', Spry 1979) (Fig. 3.7f) that syn-post (D3) kinematically replaced recrystallised quartz, carbonate and accessory phlogopite and graphite (Fig. 5.2b & c).

Individual prismatic tremolite crystals are less common. These crystals are generally unstrained, though some are boudinaged, and weakly aligned parallel to the  $S_2$  schistosity (Fig. 5.2b & c), indicating syn-D2 growth.

Scapolite occurs in the graphitic units Unit 2 and Unit 4 as randomly orientated coarse grained (up to 5cm), idiomorphic, scapolite prisms (Fig. 5.3d). Graded scapolite layers, up to 20 cm thick, occur in Unit 2 (Fig. 3.7d). In these bands, scapolite decreases in abundance upwards and becomes intergrown with dolomite. In thin section the scapolites are sieve like, idiomorphic to corroded porphyroblasts, with diameters up to 0.5 cm. They include fine grained, relatively unstrained, quartz, albite and muscovite and occasionally coarser grained annealed calcite (Fig. 5.3d). Retrogression of scapolite to plagioclase & quartz aggregates (with carbonate and phlogopite) commonly occurs (Fig. 5.3e & f).

In some cases assymmetric pressure shadows, containing calcite and quartz, are found around rotated, rounded, scapolite porphyroblasts (Fig. 5.3e & f). The pressure trails lie parallel to D2 foliation planes with the scapolites syn-tectonically overgrowing D2 folded  $S_1$  graphitic seams. These scapolite grains clearly grew during the D2 deformation. Boudinaged, prismatic, scapolite crystals occur aligned parallel to D3 fold axes in the Black Angel mine and indicate syn-D3 growth.

Phlogopite is ubiquitous in the Marmorilik Formation. It defines both D1 & D2 foliations (Fig. 5.3b & c), D1 'C' fabric planes (Fig. 3.4f), anastomosing cleavages that wrap around D2 porphyroblasts (Fig. 5.3e & f) and flattening lineations parallel to F1 and F2 axes. The phlogopite recrystallised during D2 deformation, but is itself strained about some D2 closures where it occurs in polygonal arches. Very fine grained felted

## Figure 5.3 Phlogopite and scapolite microtextures.

### Phlogopite microtextures

A) Photomicrograph of a very fine grained felted phlogopite (Ph) foliation anastomosing around, and in places replacing, calcite (Ca) and quartz (Q) grains. Thin section PPL. Scale bar 500 $\mu$ .

B) Medium grained phlogopite forming an  $S_1$  foliation/schistosity in between more siliceous quartzitic (Q) bands. Pyrite euhedra (PY) occur in the quartz. PPL. Scale bar 500 $\mu$ .

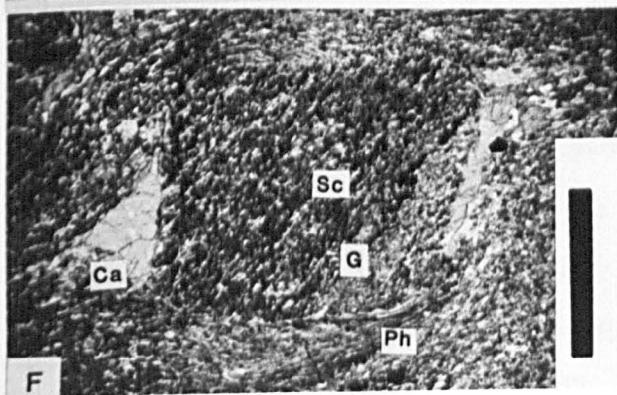
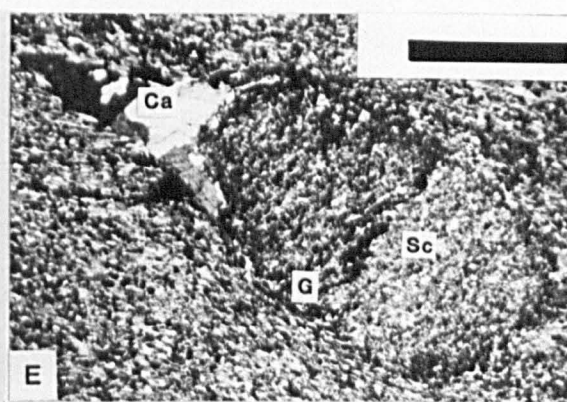
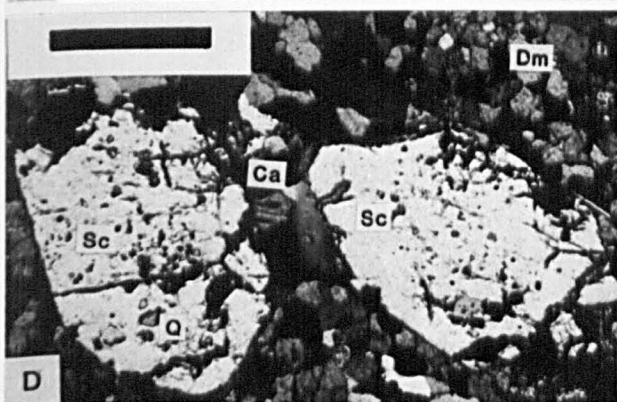
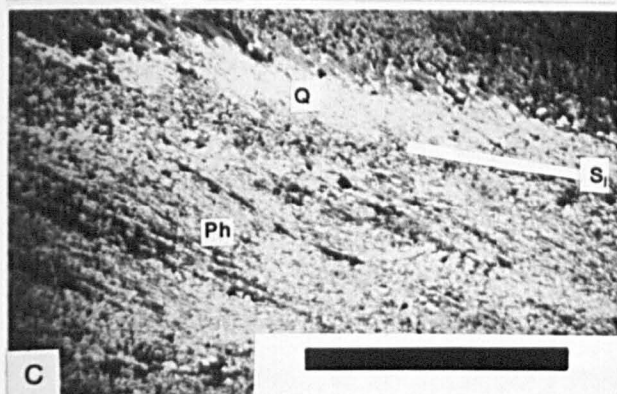
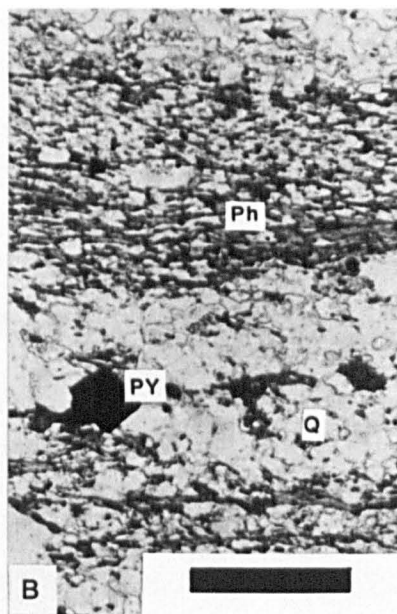
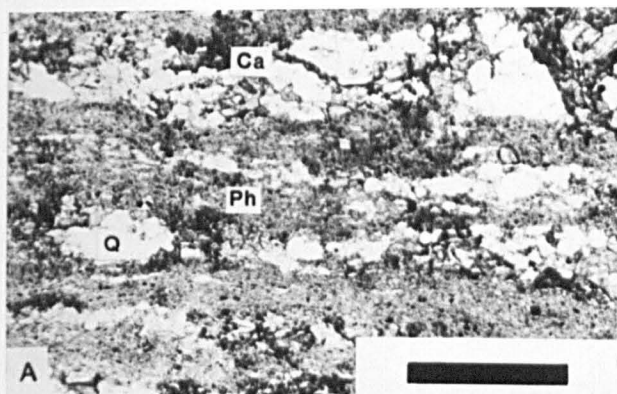
C) Photomicrograph of a strongly developed  $S_2$  phlogopite foliation which crenulates the earlier  $S_1$  fabric. Thin section 245a from siliceous pelite, Unit 1 Marmorilik Formation. PPL. Scale bar 1000 $\mu$ .

### Scapolite microtextures

D) Poikiloblastic coarse grained scapolite including and replacing a medium grained, granular, siliceous (Q) calcite (Ca) dolomite (Dm) matrix of Unit 4, Marmorilik Formation. Thin section V 217a, Drill hole V 217. Black Angel Mountain. XPL. Scale bar 500 $\mu$ .

E) A rotated, post D1 - pre D2 scapolite grain (Sc) now retrogressed to plagioclase and quartz. The scapolite overgrew a folded graphite band (G), in a graphitic calc/dolomite matrix. D2 rotation of the scapolite has formed an asymmetric calcitic pressure shadow (Ca), and a discordance between the internal and external graphite band. Thin section Scapolite 9. South Lakes area. Unit 2 Marmorilik Formation. Scale bar 500 $\mu$ .

F) An altered, rotated, scapolite porphyroblast (now plagioclase and quartz). Rotation of the porphyroblast has developed an asymmetric calcitic pressure shadow (Ca), and an impingement of the phlogopitic calc/dolomite fabric. Specimen as in (E).



phlogopite exists in mylonitic rocks (Fig. 5.3a). Muscovite is subordinate to, but coexists with phlogopite. In rare circumstances phlogopite is observed as a retrogressive mineral rimming tremolite porphyroblasts (Fig. 5.2e).

Talc is generally absent from the succession. It does not coexist with phlogopite, but tends to occur in narrow D3 & D4 extensional fault zones. It is also present as a retrogressive mineral in tremolite, where it occurs in fractures as felted masses (Fig. 5.2 b & c).

Metamorphism of the purer calcite and dolomite marbles manifests itself through static annealing or grain growth of the two minerals (Fig. 3.10e). Calcite crystals, up to 10 cm, occur in the footwall of, and as gangue material in, the Black Angel sulphides.

Graphite is an accessory metamorphic mineral in the Marmorilik Formation carbonates. It tends to be concentrated in the calcite-dolomite marbles as finely disseminated grains and amorphous masses overgrowing carbonate minerals or more commonly as fine grained flakes that enhance the foliation (Fig. 5.4a & b). In rare cases sub-hedral graphite grains, up to 5 mm., are found in the coarse calcite marbles (3.3.2) overgrowing the tremolite/phlogopite bearing carbonate matrix (Fig. 5.4 c & d).

### **c) Upper Karrat Group**

The following mineral assemblages are present in the metapelites of the Upper Karrat Group (Fig. 5.5):-

Talc-phlogopite-quartz-graphite

Biotite-muscovite-quartz-K-feldspar-graphite

Quartz-albite-biotite+K-feldspar

Phlogopite, biotite and subordinate muscovite grow in both D1 and D2 fabrics and are associated with graphite seams. Albite porphyroblasts overgrow these foliations and the quartzo-feldspathic matrix. The porphyroblasts occur as white spots that in some cases develop a relict

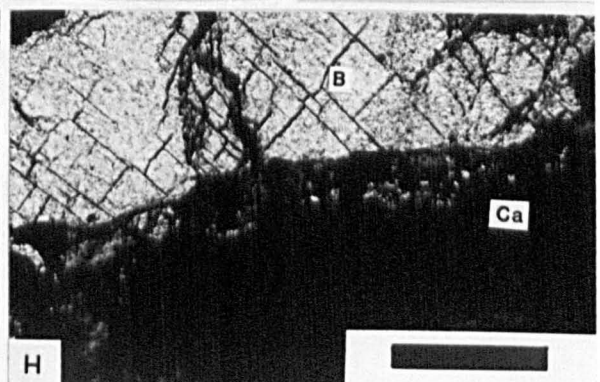
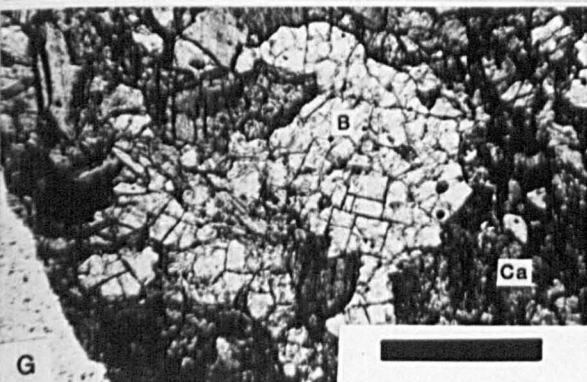
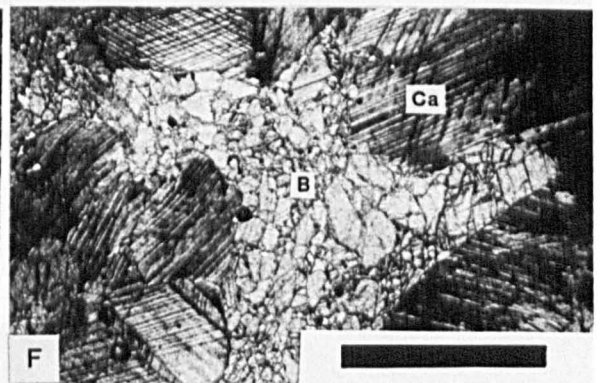
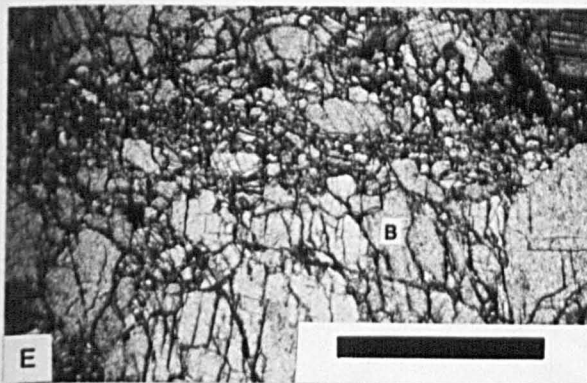
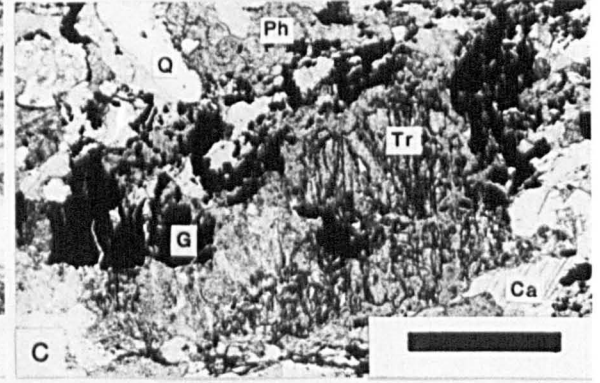
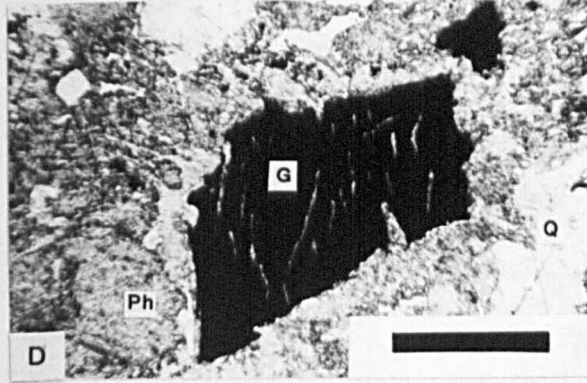
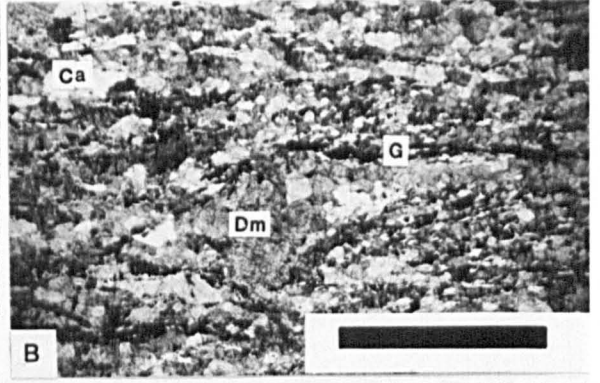
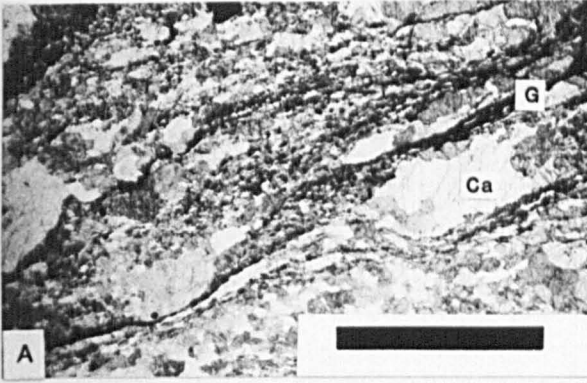
## Figure 5.4 Graphite and Baryte microtextures.

### Graphite microtextures.

- A) Thin graphitic seams (black) are developed parallel to  $S_2$  foliation. The seams wrap around elongate coarse grained calcitic augen. Thin section 389. Middle Marmorilik Formation. PPL. Scale bar 600 $\mu$ .
- B) Diffuse graphitic seams (G) wrapping around dolomitic augen (Dm). Asymmetric dolomitic augen indicates dextral shear. Ca is calcite. Thin section 407. North Marmorilik cliffwall Unit 4 Marmorilik Formation. PPL. Scale bar 600 $\mu$ .
- D) Coarse grained graphite euhedra overgrowing a phlogopite and quartz matrix. Irregular hairline fractures suggest minor rotation. Thin section V 197. Upper Marmorilik Formation. PPL. Scale bar 500 $\mu$ .
- C) Sheared graphitic flakes overgrow a matrix of quartz (Q), calcite (Ca), tremolite (Tr) and phlogopite (Ph). The tremolite shows strong retrogression to phlogopite. Thin section V 197. Upper Marmorilik Formation. PPL. Scale bar 500 $\mu$ .

### Barytic microtextures

- E) Coarse grained cataclastically fractured baryte. The baryte develops rounded fragments in the fracture zone. Specimen B 124b, B 124 Banana zone, Black Angel mine. XPL. Scale bar 600 $\mu$ .
- F) Brecciated coarsely recrystallised baryte between coarse grained calcite showing kinked deformation twins. Specimen as in (E)
- G) An amorphous coarse baryte grain held in coarse granular calcite. Specimen as in (E). XPL. Scale bar 500 $\mu$ .
- H) Coarsely recrystallised baryte (B) with strong 90° cleavage abutting a coarse (extinct) calcite grain (Ca). Along the grain boundary fine new baryte grains are developed as a result of cataclasis. Specimen as in (E). XPL. Scale bar 500 $\mu$ .



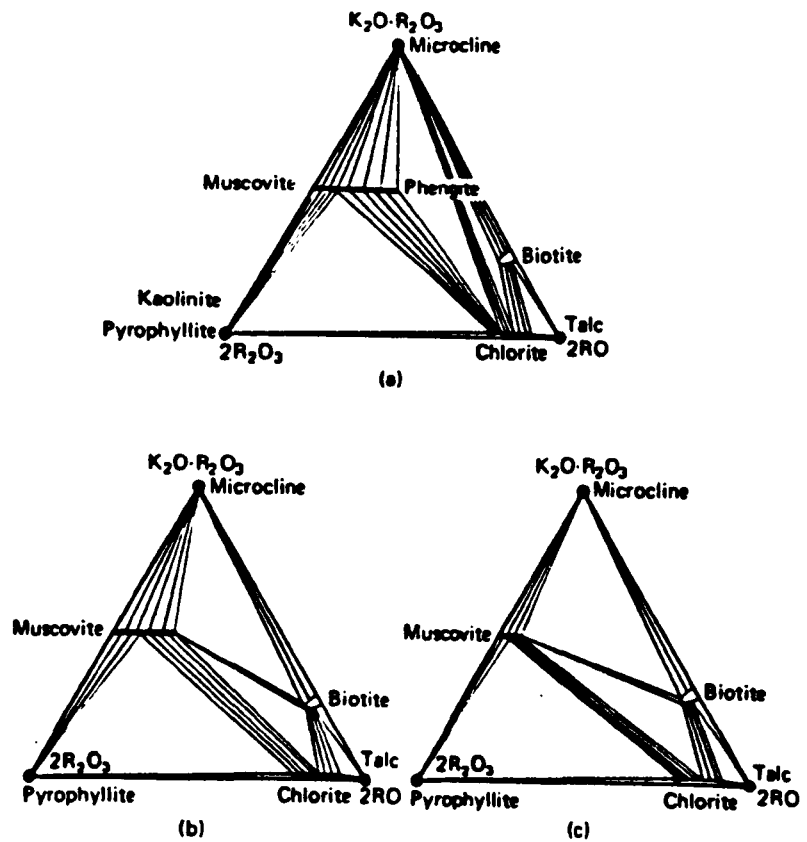


**Figure 5.5** Ternary diagram showing the mineral assemblages found in metapelites of the Karrat Group and also the progressive changes of phase relations involving muscovite and biotite (After Miyashiro, 1973)

zoning of biotite and aggregates of replacive albite, quartz  $\pm$  biotite and phlogopite. Talc occurs in late stage fractures.

#### **5.4 Mineral compositions**

Analytical work on the metamorphic minerals of the area has been limited. Microprobe work has focussed on the sulphide ores of the Black Angel deposits (6.5.7c). Garde (1978) made a number of microprobe analyses on tremolite, phlogopite and scapolite which augment the data obtained from this study (Fig. 5.6). He also determined the approximate chemical compositions of muscovite, talc and biotite from a metapelite unit in the calcite-dolomite member (Unit 3).

#### **5.5 Metamorphic grade and P/T regimes**

It is clear from both the carbonate and pelitic mineral assemblages of the Marmorilik and Nukavsak Formations that peak conditions within or slightly exceeding the greenschist facies were attained towards the end (post-D3) of the Rinkian event in the Upper Karrat Group. The presence of the Diopside-tremolite-quartz $\pm$  epidote assemblage in the Qeqertarssuaq Formation of the Tassiusaq region south west of Marmorilik, may represent a higher grade, (epidote)-amphibolite facies metamorphism, at the base of the Karrat Group.

Although it is relatively easy to define the peak metamorphic facies in the area it is much more difficult to establish precise pressures and temperatures of metamorphism. This is particularly the case in the carbonate CaO-MgO-SiO<sub>2</sub>-H<sub>2</sub>O-CO<sub>2</sub> system where mineral stabilities are strongly dependent on X<sub>CO<sub>2</sub></sub>. Much experimental work on the CaO-MgO-SiO<sub>2</sub>-H<sub>2</sub>O-CO<sub>2</sub> system has been carried out (Winkler, 1979). Fifteen basic mineral transformations have been documented within the prograde metamorphism of siliceous carbonates, talc-tremolite-diopside-forsterite, of which only six concern the

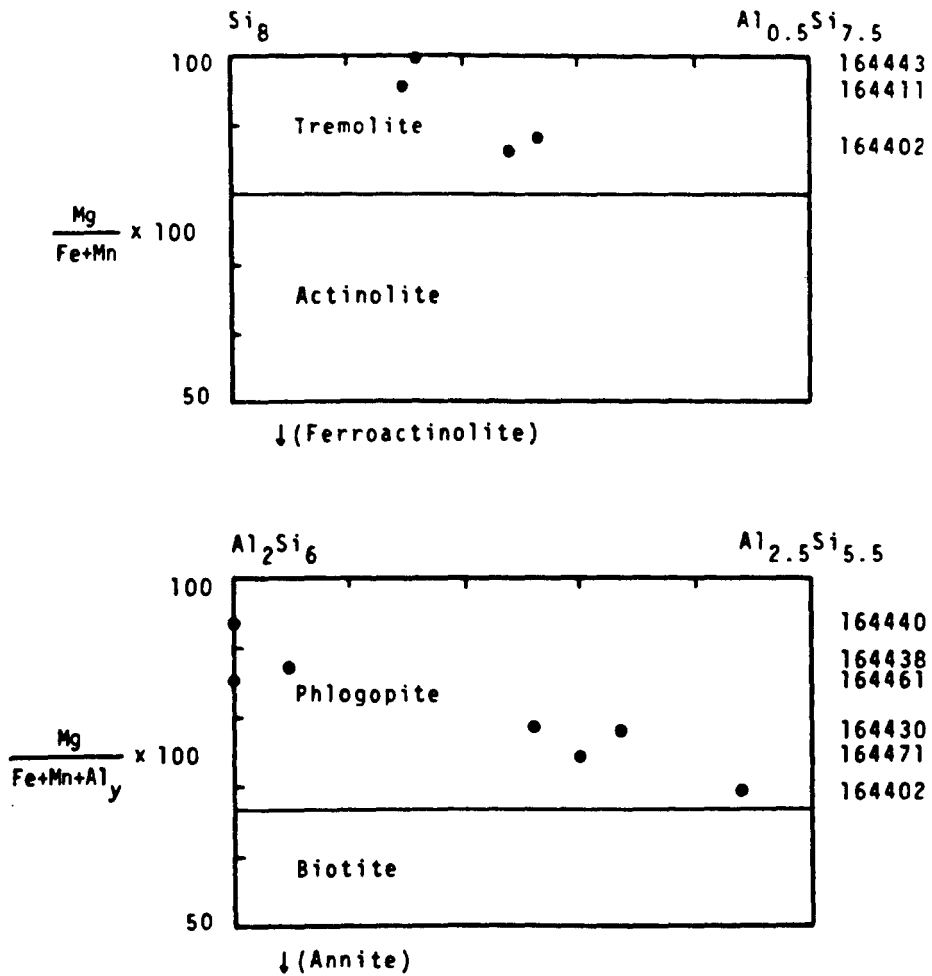


**Figure 5.6** Chemical composition diagrams of tremolite and phlogopite (From Garde, 1978)

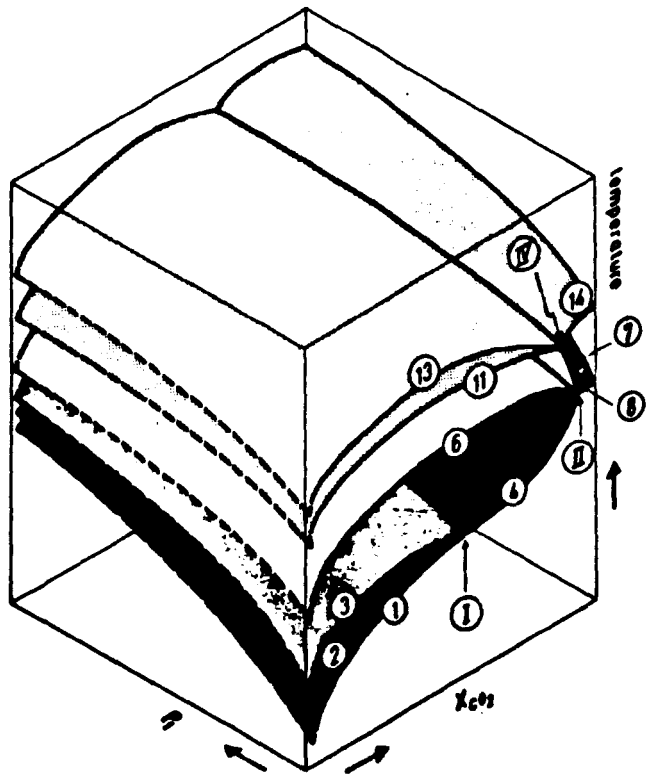


**Figure 5.7** Isobaric Pf-T-Xco<sub>2</sub> diagram for reactions in siliceous dolomite marbles (From Winkler, 1979)

metamorphism of the Karrat Group carbonates. These reactions are:-

- (1)  $3 \text{ Dolomite} + 4 \text{ Quartz} + 1 \text{ H}_2\text{O} = 1 \text{ Talc} + 3 \text{ Calcite} + 3 \text{ CO}_2$
- (2)  $3 \text{ Dolomite} + 1 \text{ K-feldspar} + 1 \text{ H}_2\text{O} = 1 \text{ Phlogopite} + 3 \text{ Calcite} + 3 \text{ CO}_2$
- (3)  $5 \text{ Talc} + 6 \text{ Calcite} + 4 \text{ Quartz} = 1 \text{ Tremolite} + 6 \text{ CO}_2 + 2 \text{ H}_2\text{O}$
- (4)  $2 \text{ Talc} + 3 \text{ Calcite} = 1 \text{ Tremolite} + 1 \text{ Dolomite} + 1 \text{ CO}_2 + 1 \text{ H}_2\text{O}$
- (5)  $5 \text{ Dolomite} + 8 \text{ Quartz} + 1 \text{ H}_2\text{O} = 1 \text{ Tremolite} + 3 \text{ Calcite} + 7 \text{ H}_2\text{O}$
- (6)  $1 \text{ Tremolite} + 3 \text{ Calcite} + 2 \text{ Quartz} = 5 \text{ Diopside} + 3 \text{ CO}_2 + 1 \text{ H}_2\text{O}$

Schematic and precise isobaric T-Xco<sub>2</sub> diagrams for the CaO-MgO-SiO<sub>2</sub>-H<sub>2</sub>O-CO<sub>2</sub> system have been produced by Winkler (1979) (Figs. 5.7, 5.8 and 5.9). It has been documented experimentally (Tilley, 1948) that talc is expected to form before tremolite in progressively metamorphosed siliceous dolomites by reaction 1. In the Marmorilik area, talc is generally absent with phlogopite being the dominant low grade metamorphic mineral. Phlogopite is produced by reaction 2 and has been studied experimentally by Puhon and Johannes (1974) at 1Kb., and at higher pressures by Puhon (1976). The production of phlogopite requires the presence of high potassium and aluminium contents and high Xco<sub>2</sub> values and occurs at temperatures 10-20°C lower than the talc-producing reaction (Fig. 5.8 & 5.9).

Tremolite is the product of several decarbonation reactions (e.g. equations 3, 4 & 5) that occur over a considerable P/T range. This wide thermo-barometric range is of little help in establishing a tight P/T control on the Rinkian metamorphism. In spite of the widespread occurrence of rocks of suitable composition for the production of tremolite, the mineral is present sporadically in the Karrat Group. This probably indicates that large variations in Xco<sub>2</sub> occurred throughout the carbonate succession during prograde metamorphism.

The transition to peak metamorphic grade of (epidote)-amphibolite

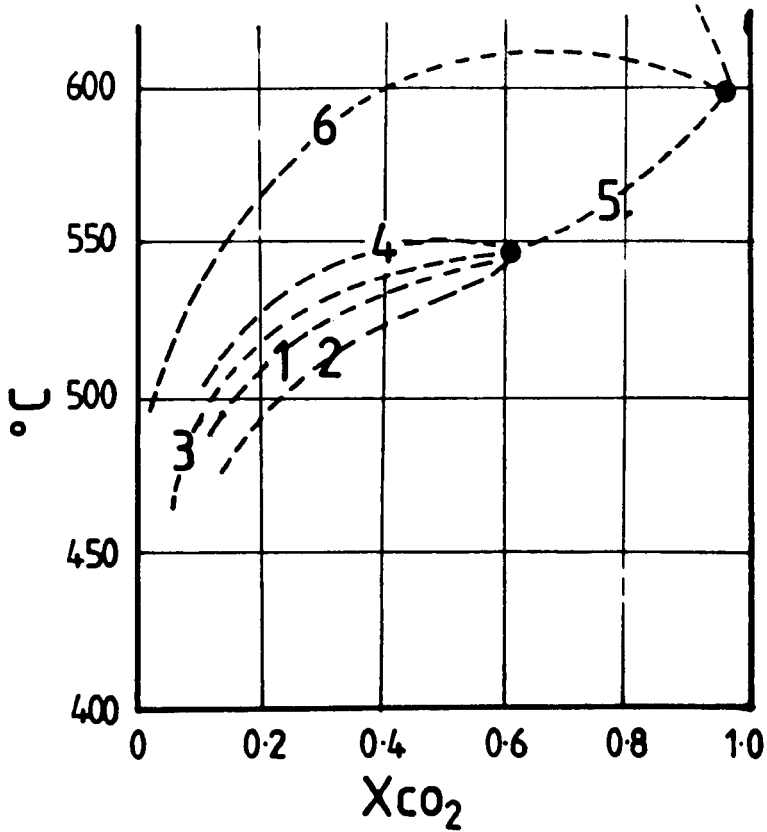


**Figure 5.9** Isobaric T- $X_{CO_2}$  diagram at 5 kb. pressure for reactions in siliceous dolomite marbles (From Winkler, 1979)

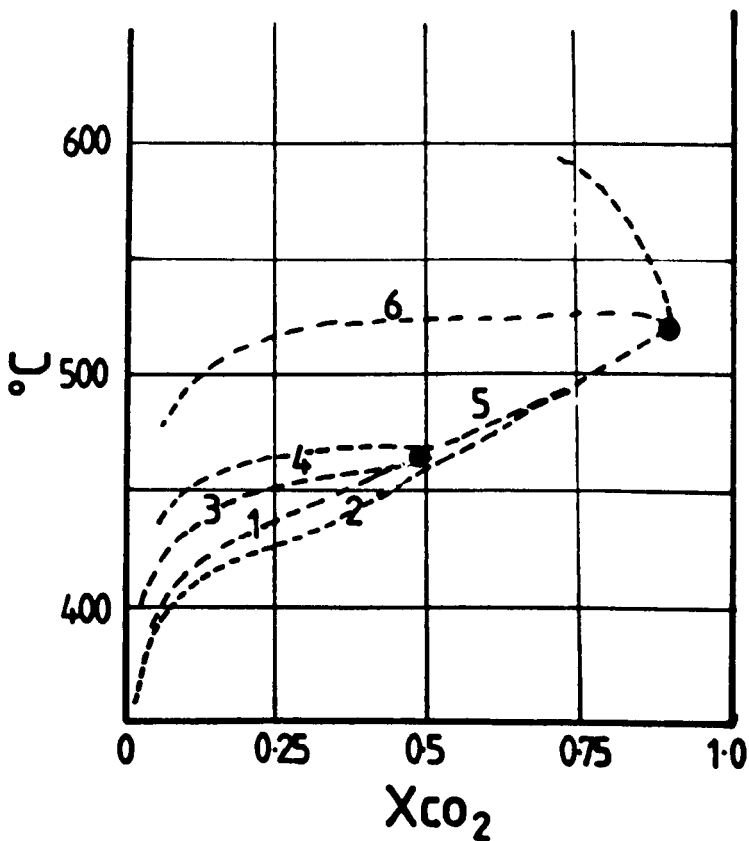


**Figure 5.8** Isobaric T- $X_{CO_2}$  diagram at 2 kb. pressure for reactions in siliceous dolomite marbles (From Abercrombie et al., 1987)

facies is reflected by the occurrence of diopside. The temperature of diopside formation (reaction 6) does not vary considerably if  $T-X_{CO_2} > 0.4$  (Winkler, 1979) (Fig. 5.7, 5.8 & 5.9), but is strongly dependent on the total fluid pressure: at 2kb. diopside may be formed at 510°C (Skippen, 1974)(Fig. 5.8) but at an increased pressure of 5kb. diopside doesn't form at less than 600°C (Winkler, 1979) (Fig. 5.9). However, F-OH substitution in tremolite, talc and phlogopite can shift the univariant points and stability fields in metacarbonates to higher temperatures (Abercrombie et al., 1987).

Graphite in the Marmorilik Formation may have been derived from organic material or it may have formed through metamorphic reaction between dolomite and quartz:-



The near total absence of iron oxides in the Marmorilik Formation (chapter 6) is consistent with this reaction and also gives clues as to the  $f_{O_2}$  and  $f_{S_2}$  conditions during metamorphism. The association of sphalerite and graphite and absence of rutile and the presence of pyrite with minor pyrrhotite suggests that metamorphism occurred under low  $f_{O_2}$ ,  $\log f_{O_2} < -21$ , and high but slightly variable  $f_{S_2}$  conditions,  $\log f_{S_2} \approx -2.5$ , (Nesbitt and Kelly, 1980)(Fig. 5.10).

The mineral assemblages of the metapelitic succession do not define any P/T regimes, as biotite is stable over a wide P/T range. The lack of garnet may suggest that metamorphism in the Marmorilik area took place at less than 500°C and 4kb (minimum P/T of garnet production). However, garnet may not have formed simply because the chemistry of the protolith was not compatible with its production.

A more precise way of determining the P/T regime in the area is

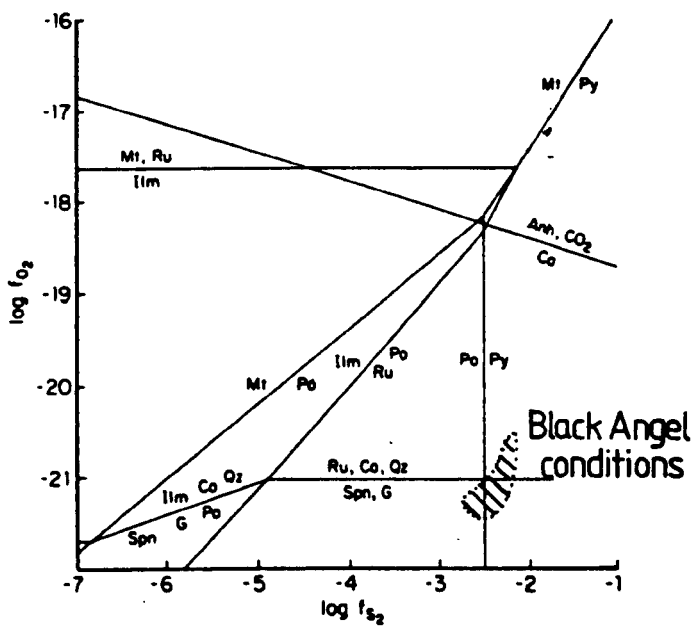


**Figure 5.10** Phase stabilities in the C-O-S-Ca-Ti-Fe system as a function of  $f_{S_2}$  and  $f_{O_2}$  and 6 kb, 550°C  
(After Nesbitt and Kelly, 1980)

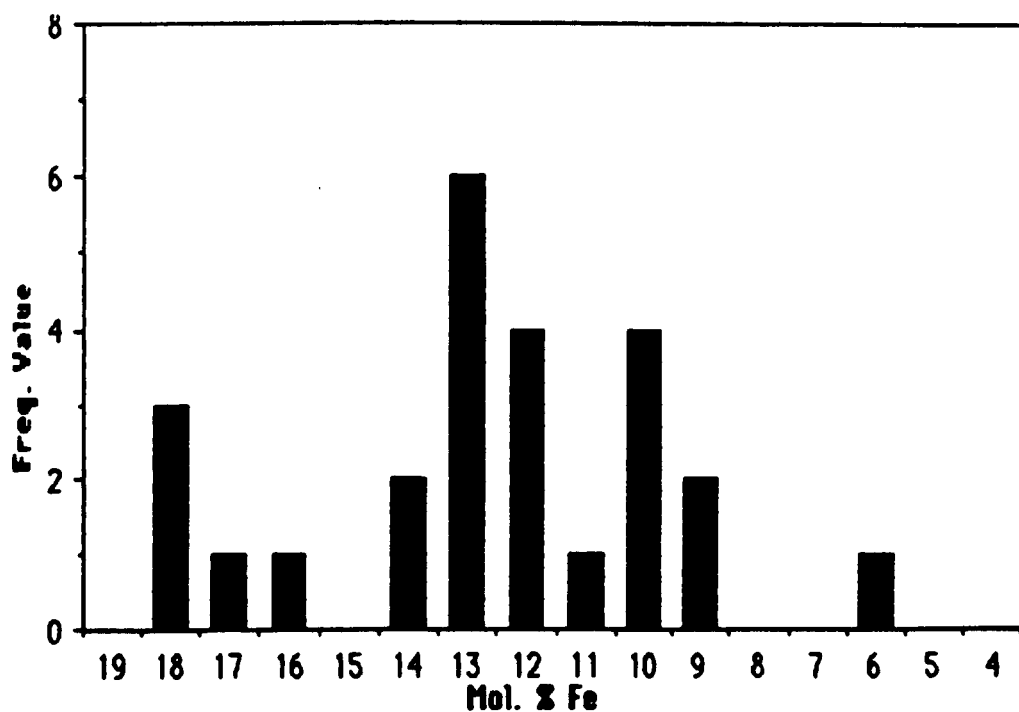


**Figure 5.11:** Mole % Fe content in sphalerite encapsulated within D3 pyrite from the Black Angel deposits.

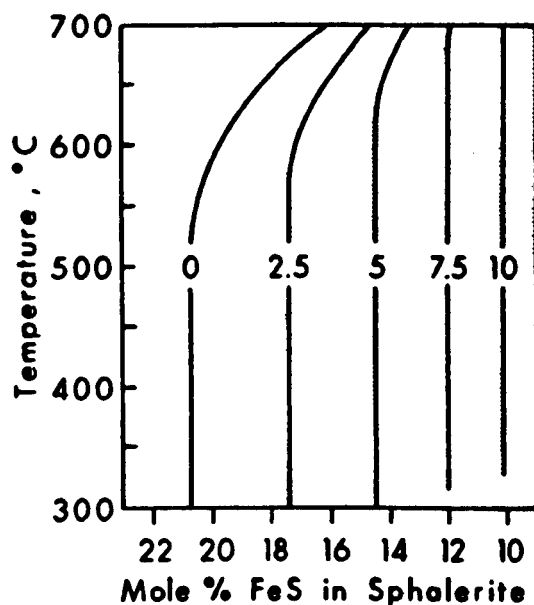


**Figure 5.12** Temperature-composition section along the ZnS-FeS join of the system ZnS-FeS-S of sphalerite + pyrite + hexagonal pyrrhotite equilibria as a function of pressure (in kbar). Temperature independent portion of the isobars is shaded. (From Scott, 1983)

**Table 5.1a: Microprobe Analyses of Pyrite Encapsulated**

**Sphalerite (in wt.%) from the Black Angel and  
Mungarut deposits**

Zn	Fe	S	Co	Ni	Cr	As	Total	Location	Mol. %Fe
50.24	13.73	33.96	0.07	---	0.06	0.44	98.43	T172	24.2
51.37	13.18	30.39	---	---	0.24	0.83	96.01	T172	23.0
54.20	13.34	32.43	---	---	---	---	99.99	1170 b	22.4
54.51	10.89	32.46	---	---	0.54	0.50	98.90	T172	18.9
55.97	11.09	30.70	---	---	---	0.73	98.55	T172	18.9
56.84	10.67	30.92	---	0.14	---	0.18	98.81	T172	18.0
59.14	10.73	32.57	0.22	0.03	0.29	0.53	103.51	T172	17.6
58.68	10.29	30.68	0.16	---	---	---	99.82	T 188a	17.0
59.59	9.93	30.42	0.10	---	---	---	100.04	1170 b	16.3
60.57	8.99	30.92	---	---	---	---	100.51	T 188a	14.8
60.92	8.88	31.30	---	---	---	---	101.11	T 188a	14.6
61.62	8.99	32.74	---	0.16	0.07	0.83	104.47	T172	14.6
59.01	8.38	32.61	---	---	---	---	100.00	1170 b	14.2
61.26	8.43	30.27	---	---	---	---	99.99	1170 b	13.9
61.31	8.24	30.06	---	0.28	---	---	99.88	1170 b	13.6
57.78	7.70	29.96	0.26	---	---	0.58	96.45	T172	13.5
61.45	8.09	30.24	0.24	---	---	---	100.02	1170 b	13.4
61.82	7.93	30.15	---	0.08	---	---	99.98	1170 b	13.1
61.10	7.88	30.70	---	---	---	---	99.66	T 188a	13.0
61.49	7.89	30.14	---	0.13	---	---	99.67	1170 b	13.0
61.19	7.68	31.00	---	---	---	---	99.94	T 188a	12.8
62.48	7.70	30.20	---	0.11	---	---	100.51	1170 b	12.6
61.63	7.56	30.39	0.27	0.08	---	---	99.83	1170 b	12.5
63.77	7.76	32.42	0.06	---	---	0.34	104.47	T172	12.4
62.40	7.37	30.10	---	0.11	---	---	99.99	1170 b	12.1
61.29	6.83	30.94	---	---	---	---	99.12	P 59	11.5
61.23	5.91	30.76	0.11	---	---	0.83	98.89	T172	10.2
61.81	6.04	30.33	0.11	---	0.36	0.17	98.86	T172	10.2
62.60	6.11	30.81	---	---	---	---	99.55	P 59	10.2
62.38	5.94	31.08	---	---	---	---	99.41	P 59	10.0
62.91	5.90	30.80	---	0.18	---	---	99.79	P 69	9.9
62.92	5.55	30.32	0.22	0.25	---	---	99.26	P 59	9.3

**Table 5.1b: Microprobe Analyses of Matrix Sphalerite (in wt.%)**

**from the Black Angel and Mungarut deposits**

Zn	Fe	S	Co	Ni	Cr	As	Total	Location	Mol. % Fe
65.764	3.828	30.381	---	---	---	---	100.003	B 124	6.4
65.745	3.512	30.565	---	---	---	---	99.832	B 124	5.9
65.238	3.526	30.448	---	---	0.09	---	99.302	B 104	5.9
65.304	3.423	31.273	---	---	---	---	100.000	B 124	5.8
65.162	3.297	30.711	---	0.19	---	---	99.360	B 104	5.6
65.845	2.857	30.658	---	---	---	---	99.360	B 104	4.8
65.600	2.811	30.872	---	---	---	---	99.283	B 104	4.8
66.095	2.657	30.829	---	0.14	0.05	---	99.771	B 104	4.5
66.961	2.511	30.460	---	---	---	---	99.932	B 124	4.2
65.753	2.448	30.790	---	---	---	---	98.991	B 104	4.2
64.935	2.188	31.738	---	---	0.15	---	99.011	M 160	3.8
66.021	2.125	31.699	---	---	---	---	99.845	M 160	3.6
68.213	1.245	30.393	0.14	---	---	---	99.991	B 124	2.1
66.502	1.093	31.627	---	---	---	---	99.222	M 160	1.9
66.449	1.090	31.252	---	---	---	---	98.811	M 160	1.9
66.390	1.055	31.397	---	---	0.09	---	98.932	M 160	1.8
66.719	0.940	31.591	---	---	0.05	---	99.300	M 160	1.6

by geothermometry and geobarometry. Calcite/dolomite solvus geothermometry (Goldsmith and Newton, 1969; Puhan, 1976; Bickle and Powell, 1977) was carried out on the Marmorilik Formation by Garde (1977) who found a mean of 3.3 mol % calcite in dolomite. This corresponds to a temperature of  $\approx 440^{\circ}\text{C}$ . Fluid inclusions in quartz of the Black Angel ore deposits (Pedersen, 1981) gave a temperature of  $450^{\circ}\text{C}$  at a pressure of 1-1.5 kb for peak metamorphism.

Garde (1978) and Pedersen (1980a) calculated the approximate minimum lithostatic pressure at the base of the Karrat Group by estimating that there was 7km of overburden during deformation (5 km. for the Nukavsak Formation and 2 km. for the tectonic thickness of the Marmorilik Formation). This corresponds to a minimum pressure of 2kb. A more accurate measurement of the lithostatic pressure was attempted by using the iron content of sphalerite as a geobarometer (method as in Scott, 1983). The maximum mole fraction FeS in sphalerite, from the Black Angel deposits, of 18% (Table 5.1 a & b, Fig. 5.11) corresponds to pressures of 2.5 - 3.0 Kb. (Fig. 5.12) at the time of D3 pyrite annealing.

In summary, metamorphic grades determined from the mineral assemblages of both carbonate and pelitic rocks in the Karrat Group correspond to a prograde greenschist facies metamorphism at temperatures of  $<540^{\circ}\text{C}$  (Minimum temperature of Diopside formation under high  $X_{\text{CO}_2}$ ) and pressures of  $<4\text{kb}$  under  $>0.4 X_{\text{CO}_2}$ . During D1 and D2 deformation lower greenschist facies metamorphism was attained suggesting somewhat lower temperatures, with pressures of between 1-1.5 kb (Pedersen, 1981). Localised higher grade (epidote)-amphibolite facies metamorphism occurred in the Qeqertarsuaq Formation. A peak metamorphic pressure of 2.5 - 3.0 Kb. has been determined by the sphalerite geobarometer, with estimates of temperatures varying from  $440^{\circ}\text{C}$  (calcite/dolomite geothermometry)  $450^{\circ}\text{C}$  (fluid inclusion studies)

to a maximum of 510°C (Diopside production at 3.0kb).

Geothermal gradients calculated for the mid-Proterozoic Rinkian event correspond to high temperature-low pressure metamorphism of between 50-60°C / km.

## **5.6 Primary sediment chemistry**

Calcite marbles and siliceous dolomite marbles dominate the metasedimentary pile. The ubiquitous presence of phlogopite, with accessory biotite, indicates that significant potassium and aluminium concentrations were present throughout the Karrat Group. More localised metamorphic minerals such as scapolite, tremolite/actinolite and graphite may indicate the presence of sedimentary chemical variation.

Graphite may represent organic material or may be a metamorphic derivative (section 5.5). The calcic amphiboles, tremolite and actinolite, are concentrated in massive bands and units both within the Qeqertarsuaq Formation and the Marmorilik Formation. The presence of quartz throughout the succession indicates that magnesium (tremolite) and iron (actinolite) concentrations are higher in these particular units than elsewhere. The predominance of actinolite in the west indicates that Fe-content increases westwards.

The presence of marialitic scapolite (Garde, 1978) indicates the presence of high sodium and chlorine contents. Scapolite may be produced by both metamorphic (Kwak, 1977) and metasomatic (Edwards and Baker, 1954) processes. At Marmorilik the presence of scapolites in graded beds (Fig. 3.7d) is taken to represent a primary origin for the sodium & chlorine variations in the dolomitic units of the Lower Marmorilik Formation. Primary scapolite has been recognised in carbonate units of the Pinkie Group, Forland complex, Svalbard (Manby, 1983). The mechanism proposed for the generation of this scapolite involves the entrapment of connate brines in the sediments during compaction. The sodium and chlorine rich brines are presumed to crystallise as halite which later react with

calcite, quartz and clay minerals to give meionitic scapolite (von Englehart, 1961; Manby, 1983). A review of scapolite-bearing rocks from other Precambrian units by Serdyuchenko (1975), has concluded that scapolite resulted from metamorphism of evaporites, and that the carbonate-sulphate-halide sedimentation took place under littoral and lagoonal conditions.

Anhydrite (Fig. 3.10b) and gypsum represent highly localised chemical anomalies. Evaporitic origins are given to these minerals. Mn calcites (rhodocrosite), fluorite, and baryte (Fig. 5.4e-h) represent even less widespread minerals and are found in association with the Black Angel deposits indicating high barium, fluorine, manganese contents in this area.

Carbonates form in a wide range of environments, which often reflect many transgressive and regressive cycles. The presence of sulphates and scapolite in the Marmorilik Formation suggests that sedimentation at times took place under littoral and/or lagoonal conditions (Serdyuchenko, 1975). The high K, Na, Mg, component to the carbonates suggests a saline environment, that was often oxygenated during sulphate production. The high graphite contents through parts of the Lower and Middle Marmorilik members suggest that areal or near-shore accumulation of organic substances occurred, possibly through flooding of the lagoonal basins and near-shore marine zones. The relatively purer Upper Marmorilik Formation calcite marbles are interpreted to have been deposited in a more stable, deeper water platformal environment.

## Chapter 6. Mineralisation of the Black Angel deposits and Marmorilik area.

### 6.1 Introduction.

This chapter is an overview of the geological setting of the mineralisation of the Marmorilik area.

The predominant mineralisation in the Marmorilik area occurs as Fe-Zn-Pb-(Ag) carbonate-hosted sulphides (Fig. 6.1). Minor Cu, Fe oxides are present in siliceous units of the Qeqertarssauq Formation (Garde, 1978; Pedersen, 1980) (Fig. 6.2). Massive to disseminated pyrrhotite and pyrite are set in the black graphitic pelites of the Nukavsak Formation (Pedersen and Gannicott, 1980; Allen and Harris, 1979; Nichols, 1981) (Fig. 6.2).

The sulphide mineralisation consists of sphalerite, galena, pyrite, chalcopyrite, tennantite and arsenopyrite which occur as; i) disseminated and stringer like stratabound to stratiform horizons and discordant recrystallised veins at ten tectono-stratigraphic levels (King, 1981) and ii) as massive to semi-massive bodies at four horizons (Fig. 6.2). These are:-

- 4) Black Angel deposits: Upper Marmorilik Formation (unit 4)
- 3) MP 5-Uvkussigsat-Agpat: Middle Marmorilik Formation (unit 3)
- 2) Nungarutt: Lower Marmorilik Formation (unit 2)
- 1) (Della Valle)-Myers-SLGL-Ark-Garde: Lower Marmorilik Formation (unit 2)

Details of each drilled showing in the Marmorilik area are given in table 6.1. Sulphide ore has been exploited since 1974 in the Black Angel Mine (Fig. 6.1) and has been drilled off at the Nunngarut deposit (Figs. 6.1 & 6.7) on the Marmorilik plateau (Harris, 1981; Della Valle, 1977). Reserves calculated for both deposits, on the basis of an 8% combined Zn-Pb cut-off, are (Table 6.1 & 6.2):-

Black Angel Mine: 13.5 M.T. @ 5.5% Pb, 15% Zn, 22% Fe, 32g/T Ag.  
Nungarutt Deposit: 0.357 M.T. @ 3.9% Pb, 8.8% Zn, 20.4% Fe, 34g/T Ag.

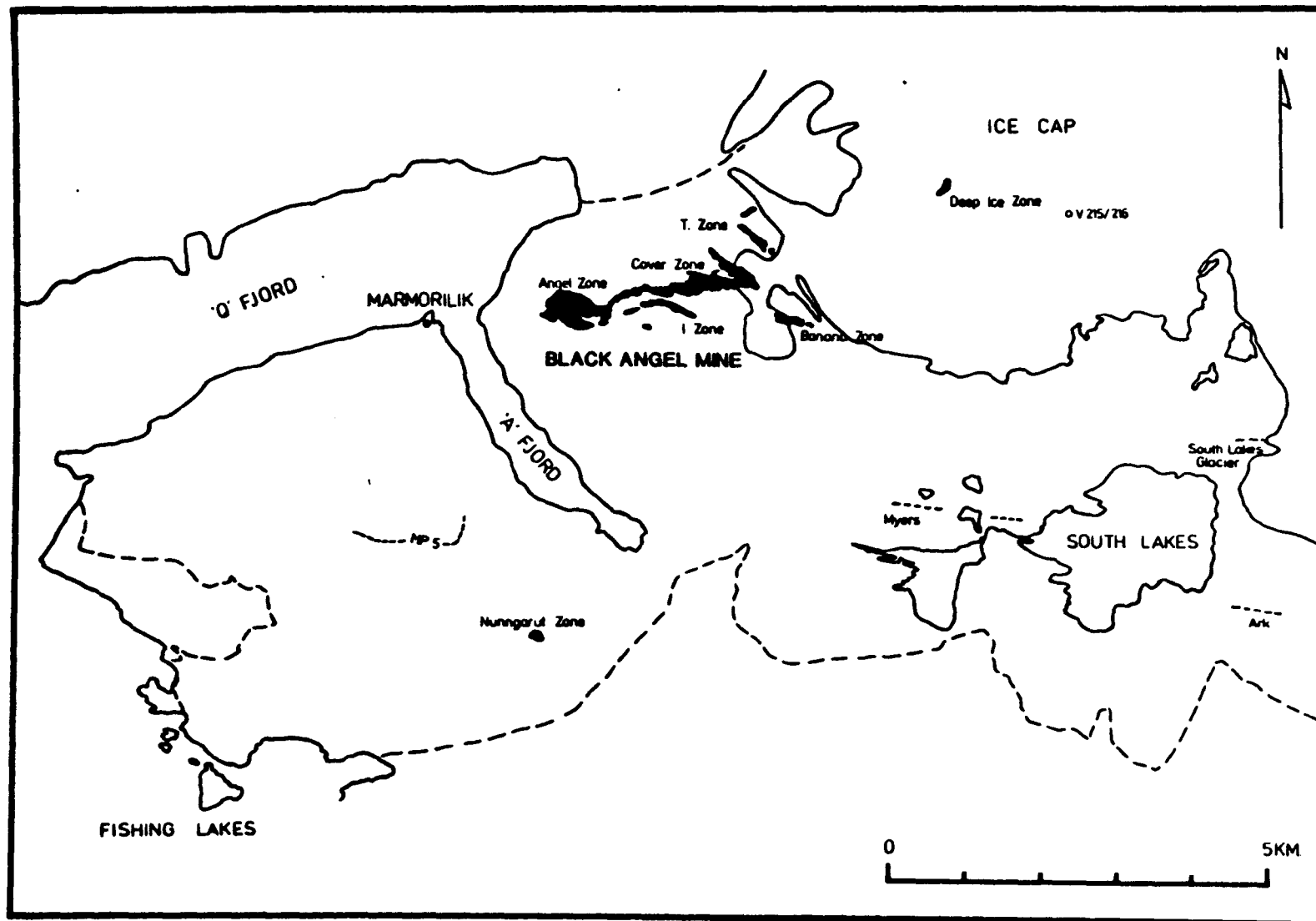


**Figure 6.1** Location map of mineralised zones in the Marmorilik area

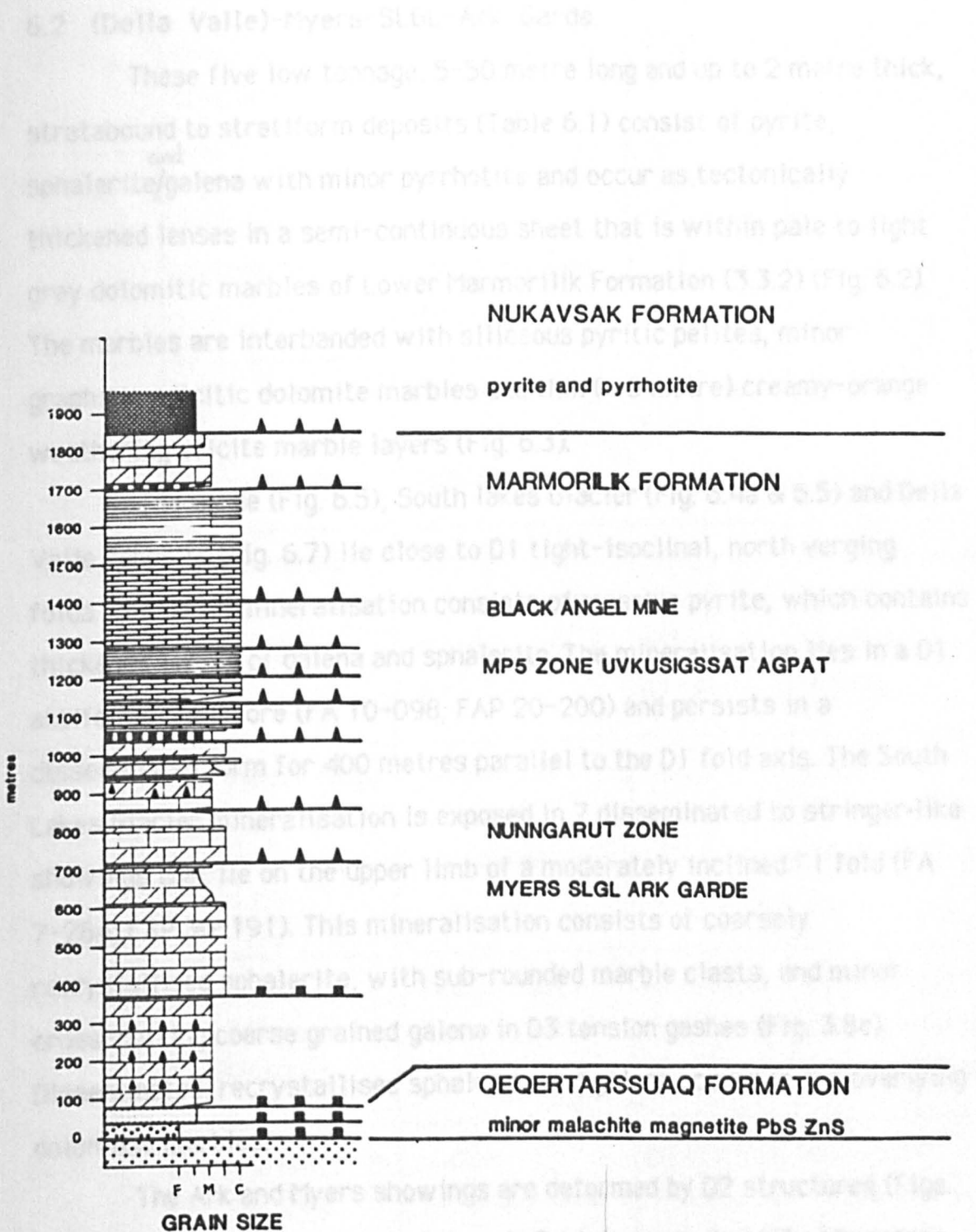


**Figure 6.2** Stratigraphic location of mineralised zones of the Marmorilik area

## 6.2 (Della Valle)-Myers-SLGL-Ark-Garde.

These five low tonnage, 5-50 metre long and up to 2 metre thick, stratabound to stratiform deposits (Table 6.1) consist of pyrite, sphalerite<sup>and</sup> galena with minor pyrrhotite and occur as tectonically thickened lenses in a semi-continuous sheet that is within pale to light grey dolomitic marbles of Lower Marmorilik Formation (3.3.2) (Fig. 6.2). The marbles are interbanded with siliceous pyritic pelites, minor graphitic calcitic dolomite marbles and thin ( $\approx$  5 metre) creamy-orange weathering calcite marble layers (Fig. 6.3).

The Garde (Fig. 6.5), South lakes Glacier (Fig. 6.4a & 6.5) and Della Valle deposits (Fig. 6.7) lie close to D1 tight-isoclinal, north verging folds. The Garde mineralisation consists of massive pyrite, which contains thickened lenses of galena and sphalerite. The mineralisation lies in a D1 antiformal fold core (FA 10-098; FAP 20-200) and persists in a disseminated form for 400 metres parallel to the D1 fold axis. The South Lakes Glacier mineralisation is exposed in 7 disseminated to stringer-like showings that lie on the upper limb of a moderately inclined F1 fold (FA 7-264; FAP 30-191). This mineralisation consists of coarsely recrystallised sphalerite, with sub-rounded marble clasts, and minor cross-cutting coarse grained galena in D3 tension gashes (Fig. 3.8e). Disseminated, recrystallised sphalerite and galena occurs in the overlying dolomitic marbles.

The Ark and Myers showings are deformed by D2 structures (Figs. 6.4b, 6.5 & 6.6). The Ark deposit trends E-W, is approximately 10 metres long by 1.2 metres thick, and consists of massive sphalerite, galena and pyrite with some quartz. The showing lies on the overturned limb of a tight, south verging F2 synform (Fig. 6.5) and is transected to the west by a D3 sinistral shear zone. The south verging folds lie above a north dipping D2 tectonic slide, which reactivated a D1 extension fault.

The Myers showing consists of massive pyrite with lesser sphalerite and galena and is situated in the footwall of the imbricated D2

**Table 6.1 Geological characteristics of the mineralised zones in the Marmorilik area (apart from the Black Angel).**

SHOWING	STRATIGRAPHIC SETTING	MINERALISATION STYLE	SIZE	TONNAGE & GRADE
<b>Uvkusigssat</b>	Mid. Marmorilik Fm. Unit 3 graphitic calcite-dolomites.	Massive and Dissem. Breccia-textured and recrystallised ore	2 layers 400 m long	± 1000 000 T
<b>Agpat</b>	Mid. Marmorilik Fm. Unit 3 Graphitic Calcite-dolomite	Massive-Semi massive breccia-textured ore.	120m. long 3-4 m. thick	?
<b>Nunngarut</b>	Lwr. Marmorilik Fm. Unit 2 Calcite with siliceous pelites.	Massive Breccia-textured and recrystallised ore	200m. wide 18m. thick 500 m long in F1 hinge	357 000 Tonnes of 3.9% Pb, 8.8% Zn 20.4% Fe, 34 g/t Ag.
<b>Ark</b>	Lwr. Marmorilik Fm. Unit 2 Lt. grey massive dolomite	Massive-dissem buckshot to recrystallised ore	10m. long .7-1.3 m. wide 1400 m long in dissem. form	± 100 000 T .15% Pb, 22% Zn 20% Fe, 18g/t Ag
<b>South Lakes Glacier</b>	Lwr. Marmorilik Fm. Unit 2 lt. grey dolomite marble	Stringer-dissem recrystallised to buckshot textured	Folded 200m sheet, 1m wide 50 m. long	approx. 30 000 T .52% Pb, 4.9% Zn 5.5% Fe, 18g/t Ag
<b>Gerde</b>	Lwr. Marmorilik Fm. Unit 2 Lt. grey dolomite marble	Massive recrystallised ore. Disseminated massive pyrite	0.1-2 m. wide 40 m. long 500 m long	approx 1000T 15% Pb, 27% Zn
<b>Myers</b>	Lwr. Marmorilik Fm Unit 2 Lt grey dolomite marble	Massive buckshot ore Stringer horizons	.1-.4 m thick .4-.5 m thick 900m Dissem.	23% Pb & Zn 8% Pb & Zn
<b>Wedge</b>	Lwr. Marmorilik Fm. Unit 2 lt grey dolomite marbles. Extension of Ark	Small massive showings and longer disseminated zones	30 cm. thick 2-3 m. wide 300 m long over 2 m. wide	20% Pb & Zn 5% Pb & Zn

tectonic slide zones of the middle Marmorilik area (Fig. 6.1 & 6.6). It lies on the structurally correct way up limb of a sheared D2 synform.

### **6.3 The Nunngarut deposit.**

#### **6.3.1 Introduction**

The Nunngarut deposit is a stratabound, massive to semi massive Fe-Zn-Pb-(Ag) 357,000 tonne ore body (Figs. 6.7 & 6.9) of 12.7% combined Zn-Pb (Table 6.1), situated at an elevation of 650 metres, 4.5 km. to the south of Marmorilik (Fig. 6.1). It occurs in white calcitic marbles and calcite-pelite rythmites (Figs. 6.3 & 6.9) of the Lower Marmorilik Formation which lie at a slightly higher stratigraphic level than the Myers-Ark horizon (Fig. 6.3). Gossanous Zn-Pb showings occur at four other localities near the Nunngarut deposit (Fig. 6.7). To the northwest of the orebody, Plateau showings 1,3 & 4 are present in the stratigraphical hangingwall (Figs. 6.7 & 6.8). The P1 and P3 showings occur in white to light grey, siliceous to vuggy, saccaroidal dolomite marbles. The P4 showing is hosted in massive tremolitic marbles with calcite-dolomite marble containing graphite folia, which are interbanded with the dolomite marbles. The stratigraphical footwall of the deposit consists of barren light grey to grey, massive, medium to fine grained, dolomitic marbles.

#### **6.3.2 The Nunngarut Orebody: Form and Structure**

The Nunngarut ore body is irregular in plan view and defines a distorted NNW-SSE trending ellipse, with a concordant northerly limb-like offshoot (Fig. 6.7). The horizon is up to 250 metres long, 150 metres wide and 19.5 metres thick (Figs. 6.7 & 6.9). To the west and northwest the ore becomes disseminated. Disseminated mineralisation also extends towards the P2 showing to the east (Fig. 6.7).

The deposit lies in a north verging, tight-isoclinal F1 synform, known as the Nunngarut fold (Figs. 6.8a & 6.9), which occurs in a D2 tectonic slide block. The synform is part of a sequence of D1 cascade folds

that are believed to have formed above a curvilinear, east-west trending, D1 listric extension fault (Figs. 6.8a & 6.8b). Strong axial planar cleavages, non-cylindrical fold axes and extensional crenulation cleavages occur in association with this synform. A major D3 listric, northwest side down, sinistral shear fault (the Tributary-Nunngarut fault) runs to the west of the deposit, through the P1-P4 area and across to the western 'A' fjord cliffwall (Fig. 4.26 & 6.7).

The ore body contains massive to breccia-textured ore characterised by sub-rounded pyrite porphyroblasts, up to 3 mm, in a medium grained sphalerite-galena matrix containing accessory pyrrhotite. The matrix contains irregular to tabular pelitic fragments, grey white calcite clasts, ragged and ellipsoidal recrystallised quartz eyes and minor bitumen. Small amounts of recrystallised galena and sphalerite occurs at the hangingwall contact of the deposit.

#### **6.4 Uvkussigsat and MP 5 zone**

Zn-Pb mineralisation in the Middle Marmorilik Formation occurs as a highly sheared, discontinuous sheet for over 30 Km. Massive mineralisation occurs on the Uvkussigsat Peninsula (Fig. 4.13) (Della Valle, 1976; Pedersen, 1980; King 1981) and the Agpat Island (Fig. 1.3) (Gannicott, 1976; Della Valle, 1976; King 1981), and is correlated with the MP 5 zone semi-massive mineralisation of the Middle Marmorilik Plateau (Figs. 6.1, 6.2 & Table 6.1). The Uvkussigsat showing contains coarsely recrystallised high grade pods of galena and sphalerite in open D3 folds, which lie within a more massive sheared ore (synonymous with the porphroclastic ore facies, section 6.5.6).

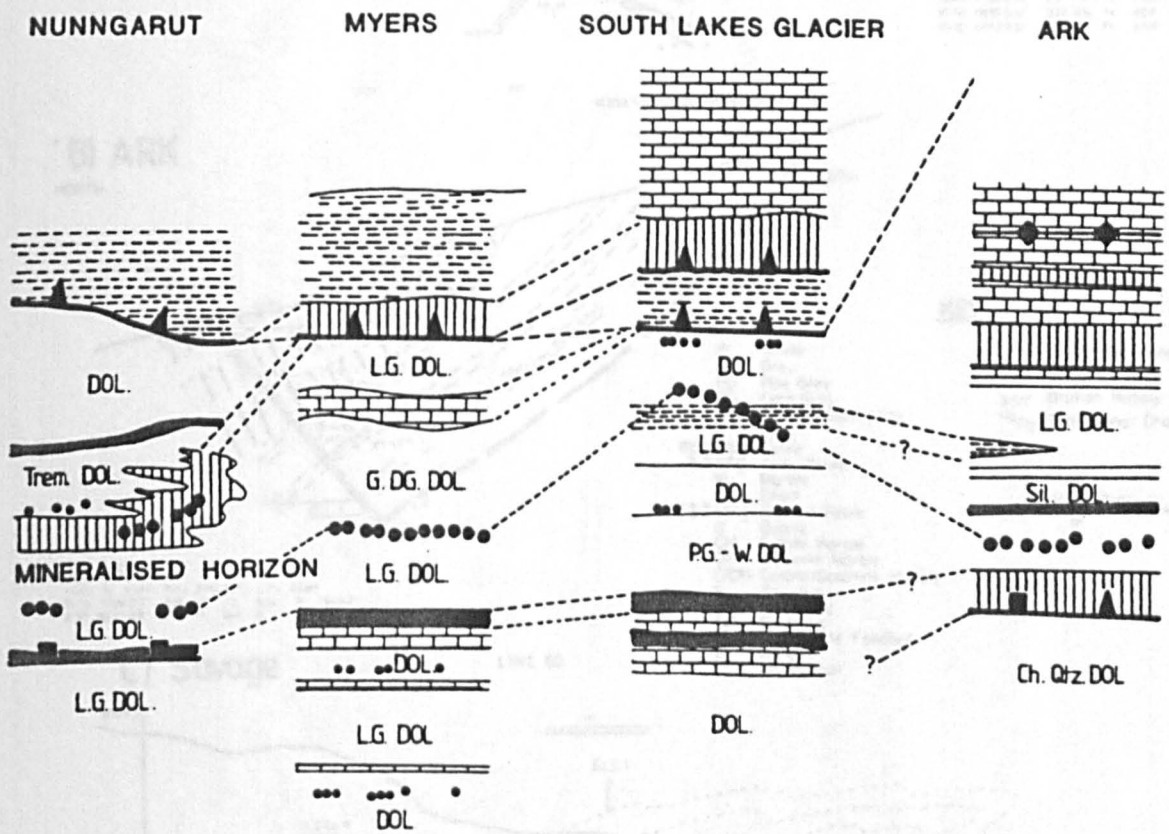
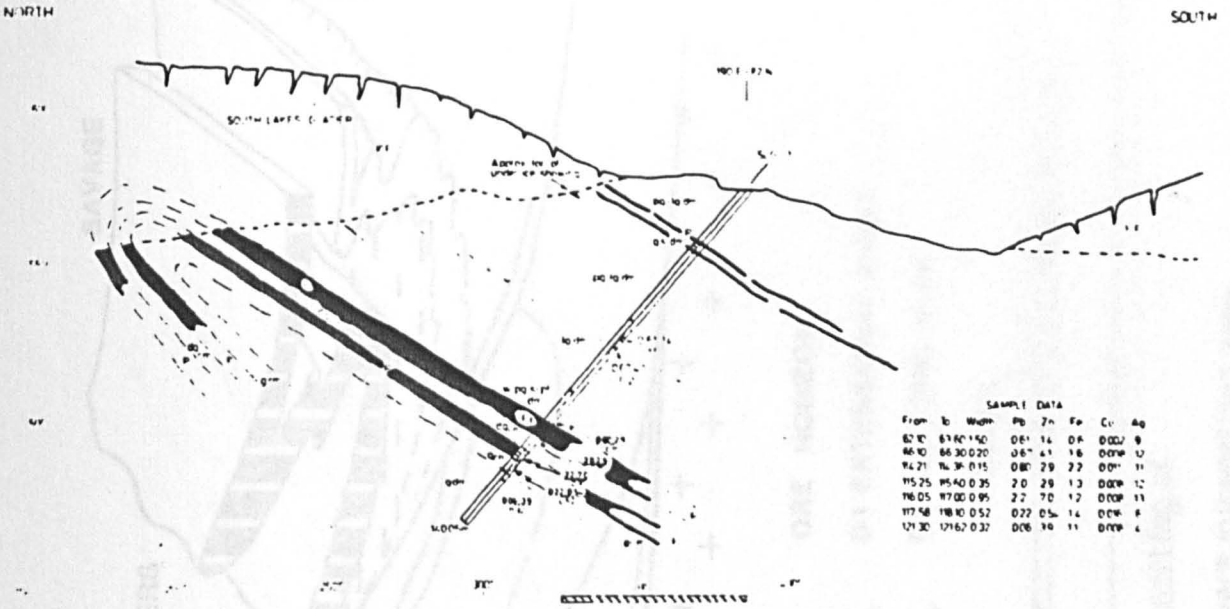
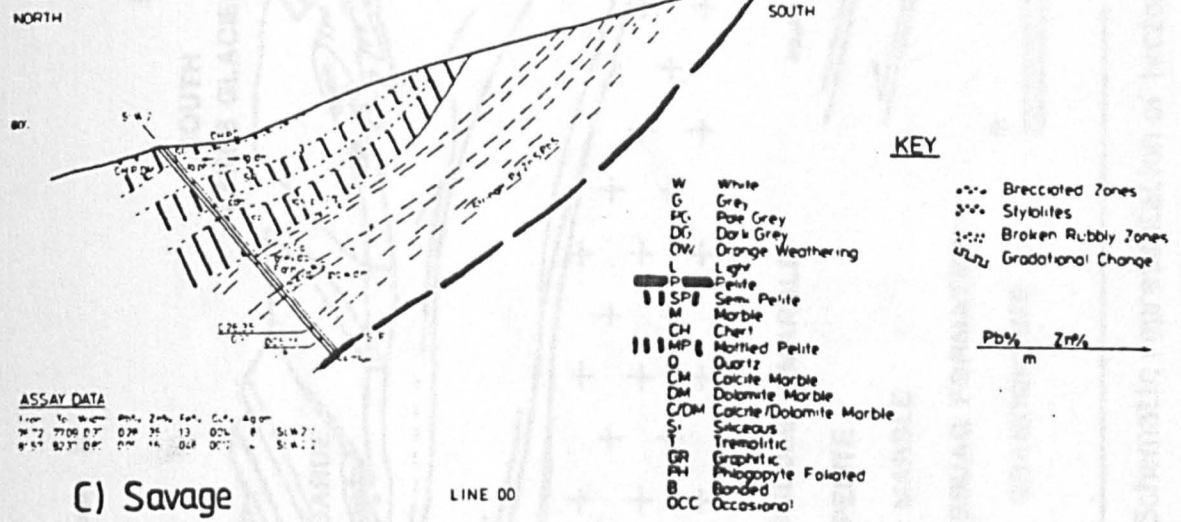


**Figure 6.3** Stratigraphic setting and the correlation of mineralisation in the Lower Marmorilik Formation Myers-Ark zone

A) South Lakes Glacier



B) ARK



**ASSAY DATA**

From	To	Width	Pb	Zn	Fe	Cu	Ag
74'72"	77'00"	0.27	0.24	2.6	1.3	0.01	1.5
81'57"	82'37"	0.40	0.14	0.47	0.01	0.01	0.01

C) Savage

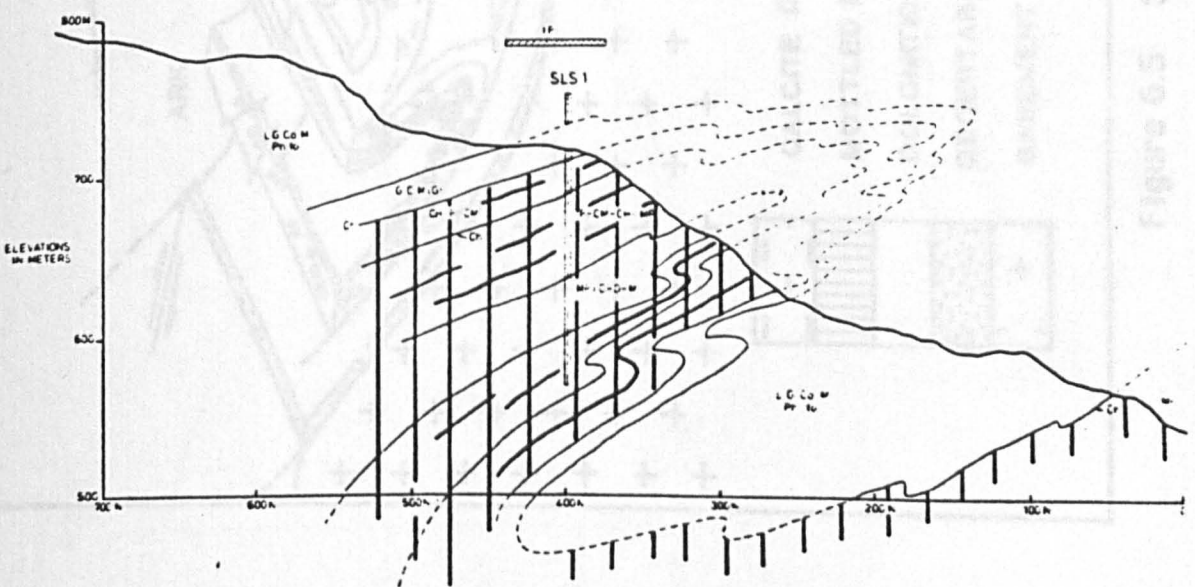
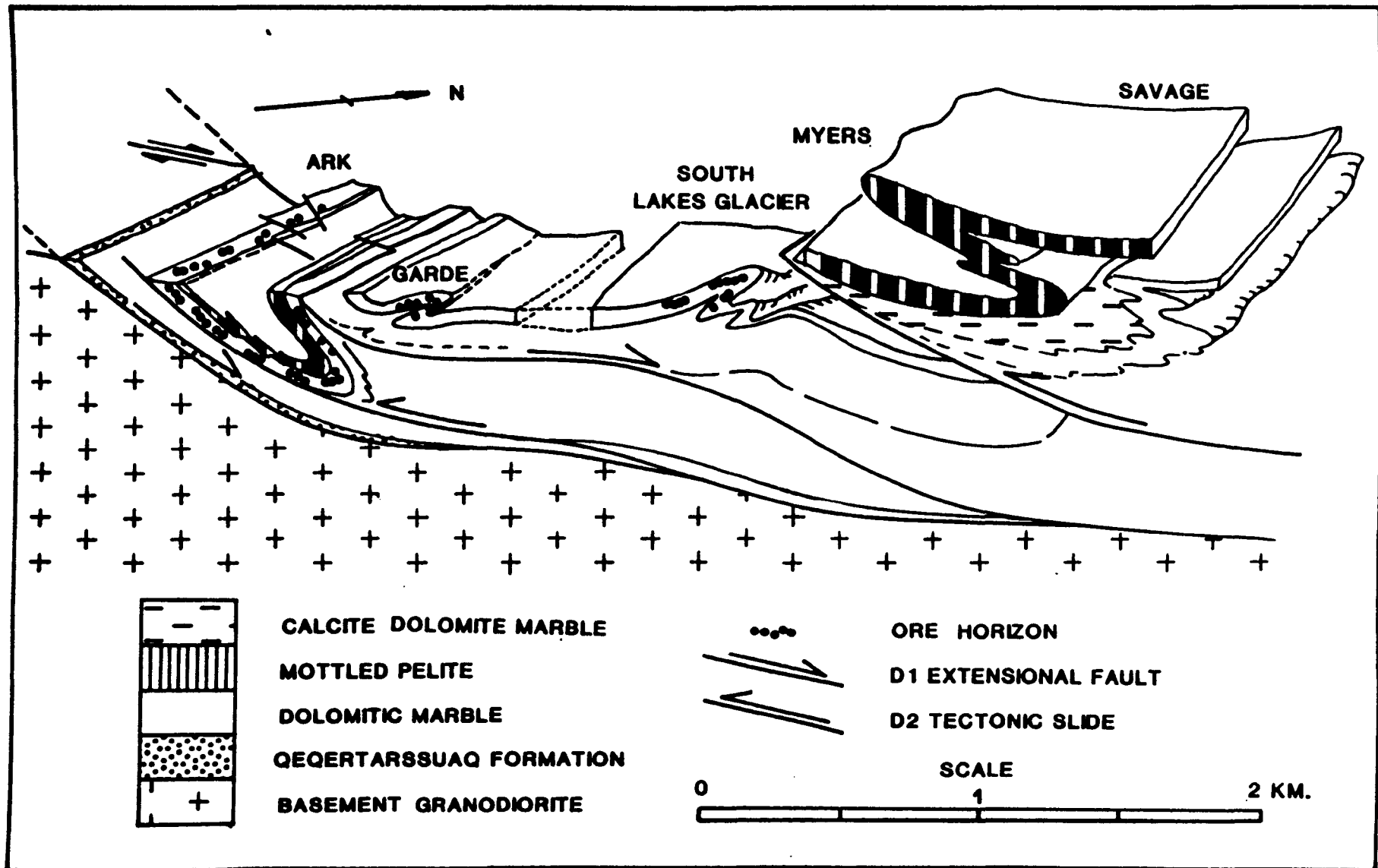
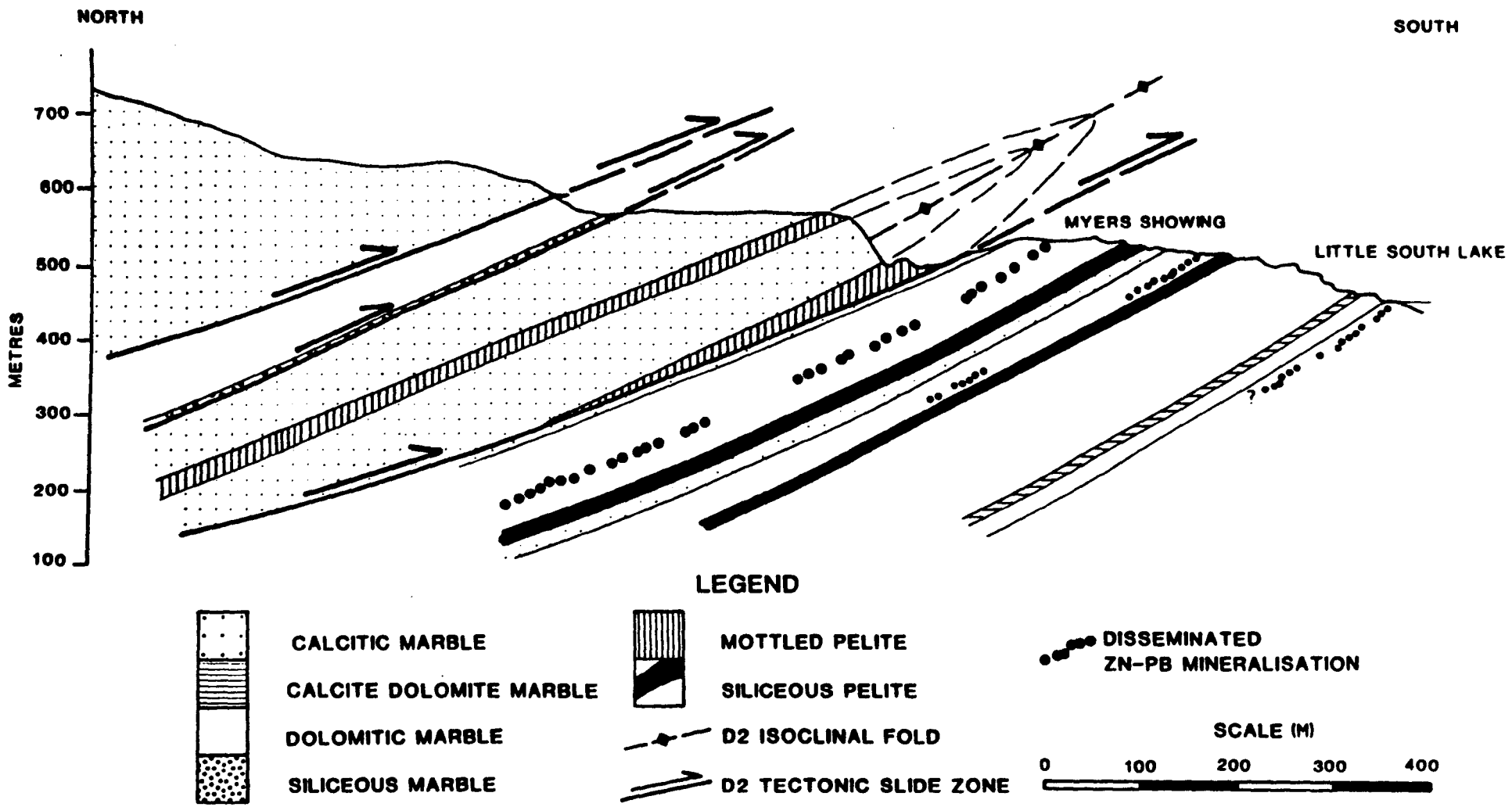


Figure 6.4 Stratigraphic and tectonic setting of mineralisation in the Lower Marmorilik Formation



**Figure 6.5** Schematic representation of tectonic setting of the Ark-Garde-South Lakes Glacier-Myers mineralised zone



**Figure 6.6** Cross-section through the Myers mineralised zone. (Modified from Harris, 1982)

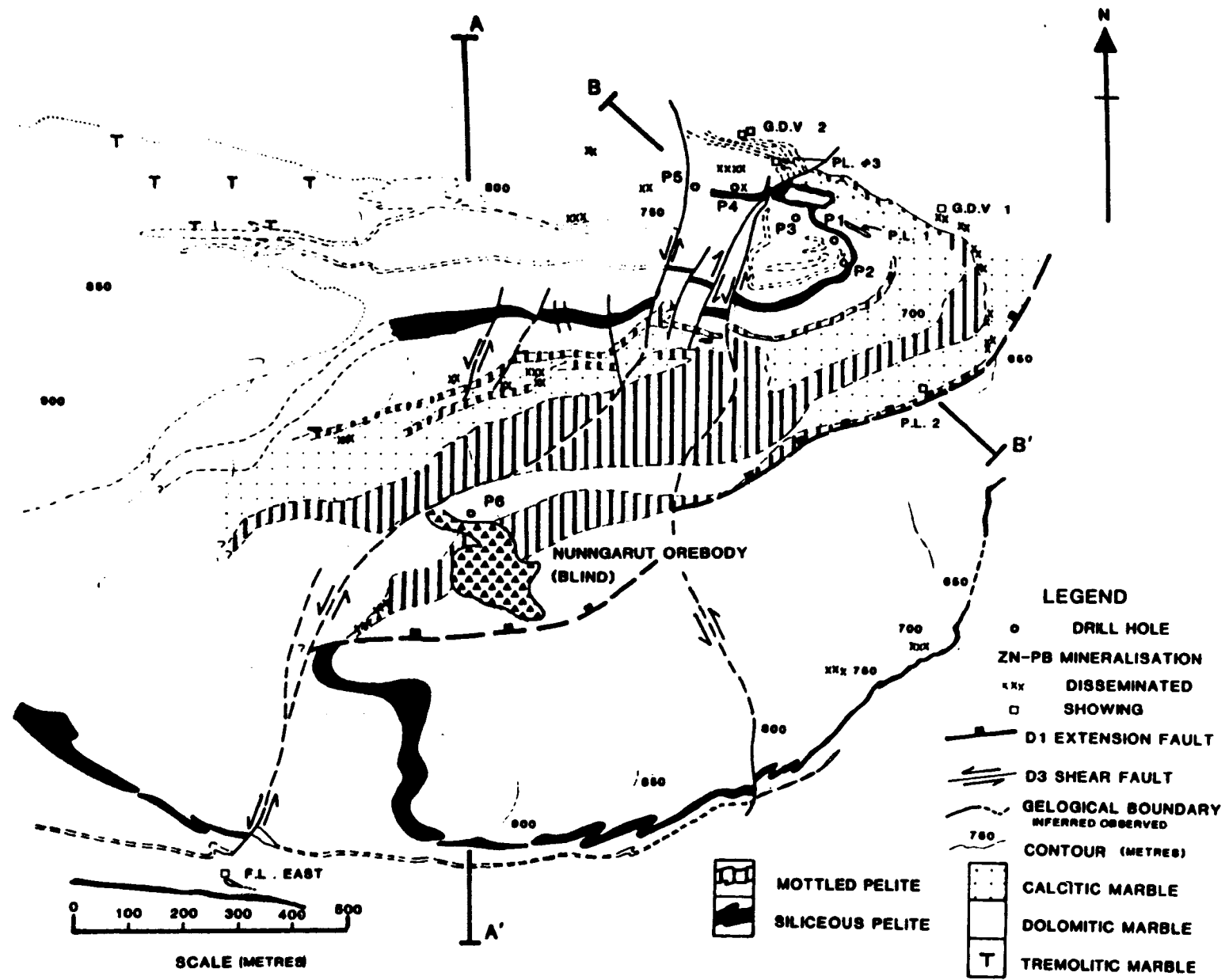


**Figure 6.7** Geological map of the Nunngarut deposit. The folded, sub-surface Nunngarut deposit has been projected to the surface

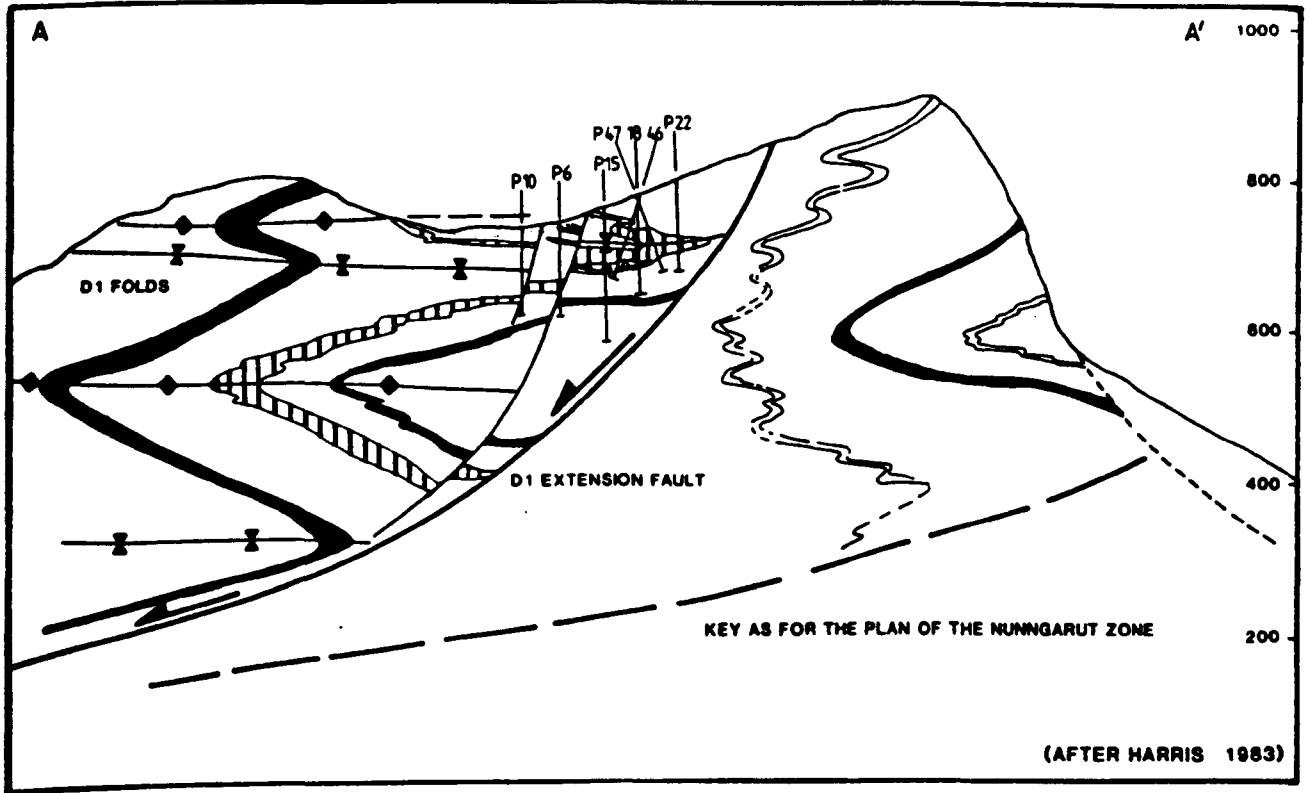


Figure 6.8a Cross-section through the west Nunngarut zone

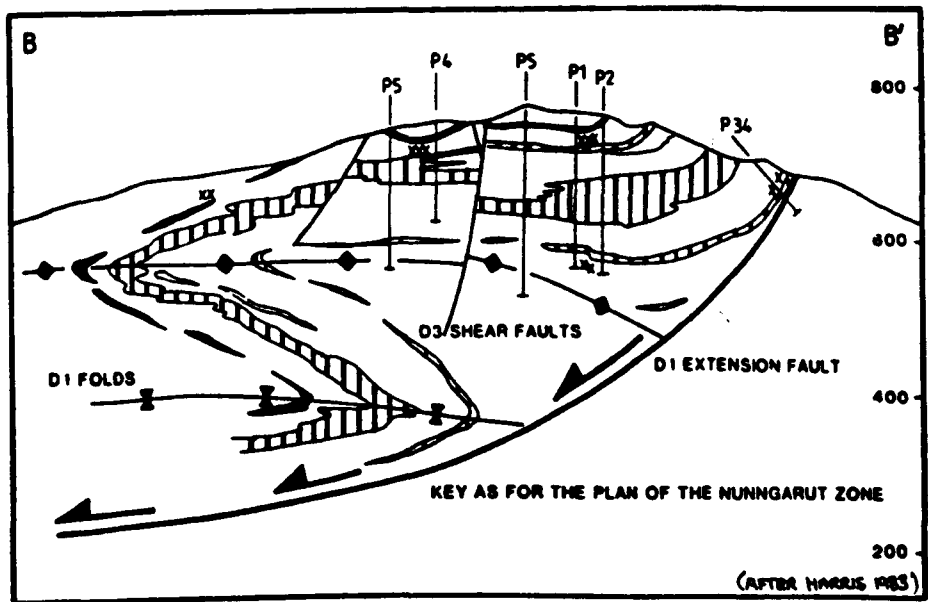
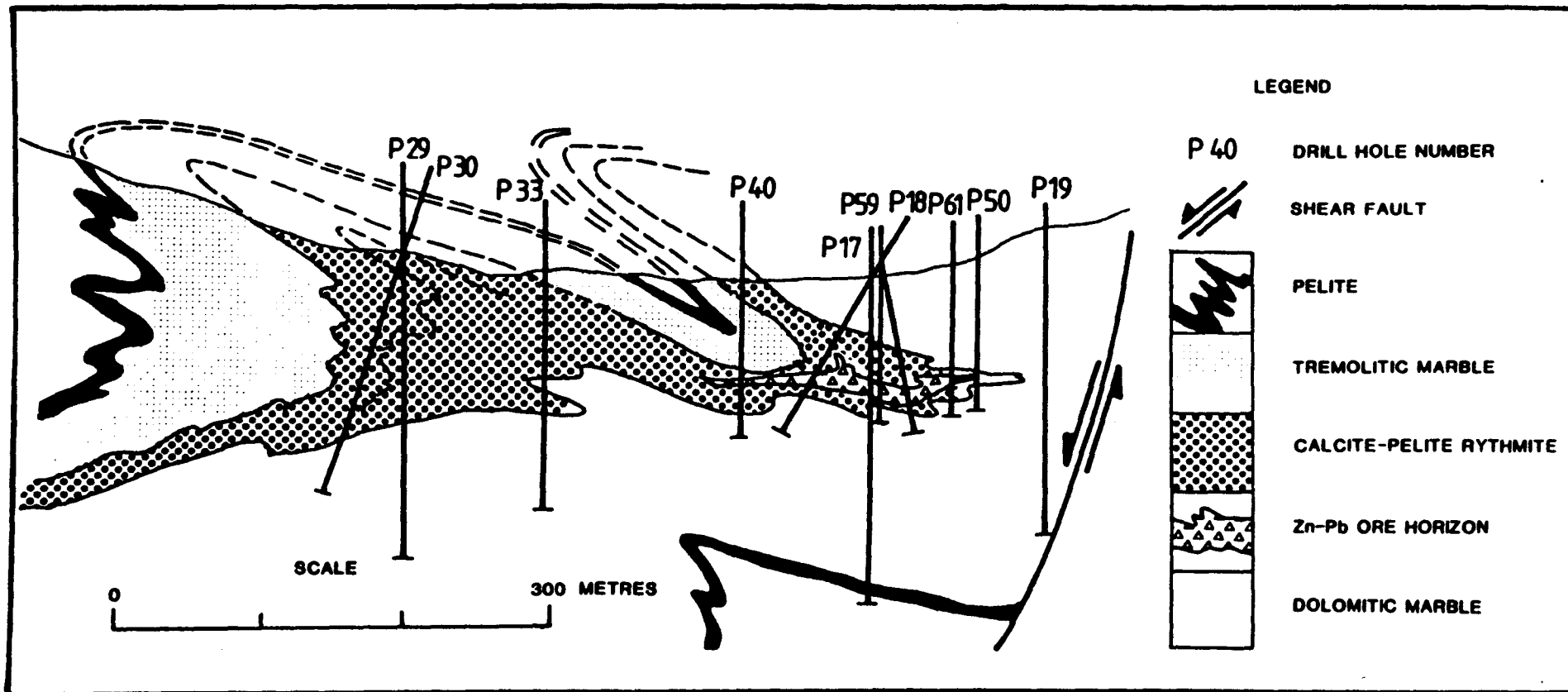


Figure 6.8b Cross-section through the east Nunngarut zone



**Figure 6.9** Detailed section through the Nunngarut deposit

## **6.5 The Black Angel deposits**

### **6.5.1 Introduction**

The Black Angel deposits are poly-metamorphosed massive, stratabound, and in places tectonically discordant Fe-Zn-Pb-Ag sulphide deposits, consisting of six ore zones namely the; Angel, Cover, Tributary, I, Banana and Deep Ice zones (D.I.Z.) (Fig. 6.1 & Table 6.2). These zones occur in a narrow, 5 km. long, west-east trending mineralised belt extending from the Black Angel cliffwall and persisting under the inland ice cap as far as V 205 & V216 drill hole intersections (Fig. 6.1). The ore deposits occur as elongate, boudinaged pods and lenses in two tectonically separated horizons namely the Angel-Cover-Tributary zone horizon (A-C-T) and the I-Banana zone horizon (I-B) within a disseminated mineralised sheet in the Unit 4 marbles. The mineralised sheet was folded about the Black Angel nappe during D1 deformation and transected by tectonic slides in the D2 event, so that the A-C-T zone now occurs at a higher topographic level than the I-B zone horizon (Fig. 6.10).

### **6.5.2 Previous mine work**

Previous work on the Black Angel deposits has included surface exploration drilling supervised by Cominco Europe Ltd. exploration geologists and underground mine mapping by Greenex A/S geologists. Detailed stope wall mapping by the mine geologists concentrated on the form and extent of the ore horizon rather than on mineralogy, texture and structural relationships. A detailed study of the mineralogy and structure of the Angel Zone was carried out by Pedersen (1980b & 1981) who produced an isometric cross-section and an ore facies map of the Angel zone. As Pedersen failed to recognise certain tectonic events in the Marmorilik area (section 4.1), several of his interpretations of the sulphide deformation textures are flawed.

Many new ore zones have been opened to production and/or subjected to extensive exploration drilling since this earlier work which

ORE ZONE	STRATIGRAPHIC SETTING	MINERALISATION STYLE	SIZE	TONNAGE & GRADE
Angel	White anhydritic calcitic marbles	Massive stratabound sheet of layered recrystallised pyritic and porphyroclastic ore facies	30 m thick 600 m wide 1000 m long	7 M. Tonnes 5.1% Pb 15.7% Zn 17% Fe 30 g/t Ag
Cover	White-lt. grey calcite marbles	Massive stratabound porphyroclastic ore with layered and recrystallised pods	Refolded 5 m. thick 350 m. wide 3000 m long.	2-3 M. Tonnes
Tributary	White anhydritic calcitic marbles	Massive stratabound mega-boudins of layered and porphyroclastic ore with pyrrhotite	2-3 m. thick 150 m. wide 700 m. long	0.7-1 M. Tonnes
'J'	Calcitic marbles with dark grey siliceous dolomite marbles and pelites	Massive steeply dipping stratabound to discordant ore lens of porphyroclastic ore	3-5 m. thick 150 m. wide 1000 m long	1 M. Tonnes
Banana	Calcitic marbles with dark grey siliceous dolomites and pelites. Barite in Footwall.	Massive stratabound to discordant arched horizon of porphyroclastic ore	0.5-3 m. thick 120 m. wide 500 m. long	0.5-1 M. Tonnes
Deep Ice	Massive calcites with interbanded calcite and dolomite marbles & py.	Massive stratabound recrystallised ore pods with layered ore	0.5-5 m thick 100 m. wide 250 m. long	0.6-1.0 M. Tonnes 8.1% Pb 33% Zn 14% Fe 28 g/t Ag
V215/216	Interbanded white-lt grey calcite and dolomite marbles	Massive stratabound recrystallised ore pods.	limited drill intersections	

**Table 6.2** Characteristics of the main mineralised zones in the Black Angel deposits and possible correlatives.

has provided a considerable amount of new data.

### 6.5.3 The Black Angel ore zones

The Angel zone contains the largest ore concentration in the mine (Table 6.2). It is sheet-like (1000m long, 600 metres wide and up to 30 metres thick) and dips at  $\approx 20^\circ$  N (Fig. 6.11). It passes into the Cover zone via a thin refolded mineralised unit (Fig. 6.17). The Cover zone is a relatively thin (Table 6.2) and strongly sheared lensoid ore body which has a hook like eastern closure (Fig. 6.15). The Tributary Zone lies to the northwest of the Cover Zone and consists of three boudinaged ore grade pods.

The I zone is a very thin, (2-3 m), W-E trending, north dipping ( $30^\circ - 60^\circ$ ) orebody (Fig. 6.21). Disseminated mineralisation extends eastwards from the I zone into the Banana zone. This zone is less elongate than the I zone. The ore horizon is arched over a D3 antiform (Fig. 6.15) so that the central ore zone is flat-lying, while the northern margin dips very steeply ( $80^\circ$ ) northwards in places.

The Deep Ice zone, which is presently in an early stage of production, is a satellite ore body which occurs 2.5 km. ENE of the Cover zone (Fig. 6.1). Mineralisation occurs at three tectono-stratigraphic levels and is folded into a dome-like structure. The lowest mineralised level contains irregular, high grade, recrystallised ore pods (Table 6.2).

### 6.5.4 Mine stratigraphy.

#### a) Introduction.

The lithologies hosting the Black Angel deposits conform to three broad tectono-stratigraphic panels. These are (with respect to the mineralisation):- i) the hangingwall sequence: ii) the mineralised sequence: iii) the footwall sequence (Fig. 6.10).

The hangingwall sequence consists of the pyritic and pyrrhotitic pelites and biotite schists of the Nukavsak Formation (3.3.3) and the

uppermost calcite-dolomite marbles (with interbands of siliceous pelites) of the Marmorilik Formation (3.3.2).

The mineralised sequence that hosts the A-C-T zone horizon and the I-Banana zone horizons are bounded by two D2 tectonic slide zones (Fig. 6.10). The stratigraphy is highly deformed and the host rocks and the ore horizon are repeated and tectonically inverted many times in parasitic folds of the Black Angel nappe. Highly sheared siliceous pelitic schists in the footwall of the I-Banana zone mineralisation (Fig. 6.12 & 6.21) mark the boundary between the mineralised and footwall sequences in the mine.

The footwall sequence consists of a tectonically folded and imbricated succession of dark grey pyritic siliceous pelites which occur in layers up to 20 m thick, and are interbanded with white to light grey siliceous carbonates and grey banded graphitic calcite and dolomite marbles (unit 3; sect. 3.3.2).

Ore/gangue contacts in the A-C-T zone horizon are generally sharp and conformable with the host rock foliation (Fig. 6.25). In the Cover, I and Banana zones many contacts are discordant and strongly sheared (Fig. 6.27).

## **b) Stratigraphic location of the ore zones.**

### **1) The A-C-T zone horizon**

The A-C-T zone horizon is hosted in monotonous coarse to medium grained white calcitic marbles (Figs. 6.12 & 6.13) with randomly distributed prismatic scapolite and prismatic to rosetteform tremolite. Thin (1 cm - 10 cm) white-lilac-pale purple anhydritic layers are interbanded with the calcitic marbles (Fig. 3.10b). The marbles are purer in the north west Angel zone. A relatively consistent hangingwall and footwall stratigraphy is maintained along strike, despite strong localised faulting and shearing.

The marbles become interbanded with light to dark grey, fine grained graphitic, phlogopitic and pyritic dolomitic marbles southwards

from the Angel zone and also eastwards towards the Cover zone (Figs. 6.12 & 6.13). In the southernmost Angel zone (G and H areas) the ore horizon is thrust against indurated black graphitic siliceous pelites (Fig. 6.13).

The footwall stratigraphy of the A-C-T zone horizon is a complexly folded and interbanded succession of dark grey dolomitic marbles and fine grained indurated pelites with light grey siliceous calcitic marbles (Fig. 6.17). In the Tributary area phlogopite-calcite marbles and salmon pink, manganese-rich calcite marbles are interbanded with these footwall units and can be traced through to the the the Deep Ice Zone, where they also form the footwall succession.

#### **ii) I-Banana zone Stratigraphy**

The I-Banana zone mineralisation occurs in white to light grey calcitic and dolomitic marbles (Figs. 6.12 & 6.13), which do not persist in the footwall succession where they give way to pelitic shists interbanded with dark grey dolomitic marbles. In the south and east of the I zone the footwall contact is sharp and highly sheared (Fig. 6.14). The ore horizon is thrust against dark grey dolomitic marbles (Fig. 6.21), with coarse calcite-filled joints, and black graphitic siliceous pelites (Fig. 6.13). The pelites are indurated and in places (I 170) contain chlorite and biotite books associated with recrystallised quartz (Fig. 6.38). The ore zone stratigraphy is consistent between the I and Banana zones.

The Banana zone ore horizon is hosted by wispy pyrite and phlogopite-bearing foliated, calcitic and dolomitic marbles (Figs. 6.12 & 6.13 ). The footwall succession is dominated by tan coloured siliceous dolomite marbles (Fig. 4.21d & e) which are underlain by dark grey graphitic dolomites and siliceous pelites containing lenses (up to 10 m thick) of siliceous calcite marbles. Chlorite-biotite-quartz is present in the footwall succession of the Banana zone, associated with pods of recrystallised and sheared baryte (Fig. 6.13). The baryte pods occur in contact with the ore horizon as east-west trending bodies, up to 2 metres

thick and 30 metres long.

### **iii) Deep Ice zone stratigraphy.**

The exact stratigraphic location of the Deep Ice zone mineralisation (Fig. 6.1) is uncertain. Mineralisation is present at three tectono-stratigraphic levels. The highest of these occurs in graphitic calcite-dolomite marbles of the Upper Marmorilik Formation (Fig. 3.11) correlating with the hangingwall sequences in the A-C-T zone. The two lower ore sequences are clearly seen to lie below the Tributary zone horizon in drill holes intersections located between the two ore zones. Coarsely crystalline, high grade, sphalerite and galena occur in irregular pods and are hosted in white, grey and occasionally dark grey dolomitic marbles. These are interbanded on a millimetre to metre scale with white, tremolite and scapolite bearing, calcitic marbles. Thin siliceous pelite bands are also interlayered with the carbonates (Fig. 4.21d & e). These units are consistent with those which occur in the I-Banana zone.

The footwall is a distinctive white and predominantly dolomitic marble with wispy, folded and sheared out pyritic laminae (Fig.4.29e).

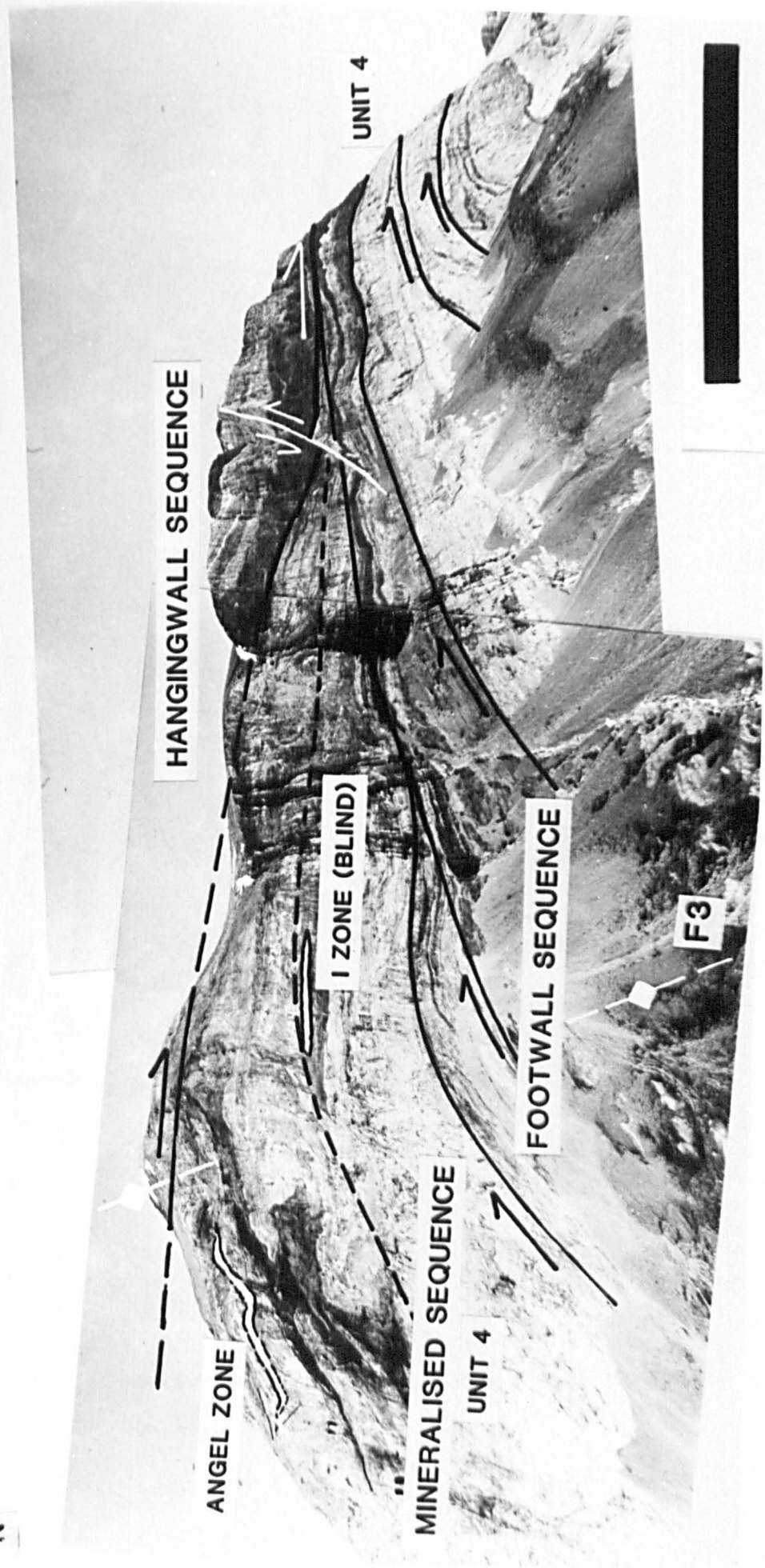
### **c) Hangingwall and footwall stratigraphic variation.**

There are strong consistencies between the immediate hangingwall and footwall lithologies of the ore zones (Figs 6.12 & 6.13). Variations exist in the southern Angel zone, the I zone and the Banana zone, but these are tectonically rather than stratigraphically controlled. The major lithological variations are associated with D2 tectonism, which caused the hangingwall lithologies to be carried over the footwall lithologies on the ductile ore. A good example of this is observed in the eastern I zone, where the ore horizon and overlying folded dolomitic marbles, are thrust onto imbricately stacked pelitic schists of the footwall (Fig. 6.14).

## Figure 6.10 Eastern Agfardlikavsa Cliffwall and Black Angel deposits

A photographic montage showing the eastern 'A' fjord cliffwall. To the north the D1 Black Angel nappe, and the subjacent strongly transposed interbanded pelites calcite and dolomite marbles, are deformed into a D3 rollover structure. The Black Angel nappe and ore horizon (thin dark grey boudinaged strip above the nappe), are held in a southerly tapering D2 tectonic wedge. Imbricated D2 tectonic slide zones associated with D2 folds are concentrated towards the southern end of the cliffwall, and transect D1 isoclinal folds. Scale bar 500 metres.

S



N

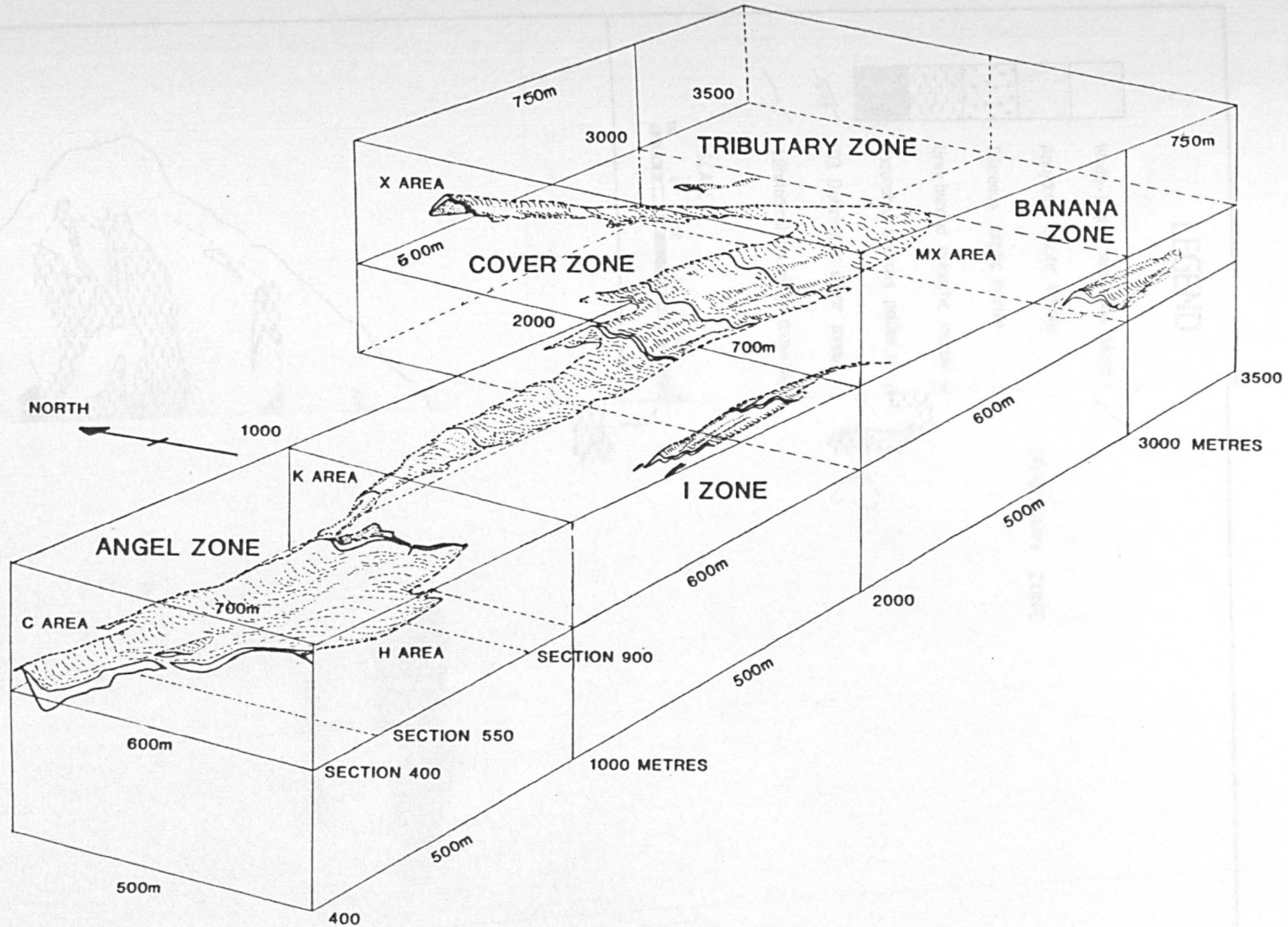


Figure 6.11 Isometric 3D section of the Black Angel deposits

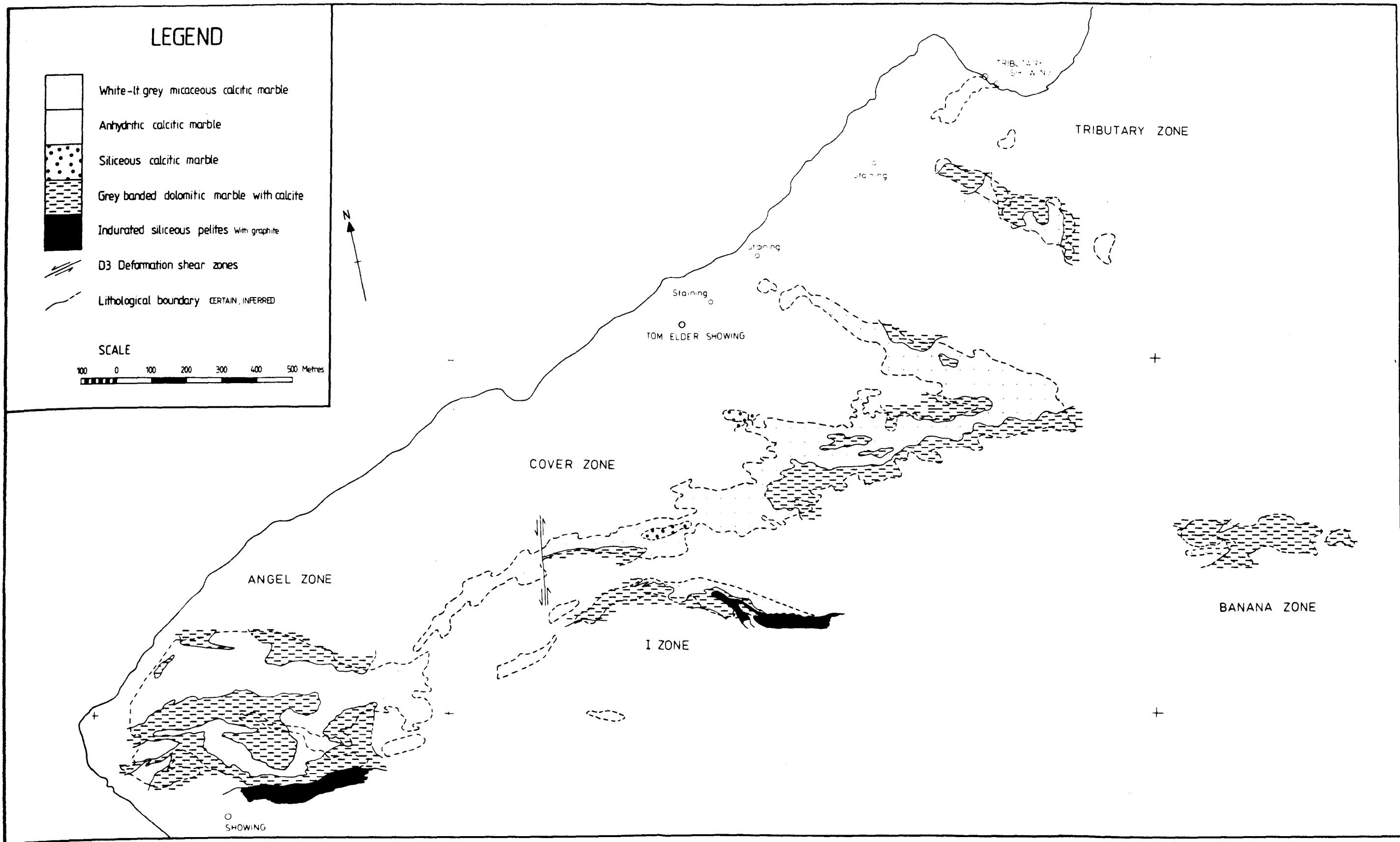


Figure 6.12 Hangingwall lithological map

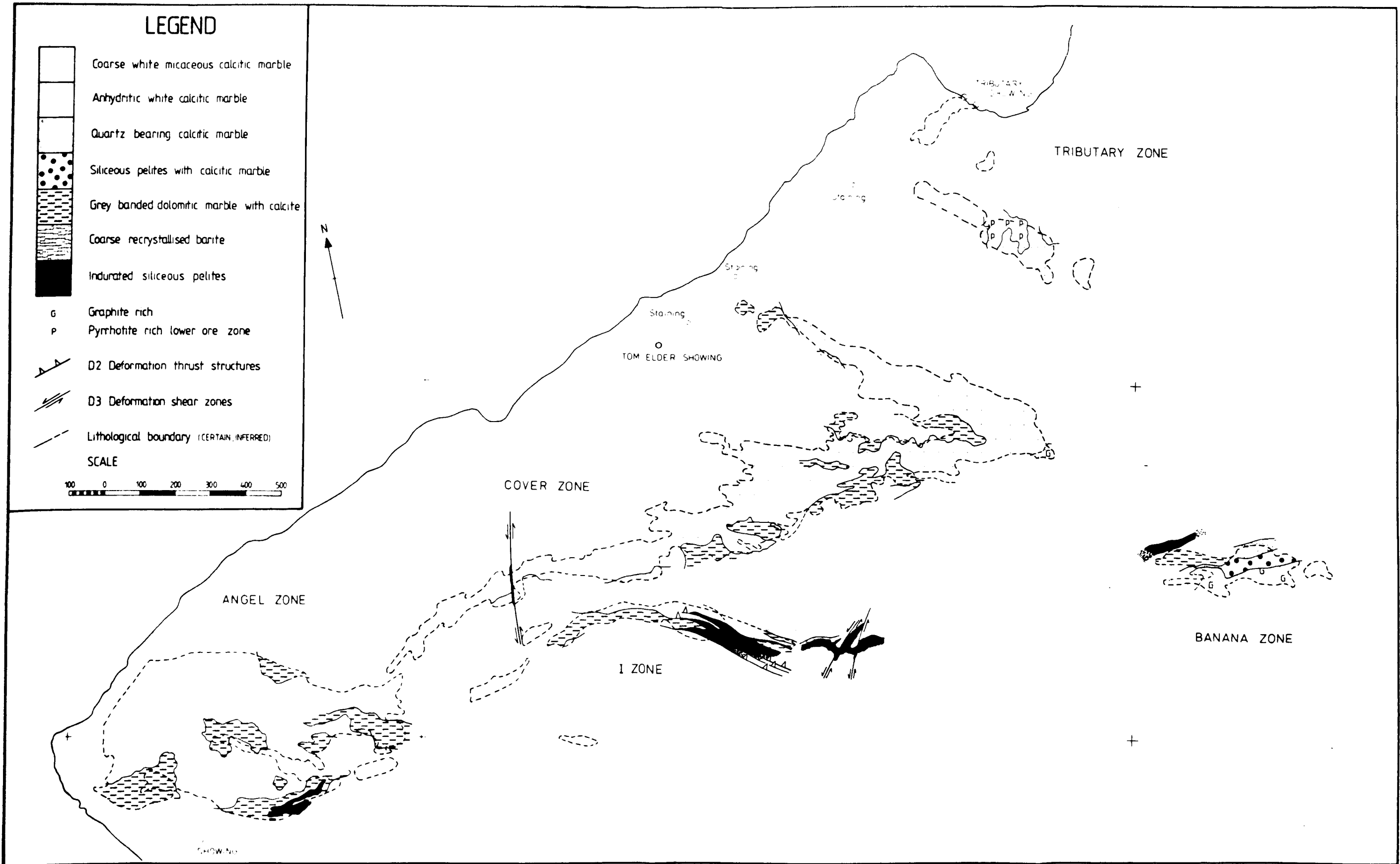


Figure 6.13 Footwall lithological map

### 6.5.5 Mine structure.

The Black Angel deposits have been polydeformed during the Rinkian event. They were deformed in; the northern contractional domain during D1 deformation (section 4.2.3), the transition between the northern fold belt (section 4.3.2) and the central contractional belt (section 4.3.3) during D2 deformation, and the oblique slip rollover (section 4.4 & Fig. 4.27) during D3 deformation.

The major structural features of the Black Angel deposits are depicted in Figure 6.15. The most obvious features are ESE-WNW trending D3 folds that refold D1 isoclinal, D2 folds and D2 tectonic slides.

#### a) D1 structures

D1 deformation folded the Black Angel ore horizon about the D1 Black Angel nappe (Fig. 6.10). The resulting ore horizons (A-C-T and I-B) are transposed parallel to the D1 fold axial plane. The A-C-T horizon is elongate parallel to the F1 fold axis (080-260°) (Fig. 6.15).

D1 structures are largely obscured in the mine by the more pervasive D2 structures. They are more easily recognised on mine cross sections (Fig. 6.17). In the central Angel zone (Fig. 6.15) and the northern Banana zone (Fig. 6.15) they are represented by large scale north verging, non-cylindrical, recumbent folds (Figs. 4.14 & 6.18) with nipple like accommodation features (Fig. 6.19), and more rarely by low angle tectonic slide zones (Fig. 6.18). The nipple structures are a response to the competency contrast between the sphalerite (more ductile) and pyrite bands.

The upper surface of the ore horizon is characterised by rootless folds with axial planar seams of semi-massive and stringer-like mineralisation that penetrate the host rocks (Fig. 6.17 & 6.20). Sulphides near the footwall of the ore horizon are folded into D1 cusped antiforms and 'pinched in' synclines (Fig. 6.17 & 6.20) which are similar to the cusp and piercement structures described by Maiden et al. (1986). The less

competent sulphides form pinched in synforms against the more competent carbonates, while piercement structures are developed in fold hinge zones where the host rock deformed by brittle fracture.

#### b) D2 structures

The D2 structures are represented by south-verging inclined folds with 'out of syncline thrusts' (Fig. 4.21) and imbricated tectonic slide zones (Figs. 6.14 & 6.21). Although these have been refolded by D3 folds they maintain a north-east to south-west trend (Fig. 6.15) and are dominantly north-west plunging. Slip vectors ( $32^{\circ}$ - $356^{\circ}$ , Table 4.2), determined from mineral stretching lineations, indicate a south-eastward tectonic transport of the imbricated fault blocks.

D2 tectonic slides thin the ore horizon, in the southern Angel zone, much of the Cover zone, and especially in the L,M and P areas (Fig. 6.41), where large tectonic discordances between the ore horizon and host rocks occur (Fig. 6.27 & 6.33 a& b). D2 southerly verging inclined folds (Fig. 4.21) refold the ore horizon and D1 isoclinal folds (Fig. 6.23 b & f) into type 3 fold interference patterns (Fig. 6.17 section 900) (Ramsey, 1967), and produce steeply dipping ore shoots. Good examples of the latter feature are found in the I zone (Fig. 6.21), and are similar to the 'droppers' in the Broken Hill deposit (N.S.W.) (Maiden et al., 1986). These ore shoots are uneconomic, even though they are commonly high grade, because of the length of drifting required for their exploitation.

D2 en-échelon arrays of shallowly north dipping, imbricated and duplexed tectonic slide zones occur in and between the Cover and I zones (Fig. 6.21). As the tectonic slides accommodate a large amount of shortening, the number of slides and the amount of displacement upon them controls the separation between the Cover zone and the I/Banana zone. D2 duplexes and antiformal stacks thicken the ore horizon (Fig. 6.14).

### **c) D3 structures**

The most common D3 structures are south dipping, north verging, open to closed periclinal folds (Fig. 4.29a & 6.16). In the eastern Cover zone an array of parasitic folds occur on the limbs of a major D3 antiform-synform pair (Fig. 6.15). The fold axial traces of this fold pair run through the MX and southern KM areas and extend into the Banana zone (Fig. 6.15). Major D3 folds also occur in the northern C area of the Angel zone (Fig. 6.17 & 6.20) and the Banana zone (Fig. 6.15). Severe tectonic thickening of the ore horizon occurs within the D3 hinge zones (Fig. 6.20). The D3 fold limbs are attenuated and are often characterised by pinch and swell structures (e.g. northern Angel zone).

The D3 structures refold the already polydeformed ore horizon, creating very complex outcrop patterns (Fig. 6.16). Two major N-S trending, west dipping, D3 sinistral shear zones (the section 1600 shear zone and the Tributary-Nunngarut fault) cross-cut all earlier structures. The section 1600 shear zone (Fig. 6.15) locally causes vertical/oblique west-side down displacements in the ore horizon of up to 30 metres. The Tributary-Nunngarut fault occurs as a transtensional duplex zone in Drift 23 (Fig. 6.16).

### **d) D4 structures**

North-south trending west side down, extension faults and numerous close spaced joints occur throughout the mine. These D4 structures have little effect on the geometry/morphology of the ore horizon, but contribute greatly to slabbing and pillar failure in the mine (i.e. Angel zone) and can considerably hinder production.

### **e) Summary**

The Black Angel deposits are folded about the D1 Black Angel nappe. D2 imbricated tectonic slides transect and severely thin the ore horizon, whereas considerable thickening of the ore horizon occurs in D3

fold structures. Large competence contrasts exist between the ductile ore and the host rocks which has caused much plastic deformation to be concentrated within and around the ore deposits. Folds and joints are commonly rooted in the ore horizons, and D2 tectonic slide zones have exploited the naturally high viscosity/anisotropy contrasts at the ore-gangue contacts.

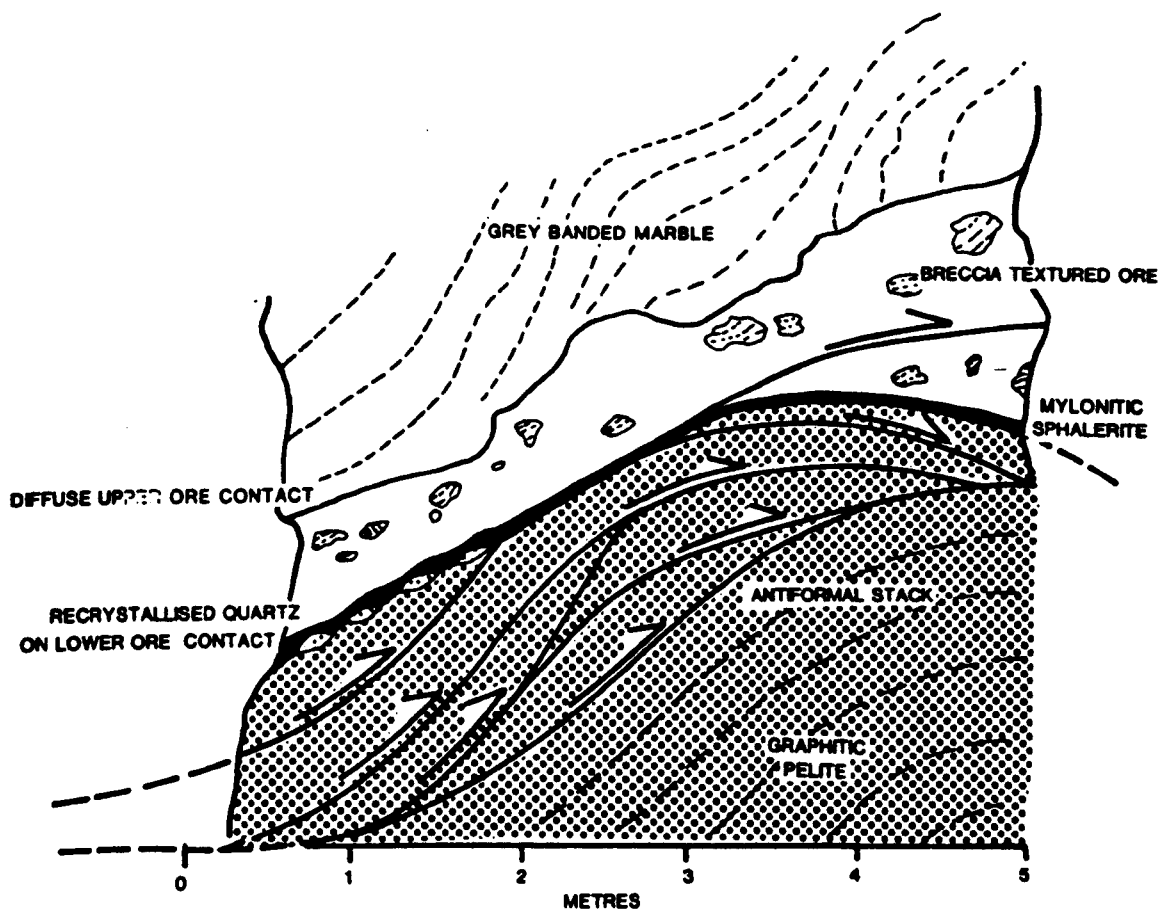


**Figure 6.14** I zone ore horizon showing discordant hangingwall contacts and highly sheared mylonitic footwall contact. Note the D2 antiformal stacking of the siliceous pelites in the footwall to the ore. Slope I 170



## Figure 6.18. North verging F1 isoclinal nappe

Photograph of a sub-horizontal F1 isoclinal nappe developed in interbanded calcite-dolomite marbles. Breccia-textured ore (B) is present along the hinge zone. Note the decollement horizon at the base of the ore and the downcutting of the ore into the footwall with a consequent incorporation of host rock. Tight north verging parasitic folds occur on the upper limb of the nappe with cusps and axial planar seams of mineralisation. West wall T-1 Ramp, T zone. Metre rule for scale.



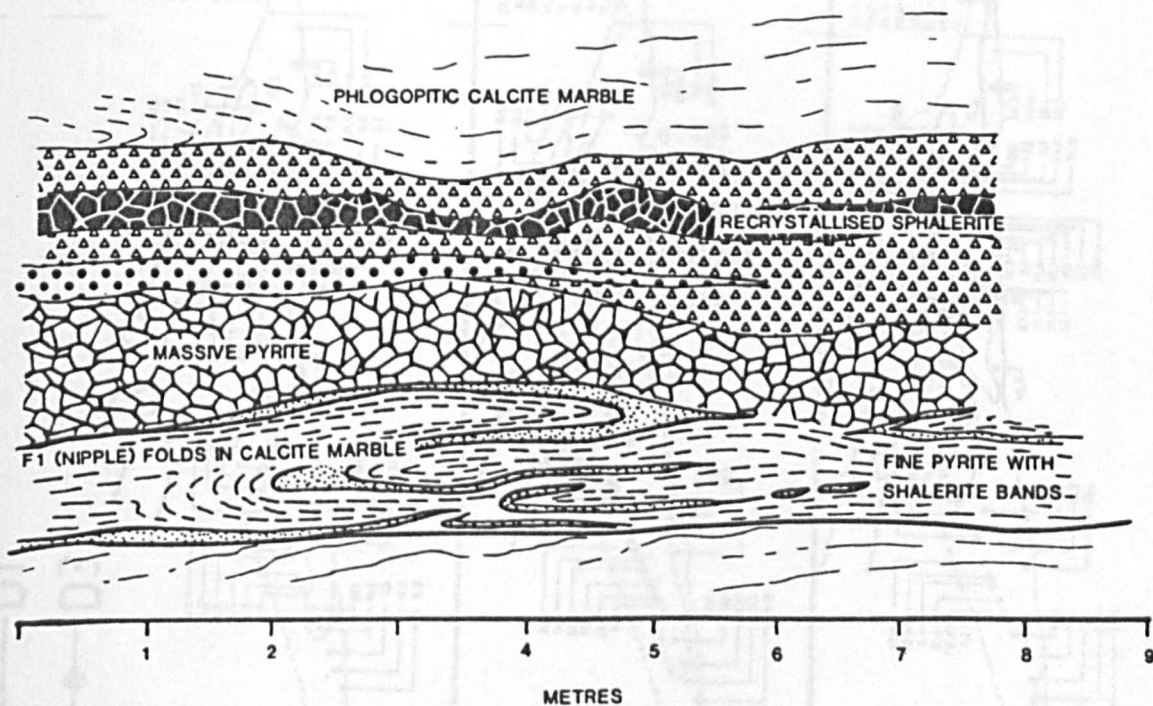


**Figure 6.19** Isoclinal F1 nipple folds in the K area, Cover zone

The folds are formed in layered ore tectonites which are overlain by coarsely recrystallised massive pyrite ore tectonites. Sheared porphyroclastic ores occur toward the hangingwall contact

Figure 6.20 Vertical sections of Stop E 60 displaying assay data of Zn, Pb and Fe. Note that high Zn and Pb values are present in the G3 fold, which

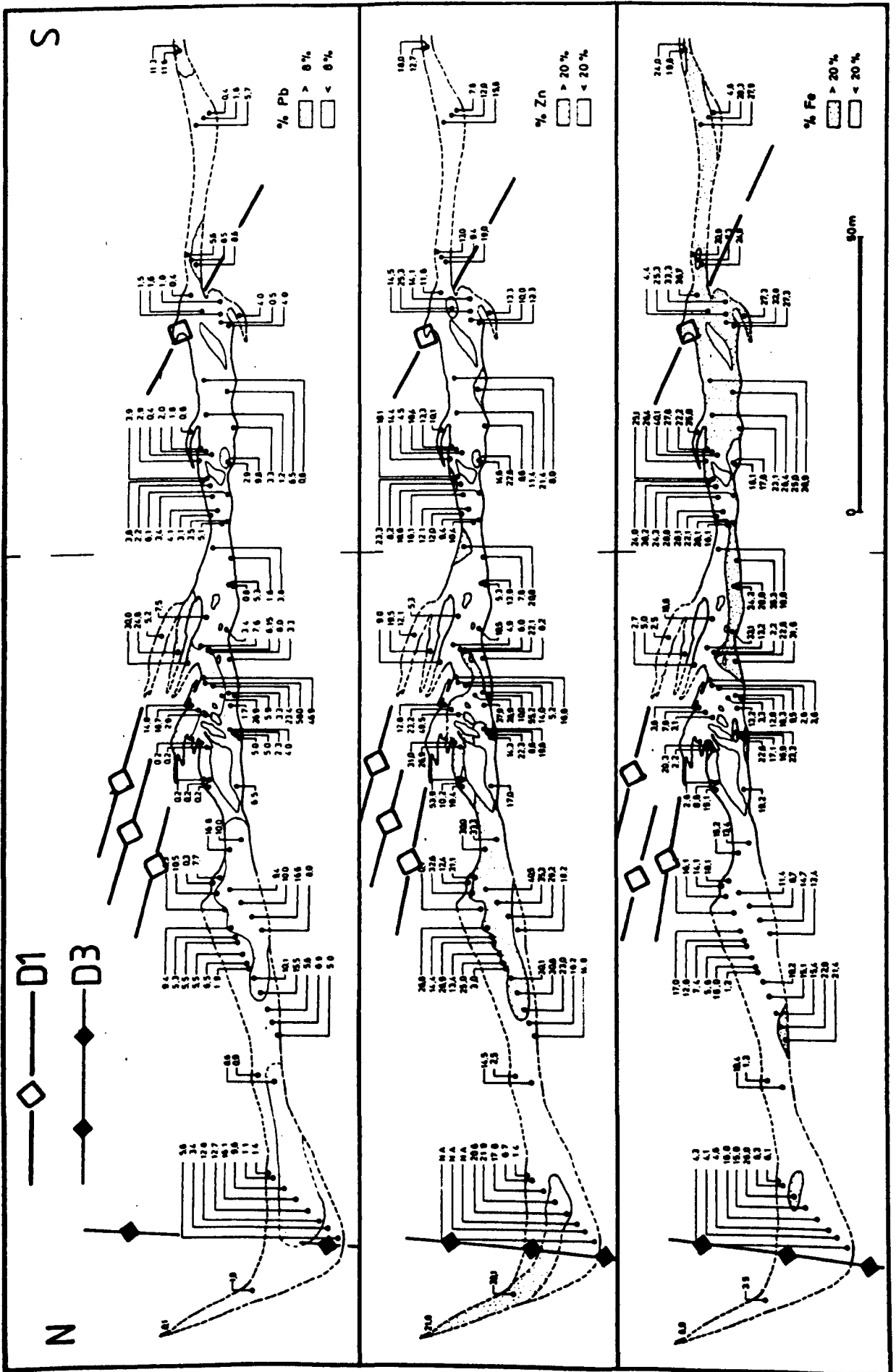


**Figure 6.20** Vertical sections of Stope E 60 displaying assay data of Zn, Pb and Fe. Note that high Zn and Pb values are present in the D3 fold, which is Fe deficient. (Modified from Pedersen, 1980b)

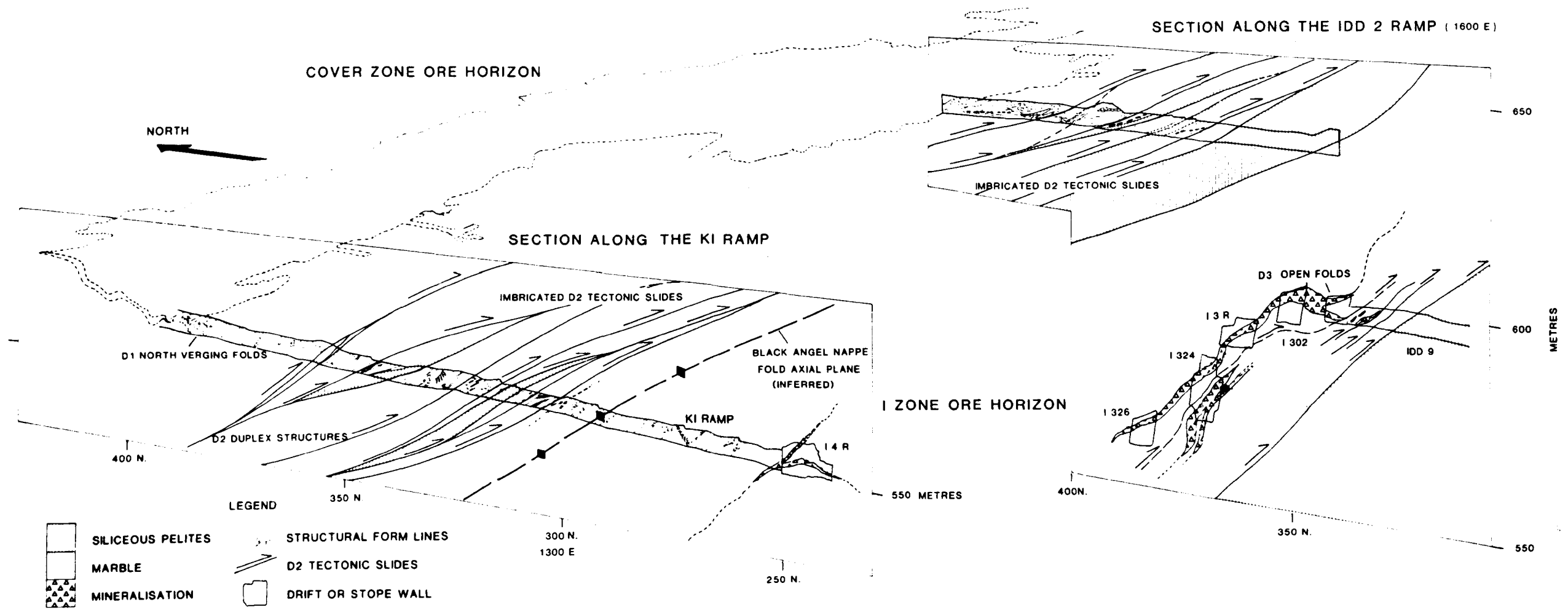


**Figure 6.21** Simplified sections along the KI and CB II ramps showing the complex D2 imbricated tectonic slide systems between the Cover and I-B zones

## 6.5.6 Ore petrology.

### a) Introduction

This section documents the ore mineralogy, texture, ore horizon geochemistry and mineral chemistry of the Black Angel deposits. The ore horizon contains pyrite, sphalerite and galena with minor pyrrhotite, chalcopyrite, arsenopyrite, and tennantite. Subordinate stannite, cubanite, electrum, polybasite, rutile, hematite, magnetite have been reported by Pedersen (1980). Fluorite, baryte and graphite also occur. The severe deformation in the Marmorilik area has largely obliterated the primary mineral textures. The sulphide horizons now consist of nine types of ore tectonite (Table 6.3) which display a variety of buckled, layered, sheared and recrystallised fabrics. On the basis of mineralogical and textural variations, the ore tectonite types have been classified into four ore facies associations (Table. 6.3). The ore facies associations are namely; the banded ore facies, porphyroclastic ore facies, recrystallised ore facies and the massive pyritic ore facies. The ore facies associations (Fig. 6.22) have been mapped and their distribution is discussed with respect to the structural architecture of the ore zones.

ORE FACIES	TYPES OF ORE TECTONITE	MINERALOGY	DEFORMATION TEXTURES	PRIMARY TEXTURES	STRUCTURAL ASSOCIATION OF ORE TECTONITES
BANDED	layered ore	banded py and sp with cpy and gn.	In py; grain elongation and flattening with slip lines, deformation bands, D3 polygonisation and annealing in sp; grain growth and defn. twins.	Coliform, collobal growths twinned and single ribbons of marcasite pseudomorphed by py.	Deformed into tectonic D1 folds with sheared out north verging hinges.
POORLY-DEFORMED	bracketed-textured	Massive ore marble clasts Minor quartz	Matrix of sp and gn showing elongate grains with defn. twins, later kinked. Py, poikiloblasts overgrow matrix with annealed texture.	Minor collobal growths in py.	Ore forms in D1 and D2 folds and above D1 and D2 tectonic slides.
	buckshot textured	Fine grained grey coloured ore with py & quartz eyes	Dynamically recrystallised sp. with intergrowths of polygonal gn. overgrown by fragmented elongate and relict py. Grain boundary migration textures in py. Includes matrix with gn & cpy in fractures.	Mostly absent, some seen as fragmented growths.	Forms adjacent to/or within bracketed-textured ore, in association with south verging D2 tectonic slides & folds.
	pyrrhotite ore	Po with sp clasts & py poikiloblasts. Minor cpy & arsenopyrite.	Highly elongate po, later grain size reduction due to polygonisation, with elongate & annealed sp. Sp clasts coarse grained aggregates show minor grain boundary migration. Py poikiloblasts overgrow matrix.	Absent	Forms at the base of the ore horizon abutting D2 tectonic slides in the I zone. Strong S2 foliation.
	mylonitic sphalerite	brown near-monomineralic embayting bands of sp	Dynamically recrystallised grains ment to coarse D1 relict sp. in which defn. twins and sub-grains form. Minor very fine py. poikiloblasts. Annealing twins in dynamically recr. sp.	Absent	Occurs internally to the buckshot ore tectonites in association with D2 slides in highly sheared areas of the Cover zone.
RECRYSTALLISED ORE	Coarse galena	Coarse gn with qz, sp py & tn	Grain growth textures, subhedral grains, polygonal shaped overgrowths formed by grain boundary migration. Strong annealing textures.	Absent	Formed in D3 fold hinges and pinch and swell structures.
	coarse sphalerite	Coarse brown sp with py and calc-sphalerite clasts.	Grain growth textures with cupolate grain boundaries. Defn. twins overgrown by U-shaped annealing twins. Cpy included along earlier defn. twins and grain boundaries, causing grain pinning.	Absent	In association with D3 fold structures.
	blubby sphalerite	brown rec. sp clasts in a sheared gn. & rec. qz. mb. Minor py.	Strongly elongate gn. adjacent to sp. Inclusions. Elongate grains form sub-grains and links perpendicular to the elongation. Polygonal gn. occurs away from sp., with dentate and cusped boundaries. The sp. inclusions are polycrystalline aggregates with defn. twins overgrown by annealing twins. Sheared gn. is included in sp.	Absent	Formed in D3 shear zones and limb regions of D3 folds.
MASSIVE PYRITIC ORE FACIES	fine textured pyrite	Medium sized subhedral py. Includes marble Minor cpy/epi	Strong polygonal grains, with straight grain boundaries 120° triple junctions. Grains tend to elongate parallel to produce large grains. Grain size reduction of primary textures by polygonisation.	Common primary coliform and collobal growths. Euhedral twinned marcasite pseudomorphs overgrown by zoned primary py.	Forms with coarse pyritic ore in relatively undeformed masses.
	massive pyrite	Massive coarse py, with some py & marble.	Grain aggregation and grain growth textures. Grain boundary pinning by zoned inclusions.	Not observed in section, but smaller textures to those of the fine textured ore.	Forms as recrystallised masses in relatively resistant blocks in the central Angel zone and on D3 fold limbs.

Table 6.3 Summary of the mineralogy and textures in the ore facies of the Black Angel deposits

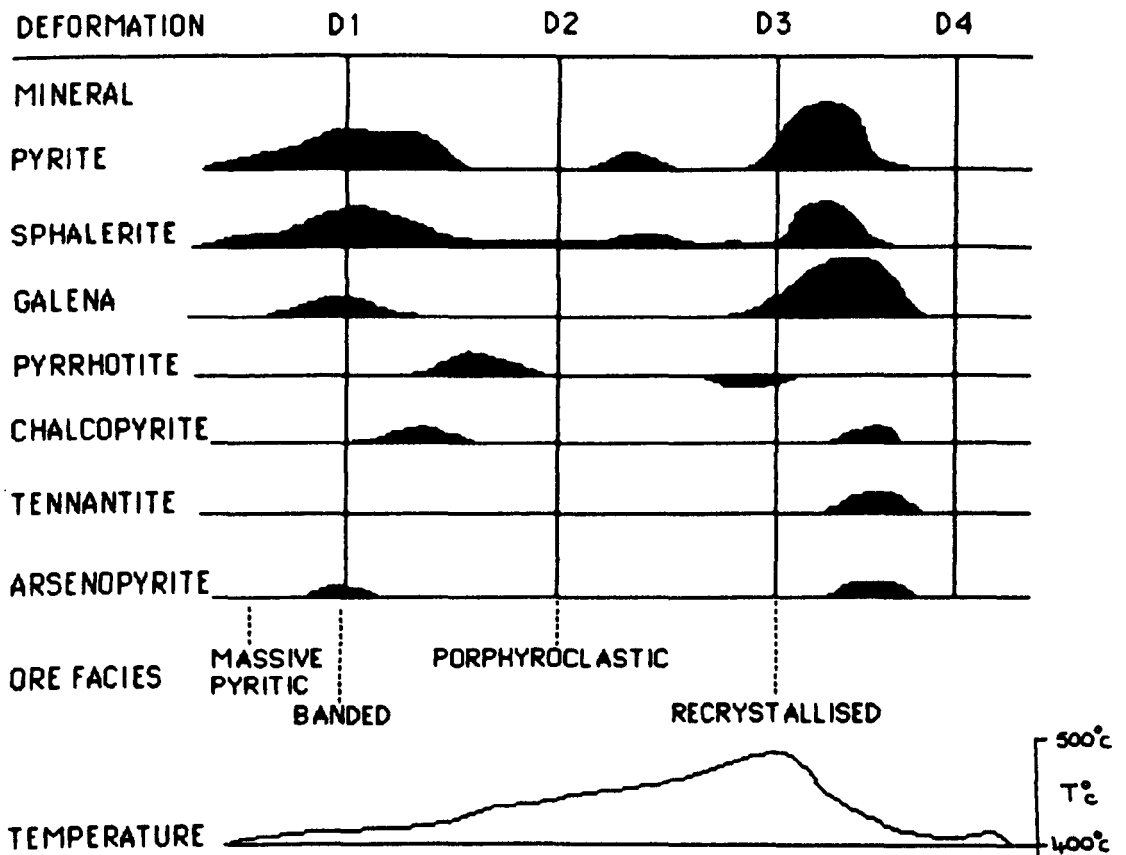


**TABLE 6.4 Schematic relationship between mineral deformation, ore facies, temperature and tectonic event**

### **6.5.6.b Ore facies.**

#### **Banded ore facies**

The Banded ore facies is characterised by the layered ore tectonite type which occurs in sheared out D1 isoclinal closures (Fig. 6.23e) within the northern Angel zone, M-X area of the Cover zone, the T zone (Fig. 6.22) and the lower ore stratigraphy of the I and Banana zones. The layered ore tectonite consists of discontinuous cm-dm bands of granular, poikiloblastic pyrite (up to 1mm) (Fig. 6.23c), coarsely recrystallised sphalerite (Fig. 6.23), and coarsely recrystallised fluorite bands (1-5 cm).

In some cases the pyrite grains are elongate. Internal dislocation etch pits (McClay and Ellis, 1983) are oriented sub-parallel to this elongation direction (Figs. 6.24 g & h) and to increase in density towards grain boundaries and fractures (Fig. 6.24h). Chalcopyrite, sphalerite and galena are included along relict triple junctions and in both early and late extensional fractures. These early fractures have been healed and overgrown during later annealing processes. The chalcopyrite and sphalerite inclusions contain minor subhedral-euhedral arsenopyrite rhombs which replace the chalcopyrite in a boxwork texture.

Sphalerite bands contain minor inclusions of pyrrhotite and chalcopyrite along broad intragranular annealing twins and at grain boundaries. In some cases the pyrrhotite inclusions themselves poikilitically enclose fine grained anhedral sphalerite. Fine-medium grained, euhedral-subhedral, pyrite poikiloblasts overgrow the coarse sphalerite (Fig. 6.23c).

#### **Porphyroclastic ore facies**

The porphyroclastic ore facies is predominant in the southern Angel, Cover (apart from the M-X area), I, Banana and T zones (Fig. 6.22). It consists of four types of ore tectonite that contain sheared deformation textures. These are masked to a large extent by later grain growth textures. The ore tectonite types are namely; 1) breccia textured ore 11)

buckshot textured ore and iii) pyrrhotitic ore, and iv) mylonitic sphalerite ore. Gradational contacts often occur between the breccia textured ore tectonite and the banded ore facies. The buckshot textured ore and the mylonitic sphalerite ore tectonites occur against or sandwiched between the breccia textured ore (Fig. 6.25 & 6.42b).

### **Breccia textured ore tectonite**

The breccia textured ore tectonite consists of poikiloblastic and fragmented pyrite (up to 3mm) in a massive, moderately sheared, matrix of medium-coarse grained (up to 4mm) sphalerite (Fig. 6.28), with coarsely recrystallised galena and minor chalcopyrite (Fig. 6.28b). Tabular to rounded marble inclusions (Fig. 6.26 & 6.33a & b), pelitic fragments and smaller recrystallised quartz clasts are incorporated into the ore. Clasts lying near the centre of the ore horizon are more rounded than those near the ore horizon boundaries (Fig 6.25 & 6.26). The inclusions have been delaminated from the host rocks by shearing along perturbations on the ore horizon boundary (Fig. 6.26). Once incorporated, the clasts or 'rafts' were boundinaged, subsequently rounded (Fig. 6.25) and took on classic 'durchbewegung' textures. Micas occur close to the quartz clasts and overgrow and include deformed and later annealed sphalerite (Fig. 6.28e). The inclusions are aligned along slightly bent cleavage traces (Fig. 6.29d).

Grain rotation, grain boundary impingement and fracturing occur in the pyrite. Fine new grains (Fig. 6.24e & f) which surround sub-hedral, internally strained, grains (Fig. 6.24i & j) are developed.

The matrix is dominated by aggregates of embayed to irregular (Fig. 6.28 c-f), medium to coarse grained sphalerite (Fig. 6.28a) with minor sub-grain development and lanceolate deformation twins, overgrown by broad annealing twins (Fig. 6.28 c & d). The sphalerite is intergrown with polygonal, coarsely recrystallised and annealed galena grains (Fig. 6.28c & d). The sphalerite aggregates have cusped grain boundaries, which indicate that later annealing and grain growth took place (Fig. 6.28a). This

recovery led to sphalerite overgrowth and inclusion of the galena. Rotated pyrite poikiloblasts embay the matrix sphalerite, which exhibits bent deformation twins and sub-grain development adjacent to the pyrite (Fig. 6.28e).

### **Buckshot textured ore tectonite**

This type of ore tectonite occurs in bands mostly between 10-30 cms thick (Fig. 6.25), but locally reaching as much as 1.1 metres thick (for instance in the K area, Cover zone Fig 6.42). The bands occur within and juxtaposed against the breccia textured ore (Fig. 6.25). Buckshot textured ore tectonites are vaguely banded and characterised by fragmented, xenomorphic-idioblastic, pyrite poikiloblasts (up to 4mm) with embayed and cusped boundaries in a fine grained, sphaleritic matrix (Figs. 6.33 c & d). Minor galena and chalcopyrite are present. Coarse grained dark brown sphalerite recrystallises around included gangue material and pyrite poikiloblasts (Fig. 6.33c). Elongate, coarse grained, strongly rounded clasts of calcite marble and opaque to clear, augen-like quartz clasts, up to 10 cm, (Fig. 6.33c) are aligned parallel to the pyrite banding (Fig. 6.25). Some of the the quartz inclusions contain small amounts of disseminated galena and sphalerite

The pyrite grains are boudinaged, shattered, rounded, (Figs. 6.24 a & b, & 6.33d) and show two stages of fracturing. Spindle and wedge-shaped inclusions of sphalerite, galena and chalcopyrite occur in the pyrite and represent healed extension fractures. Many grains are also elongate. Cross-hatched or linear dislocation pits are concentrated into a dominant slip direction and these occur in inclined kink bands. A reorientation of fractured pyrite grains occurs across late stage fracture zones.

The matrix is dominated by both coarse (up to 4mm) and fine (up to 0.1 mm), grained grey sphalerite with minor coarse grained galena and chalcopyrite (Fig. 6.33d). Fine grained, embayed-irregular, sphalerite crystals mantle the coarser sphalerite (Fig. 6.33h) in which lanceolate

deformation twins are overgrown by broad annealing twins. Broad annealing twins also occur in the unstrained fine, sub-idiomorphic, straight to slightly curved sphalerite grains. Sphalerite grain boundaries are pinned by included marble, galena and interstitial chalcopyrite.

Coarse grained polygonal galena occurs in the sphalerite matrix as interstitial material, that develop  $120^\circ$  triple junctions and straight to curved grain boundaries. Chalcopyrite occurs as rare embayed, (0.1-0.5mm) inclusions, sometimes with broad annealing twins, trapped at triple junctions in the sphalerite matrix.

Sub-rounded, embayed marble inclusions (up to 0.1mm) occur in the fine grained sphalerite matrix. Coarse calcite overgrows the sphaleritic matrix, whilst pyrite grains indent the calcite clasts. Micas are crenulated and include the mineralisation along cleavage traces (Fig. 6.29d). Included, embayed, quartz clasts themselves include sphalerite and galena.

A galena-rich variation of the buckshot textured ore tectonite occurs in the K and F areas of the Angel zone. The matrix consists of duplex-textured recrystallised polygonal galena grains and sphalerite aggregates (Fig. 6.28g & h).

The aggregates occurs as cauliflower-like masses of (0.1-1 mm) sphalerite crystals (Fig. 6.28g) with small, embayed, irregular, inclusions of galena. The larger crystals are mantled by sub-idiomorphic smaller grains which have cusped grain boundaries against the galena matrix and both straight and bent annealing twins (Fig. 6.28i). Idiomorphic pyrite poikiloblasts overgrow the duplex textured matrix (Fig. 6.28j).

Deformed and undeformed micas replace the sphalerite aggregates. Augen like quartz grains include annealed sphalerite and small pyrite poikiloblasts (Fig. 6.28 g & h). Quartz grains also occur at triple junctions in sphalerite and polygonal galena, where they pin grain boundaries (Fig. 6.28j).

## Pyrrhotitic ore tectonite

Pyrrhotite-rich ore tectonites occur at the base of the ore horizon in the Tributary zone (Fig. 6.43); at sheared, conformable and disconformable contacts against calcite-dolomite marbles and pelitic schists in the eastern I zone; and in the Banana zone where they are associated with the basal breccia textured ore.

This type of ore tectonite is characterised by massive and foliated pyrrhotite with subordinate sphalerite and minor chalcopyrite. The pyrrhotite encloses fractured and boudinaged, tabular to lenticular, sphalerite aggregates (Figs. 6.30 & 6.31a & b) together with inclusions of quartz and marble. The sphalerite aggregates are orientated parallel to the pyrrhotite foliation and contain coarse sphalerite grains with broad annealing twins. Chalcopyrite and lesser amounts of pyrrhotite are included as interstitial material (Fig. 6.31b) along cusped to straight grain boundaries and broad annealing twins.

The matrix of the more massive pyrrhotitic units exhibits fine grained duplex textures (Fig. 6.32) of sub-idiomorphic pyrrhotite (0.3-0.05 mm.) and sphalerite (0.5-0.1 mm.). The foliated units contain strongly elongate, very fine grained pyrrhotite in en-échelon shear zones adjacent to the included sphalerite clasts (Fig. 6.31c & d). Inclined bands of polygonal to slightly elongate pyrrhotite, considered to be relict kink bands, lie between the throughgoing shear zones (Fig. 6.31c).

Idiomorphic quartz crystals are included within the ore matrix. These are commonly rimmed by calcite. Phlogopite books are present at the base of the ore horizon. Coarsely recrystallised, embayed, rounded to ellipsoidal calcite clasts (1-5 cm) lie parallel to the pyrrhotite schistosity. The calcite inclusions consist of strongly annealed polygonal calcite crystals and themselves enclose quartz augen and small amounts of matrix sphalerite/pyrrhotite.

The sulphide matrix is locally replaced by pyrite (Fig. 6.32) and arsenopyrite (Fig. 6.36e) porphyroblasts. The pyrite occurs as sieve-like

sub-idiomorphic to idiomorphic pyrite poikiloblasts up to 5 cm (Fig. 6.32) which include sphalerite and quartz in a zoned manner (Fig. 6.32a & f). Pyrrhotite depletion halos occur adjacent to the poikiloblasts (Fig. 6.32a,c & f). The pyrrhotite foliation often anastomoses or is displaced around the pyrite (Fig. 6.32a & b). Pyrrhotite in some cases is included in the pyrite grains (Fig. 6.32c & e). Arsenopyrite is uncommon, but occurs as large (upto 3mm) porphyroblastic laths that also overgrow the pyrrhotite matrix (Fig. 6.36e).

### **Mylonitic sphalerite ore tectonite**

The mylonitic sphalerite ore tectonite type occurs in the central Cover zone; the I,T and Banana zones, and as disaggregated fragments in the recrystallised ore of the southern Angel zone. It is a near-monomineralic, dark brown, fine grained, sphalerite rock that occurs in sharp, discontinuous, (1-15 cm thick) bands which anastomose around included quartz and marble clasts within buckshot textured and breccia textured ore tectonite types (Fig. 6.25).

The sphalerite bands are composed of coarse (1-1.5 mm) elongate xenomorphic, ragged, embayed and serrated grains mantled by fine grained sphalerite (Fig. 6.33e & f). Thin, kinked and cross twinned, lanceolate deformation twins occur in the coarse sphalerite. These are orientated obliquely/sub-parallel to the grain elongation (Fig. 6.33f). Sub grains are present towards the grain margins (Fig. 6.33e). The finer (0.01mm-0.1mm) grains have broad annealing twins (Fig. 6.33a & b) and are concentrated into thin (1mm-1cm) anastomosing shear bands (Fig. 6.33f). The straight and cusped-lobate grain boundaries are pinned by minor quartz and marble inclusions (fig. 6.33g).

Fine grained, sub-idomorphic to idiomorphic, poikilitic pyrite crystals occur in a discontinuous spotted form and overgrow the fine grained sphalerite shear bands (Fig. 6.33g).

## **Recrystallised ore facies**

The recrystallised ore facies consists of 3 coarse grained ore tectonite types (Table 6.3) namely:-i) Coarse sphalerite (with pyrite and quartz) ii) Coarse galena (with quartz and tennantite) and iii) Bleby sphalerite. These tectonites occur in D3 folds, in the C area and M-X area, in large-scale boudins in the H and G areas, and as isolated pods in the breccia textured ore of the K area, Cover zone (Fig. 6.22).

## **Coarse sphalerite ore tectonite**

This ore type is common in the northwestern Angel zone (Fig. 6.42), where massive bands (up to 2 metres thick) of coarse grained, sub-idioblastic to irregular, sphalerite exhibiting cusped, stepped to slightly serrated grain boundaries, are interleaved with coarse pyritic units. Bent and kinked lanceolate deformation twins occur within the sphalerite which are overgrown by broad annealing twins. Very fine grained chalcopyrite occurs as embayed to irregular crystals at sphalerite grain boundaries and annealing twins.

The sphalerite varies in colour from black in the Tributary zone, through green in the M area of the Cover zone, to a very light honey colour in the L area, Cover zone. This colour change is due to the varying iron content (Scott 1983 & Barton and Toulmin 1966. Table 5.1). Most of the sphalerite occurs as coarsely crystalline irregular bodies associated with large (20cm) idiomorphic pyrite porphyroblasts (Fig. 6.34a). It is less commonly associated with quartz crystals. Rounded, coarsely recrystallised, calcitic/dolomitic clasts (upto 50cm), have become included in the ore, through fracturing the host rock and invasion by sphalerite (Fig. 6.34c).

### **Coarse galena ore tectonite**

Massive coarse galena layers (upto 1.3 metres thick) occur in the E, C, G, H areas of the Angel zone (Fig. 6.42); in the X area of the Cover zone and in the northern Banana zone. Coarse galena (upto 1cm) is often strongly kinked and sheared against D3 fault surfaces. It is associated with minor pyrite, coarse sphalerite, tennantite, isolated quartz crystals, up to 10cms (Fig. 6.34e & f) and large (50 cm) marble inclusions (Fig. 6.34f). The clasts are derived from the adjacent host rock by host rock fracturing and galena invasion (Fig. 6.34b).

Tennantite-rich galena ore occurs in the C area of the Angel zone and the K area of the Cover zone. Coarse grained, xenomorphic, tennantite replaces galena (Fig. 6.35a & b). Pyrite cubes (Fig. 6.35a), which are commonly rimmed by duplex-textured inclusions of chalcopyrite and arsenopyrite rhombs (Fig. 6.36 a,b & c), occur with the tennantite.

### **Bleby sphalerite ore tectonite**

This type of ore tectonite occurs in the E and H areas of the Angel zone (Fig 6.42) between the coarse galena and the coarse sphalerite ore tectonites (Fig. 6.34d). It is characterised by (1-4 cm) rounded, ragged and cuscate dark brown sphalerite aggregates, quartz augen (1mm-15cms) and pyrite porphyroblasts in a medium to coarse grained, foliated, galena matrix. The matrix consists of strained, coarse, sub-idioblastic to xenomorphic, cuscate-embayed, grains (Fig. 6.37a) which are reduced in size towards the sphalerite blebs. These galena grains are strongly elongate (Fig. 6.37 b & d). Kinked, polygonal sub-grains occur in the elongate crystals (Fig. 6.37e). The kinks are perpendicular to the grain elongation.

The sphalerite aggregates consist of coarse, rounded-irregular grains with thick annealing twins (Fig. 6.37a) which include minor chalcopyrite and galena. Grain size decreases towards the ragged sphalerite aggregate margins which are composed of strongly annealed,

finely recrystallised, polygonal grains (Fig. 6.37a). The aggregates are themselves disaggregated. Single sphalerite grains or fine grained, annealed, aggregates with small irregular quartz, marble and sheared galena inclusions (Fig. 6.37a & b) are commonly incorporated into the galena matrix.

The presence of sheared galena inclusions in these disaggregates suggests that a late stage of annealing of sphalerite occurred, which resulted in a replacement and inclusion of the sheared matrix galena.

Xenomorphic poikilitic tennantite replaces the galena matrix (Fig. 6.35c) enclosing galena, sphalerite, chalcopyrite, arsenopyrite and quartz. It is itself replaced by idiomorphic poikilitic pyrite (0.1 mm) which also replaces the sphalerite aggregates. Coarser (3mm) pyrite poikiloblasts replace and enclose both sphalerite aggregates and matrix galena (Fig. 6.37f). Late stage fractures cross-cut all the matrix material (Fig. 6.37b).

### **Massive pyritic ore facies.**

This ore facies consists of two types of ore tectonite (Table 6.3), namely:-i) foam textured ore and ii) massive pyrite ore. These occur in the central E area, where massive pyrite is up to 4.5 metres thick (Fig. 6. 42), the northern D and eastern G areas of the Angel zone; the northern P area, southern M area and the northeastern X area of the Cover zone (Fig. 6.22). This ore facies occurs in association with both the banded and recrystallised ore facies.

### **Foam textured ore tectonite**

The foam textured ore is concentrated in D3 folds of the M-X area (Cover zone) and D3 axial planar structures in the eastern I zone (Fig. 6.38 & 6.39a & c). It consist of medium to coarse grained (up to 3mm) granular pyritic ore (Fig. 6.39d) containing chalcopyrite, sphalerite, arsenopyrite, tennantite and marble fragments. The granular pyrite metamorphically

overgrows primary zoned crystals (Fig. 6.40). It is associated with recrystallised sphalerite and quartz (Fig. 6.39c).

### **Massive pyrite ore tectonite**

This tectonite type occurs as a core of pyrite in the central Angel zone (Fig. 6.42). It consists of very coarse grained (up to 20 cm) idiomorphic, fractured and bent pyrite porphyroblasts and pyrite aggregates. It occurs in both pyritic foam textured ore and in coarsely crystalline calcite matrices which contain minor intergranular quartz.

### **Primary textures**

Early diagenetic or epigenetic mineral textures (primary textures as used in this thesis) are only preserved as mantled growths in metamorphic pyrite (Fig. 6.40) of the massive pyritic ore facies and the pyrite units of the banded ore facies (Table 6.3). Minor primary textures are retained in pyrite poikiloblasts of the breccia-textured ore. The more highly deformed buckshot textured ore and remobilised ore facies do not retain any primary features.

In order to study the primary features, the pyrite porphyroblasts were etched in 10%  $\text{HNO}_3$  at 60-70°C for between 30 seconds and 5 minutes. A wide range of primary textures are revealed by the presence of carbonate inclusions, which were trapped during early mineral growth.

The main types of primary textures are unstrained, void fill features which include colloform (up to 2mm in diameter) and colloidal textures. The colloform textures contain bands of rounded variably sized carbonate inclusions, which possibly indicate changing colloform growth rates (Fig. 6.40a). Cuspate and embayed masses of fine grained rounded carbonate or siliceous material are commonly overgrown by metamorphic pyrite (Fig. 6.40b). These masses probably represent colloidal crystallisation of early marcasite/pyrite (possibly sphalerite) with carbonate.

Other relict primary textures include unstrained, idiomorphic, twinned and zoned rhombs (Fig. 6.40c & d), twinned (Fig. 6.40e) and rosette-like and skeletal prismatic crystals (Fig. 6.40f), and boxwork laths (Fig. 6.40i & j). All of these crystal forms are interpreted to represent the presence of early marcasite growing both in a bladed and a more stubby prismatic form. The skeletal crystals possibly represent rapid growth rates.

Zoned cubic grains, probably of later diagenetic pyrite, often mantle these early marcasite grains (Fig. 6.40d). Thus alteration of marcasite to pyrite occurred relatively early in the history of the ore deposit. Cubic and colloform banded primary pyrite grains, with overgrowths of lath-like crystals, occur in the pelitic units of the Nukavsak Formation (Fig. 6.40g & h)

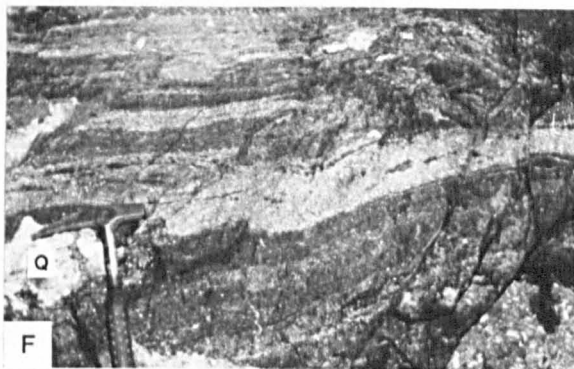
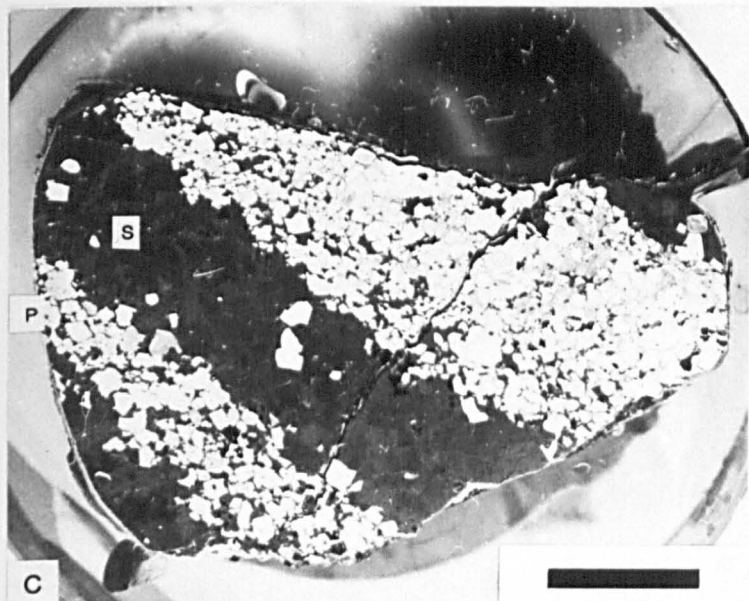
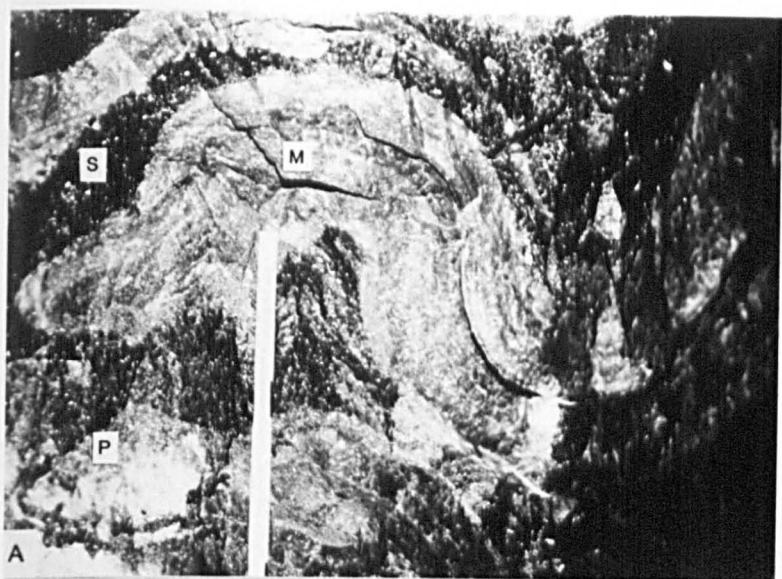
The presence of euhedral, zoned and rosette-like marcasite and colloform shaped textures and the lack of framboidal textures indicates that most primary mineralisation took place as void fill mineralisation in a low-temperature epigenetic regime. A later pseudomorphing of marcasite by pyrite represents a change in the FeS stability field during late stage diagenesis.



Figure 6.22 Ore facies distribution map

### Figure 6.23. Layered ore tectonite

- A) Banded ore tectonite showing D3 folded pyrite (P) and coarser sphalerite (S) bands enclosing boudinaged, phlogopite banded, marble (M) fragments. Stope D 26, Angel zone
- B) Rhythmically banded sphalerite (mid-grey) and pyrite (light grey) layers deformed into D2 south verging asymmetric folds. E sillpillar, Angel zone.
- C) Polished block of banded ore, showing euhedral pyrite (P) with interstitial sphalerite and dark brown sphalerite (S) bands of annealed grains enclosing a few pyrite euhedra. Specimen E36a. Stope E 36, Angel zone. Brebrick and Scanlon etch 120 secs. 70°C.
- D) Weakly banded ore. Sphalerite layers are boudinaged within the more massive pyrite bands. Lenses and pods of recrystallised calcite (white) are incorporated in the ore and aligned parallel to the banding. Stope M 110, Cover zone.
- E) Moderately well banded layered ore. The darker sphalerite bands are deformed into isoclinal folds. Northerly dipping discordant footwall contacts and a sheared, relatively concordant, hangingwall contact are observed. Stope E 82, Angel zone.
- F) Massive pyrite bands (10 cm. thick) hold boudinaged sphalerite fragments, that are both deformed into D2 south verging asymmetric folds. Large quartz clast (Q) is held in the sphalerite. E sillpillar, Angel zone.



## Figure 6.24. Pyrite microtextures

A) Cataclastically deformed pyrite (P) with blow apart texture, infilled by chalcopyrite and minor sphalerite, in a breccia to buckshot textured ore. Specimen B 124. Stope B 124, Banana zone. Unetched. Scale bar 500 $\mu$ . (x.p.l)

B) Boudinaged, rotated and disaggregated pyrite poikiloblast producing fine grained pyrite cubes within a sphaleritic (S) matrix. Breccia to buckshot textured ore. Specimen, B 160a. Stope B 160, Banana zone. Scale bar 500 $\mu$ . (x.p.l)

C) Annealed polygonal pyrite grains with well developed 120° triple junctions cut by D4 extension fractures. Interstitial chalcopyrite (CPY) and marble (black). Layered ore. Specimen E 36a. Stope E 36, Angel zone. Scale bar 500 $\mu$ . (p.p.l)

D) Intense D4 fracturing in pyrite poikiloblasts from breccia-textured ore. Sphalerite (S) galena (Light grey) matrix and quartz (Q) eye are undeformed. Specimen A7.2T, Stope D16, Angel zone. Scale bar 500 $\mu$ . (x.p.l)

E) Grain impingement and concomitant cataclastic fracturing of idiomorphic pyrite crystals in a marble (M) matrix. Breccia-texture ore. Specimen A7.1T, Stope D16, Angel zone. Scale bar 500 $\mu$ . (p.p.l)

F) Close up of (E) showing new fragmented elongate and subhedral pyrite grains associated with the fracture zones. Scale bar 100 $\mu$ . (p.p.l)

G) Polygonal pyrite grains showing dislocation etch pits. The etch pits have preferred orientations in each grain. Marble matrix. Etched in 50% HNO<sub>3</sub>, 90 secs at 60°C. Specimen E 36a layered ore tectonite. Stope E 36, Angel zone. Scale bar 250 $\mu$ . (p.p.l).

H) Close up of a grain boundary from (G), showing L-R aligned dislocation etch pits in the left hand grain and NE-SW etch pits in the right hand grain. The etch pits form tangles at the grain boundary. Scale bar 100 $\mu$ . (p.p.l).

I) Etched polygonal pyrite grains, showing high relief zones signifying the presence of deformation twins or kinks. Pyrite band in buckshot-textured ore. Etched in 50% HNO<sub>3</sub>, 30 secs at 60°C. Specimen K 152, Stope K 152, Cover zone. Scale bar 500 $\mu$ . (p.p.l.)

J) Close up of triple junction and deformation twins/kinks from (I). Scale 250 $\mu$  (p.p.l.)

One of these  
is wrong.

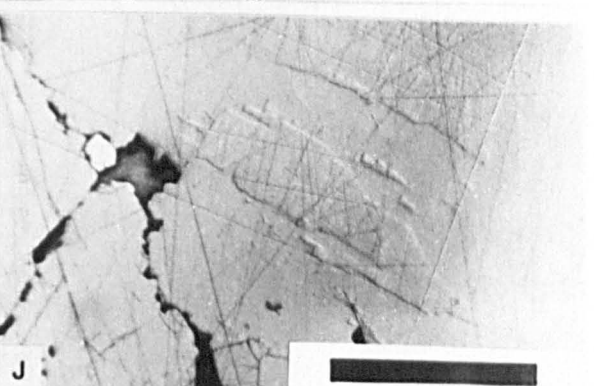
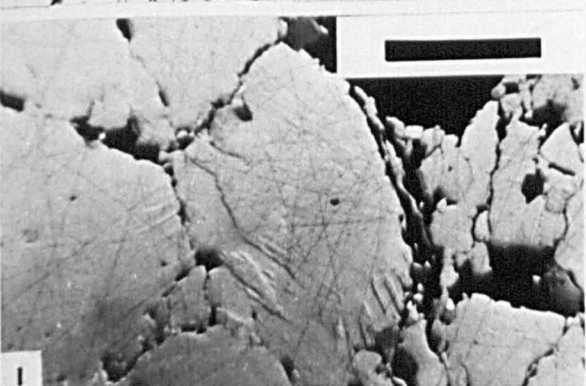
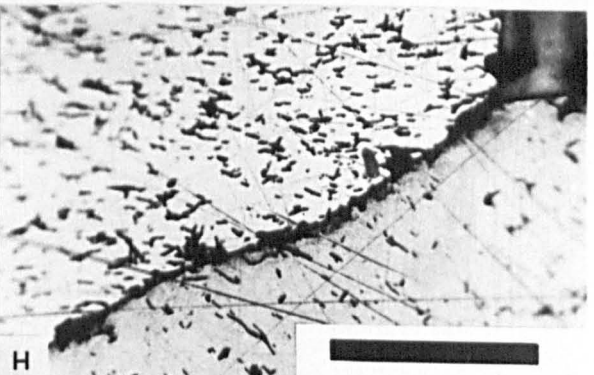
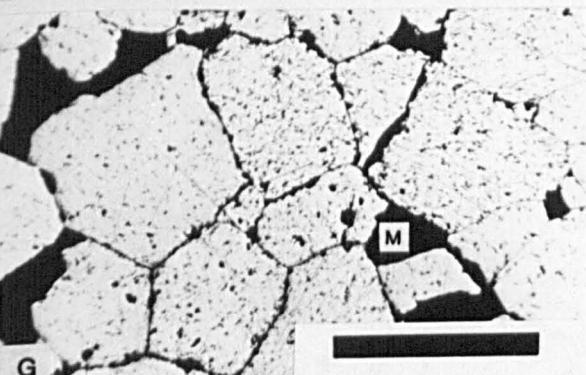
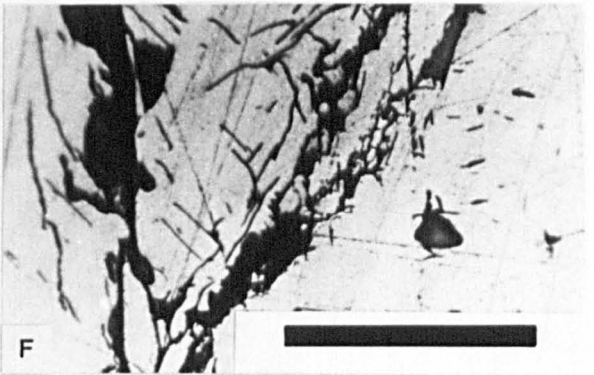
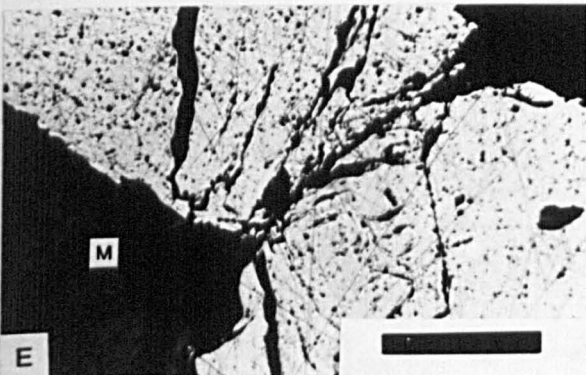
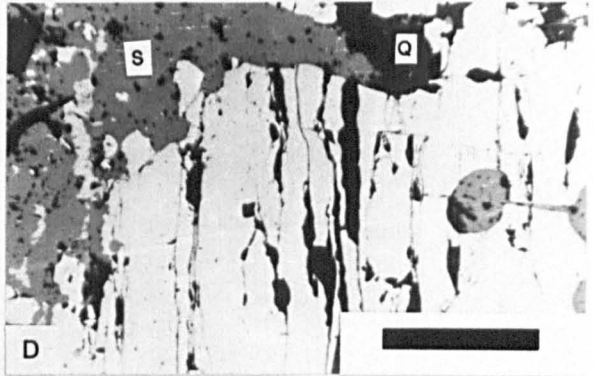
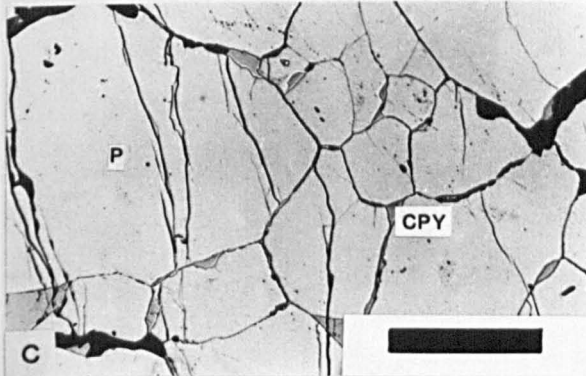
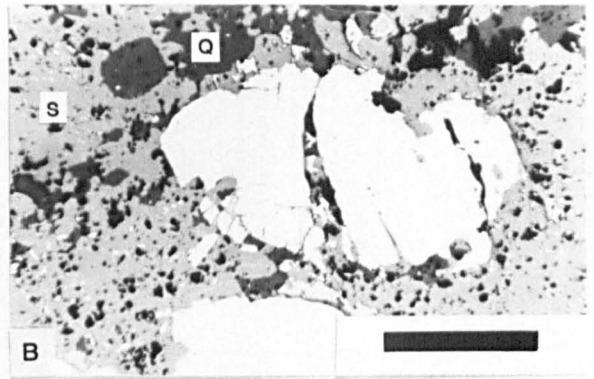
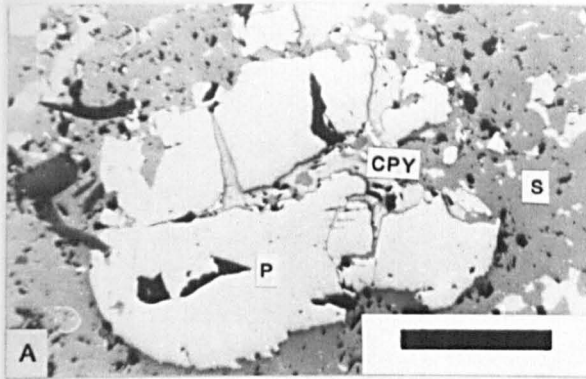


**Figure 6.25. Porphyroclastic ore facies**

Complex ore stratigraphy developed in the porphyroclastic ore facies. Breccia and buckshot textured ore sandwich a thin, sharply defined band of mylonitic sphalerite ore tectonite (dark grey), which anastomoses around an included marble lens. Rounded and slightly ragged coarse grained marble clasts are included in the buckshot textured ore tectonites ore. Less deformed layered ore tectonites (Banded ore facies) occur towards the bottom left of the photo. Some pyrite layering is retained in the sheared breccia textured ore tectonite. The hangingwall contact is sheared and conformable whereas the footwall contact is irregular. Stope M 72w, central Cover zone. Metre rule for scale.

Buckshot textured ore tectonite

Mylonitic sphalerite ore tectonite

Layered ore tectonite grading into  
breccia and buckshot textured ore  
tectonites



## Figure 6.26 Breccia textured ore tectonite

A photograph of massive breccia-textured ore. The ore is seen to include a delaminated and subsequently boudinaged marble block. The marble blocks are smaller and more rounded towards the centre of the ore. Note the delaminated block occurs in a finer grained (highly sheared) ore matrix. Greater pyrite exists towards the footwall. The hangingwall contact is sharp and conformable with the host rock foliation. Irregular marble clasts occur along the disseminated footwall contact, where thin galena and pyrite stringers are present. Stope L 66n, Cover zone.



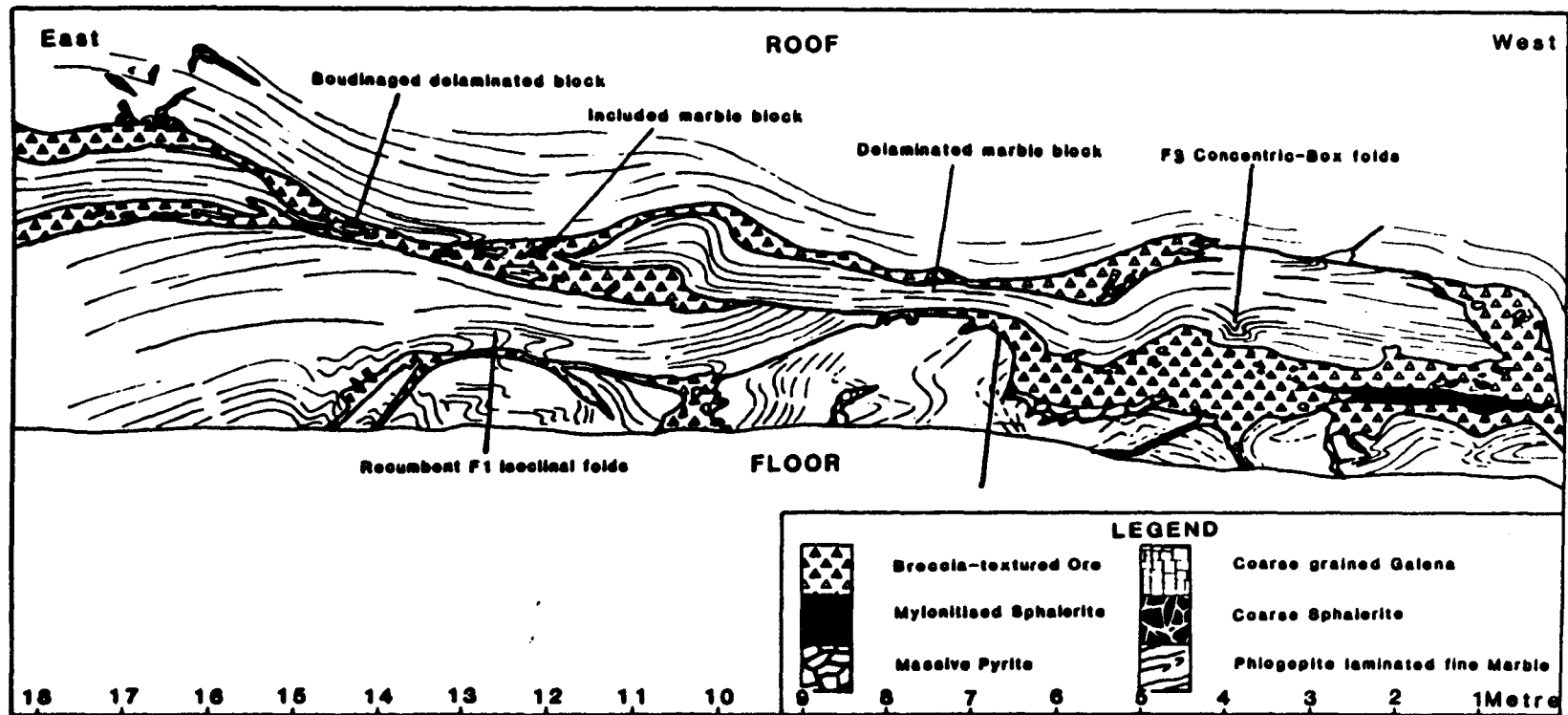


**Figure 6.27** Breccia-textured ore tectonite in Stope L66, Cover zone.

## Figure 6.28. Breccia and buckshot textured ore tectonite microtextures

A) Photomicrograph of breccia-textured ore. The sphalerite and galena matrix is overgrown by a coarse grained sub-idioblastic pyrite poikiloblast. The sphalerite (S) occurs in clots that replace and include the medium grained galena (G) along cusped boundaries. Unetched. Specimen 357. Stope F 54, Angel zone. Scale bar 500 $\mu$ . (x.p.l.).

B) Coarse xenomorphic pyrite (P) grains in a matrix of sphalerite (S) and chalcopyrite (CPY). The pyrite is strongly fractured and infilled by chalcopyrite. Small quartz grains (grey black) are present. Unetched. Specimen T 188T. Stope T 188n, Tributary zone. Scale bar 700 $\mu$ . (p.p.l.).

C) Specimen 357 (as in A) but etched. A large pyrite poikiloblast overgrows the medium grained sphalerite-galena matrix. The sphalerite consists of aggregates of sub-hedral slightly elongate annealed grains. The galena has a more polygonal texture. Brebrick and Scanlon etch, at 75°C for 30 secs. Scale bar 500 $\mu$ . (p.p.l.)

D) Photomicrograph of the matrix textures in a typical breccia textured ore. Broad annealing twins overgrow thinner bent deformation twins in anhedral sphalerite. Galena (G) is coarse grained and polygonally recrystallised. An anhedral pyrite poikiloblast overgrows the partially annealed sphalerite matrix. Brebrick and Scanlon etch, at 75°C for 30 secs. Specimen I 170. Stope I 170, I zone. Scale bar 500 $\mu$ . (x.p.l.).

E) A photomicrograph showing sub-grain development and bending of deformation twins in sphalerite due to grain impingement by an anhedral pyrite grain (P). Also in the matrix kinked phlogopite (Ph), galena and quartz. Brebrick and Scanlon etch, at 75°C for 50 secs. Specimen K 130. Stope K 130, Cover zone. Scale bar 500 $\mu$ . (x.p.l.).

F) Sphalerite (S) matrix composed of irregular grains that show annealing twins overgrowing deformation twins. Quartz eyes (Q) and marble have cusped grain boundaries and include sphalerite. Brebrick and Scanlon etch, at 75°C for 30 secs. Specimen B 126. Stope B 126w, Banana zone. Scale bar 500 $\mu$ . (x.p.l.).

## Galena-rich buckshot textured ore tectonite microtextures

G) Irregular sphalerite clots composed of fine to medium grained annealed crystals replace and include the galena rich matrix. The galena shows polygonal, granoblastic textures. (Q)= quartz. Brebrick and Scanlon etch, at 60°C for 90 secs. Specimen F 56. Stope F 56, Angel zone. Scale bar 500 $\mu$ . (x.p.l.).

H) Close up of granular and slightly elongate grains in the polygonal galena matrix (G), which are replaced and included by annealed sphalerite grains. Specimen as in (G). Scale bar 160 $\mu$ .

I) Photomicrograph of bent annealing twins in sphalerite. Specimen as in (G). Scale bar 160 $\mu$ .

J) Photomicrograph of a pyrite poikiloblast overgrowing the sphalerite/galena matrix. Specimen as in (G). Scale bar 160 $\mu$ .

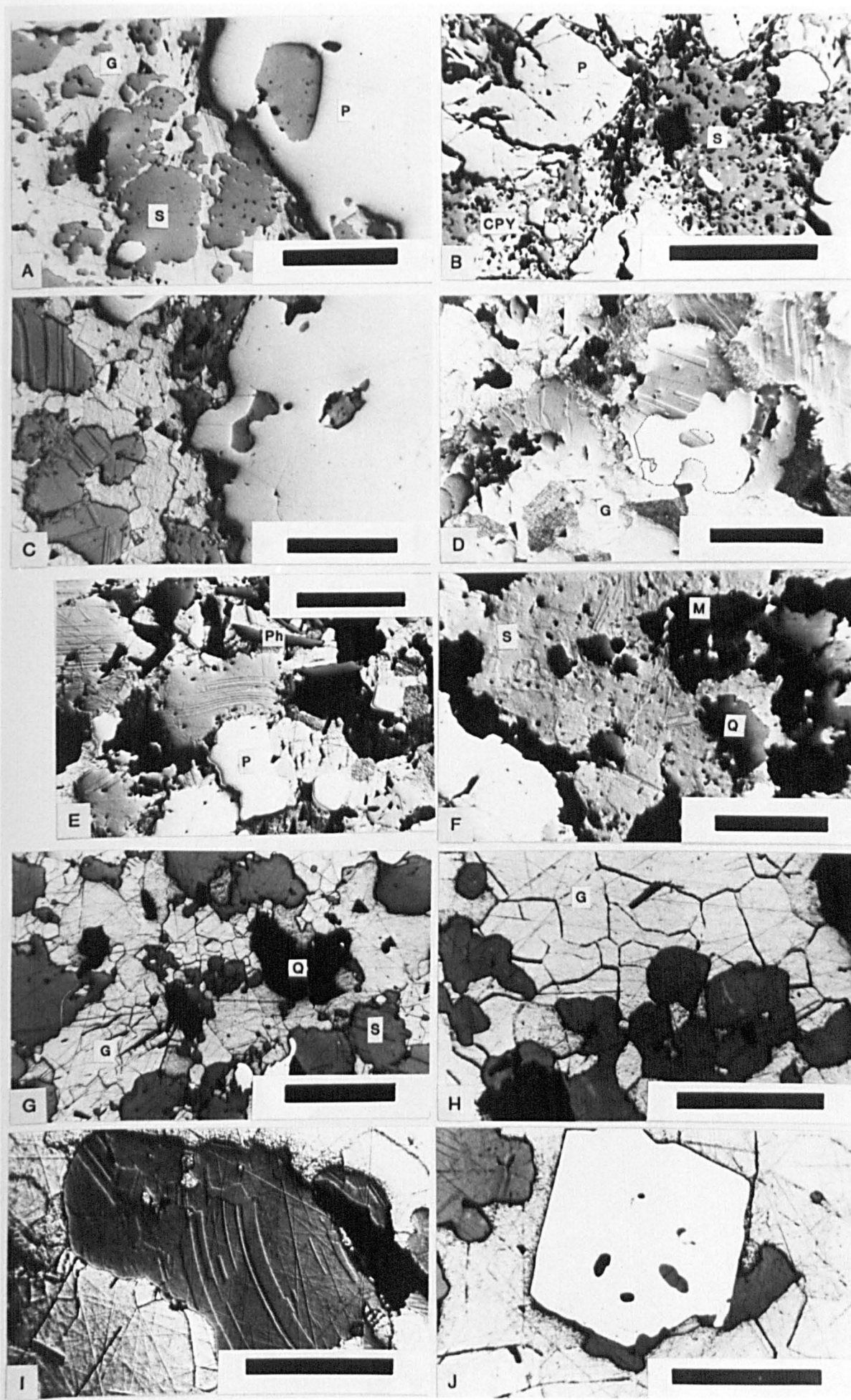


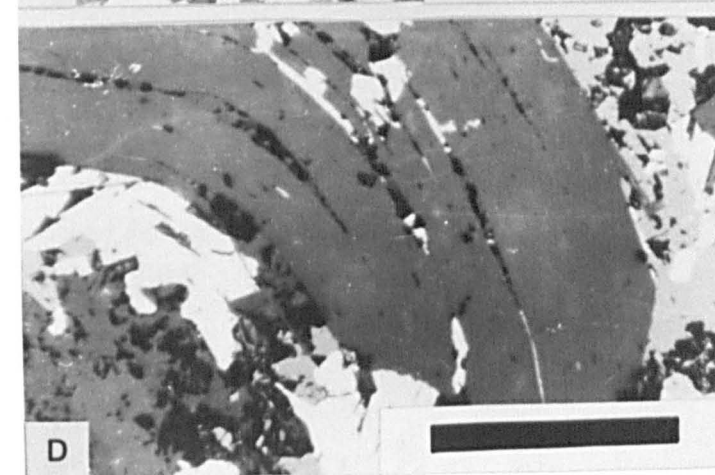
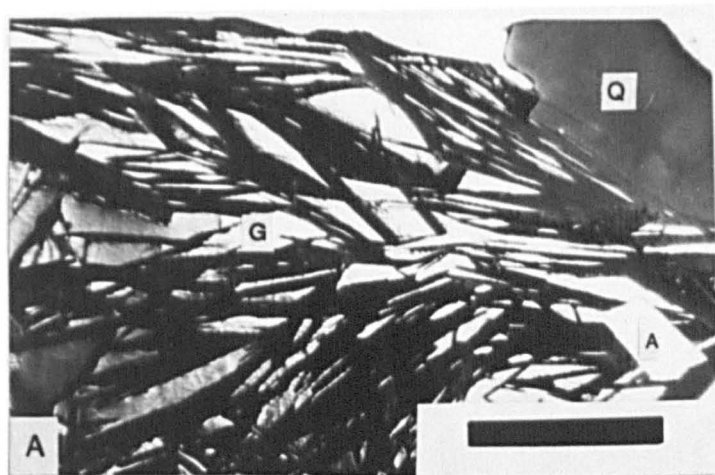
## Figure 6.29 Micaceous microtextures

A) Phlogopite intergrown with galena (g). A slightly irregular quartz (q) grain occurs to the top right. An idiomorphic arsenopyrite rhomb replaces the galena and phlogopite. Sample K 152, recrystallised ore facies, Stope K 152 Cover zone. Scale bar 200 $\mu$ .

B) Complex intergrowth between galena (white) and a curved band of bent phlogopite crystals. Quartz occurs in the matrix as a rounded slightly annealed grain. Arsenopyrite (A) rhombs replace both the mica and galena. Specimen as in (A). Scale bar 500 $\mu$ .

C) Randomly orientated phlogopite crystals in a galena (with sphalerite matrix). Pelitic fragment with minor galena occurs to the top right. Specimen B 124P, Stope B 124, Banana zone. Scale bar 500 $\mu$

D) Close-up of a bent phlogopite crystal replacing a galena (white) sphalerite (mid-grey) matrix. The ore matrix is included along the phlogopite cleavage. Specimen A 7.2T, Stope E 16 Angel zone. Scale bar 200 $\mu$ .



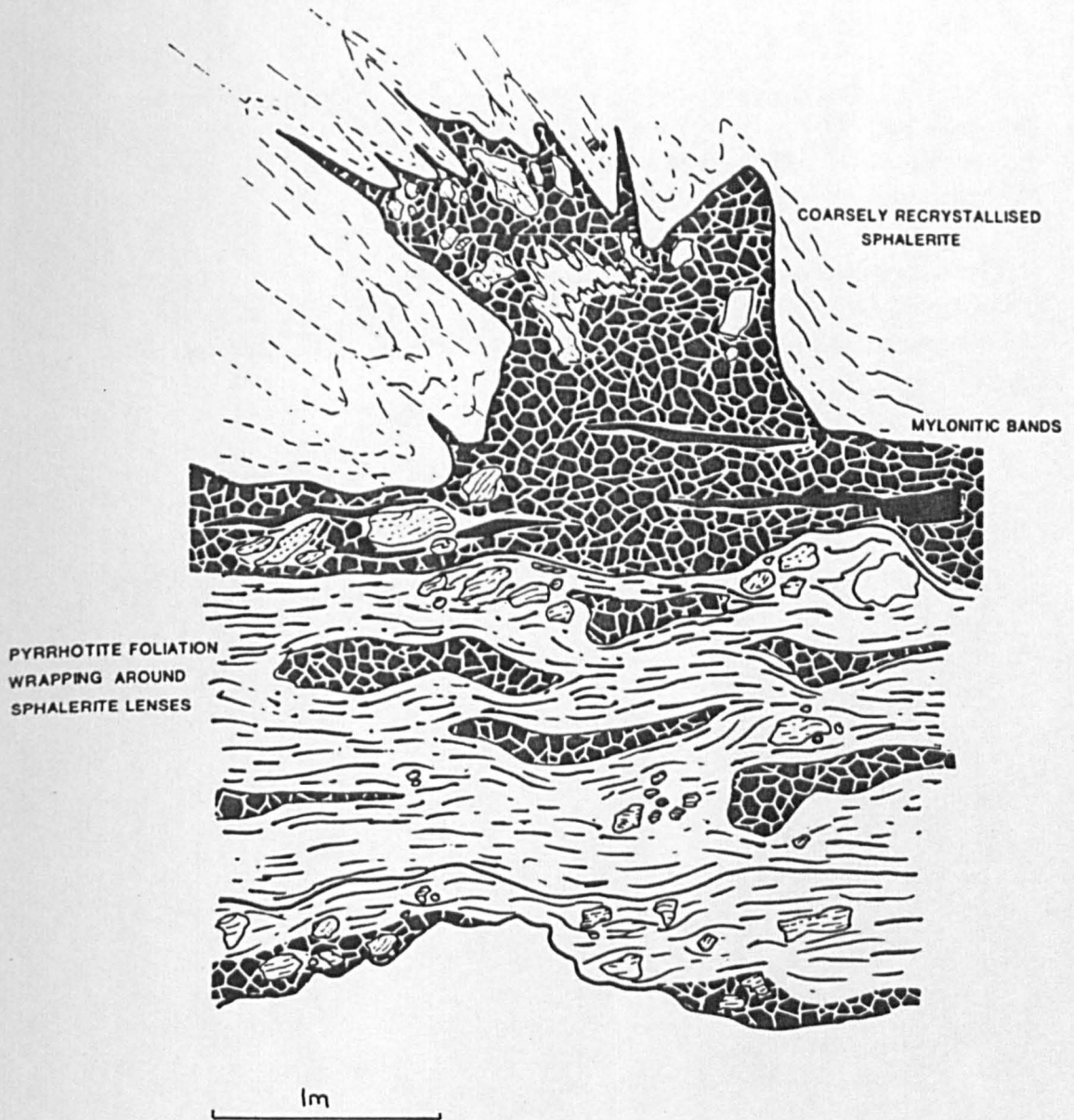


**Figure 6.30** Sketch of foliated pyrrhotite ore from Stope T 188, Tributary zone

### Figure 6.31. Pyrrhotite ore tectonite microtextures

A) Photograph of a polished block containing thin brecciated and boudinaged sphalerite (S) bands held in a foliated pyrrhotite (PY) and chalcopyrite (CPY) matrix. The matrix sulphides are seen replacing marble (M). Unetched. Specimen T188. Stope T188n, Tributary zone. Scale bar 1cm.

B) Close up of a pulled apart sphalerite band (S). The sphalerite encloses blebs of chalcopyrite (minor galena) along grain boundaries and annealing twins. The matrix of pyrrhotite (PY: white) and chalcopyrite (CPY: light grey), forms a duplex texture, which replaces the sphalerite and infills the fracture zone. Specimen as in (A). Scale bar 500 $\mu$ . (p.p.l.).

C) Photomicrograph of a very fine grained pyrrhotite rich shear zone abutting the sphalerite band (S). Two throughgoing shear zones are present at the top and bottom of the pyrrhotite unit. Between these zones elongate to polygonal pyrrhotite form in a NE-SW orientation. Specimen as in (A). Scale bar 160 $\mu$ . (p.p.l.).

D) Photomicrograph showing two conjugate pyrrhotite shear zones (meeting at the left of the figure). Fine elongate grains occur in these shears while coarser grained sub-equant pyrrhotite is present between them. Specimen as in (A). Scale bar 160 $\mu$ . (p.p.l.).

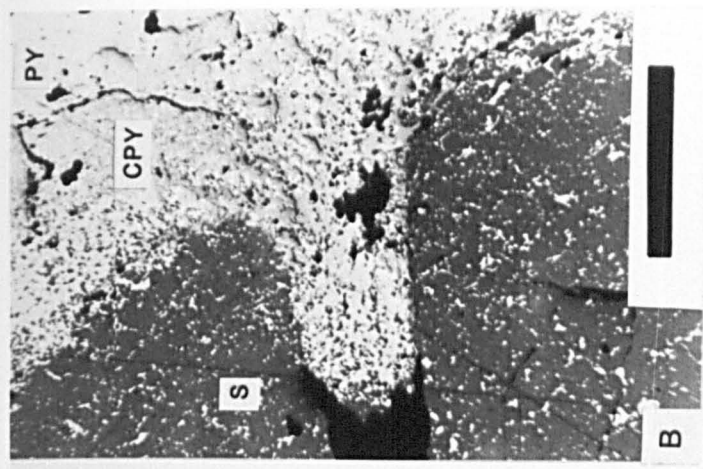
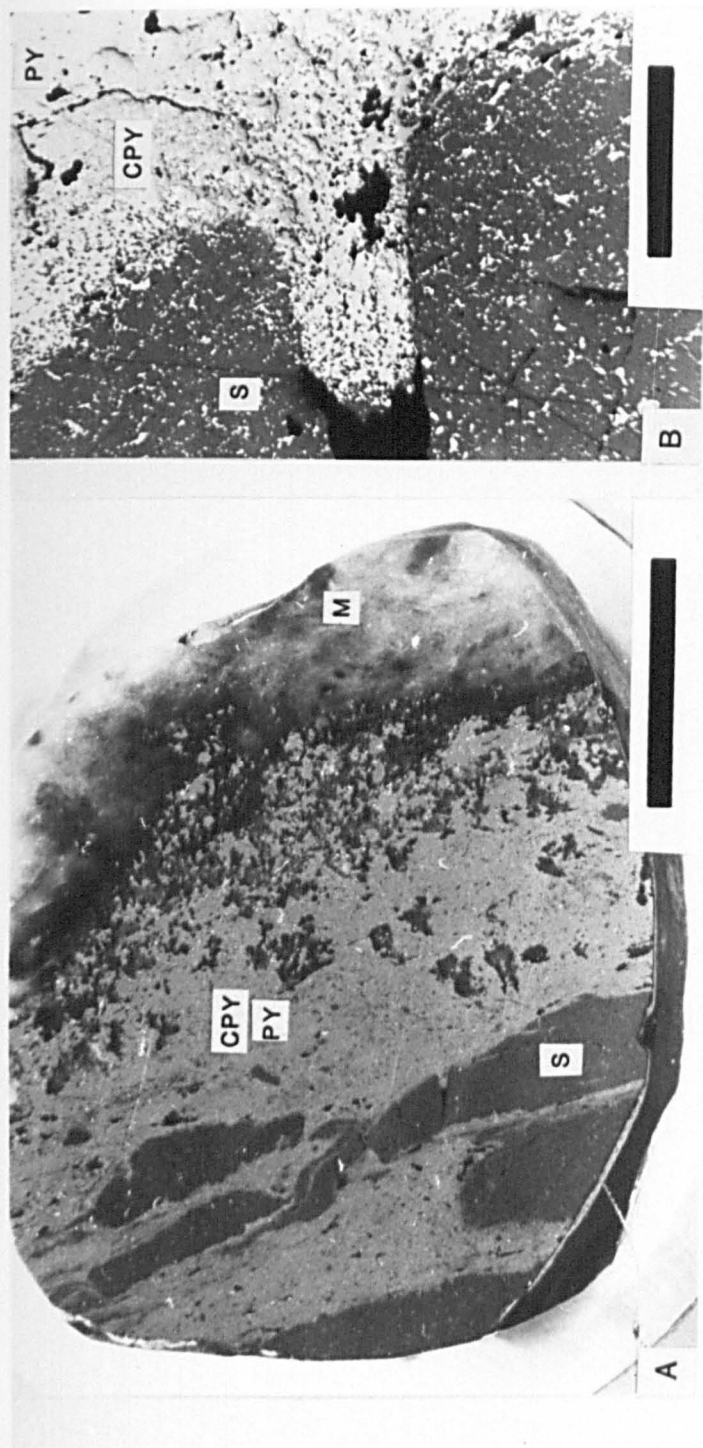


### Figure 6.32. Pyrite / pyrrhotite microtextural relationships

A) A slightly rotated sub-idiomorphic pyrite poikiloblast, including sphalerite in a vaguely zoned pattern, in a duplex textured matrix of pyrrhotite (PY) and sphalerite (S). A zone depleted in pyrrhotite occurs around the pyrite. Unetched. Specimen I 170. Stope I 170s, I zone. Scale bar 500 $\mu$ . (Normarski interference prism (N.I.)).

B) Boudinaged and cataclastically fractured pyrite poikiloblast enclosing sphalerite. The pyrite grains are rotated causing the vaguely foliated pyrrhotite/sphalerite matrix to wrap around the grain. Specimen as in (A). Scale bar 500 $\mu$ .

C) Pyrite poikiloblast (near skeletal), overgrowing and enclosing pyrrhotite and sphalerite. Specimen as in (A). Scale bar 500 $\mu$ .

D) Two large anhedral poikiloblasts of pyrrhotite (PY: light grey) and pyrite (P: white) abutting each other with a straight grain boundary. Unetched. Specimen T 188b. Stope T 188n, Tributary zone. Scale bar 500 $\mu$ . (N.I.).

E) Pyrite poikiloblast overgrowing, replacing and including pyrrhotite, in association with sphalerite (dark grey). Note these sphalerite inclusions were analysed in order to estimate peak metamorphic pressure. Specimen as in (D). Scale bar 160 $\mu$ . (N.I.).

F) A pyrite poikiloblast with zoned sphalerite inclusions, in a pyrrhotite/sphalerite matrix. A pyrrhotite depletion halo occurs around the metamorphic pyrite. Specimen as in (D). Scale bar 500 $\mu$ . (N.I.).

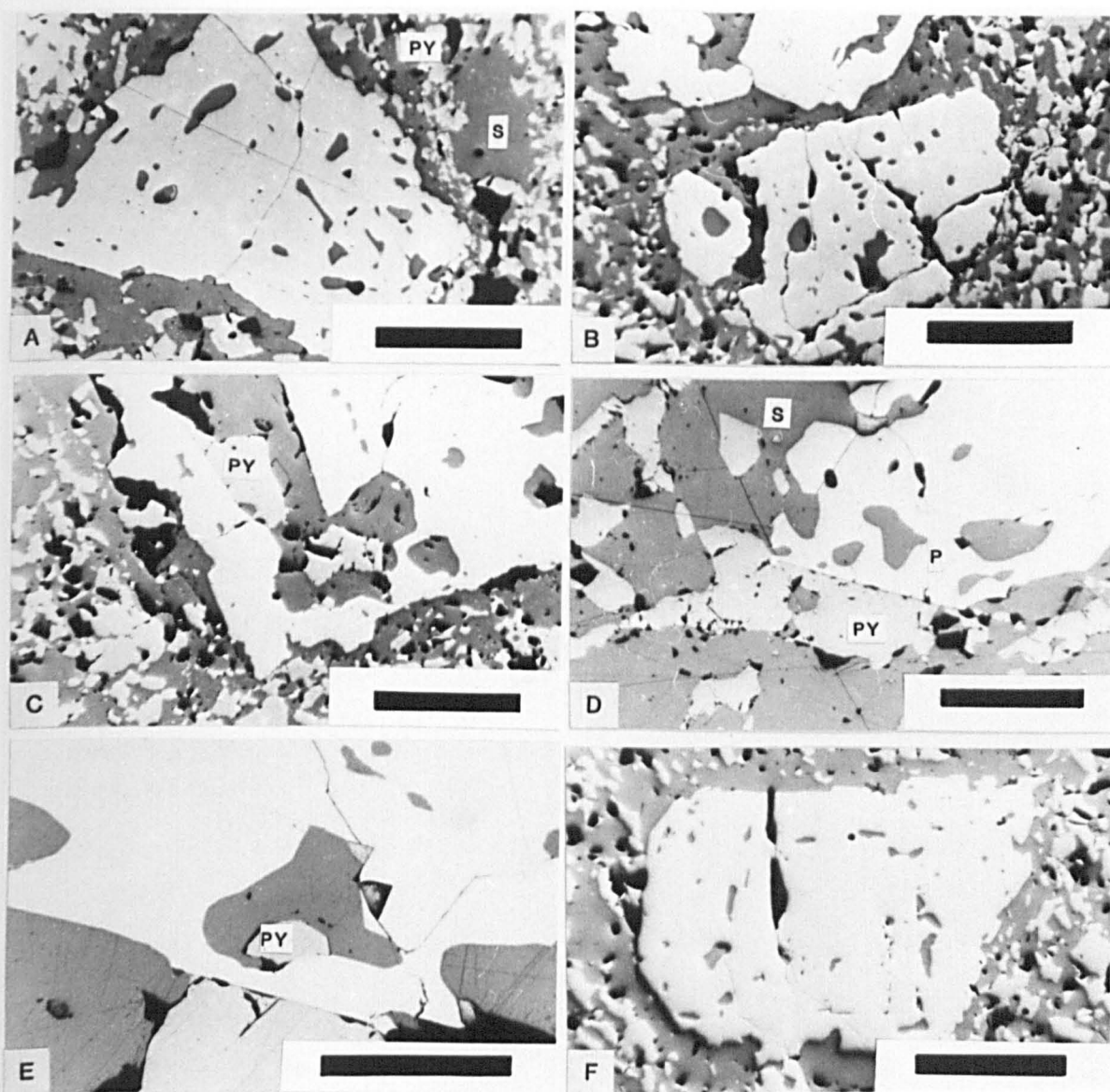


### Figure 6.33 Field relationships and microtextures of tectonites from the porphyroclastic ore facies

A) Mine photograph showing the irregular form of the conformable and cross-cutting relationships of the breccia-textured ore. To the left the ore is held in a south verging D2 fold. On the upper fold limb large marble blocks are incorporated into the ore. Stope P 72e, central Cover zone. Scale bar 1 metre.

B) Discordant contact between massive breccia-textured ore (dark grey) and partially included phlogopite laminated marble raft. Stope L 66w, Cover zone.

C) Close up of a slab of Buckshot textured ore. Note the massive speckled appearance and the inclusion of small < 1 cm. 'quartz eyes' (black) and recrystallised calcite (white). Stope M 72w, Cover zone.

D) Photograph of a polished block of buckshot textured ore. Rounded, sub-hedral, and elongate, angular, strongly deformed shattered pyrite poikiloblasts and finer grained disaggregated cleaved pyrite fragments are held in a fine grained, predominantly sphalerite matrix. Fine grained quartz inclusions (black) are formed in the block. They are weakly aligned in a N-S orientation. M = marble. Specimen A 11. Stope M 72w, Cover zone. Scale bar = 1 cm.

E) Photomicrograph of mylonitic sphalerite ore showing a large rounded sphalerite grain, with bent lenticular internal deformation twins, surrounded by a finer grained less strained serrated sphalerite grains. Very fine grained equant new grains form interstitially to the serrated grains. Brebrick and Scanlon etch at 50°C for 120 secs. Specimen A 7. Stope M72w, Cover zone. Scale bar 500µ. (p.p.l.)

F) Large tabular sphalerite grain, with bent internal deformation twins, in a dynamically recrystallised matrix of finer grained sub-equant sphalerite, with serrated and straight grain boundaries. Specimen as in (A). Scale bar 500µ. (p.p.l.)

G) Close up of dynamically recrystallised sphalerite matrix. The equant unstrained sphalerite grains (striped) have broad annealing twins, and have overgrown dynamically recrystallised grains. Minor fine grained idiomorphic pyrite poikiloblasts (P) overgrow the sphaleritic matrix. Specimen as in (A). Scale bar 160µ.

H) Photomicrograph of a buckshot textured ore showing coarse cataclastically deformed pyrite poikiloblasts overgrowing a dynamically recrystallised sphaleritic matrix. Brebrick and Scanlon etch at 50°C for 120 secs. Specimen E 46, Stope E 46, Angel zone. Scale bar 500µ. (x.p.l.) (N.I.).

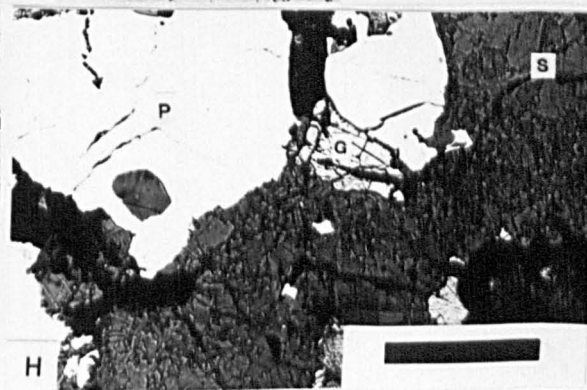
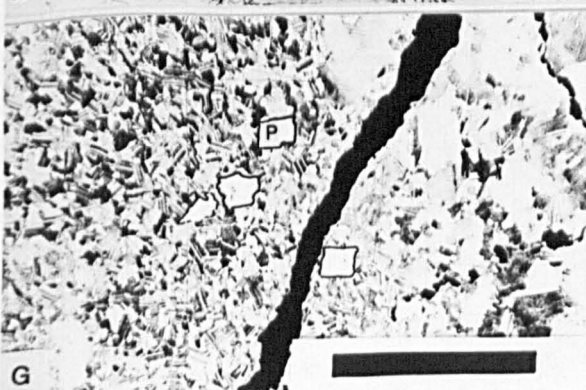
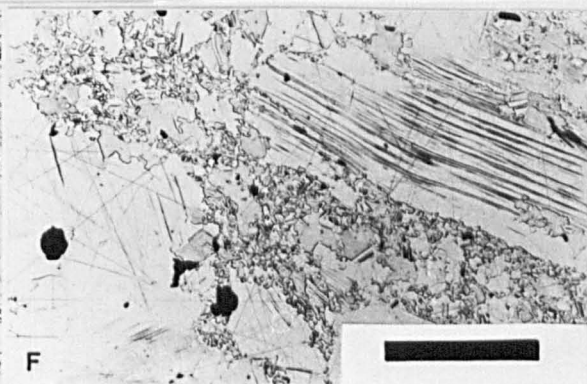
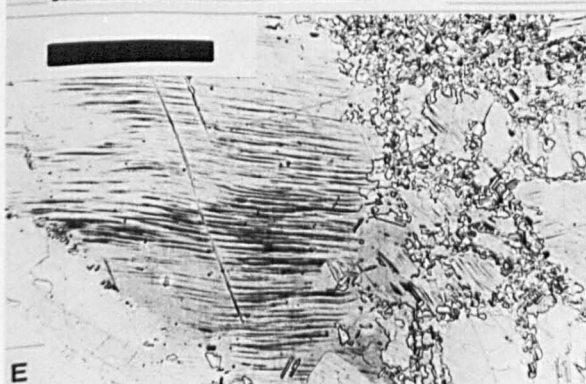


## Figure 6.34. Recrystallised ore facies

A) Coarsely recrystallised sphalerite-galena-pyrite ore tectonite. Pyrite megacrysts (P) lie in a coarse grained sphalerite (S)-galena (G) matrix. Coarsely recrystallised calcite clasts (C) are included in the ore. An irregular contact is made with the host marbles. Stope D 20, Angel zone. Ruler in 20cm. sections.

B) A recrystallised ore band containing large pyrite cubes (P) in a coarse galena (G) matrix. The galena has invaded a footwall of recrystallised quartz (Q) along splayed fractures. M = marble hangingwall. Stope M 72, Cover zone.

C) Coarsely recrystallised monomineralic sphalerite lying above breccia-textured ore tectonites. The coarse sphalerite is seen to have delaminated a calcitic marble raft (C), and to have fractured the hangingwall phlogopite marbles. Stope K 118, Cover zone. Width of view 3 metres.

D) Bleby sphalerite (dark grey) and recrystallised quartz in coarse galena that has formed in a D3 shear zone between layered ore tectonites (upper unit) and coarse sphalerite ore tectonites. The sphalerite blebs are incorporated into the ore through brecciation of the coarse sphalerite bands. Stope E 36, Angel zone. Scale bar 2 metres.

E) Coarsely recrystallised galena and quartz ore tectonite. Recrystallised rounded/ragged quartz crystals are held in a coarse grained galena (G: Light grey) matrix. Stope E 46, Angel zone. Metre rule for scale.

F) Photograph showing the strongly discordant character of the recrystallised massive sphalerite (S) and galena (G) ore tectonite. Marble clasts, up to 1 metre (M) have been delaminated from the host marbles and rotated within the ore. Stope E 46n, Angel zone. Map board for scale. Scale bar 1.5 metres.

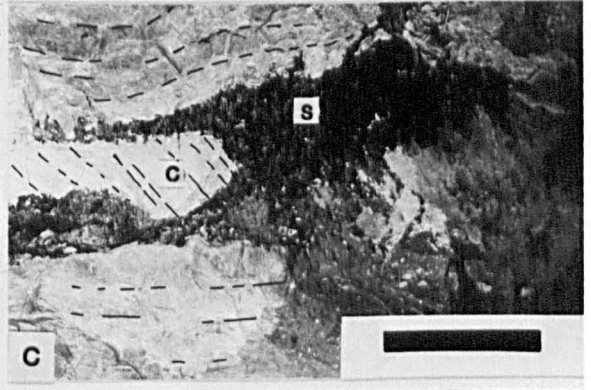
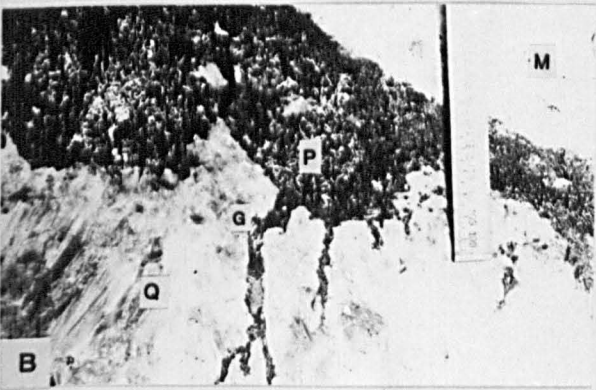
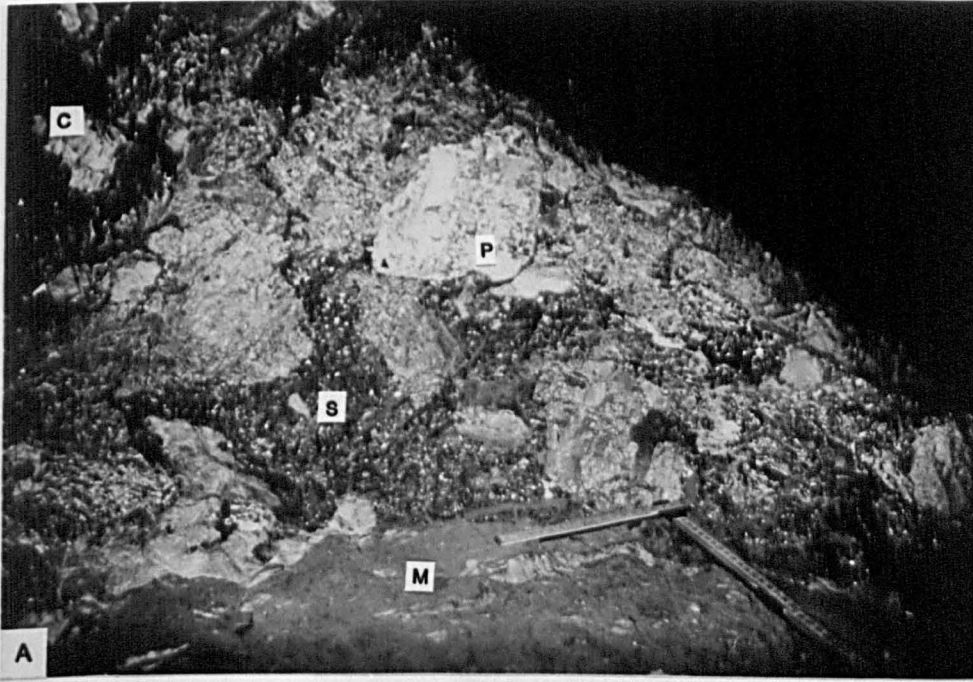


### Figure 6.35. Microtextures of tennantite-rich ore

A) Photograph of a polished block containing coarse tennantite (T: mid-grey) replacing and including galena (G: white-grey) and enclosing fractured sphalerite clasts (S). Pyrite poikiloblasts (P: light grey) overgrow this coarse grained matrix. C = calcite. Unetched. Specimen K 124T. Stope K 124, eastern Cover zone. Scale bar 1 cm.

B) Photomicrograph showing tennantite (T) with cusped grain margins replacing galena (G). Unetched. Specimen K 124T. Stope K 124, eastern Cover zone. Scale bar 500 $\mu$ . (N.I.).

C) Photomicrograph of coarse irregularly shaped tennantite (T: pale grey), in a matrix of coarse galena, with an elongation parallel to a ragged sphalerite aggregate boundary. Unetched. Specimen E 46 Bleby sphalerite. Stope E 46, Angel zone. Scale bar 500 $\mu$ . (p.p.l.).

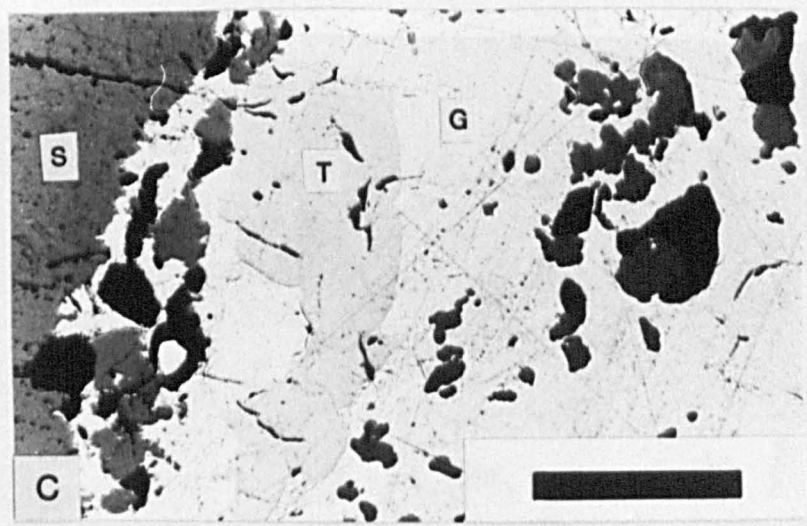
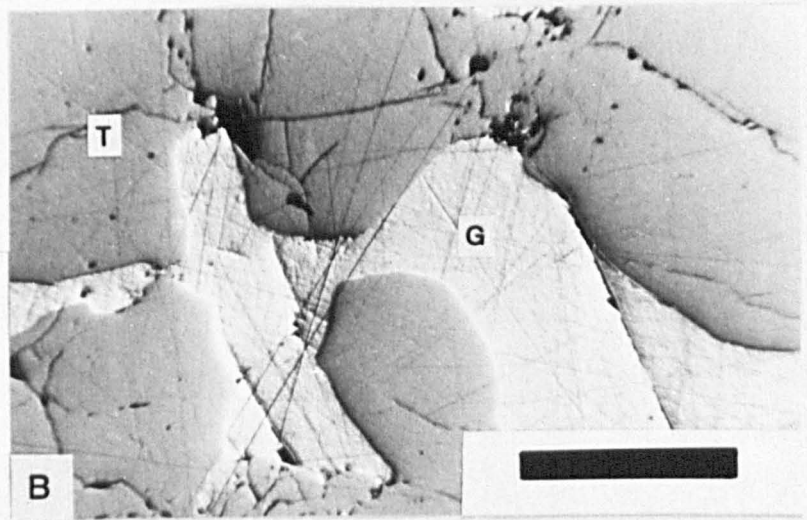
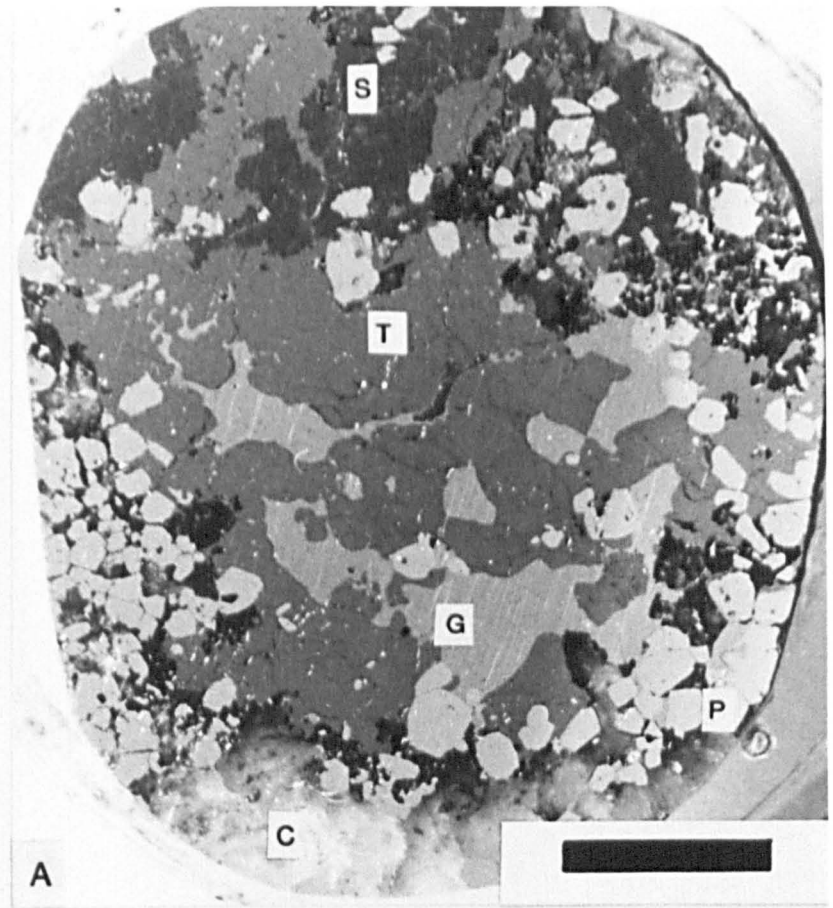


### Figure 6.36. Arsenopyrite microtextures

A) Arsenopyrite (Apy) and chalcopyrite (CPY) rim separating a large fractured pyrite poikiloblast (P) from coarse grained tennantite (T). Cuspate grain boundaries, synonymous with grain boundary migration, in the tennantite abutt the chalcopyrite. Unetched. Specimen K 124T, Stope K 124, Cover zone. Scale bar 500 $\mu$ . (p.p.l.)

B) Idiomorphic twinned rhombs of arsenopyrite (Apy) poikiloblastically overgrowing chalcopyrite (CPY). The chalcopyrite matrix is set in coarse grained tennantite (T). Specimen as in (A). Scale bar 500 $\mu$ . (p.p.l.).

C) Close up of arsenopyrite rhombs from (B), with chalcopyrite (CPY) inclusions. (T) = Tennantite. Specimen as in (A). Scale bar 160 $\mu$ . (p.p.l.).

D) Euhedral arsenopyrite rhombs observed overgrowing phlogopite (Ph) and coarse grained galena (G). The phlogopite and quartz grain also occur in the galena matrix. Unetched. Specimen K 126, Stope K 126s, Cover zone. Scale bar 500 $\mu$ . (p.p.l.).

E) A coarse grained arsenopyrite lath set in a pyrrhotitic (PY) matrix with interstitial sphalerite (S). Unetched. Specimen T 188, Stope T 188n, Tributary zone. Scale bar 500 $\mu$ . (p.p.l.).

F) Xenomorphic pyrite (P) replacing an arsenopyrite (Apy) lath. The matrix consists of sphalerite (S: mid-grey), galena (Light grey) and an abundance of quartz (Q: deep grey). Unetched. Specimen T 188a, Stope T 188n, Tributary zone. Scale bar 500 $\mu$ . (p.p.l.).

G) Arsenopyrite in a fine grained footwall siliceous pelite. Sphalerite (S) occurs in irregular masses replacing the arsenopyrite and the siliceous pelite. Unetched. Specimen B 124bp, Stope B 124, Banana zone. Scale bar 500 $\mu$ . (N.I.).

H) Arsenopyrite with phlogopitic seams (Ph). Specimen as in (G). Scale bar 160 $\mu$ .

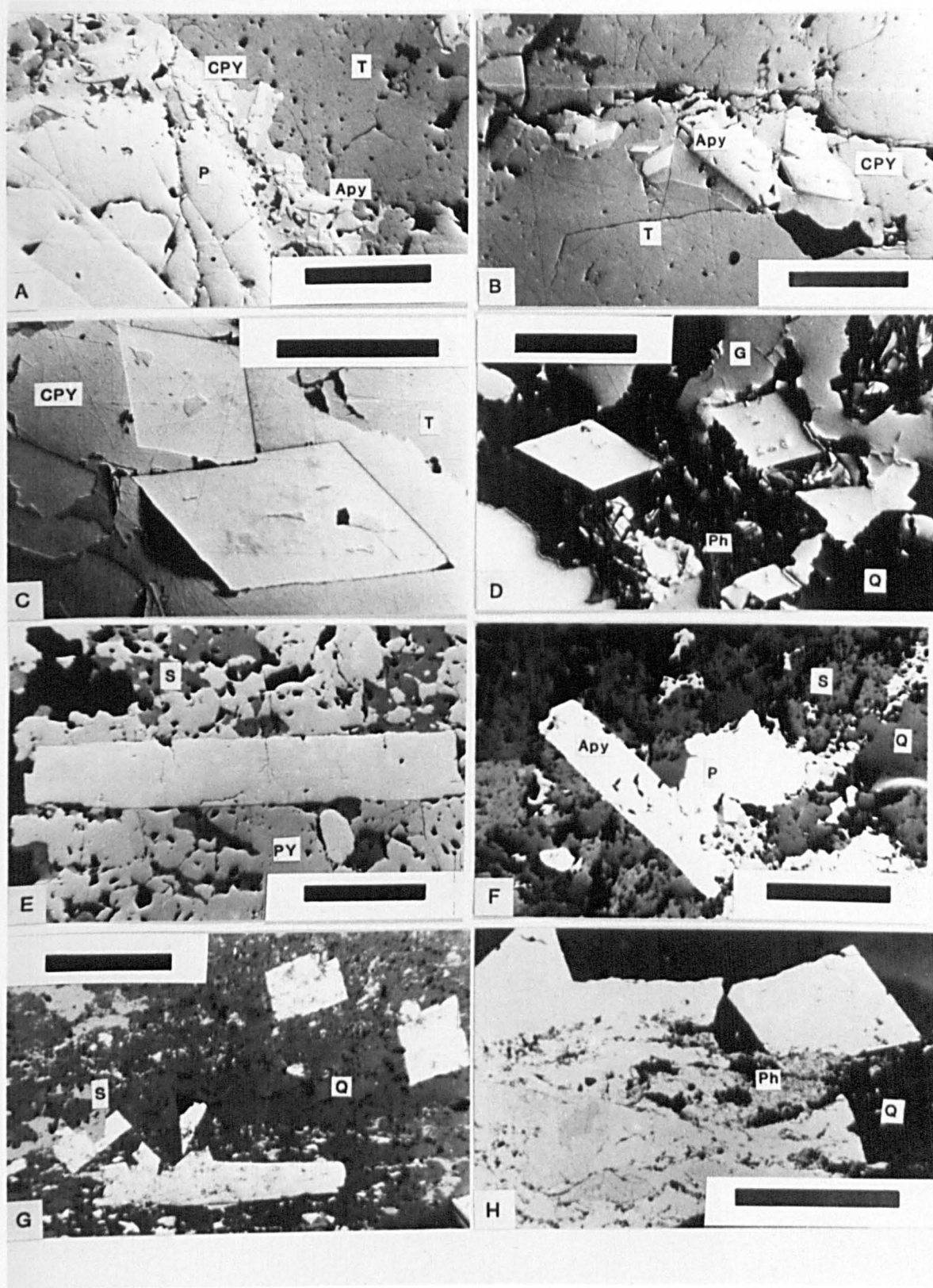


## Figure 6.37. Bleby sphalerite and sheared galena microtextures

A) Bleby sphalerite in coarse galena. The sphalerite grains are ragged and consist of annealed crystal aggregates, that on their extremities overgrow sheared galena. Very fine grained, elongate, foliated, galena (g) abutts and anastomoses around the sphalerite blebs. Away from the sphalerite the galena matrix develops a coarser grained, polygonal, grain growth texture. Recrystallised quartz grains with ragged (fragmented? and annealed) margins are rotated within the foliated galena matrix. Etched in Brebrick and Scanlon etch at 60°C for 120 secs. Specimen A7, Stope E 46, Angel zone. Scale bar 1 cm.

B) Bleby sphalerite ore showing fine grained elongate foliated galena (mottled grey, through differential etching), incorporating sphalerite blebs (S). Later stage annealing occurs in the disaggregated sphalerite blebs, which causes inclusion of the sheared galena. Etched in Brebrick and Scanlon etch at 60°C for 120 secs. Specimen A7, Stope E 46, Angel zone. Scale bar 160 $\mu$ . (p.p.l.).

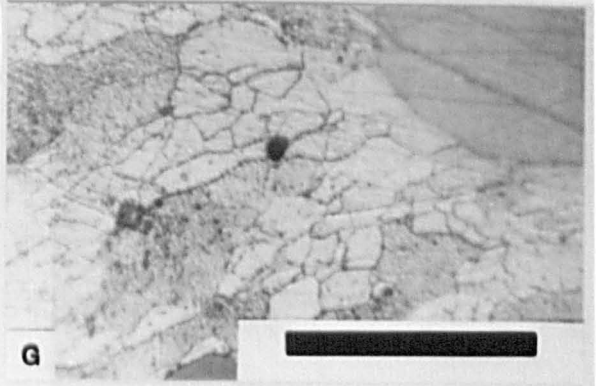
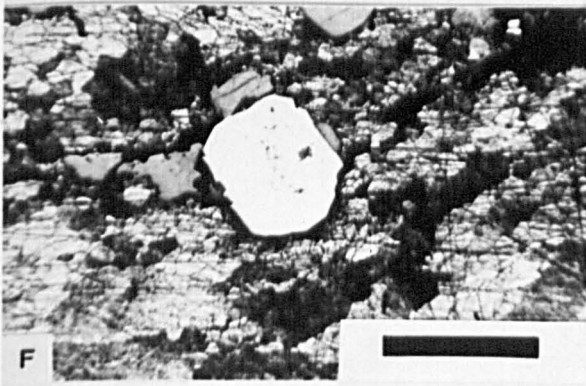
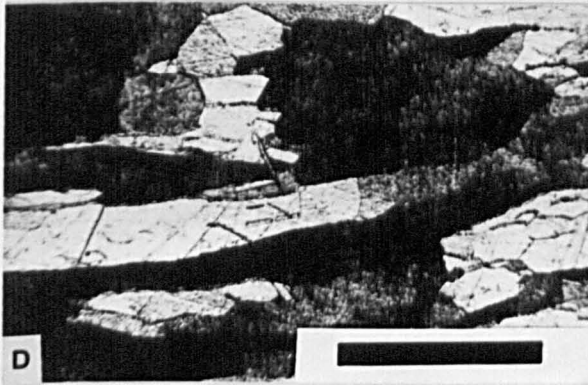
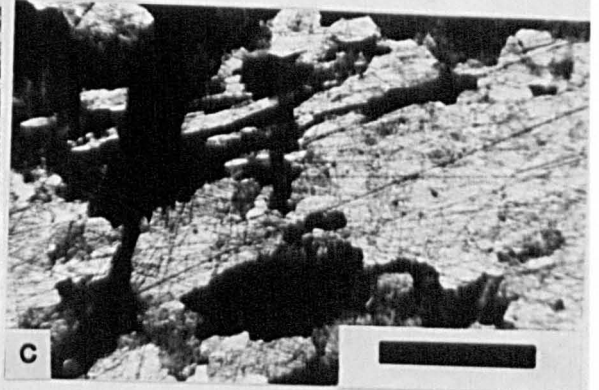
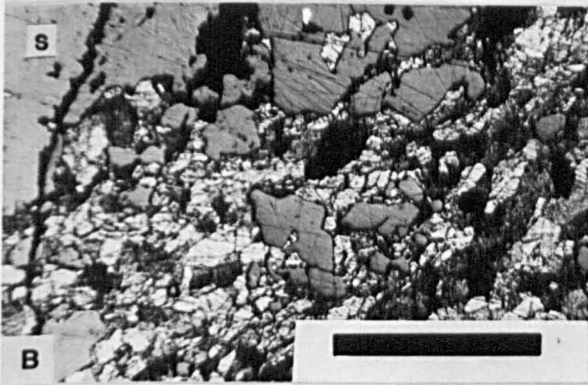
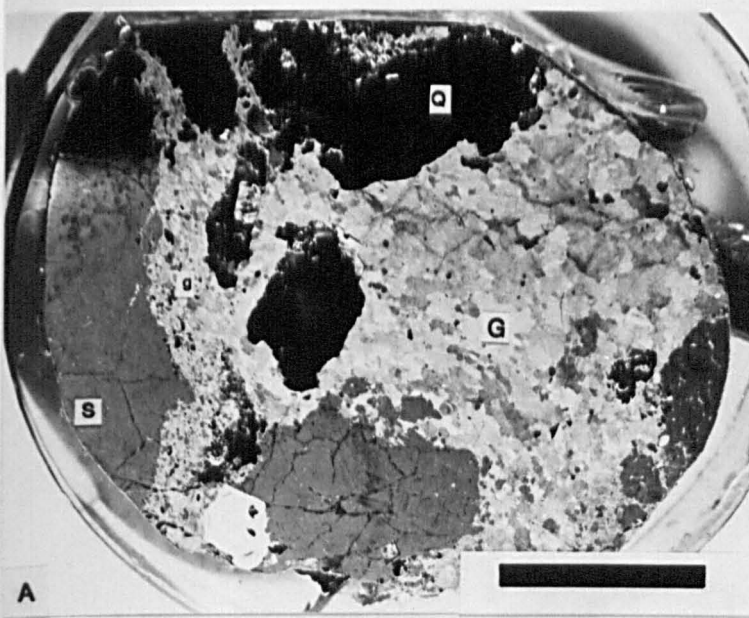
C) Large sub-equant galena grains showing faint elongate sub-grain development. Elongate grains mantle these large galena cores. Specimen as in (A). Scale bar 500 $\mu$ .

D) Close up of highly elongate galena grains and ribbons, showing internal sub-grain development and polygonisation. Specimen as in (A). Scale bar 160 $\mu$ .

E) N-S orientated kink bands developed in a polygonal sub grain within a galena ribbon. Specimen as in (A). Scale bar 100 $\mu$ .

F) Pyrite poikiloblast overgrowing and enclosing sphalerite blebs (S) within the sheared galena matrix. Specimen as in (A). Scale bar 500 $\mu$ .

G) Close up of a polygonised galena ribbon (white) adjacent to an annealed sphalerite bleb. 120° triple junctions and straight to slightly curved grain boundaries are well developed. Specimen as in (A). Scale bar 100 $\mu$ .



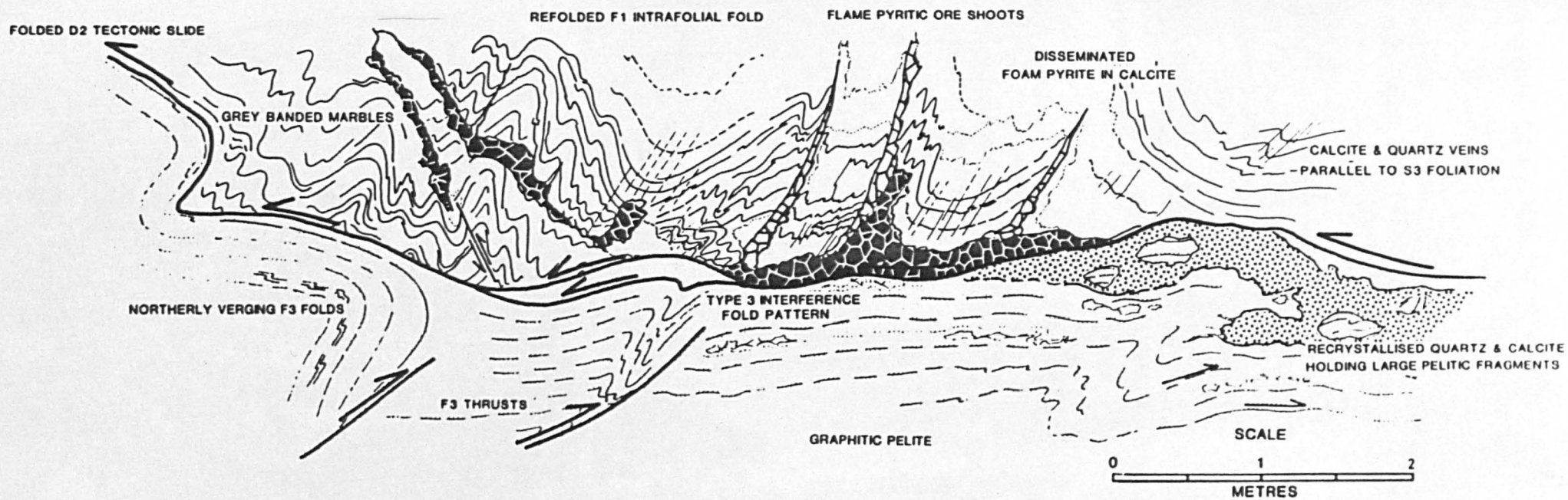


**Figure 6.38** Detailed mapping of Stope I 170, I zone, showing Foam textured pyrite ore and recrystallised sphalerite forming axial planar to D3 folds above a folded D2 south verging tectonic slide.

## **FIGURE. 6.39. Field relationships and microtextures of the foam textured ore tectonite**

A) Mine photograph of D3 folds with a strong axial planar fabric affecting an ore band. Foam textured ore and recrystallised sphalerite occur in upright axial planar alteration zones. Stope I 170s, I zone. Hammer for scale.

B) Close up of foam textured ore within an axial planar zone. A folded quartz layer and recrystallised marble clasts are incorporated within fine grained pyrite (light grey). Recrystallised sphalerite and quartz occur at the base of the massive pyrite.

C) Photograph of a thin D3 axial planar foam textured mineralised band associated with recrystallised quartz (white) which crosscuts the intense S2 graphitic calcite-dolomite fabric. Coarse grained sphalerite (Black) is partially injected along the D3 structure. South wall of Stope I 170s, I zone.

D) Photograph of a polished block of a foam textured ore tectonite. Equant, granular, pyrite (P) are set in a marble and sphalerite (S) matrix. A large pyrite poikiloblast is near the left hand edge of the block. It formed through aggregation of smaller grains. Ca = calcite clast. Unetched. Specimen M-X area, western Cover zone. Scale bar 1 cm.

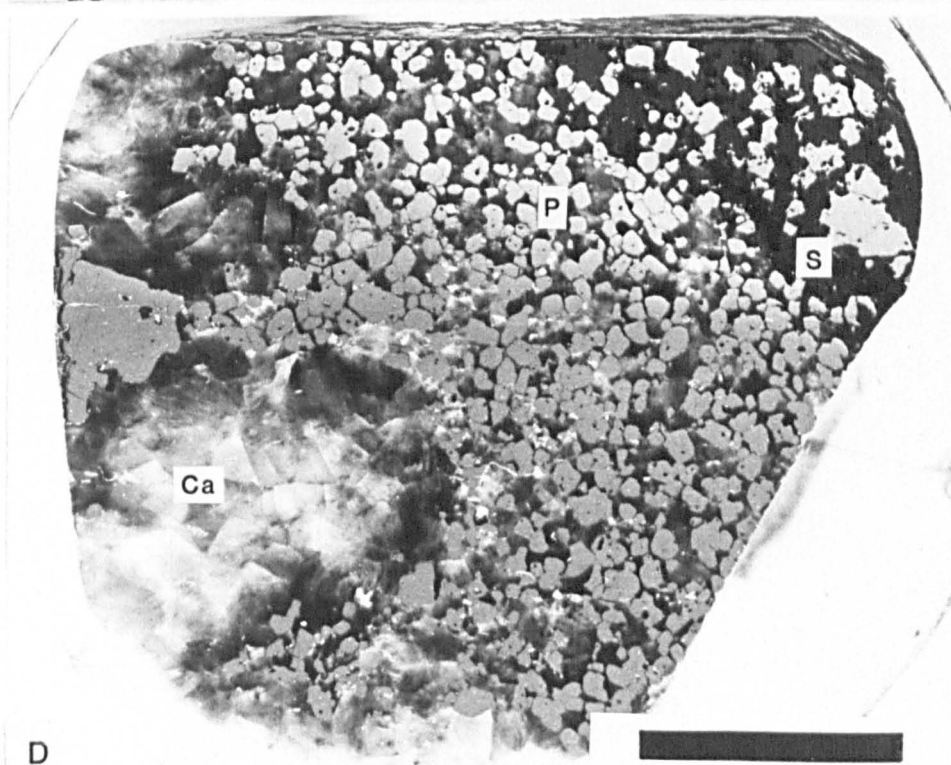
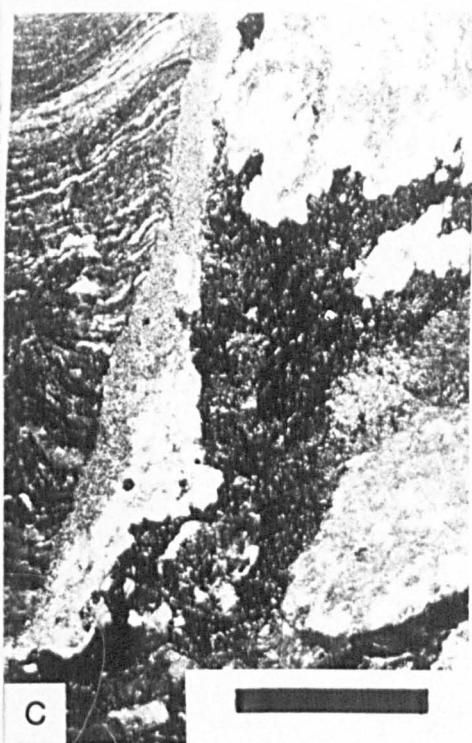
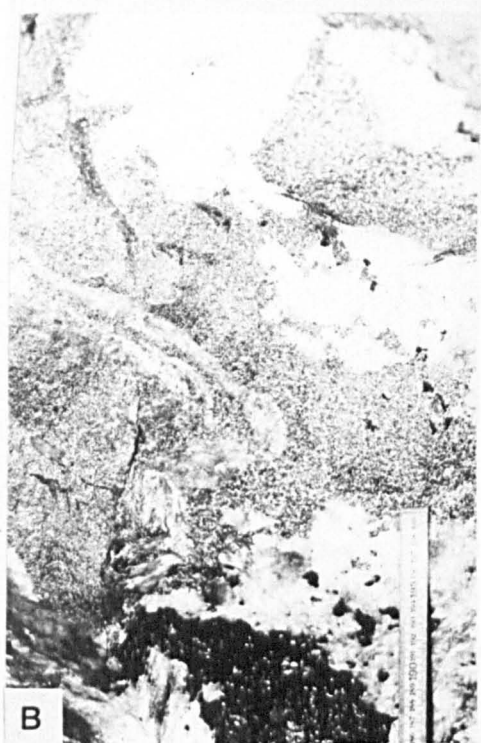


## Figure 6.40. Primary microtextures

A) Colloform shaped growth of zoned colloidal pyrite and marble overgrown and mantled by a sub-hedral metamorphic pyrite grain. Foam textured ore. Etched in 50%  $\text{HNO}_3$ , 120 secs at 60°C. Specimen A 10. Stope K 306, Cover zone. Scale bar 500 $\mu$ . (p.p.l.).

B) Irregularly shaped, co-precipitated, colloidal intergrowths of carbonate and iron sulphide overgrown by metamorphic annealed pyrite, that has caused a grain size reduction in the early mineralisation. Specimen as in (A).

C) Relict twinned rhombs, possibly after marcasite, picked out by marble inclusions (black), overgrown by metamorphic pyrite. Minor cataclastic fracturing. Layered ore. Etched in 50%  $\text{HNO}_3$ , 120 secs at 60°C. Specimen DIZ b. Deep Ice zone. Scale bar 160 $\mu$ . (p.p.l.).

D) Twinned rhombs, after marcasite, rimmed by a overgrowth of small cubic grains and carbonate inclusions. Overgrown by a large cubic grain and subsequently by a metamorphic pyrite. Layered ore. Etched in 50%  $\text{HNO}_3$ , 120 secs at 60°C. Specimen A 5. Stope E 38, Angel zone. Scale bar 500 $\mu$ . (p.p.l.).

E) Metamorphic pyrite holding a twinned lath, after marcasite (?), rimmed by a overgrowth of finer laths and interstitial marble. Specimen as in (D). Uneven etch. Scale bar 200 $\mu$ .

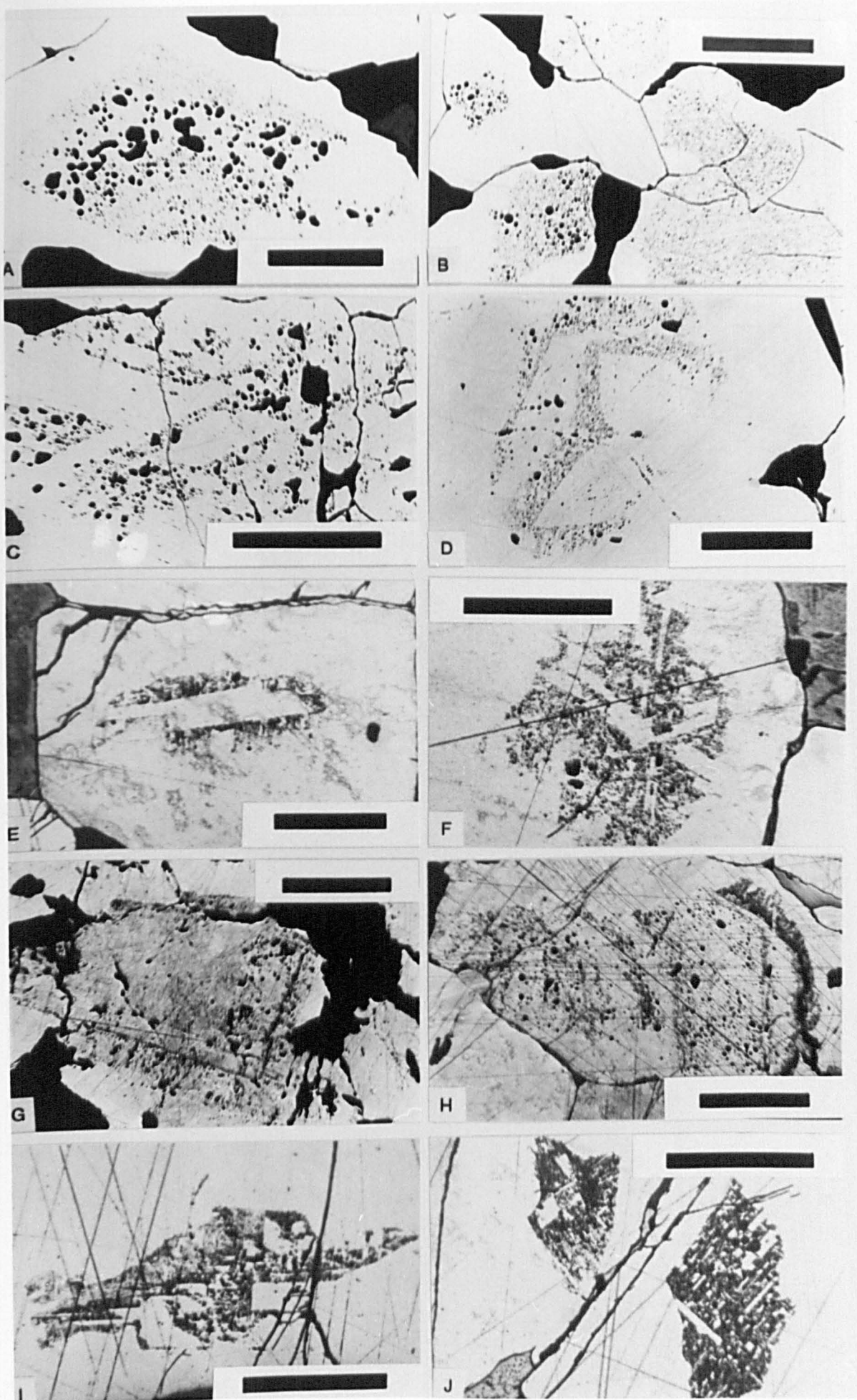
F) Rounded primary inclusion, within a metamorphic pyrite, consisting of skeletal prisms forming a rosette, with interstitial marble and sulphide. Specimen as in (D). Scale bar 160 $\mu$ .

G) Large zoned cubic grain, possibly after pyrite, overgrown by pyrite. Late stage annealing has caused grain size reduction. Massive pyrite from Nukavsak Formation. Etched in 50%  $\text{HNO}_3$ , 60 secs at 50°C. Specimen NUK 3. Drill core from Y 216. Scale bar 500 $\mu$ . (p.p.l.).

H) Concentrically zoned, colloform (?), growth rimmed by a corona of fine acicular laths, and subsequently overgrown by pyrite. Specimen as in (D). (N.I.) Scale bar 500 $\mu$ . (p.p.l.).

I) Irregular diamond shaped corroded primary clast consisting of cubic and acicular laths with interstitial marble inclusions. Overgrown by pyrite. Specimen as in (D). (N.I.) Scale bar 160 $\mu$ . (p.p.l.).

J) Corroded and embayed primary clasts containing pseudomorphed acicular laths. Overgrown by pyrite that is cataclastically fractured. Specimen as in (D). Scale bar 500 $\mu$ . (p.p.l.).



### c) Ore facies distribution.

The ore facies have been carefully mapped in order to determine their relationship to the structure and to examine the concomitant control on the metal distributions in the deposits.

The Angel zone contains both the greatest diversity of ore tectonite types and ore facies association, and the most complex deformation patterns of any of the Black Angel ore zones (Fig. 6.15 & 6.22). The northern Angel zone is dominated by layered ore tectonites and D1 fold structures (Figs. 6.15, 6.17 & 6.20). The layered ore tectonites grade southwards into massive breccia textured ore tectonites of the porphyroclastic ore facies. Elongate ESE-WNW lenses and circular pods of the recrystallised ore facies which are localised within D3 fold structures (Fig. 6.15 & 6.20) occur in the C and Northern E areas of the Angel zone (Fig. 6.22) and are responsible for the high metal grades (Fig. 6.20, 6.44 & 6.45) of the northern Angel zone. The central Angel zone consists of a low grade core of the massive pyritic ore facies (Fig. 6.22). The pyrite core occurs within minor D1 folds (fig. 6.20), which lie on D3 fold limbs. The core was largely resistant to deformation. To the south of this massive pyritic ore facies, the ore horizon is thinned (0.5 - 10 metres) and transected by D2 tectonic slides, and dominated by the porphyroclastic ore facies (Fig. 6.15 & 6.22). An isolated irregularly shaped banded ore facies lens (western G area), and three pods<sup>of</sup> the recrystallised ore facies occur within this porphyroclastic ore (Fig. 6.22).

The ore horizon in the Cover zone is thinner and more sheared than in the Angel zone (Fig. 6.41). It varies in thickness between 0.5 - 5 metres (average  $\approx$  1-2 metres) (Fig. 6.41 & 6.42). It is deformed by a system of D2 tectonic slide zones and open D3 folds. The porphyroclastic ore facies, composed largely of breccia-textured ore tectonites, dominates the western Cover zone. The more sheared buckshot ore and mylonitised sphalerite ore tectonites occur locally in the M and P areas of the central Cover zone. Small remobilised ore facies pods occur in the K

area.

The eastern Cover zone contains a number of ore tectonite types and facies associations (Fig. 6.22). Banded and porphyroclastic ore facies dominate the southern flanks and the outer hinge zone of the MX area D3 flexure (Fig. 6.15 & 6.22), whilst porphyroclastic ores occur in the southern X area (Fig. 6.22). Massive pyritic ore facies occur in irregular masses about the D3 flexure and are associated with the tectonites of the banded ore facies. Ore tectonite types of the recrystallised ore facies are present in the D3 fold hinge, and also as irregular lenses and pods on the northwesterly limb of the D3 flexure. In the northern X area (Fig. 6.22) the porphyroclastic ores grade into massive pyritic and weakly sphalerite banded ores.

The ores of the I, Banana+T zones are less variable than the sulphides of Angel and Cover zones, and are dominated by porphyroclastic ore facies associations. In the I zone, these ores occur in a D2 tectonic slide system (Fig. 6.21). The lower units of the eastern I zone contain breccia-textured ore tectonites and sheared pyrrhotitic tectonites. The Banana zone consists of breccia-textured tectonites in which a small pod of the banded ore facies is present (Stope B101) (Fig. 6.22). Coarse sphalerite ore tectonites occur in the north of the zone which occur with coarse baryte (Fig. 5.4 e-h).

Some ore tectonite variation occurs in the Tributary zone. The basal sections of the central T zone are marked by pyrrhotitic ore tectonites (Fig. 6.43). Recrystallised ores occur to the north of this pyrrhotitic core and also as very small recrystallised pods in the T2 area. Massive to porphyroclastic ores dominate the outer areas of the T zone (Fig. 6.43).

The Deep Ice zone consists of irregular pods of recrystallised ore facies together with minor banded ore facies. These ore facies associations are similar to those found within D3 folds of the northern Angel zone and the MX area of the Cover zone. This may suggest that a

previously unrecognised D3 fold exists in the Deep Ice zone.

In summary, it is evident that the distribution and generation of ore facies are directly related to particular deformation structures (Fig. 6.15 & 6.22) and specific tectonic events (Table. 6.3 & 6.4). The banded ore facies is associated with large D1 overfolds. Any primary layering that may have been present prior to deformation would have been accentuated by a transposition of fabrics during the D1 event. The breccia-textured ore of the porphyroclastic ore facies occurs in both D1 and D2 fold structures above decollement zones. The buckshot and mylonitic sphalerite ore tectonite types of this facies are associated with the D2 tectonic slides. The recrystallised ore facies is present in the D3 structures. The coarser unstrained tectonites of this facies e.g. coarse sphalerite and coarse galena ore tectonite types, occur in D3 fold hinges. The sheared bleby sphalerite ore tectonite occurs in slightly later D3 shear zones.

The massive pyritic ore facies occurs on D3 fold limbs in the central Angel zone and eastern Cover zone. This ore facies is little deformed and probably approximates original (primary) pyrite distributions.

#### **d) Ore stratigraphy**

The ore facies distribution map (Fig. 6.22) is a somewhat simplified 2D representation of the ore facies distribution. In many cases several ore tectonite types and ore facies occur at the single locations, but only the dominant ore facies is represented on the map (Fig. 6.22). More detailed 3D representations of the tectonite type distribution based on measured and logged sections are given in Fig. 6.42, 6.43.

The Angel zone ore horizon varies considerably in thickness between 0.5- 35 m. It contains all ten ore tectonite types and all four ore facies associations. Stratigraphic correlation between sections is poor (Fig 6.42a) and rapid changes in ore facies and tectonite types occur

throughout the zone. A good example of this is observed in Stope E 44-46 (Fig 6.41a). The ore horizon consists of D1 layered ores at the hangingwall contact which grade into D2 related breccia textured ores of the porphyroclastic ore facies. Buckshot textured ore tectonites are developed towards the footwall contact, whilst coarse sphalerite and coarse galena ore tectonites with bleby sphalerite ore tectonites occur at the centre of the horizon. However, 70 m west (i.e. Stope E 48-52) only the basal breccia textured ore is retained. The rest of the horizon consists of the massive pyrite ore tectonite type.

In comparison to the Angel zone, tectonite types can be closely correlated between measured sections in the central Cover zone (Fig. 6.41b), where a well defined ore stratigraphy composed mainly of breccia-textured ore tectonite types occurs (Fig. 6.25 & 6.41b). The most variable ore stratigraphy is present in the more highly deformed and sheared, central parts of the zone e.g. Stope M72 W (Fig. 6.25 & 6.41b). Here the ore horizon (Fig. 6.25) contains a thin unit of D1 layered ore tectonites at the hangingwall and footwall contacts. D2 porphyroclastic ore facies occur within the layered ore. The tectonites grade from breccia-textured ores to buckshot textured ores and finally mylonitic sphalerite towards the centre of the ore horizon. Minor D3 folds occur in the Cover zone and result in formation of the recrystallised ores that are commonly found towards the base of the ore horizon (Stopes KDD, K 188 and M72 W, Fig. 6.41b).

The rapid changes in ore tectonite type through the Angel zone are due to the complex style of deformation within the zone (and the pre-existing mineral distributions) (Fig. 6.15). The more consistent ore stratigraphy of the eastern Cover zone results<sup>in</sup> the ore horizon having been deformed by one major tectonic event. D2 tectonic slide structures are dominant in the zone (Fig. 6.15). The ore stratigraphy becomes more highly sheared and therefore more variable towards tectonic slide zones of greater displacement.

Figure 6.41 ORE THICKNESS IN THE BLACK ANGEL MINE

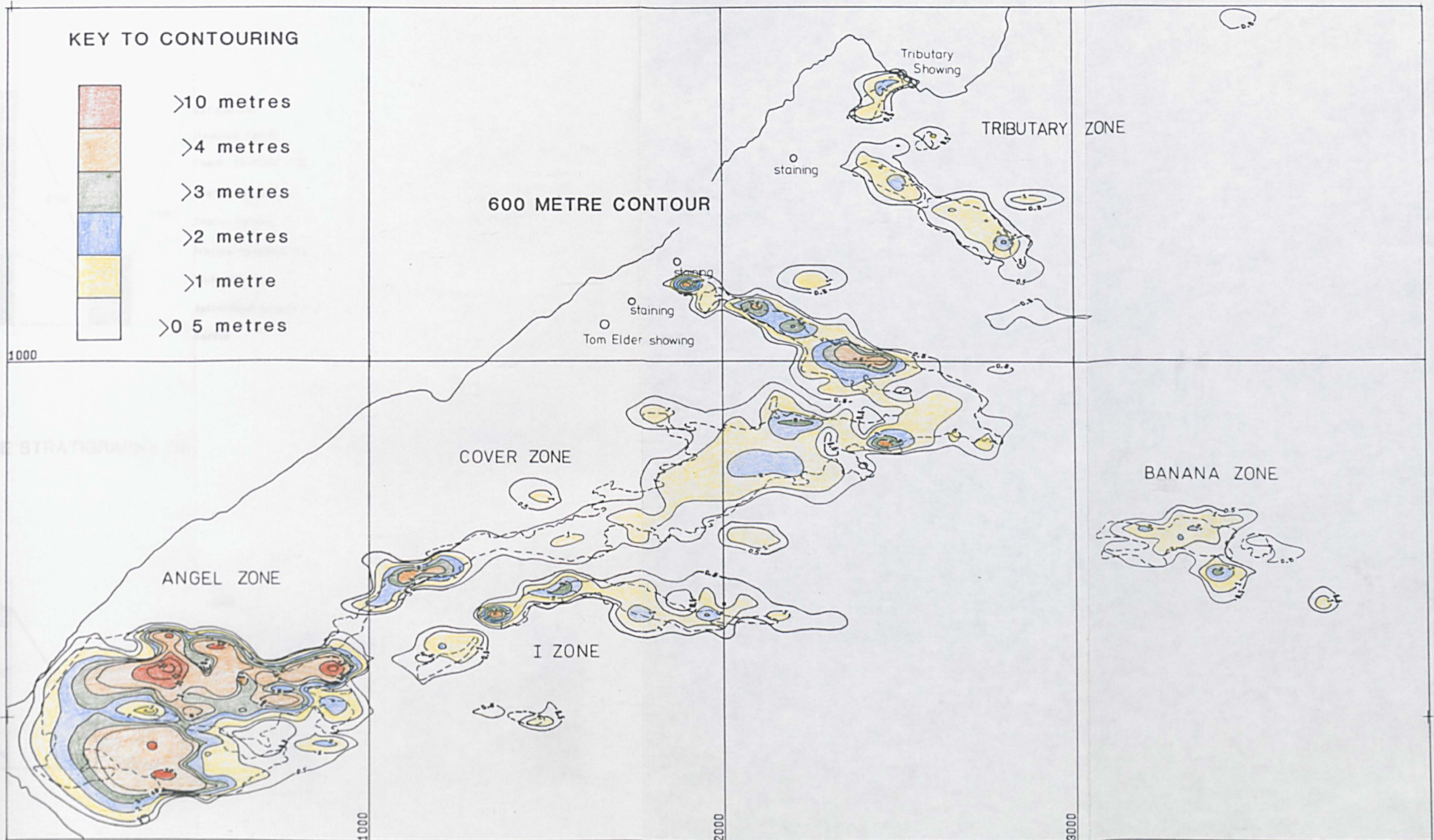
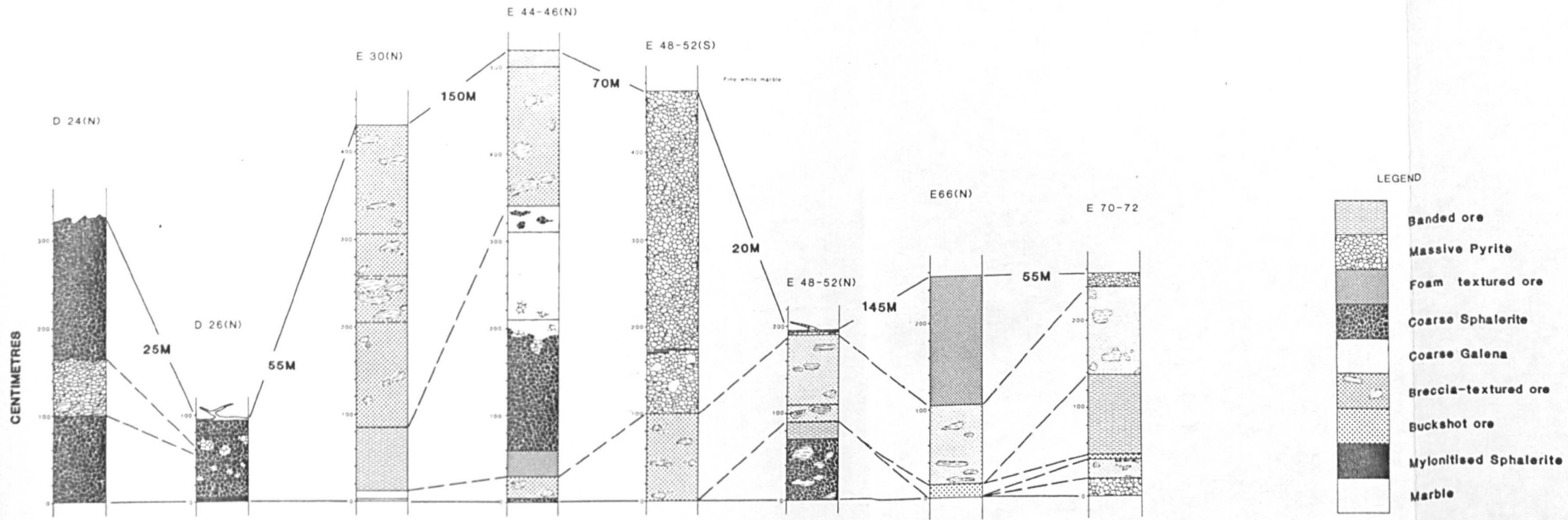
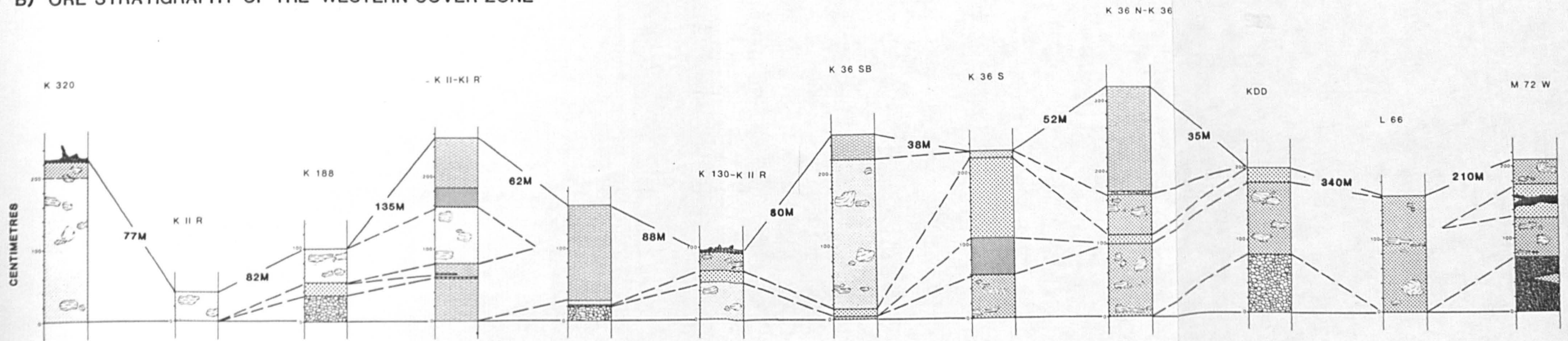


FIGURE 6-42

A) ORE STRATIGRAPHY OF THE NORTHERN ANGEL ZONE



B) ORE STRATIGRAPHY OF THE WESTERN COVER ZONE



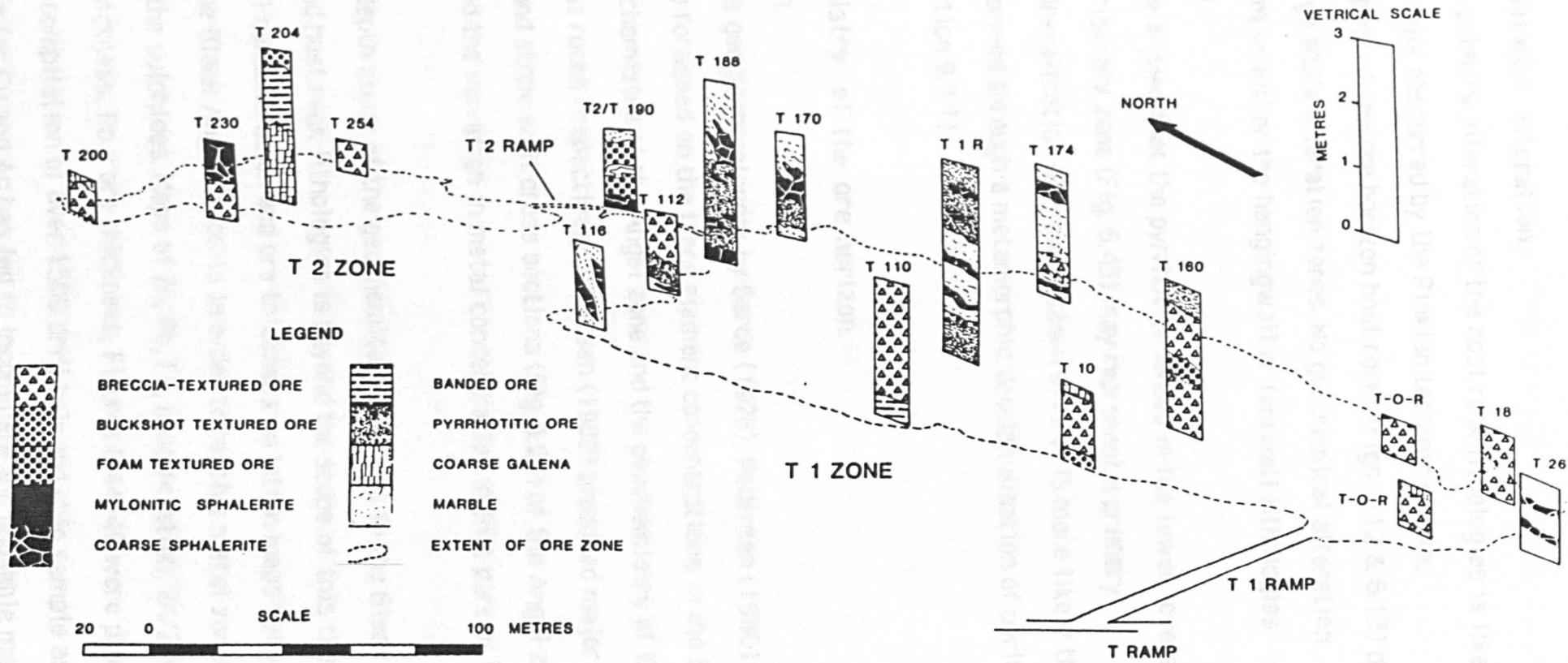


Figure 6.43 Fence diagram of Tributary zone ore stratigraphy

### **e) Hanging / Footwall alteration.**

Although primary alteration of the host rock lithologies is likely to have been strongly obscured by the Rinkian tectonic events, lithological mapping of the ore horizon host rocks (Figs. 6.12 & 6.13) did not show any large scale alteration zones. No geochemical alteration haloes are present in either the hangingwall or footwall lithologies (Edmunds, 1981).

It may be argued that the pyrrhotite lenses in the lower levels of the I zone and Tributary zone (Fig. 6.43) may represent a primary hydrothermal mineralisation (Finlow-Bates, 1977). It is more likely that the pyrrhotite formed through a metamorphic desulphidisation of pyrite (Hall, 1986)(section 9.3.1).

## **6.5.7 Geochemistry of the ore horizon.**

### **a) Introduction.**

Previous geochemical work by Garde (1978), Pedersen (1980) and Edmunds (1981) focussed on the trace element concentrations in the South Lakes area, geochemistry of the Angel zone and the geochemistry of the Black Angel host rocks respectively. Pedersen (1980) produced major element maps and stope wall cross sections (Fig. 6.20) of the Angel zone that documented the variation in metal concentration in that part of the mine.

An in-depth study of the geochemical variations in the Black Angel ore deposits and host rock lithologies is beyond the scope of this thesis. However, metal concentration and ore thickness variation maps have been produced for the Black Angel deposits in order to resolve metal zonation trends within the sulphides. Maps of Zn, Pb, Fe, concentration, Zn/Zn+Pb, and Zn x Ore thickness, Pb x ore thickness, Figures 6.44-49 were produced by a computer compilation of over 1500 drill hole and chip sample assays. Scant analysis for Cu and Ag has led to incomplete and unusable maps. A tectonic map of the Black Angel mine has been presented (in back pocket)

to overlay upon Figures 6.44 to 6.49 in order to study the variations of metal concentrations etc. with structure.

#### **b) Metal distribution patterns.**

The Zn and Pb distributions (Figs. 6.44 & 6.45) are generally similar throughout the Black Angel deposits. ESE-WNW trending high grade Zn and Pb areas which correlate with the D3 associated recrystallised ore facies (Fig. 6.22) occur in the northern and southern Angel zone (fig. 6.44). Outside the Angel zone, high Zn concentrations in D3 folds are present in the western K zone, the M and P zones (where the D3 folds interfere with a D2 tectonic slide zone that thickens the ore horizon), and the southern X area of the Cover zone (Fig. 6.44). High Pb concentrations in the Cover zone are restricted to two medium sized (100 metre long) lenses in the M and P areas (Fig. 6.45). These lenses are associated with a system of D2 tectonic slides which tectonically thicken the ore horizon. Two small rounded pods occur to the north and south of the X area in a D3 synform (Fig. 6.45).

In the I zone, high Zn & Pb concentrations are restricted to the central and western I zone, where the horizon is tectonically imbricated and thickened by minor D3 folds (Fig. 6.21). An elongate ESE-WNW trending, 500 metre long, high grade Zn body occurs in the central Banana zone, which incorporates a 200 metre long, high grade Pb lens. High grade Zn and Pb zones are also present southeast of the Banana zone (Figs. 6.44 & 6.45). These high grade zones correspond to D3 folds. The Tributary zone consists of five medium to small sized high grade Zn pods, but only one high grade Pb pod. These have possibly formed as D3 pinch and swell structures on an elongate D1 structure.

High Fe concentrations occur throughout the Angel and Cover zones (Fig. 6.46). The Tributary zone (apart from the northerly T3 area) the western Banana zone and the western I zone are relatively Fe-poor areas. However the eastern I zone has a high Fe concentration which coincides with the location of pyrrhotite rich ores. The high grade iron zones tend to

Figure 6.44 PERCENTAGE ZINC CONCENTRATION IN THE BLACK ANGEL MINE

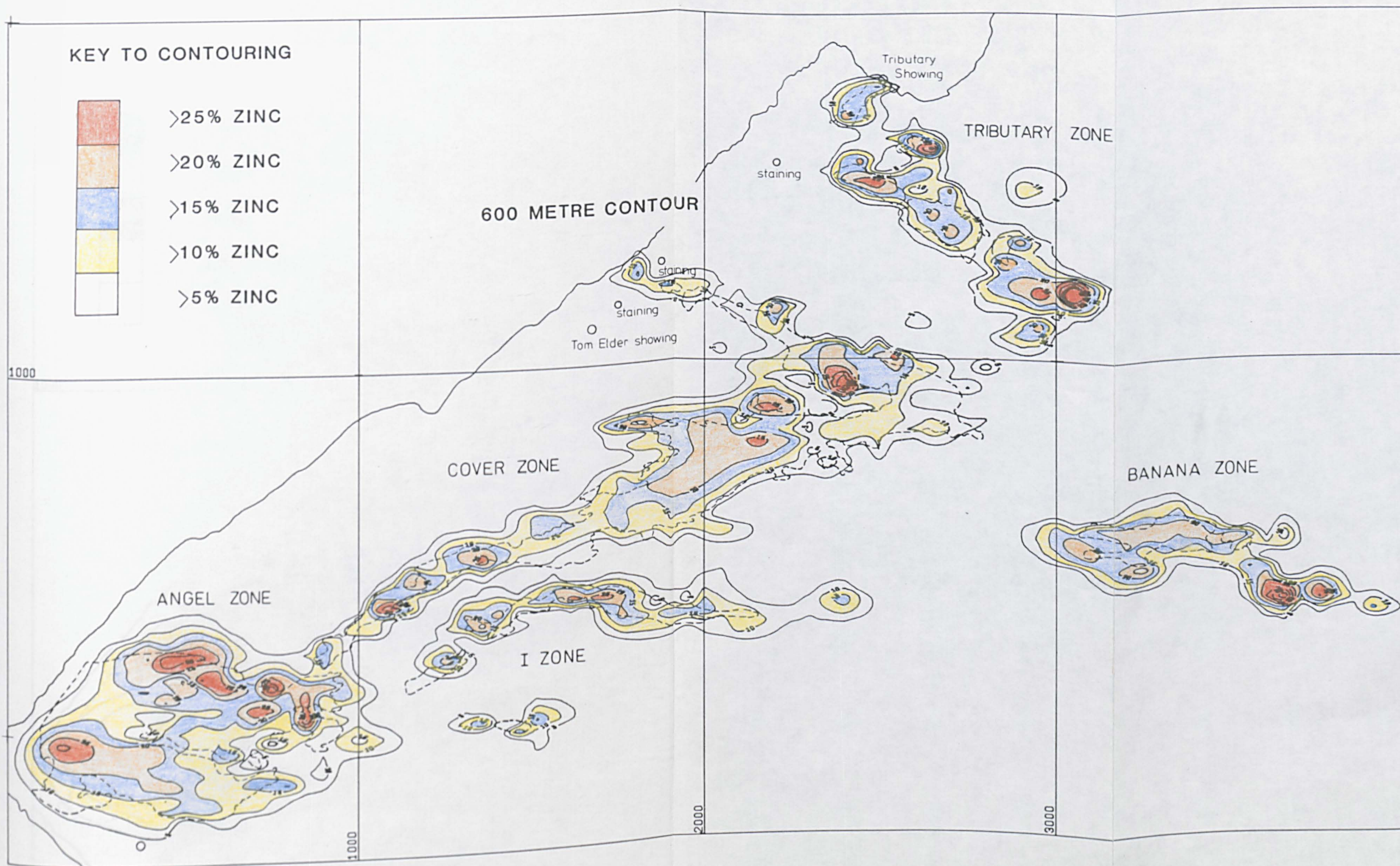


Figure 6.45 PERCENTAGE LEAD CONCENTRATION IN THE BLACK ANGEL MINE

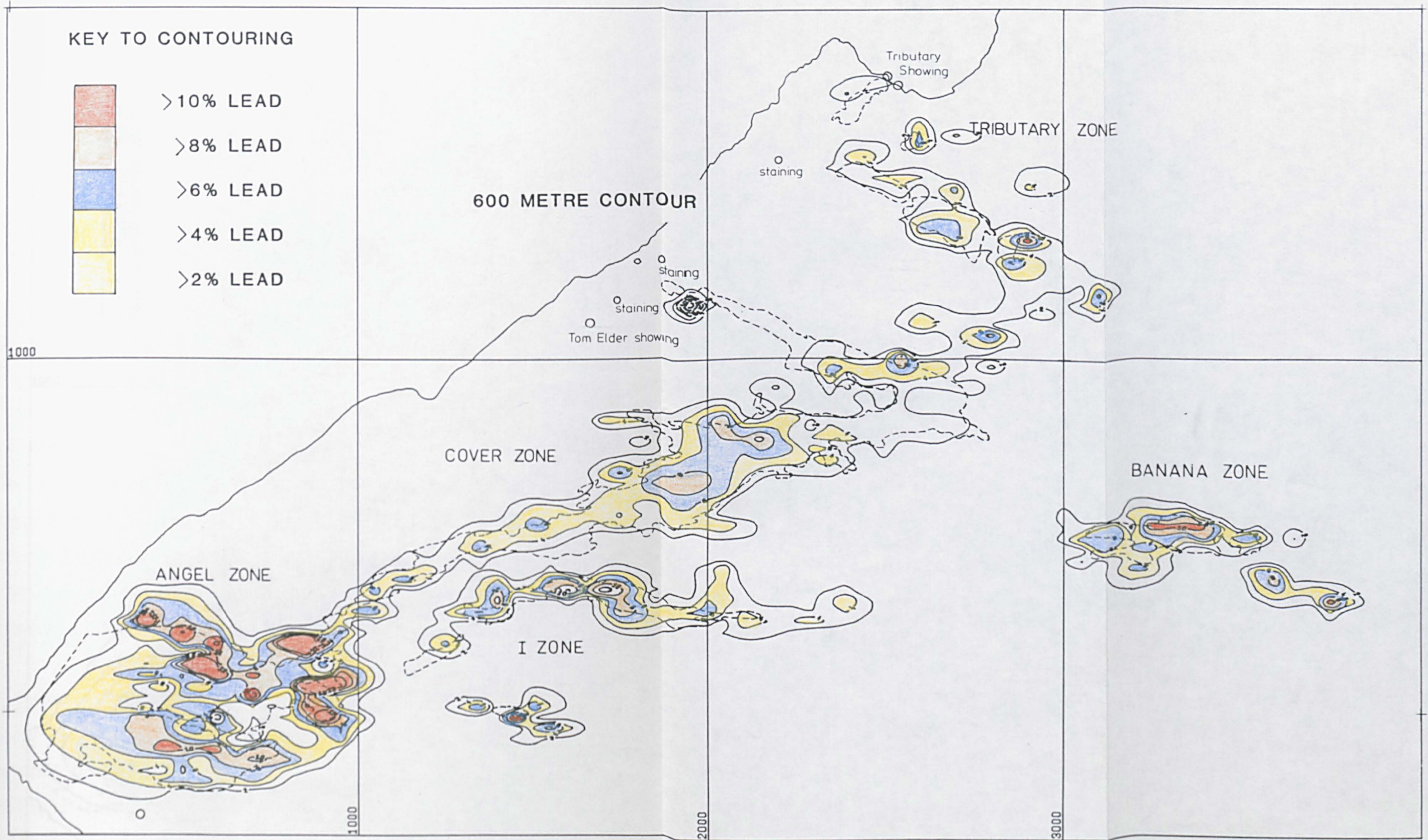
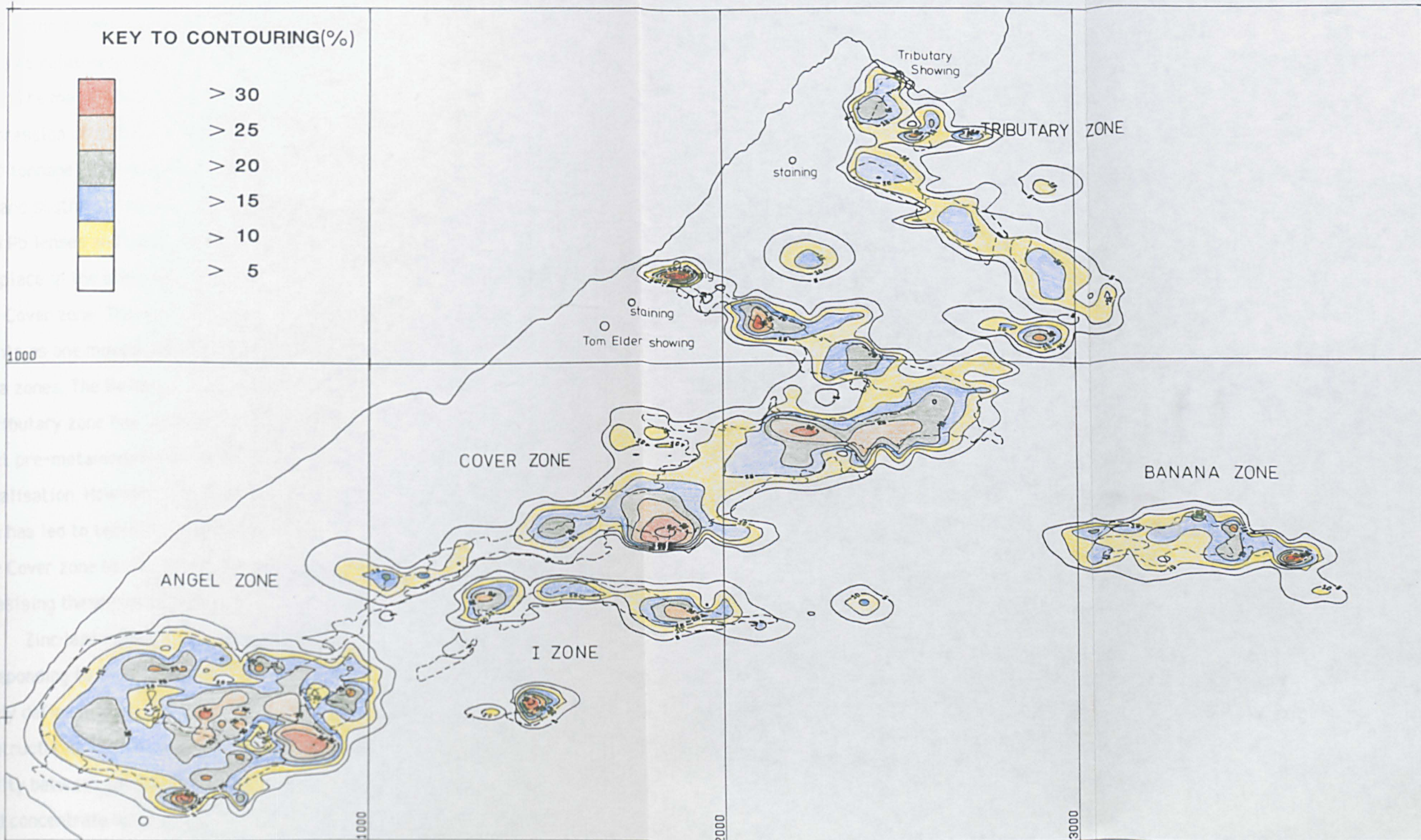


Figure 6.46 PERCENTAGE IRON CONCENTRATION FOR THE BLACK ANGEL MINE



be formed on D3 fold limbs (Fig. 6.20) e.g. MX area, eastern Cover Zone. However the pyrite core of the Angel zone (Fig. 6.22) corresponds with a major D1 overfold.

Large variations exist between the Zn & Pb maps and the Fe plot. This is probably due to the differential mobilisation during deformation of lead and zinc to low stress zones, i.e. D3 hinge zones, while the immobile Fe became relatively enriched on the fold limbs.

The metal concentration x thickness maps (Fig. 6.47 & 6.48) give an impression of the distributions of the total economic metal content (metal tonnage). The Angel zone contains two high scoring regions to the north and southwest of the zone in equivalent locations to the high grade Zn and Pb lenses and is by far the richest ore zone in the mine. The only other place in the mine where a factor index >100 occurs is in the X area of the Cover zone. The ore bodies show a general decrease in metal contents as one moves eastwards from the Angel zone to the Tributary and Banana zones. The Banana zone has the smallest amounts of zinc, whereas the Tributary zone has the least lead. These factor indexes are thought to reflect pre-metamorphic variations in the grade and thickness of the mineralisation. However, the complex deformation in the Angel zone, which has led to tectonic thickening of the ore, and the tectonic thinning of the Cover zone (on D2 tectonic slides) may be responsible for emphasising these pre-metamorphic variations.

Zinc:lead ratios of the mined ore vary between 2:1 and 4:1 corresponding to 70%-80% Zn /Zn+Pb (Fig. 6.49). High Zn/Zn+Pb ratios vaguely define E-W to ENE-WSW trends (Fig. 6.49), which correspond to D3 fold structures. This E-W grain may be caused by the differences in mobility between galena and sphalerite. Galena is more mobile and hence would concentrate more quickly within the D3 fold hinges. The D3 fold limbs would therefore become relatively enriched in sphalerite with respect to galena.

In all of the metal concentration maps, it is apparent that the

Figure 6.47 PERCENTAGE ZINC CONCENTRATION x ORE THICKNESS IN THE BLACK ANGEL MINE

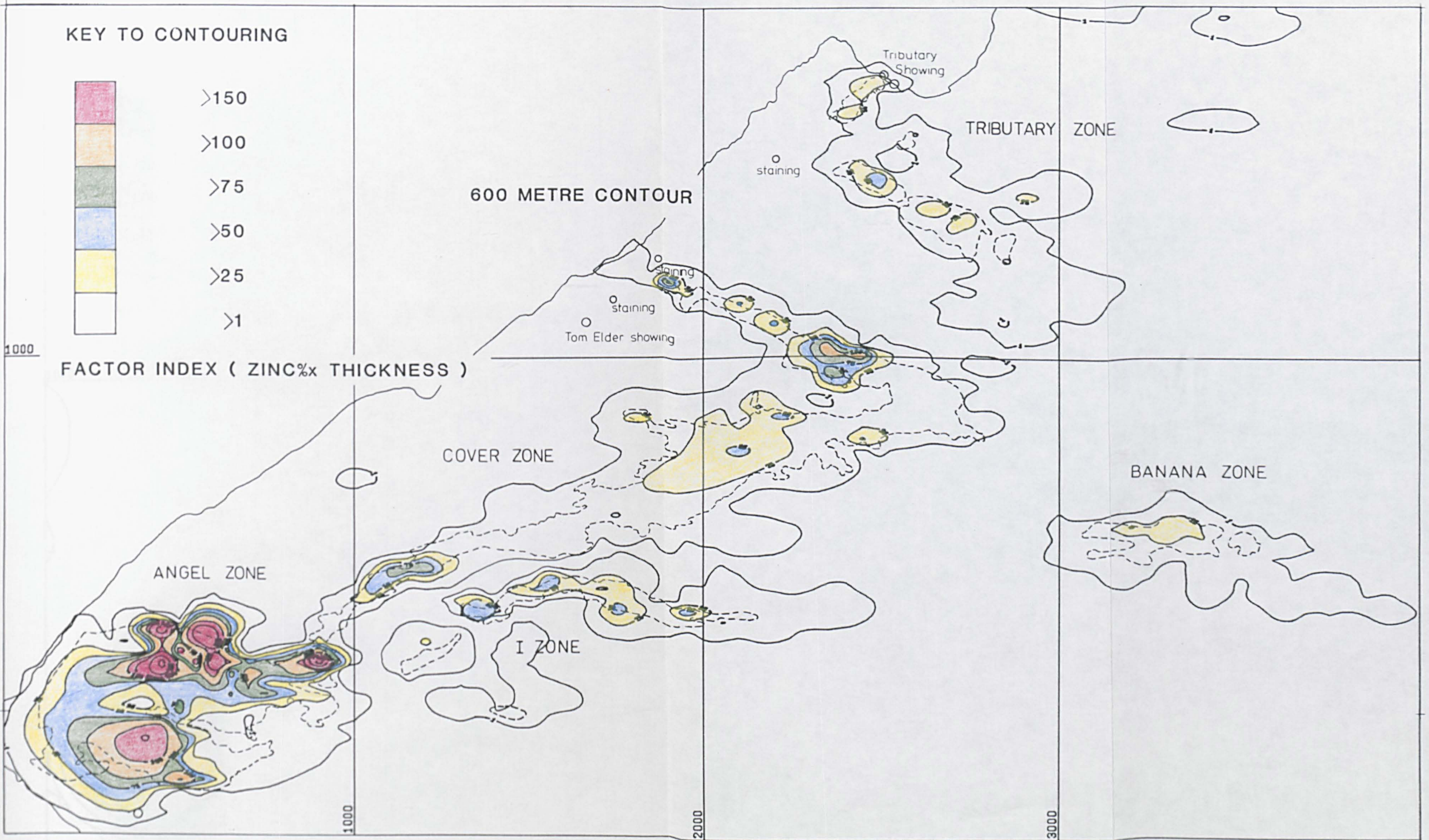


Figure 6.48 PERCENTAGE LEAD CONCENTRATION x ORE THICKNESS FOR THE BLACK ANGEL MINE

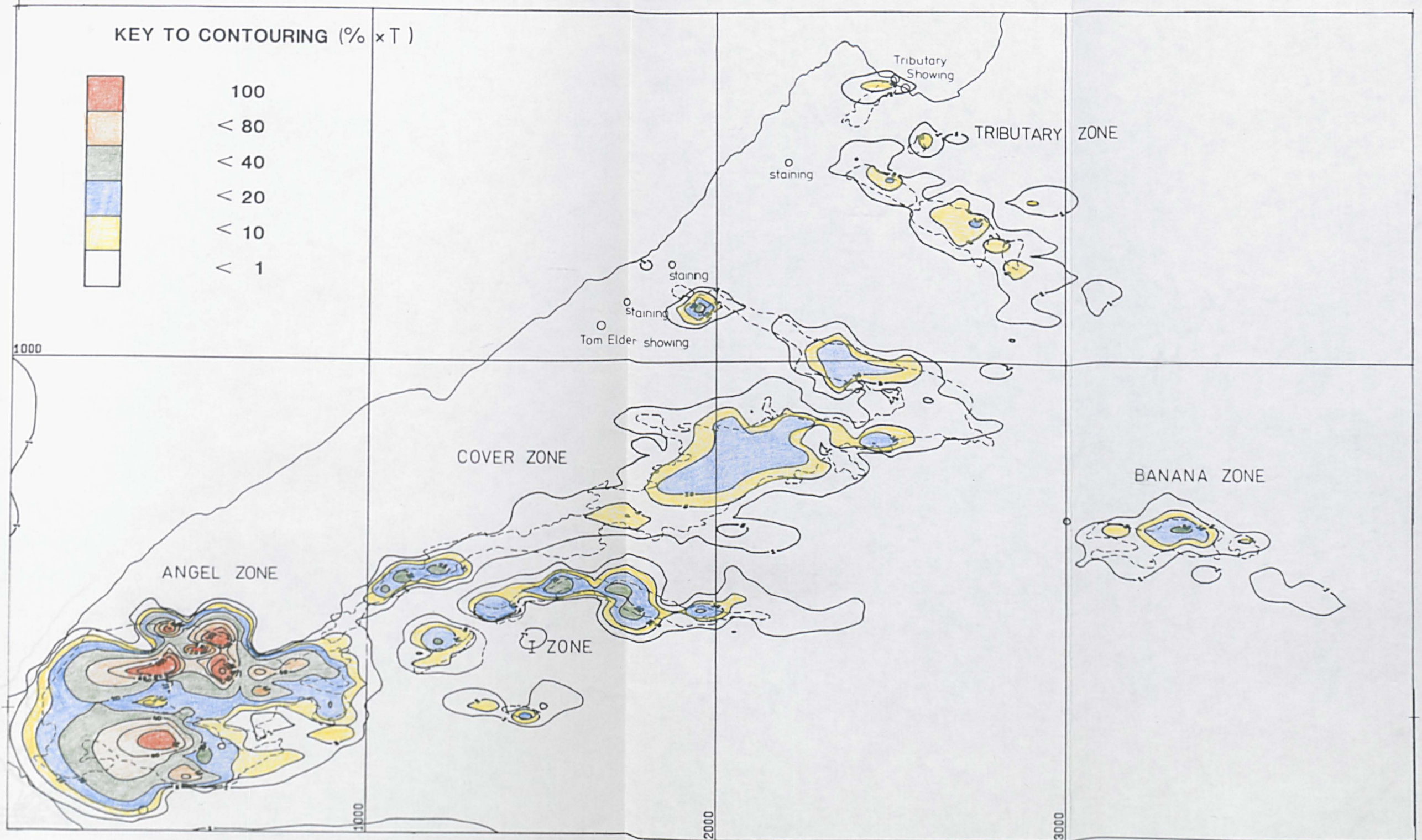
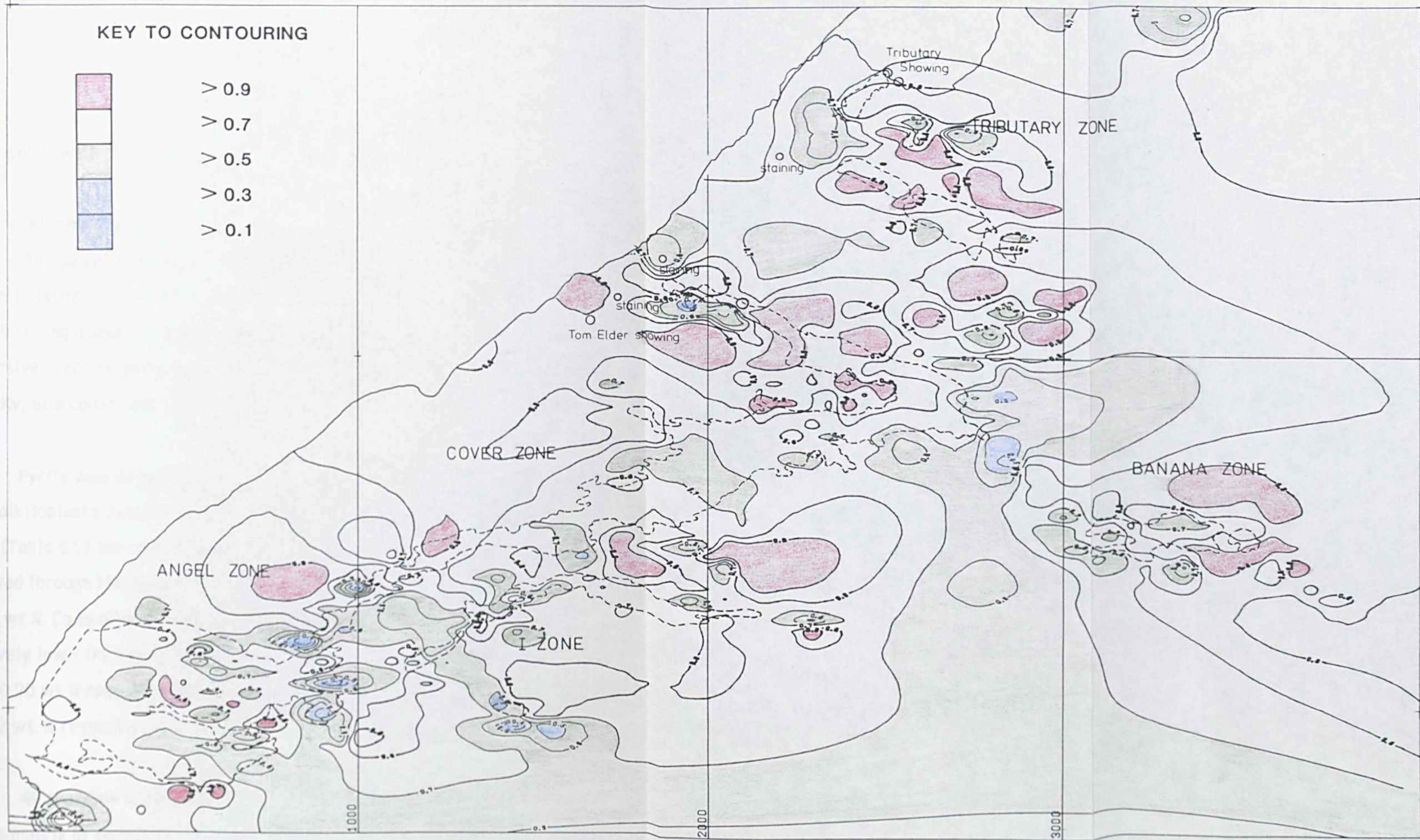


Figure 6.49 ZINC CONCENTRATION AS A PERCENTAGE OF THE TOTAL ECONOMIC METAL CONTENT FOR THE BLACK ANGEL MINE



metal grades, ratios and ore thicknesses are strongly controlled by Rinkian tectonism. D3 structures present the best evidence for the association between tectonism and mineralisation. The fold hinges act as natural beneficiation zones for the ore, as galena and sphalerite are differentially mobilised (at the expense of pyrite) towards these low stress zones. This results in greatly increased ore grades and thickness within these zones. Similar processes probably took place during the D1 event, although due to tectonic overprinting this cannot be substantiated. D2 tectonic slides thin the ore horizon, although tectonic thickening in the central Cover zone corresponds with the highest metal tonnages.

### **c) Mineral chemistry**

Microprobe analyses of ore minerals from specially selected ore tectonite types are given in tables 5.1 and 6.5 to 6.8. The analyses were made by using a JEOL microprobe fitted with a link systems e.d.s. (energy dispersive spectrometer) analytical system using an accelerating voltage of 15 Kv, at a count rate of 2000cps for 90 secs.

Pyrite was selected for analysis from coarse grained aggregates and poikiloblasts in the breccia-textured and pyrrhotite ore tectonite types (Table 6.5). No systematic trace element variation in pyrite has been observed through the deposit in this study. Co and Ni values are generally < 0.20 wt.%. Co is often below the detection limit. Cu values are also relatively low < 0.25 wt.%. Zn and As values average between 0.5 - 0.6 wt. % and 0.20 wt % respectively, but in some cases can be as high as 1.8 wt. % and 1.2 wt. % respectively.

49 analyses were conducted on sphalerite (Tables 5.1 a & b) from the ore matrix of tectonites from the recrystallised ore facies and from sphalerite poikilitically enclosed in pyrite of the breccia-textured ore, pyrrhotite ore and buckshot ore tectonites. These analyses show that there

**Table 6.5: Microprobe analyses of pyrite (in wt.%) from the Black Angel and Nunngarut deposits**

Fe	Cu	Zn	As	Co	Ni	S	Total	Sample
48.354	0.14	0.29	0.11	---	0.31	50.726	99.930	T 172*
48.310	0.28	---	0.28	---	---	51.130	100.020	1170b*
48.248	0.19	---	---	0.13	---	51.451	100.019	1170b*
48.080	0.16	0.35	---	0.16	0.25	50.980	99.980	1170b*
48.070	---	0.09	---	---	---	51.858	100.018	M 160
48.046	0.12	---	0.20	---	0.27	51.324	99.960	T 172*
47.787	0.14	0.17	0.04	---	---	51.820	99.987	P 19
47.662	0.25	0.65	---	---	0.07	51.319	99.951	B 124
47.516	0.23	0.44	0.08	---	0.06	51.599	99.925	M 160
47.356	0.15	0.44	---	---	---	52.018	99.964	T 172*
47.344	0.18	0.92	0.14	---	---	51.415	99.999	M 160
47.119	---	0.35	---	---	0.12	52.352	99.981	P 19
46.985	---	0.88	0.35	---	---	51.821	100.036	B 104
46.968	0.06	0.79	0.13	---	0.28	51.780	100.008	M 160
46.779	---	0.86	1.21	---	---	51.209	100.058	M 160
46.637	0.06	1.88	---	---	---	51.303	100.010	M 160

\* pyrite in pyrrhotite ore tectonite

**Table 6.6: Microprobe analyses (in wt.%) of arsenopyrite from the Black Angel deposits**

Fe	As	S	Co	Ni	Sb	Total	Location	Mole % Fe
43.244	38.938	17.300	---	---	---	99.482	K 126	40.2
44.032	37.679	17.200	---	---	---	98.941	K 126	39.0
42.616	39.572	17.400	---	---	---	99.588	K 126	40.9
42.888	39.332	16.400	---	---	---	98.620	K 126	40.6
44.276	38.358	16.800	0.17	---	---	99.604	K 126	39.2
44.231	38.012	16.800	0.10	0.17	---	99.313	K 126	39.0
44.319	37.939	17.200	0.09	0.20	0.06	99.808	K 126	38.9
43.426	37.459	17.200	0.23	---	0.18	98.495	K 126	39.1
43.996	38.602	16.200	---	---	---	98.798	K 126	39.5

is large variation in the minor element composition, especially the iron and arsenic content. The matrix sphalerite has markedly lower iron (3.83-0.94 wt.%) and arsenic (totally depleted) contents than in the poikiloblastically enclosed sphalerite where iron is 13.73-5.55 wt.% (i.e. 24.2-9.3 mol. %) and arsenic is up to 0.83 wt. %. Maximum values of Co and Ni are 0.27 wt. % and 0.25 wt. % respectively. Cr may be up to 0.54 wt. % and Cd 0.50 wt. %. Although in many cases these minor element concentrations were below the detection limits.

Arsenopyrite analyses (Table 6.6) are of idiomorphic grains in a chalcopyrite matrix associated with tennantite and galena. Application of the arsenopyrite geothermometer (Scott, 1981) is precluded by the absence of equilibrium apy-po assemblages in the Black Angel deposits.

Pyrrhotite was analysed from the footwall pyrrhotitic lenses of the I zone and T zone and also from interstitial material in the Nunngarut deposit and the K zone (Table 6.8). The iron content is fairly constant at 62 wt. % (49 mol. %). Zn content is variable, but may be as high as 1.34 wt. %. When high Zn values are observed low iron values occur, indicating Zn-Fe substitution. Cu values are very low < 0.08 wt. %. Co and Ni values are quite variable up to 0.56 wt. % and 0.26 wt. % respectively. The Co/Ni ratio is  $\approx$  1:1, although absolute ratios cannot be predicted due to the errors involved in e.d.s. analysis.

The tennantite analyses (Table 6.7) are from coarse grained samples that overgrow galena (Fig. 6.35). As values vary between 17-19 wt. %, whilst Sb values are low, < 0.72 wt. %. Fe and Zn ( $\approx$ 4.5 wt. %) substitute for Cu which varies between 51.08 and 52.38 wt. %. Ni occurs in small amounts < 0.11 wt. %, whilst Co was not detected. Ag values are quite constant at approximately 0.5 wt. %, which is low in comparison to those reported in fahlore from the Broken Hill deposits (N.S.W.), where Ag

**Table 6.7: Microprobe analyses of tennantite (in wt.%) from the Black Angel deposits**

Cu	As	Zn	Fe	Ni	Sb	Ag	S	Total	Location
52.11	17.66	4.76	4.68	---	---	0.58	20.17	99.960	K 124
51.33	19.68	4.30	4.85	0.11	---	0.45	19.68	100.400	K 124
52.38	17.34	4.55	4.72	---	0.38	0.40	20.05	99.820	K 126
51.05	17.33	4.91	4.90	---	0.72	0.63	20.18	99.720	K 126
51.78	18.03	4.10	4.77	0.08	0.33	0.52	20.11	99.720	K 126

**Table 6.8: Microprobe analyses of pyrrhotite (in wt.%) from the Black Angel and Nunngarut Deposits**

Fe	Co	Ni	Zn	Cu	S	Total	Location
62.47	0.23	0.21	0.28	---	36.83	100.05	1170b
62.50	0.30	0.26	0.76	0.08	36.20	100.10	1170b
60.90	---	0.19	1.34	---	36.97	99.40	T 172
62.10	---	---	0.20	---	37.07	99.54	K 124
62.00	0.56	---	0.18	---	36.87	99.61	P 19

may be as great as 50 wt. % in some tetrahedrite samples (Both and Stumpfl, 1987). This low Ag content in the tennantite suggests that much of the Ag from the Black Angel deposits (30 p.p.m., Table 6.2) is contained within galena.

Quantitative e.d.s. analysis of galena is not possible because of S-Pb x-ray interference. Semi-quantitative analysis suggested that Ag content was below the detection limit.

## **Chapter 7: Lead Isotope Analysis of the Black Angel Deposits and Mineralisation of the Marmorilik Region.**

### **7.1 Introduction**

A lead isotope analysis of galena and pyrite samples from the Black Angel ore zones and the disseminated mineralisation in the Marmorilik region was conducted at the British Geological Survey lead isotope laboratory, Grays Inn Road, London under the supervision of Dr. Ian Swainbank. The principal aims of the isotopic study were:-

- i) to determine the model age dates for the Zn-Pb mineralisation.
- ii) to predict a source or sources of the lead in the mineralised occurrences and
- iii) to place constraints on the evolution of the Black Angel sulphides and regional mineralisation in the Marmorilik area.

Previous lead isotope analyses in the Marmorilik area have been limited. A lead isotope study on galena from the Black Angel deposits was undertaken by Pedersen (1980a). Pb/Pb dating of the tremolitic and diopsidic marbles of the Marmorilik Formation has been carried out by Kalsbeek, Taylor and Hendrickson (1984) and Taylor and Moorbath (1986). These studies yielded ages of 1.85 Ga. for the carbonates.

### **7.2 Methods of Study**

In this study 32 galena and 5 pyrite samples were analysed for their Pb isotope ratios. The samples were selected from ore zones throughout the Black Angel mine (Fig. 7.1) and from the Nunngarut deposit, the South Lakes Glacier mineralisation, the Ark mineralisation and the V 215 and V 216 drill hole intersections (Fig. 6.1).

The galena analysed was dominantly coarse grained material of the recrystallised ore facies (6.5.6). 3 samples (P72E, P74W, P78W) of fine grained galena from the porphyroclastic ore facies were also analysed, along with 5 coarse grained metamorphic pyrites, with relict primary

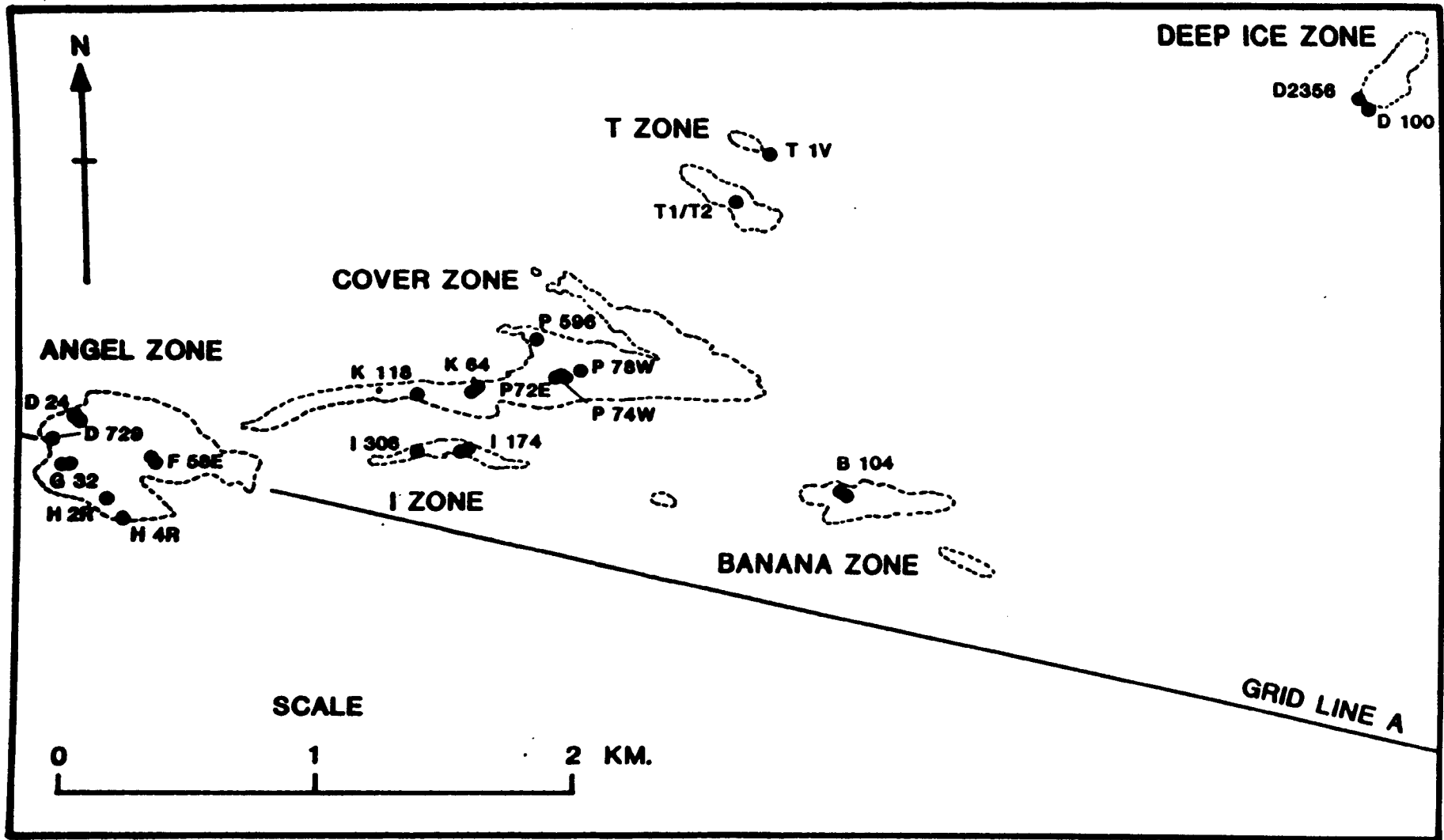


Figure 7.1 LOCATION MAP OF SAMPLES TAKEN FROM THE BLACK ANGEL MINE FOR Pb ISOTOPE ANALYSIS

textures. The pyrite analyses were carried out in an attempt to determine if the lead isotope ratios varied between primary mineralisation and subsequent recrystallisation, and possible remobilisation, during the Rinkian event.

The samples were analysed using a single filament silica gel technique described in appendix 1. The results obtained from these analyses are given in table 7.1.

### 7.3 Results

The lead isotope compositions (table 7.1) have been standardised to the National Bureau of Standards 981 value. The replication of results was possible with a precision of 0.0013%  $Pb^{206}/Pb^{204}$ , 0.002%  $Pb^{207}/Pb^{204}$  and 0.007%  $Pb^{208}/Pb^{204}$  (standard error of the mean).

Sources of error within the analyses may arise from trace amounts of Mercury and Thallium (although none was detected in this study) but the main error is in the precise measurement of the  $Pb^{204}$  isotope (known as the 204 error). Isotopic fractionation during sample preparation and analysis contributes to this error. Fractionation was observed during the running of some samples. These analyses were therefore repeated.

The galena lead isotope analyses (Table 7.1) show a bimodal distribution (Fig. 7.2 a & b). However, the isotopic ratios within individual showings are homogeneous. The main population (population I) encompasses all mineralisation from the Black Angel deposits, the Nunngarut deposit and the South Lakes Glacier showings. Population II encompasses samples from the Ark and the drill hole intersections of V215 and V 216. No significant variation in lead isotope ratios is evident between the different ore tectonite types of the Black Angel deposit.

On the  $Pb^{206}/Pb^{204}$  v  $Pb^{206}/Pb^{204}$  plot (Figure 7.2a) population II has a lower  $Pb^{206}/Pb^{204}$  ratio than population I, suggesting thorium depletion. In Figure 7.2b, Population I can be considered homogeneous,

**Table 7.1: Lead Isotope Ratios From the Black Angel deposits and Marmorilik mineralisation.**

206/204	207/204	208/204	207/206	208/206	LOCATION	SPECIMEN DETAILS
16.2046	15.4391	36.4998	.95277	2.25241	k306	Coarse pyrite
16.1214	15.4241	36.4673	.95675	2.26204	E38	Coarse pyrite
16.1064	15.3980	36.3748	.95596	2.25841	MR-MX	Coarse pyrite
16.1425	15.4582	36.5557	.95761	2.26457	HR	Coarse pyrite
16.1705	15.4522	36.5396	.95558	2.25964	T1/T2	Coarse pyrite
16.1004	15.3877	36.3571	.95574	2.25861	B104	Galena in coarse calcite
16.0991	15.3737	36.3028	.95494	2.25496	D24	Coarse galena and rex quartz
16.0876	15.3705	36.2935	.95543	2.25600	H4R	Coarse galena
16.0898	15.3747	36.3187	.95556	2.25725	P74W	Coarse galena sheared sphal.
16.1024	15.3855	36.3530	.95548	2.25762	I306	Coarse galena in banded ore.
16.0817	15.3675	36.2889	.95558	2.25653	F58E	Coarse galena and rex quartz
16.0855	15.3925	36.3300	.95692	2.25856	T1V	Coarse galena and fine pyrite
16.0900	15.3698	36.3077	.95524	2.25654	Kii K118	Coarse galena & brown sphal
16.0757	15.3745	36.2864	.95638	2.25721	G32	Coarse galena
16.0833	15.3751	36.3038	.95596	2.25722	I592	Coarse galena
16.0909	15.3866	36.3033	.95623	2.25614	T1/T2	Coarse galena pyrite & sphal
16.0995	15.3904	36.3546	.95596	2.25813	K64	Coarse galena
16.0772	15.3870	36.2840	.95707	2.25685	H2R	Coarse galena & bleby sphal.
16.0936	15.3770	36.3119	.95547	2.25630	P792	Coarse galena and rex quartz
16.0854	15.3668	36.2836	.95532	2.25568	D100	Coarse galena and rex. sphal.
16.1080	15.3918	36.2995	.95554	2.25351	I174	Sheared galena, euhedral qtz
16.0969	15.3843	36.3252	.95576	2.25673	P74W	Minor galena in sheared ore
16.0860	15.3858	36.3095	.95653	2.25716	G32	Coarse galena
16.0739	15.3752	36.2524	.95652	2.25534	H2R	Coarse galena in late D3 joint
16.1068	15.3964	36.3606	.95591	2.25787	K64	Galena, quartz
16.1149	15.4096	36.4019	.95626	2.25887	F58E	Coarse galena and rex quartz
16.2105	15.4216	36.2223	.95134	2.23461	SLA13*	Dissem. galena
16.2162	15.4393	36.2282	.95208	2.23401	V215*	Coarse galena & green sphal
16.0939	15.3796	36.3068	.95564	2.25607	B104	Coarse galena and rex quartz
16.1041	15.3849	36.3550	.95538	2.25767	P596	Minor galena in sheared ore
16.1093	15.3941	36.2815	.95569	2.25226	CSL12	Coarse galena rex sphalerite
16.0973	15.3776	36.3286	.95530	2.25691	P59a	Galena in sheared ore
16.2144	15.4152	36.1802	.95076	2.23140	SLA19*	Dissem. galena
16.0900	15.3750	36.2999	.95554	2.25597	P78W	Sheared galena & sheared ore
16.0857	15.3740	36.2994	.95577	2.25667	P72E	Sheared galena & sheared ore
16.1089	15.3871	36.3188	.95524	2.25456	D2356	Coarse galena rex sphalerite
16.2141	15.4332	36.2137	.95183	2.23343	V216*	Coarse galena in banded ore

\* = Population II data

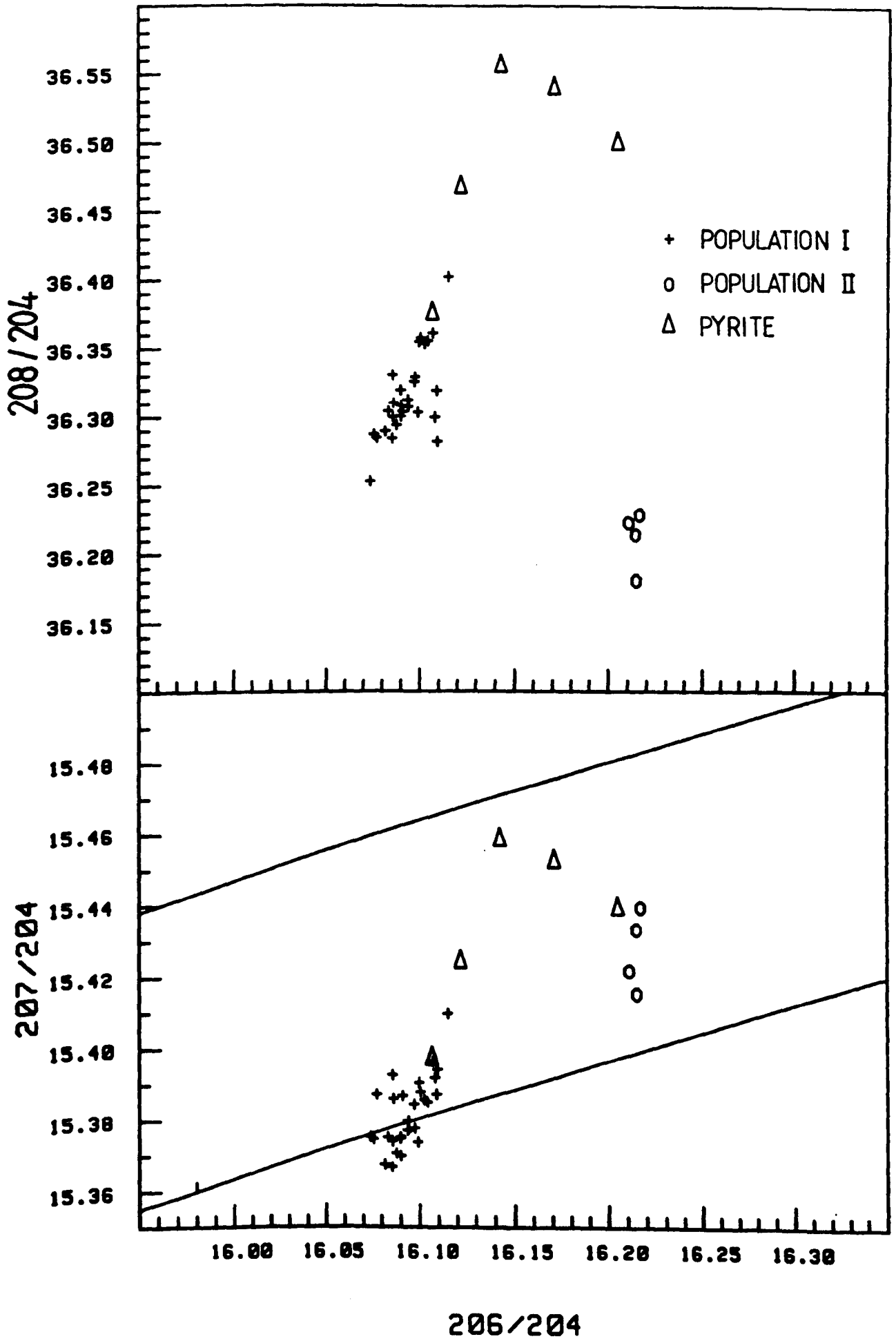


**Figure 7.2** Distribution patterns of lead isotope analyses from the Black Angel deposits and surrounding mineralisation

although a  $Pb^{204}$  fractionation trend is depicted (Fig. 7.2). Population II is seen to be slightly more radiogenic (i.e. higher  $Pb^{206}/Pb^{204}$  values) than Population I. Average source conditions for the two populations are:-

Population I  $\mu = 8.83 - 8.90$   $K = 4.37$

Population II  $\mu = 8.97 - 9.04$   $K = 4.24 - 4.25$

where  $\mu$  is  $(U^{238}/Pb^{204})$ ,  $K$  is  $(Th^{232}/U^{238})$

The pyrite lead isotope data are scattered (Fig. 7.2). In Figure 7.2b, the data define a curved distribution trend that links the two galena lead isotope populations. In Figure 7.2a the data define a curved trend which is linked to population I. These curved trends may be partially the result of  $^{204}Pb$  fractionation.

#### 7.4 'Model Age' dates

Model age dates for the Black Angel mineralisation have been calculated using two theoretical models of lead isotope evolution, namely the; two-stage lead isotope model (Stacey and Kramers, 1975), lead isotopes in a continually changing earth (Cumming and Richards, 1975).

##### a) Stacey and Kramers (1975) : Two stage lead isotope model

This model involves a two stage lead isotope evolution separated by an event at 3.7 Ga. where differentiation processes in the Earth brought about the conditions which gave rise to an average lead isotope composition.

On plotting the Black Angel data set onto Stacey and Kramers  $Pb^{207}/Pb^{204}$  v  $Pb^{206}/Pb^{204}$  average growth curve (Figure 7.3) the data lie close to the evolution curve at the 1.5Ga. isochron. The 'model ages' of the ore deposit when computed using this model are  $1502 \pm 7$  ma. for population I and  $1480 \pm 4.5$  ma. for population II.

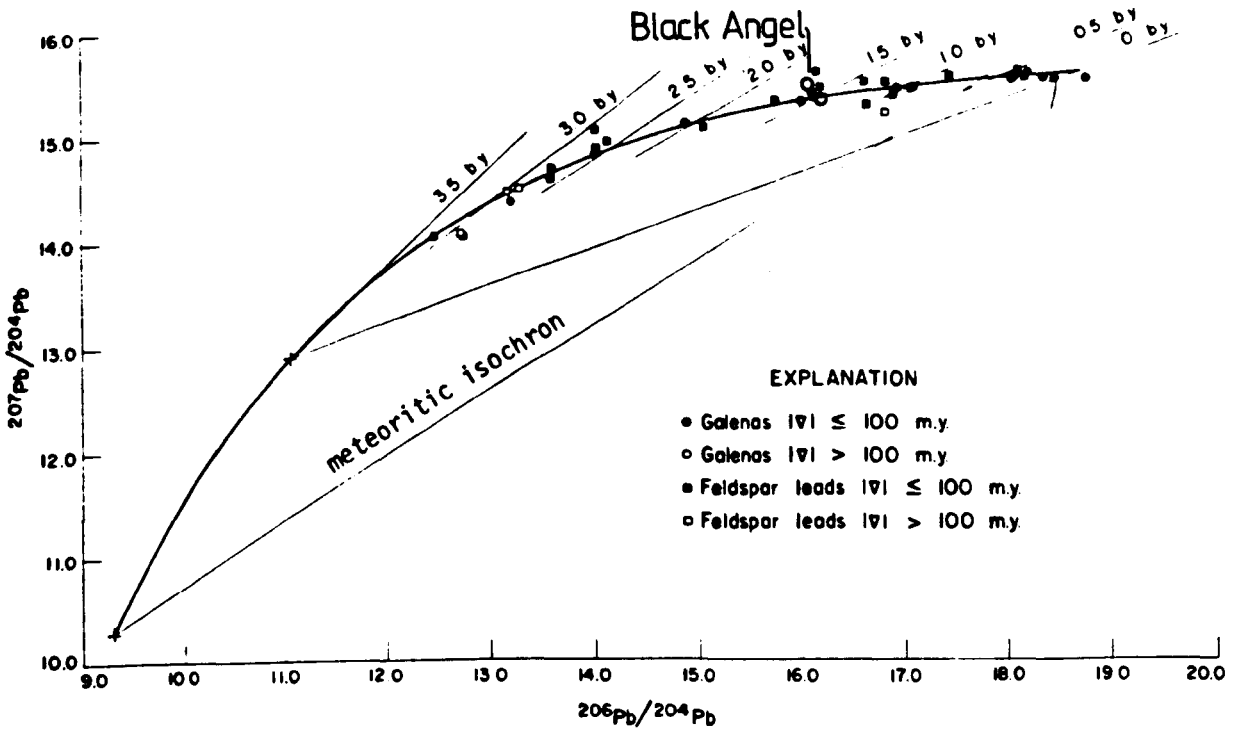


**Figure 7.3** Black Angel data plotted onto Stacey and Kramers (1975) two stage model growth curve. Closed symbols are used for lead samples where the model age is within 100ma. of the accepted age  $\mu_1 = 7.19$ ;  $\mu_2 = 9.74$  for average modern lead. Second stage beins at 3.7 b.y. ago.

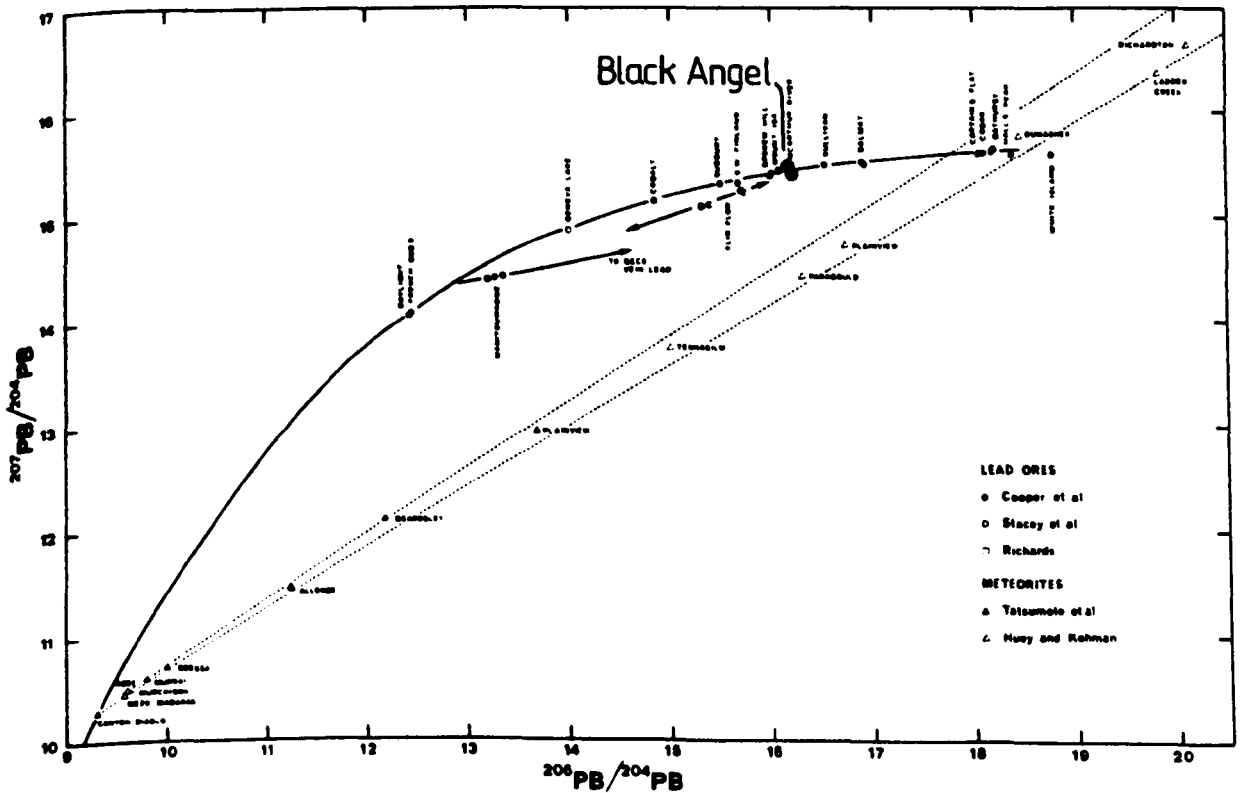


**Figure 7.4** Black Angel data plotted onto Cumming and Richards (1975) single stage growth curve ( Solid line), along with other  $^{207}\text{Pb}/^{204}\text{Pb}$  vs  $^{206}\text{Pb}/^{204}\text{Pb}$  ratios for some ore leads and meteorites.

b) Cumming and Richards (1975) : lead isotopes in a continuously changing Earth.

This model invokes continually evolving U/Pb and Th/Pb ratios in the Earth to explain the discrepancies between lead isotope 'model ages' and geologically inferred ages. This model is the second approach to a mathematical modelling of the Earth's Lead isotope system and develops an average growth curve as seen in Figure 7.4.

On plotting the data from this present study onto Cumming and Richards (1975) single stage growth curve (Fig.7.4) it is seen that the two populations lie close to the growth curve. Model ages computed from this model are for population I of  $1470 \pm 7.2$  ma., population II  $1441 \pm 10.7$  ma. These ages are slightly younger than those calculated from Stacey and Kramers model.

The 'model age' dates computed from these theoretical models give ages of mineralisation at  $\approx 1500-1440$  ma., which are anomalous (too young) with respect to the published age of  $1860-1680$  ma. (Rb-Sr and K-Ar analyses) for the Rinkian event (Larsen and Møller 1968; Bridgewater 1971; Kalsbeek 1981; Andersen and Pulvertaft 1986). The 'model ages' therefore do not represent the true age of mineralisation and the lead isotope ratios are radiogenic.

It is likely that the radiogenic and homogeneous character of the lead isotope ratios are the result of metamorphism and remobilisation of the Black Angel sulphide deposits during the Rinkian event.

However as radiogenic lead is concentrated in incompatible and interstitial sites in the host material (LeHuray, 1984), the presence of radiogenic lead in the Black Angel deposits may imply that the lead was leached from upper crustal source rocks by hydrothermal fluids (Ludwig and Silver, 1977).

## 7.5 Discussion

### 7.5.1 Lead source

Doe and Zartman (1979, 1981) developed a lead isotope evolution model called 'Plumbotectonics' that stressed the role of dynamic geological processes of the mantle and crust in determining lead isotope composition. The Plumbotectonics model (Doe and Zartman, 1979 & 1981) is an attempt to model the geochemical behaviour of U, Th, Pb, through geological time. In this model three lead reservoirs (the upper crust, the lower crust and the mantle) are in dynamic communication with each other through the orogene growth curve. The orogene growth curve is derived from Cumming and Richards (1975) single stage growth curve and may be taken to represent the average growth curve for lead isotope evolution (Fig. 7.5). The orogene itself represents an efficient homogenising process of sedimentation, volcanism, plutonism, metamorphism, and rapid erosional turnover, which tends to erase much of the lead isotope diversity that accrues in the mantle, upper crust and lower crust. Thus the 'Plumbotectonics' model has great applications in defining the source of ore lead.

On the 'Plumbotectonics'  $Pb^{208} / Pb^{204}$  v  $Pb^{206} / Pb^{204}$  plot (Fig. 7.5a), the data lie between the orogene and lower crustal evolution curves. This suggests that the lead evolved in slightly enriched Th/U environment (Fig. 7.6). Population I data and the pyritic data plot closer to the lower crustal growth curve than population II data. The dispersion of population I data (Fig. 7.5a), between the orogene curve and the lower crust evolution curve, suggests a lower crustal contamination possibly from Archean derived sediments. Population II data is relatively depleted in thorium and therefore represents a higher crustal lead source than population I data.

Population I data lie very close to the orogene curve in the  $Pb^{207} / Pb^{204}$  v  $Pb^{206} / Pb^{204}$  plot (Figure 7.5b), whereas population II data tend to be displaced towards the upper crustal curve. The pyritic data is strongly displaced towards the upper crustal curve.

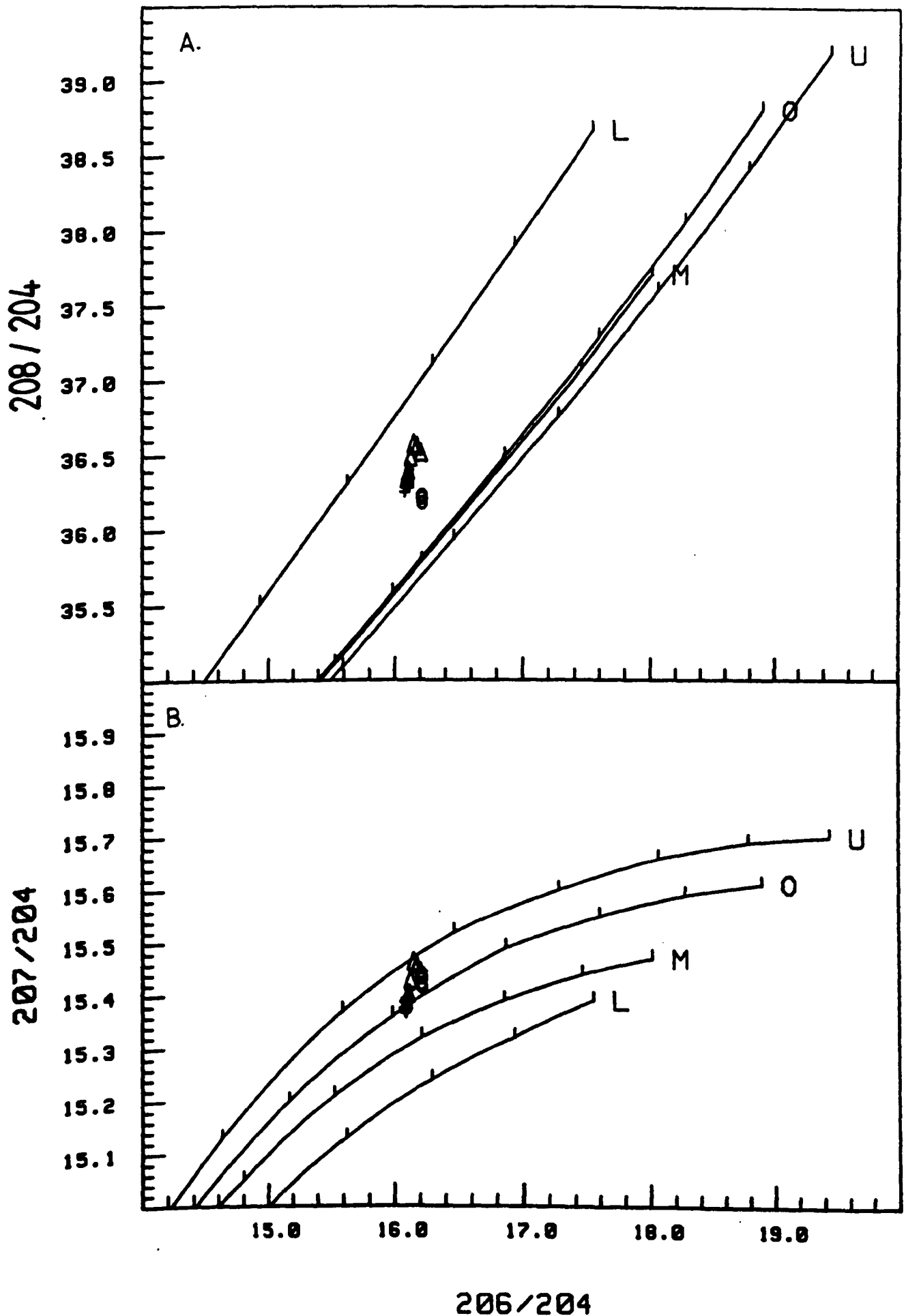


**Figure 7.5** Black Angel lead isotope data plotted onto an expanded Plumbotectonics plot (Doe and Zartman, 1979). M= Mantle growth curve; O= Orogene growth curve; L= Lower crustal growth curve and U= Upper crustal growth curve. Tick marks along each curve represent 0.4 b.y. increments.

The two homogeneous data sets may be accounted for if Rinkian deformation brought about partial re-equilibration of the sulphides during the polyphase event; if the lead was derived from slightly differing source regions; or if mineralisation occurred at slightly different times, as suggested by the 'model age' dates (section 7.4). Pyritic lead isotope compositions plot between the two galena populations. This possibly suggests that mixing took place during mineralisation between lead isotope compositions that were derived from separate sources.

The affinity of the isotopic data to the orogene and upper crustal lead curves (Figs. 7.2b & 7.5b), predicts that the ore lead was derived from an upper crustal source with reworking during the Rinkian event. The homogeneity of data also points to an upper crustal source of lead from a reworked sedimentary basin. For as Vaasjoki and Gulson (1986) have stated:-

'isotopically homogeneous leads, whether radiogenic or not, are most likely to occur in areas where the emplacement of thick sedimentary piles has allowed the homogenisation of lead through prolonged mechanical and geochemical reworking and lateral transportation into zones favourable for ore deposition.'

If the ore leads were derived from an upper crustal lead source, it is likely that the lead was leached from feldspathic material within the meta-quartzites and psammities of the Qeqertarsuaq Formation (see section 9.4.3 a). Uranium and thorium do not substitute into the feldspar lattice. Therefore feldspar leads tend to be non-radiogenic as compared to values for bulk crustal leads. The Qeqertarsuaq Formation may have acted as a 'holding sediment' (Doe and Delevaux, 1972) prior to the final transport of the metals. A repetition of two cycles of erosion-sedimentation-remobilisation (leaching) can result in isotopically homogeneous lead (Vaasjoki and Gulson, 1986).

The lithologies of the Nukavsak Formation are not regarded as a

suitable lead source. Uranium and thorium are preferentially bonded to clay minerals. . . . Leaching of lead from the U/Th-rich pelitic lithologies would generate highly radiogenic 'J' type leads.

The presence of lower crustal (thorogenic) isotopic characteristics in the lead (Fig. 7.5a) may be due to the lithologies of the Qeqertarsuaq Formation having been derived from the Basement Archean Umanak Gneiss (section 3.2).

### 7.5.2 Comparison of Black Angel lead isotopic data with other carbonate-hosted deposits

In this section, an attempt is made to compare the isotopic signatures of the Black Angel deposit with those of other major carbonate hosted Zn-Pb deposits. However the lead isotope compositions have been strongly homogenised during the Rinkian tectono-metamorphic event, and consequently their pre-metamorphic composition may be severely masked.

Doe and Zartman (1979) observed that lead isotope data for carbonate hosted ore deposits fell into three distinct categories, namely:-

- i) Normal homogeneous data: as in the case of Pine Point (Cumming and Robertson, 1969; Godwin et al., 1982), Irish deposits of Silvermines and Tynagh (Boast et al., 1981) and the Silesian deposits (Ridge and Smolarski, 1972; Zartman et al., 1979).
- ii) Slightly radiogenic homogeneous data: as in the case of Sorby Hills (Vaasjoki and Gulson 1986)
- iii) Highly radiogenic heterogeneous data ( $Pb^{206}/Pb^{204} > 20$ ): as in the case of the Mississippi Valley type (M.V.T.)(Heyl et al., 1974)

The lead isotope distributions for Black Angel deposits and the Marmorilik mineralisation (Figs. 7.2 & 7.5) represent 'normal' leads when compared with the deposits in these categories (Fig. 7.6). Figure 7.6 suggests a relationship between the Black Angel mineralisation and the deposits of category (i). However, the difference between the 'model age'

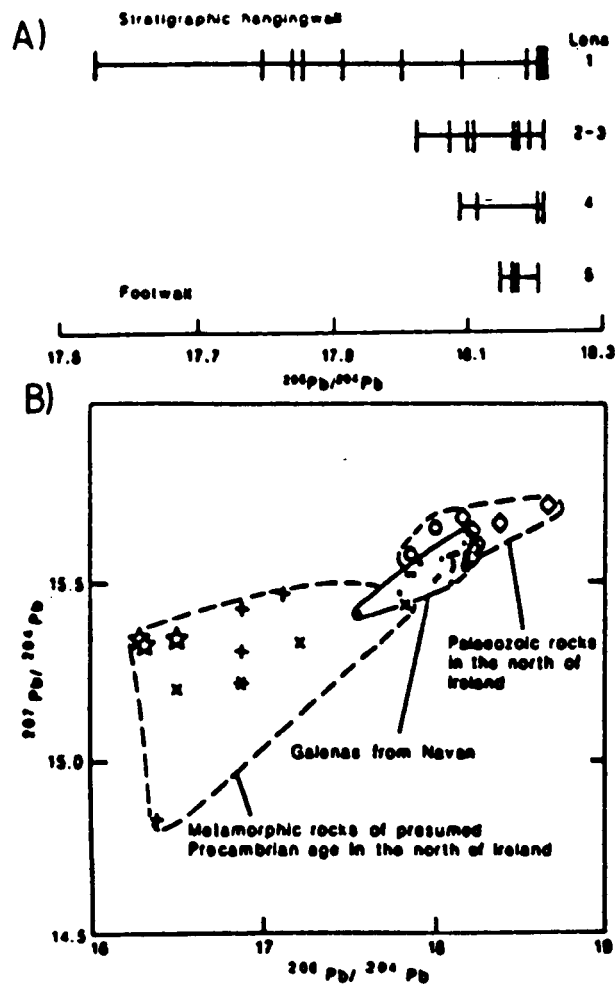


**Figure 7.6** a) Variation in  $^{206}\text{Pb}/^{204}\text{Pb}$  in galenas with stratigraphic height in the Navan orebody (After Mills et al., 1987).  
 b) Lead isotope data for Navan galenas compared with age corrected data for rock types in the north of Ireland.

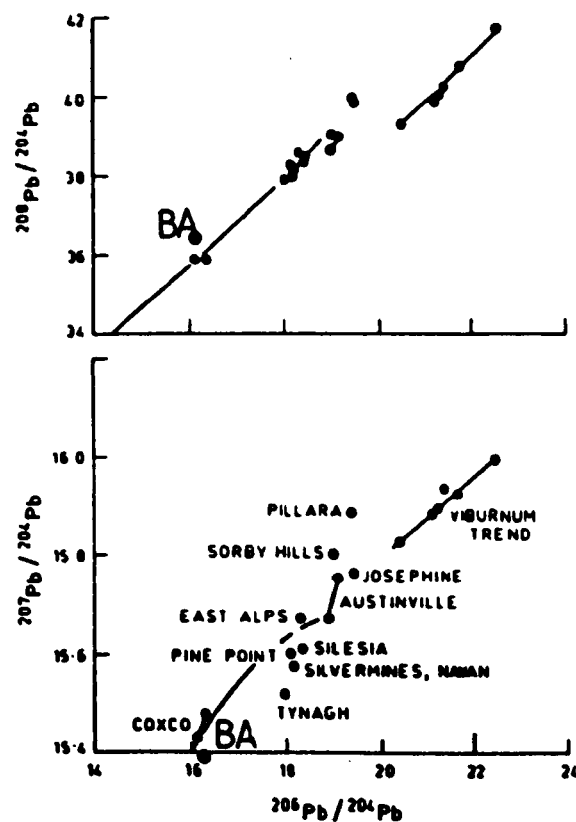


**Figure 7.7** Comparison of high quality lead isotope data from carbonate-hosted base metal deposits with the black Angel deposits. Growth curve from Cumming and Richards (1975). (Modified from Vaasjoki and Gulson, 1986).

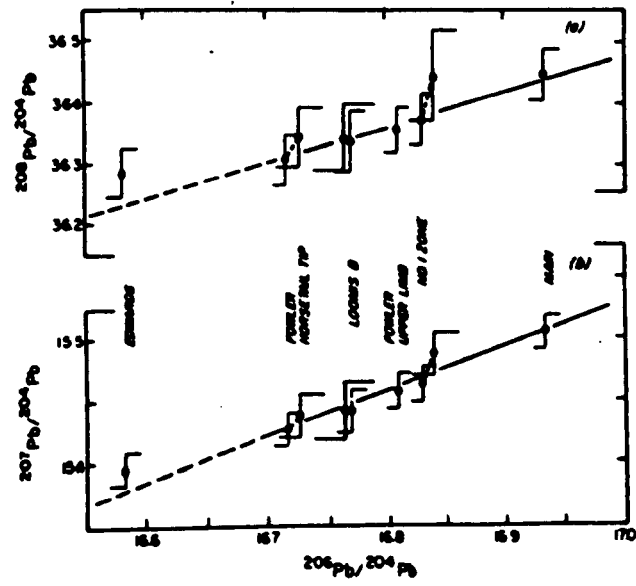


**Figure 7.8** Lead isotope compositions of Balmat-Edwards galenas. (After Fletcher and Farquhar, 1982).

and real age of mineralisation infers that the lead is radiogenic (section 7.4). The Black Angel deposits clearly do not compare isotopically to the highly radiogenic distributions typical of M.V.T mineralisation.

Recent studies of the Navan base-metal deposits (Boast et al., 1981; Mills et al., 1987) have shown that lead isotope compositions become increasingly diverse, but on average less radiogenic, with time (Fig. 7.7). This isotopic distribution has been explained by the theory that the deposits formed through expulsion of downward excavating, hydrothermal brines (Russell, 1983) (section 9.4.4 a), which scavenged progressively less radiogenic basement rocks. The isotopic characteristics of the Navan deposit are not compatible with the Black Angel data. The close genetic associations between the Navan and the Tynagh and Silvermines deposits, may suggest that Black Angel deposits are more closely related isotopically to the Pine Point and Silesian deposits of category (I).

Possibly the closest geological analogue of the Black Angel deposits are the polydeformed, metamorphic Balmat-Edwards Zn-Pb deposits. These sulphide deposits have recently been interpreted as syn-sedimentary ores (Whelan et al., 1984). Lead isotope compositions show a small but distinct range of values (Fletcher and Farquhar, 1982) which lie on linear mixing lines (Fig. 7.8). The lead is interpreted to be derived from both a radiogenic and a non-radiogenic source with a significant mantle component. The latter source is likely to be the Grenville series metasediments and volcanoclastics. The Black Angel isotopic data does not compare well with these isotopic distributions.

In summary, the Black Angel lead isotope compositions are more closely related to the Pine Point and Silesian deposits than any other carbonate-hosted deposits.

## Conclusions

i) Lead isotopic 'Model ages' of mineralisation, at 1502-1440 ma., are young with respect to the inferred geologic age, 1860-1680 ma. and therefore represent radiogenic lead.

ii) The galena lead isotope ratios from the Black Angel deposits and mineralisation in the Marmorilik area give a bimodal distribution. This may reflect changing lead isotope U/Th/Pb compositions in the source environment. Pyrite lead isotope compositions lie between the two data sets. This possibly suggests that mixing took place between lead isotope compositions from separate sources during mineralisation.

iii) The homogeneity of data is likely to be a response to the remobilisation and metamorphism of the sulphide ores during Rinkian metamorphism and deformation.

iv) The close affinity of the data to the orogene/upper crustal evolution curves in the Plumbotectonics model suggests a derivation of ore lead from a reworked sedimentary basin with no mantle contribution. The feldspar-rich psammites of the Qeqertarsuaq Formation are the most probable lead source. The thorogenic nature of the lead may be due to an Archean Basement derivation for the Qeqertarsuaq Formation psammites.

## **Chapter 8. A stable isotope study of the Black Angel sulphides and host rocks**

### **8.1 Introduction.**

This chapter presents the results of a stable carbon, oxygen and sulphur isotope study on the Black Angel sulphides, the surrounding Zn-Pb mineralisation, and the carbonate lithologies of the Karrat Group. The analyses were carried out at the British Geological Survey Sulphur Isotope Laboratories, Gray's Inn Road, London, under the supervision of Dr. Baruch Spiro. Several analyses were also carried out at Wallingford and the Scottish Universities Research Reactor Centre (S.U.R.R.C.), East Kilbride, due to failures of the mass spectrometer at the British Geological Survey.

No previous sulphur isotope work has been carried out on the Black Angel deposits. However, Garde (1977) carried out a carbon and oxygen isotope study on the Marmorilik Formation carbonates.

This isotopic study is aimed at determining:-

- (i) the stable isotopic characteristics of the massive Black Angel sulphides and mineralisation in the host rock carbonates and metapelites.
- (ii) the equilibration temperatures of ore sulphides and host rocks,
- (iii) the significance of the isotopic characteristics to ore formation, metamorphism and remobilisation.

## 8.2 Methods of Analysis

20 sulphur isotope analyses were carried out on; pyrite poikiloblasts and sphalerite/galena pairs from the Black Angel ore bodies, on pyrite from the Agpat Nunngarut and South Lakes Glacier deposits, and pyrite and pyrrhotite from the metapelites of the Nukavsak Formation (Fig. 6.1 & 6.2).

18 carbon isotope analyses were performed on graphite/carbonate pairs from graphitic marbles of the Marmorilik Formation. The analyses were aimed at defining the peak metamorphic temperature throughout the Marmorilik Formation by using the graphite/carbonate geothermometer (Bottinga, 1969; Wada, 1977; Ohmoto and Rye, 1979). 9 oxygen isotope analyses were also carried out on the carbonate samples.

Details of the preparation techniques used for the mass-spectrometric measurements are given in appendix 2. Sources of error in the analyses may be obtained from trace amounts of mineral contaminant. The main error is in the accurate determination of  $\delta^{34}\text{S}$ ,  $\delta^{13}\text{C}$  or  $\delta^{18}\text{O}$  isotope. Isotopic fractionation during sample preparation led to one sulphur sample being lost.

## 8.3 Results

### 8.3.1 Carbon Isotopes

The results of the carbon isotope analyses have been standardised to the PDB standard. The carbon isotopic compositions are expressed, in per mil, as:-

$$\delta^{13}\text{C}_{\text{sample}} = \left[ \left( \frac{^{13}\text{C}}{^{12}\text{C}} \right)_{\text{sample}} / \left( \frac{^{13}\text{C}}{^{12}\text{C}} \right)_{\text{standard}} - 1 \right] \times 1000$$

Results from the carbon isotope analyses are given in table 8.1a and depicted in figure 8.1. The graphite shows a narrow range of  $\delta^{13}\text{C}$  values between - 6.89 to -10.42 ‰. The  $\delta^{13}\text{C}$  values for the graphite

**Table 8.1a: Carbon and oxygen isotope data from the Marmorilik Formation carbonates**

Location	$\delta^{18}\text{O}_c$	$\delta^{13}\text{C}_c$	$\delta^{13}\text{C}_g$	$\Delta_{c-g}$	$T^\circ\text{C}$	Lithological description
V 215 F	-11.31	-0.06	-8.28	8.22	432	Fine graphite in Up. Marmorilik
V 197	13.17	-2.13	-6.89	4.76	753	Dark grey graphitic calcite marble
DIZ	-13.76	-0.06	-7.80	7.74	472	Wispy graphite in calcite marble
DIZ 1620	-7.50	+0.51	-10.32	10.83	319	Footwall Black Angel deposits
MX	-13.83	-1.03	-9.45	8.42	420	Grey banded calcite dolomite marble
I 413	-11.77	-5.82	-9.09	3.27	1170	Footwall I zone, graphitic calcite
389	-11.61	-1.32	-9.09	7.77	476	Unit 3 Graphitic calc-dolomite (T 1)
408	-10.50	-1.76	-10.42	8.66	408	Unit 3 Grey calcite dolomite. MP 5
858	-8.29	+0.23	-10.04	10.27	330	Graphitic dolomite, Unit 1

**Table 8.1b Sulphur isotope compositions of sulphides from the Black Angel deposit and surrounding mineralisation**

Location	$\delta^{34}\text{S}_p$	$\delta^{34}\text{S}_{sp}$	$\delta^{34}\text{S}_g$	$\Delta^{34}\text{S}$	$T^\circ\text{C}$	Lithological setting
E. 40	---	3.96	2.66	1.30	410	Coarse rex. sp-gn pair
L. 66	---	3.54	2.57	0.97	477	Coarse rex. sp-gn pair
D.I.2 2356	---	2.57	1.59	0.98	475	Coarse rex. sp-gn pair
V. 216	---	2.45	0.50	1.95	328	Coarse rex. sp-gn pair
M.72	2.83	---	---	---	---	Py. Poikiloblast in sheared ore
E.36	4.76	---	---	---	---	Coarse rex py.
T.2	4.96	---	---	---	---	Coarse rex py.
E. 46	4.99	---	---	---	---	Coarse rex py.
CSL. 12	4.52	---	---	---	---	Dissem. fine py.
Nungerutt	6.72	7.22	---	---	---	Py. idioloblast in sheared sp. ore
Agpat	9.00	---	---	---	---	Py. idioloblast in sheared sp. ore
Sorte Nunatak	7.42	---	---	---	---	Massive py. in pelitic schist
V133 (* = po)	11.78*	---	---	---	---	Rex. po. in graphitic schist

	Avg. wt % carbonate	$\delta^{18}\text{O}$	Mean	$\delta^{13}\text{C}$	Mean	Reference
<b>Granulite Facies Marbles</b>						
54 calcites, Adirondack Mts., N.Y.	62	12.3 to 26.1	19.0	-7.2 to 2.4	0.0	(1)
6 calcites, Grenville Province, Ont.		16.6 to 23.6	20.7	0.5 to 5.0	1.7	(2)
12 calcites, Gour Oumelalen, Algeria		15.7 to 22.8	19.7	-2.8 to 0.0	-0.9	(3)
10 calcites, Limecrest Quarry, N.J.		17.7 to 19.5	18.6	-0.6 to 0.1	-0.1	(3)
<b>Middle and Upper Amphibolite Facies Marbles</b>						
21 calcites, Adirondack Mts., N.Y.	87	16.8 to 27.2	21.8	-4.6 to 5.0	0.3	(1)
8 dolomites, Adirondack Mts., N.Y.	94	21.0 to 23.8	22.1	-0.3 to 2.9	1.3	(1)
9 carbonates, Balmat Zn-Pb Mine, N.Y.		24.8 to 27.0	25.6	-1.6 to 1.4	0.8	(4)
13 calcites, Grenville Province, Ont.		16.2 to 27.8	22.2	-1.5 to 3.7	0.8	(5)(6)
<b>Lower Amphibolite and Greenschist Facies</b>						
47 calcites, Grenville Province, Ont.	53	18.1 to 28.1	21.4	-0.3 to 5.6	3.0	(5)
<b>Unmetamorphosed Carbonates, 1.0-2.0 b.y.</b>						
37 calcites and dolomites		11.3 to 26.2	20.7	-6.0 to 6.0	0.3	(7)

References: (1) Valley and O'Neill (1984). (2) Valley and O'Neill (1981). (3) Pincus et al. (1976). (4) Whelan et al. (1984). (5) Dunn and Valley (1983). (6) Shih et al. (1976). (7) Veizer and Hoefs (1976).

**Table 8.1c Oxygen isotopic ratios for carbonate in unmetamorphosed carbonates to granulite facies marbles (After Valley, 1986).**



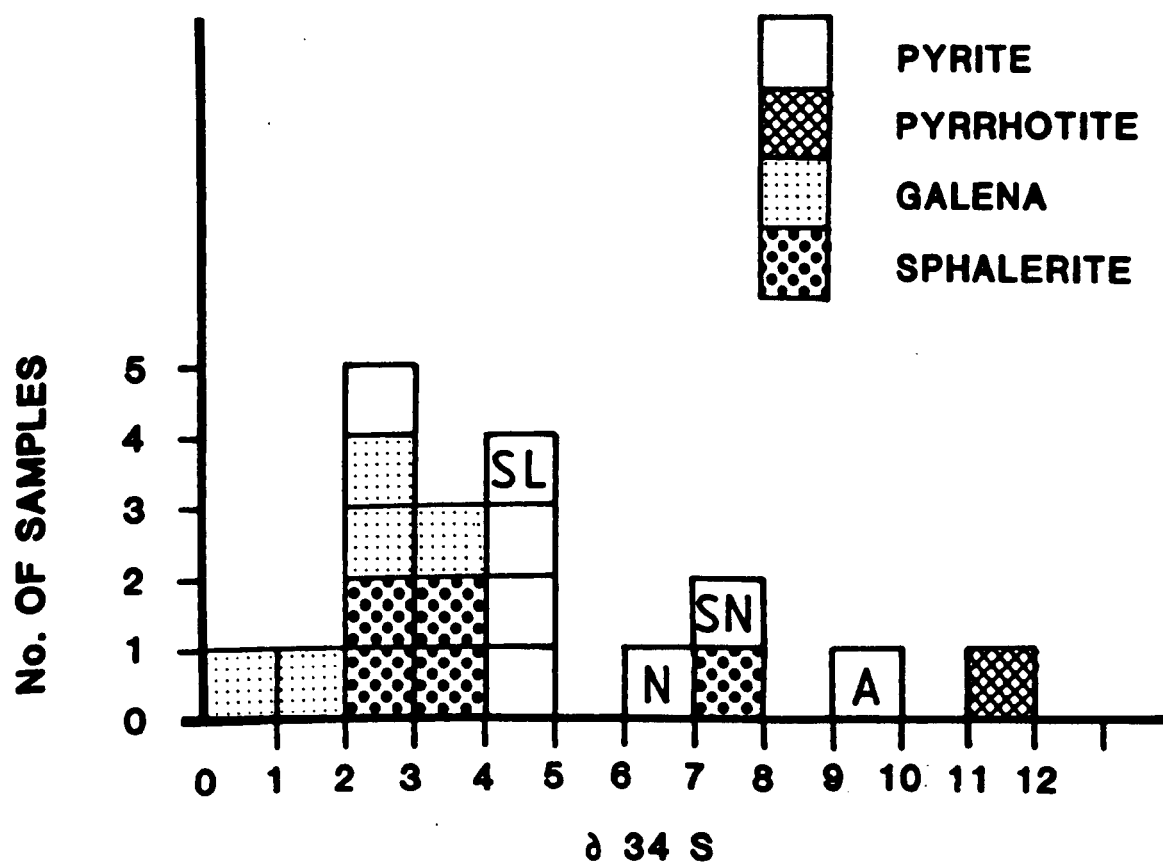


**Figure 8.2** Schematic representation of sulphur isotopic data from the Black Angel mine and surrounding mineralisation. SL - South Lakes, N - Nunngarut, SN - Sorte Nunatak (Nukavsak Formation), A - Agpat.

Compounds	(T in °K)				T(°C) Range
	A	B	C	D	
CaMg(CO <sub>3</sub> ) <sub>2</sub> <sup>a</sup>	-8.914	8.737	-18.11	8.44	≤ 600
CaCO <sub>3</sub> <sup>b</sup>	-8.914	8.557	-18.11	8.27	≤ 600
HCO <sub>3</sub> <sup>-c</sup>	0	-2.160	20.16	-35.7	≤ 290
CO <sub>3</sub> <sup>2-d</sup>	-8.361	8.196	-17.66	6.14	≤ 100
H <sub>2</sub> CO <sub>3</sub> (ap) <sup>e</sup>	0	0	0	0	≤ 350
CH <sub>4</sub> <sup>f</sup>	4.194	-5.210	-8.93	4.36	≤ 700
CO <sup>g</sup>	0	-2.84	-17.56	9.1	≤ 330
C(graphite) <sup>h</sup>	-6.637	6.921	-22.89	9.32	≤ 700

<sup>a</sup>Based on empirical fractionation factors between dolomite and calcite of Sheppard and Schwarcz (1970).

<sup>b</sup>Polynomial fit of values calculated by Bottinga (1969).

<sup>c</sup>Polynomial fit of experimental data of Malinin et al. (1967), Deuser and Degens (1967), Wendt (1968), Emrich et al. (1970), Mook et al., (1974), and Vogel (1961).

<sup>d</sup>Polynomial fit of values calculated by Thode et al. (1965).

<sup>e</sup>Estimated in Ohmoto (1972) on the basis of H<sub>2</sub>CO<sub>3</sub>(ap) = CO<sub>2</sub>(aq) + H<sub>2</sub>CO<sub>3</sub>.

<sup>f</sup>Polynomial fit of values calculated by Bottinga (1968).

<sup>g</sup>Polynomial fit of values calculated by Urey (1947).

**Table 8.2** Equilibrium isotopic fractionation factors of carbon compounds with respect to CO<sub>2</sub>. (From Hoefs, 1980)

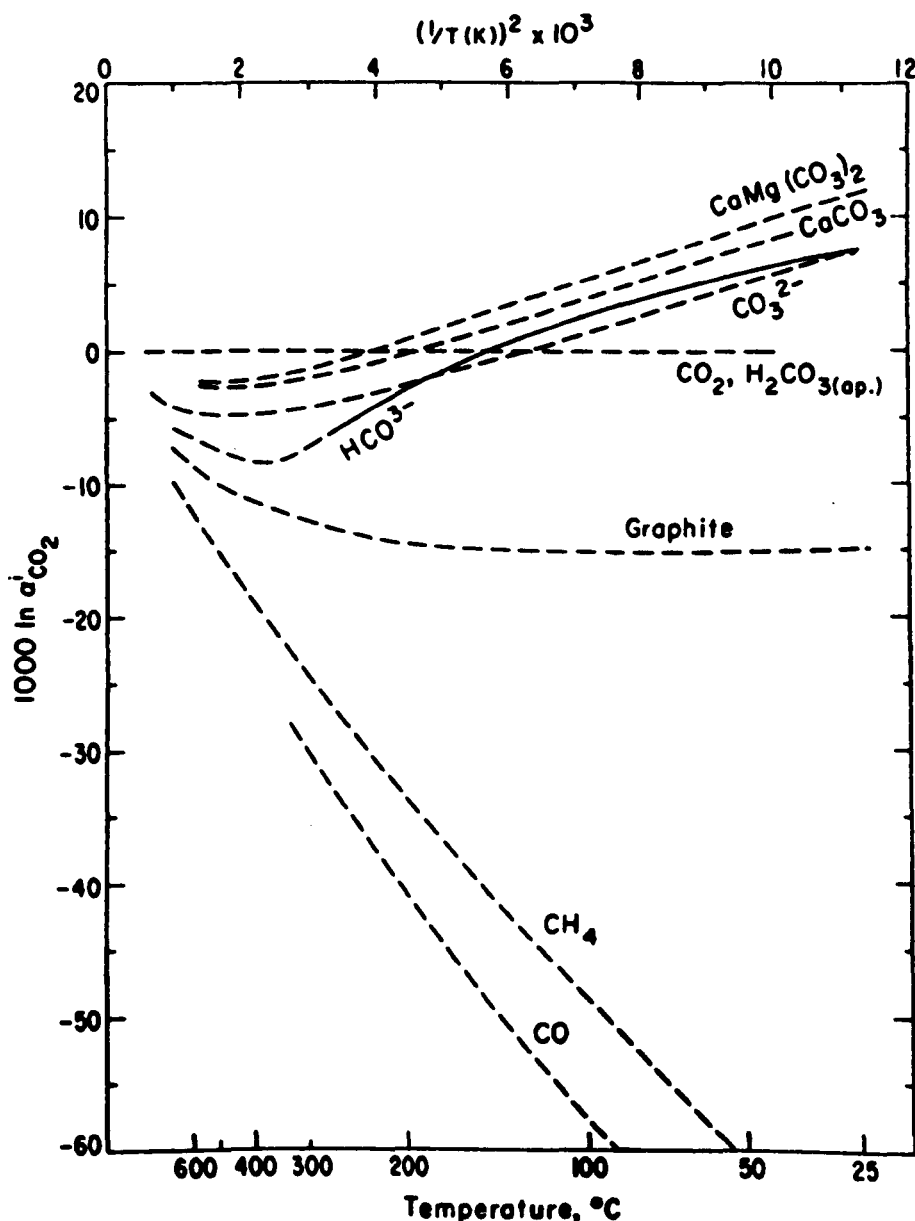


**Figure 8.3** Equilibrium isotopic fractionation factors among carbon compounds relative to H<sub>2</sub>CO<sub>3</sub>(ap), where H<sub>2</sub>CO<sub>3</sub>(ap) = H<sub>2</sub>CO<sub>3</sub> + CO<sub>2</sub>(aq). (From Ohmoto and Rye, 1979)

hosting carbonates range between + 0.51 to - 5.82 ‰, with an average of  $-1.27 \pm 1.0\%$   $\delta^{13}\text{C}$ . These values are in close agreement with the data obtained by Garde (1977) (Carbon isotope ratios of forty calcite and dolomite samples gave the following ratios:  $-0.2 \pm 1.0\%$   $\delta^{13}\text{C}_c$ , -9.6 to  $-14\%$   $\delta^{13}\text{C}_{gr}$  (Fig. 8.1)) and are consistent with the  $\delta^{13}\text{C}$  values obtained for unmetamorphosed Pre-cambrian marine carbonates (Schidlowski et al., 1975). The  $\delta^{13}\text{C}_{gr}$  values correspond to both an organic and a metamorphic origin. Carbon isotope analysis cannot define whether graphite is a metamorphic or organic derivative (Wada, 1977).

Experimentally determined carbon isotope fractionations have been carried out by a number of people for exchange amongst graphite, calcite, carbon dioxide, and methane (Bottinga, 1969; Monk et al., 1974; Ohmoto, 1972). The calculated fractionation curves (Table 8.2 & Fig. 8.3) between carbonate and graphite have been used in this study as a geothermometer for the Marmorilik Formation. Samples V 197 and I 413 are interpreted to reflect graphite / carbonate disequilibrium. The  $\Delta^{13}\text{C}_{c-g}$  values calculated for the other carbon isotope analyses (Table 8.1a) correspond to temperatures of between  $319^\circ\text{C} - 472^\circ\text{C}$  ( $\pm 20^\circ\text{C}$ ). The highest temperatures calculated for the equilibrated, graphite/carbonate pairs fit very well with other geothermometric data established for the peak metamorphic grade in the area (section 5.5 & section 8.4).

### 8.3.2 Oxygen Isotopes

The results of the oxygen isotope analyses have been standardised to the SMOW standard. The oxygen isotopic compositions are expressed, in per mil, as:-

$$\delta^{18}\text{O}_{\text{sample}} = \left[ \left( \frac{^{18}\text{O}}{^{16}\text{O}} \right)_{\text{sample}} / \left( \frac{^{18}\text{O}}{^{16}\text{O}} \right)_{\text{standard}} - 1 \right] \times 1000$$

The oxygen isotope compositions range in value between - 7.5 & -13.76 ‰ (Table 8.1a). These compositions are in close agreement with the results obtained in Garde's (1977) study ( $-9.9 \pm 1.5\%$   $\delta^{18}\text{O}$ ) (Fig. 8.1), who stated that the values were compatible with the isotopic compositions of unmetamorphosed limestones of equivalent age. This is clearly not the case. The oxygen isotopic compositions are very strongly depleted with respect to both unmetamorphosed (range of  $\delta^{18}\text{O}$ ; 11.3 - 26.2 ‰) and metamorphosed carbonates (range of  $\delta^{18}\text{O}$ ; 18.1- 28.1) of equivalent age (Table 8.1c) (Valley, 1986).

A strong similarity exists in the oxygen isotope compositions of the greenschist-granulite facies marbles of the Grenville province and those of unmetamorphosed carbonates (Table 8.1c). This isotopic similarity has been taken as evidence in favour of fluid-absent metamorphism (Valley, 1986).

Therefore the strongly depleted character of the Marmorilik Formation carbonates may suggest high fluid flow during Rinkian metamorphism. The fluids were probably relatively hot, meteoric waters ( $\delta^{18}\text{O}$  0 to - 50 ‰ ), that interacted with the unmetamorphosed carbonate so as to leave the rock strongly depleted in  $\delta^{18}\text{O}$  and the fluids relatively enriched (Criss and Taylor, 1986). This metamorphic fluid-flow is likely to have been active in homogenising lead (section 7.3) and sulphur isotope compositions (section 8.3.3). The carbon isotope compositions remained relatively unchanged as carbon isotopes are particularly resistant to isotope exchange (section 8.5.1).

The oxygen isotope depletion is widespread throughout the Marmorilik Formation (Table 8.1a & Fig. 8.1). Thus no evidence exist to suggest that hydrothermal fluid flow (such as in the production of SEDEX deposits, section 9.4.4) was restricted to the Black Angel deposits.

### 8.3.3 Sulphur Isotopes

The results of the sulphur isotope analyses have been standardised to the Canon Diablo iron meteorite standard. The sulphur isotopic compositions are expressed, in per mil, as:-

$$\delta^{34}\text{S}_{\text{sample}} = \left[ \left( \frac{^{34}\text{S}}{^{32}\text{S}} \right)_{\text{sample}} / \left( \frac{^{34}\text{S}}{^{32}\text{S}} \right)_{\text{standard}} - 1 \right] \times 1000$$

The sulphur isotope data is presented in Table 8.1b and Figures 8.1 & 8.2.  $\delta^{34}\text{S}$  values have been obtained from four sphalerite-galena equilibrium pairs, ten pyrite and one pyrrhotite sample. Sulphates are found in the Marmorilik area, but analyses of these sulphates are incomplete at the time of writing this thesis.

The isotope values obtained for galena, sphalerite and pyrite are relatively homogeneous throughout the mine (Fig. 8.2). Pyrite is approximately 1‰ heavier than the sphalerite data, with the sphalerite approximately 1‰ heavier than galena. This is consistent with the equilibrium fractionation curves for these particular minerals (Table 8.3 & Fig. 8.4) and represents that the minerals are in equilibrium. Pyrite values range from 2.83 to 4.99 ‰, with a mean of 4.39 ‰. The value of 2.83 ‰, from the highly sheared porphyroclastic ore of the middle Cover zone (M 72W), is slightly anomalous, probably representing a minor premetamorphic variation in the isotopic distribution. The isotopic distribution for sphalerite shows a narrow cluster of data between 2.45 to 3.96 ‰  $\delta^{34}\text{S}$ , and the galena 0.50 to 2.66 ‰  $\delta^{34}\text{S}$ . The sphalerite-galena mineral pairs become isotopically lighter as one moves east in the mine.

Pyrite from mineralised units away from the Black Angel ore bodies give heavier isotope values e.g. the Nunngarut (6.72‰) and Agpat (9.00‰) pyrites, as is a sphalerite sample (7.22‰) from the Nunngarut (Fig. 8.1). The pyrite from the South Lakes Glacier showing (CSL 12) is

consistent with the Black Angel data (Figs. 8.1 & 8.2).

Pyrite from metapelite of the Nukavsak Formation is also heavier (7.45‰) than the pyrite in the Black Angel mineralisation, but it lies within the general  $\delta^{34}\text{S}$  range of pyrite from the carbonate hosted mineralised showings in the Marmorilik Formation. The pyrrhotite of the Nukavsak Formation is heavier (11.78‰) than all other minerals, and is not in equilibrium with the pyrite (Fig. 8.4).

#### **8.4 Sphalerite-Galena Geothermometry**

The experimental calculation of isotopic equilibrium fractionation curves (Table 8.3 & Fig. 8.5) amongst sulphur compounds (Rye and Ohmoto, 1979) has allowed many coexisting sulphur bearing mineral pairs to be used as geothermometers. The suitability of mineral pairs for geothermometry varies according to the separation of the equilibrium curves for any two minerals. The larger the separation the more sensitive the geothermometer. Recrystallised sphalerite and galena mineral pairs, from the D3 related recrystallised ore facies (section 6.5.6b), were found to be the most favourable for sulphur isotope geothermometry. The rocks were coarse grained, therefore uncontaminated samples were easily obtained by microdrilling.

The sphalerite-galena system has been studied in detail by Grootenboer and Schwarz (1969), Kiyosu (1971), Kajiwarra and Krouse (1971), Czamanske and Rye (1974) and Smith (1977). These workers have constructed equilibrium curves (Fig. 8.5) for the sulphur isotopic fractionation between sphalerite and galena ( $\Delta^{34}\text{S}_{\text{sp-gn}}$ ) at temperatures between 50 - 500°C (Fig. 8.5). Rye (1974) has argued that the Czamanske and Rye (1974) curve gives the best agreement with filling temperatures of fluid inclusions over the temperature range from 370°C to 125°C. In this study this curve has been taken as the best estimate for equilibration temperatures of sphalerite and galena.

Compound <sup>a</sup>	(T in K)			T(°C) Range
	A	B	C	
CaSO <sub>4</sub>	5.26		6.0 ± 0.5	200-150
CaSO <sub>4</sub> · 2H <sub>2</sub> O				
SrSO <sub>4</sub>				
BaSO <sub>4</sub> <sup>b</sup>				
Aqueous sulfates	(8.0)		(±1.0)	> 400
Sulfites <sup>b</sup>	(4.12)	(5.82)	(-5.0)	> 25
SO <sub>2</sub>	4.70		-0.5 ± 0.5	150-1050
SCl <sub>2</sub> <sup>c</sup>	(0.67)	(0.43)	(-1.15)	> 25
CaS <sup>d</sup>	(0.6 ± 0.1)			
SrS <sup>d</sup>	(0.6 ± 0.1)			
BaS <sup>d</sup>	(0.6 ± 0.1)			
MgS <sup>d</sup>	(0.5 ± 0.1)			
MoS <sub>2</sub> <sup>d</sup>	(0.45 ± 0.1)			
FeS <sub>2</sub>	0.40 ± 0.08			200-700
CoS <sub>2</sub> <sup>d</sup>	(0.4 ± 0.1)			
NiS <sub>2</sub> <sup>d</sup>	(0.4 ± 0.1)			
MnS <sub>2</sub> <sup>d</sup>	(0.4 ± 0.1)			
ZnS	0.10 ± 0.05			50-705
MnS <sup>d</sup>	(0.10 ± 0.05)			
FeS	0.10 ± 0.05			200-600
CoS <sup>d</sup>	(0.10 ± 0.05)			
NiS <sup>d</sup>	(0.10 ± 0.05)			
CuFe <sub>2</sub> S <sub>3</sub> <sup>d</sup>	(0.05 ± 0.05)			
H <sub>2</sub> S (g.aq.)	0			
CuFeS <sub>2</sub>	-0.05 ± 0.08			200-600
S (=S <sub>8</sub> )	-0.16		±0.5	200-400
HS <sup>-</sup>	-0.06 ± 0.15		-0.6	50-350
Cu <sub>3</sub> FeS <sub>4</sub> <sup>d</sup>	(-0.25 ± 0.1)			
CdS <sup>d</sup>	(-0.4 ± 0.1)			
CuS <sup>d</sup>	(-0.4 ± 0.1)			
SnS <sup>d</sup>	(-0.45 ± 0.1)			
PbS	-0.63 ± 0.05			50-700
HgS <sup>d</sup>	(-0.7 ± 0.1)			
Cu <sub>2</sub> S <sup>d</sup>	(-0.75 ± 0.1)			
Sb <sub>2</sub> S <sub>3</sub> <sup>d</sup>	(-0.75 ± 0.1)			
Ag <sub>2</sub> S <sup>d</sup>	(-0.8 ± 0.1)			
S <sup>2-</sup>	(-0.21)	(-1.23)	(-1.23)	> 25

**Table 8.3** Equilibrium isotopic fractionation factors of sulphur compounds with respect to H<sub>2</sub>S. (From Hoefs, 1980)

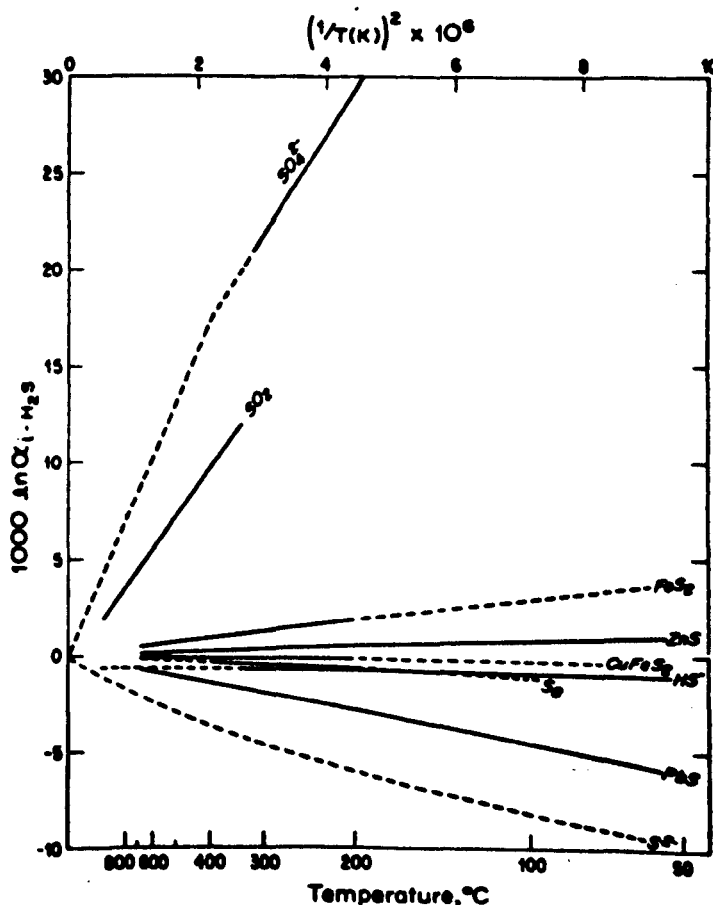


**Figure 8.4** Equilibrium isotopic fractionation factors among sulphur compounds relative to H<sub>2</sub>S. Solid lines - experimentally determined. Dashed lines - extrapolated or theoretically calculated. (From Ohmoto and Rye, 1979)

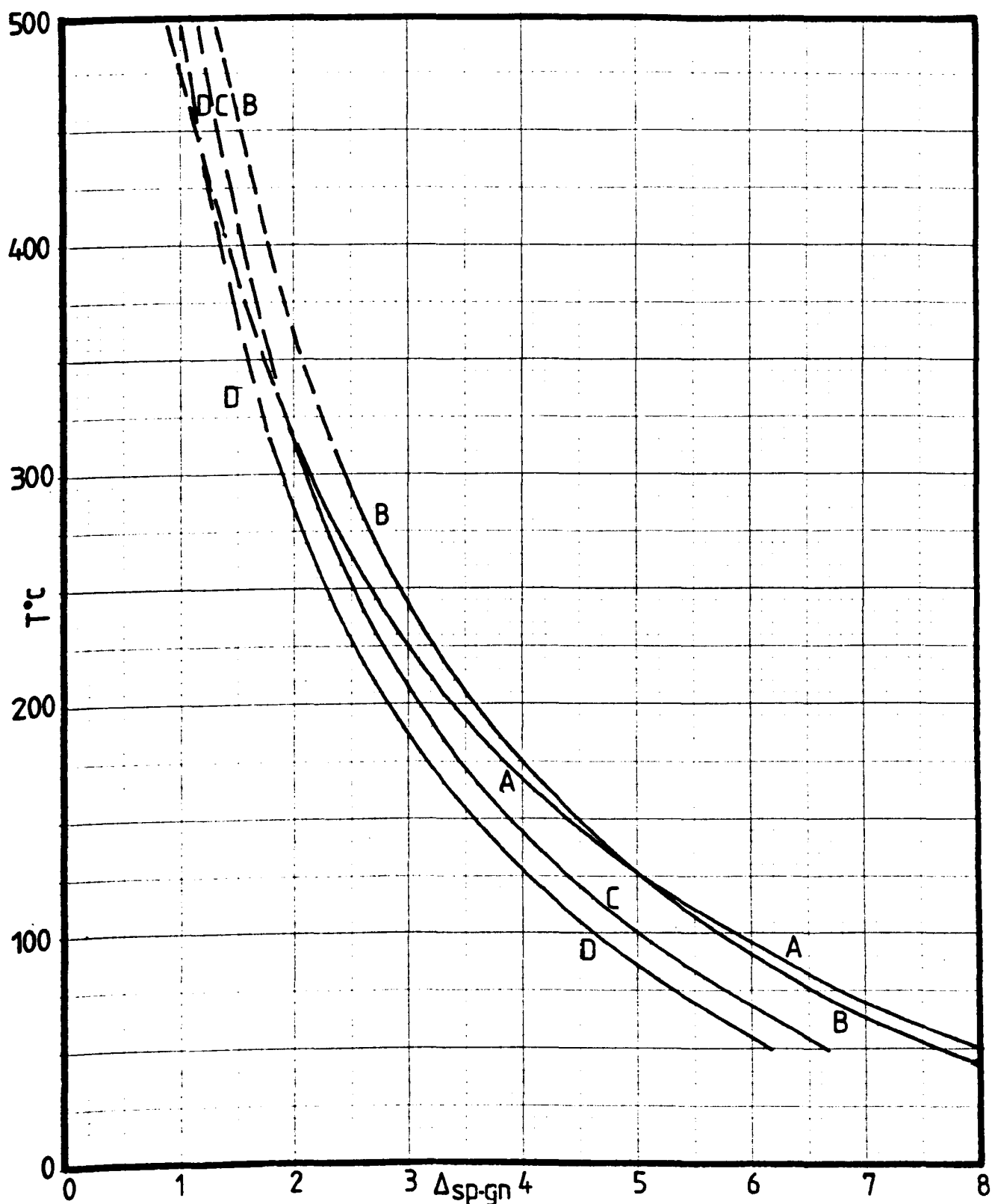


**Figure 8.5** Calibration curves for the fractionation of sphalerite and galena vs temperature. A= Kiyosu (1973); B= Kajiwara and Krouse (1971); C= Czamanske and Rye (1974); D= Grootenboer and Schwarz (1969).

The anomalous  $\Delta^{34S}$  figure for pair four (V216) has been discounted because of galena fractionation during analysis. The remaining sphalerite galena pairs give  $\Delta^{34S}_{sp-gn}\%$  values of 1.30 % to 0.95 % (table 8.1b) which corresponds to a range in the equilibration temperatures of 410° to 477°C. The equilibration temperatures calculated from the mineral pairs agree well with the inferred peak metamorphic conditions of upper greenschist facies in the Upper Marmorilik Formation (section 5.5).

## 8.5 Discussion

### 8.5.1 Effect of metamorphism on Carbon and Sulphur isotope compositions

It has generally been found in metamorphic ore deposits that (Rye and Ohmoto, 1974; Ohmoto and Rye, 1979; Hoefs, 1980; Ohmoto, 1986):-

i) Carbon isotopes are particularly resistant to isotopic exchange. The distribution of the isotopes is largely a pre-metamorphic distribution.

ii) large scale premetamorphic  $\delta^{34S}$  variations are retained during metamorphism, with the average  $\delta^{34S}$  of major units being unchanged.

iii) Small scale sulphur isotope changes can be superimposed on the original isotopic distribution during metamorphism, such as; redistribution of sulphur isotopes among coexisting minerals that define the temperature of metamorphism, and local  $\delta^{34S}$  variations that reflect the structural or chemical metamorphic history.

No large scale variations are observed in the sulphur isotopic data of the Black Angel deposits (Table 8.1b). However, the pyrite of M72W is somewhat anomalous and a variation in  $\delta^{34S}$  of sphalerite and galena pairs occurs as one moves east in the mine. The  $\delta^{34S}$  of pyrite is more variable throughout the Karrat Group.

On comparing the sulphur isotopic distributions of relatively undeformed carbonate hosted deposits, such as MVT (Fig. 8.6), SEDEX 'Irish type' deposits (Fig. 8.7) and McArthur River deposits (Fig 8.8) with those of

higher grade metamorphic carbonate hosted deposits, such as the Balmat-Edwards (Whelan et al., 1984) and the Black Angel deposits, it is clear that a much tighter isotopic distribution occurs in the metamorphosed deposits. This suggests that strong metamorphic homogenisation of the Black Angel sulphur isotope compositions has occurred. However, Rye and Ohmoto (1979) and Goodfellow (1987) have suggested that a homogeneous sulphur isotopic distribution indicates that the ore-bearing mineral sulphur was derived from the same sulphur source and was precipitated under the same chemical conditions.

### 8.5.3 Sulphur Isotopes and ore genesis

In many carbonate hosted ore deposits stable isotopes have been used as a tool in determining modes of ore genesis (Heyl et al., 1974; Rye, and Ohmoto, 1979; Whelan et al., 1984; LeHuray, 1984; Powell and MacQueen 1984; Muir et al., 1985; Caulfield et al., 1986). In the following section the possible sources of ore sulphur are discussed and the isotopic signatures of the Black Angel deposits are compared with those of other carbonate hosted sulphides. However there must remain doubt as to the significance of the metamorphically equilibrated Black Angel sulphur isotopic signatures (section 8.5.2). In addition the limited number of analyses and the broad lithological range over which the samples were taken in this study present statistical limitations as to the significance of the results.

#### a) Sulphur source

The source of sulphur in the Black Angel deposits is hard to assess. Ohmoto<sup>and Rye</sup> (1979) argued that it is necessary to calculate the total sulphur isotope content ( $\delta^{34}\text{S}_{\Sigma\text{S}}$ ) of the mineralising system before the sulphur sources can be worked out. In most ore deposit studies, the total isotope content cannot be calculated.

Sulphur is likely to be introduced into ore forming fluids of carbonate hosted deposits either directly or indirectly from seawater.

Sangster (1976) noted that marine hosted stratabound deposits have generally derived their sulphur from bacterial reduction of seawater sulphate, with most stratabound sedimentary deposits showing a 15 ‰ depletion in  $\delta^{34}\text{S}$  relative to coeval seawater sulphate. However, sulphur isotope data on stratabound deposits have indicated other sulphur sources

Sea water sulphur is recycled within the sedimentary system by a number of processes and may be introduced into ore forming fluids by dissolution of pre-existing evaporitic minerals followed by inorganic (Barton, 1967) or organic (Shearman, 1971; Trudinger, 1981) reduction of sulphate (Fig. 8.9). Alternatively, it may be introduced into the ore-fluids as reduced sulphur by:-

- i) mixing of the sulphide brines with water enriched in  $\text{H}_2\text{S}$  by bacterial sulphate reduction (Jackson and Beales, 1967).
- ii) dissolution of pre-existing sulphides (Lovering, 1961)
- iii) thermal degradation of organic sulphur bearing hydrocarbons in petroliferous material (Skinner, 1967).

If seawater sulphate is considered as a possible source of sulphur for the Black Angel mineralisation, then the sulphur isotopic composition of Proterozoic sea-water needs to be known. This may be approximated by analyses of sulphate minerals. Unfortunately no results have been obtained from sulphate minerals in the Marmorilik Formation, but the  $\delta^{34}\text{S}$  values of contemporaneous seawater for approximately 2000 Ma. (encompassing the Black Angel and McArthur River deposits) has been estimated at  $+20 \pm 5 \text{ ‰ } \delta^{34}\text{S}$  (Vinogradov, 1972; Claypool et al., 1980; Muir et al., 1985).

The Black Angel sulphides are depleted in  $\delta^{34}\text{S}$  by approximately 15 ‰ relative to this value for Early Proterozoic sea-water sulphur. Thus the possibility exists that the Black Angel sulphur was derived by bacterial reduction of seawater sulphate. However, a direct fixation of seawater sulphur during syn-genetic or early diagenetic mineralisation

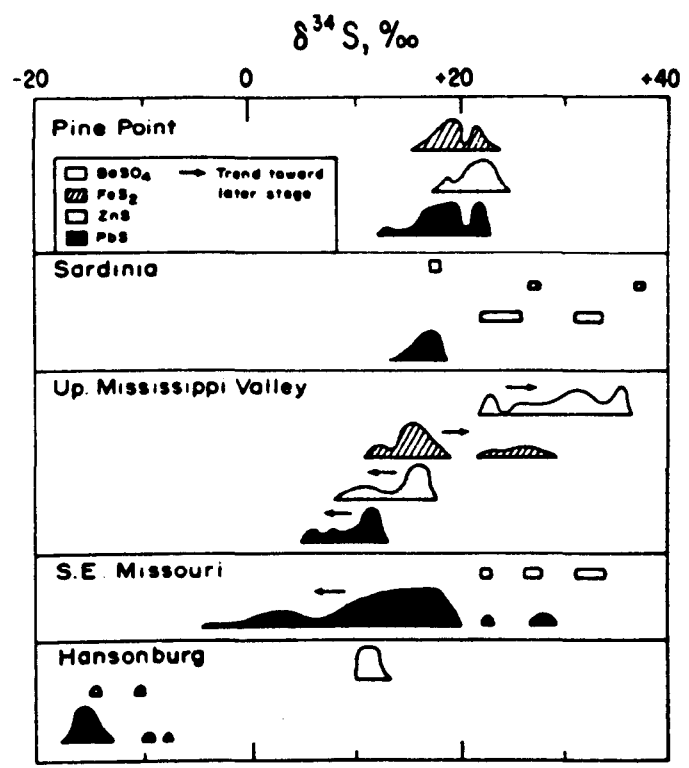


Figure 8.6a Schematic presentation of sulphur isotopic data of some Mississippi Valley type deposits.(From Ohmoto and Rye, 1979)

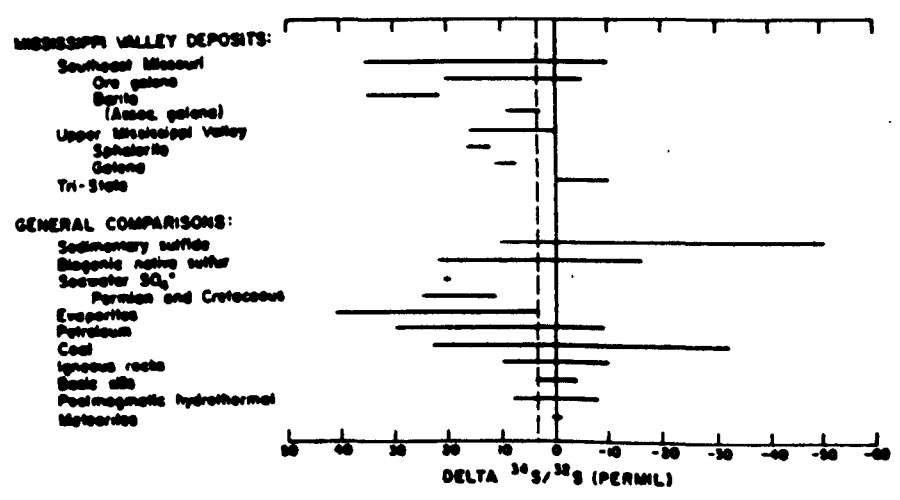
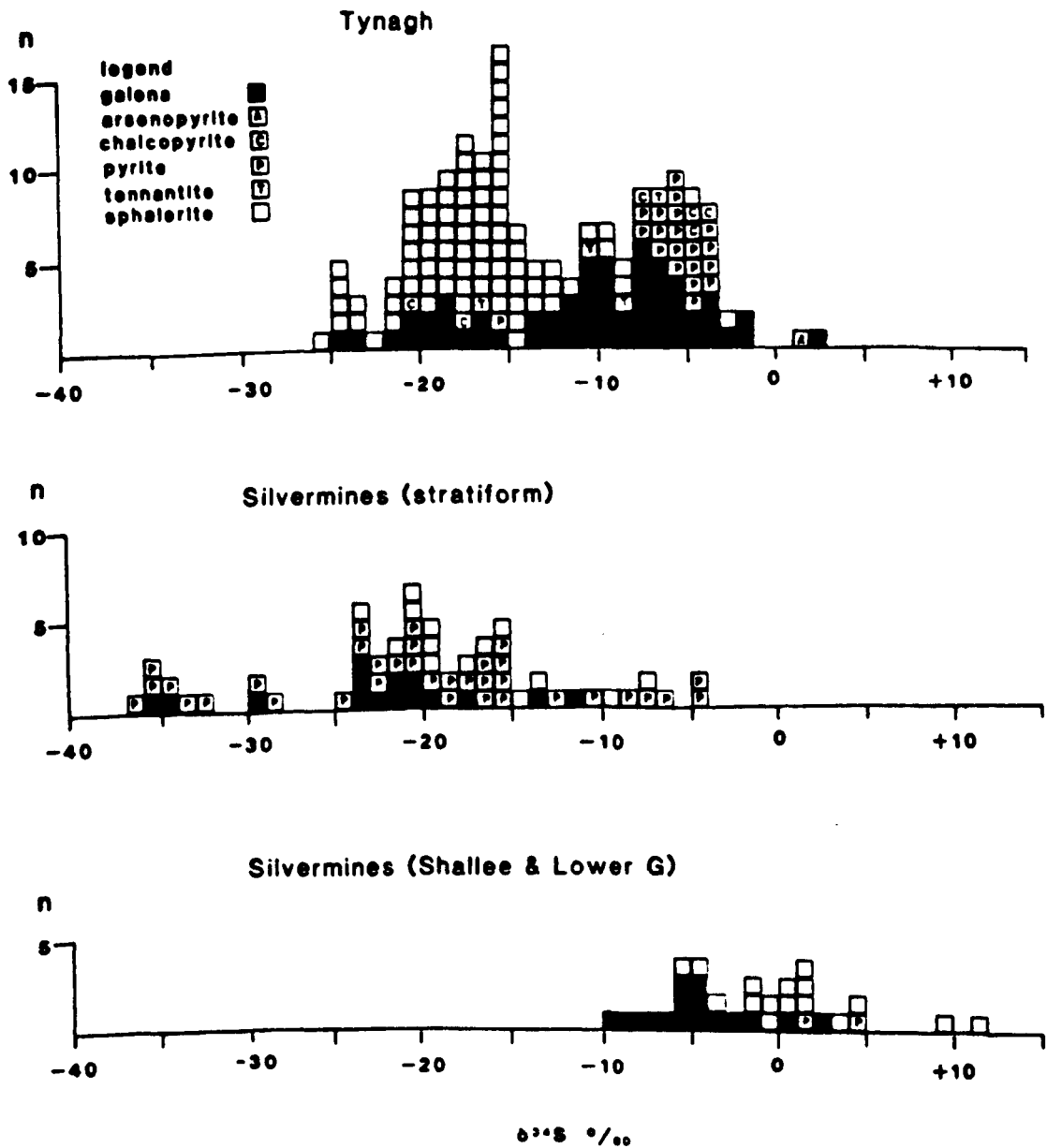
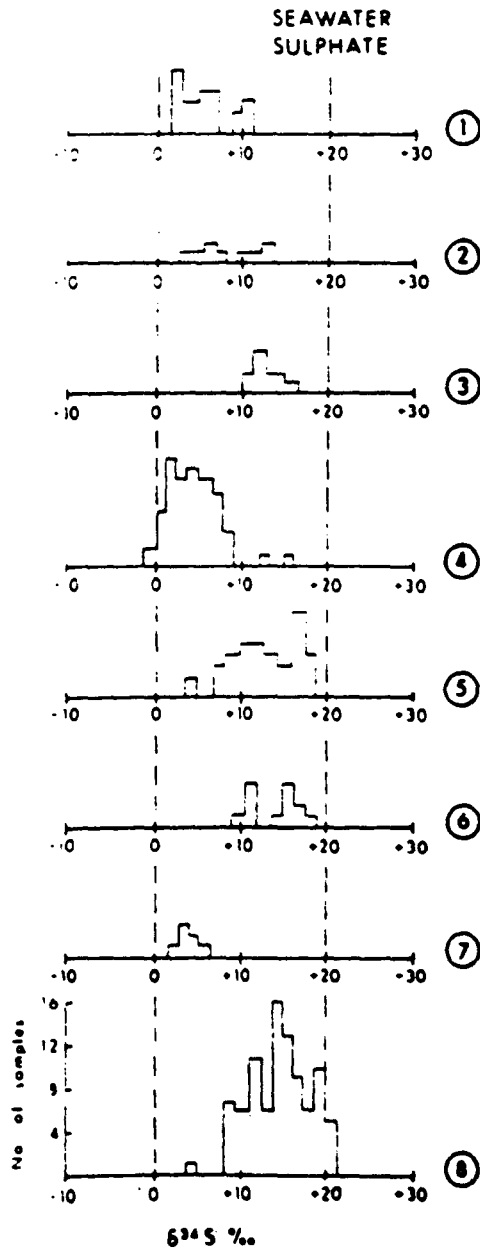


Figure 8.6b Sulphur isotope distributions of Mississippi Valley type ores compared to other sulphur bearing environments. (From Omoto and Rye, 1979)



**Figure 8.7** Sulphur isotopic composition of ore stage sulphides at Silvermines; (a) discordant mineralisation, (b) stratiform mineralisation. (c) sulphur isotopic composition of ore stage sulphides at Tynagh (After Caulfield et al., 1986)



**Figure 8.8** Sulphur isotope distributions for present day sea floor emanations (1), the Proterozoic McArthur River basin deposits (2) (3) & (4) and shale hosted Mount Isa (5), Lady Lorretta (6), Dugal River (7) and Rammelsberg (8). (from Muir et al., 1985)

seems unlikely (section 8.5.3 b).

The possibility also exists that the sulphide sulphur was partly derived by dissolution of pre-existing evaporitic minerals (section 3.2.3), or a mixing of sulphide brines with fluids enriched in  $H_2S$ . Unfortunately no data are available as to the sulphur isotope compositions of the evaporitic minerals, and so conclusions cannot be drawn as to <sup>the</sup> relative importance of this mechanism as a source of ore sulphur. On the other hand as the isotopic composition of pyrite both within the Black Angel deposits and in the Karrat Group is comparable, it is possible that some sulphur was introduced into the Black Angel deposits in the form of reduced sulphur by hydration (dissolution) of pyrite (Ohmoto and Rye, 1979).

In summary, it is suggested that most of the ore bearing sulphur was derived by bacterial reduction of sea-water sulphate. However, minor amounts of sulphur may have been derived from the Marmorilik Formation by both the partial dissolution of pre-existing evaporitic minerals and the hydration of pyrite.

### **b) Isotopic signatures in carbonate-hosted deposits**

Mississippi Valley type (M.V.T.) mineralisation displays a wide range of generally enriched sulphur isotopic compositions between -10 & +40‰ (Fig. 8.6). The individual deposits do not show such large isotopic ranges, and in the case of Pine Point a relatively narrow isotopic distribution is produced (Fig. 8.6a). The isotopic compositions of M.V.T. mineralisation spans the data from the Black Angel ore bodies. As in many M.V.T. deposits, there is a correlation in Black Angel galena samples between the radiogenicity of lead and a depletion in  $\delta^{34}S$  compositions (Fig. 8.10). The variation in lead and sulphur isotopes in the Black Angel deposits is very small in comparison with the isotopic diversity in the heterogeneous M.V.T. deposits. Even so this observation has been interpreted to suggest that the lead and sulphur were transported together

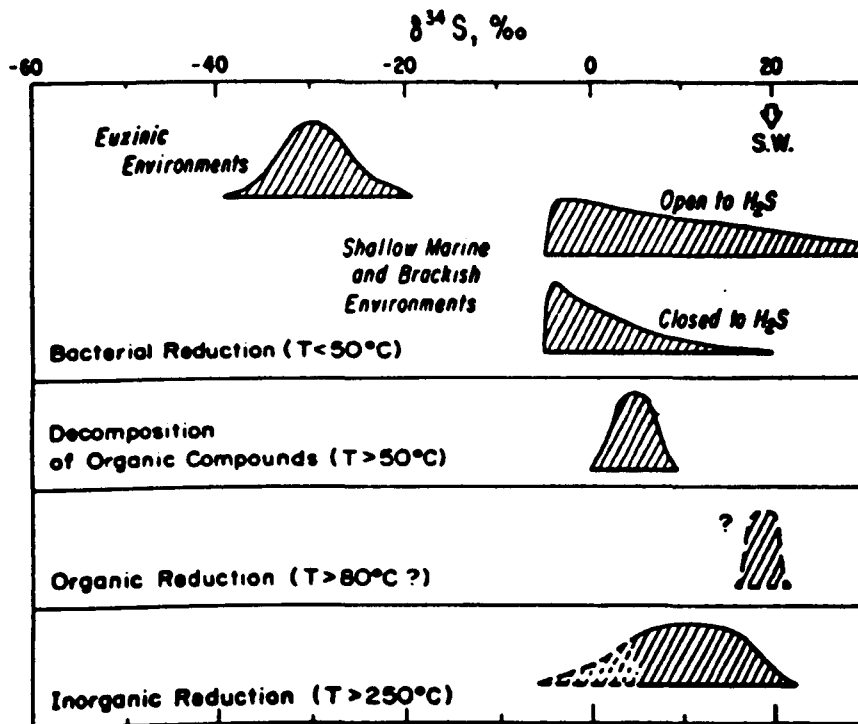


**Figure 8.9** Distribution pattern for  $\delta^{34}\text{S}$  values of  $\text{H}_2\text{S}$  and sulphide minerals when sulphate of  $\delta^{34}\text{S} = +20\text{‰}$  is reduced by various mechanisms. SW is sea water. (From Ohmoto and Rye, 1979)

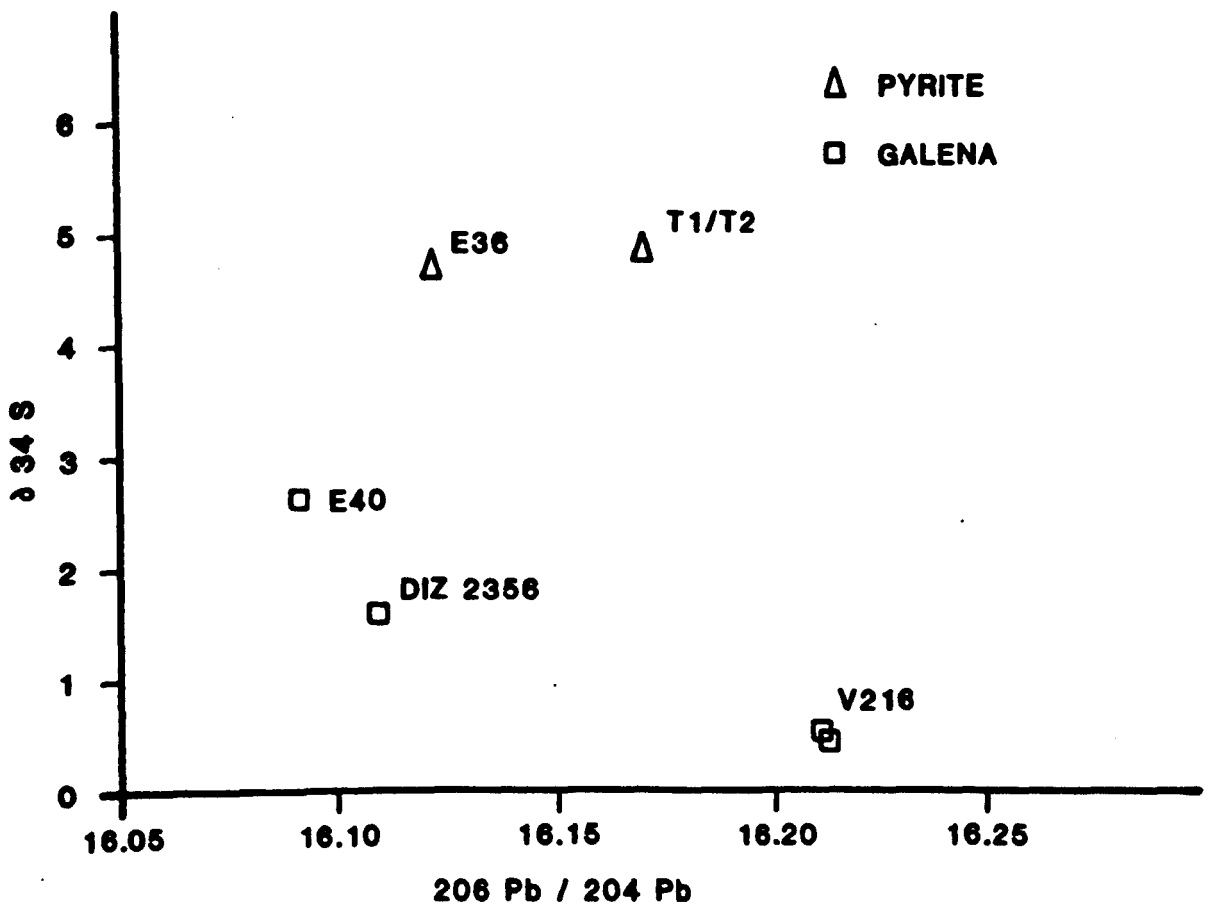


Figure 8.10 Plot of  $\delta^{34}\text{S}$  against  $^{206}\text{Pb} / ^{204}\text{Pb}$  for galena and lead-bearing pyrite from the Black Angel mine.

in the same ore solutions, and that the solutions varied in isotopic composition through time (Rye and Ohmoto, 1974; Sverjensky et al., 1979; Sverjensky, 1981)

In the carbonate-hosted 'Irish type' deposits the sulphur isotope ratios are highly variable and isotopically lighter than the Black Angel deposits (Fig 8.7). There is no correlation between lead isotopic data and  $\delta^{34}\text{S}$  values within these deposits. A dual sulphur source has been predicted for the 'Irish type' deposits (Coomer and Robinson, 1976; Caulfield et al., 1986; Samson and Russell, 1983 & 1987), a deep seated crustal source forming sulphides with  $\delta^{34}\text{S}$  values close to 0‰ and a sea water sulphate source forming sulphides by bacterial reduction of sulphate with variably depleted  $\delta^{34}\text{S}$  values. Sulphur isotope estimates for seawater during the formation of the Irish deposits are almost equivalent to those for estimates of Proterozoic seawater sulphur (e.g. 15‰), but as the isotopic signatures for the Black Angel and 'Irish type' deposits are dissimilar, it is highly unlikely that the same isotopic processes were active during the generation of the 'Irish type' and Black Angel deposits.

The McArthur River deposits (Fig. 8.8) have relatively homogeneous sulphur isotopic distributions between +3.5 and +15 ‰  $\delta^{34}\text{S}$  (Muir et al., 1983) that are also comparable with Mt. Isa, Lady Lorreta and the Rammelsberg deposits (Fig. 8.8). The Black Angel isotopic signatures lie within this isotopic range.

In the Balmat-Edwards deposits (Whelan, 1984) Zn-Pb sulphur isotope compositions are heavier ( $\delta^{34}\text{S} \approx 11-17$  ‰) than in the Black Angel deposits, but are similar in that they show a strongly homogeneous distribution.

## 8.6 Conclusions.

Although the stable isotope studies of the Black Angel deposits and surrounding mineralisation were quite limited, several broad conclusions may be drawn:-

i) large scale homogenisation of the Black Angel sulphur isotope compositions has occurred during Rinkian metamorphism. This homogenisation is also present in the Balmat-Edwards deposits.

ii)  $\delta^{18}\text{O}$  values (Garde, 1977) for the Marmorilik Formation carbonates are strongly depleted. They probably represent interaction of the carbonates with depleted waters either during late diagenesis or Rinkian metamorphism. Carbon isotope variations have suffered little or no metamorphic homogenisation.  $\delta^{13}\text{C}$  values are indicative of 'normal' marine carbonates.

iii) equilibration temperatures of between 410-477°C have been estimated for peak Rinkian metamorphism from sulphur isotope geothermometry of sphalerite and galena pairs from the D3 related recrystallised ore facies. The graphite/carbonate geothermometer gave more variable results with a value of 476°C for peak metamorphism.

iii) sulphide sulphur was probably derived by the reduction of sea-water sulphate, with minor sulphur contributions from the dissolution of pre-existing evaporites or by the hydration of pre-existing pyrite. (Proterozoic sea-water sulphate is estimated at 15%.)

iv) a positive correlation exists between galena lead radiogeneity and decreasing  $\delta^{34}\text{S}$ . This possibly indicates that sulphur and lead were transported in the same ore forming solution during ore formation.

v) sulphur isotope compositions of the Black Angel sulphides lie within the range of the MVT, McArthur River and Proterozoic shale-hosted deposits, but are dissimilar to the sulphur isotope compositions of the 'Irish type' deposits.

## **Chapter 9 Discussion.**

### **9.1 Introduction**

This chapter deals with i) the tectonic evolution of the Marmorilik area with respect to the Rinkian mobile belt. The mechanisms of gneiss dome formation are discussed, as their formation so directly affects the deformation style and processes which occurred within the overlying supracrustal units ii) the processes and mechanisms of ore deformation and the iii) problems of classifying and constraining genetic models for the Black Angel sulphides.

### **9.2 Tectonic evolution of the Marmorilik area**

#### **9.2.1 Mechanisms of gneiss dome formation**

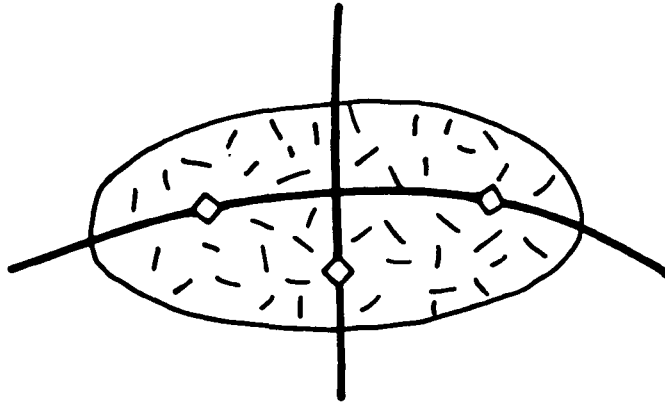
Basement massifs are recognised in a number of tectonic belts characterised by high temperature-low pressure metamorphism. Their formation has been ascribed to many tectonic processes (Fig. 9.1). Basement domes are observed in:- i) In the Loch Monar district (Ramsay, 1967) where the domes are formed through buckling, either by the interference of two antiformal folds or by the development of non-cylindrical folds; ii) In the Alpine (and Norwegian) thrust systems (Williams, 1982) as culminations iii) In the Svecokarrelidés (Ramberg, 1967 & 1980) where the domes have been interpreted to have developed through gravitational instabilities set up between basement and supracrustals; iv) the eastern Pyrenees (Soula, 1982) where gneissic, plutonic and metamorphic domes have been interpreted as forming through diapirism during major regional shortening; v) In the basin and range province U.S.A. (Spencer, 1984 & Allmendinger and others, 1987) as tectonically denuded extensional core complexes.

The characteristic tectonic features recognised in the basement massifs of the Marmorilik area are compared with the structures formed within these major tectonic systems (table 9.1).

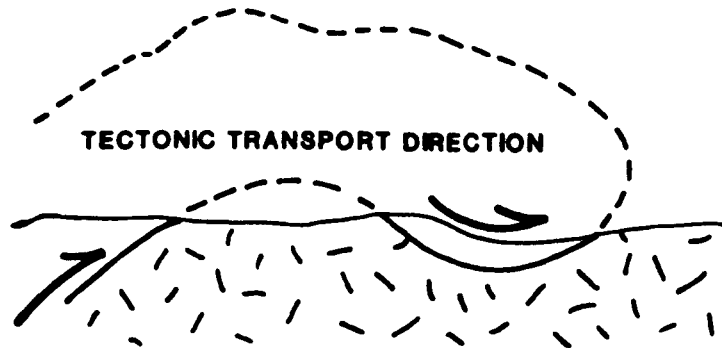
**Table 9.1** A comparison of the tectonic features of basement massifs in the Marmorilik area with the features of basement massifs formed during different tectonic processes.

Marmorilik area and Rinkian belt	Contraction	Diapirism	Extension	Transtension
Domes and ENE-WNW Antiformal ridges	As culminations	Common	Ridges common (tectonic collapse)	Oblique periclinal ridges common
Massif contains high angle normal faults	Rotated thrusts on backthrust	Vertical extension at centre of dome	Uncommon	Uncommon
Mylonitic decollément.	Associated with tectonic slides	Highly attenuated units above dome	Common	Common
Polydirectional tectonic transport vergence away from the basement/cover contact	Unidirectional modification by backthrusts	Polydirectional vergence away from dome	Unidirectional	Unidirectional/oblique modified by periclinal ridges
Stacked tectonic slides in basement and cover	Common	Gravity collapse of dome	None	None
Recumbent folds form in extensional fault sheets.	None	Common	Common	Common
C/S fabric & stretching lineation on the basement/cover contact.	Opposite sense of shear	Common	Common	Oblique slip common
Fanning extensional to compressional cleavages	None	Common	Common	Uncommon
Basement extensional fabrics translate into compressional fabrics	Contraction into extension	similar fabrics on upturned domal margin	Uncommon	Uncommon

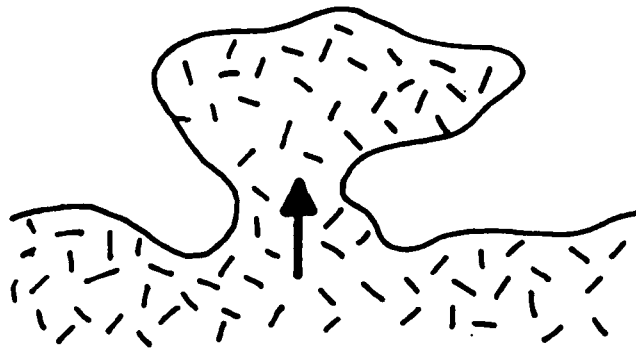
## A) BUCKLING MODEL



## B) THRUSTING MODEL



## C) DIAPYRIC MODEL



## D) EXTENSIONAL MODEL

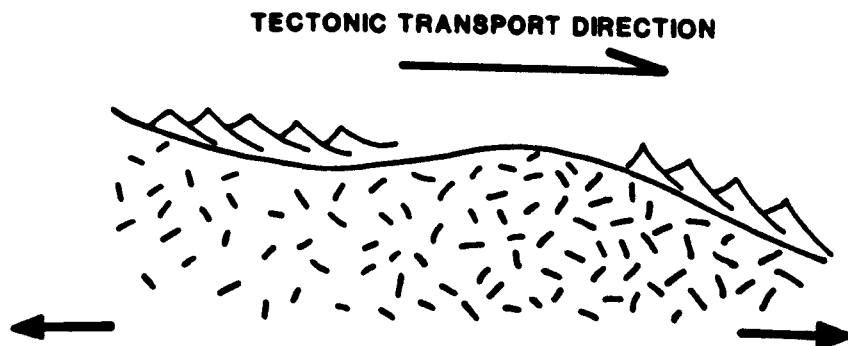


Figure 9.1 Tectonic models for the formation of basemnet gneiss domes.

### **a) Intersecting fold model**

In the Marmorilik area, as well as other parts of the Rinkian mobile belt, there is no evidence of intersecting fold phases or non-cylindrical folding during the development of the basement massifs.

### **b) Thrusting model**

The formation of basement massifs as culminations within a thrust sheet (Fig. 9.1) or possibly as transported basement slices within a thick skinned compressional system i.e. D2 deformation in Marmorilik (Fig. 9.2) is well documented and has been suggested as a mechanism for gneiss dome production in the Svartehuk Halvø (Grocott, 1987) (Fig. 2.8).

Kinematic indicators and strain trajectories within thrust sheets are generally unidirectional and indicate a dominant tectonic transport direction (Fig. 9.1), though the development of backthrusts at the sticking point in a sole thrust will form structures with opposing tectonic transport directions (Fig. 9.2). The presence of polydirectional verging structures above the gneiss domes (section 2.3.3) in the Marmorilik area and the Rinkian mobile belt, suggests that a thrusting model was not the mechanism responsible for generating the mantled gneiss domes. However, the domes are modified by tectonic slides on the Alfred Wegener (Fig. 4.34) and Nunnarssugssuaq peninsulas (Fig. 4.13).

### **c) Diapiric model**

Diapirism has long been a favoured mechanism for gneiss dome formation, since Ramberg (1967) produced his classic centrifuge models of diapiric structures.

Insights into the strain patterns developed during diapirism have been gained from the deformation of models with primary density inversions in a centrifuge (Ramberg, 1967 & 1980; Dixon, 1975; Schwerdtner & Troeng, 1977; Schwerdtner et al., 1978; Dixon and Summers, 1983 & 1985). The most sophisticated modelling of diapirs, or

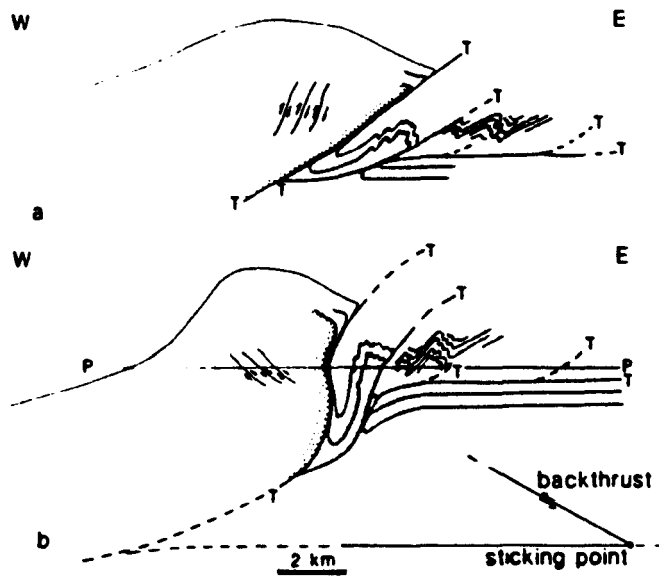


**Figure 9.2** The rotation of compressional structures by the formation of backthrusts, an example from the Svartehuk peninsula. (After Grocott et al., 1987)

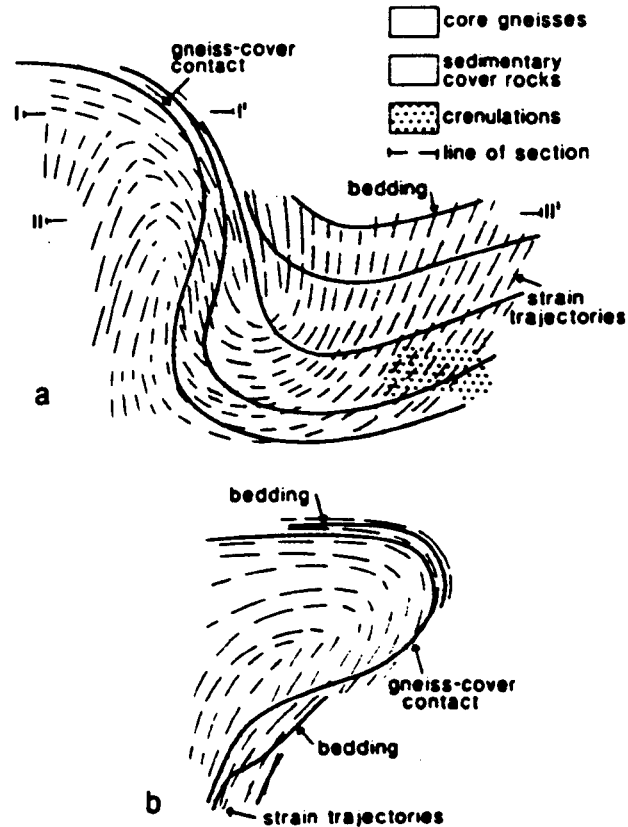


**Figure 9.3** Schematic representation of finite strain in two stages of a model diapir a) an immature dome with an extensional through to overturned basement supracrustal contact b) a mature 'mushroom shaped' dome with considerable basement overthrusting. (After Dixon, 1975).

antiformal ridges, has been performed by Dixon (1975) (Fig. 9.3) and Dixon and Summers (1983 & 1985). A cautionary note by Dixon (1975), suggests that it is often difficult to apply these finite strain models of diapirs to areas where a later pervasive deformation has been superimposed on the dome structure. Such difficulties do occur in the Marmorilik area, where D2 fabrics reactivate and overprint D1 structures. However, a number of conclusive similarities are found when structures in the basement massifs of the Marmorilik area are compared to Dixon's models (Table 9.1). These are namely:-

i) a vertical stretching and shear zones in the basement with upright axes of principal extension ii) a shear zone with a down dip stretching lineation at the basement supracrustal contact, e.g. mylonitic decollement and extensional listric fans in the supracrustals iii) fanning cleavages, consisting of extensional C/S fabrics and flattening cleavages, in the supracrustal overburden.

Recent workers have favoured this diapiric model for the genesis of the Rinkian basement massifs (Henderson, 1973; Escher and Pulvertaft, 1976; Pedersen, 1980; Grocott, 1987), but have neglected to determine the mechanisms responsible for the initiation of these diapirs.

Ramberg (1967 & 1980) suggested that diapirism was driven by the formation of unstable density gradients within the lithosphere. A primary, isothermal, density inversion may arise through compositional variations and is known as a Rayleigh-Taylor instability. Density inversions may also occur by heat flow. These instabilities are known as Rayleigh-Bernard instabilities and have been linked with dome formation in high temperature-low pressure metamorphic terranes (Talbot, 1974 & 1979; Den Tex, 1975; Soula, 1982).

Studies on the density gradients within the Marmorilik/ Rinkian lithologies have been carried out by Henderson (1969). He calculated that the specific gravity of the Rinkian lithologies were on average:-

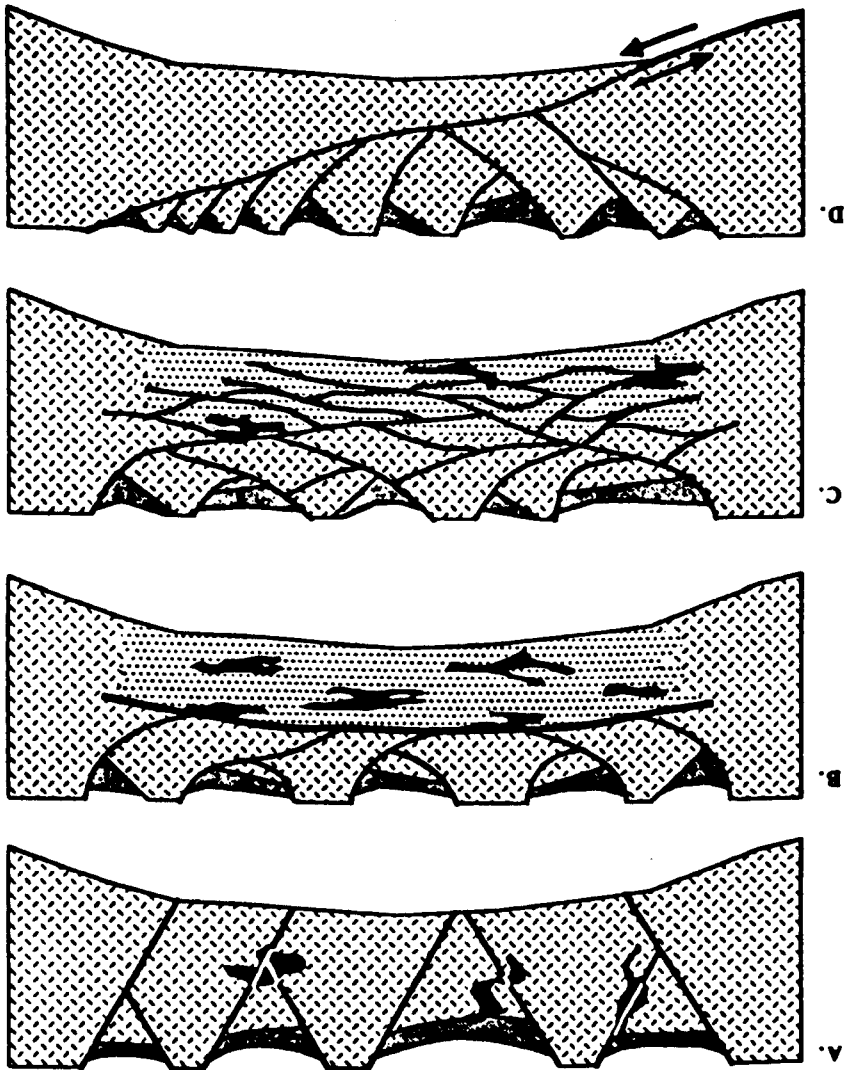
		g cm <sup>-3</sup>
	Nukavsak Formation	2.77
Karrat Group	Marmorilik Formation	2.76
	Qeqertarsuaq Formation	2.74-2.79
Archean Basement	Granodiorite	2.72
Gneiss Complex	Granulite/amphibolite gneiss	2.66

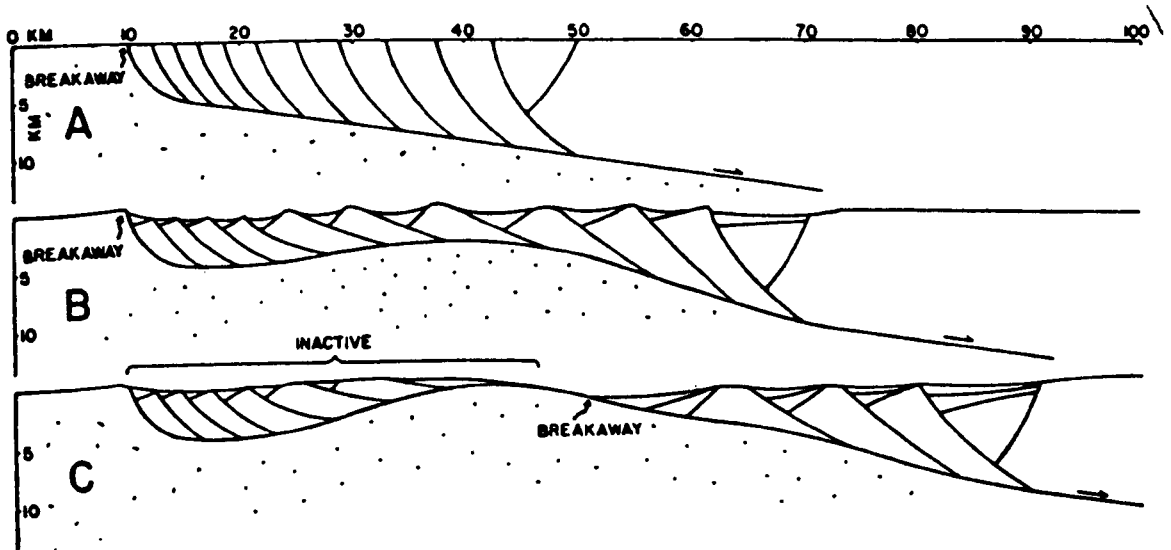
The densities of these lithologies are not likely to have altered greatly as a result of increased pressure or temperature (Soula, 1982). It is clear that the units of the Karrat Group are denser than the granulite/amphibolite gneiss by approximately 0.08-0.1 g cm<sup>-3</sup>, while the difference between the Karrat Group and the granodiorite is merely 0.02-0.05 g cm<sup>-3</sup>. In the Pyrenean gneiss domes the difference in density between the basement and supracrustals was up to 0.3 g cm<sup>-3</sup> (Soula, 1982) and in Ramberg's models (1967 & 1980) as high as 0.5 g cm<sup>-3</sup>. The differences in the Rinkian Mobile belt are very minor and are possibly not large enough to initiate diapirism on their own. Therefore some other mechanism may be responsible for 'kicking off' the diapirism.

#### **d) Lithospheric extension**

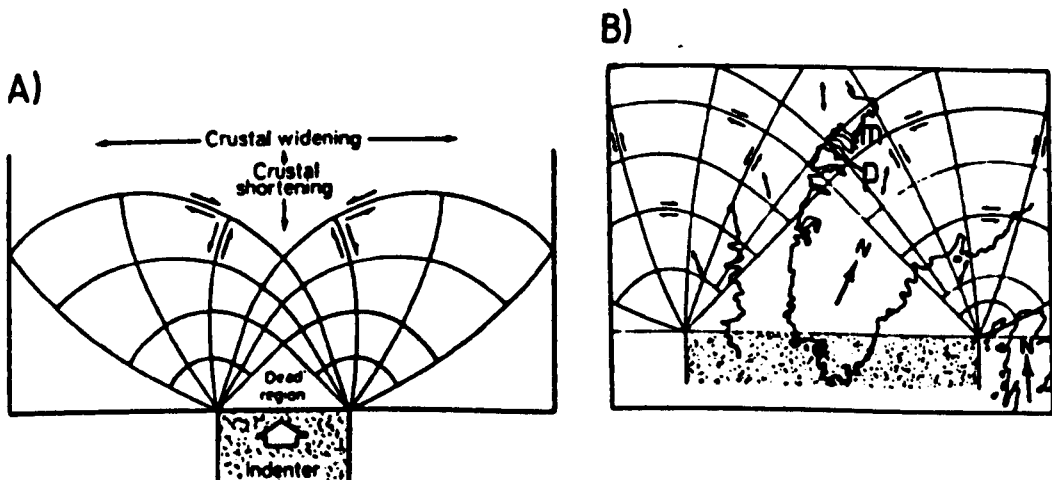
A theory not previously applied to the Rinkian mobile belt for generating basement domes is one of lithospheric extension (Allmendinger & others, 1987) (Fig. 9.4) and models analogous to core complex development (Fig. 9.1c). Antiformal uplifts of metamorphic and plutonic rocks are a common characteristic of the Cordilleran metamorphic core complexes (Coney, 1980). Their formation is attributed to the gravitational collapse of an overthickened crustal welt. The uplifts occur in low-angle normal-fault terrains and are generated by attenuation of the hangingwall panel. The inferred direction of the upper-plate transport is typically unidirectional, the upper-plate rocks appearing to have moved up one side of the uplifts and down the other (Spencer, 1984) (Fig. 9.5).

Figure 9.4 Simplified models of intracontinental extension. A) Classic horst and graben model, B) subhorizontal-decoupling zone model, C) anastomosing shear-zone or lenses model, and D) crustal-penetrating shear zone model. (After Allmendinger and others, 1987)





**Figure 9.5** Schematic diagram of warping and uplift of a detachment fault and the initiation of a metamorphic core complex. (After Spencer, 1984).



**Figure 9.6** a) Trajectories of maximum shear stresses (slip lines) for indentation model, with a rigid indenter (shaded)  
 b) Indentation model in relation to the North Atlantic craton dead triangle zone superimposed on the Archean block, and indenter on the Ketilidian showing potential transcurrent and overthrust motions. M = Marmorilik, P = Pakitsoq. (After Watterson, 1978)

Textures and tectonic packages developed at the supracrustal basement contact in the Marmorilik area (4.2.2) are somewhat analogous to those of the metamorphic core complexes developed in the Basin and Range province of U.S.A. (Davis, 1987; Naruk, 1986). However, deformation occurred at a deeper crustal level in the Rinkian mobile belt than in the Cordilleran complexes. Deformation and basement massif production may have occurred through the generation of an anastomosing set of sub-horizontal shear zones (below the brittle-ductile transition), in a manner similar to that of Figure 9.4c.

Extensional models generally assume pure dip-slip components. However, it is conceivable that oblique-slip components are active in broadly extensional systems. This has been suggested in the mixed-mode basins of Gibbs (1987).

Transtensional processes were active in the evolution of the Rinkian mobile belt. Major sinistral shear systems have been recognised at several locations, namely: at Marmorilik, where D3 sinistral shear zones occur; in the Rinks Isbrae district, where en-échelon WNW-ESE trending periclinal antiformal ridges are produced at an oblique angle to the late stage through-going shear zones (Fig 2.7); in the Ikerasak district (Grocott, 1984) as large scale throughgoing sinistral shear zones (the shear zone's age is uncertain), and in the Ata Sund district, where the Pakitsoq shear zone acts as a major boundary fault (Fig. 2.4) (Late Rinkian age) between the Rinkian and Nagssugtoquidian mobile belts (Escher and Burri, 1967).

The regional significance of these shear systems has previously been overlooked. Watterson (1978) interpreted the shear zones as Proterozoic manifestations of a northward directed continent-continent collision in a zone now represented by the Ketilidian Mobile Belt (Fig. 1.1). This collision is envisaged to have produced an array of both dextral and sinistral shear zones which wrapped around the rigid Archean block (Fig. 9.6).

The presence of these major transtensional structures, suggests that transtensional processes were responsible for the initiation of basement/supracrustal perturbations in the Rinkian mobile belt. The combined effect of these perturbations and the gravitational instabilities already present between the basement and cover sequences (9.2.1c) may have acted to translate the regional trans/extensional stresses into localised vertical (diapiric) motions within the basement.

Once the vertical motions were initiated, the rate of diapiric propagation depended on the rheological characteristics of the overburden above the massifs (Ramberg, 1967). A variation in domal uplift rates occurred in the southern Marmorilik area where the gently arched granodioritic massif and basement/supracrustal contact is rotated westwards into an upright and finally an overturned attitude (Fig. 9.7). The most rapid diapiric growth took place on the Nunarsugssuaq peninsula, where once having reached an overturned attitude the large dome progressively deformed by processes of heterogeneous simple shear and gravity spreading to produce an overthrust, imbricately stacked, non-cylindrical, basement margin (Fig. 4.13). This link between diapirism and sub-horizontal basement shear has been suggested recently by Brun and van den Driessche (1985) and supported by examples from the Shuswap terrane.

### **9.2.2 Summary of the tectonic evolution for the Marmorilik area**

On the basis of the preceding discussion it is envisaged that deformation in the Rinkian Mobile belt was initiated by continental collision between the Ketilidian belt and the stable Archean craton (Fig. 1.1) during Mid-Proterozoic times. The Ketilidian indenter is interpreted to have propagated overthrusting in the Nagssugtoqidian mobile belt (Bak et al., 1975; Watterson, 1978) and the initiation of transtensional stresses in the Rinkian mobile belt.

Sinistral shear initiated periclinal basement ridges, with a vague

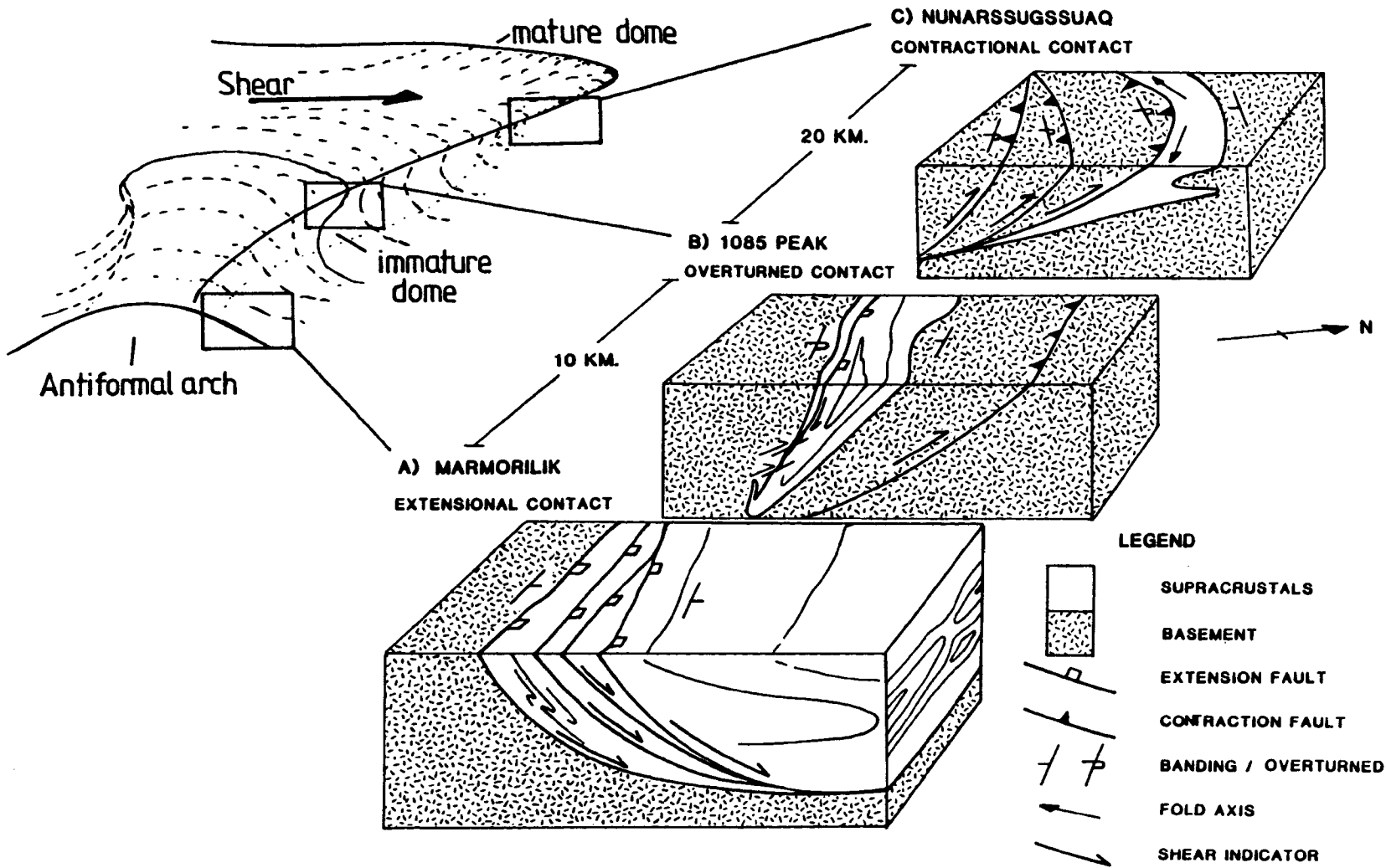


**Figure 9.7** Schematic representation of the southern basement - supracrustal contact between Marmorilik and the Nunarssugssuaq peninsula (Inset: structures in relation to an evolving basement dome).

ENE-WSW trend, which together with the pre-existing density variations between the basement and supracrustal units gave rise to more rapid diapiric movements of the basement in the upwarped ridges.

The diapirs initially developed as upward propagating structures, above which the supracrustals deformed by sub-horizontal extensional and contractional processes (Fig. 9.7 & section 4.2). As diapirism proceeded a continuum of structures developed. The slower moving zones formed upwarped ridges whilst the faster propagating zones developed 'mushroom' structures with overturned basement nappes (Fig. 9.7). As the basement domes/ridges grew, the structures in the overlying supracrustals overprinted one another. The final stages of the progressive Rinkian deformation were marked by the formation of discrete, large-scale, sinistral shear zones (Fig. 4.28).

The recognition of differentially propagating domal structures in the Marmorilik area (Fig. 9.7) may be used to reinterpret other areas of the Rinkian mobile belt and in particular the Kigarsima nappe (Fig. 2.9). An early theory suggested that the nappe was a late stage Rinkian structure (Henderson and Pulvertaft 1967). This can be dismissed as the nappe is refolded by the Snepyrmiden gneiss antiform (Fig. 2.9) (Grocott, 1987). It is predicted that the nappe originally developed as a rapidly propagating basement arch, slightly before or at the same time as the other domal complexes in the belt. The basement arch grew into a bulbous mushroom structure (similar to the Nunnarssugssuaq peninsula), which was sub-horizontally sheared at deep crustal levels to produce the present day overturned nappe.

### 9.3 Sulphide deformation and metamorphism

The recognition and understanding of the metamorphic effects imposed upon the Black Angel sulphides is imperative if the environment of deformation, and in particular the temperature, confining pressure, and the differential stress and strain rate under which the sulphides have been subjected are to be interpreted. Detailed reviews of sulphide metamorphism are given by McDonald (1967), Vokes (1969), Stanton (1972) and Mookerjee (1976)(table 9.2)

Regional metamorphic processes, active in the deformation of the Black Angel sulphides, are responsible for the following effects in sulphides: i) chemical changes in mineralogy; ii) physical changes in grain size and fabric; iii) mobilisation of minerals and elements (Table 9.3).

#### 9.3.1 Chemical changes of the Black Angel ores

Stanton (1972) stated that sulphides are less noted for their chemical changes- as they do not react readily with either the accompanying silicate or carbonate- than for their physical changes. Work by McDonald (1967) suggested that an increasing mineralogical diversity is developed in conjunction with an increased metamorphic grade. The Black Angel sulphides are not mineralogically diverse (section 6.5.6).

Chemical transformations within the Black Angel sulphides are recognised in the pyrite/pyrrhotite horizons of the Banana and T zones (Fig. 6.32 & 6.43). The pyrrhotite lenses are thought to be metamorphic products of pyrite reduction. The origin of the massive pyrrhotite units found in the Nukavsak Formation (section 3.3.3) is less clear. They may be either sedimentary exhalatives (Finlow-Bates et al., 1977; Craig, 1980 & 1983; Sunblad, 1981) or metamorphic derivatives of pyrite.

Pyrite/pyrrhotite redox reactions have been studied in nature by Barnes and Kellner (1961), Curtis and Spears (1968), Curtis (1980), Hall (1986) and Hall et al. (1987). Pyrite is the stable iron oxide in sedimentary rocks, but during metamorphism pyrite will dissociate to pyrrhotite, if a low

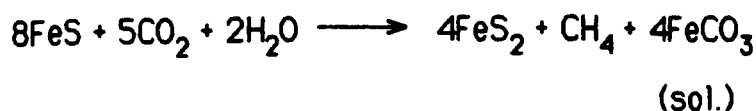
**Table 9.2 Regional metamorphism of sulphides - a summary  
(after Mookerjee, 1976)**

Ore/rock type	Observable effects	Inferred possibility of generation of new ore bodies (or ore-fluids)	Remarks/References
<i>C. Effects of regional metamorphism</i>			
(1) Sulphide ore bodies	(a) low-grade: both textural-structural and mineralogical-chemical changes initiated	(a) low-grade: expulsion of metamorphic water initiated; migration of water essentially strata-bound; solution-redeposition phenomenon influences configuration of ore-shoots within orebodies	Kalliokoski (1965); Tempelman-Kluit, (1970); Vokes (1968)
	(b) medium-grade: coarse grain size; mineralogical reconstitution, some physical remobilization, increase in Co/Ni ratio in pyrites	(b) medium-grade: physical remobilization by plastic flowage; rarely, new ore shoots adjacent to main orebody; extent of chemical remobilization, through metamorphic water of in situ origin, is likely to be inconsequential	Ito (1971); Mookherjee (1970a,b); Stanton (1972, p. 624); Vokes, (1968); Williams (1960)
	(c) high-grade: coarse grain-size; spectacular, but limited physical remobilization; "ore-dykes"; increase in pyrrhotite/pyrite ratio; narrower spread of $\delta^{34}\text{S}$ values; some veins, richer in Ag, As, Sb, and Au than the parent orebody, in adjacent rocks	(c) high-grade possibility of generation of sulphide neomagmas on a very local scale; localized meta-hydrothermal solution activity; long-distance transport of appreciable tonnage of material never proved; chemically remobilized fraction contains Ag, As, Sb and Au in much larger concentration than the parent ore body, indicating differential migration of elements	Juve, (1967); Krause (1956); Lawrence (1967); Maucher (1940); Mookherjee, (1970a,b); Ramdohr (1938); Schadlun (1960); Solomon (1963); Vokes (1963, 1966, 1969, 1971)
	(d) ultrametamorphism and palingenesis:	(d) ultrametamorphism and palingenesis:	Schreyer et al. (1964); Gavelin (1955)
	stubbornly resisting homogenization process, initiated by metamorphic convergence, until a molten or fluid phase predominates; in that stage the identity of the material, as belonging to a pre-existing ore body, is irretrievably lost in the heterogeneous milieu of magma-generating environment		

enough oxidation state is attained (the presence of graphite indicates this to be the case in the Marmorilik Formation, Fig. 5.10), by the following reaction:-



A complex growth history has occurred between pyrite and pyrrhotite in the pyrrhotite units of the Black Angel (Table 6.4). Pyrite porphyroblasts grow and are rotated within a D2 foliated pyrrhotitic matrix (Fig. 6.30 & 6.32, Table 6.3), but rarely include pyrrhotite. A zone of pyrrhotite depletion occurs adjacent to the porphyroblasts (Fig. 6.32a). It is likely that pyrite dissociated to pyrrhotite during the D1 deformation. The pyrrhotite was sheared during D2 deformation and was then oxidised (under higher  $f_{\text{O}_2}$  conditions) during D3 deformation and precipitated as pyrite. The oxidation may be considered as a retrogressive metamorphic process (Hall, 1983), which proceeds as follows:-



Other chemical changes in the sulphide mineralogy during Rinkian metamorphism are noticeable in sphalerite and may be responsible for the production of tennantite and arsenopyrite during D3 deformation (Table 6.4). Large variations in sphalerite trace element concentrations exist between sphalerite encapsulated in pyrite and that of the equilibrated ore matrix (Table 5.1a & b). It is noticeable that the D3 equilibrated sphalerite is depleted in arsenic, while arsenopyrite formed during the D3 event (Table 6.4). It is therefore likely that the arsenic released during D3 sphalerite equilibration combined with iron to produce arsenopyrite. The production of tennantite (Fig. 6.35), in the galena rich ores of the Angel and Cover zone, is probably due to a reaction between galena and arsenopyrite during D3 deformation.

The chemical equilibration of the sulphides has occurred along

with an homogenisation of lead and stable sulphur and oxygen isotopes in the Black Angel sulphides and host rocks during the Rinkian event (chapters 7 & 8).

### **9.3.2 Physical changes of the Black Angel ores**

#### **a) Introduction**

Physical changes in the texture and mineralogy of the Black Angel sulphides are the most common effects of the Rinkian metamorphism. It is interpreted, by analogy with less deformed sulphide deposits, that at the onset of metamorphism i.e. deep burial, sulphide grain size increased (Stanton, 1972). The grain growth occurred in order to maintain the minimum interfacial free energy under the prevailing P/T conditions. With an increase in metamorphic grade and the presence of directed stresses, the sulphides began to deform both in a brittle and plastic manner.

Naturally deformed sulphides have been studied principally by Ramdohr (1969) and Stanton (1964, 1972). Systematic experimental studies on sulphides deformation have been carried out by Siemes et al. (1970), Atkinson (1972, 1974, 1975a, b, and 1976), Clark and Kelly (1973), Salmon et al. (1974), Clark et al. (1977) Siemes (1976, 1977) and McClay (1978). An excellent review of sulphide deformation textures developed in low grade regional metamorphic terranes is given in McClay (1978). A summary of this data is presented in table 9.3. A summary of the mechanisms active during the plastic deformation of the Black Angel sulphides is presented in table 9.4.

The Black Angel sulphides are characterised by early layered and sheared deformation fabrics that are overprinted by late stage (D3) annealing textures. The ores may be termed 'texturally mature'. The following section discusses and interprets the various deformation textures developed in each ore forming mineral during each tectonic event (Tables 6.4 & 9.5).

SULPHIDE	GALENA PbS	SPHALERITE ZnS	CHALCOPYRITE CuFeS <sub>2</sub>	PYRRHOTITE Fe <sub>1-x</sub> S	PYRITE FeS <sub>2</sub>
STRUCTURE	Face centred cubic	Cubic - Diamond structure	Tetragonal	Hexagonal Fe <sub>1-x</sub> S above 254°C Monoclinic Fe <sub>7/8</sub> S below 254°C	Face centred cubic
SLIP SYSTEMS (and Critical Resolved Shear Stress where determined)	{100} {110} 50 bars at 20°C {110} {110} 500 bars at 20°C (Lyall and Paterson 1966)	{111} {112} {111} {011} 420 bars at 20°C 210 bars at 450°C (Siemes and Borges 1978)	{112} {110} {112} {021} (Kelly and Clark 1975)	{0001} {1120} (Clark and Kelly 1973)	not observed brittle failure only
MECHANICAL TWINNING (CRSS where measured)	{441} {110} (most common) 250-320 bars (Lyall and Paterson 1966)	{111} {112} 345 bars at 20°C 135 bars at 450°C (Siemes and Borges 1978)	{112} direction unknown	{1012} {1011} (Clark and Kelly 1973)	Interpenetrant growth twine only
KINKING	{110} {110} common	not observed	not observed	abundant kinking and phase transformations	not observed
FLOW LAW DISLOCATION GLIDE $\dot{\epsilon} = K \exp(-Q/RT) \exp(B\sigma)$ (eqn 3.1) at 10% strain	Q = 23.9 Kcal/mole B = 12.7 Kbar <sup>-1</sup> (Atkinson 1976a)	not determined	Q = 32 Kcal/mole } Roscoe B = 1.5 Kbar <sup>-1</sup> } (1975) Q = 50.5 Kcal/mole } Atkinson B = 6.0 Kbar <sup>-1</sup> } (1972)	Q = 61.4 300 - 400°C B = 16.4 (Atkinson 1972) B = 11.5 - 25 (Atkinson 1975b)	not observed
FLOW LAW DISLOCATION CREEP $\dot{\epsilon} = A(D_0 b / RT) (\sigma/\mu)^n$ (eqn 3.3) at 10% strain	Q = 22.5 Kcal/mole } up to n = 7.5 } 400°C Q = 76-247 Kcal/mole } 500- n = 4.4-5.4 } 800°C (Atkinson 1976a, 1978)	not determined	Q = 30 Kcal/mole } Roscoe n = 8.6 } (1975) Q = 55.5 Kcal/mole } Atkinson n = 11.9 } (1972)	Q = 55.3 Kcal/mole n = 14.2 300 - 400°C (Atkinson 1972)	not observed
FLOW LAW DIFFUSIONAL CREEP $\dot{\epsilon} \propto C^n$ (n = 1) (eqns 3.7 & 3.8)	Q = 60-117 Kjoules/mole n = 1.8-0.7 600° - 800°C (Atkinson 1978)	not determined	not determined	not determined	not observed
STATIC RECRYSTALLISATION TEMPERATURE	300°C (Siemes 1976, 1977)	500°C (Clark and Kelly 1973)	500°C (Gill 1969)	not determined	600 - 850°C (Read 1968)
DYNAMIC RECRYSTALLISATION TEMPERATURE	200°C (McClay and Atkinson 1977)	not observed	200 - 300°C sub-grains only (Roscoe 1975)	not determined	not observed
SOLUBILITY and comments on the possibilities of pressure solution	up to 4.5 gms/litre (Hemley et al. 1967) Pressure solution possible	up to 3 gms/litre 300°C up to 9 gms/litre 400°C (Hemley et al. 1967) Pressure solution	1.9 mg/litre at 50°C (Vukotic 1961) Pressure solution unlikely	not determined, but possible fluid assisted phase transformations	3 - 15 gms/Kgm T 192°C - 458°C probable pressure solution

Table 9.3 Synopsis of the physical properties of sulphides  
(After McClay, 1978)

**TABLE 9.4: SUMMARY OF THE DEFORMATION MECHANISMS AND MICROSTRUCTURES FORMED DURING DUCTILE DEFORMATION**

<b>DEFORMATION MECHANISM</b>	<b>P/T REGIEME</b>	<b>MICROSTRUCTURES FORMED</b>
<b>DISLOCATION GLIDE</b>	Moderate T/T <sub>m</sub> Slow strain rates	Slip lines, deformation bands, Kink bands, deformation twins, micro-fracturing, straight dislocation lines, tangles, walls and hedges, glide polygonisation. Strong preferred crystal orientation.
<b>DISLOCATION CREEP</b>	Moderate T/T <sub>m</sub> Slow strain rates	Elongate grains, deformation bands, sub-grain development, recrystallised grains, strong preferred crystallographic orientation.
<b>DIFFUSIONAL CREEP</b>	T > 0.6 T <sub>m</sub> Grain size dependency, processes Nabarro-Herring and Coble creep, Diffusive mass transfer.	Grain elongation, accumulation of phases at grain boundaries, low dislocation density, lack of crystallographic orientation, grain boundary sliding (square or rectangular grains with large areas parallel to shear direction).
<b>STATIC RECOVERY &amp; REX.</b>	T > 0.6 T <sub>m</sub> and is maintained at elevated temperatures	Polygonal sub-grains with low dislocation density, equant straight 120° grain boundaries. Tilt walls and sub-grains not found, secondary grain growth by grain boundary migration to give lobate and dentate boundaries with pinning by inclusions that may leave inclusion trails.
<b>DYNAMIC RECOVERY &amp; REX.</b>	High temperatures accelerated creep with fluctuating stress-strain curves.	Equant and elongate sub-grains, with appreciable dislocation densities, irregular grain boundaries, flattened $\perp$ to $\sigma_1$ and elongate parallel to $\sigma_3$ , deformation bands and trails.

## **b) Mineral deformation mechanisms**

### **Pyrite**

Pyrite deformed predominantly by cataclastic processes during D1 and D2 tectonic events (Table 9.5). Cataclasis is common in pyrite (Vokes, 1969, 1971; Ramdohr, 1969; Mookerjee, 1976; Sarker et al., 1980) and occurs under a wide variety<sup>of</sup> P/T conditions. Relict D1 fractures are picked out by the presence of fine, discontinuous, lens-like, inclusions of galena and chalcopyrite. Cataclastic deformation is thought to have been responsible for the nucleation of new grains that have been fragmented, rotated and elongated in many of the D2 related ore tectonites (Table 6.2).

During D1 and to a lesser extent during the D2 deformation, pyrite exhibited a degree of plasticity. Some grains are flattened and elongate. Internally dislocation etch pits are developed that combine to form slip lines and deformation bands (Fig. 6.24 f & h). These features are indicative of dislocation glide and dislocation creep processes (Table 9.3), which take place at moderate temperatures and relatively slow strain rates (Nicholas and Poirier 1976). This plasticity indicates that D1 deformation took place under medium to high grade metamorphic conditions (Mookerjee, 1971; Sarker et al, 1980; McClay and Ellis, 1983).

Grain aggregation of pyrite (Table 6.4) is responsible for many of the exceedingly coarse grained idiomorphic D3 pyrite porphyroblasts. Aggregation is achieved by static annealing and grain boundary migration, and is largely responsible for the development of the healed fractures and sieve porphyroblasts commonly found in the banded and porphyroclastic ore facies (Fig. 6.32a & b).

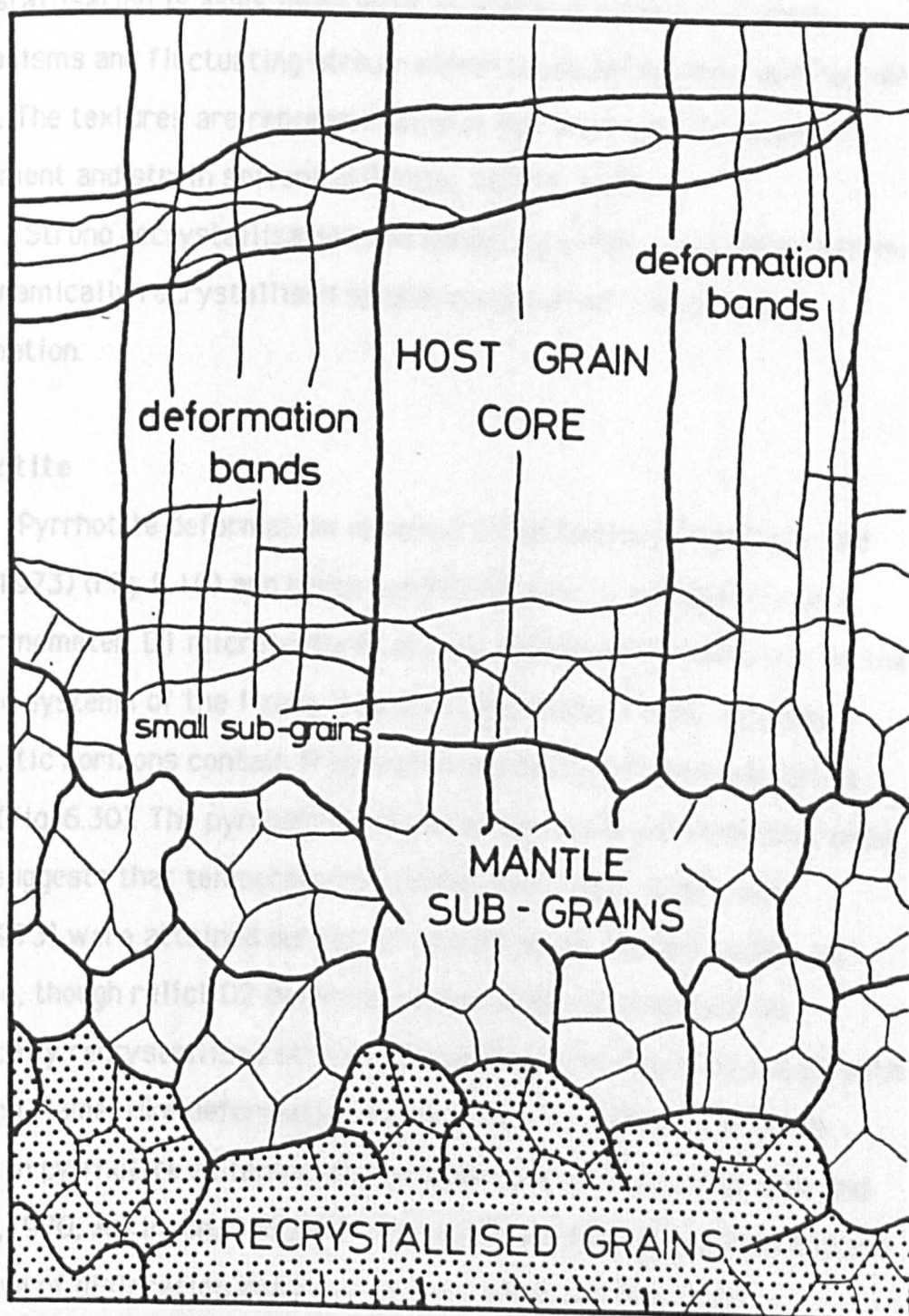
### **Sphalerite**

Sphalerite deforms by a number of processes at relatively low temperatures, and thus provides few clues as to the conditions of ore deformation. Sphalerite elongation occurred during D1 deformation. This elongation is picked out by the presence of chalcopyrite inclusions along

TABLE 9.5 MICROSTRUCTURES DEVELOPED IN THE BLACK ANGEL SULPHIDES DURING THE TECTONIC EVOLUTION OF THE MARMORILIK AREA.

MINERAL	EARLY RECUMBENT DEFORMATION	SOUTH VERGING FOLD & FAULT DEFORMATION	SINISTRAL SHEAR PHASE DEFORMATION	LATE EXTENSION PHASE DEFORMATION
<b>PYRITE</b>	Moderate grain elongation, dislocation etch pits picking out slip lines and deformation bands. Flattening on fold limbs polygonisation in hinges Many textures obscured by grain growth.	Severe cataclasis with fragmentation & rotation of grains. Elongate grains with dislocation pits, slip lines, kinks and walls.	Grain growth and polygonal grains with 120° triple junctions, lack of sub grains etc. Intense grain aggregation.	Minor cataclasis with grain fracturing of polygonal grains
<b>SPHALERITE</b>	Grain growth obscures many early textures. Minor grain elongation lanceolate deformation twins. Medium sized grains showing grain growth and annealing.	Dynamic recrystallisation with core mantle textures. Sub-grains and grain elongation preferred crystal orientation. Defm. twins	Grain growth and aggregation. Dentate cusate boundaries grain boundary pinning. Broad annealing twins Earlier defm. twins bent.	Cataclastic failure fragmentation and grain size reduction elongate irregular grains.
<b>GALENA</b>	Mostly recrystallised	Duplex textures with sphalerite. Now recrystallised but minor grain elongation, sub grains and dislocation pits. Most now recrystallised.	Coarsely recrystallised grains. Polygonal grains. 120° triple junctions. Grain boundary migration. Severe grain elongation & twinning kinking & sub-grain formation.	Remobilised into fractures and polygonal unstrained grains.
<b>PYRRHOTITE</b>	Not known	Strongly elongate grains with internal sub grains, kinks. Flame like defm twins.	Polygonisation and minor grain growth. Inclusions of sphalerite and grain boundary pinning	Not observed
<b>CHALCO-PYRITE</b>	Irregular grains included in sphalerite at old grain boundaries and defm. twins.	Grain growth and mobilisation obscures microstructures.	Grain growth and mobilisation into fractures and captured as inclusions in pyrite and sphalerite	Mobilised into late fractures.
<b>ARSENO-PYRITE</b>	Not known	Not known	Euhedral rhombs. lack of sub grains strong grain growth annealing and over-growth textures.	Fracturing and fragmentation of grains.
<b>TENNANTITE</b>	Not known	Not Known	Coarse grains with dentate and lobate overgrowths. Grain boundary migration.	Lack of fracturing. Minor mobilisation.

RECRYSTALLISATION  
CORE - MANTLE MICROSTRUCTURE



(after White 1976)

**Figure 9.9** Dynamic recrystallisation textures: Core-mantle textures

relict grain boundaries and deformation twins. Dynamically recrystallised core-mantle microtextures (Figs. 6.33 & 9.9) developed in the porphyroclastic ore facies during D2 deformation. Dynamic recrystallisation is associated with accelerated dislocation creep mechanisms and fluctuating stress-strain regimes (Nicholas and Poirier, 1976). The textures are representative of hot-working with grain refinement and strain softening (White, 1975 & 1977).

Strong recrystallisation and annealing of the plastically deformed and dynamically recrystallised sphalerite occurred during the D3 deformation.

### **Pyrrhotite**

Pyrrhotite deformation is sensitive to temperature (Clark and Kelly, 1973) (Fig. 9.10) and hence pyrrhotite acts as a relatively good geothermometer. D1 microtextures are not preserved in pyrrhotite. In the D2 slide systems of the I zone (Fig. 6.21) and in the T zone, foliated pyrrhotitic horizons contain fragmented and recrystallised sphalerite clasts (Fig. 6.30). The pyrrhotite was less competent than the sphalerite, which suggests that temperatures greater than 200°C (Clark and Kelly, 1973) were attained during this deformation. The pyrrhotite is annealed, though relict D2 deformation textures are preserved as dynamically recrystallised strongly elongate grains (Fig. 6.31 c & d), with kinks and flame-like deformation twins (Table 9.5). Kinks and twins develop in pyrrhotite at temperatures above 300°C (Gill, 1969; Graf and Skinner, 1970; Atkinson, 1972 & 1975b; and Clark and Kelly, 1973) and are indicative of dislocation deformation mechanisms (Table 9.4).

Pyrrhotite annealed during D3 deformation. Recrystallisation in pyrrhotite has been reported to occur at 525–666°C Gill (1969), though McClay (1978) states that syntectonic recrystallisation would occur at lower temperatures during natural deformation at slow strain rates. The weight of evidence compiled during this study for the peak Rinkian

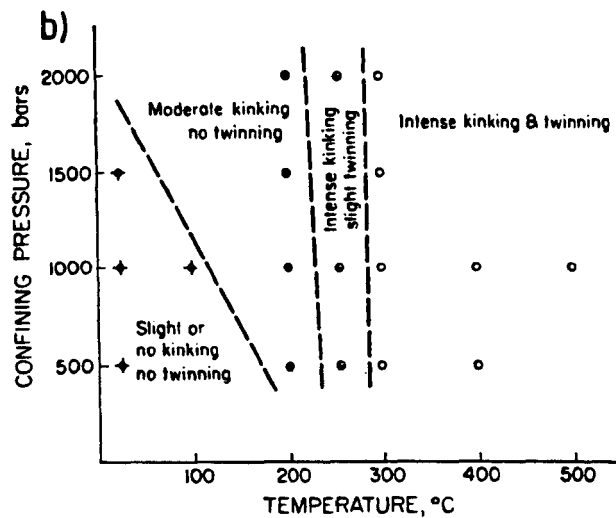
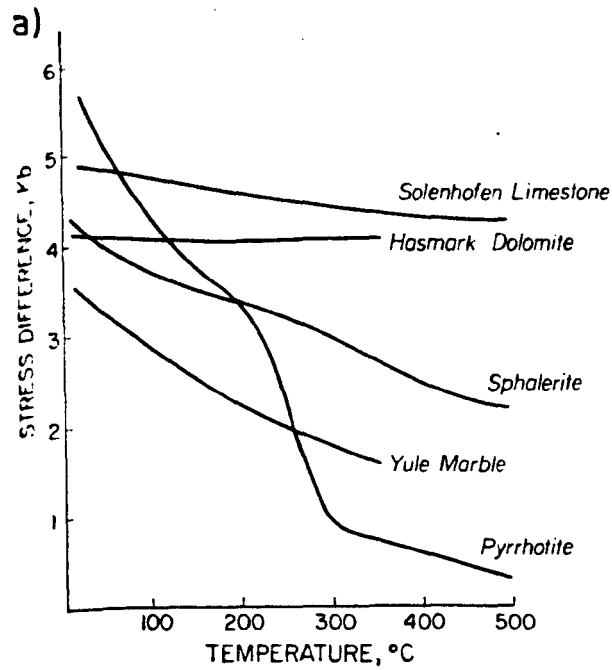


**Figure 9.10** a) Comparison of the strength of pyrrhotite with sphalerite and carbonate rocks b) deformation mechanisms observed in pyrrhotite as a function of temperature and confining pressure (After Clark and Kelly, 1973)

metamorphic grade (section 5.5) suggests that pyrrhotite must have recrystallised, in the Black Angel sulphides, at temperatures less than 500°C.

### **Galena**

D1 & D2 related galena microtextures are rare (Table 9.5). Strong grain growth recrystallisation and annealing took place during D3 deformation and peak Rinkian metamorphism (Table 6.4). Static recovery and grain growth textures (Table 9.4) such as polygonal grains with 120° triple junctions and straight grain boundaries are particularly apparent in the highly mobile galena of the recrystallised ore facies. Annealing experiments carried out on galena show that dynamic recrystallisation occurs in laboratory experiments at 200°C and strain rates of  $3 \times 10^{-7} \text{ sec}^{-1}$  (McClay and Atkinson 1977) whereas static annealing shows recrystallisation at 200°C (Clark et al., 1977) and marked recrystallisation at 400°C (Clark et al., 1977; Siemes, 1976 & 1977; Stanton and Willey, 1972).

Apart from severe grain growth, dislocation processes were active in the D3 deformation. In the bleby ore tectonite (Fig. 6.37) the galena forms highly elongate grains and internally develops subgrains, suggestive of dynamic recrystallisation, and kink bands that are aligned perpendicular to the elongation direction, suggestive of dislocation glide and creep mechanisms (Fig. 6.37). High temperature testing of polycrystalline galena by Atkinson (1972, 1974, 1976a) and Salmon et al. (1974) showed that at low temperatures 20°-200°C [001] <110> slip and kinking occurred in coarse grained galena (Salmon et al., 1974), whereas in fine grained galena Atkinson found that kinks rarely <sup>develop</sup> before 200°C.

### 9.3.3 Summary of ore deformation mechanisms

#### a) D1 deformation processes

It is difficult to predict the P/T regimes and sulphide deformation mechanisms in operation during the D1 deformation as most of the D1 deformation textures have either been overprinted or recrystallised during the later D2 & D3 tectono-metamorphic events. However, in pyrite D1 deformation was taken up by plastic, dislocation creep and dislocation glide processes, and cataclastic mechanisms operating under moderate temperatures ( $\approx +400^{\circ}\text{C}$ ) and low  $f_{\text{O}_2}$ .

A period of static recovery, grain growth and annealing is interpreted to have taken place after D1 deformation. For as Stanton (1972) suggested, at temperatures exceeding  $250\text{--}300^{\circ}\text{C}$  any pause in deformation would lead to annealing.

#### b) D2 deformation processes

The sulphides deformed by brittle failure (cataclasis) and plastic dislocation creep and dynamic recrystallisation processes during the D2 deformation. These deformation mechanisms indicate that moderate to high temperatures, associated with fluctuating strain rates, occurred during this event. The greater degree of pyrite cataclasis in D2 related ore tectonites is interpreted as an effect of both the increasingly plastic nature of the matrix, which would have allowed a greater rotation of the pyrite grains, and the increased strain rate under which deformation took place.

#### c) D3 deformation processes

Textures indicative of static recovery mechanisms are present in D3 sulphide minerals. Static recovery mechanisms result from a maintenance of elevated temperatures ( $T/T_m > 0.6$ ). These conditions are synonymous with those of peak Rinkian metamorphism (section 5.5). The excessive grain size of the late stage annealed ores, and in particular the

massive pyritic ore where pyrite grains are up to 20 cm., is thought to have resulted from a punctuated sequence of straining and annealing events (Stanton, 1972; Mookherjee, 1976). The strong mobilisation of galena, and to a lesser extent sphalerite, into fold hinges during the D3 deformation (Fig. 4.32 & 6.44) is thought to have taken place largely by dislocation processes followed by static recovery and recrystallisation mechanisms. Diffusional creep possibly influenced remobilisation in the galena, although textures synonymous with this process (Table 9.4) were not observed.

#### **d) D4 deformation processes**

Cataclastic fracturing of all sulphide minerals occurs in association with the Late extensional phase deformation. The presence of fractures in the more mobile minerals such as galena and chalcopyrite and pyrrhotite, whose strength rapidly diminishes below 200°C (Fig. 9.10) (Clark et al., 1973), suggests that this late stage deformation occurred under low temperatures <200°C and at relatively high strain rates.

#### **e) Summary**

The ores have dominantly deformed by plastic processes such as dislocation creep and glide (Table 9.4), with severe cataclasis in pyrite, during D1 and D2 deformation. Mobilisation and recrystallisation of the high grade ores, located in D3 fold hinges (Fig. 6.20), was accomplished by plastic dislocational (possibly minor diffusive processes) and static recovery processes.

## **9.4 Classification of and models of ore genesis for the Black Angel deposits**

### **9.4.1 Introduction**

Previous interpretations of ore formation have included a syn or epigenetic origin (Garde, 1978), and an early diagenetic to epigenetic sabkha-related origin, with a Marmorilik Formation metal source (F.D. Pedersen, 1980; J. Pedersen, 1980). These theories are unacceptable, as simple mass balance equations indicate that the amount of Zn-Pb needed to form the Black Angel deposits cannot be derived from the Marmorilik Formation carbonates. Also the mineralogy of the Black Angel is inconsistent (lacking Cu) with other deposits, such as the Roan (Zambia), that are interpreted to have formed through similar sabkha processes (Renfro, 1974).

### **9.4.2 A Comparison of the Black Angel deposits with carbonate-hosted deposits**

The Black Angel deposits are strongly metamorphosed and tectonically deformed carbonate-hosted sulphides. The deposits are analogous, both in terms of their stratigraphic and tectonic setting, to the Balmat-Edwards Zn-Pb deposits (Whelan, 1984). However isotopic inconsistencies exist.

In an attempt to formulate a model of ore genesis for the Black Angel sulphides, the characteristics of the deposits are compared with the i) 'Irish-type' carbonate-hosted deposits which are a genetic sub group of the SEDEX deposits (Lydon, 1986) and ii) the 'Mississippi Valley-type' (MVT) stratabound Zn-Pb deposits (Table 9.6).

#### **a) Mineralogy**

The MVT deposits usually contain Pb-Zn-Fe (py & ma) sulphides, whereas the 'Irish-type' assemblages are commonly Fe (py & po)-Zn-Pb sulphides (Table 9.6). Copper minerals are rare in both

**Table 9.6: Comparison of carbonate hosted Pb-Zn deposits with the Black Angel deposits**

Features	M.V.T deposits	Irish deposits	Black Angel deposits
Major metals	Pb-Zn-Fe.	Zn-Pb-Fe	Zn-Pb-Fe
Trace metals	generally lack Cu, Ag	Significant Ag, minor Cu	Ag, As, localised Cu (up to 0.5%)
Grade and Tonnage	low grade 8% comb. small isolated deposits	9-11% Comb. 12-18 10 <sup>6</sup> t.	18% Comb 13.5 10 <sup>6</sup> t.
Mineralisation style	stratabound in solution cavities	Discordant feeder zone with dissem.stratiform	stratabound to tectonically discordant
Age	Late Proterozoic to triassic	Carboniferous	Early Proterozoic (Met. age 1860/1680 ma.)
Tectonic setting	Basin margin tectonically stable	intracratonic fault controlled basin tectonically and thermally active	Stable basin margin, growth faults not recognised
Sedimentary Controls	Platformal carbonates with reefs, bars, slump breccias at basin margins or facies boundaries	Bank and lagoonal facies abutting growth faults	Platformal carbonates with clastic basin to the north. Carbonate structures deformed minor stromatolites
Host rock character	shallow water carbonates Unconformities within the ore sequence	Argillaceous units interbedded with muddy carbonates	Recrystallised carbonates. Mineralisation associated with Calcite/dolomite transitions above pelite. Deformation obscures U/C
Diagenetic Modification	Dolomitisation, ores in dolostones. Silicification and karstification	Early diagenetic text. partial to total rex & dolomitisation	Recrystallisation and annealing localised late dolomitisation with high porosity. Minor silicification
Barite	Common	stratiform (up to 2.3 10 <sup>6</sup> t.)	Limited stratabound to discordant and in fine schistose layers
Flourite	Common	Rare	Common, both in ore and host rocks
Red beds	Uncommon	In F.Wall fault bounded panel and basement	None
Evaporites	Back reef evaporites	Sabkha facies to North	Massive anhydrite bands and recrystallised gypsum
Volcanics	None	Minor tuffaceous units	None

Features	M.V.T deposits	Irish deposits	Black Angel deposits
Organics	Yes	Yes	Yes (Graphite films and euhedra) possibly metamorphic & bitumen
(Primary) Ore texture	Coarse colloform with disseminated replacement significant breccia mineralisation	Framboidal and colloform textures	Colloform and colloidal (?) textures and euhedral marcasite (?) rhombs overprinted by sheared annealed textures
Ore zonation	Random	Vertical and horizontal Cu-Zn-Pb from vent	Zonation controlled by deformation Cu, FeS and Barite localised to F.Wall and S.E orebodies. Central pyrite zone
Mineralising Fluids	15-25% Na-Ca-Cl Temperatures 50-175°C EPIGENETIC	10-25 wt% NaCl brines between 90 -260°C EPI-SYNGENETIC	Fluid inclusion 25 wt% NaCl. temp. 220°C (Quartz) EPIGENETIC
Lead isotopes	Highly radiogenic variable	Radiogenic but homogeneous	Slightly radiogenic homogeneous, with minor variation
Sulphur isotopes	Range < 30 ‰. zero to strongly positive	Range > 30 ‰. moderately negative	Range < 10 ‰. homogenised slightly positive
Lead/Sulphur isotopes	Negative correlation	None	Negative correlation (though homogenised data)

Compiled from Andrew (1986), Ashton (1986) Boest et al., (1981), Cathles and Smith (1983), Caulfield et al., (1986), Gustafson and Williams (1981), Heyl et al., (1974), Hitzman and Large (1986), Lydon (1986), Ohle (1980), Russell (1986) and Sangster (1976 & 1986).

classes and if present form in uneconomic amounts. Mineralogical variations do occur between the two classes, 'Irish-type' deposits commonly contain high silver and silica (usually as chert) contents. The MVT class commonly contains fluorite.

The Black Angel main sulphide assemblage of Fe-Zn-Pb-Ag is more closely related to the the 'Irish-type' rather than the M.V.T. (Table 9.6). However, the Black Angel ores contain minor copper, pseudomorphed marcasite (Fig. 6.40) and fluorite (Fig. 3.10c), which is almost exclusive to the M.V.T. ores. Greater concentrations of pyrrhotite are found in the Black Angel than would be expected in most M.V.T. ores. The pyrrhotite is interpreted to be a product of metamorphic desulphidisation rather than a primary exhalative derivative.

### **b) Tectonic setting of the deposits**

Both the 'Irish-type' and M.V.T deposits are spatially related to sedimentary basins. The 'Irish-type' deposits (Hitzmann and Large, 1986), and also the H.Y.C deposit of the McArthur River basin (Muir et al., 1985), typically occur within tectonically active fault controlled epicratonic or intracratonic marine basins, whose dimensions generally exceed 100km (Large, 1980, 1981 & 1983). The individual deposits are normally found in third order fault controlled basins, with the faults acting as channel ways for fluid migration during sedimentation (Lydon, 1986; Russell, 1986). In contrast, the MVT ore deposits appear to be located towards basin margins (Fig. 9.11)(Anderson and MacQueen, 1982) in platformal carbonates which are generally dolomites and less commonly limestones (Sangster, 1976).

Although the original stratigraphic relationships have been largely obliterated within the Marmorilik area by the Rinkian tectono-metamorphic event, the Black Angel ores occur in platformal carbonates on the southern margin of a large clastic basin (Fig. 2.5 & 9.13 ). The basin has similar dimensions to those of the M.V.T deposits (Figs. 2.8 & 9.11).

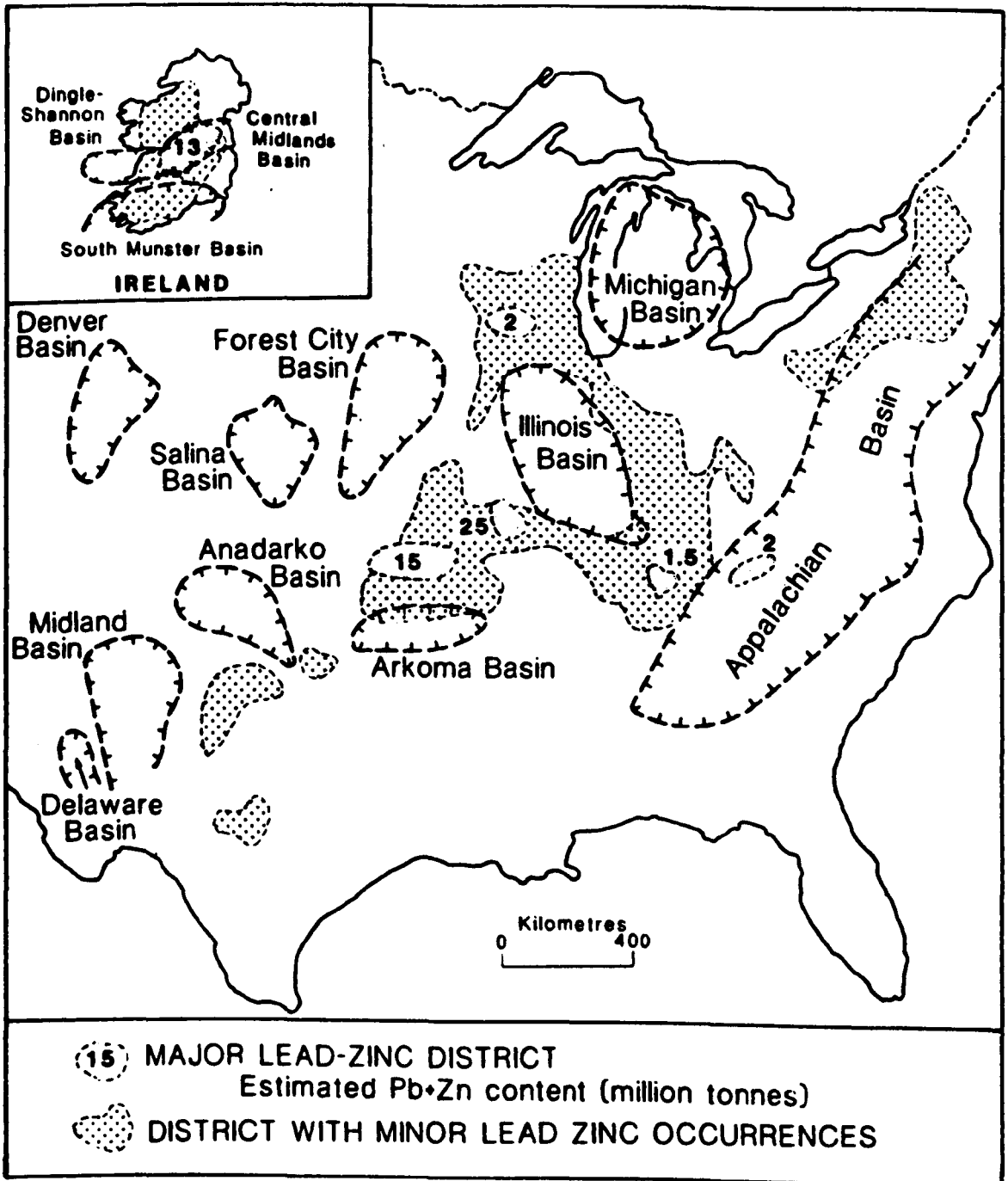


**Figure 9.11** Simplified distribution of Mississippi Valley-type ore districts of central U.S.A. showing their spatial relation to sedimentary basins. (After Lydon, 1986).

### **c) Temperature of ore formation**

Carbonate-hosted Pb-Zn ore deposits are interpreted to have formed from hydrothermal solutions (Beales and Jackson, 1967; Sverjinsky, 1981) with essentially the same chemical characteristics, at temperatures up to 250°C. Fluid inclusion filling temperatures for MVT deposits are most commonly in the range 100-150°C (Roedder, 1976), whereas the fluid inclusion and isotope data for carbonate-hosted SEDEX and 'Irish-type' deposits indicate higher temperatures of sulphide formation, i.e. up to 250°C (Gustafson and Williams, 1981; Boast et al., 1981; Samson and Russell, 1983; Nesbitt et al., 1984; Gardner and Hutcheon, 1985; Caulfield et al., 1986).

The limited fluid inclusion data from the Black Angel mineralisation (Hughes, 1981), on quartz from the Nunngarut and Ark mineralisation, gave homogenisation temperatures of 220°C - 230°C and salinities of 29 wt% NaCl. These temperatures are comparable with the formation temperatures of the 'Irish-type' deposits.

### **d) Textural characteristics and metal zonation**

'Irish-type' deposits develop a range of epigenetic-early diagenetic-syngenetic mineralisation textures. Discordant, replacement and fracture fill (epigenetic) mineralisation in the Navan deposit (Ashton et al., 1986) is associated with the fault and vent zone along which the ore forming fluids were expelled. Syngenetic textures, such as framboidal pyrite, pyritic chimneys (Boyce<sup>et al</sup>, 1983) and thin stratiform layers of sphalerite and galena (Ashton et al., 1986) are present. These are interpreted to have developed at or near the sediment/water interface. Metal zonation from copper-sphalerite-galena-pyrite is observed both upwards through and laterally outwards away from the feeder zone (Gustafson and Williams, 1981; Andrew, 1986). The deposits are generally wedge shaped in cross-section and are laterally continuous along strike (Andrew, 1986).

In M.V.T. deposits epigenetic void fill textures are predominant. Framboidal pyrite and thinly disseminated stratiform mineralisation is largely absent. Metal zonation trends are not recognised. The deposits form as random irregularly shaped pods and lenses, which vary in size from 0.5 to 15 million tonnes.

Framboidal textures, synonymous with syn-genetic mineralisation, have not been recognised in the Black Angel sulphides, whereas many epigenetic textural forms are present (Fig. 6.40). The deposits occur in both a sheet-like form (Fig. 6.11) and as irregularly distributed pods. This is largely the result of polyphase deformation. Metal zonation trends are strongly controlled by deformation processes and tectonic structures (Figs. 6.44-49), though a primary (?) iron rich core similar to that found in the Sullivan mine (Hamilton <sup>et al.</sup> 1976) occurs in the Angel zone (Fig. 6.46).

### **e) Isotopic characteristics**

Many of the lead and stable isotopic characteristics of the M.V.T. and 'Irish-type' deposits have been discussed with respect to the isotopic distributions of the Black Angel sulphides in chapters 7 & 8. The lead and stable isotopic data from the Black Angel sulphides have been strongly homogenised. Thus they are not reliable criteria on which to base a classification of the deposit

### **f) Summary**

The Black Angel mineralisation exhibits characteristics that are similar to both M.V.T and SEDEX 'Irish Type' deposits. Possibly the greater weight of evidence, namely the geological setting, minor mineral assemblage, textural and host rock characteristics, tend to be more closely linked with the epigenetic M.V.T deposits. However several characteristics such as the temperature of ore formation and the major metal concentrations are more compatible with the 'Irish-type' deposits.

### 9.4.3 Model of Ore Genesis for the Black Angel sulphides

#### a) Metal sources

Lead isotope signatures for the Black Angel deposits suggest that lead was derived from upper crustal sediments (section 7.5), which were eroded from the basement. Metal abundances of the potential source rocks are given in Table 9.7 (Krauskopf, 1967). Simple mass balance equations indicate that the amount of Zn-Pb needed to form the Black Angel deposits cannot be derived from the Marmorilik Formation carbonates. Pb-isotope analysis has predicted that the most likely lead source is from the thick sandstone sequences of the Qeqertarsuaq Formation, which occur in the clastic basin to the north of Marmorilik (Fig. 9.13). The shales and psammites of the Nukavsak Formation may have contributed Zn and Fe, but are more likely to be metal sinks (Gustafson and Williams, 1981).

#### b) Derivation and transport of ore forming fluids

Many theories exist as to the origin of ore forming fluids. The most popular theories of ore genesis are related to the dewatering of sediments during basin compaction (Noble, 1963; Jackson and Beales, 1967; Dozy, 1970; Sverjinsky, 1981 & 1984; Cathles and Smith, 1983).

Many examples exist that suggest that SEDEX and MVT deposits formed from ore fluids that were derived from the same basin, by basin dewatering. In the MacArthur River Basin (Fig. 9.12), MVT (Cooley and Ridge deposits; Walker et al, 1983) and SEDEX (H.Y.C. deposit; Rye and Williams, 1981) deposits have been interpreted on the basis of their isotopic compositions to have been derived from the same hydrothermal system. The Selwyn Basin of northern Canada is another good example of the relationship between MVT and SEDEX deposits. The shale basin contains the Anvil Range, MacPass and Howards Pass SEDEX deposits, which pass eastwards through transitional deposits containing elements of both SEDEX and MVT deposits, e.g. The Vulcan deposit (Mako and Shanks III, 1984) into platformal carbonates that host MVT deposits, e.g. Gayna River

Rock type	Source	Cu	Pb	Zn	Ag	Co
Granites (low Ca)	(5)	1-100	5-70	5-110		
	(1)	(10)	(19)	(39)	(0.037)	(1)
Intermediate rocks	(5)	<5-200	2-62	5-125		
	(6)	(35)	(15)	(72)	(0.07)	(10)
Basalts	(5)	10-260	<1-38	30-230		
	(1)	(87)	(6)	(105)	(0.11)	(48)
Ultramafic rocks	(5)	2-300		25-90		
	(1)	(10)	(1)	(50)	(0.06)	(150)
Carbonate rocks	(5)	<1-150	<1-200	<1-180		
	(1)	(4)	(9)	(20)	(0.0X)	(0.1)
Deep sea clays	(5)	10-2,000	<10-139	80-1,300		
	(1)	(250)	(80)	(165)	(0.11)	(74)
Shales	(5)	2-300	5-55	16-430		
	(1)	(45)	(20)	(95)	(0.07)	(19)
Black shales	(2)	20-500	7-260	34-7,000	1-24	7-300
	(2)	(70)	(20)	(<300)	(<1)	(10)
Sandstones	(5)	<1-155	<1-80	5-198		
	(1)	(X)	(7)	(16)	(0.0X)	(0.3)
Continental crust	(4)	(55)	(12.5)	(70)	(0.07)	(25)
Metalliferous brines						
Salton Sea brine	(3)	8	100	540		
Cheleken brine	(7)	0.9-15	3.6-77	0.9-5.4		
Mississippi brines	(8)		<2-111	<2-360		
Sources of information						
(1) Turekian and Wedepohl, 1961						
(2) Vine and Tourtelot, 1970						
(3) White, 1968						
(4) Taylor, 1964						
(5) Wedepohl, ed., Handbook of Geochemistry						
(6) Vinogradov, 1962						
(7) Lebedev, 1967						
(8) Carpenter, Trout, and Pickett, 1974						

**Table 9.7 Metal contents of potential source rocks**  
(Range and (average), all in ppm) (After Krauskopf, 1967).



and Bear Twit (Sangster, 1986).

Pb-isotope data from the Black Angel deposits, suggests that the fluids migrated laterally along the Qeqertarssuaq Formation stratiform aquifer and into the carbonate lithologies of the Marmorilik Formation. Fluid inclusion data from Hughes (1981) suggests that the Black Angel deposits ore forming solutions were highly saline, 29-33 wt.%, NaCl brines.

Studies on hydrothermal ground waters in present day basins have reported metal rich oil-field brines, carried in sodium and calcium chloride waters which range in temperature from 100°C to 140°C, that contained 370 mg/l Zn and 92 mg/l Pb (Carpenter et al., 1974).

### **c) Mineral deposition**

Ore forming fluids are undersaturated up to the site of ore deposition. Deposition of sulphides is likely to result from a) cooling of the brines b) decrease in the activities of the complex forming ligands c) increase in  $a_{S_2}$ . The degree of saturation or deposition of sulphides will increase as a consequence of i) Increased  $H_2S$  concentration which may be due to sulphate reduction, reaction from organics, or mixing with sulphide solutions. ii) Increased pH caused by either reaction with carbonates or feldspars. iii) decreased chloride concentration, resulting from dilution by meteoric waters iv) decreased temperature (Barnes, 1979).

The Black Angel sulphides contain many primary void-fill textures (Fig. 6.40), but lack syn-genetic framboidal textures. The sulphides are therefore interpreted to have formed epigenetically. It is envisaged that processes (i) and (ii) were active in the precipitation of the sulphides. It is noticeable that the Black Angel sulphides are hosted in anhydrite bearing calcitic marbles which occur in close association with graphite bearing pelitic units, both of which would be capable of increasing  $H_2S$  concentration in the ore carrying solutions.

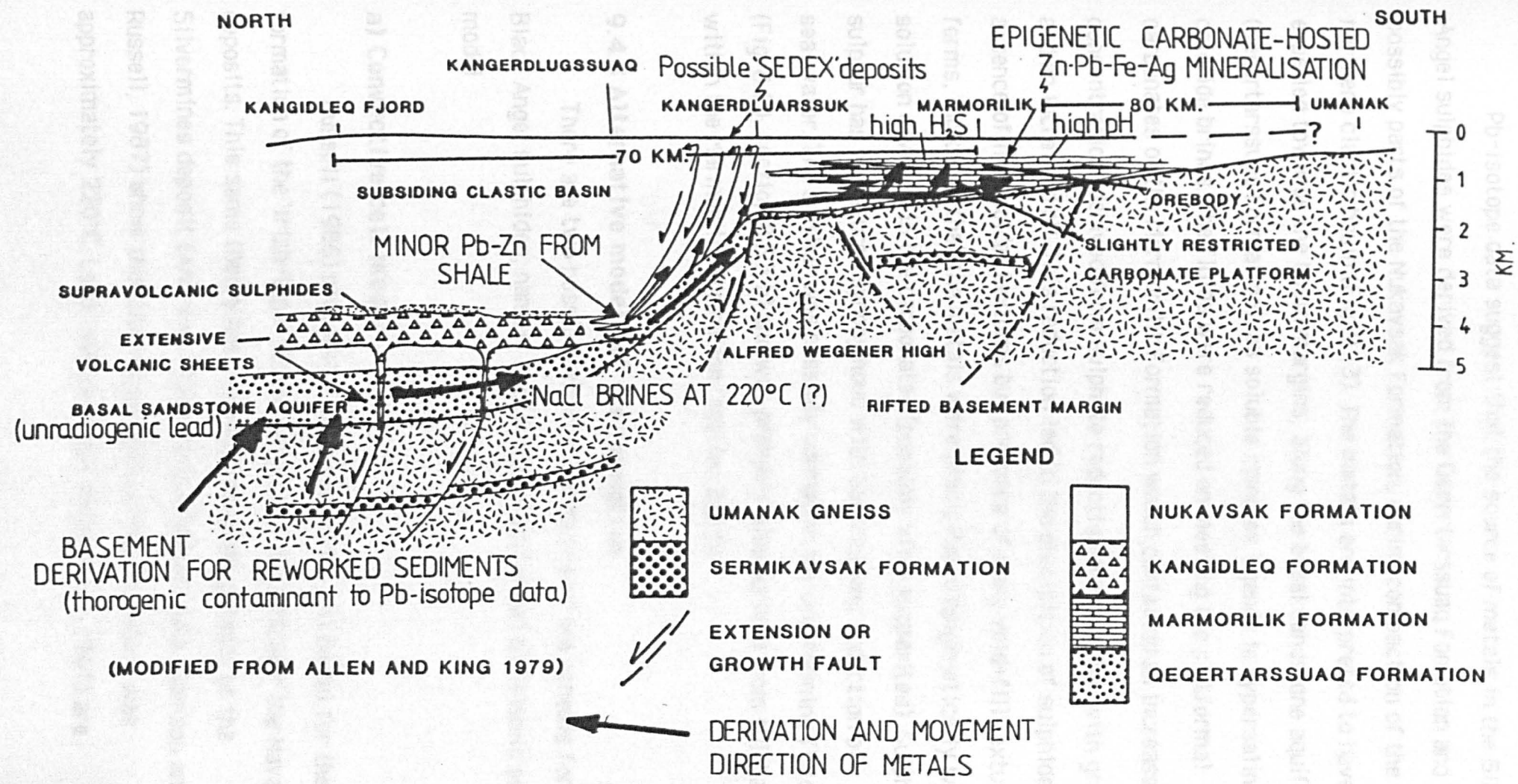


**Figure 9.13** Schematic representation of a model for the genesis of the Black Angel deposits

#### **d) Summary**

Pb-isotope data suggest that the source of metals in the Black Angel sulphides were derived from the Qeqertarsuaq Formation and possibly parts of the Nukavsak Formation, during compaction of the northern clastic basin (Fig. 9.13). The metals are interpreted to have been expelled towards the basin margins, along the basal sandstone aquifer (Qeqertarsuaq Formation), as soluble complex ligands in hypersaline chloride brines. The fluids were reduced on meeting the platform carbonates of the Marmorilik Formation which contained an increased  $H_2S$  concentration (derived from sulphate reduction and reaction with graphite) and an increased pH. This reduction led to the precipitation of sulphides. The absence of framboidal textures but presence of many void-fill textural forms, indicates that the metals were precipitated epigenetically within solution cavities in the carbonates (possibly after evaporites). Sulphide sulphur has signatures synonymous with bacterial reduction of sea-water. The sulphur was possibly carried in the ore-forming fluids (Fig. 8.10, section 8.5.3 b) and was probably also derived from sulphates within the Marmorilik Formation (section 8.5.3a)

#### **9.4.4 Alternative models of ore formation**

There are two possible alternative models of ore genesis for the Black Angel sulphides, namely a) Convective cell model b) Seismic pumping model

##### **a) Convective cell model**

Russell (1986) proposed a deep convective cell model for the formation of the 'Irish-type' SEDEX related and in particular the Navan deposits. This same theory has been applied to the genesis of the Silvermines deposit (Andrew, 1986). Fluid inclusion data (Samson and Russell, 1987) show that the temperature of ore formation was approximately 220°C. Lead isotope ratios (Mills et al., 1987) are

progressively less radiogenic the younger.

The model derived to explain the formation of the giant exhalative orebody at the downward excavating centre of extensional tectonics in the early stages of continental extension (Fig. 9.14), it is thought that the exhalative orebody is formed along extensional fractures in the brittle-ductile transition zone.

acid brines that scavenge

On meeting sea water, the hydrothermal solution precipitates their diagenetic minerals in a fault zone (it may be produced if the fault zone moves to greater depths, even though the transition zone moves

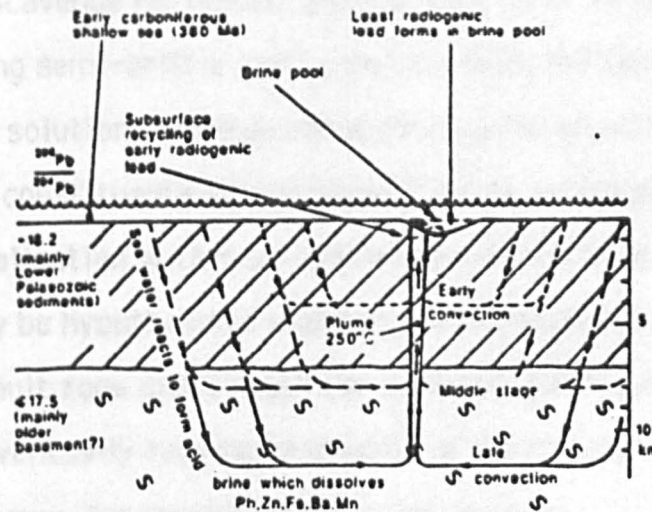


**Figure 9.14** Diagram illustrating the progress of a convection cell as it excavates downwards to tap older continental crust with less radiogenic lead which is transported upwards to form a giant exhalative orebody. (After Mills et al., 1987).

## b) Seismic pumping

This process has been invoked to explain the formation of the giant exhalative orebody at the McArthur River Basin (1975). The McArthur River Basin is a giant exhalative orebody (Mills et al., 1961). According to the model of seismic pumping (Mills et al., 1975), the exhalative orebody is formed by failure on a fault, a large amount of fluid is released from the crust and is carried to the least compressive part of the crust. This fluid is then released to the surface. This process is thought to be a result of a high differential stress in the crust. The main idea of the theory is that

progressively less radiogenic the younger the mineralisation.

The model derived to explain these characteristics is one of downward excavating convection cells, that were set up during regional extension (Fig. 9.14). It is thought that seawater penetrates the crust along extensional fractures. The fluids spread out when they reach the brittle-ductile transition. As the fluids circulate they are converted to acid brines that scavenge for metals and mix lead from the upper crust.

On meeting semi-brittle fault zones towards the basin margins, the hydrothermal solutions move upwards through the crust and precipitate their constituents syngenetically on the sea floor, or as early diagenetic mineralisation within unlithified sediments on or close to the fault zone (it may be hypothesised that epigenetic mineralisation would be produced if the fault zone didn't reach the surface). The fluids penetrate to greater depths, eventually tapping basement, as the brittle-ductile transition zone moves downwards as the crust is cooled.

The convective cell theory is not thought to be applicable to the Black Angel deposits as it relates to a tectonically active extensional basin. Also lead isotope and sulphur isotope compositions for the Black Angel sulphides do not conform to those of the 'Irish-type' deposits (sections 7.5.2 & 8.5.3b).

## **b) Seismic pumping**

This process has been invoked to explain mineralisation at McArthur River (Muir, 1979), Mt. Isa (Muir, 1981) and Tynagh (Boast et al., 1981). According to Sibson et al. (1975), as stresses build up prior to failure on a fault, a large number of extension fractures open up normal to the least compressive stress and fill with fluids, e.g. ground water. When failure occurs these fluids, rich in minerals leached from the country rocks, are rapidly expelled and precipitate their solutes at or near the surface. This process works best in wrench fault systems as a high differential stress is required. The special attraction of the theory is that

it explains the supposed pulsatory nature of mineralisation.

This process is refuted as the origin of the Black Angel deposits, for the temperatures of formation (up to 350°C) for this model far exceed those estimated during the formation of the Black Angel deposits. However, this process is likely to have had a bearing on the recrystallisation and homogenisation of the Black Angel ores.

## **9.5. Exploration potential for unfound mineralisation**

A good exploration potential exists for new Zn-Pb deposits both on a regional and a local deposit scale within the Marmorilik area and Rinks Isbrae district.

### **9.5.1 Regional exploration potential**

The theories of ore genesis for the Black Angel deposits may be particularly useful in deciding upon areas of exploration for new ore deposits. The Black Angel deposits are interpreted to be related to M.V.T deposits. If the Black Angel deposits were formed from dewatering of the northerly clastic basin (section 9.4.3 d), then there exists a great potential for SEDEX deposits to be found at the hinge zone of the northerly clastic basin (Fig. 9.14). Exploration for these SEDEX deposits should therefore focus upon the clastic basin margins, where growth faults and feeder zones for SEDEX mineralisation, would be expected. Exploration for new M.V.T. deposits should focus on calcite/dolomite (chemical) fronts, which would be favourable areas for Zn-Pb precipitation.

### **9.5.2 Local exploration potential**

Although the Black Angel deposits have been extensively drilled on a 200 metre grid from the Black Angel mountain and by exploratory diamond drilling from within the mine, there is still a high potential for the discovery of new, small tonnage, high grade deposits.

Mineralisation in the Upper Marmorilik Formation is extensive in a

thin sheet-like form for many kilometres. Ore grade mineralisation is locally formed where tectonic thickening has occurred. Not only does the Rinkian tectonism control ore grade, but <sup>it</sup> also has a major effect on the orientation of the mineralisation (Figs. 6.44-49).

D1 deformation structures have a major control on ore location. The Nunngarut deposit is located in the D1 Nunngarut fold hinge (Fig. 6.9), whilst the Black Angel deposits have been folded about the D1 Black Angel nappe (Fig. 6.14), transposed parallel with S1 fabrics and stretched along an 080 trending belt that lies parallel to the D1 fold axis. Significant mineralisation has also been intersected at the Deep Ice zone and recently at V 215, both of which lie along the D1 080 trend (Fig. 6.1).

The Black Angel deposits are held in a major D2 tectonic slide wedge (Fig. 6.10), which rapidly narrows to the south of the I zone. Exploration in the immediate area of the Black Angel sulphides should be restricted to this tectonic wedge. The Unit 4 stratigraphy which hosts the Black Angel sulphides (Fig. 6.2) is tectonically repeated along the northern margin of the South Lakes cliffwall (Fig. 6.10). Significant new, Black Angel type, mineralisation may be expected to be found within this tectono-stratigraphy, especially if evaporitic and graphitic bearing units are intersected.

Local reorientation of the ore horizon has occurred about open D3 folds. The major D3 folds have a half wavelength of approximately 2.5 km. that intersect the D1 mineralised trend at the C area, Angel zone; MX area, Cover zone; and Deep Ice zone (Fig. 6.15). As the mineralised sheets are so extensive in the Marmorilik area, it is predicted that high grade, recrystallised mineralisation (of the recrystallised ore facies) may be developed 2.5 km to the ENE of the Deep Ice zone along the D1 080 trend.

Away from the Black Angel deposits, there is potential for new finds associated with the Nunngarut zone to the east of the A fjord, below the Middle Marmorilik tectonic slide zone, on a strike parallel to the Nunngarut fold (Figs. 3.1 & 4.1a). A large north verging D1 fold is present

in this area. Drilling should focus on it's hinge zone. Elsewhere the exploration potential within the Marmorilik area is limited.

## **Chapter 10: Conclusions**

### **10.1 Introduction**

This thesis has entailed regional surface mapping of the Marmorilik area together with detailed underground mapping of the Black Angel deposits and petrographic, microprobe and isotopic analyses of the sulphides. Results from these studies have provided new insights into the understanding of the complex tectonic and metamorphic evolution of the Marmorilik area and in particular the tectono-stratigraphic setting of the Black Angel deposits, and the modes of ore deformation, mobilisation and genesis of the sulphides.

### **10.2 Stratigraphy**

Two major tectono-stratigraphic units are recognised in the Marmorilik area. They are the Basement Umanak Gneiss Complex and the Karrat Group Supracrustals. The Karrat Group lies with a sheared contact upon the basement gneisses. Significant tectonic thickening, inversion and omission of the stratigraphy occurred during the polyphase, Mid-Proterozoic, Rinkian event. In the Marmorilik area, the Karrat Group consists of the Qeqertarsuaq, Marmorilik and Nukavsak Formations. A new tectono-stratigraphy has been established for the Karrat Group supracrustals in the Marmorilik area, which has sub-divided the Marmorilik Formation into six mappable units. The Marmorilik Formation represents a platformal carbonate succession on the southern margin of a clastic basin.

### **10.3 Tectonic evolution**

The Karrat Group supracrustals have been deformed in the Mid-Proterozoic (1860-1680 Ma.), polyphase, tectono-metamorphic Rinkian event and a later extension phase deformation. Continent-continent collision between the Ketilidian and the stable Archean plates propagated deformation in the Rinkian mobile belt.

Sinistral transtensional stresses were generated within the belt, which propagated low amplitude periclinal basement folds. A diapiric rise of the basement, due to gravitational instabilities, resulted in gneiss dome formation. The domes propagated at different rates and thus developed a continuum of gneiss dome structures, from gently upwarped antiforms to large overfolded and imbricated basement nappes.

In this research, three Rinkian tectonic events have been recognised in the Marmorilik area. These are namely the:- i) D1 Early recumbent phase deformation ii) D2 South verging fold and slide phase, and the iii) D3 Sinistral shear phase.

In the Rinkian event, the basement deformed by sub-vertical motions. Basement uplift was translated into ductile sub-horizontal supracrustal deformation, which was largely accommodated by heterogeneous simple shear mechanisms. A system of ductile to semi-ductile deformation structures developed in each Rinkian event. D1 deformation was associated with southerly basement doming, which propagated a north verging gravity slide block in the overlying supracrustals. In the gravity slide block, extensional fault and slide systems formed to the south and large recumbent overfolds, such as the Black Angel nappe, formed to the north of the supracrustal sequence. The D2 deformation consisted of a south verging fold and tectonic slide system, which was generated by basement overthrusting in the northern Marmorilik area. The deformation was colinear to D1 deformation, but proceeded at higher strain rates. D3 deformation developed a major sinistral shear zone, in which a major transtensional half graben with periclinal folds were formed to the north, and a closely spaced en-échelon array of sinistral shear zones to the south-east. These shear zones progressively cross-cut the F3 fold axial traces.

The last phase of deformation occurred in the Late Pre-cambrian and consisted of N-S trending, west-side down, extension faults that are filled with dolerite dykes associated with smaller dolerite sills,

## 10.4. Metamorphism

Amphibolite to greenschist facies metamorphic grades were attained during the Rinkian tectonic event. Quantitative studies, during this project, have defined the peak metamorphic grade in the Marmorilik area as occurring at 470°C and between 2.5-3.0 Kbars under low  $f_{O_2}$  and high but slightly variable  $f_{S_2}$  conditions. These quantitative analyses were carried out by i) sulphur isotope geothermometry using equilibrated sphalerite-galena pairs ii) carbon isotope geothermometry on carbonate/graphite pairs and iii) sphalerite geobarometry using the FeS content of sphalerite inclusions within pyrite. The calculated temperatures were found to be consistent with the metamorphic grade estimated from metamorphic mineral assemblages.

## 10.5 Mineralisation

### 10.5.1 Introduction

The Black Angel Zn-Pb-Fe sulphides consist of 13.5 million tonnes of sphalerite, galena and pyrite with subordinate pyrrhotite, chalcopyrite and tennantite at grades of approximately 20% combined Zn-Pb. The sulphides occur as massive, stratabound, carbonate hosted deposits within the Upper Marmorilik Formation (Unit 4) evaporite-fluorite-barite bearing calcitic marbles. The mineralisation is developed in massive, randomly distributed pods and sheet-like horizons. Significant Zn-Pb mineralisation occurs at three other levels in the Marmorilik Formation tectono-stratigraphy.

The Black Angel deposits are texturally mature. The mineralisation was formed prior to the Rinkian event and has since undergone four phases of deformation which have generated a spectacular array of ten ore tectonite types. The ore tectonites have been classified according to their mineralogy and texture into four ore facies associations. These are the i) Banded ore facies ii) Porphyroclastic ore facies iii) Recrystallised ore

facies iv) Massive pyritic ore facies. The ore facies are directly related to specific tectonic processes and deformation events.

### **10.5.2. Deformation of the ores and host rocks**

The polyphase Rinkian deformation is the major controlling factor in the geometry and orientation of the Black Angel ore bodies, and has acted as a major influence on the ore grades, thicknesses, and textural distribution of the sulphides. The sulphides deformed plastically during the Rinkian events and in a cataclastic manner during the Late extensional deformation. However, pyrite deformed by both cataclastic and plastic processes in the Rinkian events.

In the D1 early recumbent phase deformation the mineralised horizon was folded about the Black Angel nappe. This resulted in:- two mineralised levels, the Angel-Cover-Tributary zone horizon and the I-Banana zone horizon; the transposition of the mineralisation into the plane of the F1 axial fabric; an elongation of the long axis of the sulphide sheet parallel to the F1 fold axis (O80) and the formation of the banded ore facies. Large scale recumbent folds with nipple like accommodation features and low-angle tectonic slides occur in the ore. The upper surface of the ore horizon is characterised by rootless folds with axialplanar seams of semi-massive and stringer like mineralisation.

D2 deformation caused tectonic thinning and imbrication of the ore horizon along D2 tectonic slide planes and tectonic thickening in D2 isoclinal fold hinges and antiformal imbricate stacks. An imbricated sequence of closely spaced, steeply north dipping, attenuated and discontinuous ore lenses occurs in the I zone. Intense D2 shearing occurred both within the ore horizon and along the ore-host rock boundary. The shearing generated i) an ore horizon of relatively consistent thickness and moderate grade (22% combined Zn-Pb) ii) the ore tectonites of the porphyroclastic ore facies iii) discordant tectonic contacts between the ore horizon and the host rocks in the Cover zone, southern Angel zone and

Banana zone and iv) 'durchbewegung' textures by way of gangue material being incorporated into the mineralisation by delamination and subsequent boudinage of the host rocks.

D3 deformation deformed the deposits into open, upright-northerly inclined, periclinal folds, which reorientated the ore horizon into ESE-WNW trending hook and cusp-like closures which parallel the D3 axial planar trend. Considerable tectonic thickening occurred in the synformal D3 fold closures. Coarse grained, high grade, mobilised and statically annealed ores of the recrystallised ore facies developed in the low stress fold hinges. D3 sinistral shear zones transected the ore horizon, downfaulting it to the west by up to 20 metres. The shear zones often rooted in the sulphides with the formation of bleby sphalerite and sheared galena ore tectonites.

The late extension phase deformation had little effect on the orientation or style of mineralisation, but caused local downfaulting of the ore horizon and a closely spaced fracture system within the ore horizon and host rocks. These fractures promote block rotation and rock slabbing, which has hindered production work in the mine.

### **10.5.3. Isotopic analyses**

A lead isotope analysis was conducted on galena and pyrite samples of the Black Angel sulphides and surrounding mineralisation. The galena lead isotope compositions show a closely spaced homogenised, bimodal distribution linked by the pyritic lead isotope compositions, all of which indicate a reworked upper crustal lead source. The bimodal distribution of data suggests that two separate mineralising phases existed and that a change in the isotopic composition of the source area occurred through time. Model age dates of 1500 Ma. calculated for the mineralisation are young in comparison to the calculated deformation age dates for the Rinkian mobile belt. The lead is therefore slightly radiogenic.

Stable sulphur isotope analyses carried out on the Black Angel

Zn-Pb-Fe mineralisation show a homogeneous, weakly positive, distribution of data. Strong metamorphic re-equilibration of the sulphur isotope compositions occurred during the Rinkian event. Sources of sulphur are difficult to predict due to this metamorphic re-equilibration. Stable carbon isotope analyses of the carbonates indicate normal marine origins. Stable oxygen isotope compositions of the Marmorilik Formation carbonates are strongly depleted with respect to unmetamorphosed carbonates of equivalent age. They represent an interaction of the carbonates with strongly depleted fluids, either during late diagenesis or Rinkian metamorphism.

#### **10.5.4. Genesis of the Black Angel mineralisation**

The Black Angel deposits are strongly deformed and metamorphosed carbonate-hosted sulphides. As a result of the complex tectono-metamorphic history of the deposits, conclusive evidence in favour of a particular genetic model for the evolution of the sulphides doesn't exist. Primary textural features are rare and are only preserved in metamorphic pyrite grains. Euhedral void-fill textures are present, whereas framboidal pyrite is not observed. Mineralogical and geological associations suggest that the deposits are <sup>more</sup> closely linked with the MVT class of Pb-Zn sulphides than <sup>with</sup> the SEDEX 'Irish-type' class.

It is interpreted that the Black Angel mineralisation formed epigenetically from metal rich basinal brines that were expelled from a northern clastic basin. The Qeqertarsuaq Formation acted as a basal sandstone aquifer for hydrothermal fluid flow.

#### **10.6. Exploration potential in the Marmorilik area**

There exists a good potential for as yet unfound mineralisation on both a local and regional scale. Shale-hosted SEDEX deposits are likely to be found to the north of the Alfred Wegener peninsula at the hinge zone of the northern clastic basin.

The ore grades, thickness and orientation of the Black Angel ore deposits are dominantly controlled by tectonic processes and trends, whereas the original location of <sup>the</sup> mineralisation is stratigraphically controlled. The Black Angel deposits have been folded, transposed and elongated along an O80 trending belt parallel to the fold axis of the Black Angel nappe. The deposits have subsequently been deformed into a D2 tectonic wedge. Exploration for unfound sulphides should be made along the O80 trending belt within the D2 tectonic wedge. It is predicted that high grade mineralisation exists 2.5 km. ENE of the Deep Ice Zone along the O80 trend, where F3 & F1 fold axial traces are interpreted to intersect.

Significant new, Black Angel type, mineralisation is expected to occur in Unit 4 stratigraphy that is tectonically repeated along the northern margin of the South Lakes cliffwall. There is also a potential for new finds associated with an extension of the Nunngarut zone to the east of the 'A' fjord, below the middle Marmorilik tectonic slide zone.

## Appendices

### Appendix 1: Lead isotope analyses

#### Sample preparation

32 galena and 5 pyrite samples were analysed for their lead isotope ratios from the Black Angel deposit and surrounding mineralised showings. Samples of fresh galena and pyrite were prepared by crushing to a very fine powder (-80 mesh) in an agate pestle and mortar. The mortar and pestle were cleaned between each sample using suprapure nitric acid and distilled water.

Approximately 3.45 milligrams of galena was weighed out and placed in a clean pyrex beaker and was dissolved in 3 millilitres of 7 molar hydrochloric acid. The beakers were then placed on a hot plate to evaporate the solution to dryness. The lead chloride produced was then dissolved in 2 millilitres of distilled water and 6 molar nitric acid. The solution was again evaporated to dryness. 3 milligrams of lead nitrate were produced for each sample of galena.

Before analysing pyrite the amount of lead in each pyrite sample had to be determined. This was done by a process of anion exchange chemistry. Pyrite samples were coarsely crushed and approximately 0.33 grams of each sample were placed in a 25 m.l. pyrex beaker. 1 m.l. of a  $^{206}\text{Pb}$  lead spike and 1 m.l. of a  $^{235}\text{U}$  uranium spike was added to the pyrite sample. The pyrite was then dissolved in 10 m.l. of 6 molar nitric acid and evaporated to dryness in order to obtain the lead nitrate.

#### Sample loading

The sample solution is mounted on a single rhenium filament using silica gel and orthophosphoric acid.

1) A single drop ( $\approx 2-5 \mu\text{l}$ ) of silica gel suspension was placed on the centre of the single rhenium filament. The filament was dried using a current heating (1 amp).

- 2) A drop of the sample solution ( $10^{-7}$  to  $10^{-8}$  g) was placed on the filament and dried using current heating.
- 3) A drop of orthophosphoric acid (0.75N) ultra pure grade is added and dried using current heating.
- 4) The current was raised to 2 amps for 5 minutes and then the current was raised until the filament glows red hot. The filament is kept at this temperature until a white deposit begins to form. The current is then raised further until the filament is red hot.
- 5) the bead containing the filament is loaded with other beads into a barrel which is in turn placed in the mass spectrometer.

### Sample analysis

The samples were measured 50 times and the statistical average was taken. The values were recorded along with the lead spectrum. The results were standardised against National Bureau of Standards 981 value, namely:- 206/204: 16.9371, 207/204: 15.4913, 208/204: 38.7213. Errors were due to the inaccuracy in the measurement of the 204 isotope.

## **Appendix 2 Stable isotope analyses**

### **Carbon isotope preparation**

#### **Graphite analysis**

Samples for both the oxygen and carbon isotope analyses were taken from graphitic calcite and dolomite marbles. The samples were crushed in a jaw crusher until the fragments were < 2mm. Graphite samples were purified by handpicking and acid treatment of the crushed samples. The acid treatment consisted of placing  $\approx$  100 g of sample into a conical flask with 50% HCl, the solution was diluted after a large enough amount of graphite had been released. The graphite floated as a film on the acid and was decanted off and collected by filtering through a glass filter paper. Approximately 1 g of graphite was obtained for each sample. The remaining carbonate was used in the carbon and oxygen analysis.

A few milligrams of the graphite was placed in a quartz vessel and was burnt to  $\text{CO}_2$  in pure oxygen at  $950^\circ\text{C}$ . The graphite combustion was completed by oxygen circulation and by passing the gases through a column filled with copper oxide at  $750^\circ\text{C}$ .

#### **Carbonate analysis**

The crushed carbonate from the graphite analysis was further crushed to a fine powder in a an agate pestle and mortar (-80 mesh). 10 milligrams of carbonate was reacted with 100% phosphoric acid at  $\approx 25^\circ\text{C}$  (McCrea, 1950) to liberate  $\text{CO}_2$ .

#### **Oxygen isotope preparation**

The  $\text{CO}_2$  liberated during the carbonate preparation was used in the oxygen isotope analysis. The  $\text{CO}_2$  obtained for each preparation was analysed by mass spectrometry at the B.G.S. Stable isotope laboratories Grays Inn Road, London.

## Sulphur isotope preparation

20 sulphur isotope analyses were carried out on pyrite, pyrrhotite and sphalerite-galena pairs from the Black Angel deposits and Marmorilik mineralisation. In each case a fine grained sample was obtained by microdrilling followed by grinding in an agate pestle and mortar (-80 mesh). The drill and pestle and mortar were cleaned with nitric acid and distilled water between each sample.

The pure sulphide ( $\approx 2-3$  mg) were then converted to  $\text{SO}_2$  by reaction with an oxidising agent, in this case  $\text{V}_2\text{O}_5$ . The reaction was carried out by combustion in a vacuum with a solid oxidant. This procedure minimised the presence of contaminant gases, in particular  $\text{CO}_2$ .

The resultant  $\text{SO}_2$  was analysed by mass spectrometry against the Canon diablo iron meteorite standard.

## **Appendix 3 Sulphide etches**

### **Brebrick Scanlon etch**

The Brebrick and Scanlon etchant (1957) was used in picking out grain boundaries, deformation twins, kinks and annealing twins in sphalerite and galena. The etchant was a mixture of 100 g thiourea / 1 litre of water and concentrated hydrochloric acid in the ration 5:1 respectively. This etchant was used at temperatures of 65-75°C for periods of between 30-150 seconds. The temperature and timing of the etching varied between specimen, but was critical if consistent results were to be obtained. Pyrite was resistant to this etch.

### **Pyrite etchant**

A variable etchant was used in pyrite etching. It consisted of between 10-50% nitric acid with minor amounts of alcohol ( $\approx$  10:1). The pyrite blocks were etched for between 2-4 minutes at temperatures between 55-70°C. The more concentrated acid solutions produced quicker etches. Care is to be taken at high temperatures with the 50% nitric acid to prevent boiling.

The etch was particularly useful in revealing grain boundaries and internal deformation textures such as kinks and dislocation pits. Primary growth textures were also revealed by this method.

- Abercrombie, H.J., Skippen, G.B. and Marshall, D.D. (1987): F-OH substitution in natural tremolite, talc, phlogopite. *Contrib. Mineral. Petrol.*, **97**, 305-315
- Akande, S.O. and Zentelli, M. (1984): Geologic, fluid inclusion and stable isotope studies of the Geys River Lead-zinc deposit, Nova Scotia, Canada. *Econ. Geol.* **79**, 1187-1211
- Allen, C.R. & Harris, C.J. 1979: Year end report Karrat group reconnaissance programme Marmorilik area, West Greenland. Int. Cominco report. 34 pp.
- Allmendinger, R.W., Hauge, T.A., Hauser, E.C., Potter, C.J., Klemperer, S.L., Nelson, K.D. Kruepfer, P. and Oliver, J. (1987): An overview of the COCORP 40°N transect, western United States. The fabric of an orogenic belt. *Bull. Geol. Soc. Am.*, **98**, 308-319
- Anderson, G.M. and Macqueen, R.W. (1982): Ore deposit models- 6. Mississippi Valley-type lead-zinc deposits. *Geosci. Can.*, **9**, 108-117.
- Andersen, M.C. & Pulvertaft, T.C.R. (1985): Rb-Sr whole rock 'ages' from reworked basement gneisses in the Umanak area, central West Greenland. *Bull. Geol. Soc. Denmark*, **34**, 205-212.
- \_\_\_\_\_ (1986): Occurrences of anorthositic rocks in the reworked Archean basement in the Umanak area, central West Greenland. *Rapp. Grønlands geol. Unders.* **129**, 5-18.
- Andrew, C.J. (1986): The tectono-stratigraphic controls to mineralisation in the Silvermines area, County Tipperary, Ireland. In Andrew C.J., R.W.A. Crowe, S. Finlay, W.M. Pennell and F.J. Pyne (eds.), *Geology and Genesis of Mineral Deposits in Ireland*. Irish association of economic geologists, Dublin. 377-418
- Atkinson, B.K. (1972): An experimental investigation of the rheology of some sulphide minerals. Unpublished Ph. D. thesis, Univ. of London.
- \_\_\_\_\_ (1974): Experimental deformation of polycrystalline galena, chalcopyrite and pyrrhotite. *Trans. Inst. Min. Metall.* **83(B)**, 19-28.
- \_\_\_\_\_ (1975a): Experimental deformation of polycrystalline pyrite. Effects of temperature, pressure, strain rate and porosity. *Econ. Geol.*, **70**, 473-487.
- \_\_\_\_\_ (1975b): A preliminary study of the influence of temperature and strain rate on the rheology of polycrystalline pyrrhotite ore. *N. Jb. Miner. Mh.*, **11**, 483-499.
- \_\_\_\_\_ (1976): The temperature - and strain rate- dependant mechanical behaviour of a polycrystalline galena ore. *Econ. Geol.*, **71**, 513-525.
- Badham, J.P.N. (1981): Shale hosted Pb-Zn deposits: products of exhalation of formation waters? *Trans. Inst. Min. Metall. (Sect. B)*, **90**, B70-B76.
- Bak, J., Grocott, J., Korstgård, J., Nash, D., Sørensen, K., and Watterson, J. (1975): Tectonic implications of Precambrian shear belts in western Greenland. *Nature*, **254**, 566-569
- Barnes, H.L., ed. (1979): *Geochemistry of Hydrothermal Ore Deposits*. Wiley, New York. 798pp.
- \_\_\_\_\_ and Kellerud, G. (1961): *Econ. Geol.*, **56**, 648-688.

- Barton, P.B. (1967): Possible role of organic matter in the precipitation of Mississippi Valley ores. *In*: Brown, J.S., (ed.), *Genesis of stratiform lead zinc barite deposits in carbonate rocks: Econ. Geol.*, **Mon 3**, 371-377.
- Bickle, M.J. and Powell, R. (1977): Calcite-dolomite geothermometry for iron-bearing carbonates. *Contrib. Mineral. Petrol.*, **59**, 281-292.
- Boest, A.M., Coleman, M.L. and Halls, C. (1981): Textural and stable isotopic evidence for the genesis of the Tynagh base metal deposit, Ireland. *Econ. Geol.* **76**, 27-55.
- Boest, A.M., Swainbank, I.G., Coleman, M.L. and Halls, C. (1981): Lead isotope variation in the Tynagh, Silvermines and Navan base-metal deposits, Ireland. *Inst. Min. Metall. Trans. (sect. B)*, **90**, 115-119.
- Both, R.A. and Stumpf, E.F. (1987): Distribution of silver in the Broken Hill orebody. *Econ. Geol.*, **82**, 1037-1043.
- Bottling, Y. (1969): Calculated fractionation factors for the carbon and hydrogen isotope exchange in the system calcite-carbon dioxide-graphite-methane-hydrogen-water vapour. *Geochim. Cosmochim. Acta*, **33**, 49-64.
- Boyce, A.J., Coleman, M.L. and Russell, M.J. (1983): Formation of fossil hydrothermal chimneys and mounds from Silvermines, Ireland. *Nature*, **306**, 545-550.
- Boyer, S.E. and Elliot, D. (1982): Thrust systems. *Bull. Am. Assoc. Petrol. Geol.*, **66**, 1196-1230.
- Bridgwater, D. (1971): Routine K/Ar age determinations on rocks from Greenland carried out for GGU in 1970. *Rapp. Grønlands geol. Unders.* **35**, 52-60.
- Brigo, L., Kostelka, L., Omenetto, P., Schneider, H.J., Schroll, E., Schulz, O. and Struel, I. (1978): Comparative reflections on four alpine Pb-Zn deposits. *In*, Klemm, D.D. and Schneider, H.J. (eds) *Time and stratabound ore deposits*. Springer-verlag, Berlin. 273-293.
- Brebrick, R.F. and Scanlon, W.W. (1957): Chemical etches and etch pit patterns on PbS. *J. Chem. Phys.*, **27**, 607-608.
- Brun, J.P. and van den Driessche, J. (1985) Diapiric gneiss domes in collision belts. *Abstracts of international conference on tectonic and structural processes, department of structural geology, Univ. of Utrecht*. 20-1.
- Cameron, E.M. and Garrels, R.M. (1980): Geochemical compositions of some Precambrian shales from the Canadian Shield. *Chem. Geol.*, **28**, 181-197.
- Carne, R.C. and Cathro, R.J. (1982): Sedimentary exhalative (sedex) zinc-lead-silver deposits, northern Canadian Cordillera. *Bull. Can. Inst. Min. Metall.* **75**, 66-78.
- Carpenter, A.B., Trout, M.L. and Pickett, E.E. (1974): Preliminary report on the origin and chemical evolution of lead- and zinc-rich oil field brines in central Mississippi. *Econ. Geol.*, **69**, 1191-1206.
- Cathles, L.M. and Smith, A.T. (1983): Thermal constraints on the formation of Mississippi Valley-type lead-zinc deposits and their implications for episodic dewatering and deposits genesis. *Econ. Geol.*, **78**, 983-1002.

- Caulfield, J.G.B., Lehuray, A.P. and Rye, D.M. (1986): Isotope studies of sediment hosted base-metal deposits in Ireland. Part 1, New data from the deposits in Co. Meath, Westmeath and Longford; Part 2, A review: in Andrew C.J., R.W.A Crowe, S.Finlay, W.M. Pennell and F.J. Pyne eds, *Geology and Genesis of Mineral Deposits in Ireland*. Irish association of economic geologists, Dublin. 591-618.
- Chatterjee, A.K. (1983): *Metallogenic map of the province of Nova Scotia, scale: 1:500,000*. Department of Mines and Energy, Nova Scotia.
- Chessex, R., Delaloye, M., Gulacar, F. & Escher, A. 1973: U-Pb isotopic ages of zircons from Precambrian rocks of West Greenland. *Fortschr. Miner.* **50**, 60-61.
- Clark, B.R. and Kelly, W.C. (1973): Sulphide deformation studies: I. Experimental deformation of pyrrhotite and sphalerite to 2000 bars and 500°C. *Econ. Geol.*, **68**, 332-352
- \_\_\_\_\_, Price, F.R. and Kelly, W.C. (1977): Effects of annealing on deformation textures in galena. *Contrib. Mineral. Petrol.*, **64**, 149-165.
- Claypool, G.E., Holser, W.T., Kaplan, I.R., Sakai H. and Zak, I. (1980): The age curves of sulphur and oxygen isotopes in marine sulphate and their mutual interpretation. *Chem. Geol.*, **28**, 199-260.
- Clemmey, H. (1985): Sedimentary ore deposits. *In*, Brenchley, P.J. and Williams, B.P.J. (eds), *Sedimentology: Recent developments and applied aspects*. Blackwell Scientific Publications, Oxford. 229-248.
- Coney, P.J. (1980): Cordilleran metamorphic core complexes: an overview. *In*, Crittenden, M.D., Coney, P.J. and Davis, G.H. (eds) *Cordilleran metamorphic core complexes*. *Mem. geol. Soc. Am.*, **153**, 35-78.
- Cox, S.F., Etheridge, M.A. and Hobbs, B.E. (1981): The experimental ductile deformation of polycrystalline and single crystal pyrite. *Econ. Geol.*, **76**, 2105-2117.
- Craig, J.R. (1983): Metamorphic features in Appalachian massive sulphides. *Min. Mag.*, **47**, 515-526.
- Cumming, G.L. and Richards, J.R. (1975): Ore lead isotope ratios in a continuously changing earth. *Earth Planet Sci Letters*, **28**, 155-171.
- Curtis, C.D. (1980): Diagenetic alteration of black shales. *J. Geol. Soc. Lond.*, **137**, 189-194.
- \_\_\_\_\_, and Spears, D.A. (1968): The formation of sedimentary iron minerals. *Econ. Geol.*, **63**, 257-270.
- Czamanske, C.K., and Rye, R.O. (1974): Experimentally determined sulphur isotope fractionation between sphalerite and galena in the temperature range 600°C to 275°C. *Econ. Geol.*, **69**, 17-25.
- Devis, G.H. (1980): Structural characteristics of metamorphic core complexes. *In*, Crittenden, M.D., Coney, P.J. and Davis, G.H. (eds) *Cordilleran metamorphic core complexes*. *Mem. geol. Soc. Am.*, **153**, 35-78.
- \_\_\_\_\_, (1983): Geological development of a metamorphic core complex. *Geology*, **7**, 120-124.

- Davis, G.H. (1987): A shear zone model for the structural evolution of metamorphic core complexes in S.E. Arizona. *In*, Coward, M.P., Dewey, J.F. & Hancock, P.L. (Eds.) *Continental extensional tectonics. J. Geol. Soc. Spec. Pub.*, **28**, 247-266
- Dawes, P.R. (1976): Precambrian to Tertiary of northern Greenland. *In* Escher, A. & Watt, W.S. (eds) *Geology of Greenland*, 248-303. Copenhagen: Geol. Surv. Greenland.
- Dawes, P.R. & Kerr, J.W. (eds) 1982: Nares Strait and the drift of Greenland: a conflict in plate tectonics. *Meddr Grønland, Geosci.* **8**, 392 pp.
- Della Valle, (1977): A report on field-work during 1976 & 1977 on the Uvkussigsat showing. Internal Cominco report.
- Degens, E.T. and Ross, D.A., eds. (1969): Hot brines and recent heavy metal deposits in the Red sea. Springer-verlag, New York.
- Den Tex, E. (1975): Thermally mantled gneiss domes: the case of convective heat flow in more or less solid orogenic basement. *in*, Borradaile, G.J., Ritsema A.R., Rondeel H.E. and Simon, E.J. (eds) *Progress in Geodynamics*. Koninkrijk Nederlands Akademie van Wetenschap, Amsterdam, 62-79.
- Dixon, J.M. (1975): Finite strain and progressive deformation in models of diapiric structures. *Tectonophysics*, **28**, 89-114.
- \_\_\_\_\_ and Summers, J.M. (1983): Patterns of total and incremental strain in subsiding troughs: experimental centrifuge models of interdiapir synclines. *Can. J. Earth Sci.*, **20**, 843-861.
- \_\_\_\_\_ and \_\_\_\_\_ (1985): Recent developments in centrifuge modelling of tectonic processes: equipment, model construction techniques and rheology of model materials. *J. Struct. Geol.*, **7**, 83-102.
- Doe, R.E. and Zartman, R.E. (1979): Plumbotectonics I, The Phanerozoic, *in* Barnes, H.L., ed. *Geochemistry of Hydrothermal Ore Deposits*. John Wiley and sons, New York. pp 22-70.
- Dozy, J.J. (1970): A geological model for the genesis of the lead-zinc ores of the Mississippi Valley, U.S.A. *Inst. Min. Metall. Trans. (sect. B)*, **79**, 163-170.
- Edmunds, F.R. (1981): Halo study: a preliminary report. Internal Cominco report. 21pp.
- Edwards, A.B. and Baker, G. (1954): Scapolitisation in the Cloncurry district of north-western Queensland. *J. Geol. Soc. Aust.*, **1**, 1-33.
- Eeckhout, B. van den & Grocott, J. 1982: Investigations on the Precambrian rocks of Svartenhuk Halvø, central West Greenland. *Rapp. Grønlands geol. Unders.* **110**, 22-26.
- Elder, T.G. (1967): Year end report 1967 - Vestgron Mines Ltd., Work Greenex concession. Internal Cominco report. 22pp.
- Escher, A. & Burri, M. (1967): Stratigraphy and structural development of the Precambrian rocks in the area northeast of Disko Bugt, West Greenland. *Rapp. Grønlands geol. Unders.* **13**, 1-28.
- \_\_\_\_\_ & Pulvertaft, T.C.R. (1968): The Precambrian rocks of the Upernavik-Kraulshavn area (72°-74°15' N), West Greenland. *Rapp. Grønlands geol. Unders.* **15**, 11-14.

- Escher, A. & \_\_\_\_\_ (1976): Rinkian mobile belt of West Greenland. /n Escher, A. & Watt, W.S. (eds) *Geology of Greenland*, 105-119. Copenhagen: Geol. Surv. Greenland.
- \_\_\_\_\_, Sørensen, K. & Zeck, H.P. (1976): Nagssugtoqidian mobile belt in West Greenland. /n Escher, A. & Watt, W.S. (eds) *Geology of Greenland*, 77-95. Copenhagen: Geol. Surv. Greenland.
- Fleuty, M.J. (1964): Tectonic slides. *Geol. Mag.*, **101**, 452-456.
- Finlow-bates, T., Croxford, N.J.W. and Allen, J.M., (1977): Evidence for, and implications of a primary FeS phase in lead-zinc bearing sediments, Mount Isa. *Mineral. Deposita*, **12**, 143-149.
- Gennicott, R.A. (1976): Year end report on diamond drilling programme on Agpat Island, west Greenland. Internal Cominco report. 45pp.
- \_\_\_\_\_, (1979): Year end report on diamond drilling programme on Black Angel Mountain, west Greenland. Internal Cominco report. 34pp.
- Gerde, A.A. (1977): Strontium geochemistry and carbon and oxygen isotopic compositions of Lower Proterozoic dolomite and calcite marbles from the Marmorilik Formation, West Greenland. *Precambrian Res.* **8**, 183-199.
- \_\_\_\_\_, (1978): The Lower Proterozoic Marmorilik Formation, east of Marmorilik, West Greenland. *Meddr Grønland*. **200** (3), 71 pp.
- \_\_\_\_\_, (1979): Strontium geochemistry and carbon and oxygen isotopic compositions of the Lower Proterozoic dolomite and calcite marbles from the Marmorilik Formation, West Greenland. *Precambrian Res.* **8**, 183-199.
- \_\_\_\_\_, & Pulvertaft, T.C.R. (1976): Age relations of the Precambrian Marmorilik marble formation, central West Greenland. *Rapp. Grønlands geol. Unders.* **80**, 49-53.
- Gardner, H.D. and Hutcheon, I. (1985): Geochemistry, mineralogy, and geology of the Jason Pb-Zn deposits, MacMillan Pass, Yukon, Canada. *Econ. Geol.*, **80**, 1257-1276.
- Gerven, G. and Freeze, R.A. (1984): Theoretical analysis of the role of ground water flow in the genesis of stratabound ore deposits. 2. Quantitative results. *Am. Jour. Sci.*, **284**, 1125-1174.
- Gibbs, A.D. (1984): Structural evolution of extensional basin margins. *J. Geol. Soc. Lond.*, **141**, 609-620.
- \_\_\_\_\_, (1987): Development of extensional and mixed-mode sedimentary basins. /n, Coward, M.P., Dewey, J.F. & Hancock, P.L. (Eds.) *Continental extensional tectonics*. *J. Geol. Soc. Spec. Pub.*, **28**, 19-34.
- Gill, J.E. (1969): Experimental deformation and annealing of sulphides and the interpretation of ore textures. *Econ. Geol.*, **64**, 500-508.
- Goldsmith, J.R. and Newton, R.E. (1969): P-T-X relations in the system  $\text{CaCO}_3\text{-MgCO}_3$  at high temperatures and pressures. *Am. J. Earth Sci.*, **267A**, 60-190

- Goodfellow, W (1987): Anoxic stratified oceans as a source of sulphur in sediment-hosted stratiform Zn-Pb deposits (Selwyn basin, Yukon, Canada). *Chem. Geol. (Isotope Geosci.)*, **65**, 359-382
- Graf, J.L. and Skinner, B.J. (1970): Strength and deformation of pyrite and pyrrhotite. *Econ. Geol.*, **65**, 206-215.
- Grocott, J. (1981): Structural evolution of the Ikerasak area, Umanak district, central West Greenland. *Rapp. Grønlands geol. Unders.* **105**, 33-35.
- \_\_\_\_\_ (1984): Geometry of superposed colinear deformations in the Ikerasak area, Umanak district, central West Greenland. *Precambrian Res.* **26**, 235-263.
- \_\_\_\_\_, van den Eeckhout, B. and Vissers, R.M.L. (1987): Mantled gneiss antiforms and nappes in west Greenland. *J. Geol. Soc. Lond.*, **144**, 723-744.
- \_\_\_\_\_ & Vissers, R. (1984): Field mapping of the early Proterozoic Karrat Group on Svartehuk Halvø, central West Greenland. *Rapp. Grønlands geol. Unders.* **120**, 25-31.
- Grootenboer, J. and Schwarz, H.P. (1969): Experimentally determined sulphur isotope fractionations between sulphide minerals. *Earth Planet. Sci. Letters*, **7**, 162.
- Gustafson, L.B. and Williams, N. (1981): Sediment hosted stratiform deposits of copper, lead and zinc. *Econ. Geol.*, Seventy fifth Anniversary Volume (B.J. Skinner ed.), 139-178.
- Hall, A.J. (1986): Pyrite-pyrrhotine redox reactions in nature. *Min. Mag.*, **50**, 223-230.
- Hall, A.J., Boyce, A.J. and Fallick, A.E. (1987): Iron sulphides in metasediments: isotopic support for a retrogressive pyrrhotite to pyrite reaction. *Isotope Geoscience*, **6**, 305-310.
- Hamblin, W.K. (1965): Origin of 'reverse drag' on the down-throw side of normal faults. *Bull. Geol. Soc. Am.*, **76**, 1145-1164.
- Hamilton, J. M., Bishop, D.T., Morris, H.C. and Owens, O.E. (1976): Geology of the Sullivan orebody Kimberley, B.C., Canada. *in*, Hutchinson, R.W., Spence, C.D. and Franklin, J.M. (eds) Precambrian sulphide deposits. *Geol. Assoc. Can. Special paper* **25**.
- Harding, T.P. (1985): Seismic characteristics and identification of negative flower structures, positive flower structures and positive structural inversions. *Bull. Am. Assoc. Petrol. Geol.*, **69**, 582-600.
- Harris, C.J. (1981): Report carried out on the Marmorilik Plateau June-September 1980. Year end report Greenex A/S.
- \_\_\_\_\_ (1982): Report on diamond drilling and geophysical programmes on the Marmorilik Plateau - west Greenland 1982. Internal Cominco report. 32pp.
- \_\_\_\_\_ (1985): Report on diamond drilling on the Black Angel Plateau - west Greenland 1985. Internal Cominco report. 41pp.
- Henderson, G. (1969): the use of structural contour maps in the study of gneiss-metasediment relations in the Umanak area, West Greenland. *Spec. Pap. geol. Ass. Can.* **5**, 129-142.

- \_\_\_\_\_ & Pulvertaft, T.C.R. (1967): The stratigraphy and structure of the Precambrian rocks of the Umanak area, West Greenland. *Meddr dansk geol. Foren.* **17**, 1-20.
- Henderson, J.R. & Tippett, C.R. (1980): Foxe Fold Belt in eastern Baffin island, District of Franklin. Current Research, Part a, Geol. Surv. Can., Pap. 80-1A, p.147-152.
- \_\_\_\_\_ (1981): Sheath folds with horizontal X axes in Northeast Canada. *J. Struct. Geol.* **3**, 221-232.
- \_\_\_\_\_ (1983): Structure and metamorphism of the Archean Penrhyn Group and its Archean basement complex in the Lyon Inlet area, Melville Peninsula, District of Franklin. *Spec. Bull. Geol. Surv. Can.* **324**, 50 pp.
- Heyl, A.V., Landis, G.P. and Zartman, R.E. (1974): Isotopic evidence for the origin of Mississippi Valley-Type mineral deposits: a review. *Econ. Geol.*, **69**, 992-1006.
- Hitzmann, M.W. and Large, D. (1986): A review and classification of the Irish carbonate-hosted base metal deposits. *In* Andrew C.J., R.W.A Crowe, S.Finlay, W.M. Pennell and F.J. Pyne (eds.), *Geology and Genesis of Mineral Deposits in Ireland*. Irish association of economic geologists, Dublin. 217-238.
- Hoefs, J. (1980): Stable isotope geochemistry, 2nd edition. Springer-Verlag, Berlin. 208pp.
- Hughes, R.B. (1981): A fluid inclusion study of the Zn-Pb mineralisation in the Marmorilik area, west Greenland. Unpublished BSc. thesis. Geology dept, Imperial College. 82pp.
- Hutchison, M.N. and Scott, S.D. (1981): Sphalerite geobarometry in the Cu-Fe-Zn-S system. *Econ. Geol.*, **76**, 143-153p
- Jackson, S.A. and Beales, F.W. (1967): An aspect of sedimentary basin evolution: The concentration of Mississippi Valley-type ores during late stages of diagenesis. *Bull. Can. Pet. Geol.*, **5**, 383-433.
- Kajiwara, Y.H. and Krouse, H.R. (1971): Sulphur isotope partitioning in metallic sulphide systems. *Can. J. Earth Sci.*, **8**, 1397-1408.
- Kalsbeek, F. (1981): The northward extent of the Archean basement of Greenland—a review of Rb-Sr whole rock ages. *Precambrian Res.* **14**, 203-219.
- Kalsbeek, F., Taylor, P.N. & Henriksen, N. (1984): Age of rocks, structures and metamorphism in the Nagssugtoqidian mobile belt, West Greenland. *Can. J. Earth Sci.* **21**, 1126-1131.
- King, A.R. (1981): Report on prospecting and correlation programme in the Marmorilik Formation, west Greenland. Internal Cominco report.
- Kiyosu, Y. (1971): Sulphur isotope fractionation among sphalerite, galena and sulphide ions. *Geochem. J.*, **7**, 191-199.
- Knudsen, J.C. (1980): Archean ultramafic rocks with relict spinifex textures in the Umanak area, central West Greenland. *Rapp. Grønlands geol. Unders.* **100**, 44-48.
- Krauskopf, K.B. (1967): Source rocks for metal-bearing fluids. *In* Barnes, H.L., ed. *Geochemistry of Hydrothermal Ore Deposits*. John Wiley and sons, New York. 1-30

- Kwak, T.A.P. (1977): Scapolite compositional change in a metamorphic gradient and its bearing on the identification of meta-evaporitic sequences. *Geol. Mag.*, **114**, 343-354
- Large, D.E. (1980): Geological parameters associated with sediment hosted, submarine exhalative Pb-Zn deposits: an empirical model for mineral exploration. *Geologisches Jahrbuch*, **D40**, 59-129
- \_\_\_\_\_ (1981) sediment hosted submarine exhalative Pb-Zn deposits: a review of the geological characteristics and genesis. In, *Handbook of stratiform and stratiform ore deposits* (K.H. Wolf, ed.). Elsevier, Amsterdam, **9**, 469-507
- \_\_\_\_\_ (1983): Sediment hosted massive sulphide lead-zinc deposits: an empirical model. In, *Mineralog. Assoc. Canada Short Course Handbook*, **8**, (D.F. Sangster ed.), 1-29.
- Larsen, O. & Møller, J. 1968: Potassium-argon studies in West Greenland. *Can. J. Earth Sci.* **5**, 683-691.
- LeHuray, A.P., (1984): Lead and sulphur isotopes and a model for the origin of the Ducktown deposit, Tennessee. *Econ. Geol.*, **79**, 1561-1573.
- Lister, G.S. and Snoke, A.W. (1984): S-C mylonites. *J. Struct. Geol.*, **6**, 617-638.
- Lovering, T.S. (1961): Sulphide ores formed from sulphide deficient solutions. *Econ. Geol.*, **56**, 68-99.
- Lydon, J.W. (1983): Chemical parameters controlling the origin and deposition of sediment-hosted stratiform lead zinc deposits. *Mineralog. Assoc. Canada Short Course Handbook*, **8**, 175-250.
- \_\_\_\_\_ (1986): Models for the generation of metalliferous hydrothermal systems within sedimentary rocks and their applicability to the Irish Carboniferous Zn-Pb deposits, in Andrew, C.J., Crowe, R.W.A., Finley, S., Pennell, W.M., and J.F. Payne eds., *Geology and Genesis of mineral deposits in Ireland*: Dublin, *Irish Assoc. Econ. Geologists*, 555-577.
- Mako, D.A. and Shanks III, W.C. (1984): Stratiform sulphide and barite/fluorite mineralisation of the Vulcan prospect, Northwest Territories: exhalation of basinal brines along a faulted continental margin. *Can. J. Earth Sci.* **21**, 78-91.
- MacIntyre, D. J. (1982): Geological setting of the recently discovered stratiform barite-sulphide deposits in Northeastern British Columbia. *Can. Inst. Min. Metall., Bull.* **75**, 99-113.
- Maiden, K.J., Chimbra, L.R. and Smalley, T.J. (1986): Cuspate ore-wall rock interfaces, piercement structures, and the localisation of some sulphide ores in deformed sulphide deposits. *Econ. Geol.*, **81**, 1464-1472.
- Manby, G.M. (1983): Primary scapolite from the Forland complex of Prins Karls Forland, Svalbard. *Min. Mag.*, **47**, 89-93.
- McClay, K.R. (1978): An analysis of sulphide deformation in low grade metamorphic environments. Unpub. PhD. thesis. Univ. of London. 391 pp.
- \_\_\_\_\_ and Atkinson, B.K. (1977): Experimentally induced kinking and annealing of single crystals of galena. *Tectonophysics*, **39**, 175-189.

- McClay, K.R. and Ellis, P.G. (1983): Deformation and recrystallisation of pyrite. *Min. Mag.*, **47**, 527-538.
- \_\_\_\_\_ and \_\_\_\_\_ (1987): Geometries of extensional fault systems developed in model experiments. *Geology*, **15**, 341-344.
- McDonald, J.A. (1967): Metamorphism and its effects on sulphide assemblages. *Mineral. Deposita*, **2**, 200-220.
- Mills, H., Halliday, A.N., Ashton, J.H., Anderson, I.K. and Russell, M.J. (1987): Origin of a giant orebody at Navan, Ireland. *Nature*, **327**, 323-326.
- Mook, W.G., Bommerson, J.C. and Staverman, W.H. (1974): Carbon isotope fractionation between dissolved bicarbonate and gaseous carbon-dioxide. *Earth Sci. Planet. Letters*, **22**, 169.
- Mookerjee, A (1971): Deformation of pyrite. *Econ. Geol.*, **66**, 200.
- \_\_\_\_\_ (1976): Ores and metamorphism: Temporal and genetic relationships. In, Wolf, K.D. (ed) *Handbook of stratabound and stratiform sulphide deposits*. Elsevier, Amsterdam. **4**, 203-260.
- Morikiyo, T. (1984): Carbon isotopic study on coexisting calcite and graphite in the Ryoke metamorphic rocks. *Contrib. Mineral. Petrol.*, **87**, 251-259.
- Muir, M.D. (1979): A sabkha model for the deposition of part of the Proterozoic McArthur Group on the Northern Territory, and its implications for mineralisation. Bureau of Mineral Resources, *J. Aust. Geol. Geophys.*, **4**, 149-162.
- \_\_\_\_\_ (1981): The microfossils from the Proterozoic Urquart Shale, Mount Isa, Queensland, and their significance in relation to the depositional environment, diagenesis and mineralisation. *Mineral. Deposita*, **16**, 51-58.
- \_\_\_\_\_, Donnelly, T.H., Wilkins, R.W.T. and Armstrong, K.J. (1985): Stable isotope, petrological, and fluid inclusion studies of minor mineral deposits from the McArthur Basin: implications for the genesis of some sediment hosted base metal mineralisation from the Northern Territory. *Aust. J. Earth Sci.* **32**, 239-260.
- Myers, D (1973): Geological report and electromagnetic survey report, Greenex A/S utilisation concession. Internal Cominco report. 16pp.
- Naruk, S.J. (1986): Strain and displacement across the Pinaleno Mountains shear zone, Arizona, U.S.A. *J. Struct. Geol.*, **8**, 35-46.
- Nesbitt, B.E., Longstaffe, F.J., Shaw, D.R. and Meuhlenbachs, K. (1984): Oxygen isotope geochemistry of the Sullivan massive sulphide deposit, Kimberley, British Columbia. *Econ. Geol.* **79**, 933-946.
- Nicholas, A and Poirier, P. (1976): Crystalline plasticity and solid state flow in metamorphic rocks. Wiley, London. 440pp.
- Nichols, R. (1981): Report on diamond drilling on the Black Angel Plateau. Internal Cominco report. 31pp.
- Noble, E.A. (1963): Formation of ore deposits by water of compaction. *Econ. Geol.* **58**, 1145-1156.

- Ohle, E.L. (1980): Some considerations in determining the origin in ore deposits of the Mississippi Valley-type - Part II. *Econ. Geol.* **75**, 161-172.
- Ohmoto, H. (1972): Systematics of sulphur and carbon isotopes in hydrothermal ore deposits. *Econ. Geol.* **67**, 551-578.
- Ohmoto, H. and Rye, R.O. (1979): Isotopes of sulphur and carbon. *in* Barnes, H.L., ed. *Geochemistry of Hydrothermal Ore Deposits*. John Wiley and sons, New York. 509-567.
- Pedersen, F.D. (1980a): The stratigraphy, lithology and base-metal deposits of the Lower Proterozoic Marmorilik Formation, west of Marmorilik, central West Greenland. Unpublished cand. scient. thesis. Geological Institute, Univ. of Århus. 80 pp.
- \_\_\_\_\_ (1980b): Remobilisation of the massive sulphide ore of the Black Angel Mine, central West Greenland. *Econ. Geol.* **75**, 1022-1041.
- \_\_\_\_\_ (1981): Polyphase deformation of the massive sulphide ore of the Black Angel Mine, central West Greenland. *Mineral. Deposita* **16**, 157-176.
- \_\_\_\_\_ & Gannicott, R.A. (1980): Relationships between the Precambrian metasediments of the Marmorilik Formation and the Karrat Group, Umanek area, West Greenland. Unpublished cand. scient. thesis. Geological Institute, Univ. of Århus. 20 pp.
- Pedersen, J. (1980): En geologisk og geokemisk undersøgelse af den Prækambriske Marmorilik Formation, vest Grønland, - området omkring Marmorilik by. Unpublished MSc. thesis. Geological institute, Univ. of Århus. 138pp.
- Powell T.G. and MacQueen R.W. (1984): Organic geochemistry of the Pine point Lead-zinc ore field and region, Northwest territories, Canada. *Econ Geol.*, **78**, 1-25
- Puhan, D. (1976): Metamorphic temperature determined by means of the dolomite-calcite solvus geothermometer - examples from the Central Damara orogen (South West Africa). *Contrib. Mineral. Petrol.*, **58**, 23-28
- \_\_\_\_\_ and Johannes, W. (1974): Experimentelle Untersuchung der reaktion Dolomit + Kalifeldspat + H<sub>2</sub>O - Phlogopit + Calcit + CO<sub>2</sub>. *Contrib. Mineral. Petrol.*, **48**, 23-31.
- \_\_\_\_\_ and Metz, P. (1973): In Puhan, D. and Hoffer, E. Phase relations of talc and tremolite in metamorphic calcite dolomite sediments in the southern portion of the Damara belt (S.W. Africa) *Contrib. Mineral. Petrol.*, **40**, 207-214.
- Pulvertaft, T.C.R. (1973): Recumbent folding and flat lying structure in the Precambrian of northern West Greenland. *Phil. Trans. R. Soc. Lond.* **A273**, 535-545.
- \_\_\_\_\_ (1979): Mapping in the Umanek district, central West Greenland. *Rapp. Grønlands geol. Unders.* **95**, 27-30.
- \_\_\_\_\_ (1986): The development of thin thrust sheets and basement-cover sandwiches in the southern part of the Rinkian belt, Umanek district, West Greenland. *Rapp. Grønlands geol. Unders.* **128**, 75-87.
- \_\_\_\_\_, Andersen, M.C., Jørgensen, J.B., Knudsen, J.C. & Schiøtte, L. (1980): Mapping in the Umanek district, central West Greenland. *Rapp. Grønlands geol. Unders.*

- Ramberg, H. (1967): Gravity, deformation and the Earth's crust, as studied by centrifuged models. Academic Press, London.
- \_\_\_\_\_ (1980): Diapirism and gravity collapse in the Scandinavian Caledonides. *J. Geol. Soc. Lond.*, **137**, 261-270.
- \_\_\_\_\_ (1981): Gravity, deformation and the Earth's crust: in theory, experiments and geological application. Academic Press. London 452pp.
- Ramdohr, P. (1969): The ore minerals and their intergrowths. Pergamon press, Oxford. 1174pp.
- Ramsay, J.O. (1967): Folding and fracturing of rocks. Macgrew Hill. New York. 568pp.
- Renfro, A.R. (1974): Genesis of evaporite-associated stratiform metalliferous deposits - A sabkha process. *Econ. Geol.*, **69**, 33-45.
- Rodgers, D.A. (1980): Analysis of pull-apart basin development produced by en-échelon and strike-slip faults. In, Ballance, P.F. and Reading, H.O. (eds) *Sedimentation in oblique-slip mobile zones. Spec. Pub. Int. Ass. Sedimentol.*, **4**, 27-41.
- Roedder, E. (1976): Fluid inclusion evidence on the genesis of ore in sedimentary and volcanic rocks. In, *Handbook of stratabound and stratiform ore deposits* (K.H. Wolf, ed.). Elsevier, Amsterdam, **2**, 67-110.
- Ross, D.I. & Henderson, G. (1972): New geophysical data on the continental shelf of central and northern West Greenland. *Can. J. Earth Sci.* **10**, 485-497.
- Russell, M.J. (1978): Downward excavating hydrothermal cells and Irish-type ore deposits: Importance of an underlying thick Caledonian prism. *Inst. Min. Metall. Trans.*, **87**, sec B, 168-171.
- \_\_\_\_\_ (1983): Major sediment hosted exhalative zinc and lead deposits: Formation from hydrothermal convection cells that deepen during crustal extension. In, *Mineralog. Assoc. Canada Short Course Handbook*, **8**, 251-282.
- \_\_\_\_\_ (1986): Extension and convection: A genetic model for the Irish Carboniferous base metal and barite deposits. in Andrew, C.J., Crowe, R.W.A., Finlay, S., Pennell, W.M., and J.F. Payne (eds.), *Geology and Genesis of mineral deposits in Ireland: Dublin, Irish Assoc. Econ. Geologists*, 545-554.
- Rye, D.M. and Williams, N. (1981): Studies of the base metal sulphide deposits at McArthur River, Northern Territory, Australia: III. The stable isotope geochemistry of the H.Y.C., Ridge, and Cooley deposits. *Econ. Geol.* **76**, 1-26.
- Rye, R.O. (1974): Comparison of sphalerite-galena sulphur isotope temperatures with filling-temperatures of fluid inclusions. *Econ. Geol.* **69**, 26-32.
- \_\_\_\_\_ and Ohmoto, H. (1974): Sulphur and carbon isotopes and ore genesis: a review. *Econ. Geol.*, **69**, 826-842.
- Salmon, B.C., Clerk, B.R. and Kelly, W.C. (1974): Sulphide deformation studies: II. Experimental deformation of galena to 2000 bars and 400°C. *Econ. Geol.*, **69**, 1-16.
- Sengster, D.F. (1976): Carbonate hosted lead-zinc deposits. In, *Handbook of stratabound and stratiform ore deposits* (K.H. Wolf, ed.). Elsevier, Amsterdam, **6**, 447-456.

- Sangster, D.F. (1986): Ages of mineralisation in Mississippi Valley-Type (MYT) deposits: a critical requirement for genetic modelling. *in* Andrew, C.J., Crowe, R.W.A., Finlay, S., Pennell, W.M., and J.F. Payne (eds.), *Geology and Genesis of mineral deposits in Ireland*: Dublin, *Irish Assoc. Econ. Geologists*, 625-634.
- Samson, I.M. and Russell, M.J. (1983): Fluid inclusion data from Silvermines base metal-baryte deposits, Ireland. *Inst. Min. Metall. Trans.*, **92**, sec B, 67-71.
- \_\_\_\_\_ and \_\_\_\_\_ (1987): Genesis of the Silvermines Zinc-Lead-Barite deposit, Ireland: Fluid inclusion and stable isotope evidence. *Econ. Geol.* **82**, 371-394.
- Sarker, S.C., Bhattacharyya, P.K. and Mukherjee, A.D. (1980): *Econ. Geol.*, **75**, 1152-1167
- Sawkins, F.J. (1984): Ore genesis and the episodic dewatering of sedimentary basins: application to giant Proterozoic lead-zinc deposits. *Geology*, **12**, 451-454.
- Schidlowski, M., Eichmann, R. and Junge, C.E. (1975); Precambrian sedimentary carbonates; carbon and oxygen isotope geochemistry and implications for the terrestrial oxygen budget. *Precambrian Res.*, **2**, 1-69.
- Schwerdtner, W.M. and Troeng, B. (1977): Strain distribution within arcuate diapiric ridges of silicone putty. *Tectonophysics*. **50**, 13-28.
- \_\_\_\_\_, Sutcliffe, R.H. and Troeng, B. (1978): Patterns of total strain in the crestal regions of immature diapirs. *Can. J. Earth Sci.*, **15**, 1437-1447.
- Serdyuchenko, D.P. (1975): Some Precambrian scapolite-bearing rocks evolved from evaporites. *Lithos*, **8**, 1-7.
- Shearman, D.J. (1971): Discussion: *Inst. Min. Met. Trans.*, **Sect. B**, **80**, B50-B52.
- Sibson, R.H., Moore, J. McM. and Rankin, A.H. (1975): Seismic pumping- a hydrothermal fluid transport mechanism. *J. Geol. Soc. Lond.* **31**, 653-659.
- Siemes, H. (1970): Experimental deformation of galena ores. *In*, Paulisch, P. (ed) *Experimental and natural rock deformation*. Springer-verlag, Berlin. 165-208.
- \_\_\_\_\_ (1976): Recovery and recrystallisation of experimentally deformed galena. *Econ. Geol.* **71**, 763-771.
- \_\_\_\_\_ (1977): Recovery and recrystallisation of deformed galena. *Tectonophysics*, **39**, 171-174.
- Simpson, C. and Schmid, S.M. (1983): An evaluation of criteria to deduce the sense of movement in sheared rocks. *Bull. Geol. Soc. Am.*, **94**, 1281-1288.
- Skippen, G.B. (1974): Experimental model for low pressure metamorphism of siliceous dolomitic marble. *Am. J. Sci.*, **274**, 287-509.
- Skinner, B.J. (1967): Precipitation of Mississippi Valley-type ores. *In*: Brown, J.S., (ed.), *Genesis of stratiform lead zinc barite deposits in carbonate rocks: Econ. Geol.*, **Mon 3**, 363-370.
- Smith, J.W. and Croxford, N.J.W. (1973): Sulphur isotope ratios in the McArthur lead-zinc-silver deposit. *Nature*, **245**, 10-12.

- Smith, J.W., Doolan, S. and McFarlane, E.F. (1977): A sulphur isotope geothermometer for the trisulphide system galena-sphalerite-pyrite. *Chem. Geol.*, **19**, 83.
- Soula, J.C. (1982): Characteristics and mode of emplacement of gneiss domes and plutonic domes in the central-eastern Pyrenees. *J. Struct. Geol.*, **4**, 313-342.
- Spencer, J.E. (1984): Role of tectonic denudation in warping and uplift of low-angle normal faults. *Geology*, **12**, 95-98.
- Spry, A (1979): Metamorphic textures. Pergamon press. Oxford. 350pp.
- Stacey, J.S. and Kramers, J.D. (1975): Approximation of terrestrial lead isotope evolution by a two-stage model. *Earth Planet. Sci. Letters*, **26**, 207-221.
- Stanton, R.L. (1964): Mineral interfaces in stratiform ores. *Trans. Inst. Min. Metal.*, **74(B)**, 45-79.
- \_\_\_\_\_ (1972): Ore petrology. McGraw Hill, New York. 713pp.
- \_\_\_\_\_ and Willey, H.G. (1972): Experiments on a specimen of galena from the Coeur d'Alene, Idaho. *Econ. Geol.*, **67**, 776-788.
- Sverjensky, D.A. (1981): The origin of a Mississippi Valley-Type deposit in the Viburnum trend, Southeast Missouri. *Econ. Geol.*, **76**, 1848-1872.
- \_\_\_\_\_ D.A. (1984): Oil field brines as ore-forming solutions. *Econ. Geol.* **74**, 149-153.
- Talbot, C.J. (1974): Fold nappes as asymmetric mantled gneiss domes and ensialic orogeny. *Tectonophysics*. **24**, 256-276.
- \_\_\_\_\_ (1979): Infrastructural migmatitic upwelling in E. Greenland interpreted as thermal convective structures. *PreCambrian Res.*, **8**, 77-93.
- Taylor, P.N. and Moorbath, S. (1986): Dating of carbonate rocks by the Pb/Pb method. Abstract in *Terra Cognita*. p81.
- Tchalenko, J.S. (1970): Similarities between shear zones of different magnitudes. *Geol. Soc. Am. Bull.*, **81**, 1625-1640.
- Tilley, C.E. (1948): *Min. Mag.*, **28**, 272-276.
- Trudinger, P.A. (1981): Bureau of Mineral Resources, *J. Aust. Geol. Geophys.*, **4**, 149-162
- Vaasjoki, M. and Gulson, B.L. (1986): Carbonate-hosted base metal deposits: Lead isotope data bearing on their genesis and exploration. *Econ. Geol.* **81**, 156-172.
- Vinogradov, V.I. (1972): The isotopic composition of sulphur as a factor indicating constancy of its cyclic circulation in time. *Chem. Geol.*, **10**, 99-106.
- Yokes, F.M. (1969): A review of the metamorphism of sulphide deposits. *Earth Sci. Rev.*, **5**, 99-143.
- Wada, H. (1977): Isotopic studies of graphite in metamorphosed carbonate rocks of central Japan. *Geochem J.* **11**, 183-197.

- Walker, R.N., Gulson, B. and Smith, J. (1983): The Coxco deposit - A Proterozoic Mississippi Valley-type deposit in the McArthur River district, Northern Territory, Australia. *Econ. Geol.* **78**, 214-249.
- Walker, R.N., Logan, R.G. and Binnekamp, J.G. (1977): Recent geological advances concerning the H.Y.C. and associated deposits, McArthur River, N.T. *Jour. Geol. Soc. Aust.* **24**, 365-380.
- Watterson, J. (1978): Proterozoic intraplate deformation in the light of south-east Asian neotectonics. *Nature* **273**, 636-640
- Whelan, J.F., Rye, R.O. and DeLorraine, W. (1984): The Balmat-Edwards zinc-lead deposits - synsedimentary ore from Mississippi Valley-Type fluids. *Econ. Geol.*, **79**, 239-265.
- White, D.E. (1968): Environments of generation of some base-metal ore deposits. *Econ. Geol.*, **63**, 301-335.
- White, S. (1975): Estimations of strain rates from microstructural features. *J. Geol. Soc. Lond.*, **131**, 577-583.
- \_\_\_\_\_ (1977): Geological significance of recovery and recrystallisation processes in quartz. *Tectonophysics*, **39**, 143-170
- Wilcox, R. E., Harding, T.P., and Seely, D.R. (1973): Basic wrench tectonics. *Bull. Am. Assoc. Petrol. Geol.*, **57**, 74-96.
- Williams, G.D. (1982): Thrust tectonics in the south central Pyrenees. *J. Struct. Geol.*, **7**, 11-17.
- Woodcock, N.H. and Fisher, M. (1986): Strike-slip duplexes. *J. Struct. Geol.*, **8**, 725-735
- Zartmann, R.E. and Doe, B.R. (1981): Plumbotectonics - the model. *Tectonophysics*, **75**, 135-162.
- Zartmann, R.E., Pawlowska, J. and Rubinowski, Z. (1979): Lead isotopic composition of ore deposits from Silesia-Cracow mining district. *Prace Inst. Geol.* **95**, 133-150.

## APPENDED REFERENCES

- Ashton, J.H., Downing, D.T. and Finlay, S. (1986): The geology of the Navan Zn-Pb orebody. In Andrew C.J., R.W.A. Crowe, S. Finlay, W.M. Pennell and F.J. Pyne (eds.), *Geology and Genesis of Mineral Deposits in Ireland*. Irish association of economic geologists, Dublin. p 243-280.
- Barton, P.B., and Toulmin, P. (1966): Phase relations involving sphalerite in the Fe-Zn-S system. *Econ. Geol.*, **61**, 815-849.
- Coomer, P.G., and Robinson, B.W. (1976): Sulphur and sulphate-oxygen isotopes and the origin of the Silvermines deposits, Ireland. *Mineralium Deposita*, **11**, 155-169.
- Craig (1980): *Norges Geol. Unders.*, **360**, 295-325.
- Criss, R.E., and Taylor, H.P. (1986): Meteoric hydrothermal systems. In Stable isotopes in high temperature geological processes (Eds., Valley, J.W., Taylor, H.P. and O'Neil, J.R.). Min. Soc of America spec. pub. **16**, 373-422.
- Cumming, G.L., and Robertson, D.K. (1969): Isotopic composition of lead from the Pine Point deposit. *Econ. Geol.*, **64**, 731-732.
- Doe, B.R. and Delevaux, M.H. (1972): Source of lead in Southeast Missouri galena ores. *Econ. Geol.*, **69**, 409-425.
- Fahrig, W.F., and Jones, D.L. (1969): Palaeomagnetic evidence for the extent of Mackenzie igneous events. *Can. J. Earth Sci.*, **6**, 679-688.
- Fahrig, W.F., Irving, E., and Jackson, G.D. (1971): Palaeomagnetism of the Franklin diabases. *Can. J. Earth Sci.*, **8**, 455-467.
- Fletcher, I.R., and Farquhar, R.M. (1982): Lead isotopic compositions of Balmat ores and their genetic implications. *Econ. Geol.*, **77**, 464-473.
- Godwin, C.I., Sinclair, A.J. and Ryan, B.D. (1982): Lead isotope models for the genesis of carbonate-hosted Zn-Pb, Shale-hosted Ba-Zn-Pb, and Silver-rich deposits in the northern Canadian cordillera. *Econ. Geol.*, **77**, 82-94.
- Ludwig, K.R., and Silver, L.T. (1977): Lead isotope inhomogeneity in Precambrian igneous feldspars. *Geochim. Cosmochim. Acta*, **41**, 1457-1471.
- Miyashiro, A. (1973): *Metamorphism and metamorphic belts*. George Allen & Unwin. London. 492 pp.
- Nesbitt, B.E. and Kelly, W.C. (1980): Metamorphic zonation of sulphides, oxides and graphite in and around the orebodies at Ducktown, Tennessee. *Econ. Geol.*, **75**, 1010-1021.
- Ohmoto, H. (1986): Stable isotope geochemistry of ore deposits. In Stable isotopes in high temperature geological processes (Eds., Valley, J.W., Taylor, H.P. and O'Neil, J.R.). Min. Soc of America spec. pub. **16**, 491-556.
- Piper, J.D.A. (1980): Paleomagnetism of the Swedish rapakivi suite: Proterozoic tectonics of the Baltic Shield. *Earth Planet. Sci. Letters*, **46**, 443-461.
- Piper, J.D.A. (1983): The dynamics of the continental crust in Proterozoic times. In Proterozoic geology (Eds. Medaris, L.G., Byers, C.W., Mickelson, D.M., and Shanks, W.C.). *Geol. Soc. Am. Mem.*, **161**, 11-34.

- Ramberg, H. (1949): On the petrogenesis of gneiss complexes between Sukkertoppen and Christianshaab, West Greenland. *Meddr. Dansk. Geol. Foren.*, **11**, 312-327.
- Ramsey, J.O., and Graham, R.H. (1970): Strain variation in shear belts. *Can. J. Earth Sci.*, **7**, 786-813.
- Roy, J.L., and Lapointe, P.L. (1976): The palaeomagnetism of Huronian redbeds and Nipissing diabase; post Huronian igneous events and apparent polar path for the interval 2300-1500 Me for Laurentia. *Can. J. Earth Sci.*, **13**, 749-779.
- Ridge, J.E., and Smolarska, I. (1972): Factors bearing on the genesis of the Silesian-Cracovian lead-zinc deposits in southern Poland. XIV Inst. Geol. Congress, Montreal, 1972, Sect., 6.
- Scott, S.D. (1983): Chemical behaviour of sphalerite and arsenopyrite in hydrothermal and metamorphic environments. *Min. Mag.*, **47**, 427-435.
- Sunblad, K. (1981): Chemical evidence for, and implications of, a primary FeS phase in the Ankervattnet Zn-Cu-Pb massive sulphide deposit, central Swedish Caledonides. *Mineralium deposita*, **16**, 129-146.
- Valley, J.W. (1986): Stable isotope geochemistry of metamorphic rocks. In Stable isotopes in high temperature geological processes (Eds., Valley, J.W., Taylor, H.P. and O'Neil, J.R.). Min. Soc of America spec. pub. **16**, 445-490.
- Vokes, F.M. (1971): Some aspects of the regional metamorphic mobilization of preexisting sulphide deposits. *Mineralium Deposita*, **6**, 122-129.
- von Englehart, W (1961): *Bull. Geol. Inst. Univ. Uppsala*, **40**, 189-204.
- Watkinson, A.J. (1983): Patterns of folding and strain influenced by linearly anisotropic bands. *J. Struct. Geol.*, **5**, 449-454.
- Wernicke, B and Burchfiel, B.C. (1982): Modes of extensional tectonics. *J. Struct. Geol.*, **4**, 104-115.
- Winkler, H.G.F. (1979): Petrogenesis of metamorphic rocks. Springer-verlag, Berlin. 348pp.

FIGURE 3-1b



# LITHO-TECTONIC MAP OF THE MARMORILIK AREA



**LEGEND**

**NUKAWSAK FORMATION**  
 Biotite schists  
 QEQERTARSSUAQ FORMATION  
 Quartzites and schists  
**UMANAK GNEISS**  
 Granodiorite  
 Hornblende biotite gneiss

**MARMORILIK FORMATION**  
 Grey banded marbles (unit 6)  
 Calcites and dolomites (unit 5)  
 Coarse calcitic marbles (unit 4)  
 Graphitic calc/dolomite marbles (unit 3)  
 Dolomitic marbles (unit 2)  
 Cherty dolomitic marble (unit 1)

Pelites  
 Mottled pelite  
 Mineralised zones (Zn,Pb,Fe)  
 Fault (certain, inferred)  
 Lithological boundary (certain, inferred)

N

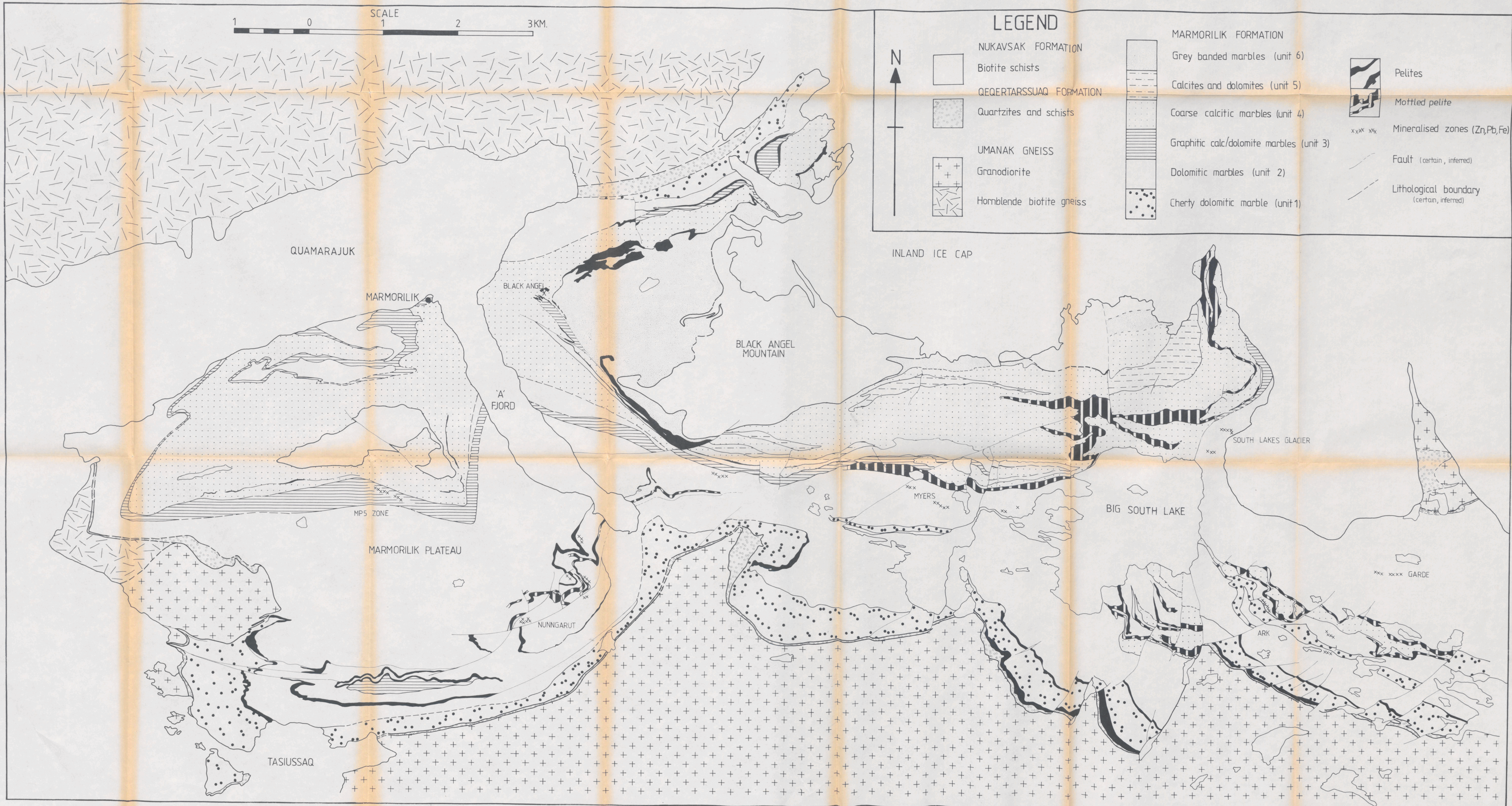


FIGURE 4-1a

# TECTONIC MAP OF THE MARMORILIK AREA

N

LEGEND

<p>— —  BEDDING</p> <p>— —  FIRST FOLIATION</p> <p>— —  SECOND FOLIATION</p> <p>—■— THIRD PHASE JOINT</p> <p>— —  F<sub>1</sub> FOLD AXIAL PLANE</p> <p>— —  F<sub>2</sub> FOLD AXIAL PLANE</p> <p>— —  F<sub>3</sub> FOLD AXIAL PLANE</p>	<p>—&gt;— F<sub>1</sub> FOLD AXIS</p> <p>—&gt;— F<sub>2</sub> FOLD AXIS</p> <p>—&gt;— F<sub>3</sub> FOLD AXIS</p> <p>—□— HIGH ANGLE EXTENSION FAULT</p> <p>—■— LOW ANGLE EXTENSION FAULT</p> <p>—△— CONTRACTION FAULT</p> <p>—&lt;=&gt;— SHEAR ZONE (WITH SHEAR SENSE)</p>	<p>—◆— D<sub>1</sub> STRUCTURES</p> <p>—◇— D<sub>2</sub> STRUCTURES</p> <p>—◆— D<sub>3</sub> STRUCTURES</p> <p>—~— OBSERVED CONTACT</p> <p>—~— INFERRED CONTACT</p>
--	--	---



# LEGEND

-  COARSE WHITE CALCITIC MARBLE
-  ANHYDRITIC CALCITIC MARBLE
-  GRAPHITIC CALCITIC MARBLE
-  QUARTZ BEARING CALCITIC MARBLE (MINOR PYRITE)
-  CHERTY PELITES WITH CALC/DOLOMITE MARBLE
-  GREY BANDED DOLOMITIC MARBLE WITH CALCITE
-  INDURATED SILICEOUS PELITES WITH GRAPHITE
-  Pb Zn MINERALISATION
-  D1 DEFORMATION FOLD STRUCTURES ANTIFORM, SYNFORM
-  D2 DEFORMATION SLIDE STRUCTURES
-  D3 DEFORMATION FOLD STRUCTURES ANTIFORM, SYNFORM
-  LITHOLOGICAL BOUNDARY CERTAIN, INFERRED
-  600 METRE MINE HAULAGE LEVEL



FIGURE 6.16





-  D1 DEFORMATION STRUCTURES
-  D2 DEFORMATION STRUCTURES
-  D3 DEFORMATION STRUCTURES
-  ANTIFORM
-  SYNFORM
-  TECTONIC SLIDE
-  SHEAR FAULT

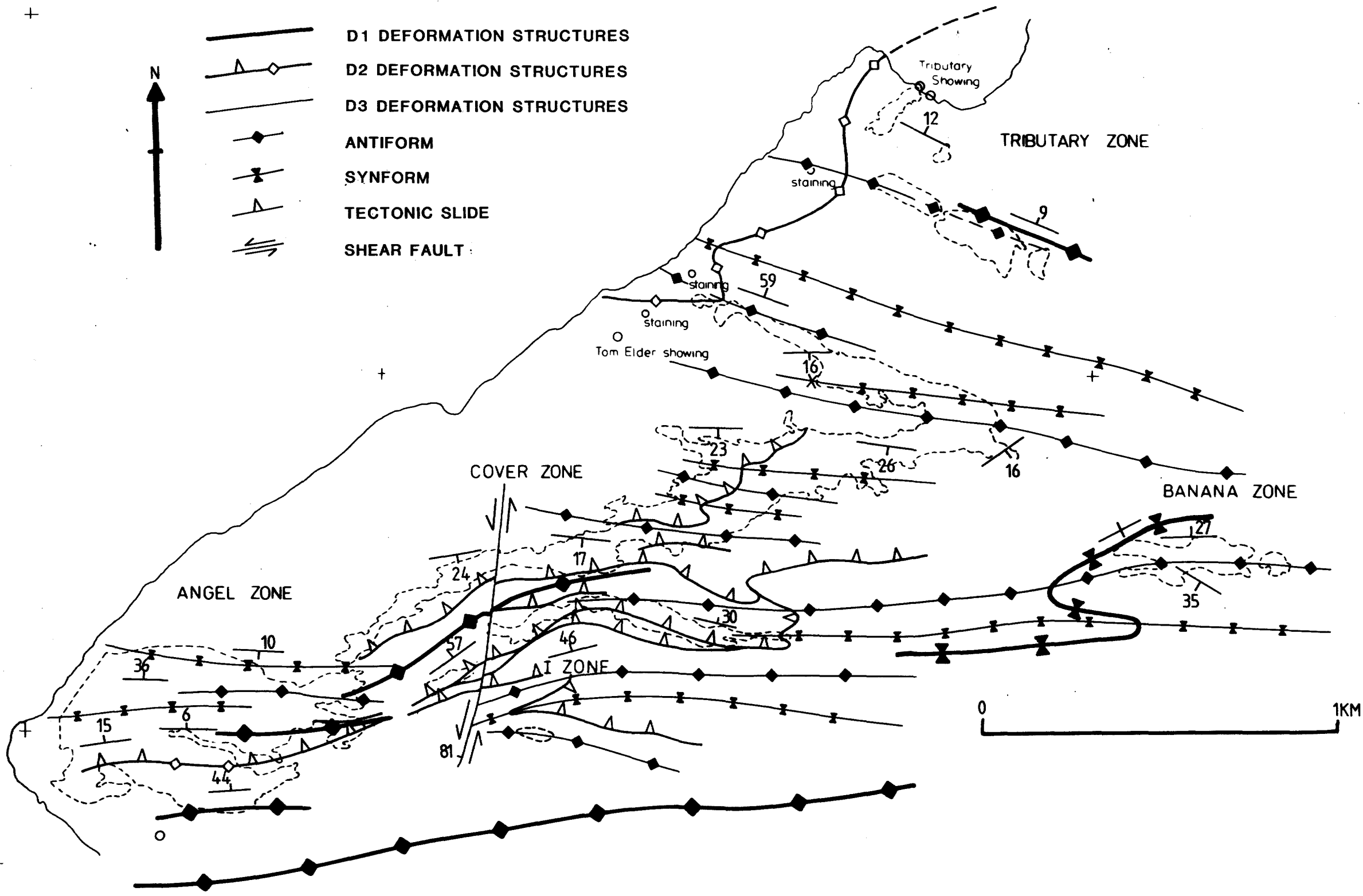


FIGURE 6-17a



GRID LINE A.

### LEGEND

-  D1 DEFORMATION STRUCTURES
  -  D2 DEFORMATION STRUCTURES
  -  D3 DEFORMATION STRUCTURES
- 
-  UNIT 6 Grey banded calcite-dolomite marbles
  -  UNIT 4 White anhydritic calcite marbles
  -  " Dark grey dolomite marbles
  -  " Siliceous pelite
  -  " Pelite banded marble
  -  Black Angel Mineralisation

SCALE



FIGURE 6.17b

# SECTION 550

(LEGEND AS FOR SECTION 400)

GRID LINE A

GRID LINE A

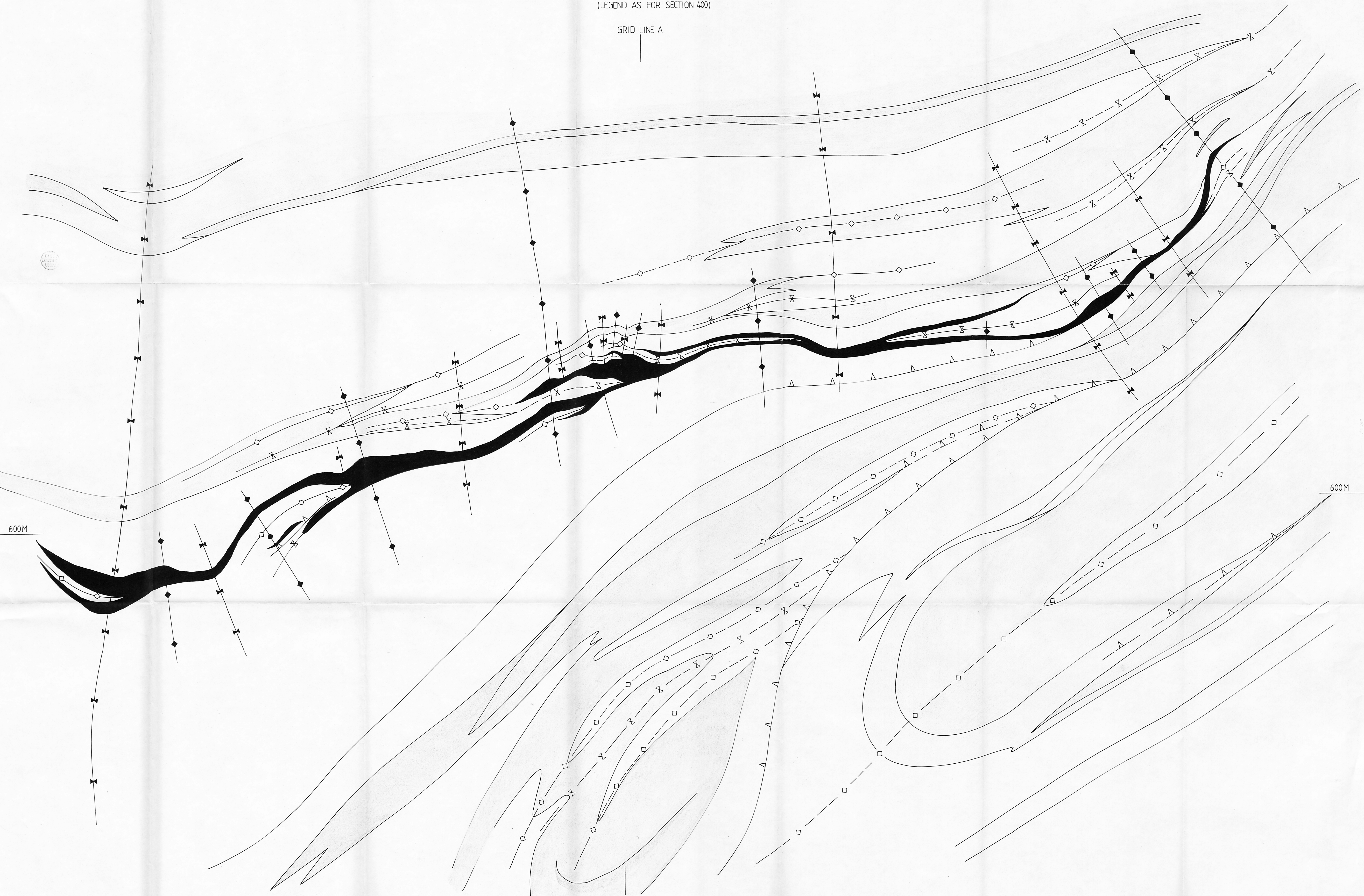


FIGURE 6-17c

# SECTION 900

(LEGEND AS FOR SECTION 400)

